

UNIVERSIDAD COMPLUTENSE DE MADRID

Facultad de Ciencias Físicas



TESIS DOCTORAL

Experimental studies of the astrophysical nuclear reaction ${}^3\text{He}(\alpha\gamma){}^7\text{Be}$.

**Estudios experimentales de la reacción nuclear con interés astrofísico
 ${}^3\text{He}(\alpha\gamma){}^7\text{Be}$**

MEMORIA PARA OPTAR AL GRADO DE DOCTOR

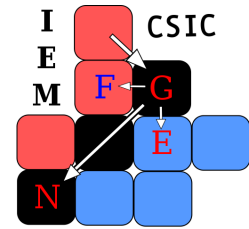
PRESENTADA POR

Mariano Carmona Gallardo

Directores

Olof Tengblad
B.S. Nara Singh

Madrid, 2014



Grupo de Física
Nuclear Experimental

Experimental Studies of the Astrophysical Nuclear Reaction ${}^3\text{He}(\alpha, \gamma){}^7\text{Be}$

Estudios Experimentales de la Reacción Nuclear con Interés Astrofísico ${}^3\text{He}(\alpha, \gamma){}^7\text{Be}$

Mariano Carmona Gallardo

MEMORIA PRESENTADA PARA LA OBTENCIÓN DEL
TÍTULO DE DOCTOR EN FÍSICA POR LA U.C.M.

MAY 2014

Directors:

Prof. Olof Tengblad
Instituto de Estructura de la Materia (CSIC)

Dr. B.S. Nara Singh
University of York

*"Physics isn't the most important thing. Love is."
Richard P. Feynman*

.....

A mis padres

CONTENTS

Contents	iii
List of figures	vii
List of tables	xi
Acknowledgements	xiii
Preface	xv
1 Introduction	1
1.1 Nuclear astrophysics: some relevant basic concepts	2
1.2 Nuclear Astrophysical Processes	6
1.3 The Sun and the Solar Neutrino Problem	8
1.4 Big-Bang Nucleosynthesis and the Primordial ${}^7\text{Li}$ problem	11
1.5 The ${}^3\text{He}(\alpha,\gamma){}^7\text{Be}$ Reaction: Experimental Previous Knowledge	16
1.6 Conclusion	19
2 Theoretical Formalism	21
2.1 Nuclear Reactions	22
2.2 Electromagnetic Transitions: Direct Radiative Capture Reactions	22
2.3 Radiative Capture Cross Section in a Potential Model	25
2.4 Phase-shifts Analysis: Elastic Scattering of ${}^3\text{He}$ and ${}^4\text{He}$ and its Relevance to $S_{34}(E)$ Data	27
2.5 Theoretical Descriptions of the ${}^3\text{He}(\alpha,\gamma){}^7\text{Be}$ Reaction	31
2.6 Conclusion	34
3 Experimental Techniques	35
3.1 The Reaction and the Methods for Cross Section Measurements	36
3.1.1 Energy range for the present work	39
3.1.2 Experimental methods: our choices	40
3.1.3 Facilities and setups for the present work	40
3.2 Activation Method @ CMAM	41
3.2.1 Experimental setup	42
3.2.2 Details of the measurements	45
3.2.2.1 Experimental energy determination	45

3.2.2.2	Observables	46
3.2.3	Setup for γ -activity measurements	49
3.2.4	Additional measurements	50
3.2.4.1	Energy calibration of the silicon detector	51
3.2.4.2	Radius of the collimator	52
3.2.4.3	Aperture angle of the collimator	52
3.2.4.4	Ni foil thickness	54
3.3	Direct Recoil Counting Method @ DRAGON	56
3.3.1	DRAGON setup	57
3.3.1.1	Gas target	58
3.3.1.2	γ -detector array	61
3.3.1.3	Electromagnetic separator	61
3.3.1.4	Double-Sided Silicon Strip Detector (DSSSD) at the focal plane	63
3.3.1.5	Electronic setup	64
3.3.1.6	Faraday cups	64
3.3.2	Details of the measurements	65
3.3.2.1	Beam purity	65
3.3.2.2	Tuning procedure for the separator	67
3.3.2.3	2011 measurements	68
3.3.2.4	2013 measurements	68
3.3.2.5	Data taking	70
3.3.2.6	Experimental determination of the beam energy	71
3.3.2.7	Observables	71
3.3.3	Additional measurements	73
3.3.3.1	DSSSD calibration	73
3.3.3.2	Beam suppression	74
3.3.3.3	Charge state distributions	76
3.3.3.4	Target density profile	79
3.4	Conclusion	86
4	GEANT Simulations of DRAGON	89
4.1	Introduction	90
4.2	Input Parameters for the Code	90
4.2.1	The gas target	90
4.2.2	The beam energy	93
4.2.3	The beam spot size and divergence	94
4.2.4	The reaction probability and reaction location	94
4.2.5	The S_1/S_0 branching ratio and the γ -rays angular distribution	96
4.2.6	The separator settings	98
4.3	First Simulations and Analysis	99
4.3.1	Tests on the DRAGON recoil energy selection procedure	102
4.4	Final Simulations using the Measured Tubes Displacements	104
4.4.1	The DSSSD and the BGO spectra: simulations and data	106
4.5	Simulations for Estimating Uncertainties in ϵ_{DRAGON}	110
4.5.1	Gas target density profile	110
4.5.2	Beam offset	114
4.5.3	Beam emittance	115
4.5.4	Beam energy	117
4.5.5	The branching ratio S_1/S_0	117
4.5.6	γ -rays angular distributions	119
4.6	ϵ_{DRAGON} Values and Uncertainties	121

5	Analysis and Results	123
5.1	Analysis I: Measurements using the Activation Method	124
5.1.1	The number of ^3He beam particles: $N^{\text{oB}}_{^3\text{He}}$	125
5.1.1.1	Error estimations	127
5.1.2	The ^4He gas target areal density: $N^{\text{oT}}_{^4\text{He}}$	127
5.1.3	The ^7Be recoils produced in the Activation Method: $Y_{^7\text{Be}}$	129
5.1.3.1	478 keV peak integration	130
5.1.3.2	Determination of the total number of ^7Be recoils produced	131
5.1.3.3	Error contributions	133
5.1.4	Estimation of the reaction energy at the centre of mass system	134
5.2	Astrophysical S-factors I: Measurements using the Activation Method	135
5.3	Analysis II: Measurements using the Direct Recoil Counting Method	136
5.3.1	Estimation of the reaction energy at the centre of mass system	137
5.3.2	The ^3He gas target areal density: $N^{\text{oT}}_{^3\text{He}}$	138
5.3.3	The number of ^4He beam particles: $N^{\text{oB}}_{^4\text{He}}$	138
5.3.4	The ^7Be recoils produced in the direct recoil counting method: $Y_{^7\text{Be}}$	145
5.3.4.1	Total counts in the focal plane DSSSD: Y_{DSSSD}	145
5.3.4.2	Experimental efficiencies: t_ℓ , ϵ_{DSSSD} and q_f	148
5.3.5	The ^7Be recoils produced in the activation method @ TRIUMF	149
5.4	Astrophysical S-factors II: Measurements using Direct Recoil Counting Method	151
5.5	Conclusion	152
6	Discussion and Future Work	153
6.1	Summary of the S-factor Results	154
6.2	Comparison with Previous Experimental Data and Discussion	155
6.3	Comparison with Theoretical Models and Discussion	156
6.4	S_1/S_0 Ratio and γ -rays Angular Distributions	159
6.5	Impact on Astrophysics	160
6.6	Future work	160
6.7	Conclusion	161
7	Conclusions	163
A	Appendix A: Silicon Detector and Electronic Modules	165
A.1	The Silicon Detector used in Activation Experiment	165
A.1.1	Electronic modules	166
B	Appendix B: Kinematics	169
B.1	From Laboratory to Centre of Mass System	169
B.2	Kinematics for Capture Reactions in the Laboratory System	171
B.3	From Kinetic Energy to Momentum	172
C	Appendix C: Errors	175
C.1	Systematic and Statistical Uncertainties	175
C.2	Statistical Treatment of Data	176
C.2.1	The Normal Distribution	176
C.3	The χ^2 Testing Method	177
C.4	Least-squares Fits and Errors	177
C.5	Error Propagation	178
C.6	Error in TRIUMF Experiment	178
C.6.1	Errors contributions to the number of ^3He target particles	179
C.6.2	Error contributions to the number of ^4He Beam Particles	179
C.6.3	Error contributions to the number of ^7Be recoils	179
C.6.4	Error contributions to the $S_{34}(\text{E})$ factor	181

D Apéndice D: Spanish Summary/ Resumen en Castellano	183
D.1 Estudios sobre la Reacción ${}^3\text{He}(\alpha,\gamma){}^7\text{Be}$: Motivación	183
D.1.1 La nucleosíntesis del Big-Bang y el problema del ${}^7\text{Li}$ primordial	183
D.1.2 El sol y el problema de los neutrinos solares	185
D.1.3 Estudios experimentales previos	186
D.1.4 Modelos teóricos	188
D.2 Técnicas Experimentales	189
D.2.1 Método de activación	190
D.2.2 Método de detección directa	192
D.3 Simulaciones del Separador DRAGON	193
D.3.1 Error sistemático de la transmisión	195
D.4 Análisis y Resultados	195
D.4.1 Método de activación	195
D.4.2 Método de detección directa	199
D.5 Discusión	202
D.5.1 Impacto en astrofísica	203
D.5.2 Conclusiones	203
E Appendix E: English Summary	205
E.1 Motivation	205
E.2 Experimental Techniques and Results	207
E.2.1 Measurements using the activation method	208
E.2.2 Measurements using the direct recoil counting method	210
E.3 Discussion and Conclusions	214
E.3.1 Impact on astrophysics	214
E.3.2 Conclusions	215
Bibliography	217

LIST OF FIGURES

1	Chart of Nuclei	xvi
1.1	Schematic diagram of a nuclear+Coulomb potentials	3
1.2	$\sigma(E)$ and $S(E)$ energy dependence	4
1.3	Gamow Peak for ${}^3\text{He}(\alpha,\gamma){}^7\text{Be}$ in the Sun	5
1.4	Astrophysical sites and nucleosynthesis processes	6
1.5	Solar nuclear reactions in the pp-chain and CNO cycle	8
1.6	${}^8\text{B}$ decay	9
1.7	Standard Solar Model neutrino spectrum	11
1.8	Big-Bang expansion timeline	12
1.9	Reaction network involved in the SBBN	13
1.10	Primordial abundances	14
1.11	Theoretical and observational likelihood for primordial elements.	15
1.12	${}^3\text{He}(\alpha,\gamma){}^7\text{Be}$ decay scheme	16
1.13	Previous astrophysical S-factors for the ${}^3\text{He}(\alpha,\gamma){}^7\text{Be}$ reaction	17
1.14	$S_{34}(0)$ values	18
1.15	$\sigma_{429}/\sigma_{g.s.}$ values	19
2.1	Electromagnetic transitions	23
2.2	Direct radiative capture reaction	24
2.3	Elastic scattering phase shifts from [TP63b]	29
2.4	Direct capture model calculation by P. Mohr	30
2.5	Electromagnetic transitions contributions to the ${}^3\text{He}(\alpha,\gamma){}^7\text{Be}$ reaction	31
2.6	Ab initio cross section calculations	33
2.7	Comparison between theoretical models	34
3.1	Reaction process	36
3.2	LUNA and ERNA setups	38
3.3	Previous information of the ${}^3\text{He}(\alpha,\gamma){}^7\text{Be}$ reaction	40
3.4	CMAM layout	41
3.5	Duoplasmatron ion source	42
3.6	Activation method sketch setup	43
3.7	Activation setup pictures	43
3.8	Electronic sketch	44
3.9	${}^3\text{He}$ straggling simulation	47

LIST OF FIGURES

3.10	⁷ Be straggling simulation	48
3.11	Beam photos from activation experiment	48
3.12	Sketch of the HPGe low background station at SOREQ	49
3.13	Pictures of the low background station at SOREQ	50
3.14	Background spectrum in the HpGe detector	50
3.15	Silicon detector calibration spectra	51
3.16	Spectra for ⁴ He elastic scattered on a C foil	53
3.17	Triple alpha spectrum without Ni foil	55
3.18	Triple alpha spectrum after crossing a Ni foil	55
3.19	TRIUMF layout	56
3.20	ISAC-I AND DRAGON	57
3.21	Schematic view of DRAGON	58
3.22	DRAGON windowless gas target layout	59
3.23	DRAGON windowless gas target picture	59
3.24	DRAGON gas control system	60
3.25	BGO detector array	61
3.26	γ -ray BGO spectrum for the ³ He(α,γ) ⁷ Be reaction @ 3.52 MeV	62
3.27	Double-sided silicon strip detector	63
3.28	Trigger electronic sketch for 2013 experiment	65
3.29	⁴ He Beam purities	66
3.30	⁴ He beam image taken with the CCD camera	67
3.31	DRAGON optics control system	68
3.32	DSSSD spectra for 5.2 and 3.5 MeV beam energies	69
3.33	DSSSD spectrum at E _{He^{beam}} = 4717(2) keV	69
3.34	DRAGON elements location	70
3.35	MD1 magnetic fields of ⁴ He ¹⁺ versus ³ He gas pressures	71
3.36	Collimated ion implanted silicon detector spectra for 5166 keV ⁴ He beam	72
3.37	DSSSD pulser linearity	73
3.38	DSSSD calibration	74
3.39	Beam suppression spectra	75
3.40	Charge state equilibrium with ¹⁶ O and ²⁴ Mg at DRAGON	76
3.41	Equilibrium charge state distributions for ¹⁶ O+ ² H	76
3.42	Charge state equilibrium for a ⁹ Be beam onto a ³ He target	78
3.43	Target density profile set up	79
3.44	Energy level diagram for the ¹² C+ ³ He reaction	80
3.45	¹² C beam purity spectrum	81
3.46	BGO spectrum for the ³ He(¹² C, ¹⁴ N γ)p reaction at the centre of the gas cell	81
3.47	Silicon spectrum at 30° for a ¹² C ion beam onto a ³ He gas target	82
3.48	Target density profile I	83
3.49	¹² C+ ³ He Breit-Wigner expression representation	84
3.50	Target density profile after energy corrections	84
3.51	Shielding effect in the BGO detector for TDP	85
3.52	Normalized final target density profile	86
4.1	DRAGON simulated geometrical areas	91
4.2	Target volumes and materials in GEANT	92
4.3	Target density profile step function	93
4.4	Simulated beam energy distribution	93
4.5	Simulated beam spot and divergence	95
4.6	GEANT 3 reaction probability	96
4.7	Theoretical fit to the S ₁ /S ₀ branching ratios	97
4.8	Stopping power for ⁷ Be recoils in ³ He gas	99
4.9	First simulation outputs	100
4.10	Simulated positions of the created recoils	101

4.11	DRAGON layout and components labels	101
4.12	Percentage of the recoils stopped throughout the separator	102
4.13	Simulation outputs using the mean energy for tuning	103
4.14	DRAGON tubes displacements	104
4.15	Output recoil angle distribution	105
4.16	Simulated stopped recoils in the DRAGON pumping tubes	105
4.17	Kinematics curves after tubes displacements	106
4.18	DSSSD simulation spectra versus data	107
4.19	DSSSD hit-maps: Simulation and data	107
4.20	Coincide BGO simulation spectra versus data	108
4.21	BGO spectra gates	108
4.22	BGO hit-maps for γ_0 -ray	109
4.23	BGO hit-maps for γ_1 -ray	109
4.24	Step target density profile function with 11.7 and 12.8 cm effective lengths	111
4.25	New steepness target density profile function	112
4.26	Stopped recoils for -1 mm beam offset	114
4.27	+0.5 mrad offset divergence in the x direction	116
4.28	Simulated BGO spectra with $S_1/S_0=1$	118
4.29	γ ray distributions from reference [TP63a]	120
5.1	Schematic of the experimental activation setup	124
5.2	Comparison of the beam particles using charge integration and scattered particles	125
5.3	Scattered beam spectra in the silicon detector	126
5.4	^3He beam particles	126
5.5	Pressure stability for the activation experiment	128
5.6	^7Be implanted γ spectra	130
5.7	γ count rate spectra	130
5.8	478 keV peak regions for integration	131
5.9	Energy loss TRIM simulation	134
5.10	Astrophysical S-factors using the activation technique	136
5.11	DRAGON setup and observables extraction	137
5.12	Gas pressure and temperature for one run in the direct recoil detection experiment	138
5.13	Trigger rates for the 30° silicon detector	139
5.14	Example for a FC1 reading	140
5.15	Si-30 and Si-57 spectra for optimum runs	141
5.16	30° silicon detector integration	141
5.17	Gas pressure and temperature for the direct recoil counting experiment	142
5.18	Normalisation R factors for the three energies measured in 2011	143
5.19	30° silicon detector spectrum for the 2013 measurements	144
5.20	Normalization factor for the 2013 measurement	145
5.21	DSSSD energy versus strips two dimensional spectra and energy projection I	146
5.22	DSSSD energy versus strips two dimensional spectra and energy projection II	147
5.23	DSSSD energy versus MPC-TAC histogram	147
5.24	2^+ charge state distribution interpolation	149
5.25	Activity spectrum for the activation measurement at TRIUMF	150
5.26	Recoil spot for activation method at TRIUMF	150
5.27	Astrophysical S-factors using the direct recoil counting technique	152
6.1	Astrophysical S-factor with total errors	155
6.2	Theoretical models and Madrid and TRIUMF results	156
6.3	Theoretical models normalised with the \mathcal{N} -factors	158
6.4	Modern data for the $^3\text{He}(\alpha,\gamma)^7\text{Be}$ reaction with normalised models	158
6.5	S_1/S_0 ratios	159

LIST OF FIGURES

A.1	Silicon Detector	166
B.1	Laboratory and centre of mass systems	170
C.1	Gaussian Distribution	177
C.2	Charge states values and error extrapolation	180
D.1	Cadena de reacciones SBBN	184
D.2	Probabilidades teóricas y observadas para la abundancia de elementos primordiales	184
D.3	Reacciones nucleares en el sol	185
D.4	Espectro de neutrinos solares según el SSM	186
D.5	Esquema de la reacción ${}^3\text{He}(\alpha,\gamma){}^7\text{Be}$	186
D.6	Datos previos sobre el factor $S_{34}(E)$	187
D.7	Comparativa de los valores $S_{34}(0)$	188
D.8	Comparación de modelos teóricos	189
D.9	Diagrama del montaje de activación	190
D.10	Diagrama del la instalación de bajo fondo en SOREQ	191
D.11	Diagrama del separador DRAGON	192
D.12	Perfil de densidad del blanco normalizada	193
D.13	Número de partículas en el haz	197
D.14	Estabilidad de la presión para el método de activación	197
D.15	Espectros de radiación γ en la estación de bajo fondo	198
D.16	Presión y temperatura en el experimento de detección directa	200
D.17	Histogramas en el DSSSD	201
D.18	Factores astrofísicos	202
E.1	Theoretical and observational likelihood for primordial elements.	206
E.2	Standard Solar Model Neutrino Spectrum	206
E.3	S-factors and theretical models for the ${}^3\text{He}(\alpha,\gamma){}^7\text{Be}$ reaction	207
E.4	${}^3\text{He}(\alpha,\gamma){}^7\text{Be}$ decay scheme	208
E.5	Activation method sketch setup	209
E.6	${}^7\text{Be}$ implanted γ spectra	209
E.7	Schematic view of DRAGON	211
E.8	Normalized final target density profile	211
E.9	DSSSD energy versus strips two dimensional spectra and energy projection	212
E.10	Astrophysical S-factors	213
E.11	Modern data for the ${}^3\text{He}(\alpha,\gamma){}^7\text{Be}$ reaction with normalised models	214

LIST OF TABLES

2.1	$S_{34}(0)$ values obtained from different models	33
3.1	Details for the ${}^3\text{He}(\alpha,\gamma){}^7\text{Be}$ reaction	36
3.2	Activation experiment details	45
3.3	α -sources energies	51
3.4	Calibration silicon detector values	52
3.5	Experimental energies for collimator angle determination	54
3.6	TRIUMF experiment details	65
3.7	Charge state distribution for a ${}^9\text{Be}$ beam onto a ${}^3\text{He}$ gas target	78
4.1	Beam emittance characteristics	94
4.2	S_1/S_0 branching ratios used in the simulations	97
4.3	Simulated tuning energies	98
4.4	Dragon transmission for the ${}^3\text{He}(\alpha,\gamma){}^7\text{Be}$ reaction	100
4.5	Simulated transmissions with different tuning energies	102
4.6	DRAGON transmissions with tube displacements	104
4.7	χ^2 values for BGO hit-maps	110
4.8	DRAGON transmissions for 11.75 cm effective length	111
4.9	DRAGON transmissions for 12.8 cm effective length	112
4.10	DRAGON transmissions for a new steepness profile I	113
4.11	DRAGON transmissions for a new steepness profile II	113
4.12	Errors in the transmissions due to the uncertainty in the target density profile	113
4.13	Transmissions including beam x displacements	114
4.14	Transmissions including beam y displacements	115
4.15	Errors in the transmissions due to the uncertainty in the beam offsets	115
4.16	Transmissions including changing in the beam transmissions	116
4.17	Errors in the transmissions due to the uncertainty in the beam emittance	117
4.18	Errors in the transmissions due to the uncertainty in the mean beam energy	117
4.19	Transmissions with different S_1/S_0 ratios	118
4.20	γ_1/γ_0 experimental and simulated values	119
4.21	DRAGON transmissions with Tombrello and Parker angular distributions	120
4.22	BGOs χ^2 values with Tombrello and Parker distributions	121
4.23	Final DRAGON transmissions and associated errors	121
4.24	Simulated parameters and associated systematic errors.	122

LIST OF TABLES

5.1	Error contribution to the number of beam particles using the scattered beam	127
5.2	Resonance in $^{10}\text{B}+\alpha$ at 1.518 MeV	128
5.3	Target density parameters values	129
5.4	Variables for determining the ^7Be recoils	133
5.5	Systematic error contribution to the number of ^7Be recoils	133
5.6	Results for activation measurements	135
5.7	Pressure, temperature and center of mass energy for the <i>direct counting experiment</i>	137
5.8	^7Be recoil energies and charge states	145
5.9	t_ℓ , ϵ_{DSSSD} , and q_f values	148
5.10	Created recoils energies dependent on the position of the reaction and emitted γ angle	149
5.11	Parameters for activation measurement at TRIUMF	151
5.12	Results for direct measurements	151
6.2	χ^2 values respect to other experiments	156
6.3	\mathcal{N} -factors for the different theoretical models	157
C.1	Systematic errors contributions to S_{34}	181
C.2	Statistical errors contributions to S_{34}	181
D.1	Valores de $S_{34}(0)$ obtenidos con diferente modelos teóricos	188
D.2	Transmisiones de DRAGON	194
D.3	Errores asociados a las transmisiones de DRAGON	195
D.4	Parametros simulados y error sistemático asociado	196
D.5	Resultados para el método de activación	199
D.6	Valores de los parámetros t_ℓ , ϵ_{DSSSD} , q_f y Y_{DSSSD}	200
D.7	Resultados para el método de detección directa	201
D.8	Valores χ^2 respecto a otros experimentos	202
E.1	Results for activation measurements	210
E.2	t_ℓ , ϵ_{DSSSD} , q_f , Y_{DSSSD} and ϵ_{DRAGON} values	212
E.3	Results for direct measurements	213
E.4	χ^2 values respect to other experiments	214

ACKNOWLEDGEMENTS

I think the first page of this thesis should be devoted to say thanks to all people who made this work possible.

First of all, I would like to thank both Olof and Nara Singh for giving me the opportunity of doing something I love. Thanks for all the support, fruitful discussions, wise counsel and, above all, for their patience. Special thanks are due to Olof for encouraging me all these years and giving me the opportunity for learning physics by participating in different kinds of experiments and to attend conferences and courses. I will never forget the first time when I saw Olof in the lab with thousands of cables around and I thought: "oh my god! this is crazy I will never understand anything here". Now, long time since then, thanks to him, I am proud of understanding much more about setting up nuclear physics experiments, electronics and many more things. Thanks, Nara Singh; from you I learnt a lot of physics, our discussions were always very useful for me and without your experience and my trips to York to work with you, this thesis could have never happened. From the beginning to the last moment you have always been an important support, in not only doing physics, but in general aspects such as nice conversations and going out.

Thanks are also due to María José, first of all for trusting me when I contacted her long ago and for supporting me to get my scholarship. Thanks to her tenacity and experience, I can now write and give presentations in a better way, even in Spanish. Thanks to her for giving me valuable advice, being patient with me and worrying about me.

I am also indebted to all the people from the DRAGON group, for teaching me a lot about astrophysics, reactions, separators and techniques. Thanks to Jennifer Fallis, Greg Christian, Lars Martin, Ulrike Hager, Sarah Reeve, Dave Hutcheon and specially to Barry Davids and to Chris Ruiz, for giving me all the help, support and passing me their experience. Thanks a lot to Alex Rojas, without him and his help the TRIUMF experiment could have not been possible, gracias. Thanks are also due to Michael Hass for the fruitful conversations at TRIUMF and to the CMAM crew: Ángel Muñoz, Arantza, Jaime, Antonio... the Madrid experiment was a success only because of your support.

And now, even most important is to say thanks to my colleagues and good FRIENDS who shared with me the most enjoyable discussions about physics, politics, sex or whatever, and who also suffered from my stress and bad mood from time to time. Thanks to Manoli, Miguel, Martín, Ricardo, Carlos, Jorge, Riccardo, Mario, Jan, Irene, Ángel, Ale, Kike, Andrés, Jose, Guille, Vicente and thanks to Briz, always a big friend and person who I started this adventure with. It was a pleasure for me to share this time with all of you and I will never be grateful enough to each of you.

Special thanks to Xan, for the continuous support and for so many things.

And of course, finally thanks to my family, which I am really proud of. To my parents and to my sisters, for understanding and encouraging me to do what I like, even though they were worried and suffering a little with my madness and each time I had to take a flight to cross the ocean. Without your support I could have never reached this. Thanks, thanks and thanks.

Thank you all, this thesis is not only mine, is yours as well.

Mariano.

"Physics is like sex. Sure, it may give some practical results, but that's not why we do it"

Richard P. Feynman

PREFACE

It has been long time, since the first theories of the composition of matter were postulated. The concept of atom was already introduced in the IV century B.C. by the Greek philosopher Democritus referring to the basic component of matter, which could not be divided into smaller pieces. This idea remained during the next 25 centuries, until the experimental works of Dalton, Avogadro and co-workers, that allowed elucidating the phenomenological laws governing the different kind of atoms and their combinations. New developments of experimental techniques played crucial roles in investigating the structure of small microscopic objects. One highlight in 1895, that astonished the world due to their applicability in various fields including crystal structures, was the discovery of X-rays by the German physicist Wilhelm Röntgen.

In 1896 the French scientist Henry Becquerel studied uranium compounds, which emitted radiation continuously without requiring any gas-discharge tube to be switched on. Becquerel found that any of the uranium or its compound emitted this kind of radiation. Further investigations in this field led to identify some other radioactive substances, such as thorium by the Polish scientist M. Curie in 1898. At this time, the British physicist J.J. Thomson, who was interested in why the X-rays made air conduct electricity, discovered that the so-called cathode rays were particles, which he called corpuscles. The name **electron** was given afterwards by the Irish physics George FitzGerald.

The New Zealand-born physicist E. Rutherford went to Britain to work with Thomson. He classified the radiation according to its penetrability: *alpha*-radiation gets easily absorbed by matter, *beta*-radiation is more penetrating and *gamma*-radiation can even pass through several centimetres of lead. With this knowledge, he used the radiation to probe the atom itself. In one of the most famous physics experiment by H. Geiger and E. Marsden carried out in 1909 under the supervision of Rutherford, alpha particles impinged onto a Gold foil and the angular distribution of the scattered particles was studied. The interpretation of the results lead Rutherford to suggest in 1911 that the atom is composed of a positively-charged atomic nucleus concentrated in a reduced volume at the centre of the atom leaving the electrons to orbit around it. This model discarded the plum-pudding atomic model of Thomson and meant the discovery of the **atomic nucleus** and a new research field, **Nuclear Physics**, was born.

A large number of experiments have been and still are devoted to study the atomic nucleus and its properties since 1911. The name **proton** was given by Rutherford to the lightest nucleus, hydrogen, as possible candidate for being one of the building blocks of nuclei, as these were emitted from nitrogen atoms when alpha particles collided with them. Later, in 1932, the English physicist J. Chadwick discovered the other type of particle present in atomic nuclei, the **neutron**, which have similar mass to the proton but no electric charge.

Today, the nuclei are still seen in the same way; a collection of protons and neutrons interacting between themselves by the strong, weak and electromagnetic forces. Since the Rutherford experiment there has been rapid progress in understanding of nuclear phenomena due to focused experimental efforts and the development of particles accelerators. Since the first linear accelerator build by Cockroft and Walton in 1930, first cyclotron by Lawrence in 1939 and first synchrotron in 1940, radiative

ions beam (RIB) production has become possible using highly sophisticated accelerators even allowing exploration of highly unbound nuclei.

With the recent artificial production of the element with $Z=117$ [OAB10], the periodic table, where all natural or artificial chemical elements are represented, completes all species between $Z=1$ and $Z=118$. For each of the chemical elements, characterised by its number of protons, nuclei with different number of neutrons, called isotopes, exist. All these isotopes are represented in the *Chart of nuclei*, where all known nuclei (around 3000) are classified according to their number of protons and number of neutrons. It is worth noting that ~ 3000 more are predicted to exist but not experimentally observed. Figure 1 shows a diagram of the *Chart of Nuclei* with neutron and proton numbers on x and y axes, respectively. Here the different colours indicate how the nuclei decay, see the caption for more details. A review about the evolution, properties and the information displayed in the chart is available, for example, in reference [NM10].

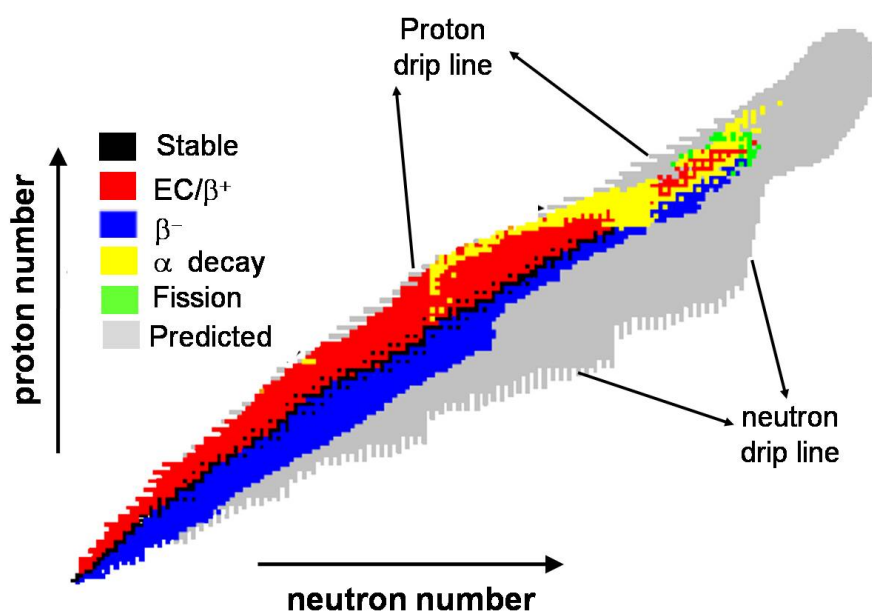


Figure 1: A diagram of the *Chart of Nuclei* with the horizontal and vertical axes showing the number of neutrons and protons, respectively. All the stable isotopes and those whose half life is higher than the Universe life time are shown in black. The β^+ /electron capture decaying nuclei (red), those decaying by β^- process (blue), the α particle emitters (yellow), and those decaying by spontaneous fission (green) are also shown. The theoretically predicted nuclei that are not experimentally produced so far are displayed in grey. The whole region is bounded by the proton and neutron drip lines, which indicate for each element (same atomic number Z) the minimum (proton drip line) and maximum (neutron drip line) numbers of neutrons that can form a bound nuclei.

The nuclear landscape is still an open play ground to understand the properties of all nuclei, how they form and how they interact. The nucleus contains 99% of the total mass of the ordinary matter therefore, information of nuclear properties and interactions is crucial in the understanding the synthesis of elements in the universe, i.e. the observable matter itself. Studying the atomic nucleus is much more rich and interesting due to its applicability in fields beyond fundamental science. Example of scientific fields where understanding of nucleus is directly applicable include medical imaging, hadron-therapy and nuclear energy.

The expert committee *Nuclear Physics European Collaboration Committee (NuPECC)* published in 2010 the *Long Range Plan: Perspectives of Nuclear Physics in Europe*. Among other issues, they review the recent achievements and current state of the art in Nuclear Physics and identify the open problems to be solved, which forms a broad part of motivation for our work. The documents is available at <http://www.nupecc.org/index.php?display=lrp2010/main>.

The work presented in this thesis has direct relevance to the *Nuclear Astrophysics*. However, direct implications on *Nuclear Structure and Dynamics* are also expected. Directly from the NuPECC Long Range Plan 2010, the key questions to be answered from nuclear astrophysics include:

- How and where are the elements made?
- Can we understand, and recreate on Earth, the critical reactions that drive the energy generation and the associated synthesis of new elements in Stars?
- How does the fate of a star depend on the nuclear reactions that control its evolution?
- What are the properties of dense matter in a compact star such as a neutron star or a hypothetical quark star?

The studies here presented aim to address part of the first question. Specifically, we study the production of the isotope ${}^7\text{Be}$ via the ${}^3\text{He}(\alpha, \gamma){}^7\text{Be}$ nuclear reaction. This reaction is important in two astrophysical scenarios. Firstly, it is relevant to the Big-Bang Nucleosynthesis, that is responsible for the abundance of the primordial ${}^7\text{Li}$ element in the universe. Secondly, it plays an important role in the helium burning stage in the stars. Specifically, this reaction is important in order to explain the high energy neutrino flux from the Sun.

This thesis is divided into seven main chapters. In the first chapter, general concepts used in nuclear astrophysics will be discussed. Different astrophysical processes responsible of creating the nuclei will also be briefly explained and those where our reaction plays a determining role will be detailed. In addition, previous experimental knowledge of this reaction will be explained. In the second chapter, the theoretical formalisms used to describe the underlying physics are discussed. In the third chapter, the two experimental techniques used to determine the capture cross sections will be described in detail. In the fourth chapter, the simulations performed in order to determine the acceptance of DRAGON will be presented. The fifth chapter gives the analysis techniques used to extract different experimental observables that lead to the results. In the sixth chapter, discussions about the experimental results comparing with other experiments and theories as well as future work will be presented. Finally, in the seventh chapter, the main outcomes of this research are listed.

Writing, I have tried that whoever physicist reading this thesis can understand both the physics case and the procedure, results and discussion. For this reason I have added three appendix at the end. In the first appendix, (A), how a silicon detector (kind of detector used in our experiments) works is explained. Also the electronic used is explained as an example of typical nuclear physics modules used to process electric signals. In appendix B, the centre of mass reference system, commonly used when describing nuclear reaction and therefore throughout this thesis, is explained. Moreover, the kinematics of the reaction is detailed for reference. Finally, in appendix C, general concepts related to error estimation are briefly recalled and how the errors are estimated for one of the experiments is detailed. Appendixes D and E are Spanish and English summaries, respectively.

"Learn from yesterday, live for today, hope for tomorrow. The important thing is to not stop questioning."

Albert Einstein

CHAPTER 1

INTRODUCTION

Abstract: *In this chapter some of the essential nuclear astrophysics concepts are introduced in order to understand the capture reaction studied in this thesis. Concepts such as the astrophysical S-Factor and the Gamow Peak will be discussed. In continuation, the nuclear astrophysical processes responsible for producing different nuclear isotopes and the astrophysical sites where they originate will briefly be presented. The two distinct scenarios where the ${}^3\text{He}(\alpha,\gamma){}^7\text{Be}$ reaction plays an important role, namely "The solar neutrino flux" and "The primordial ${}^7\text{Li}$ production" will be briefly introduced. Finally, previous experimental studies will be discussed.*

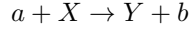
Since the beginning of time the Human Being has wondered, What are we? Where do we come from?, or What is the origin of the Universe?. Answering these metaphysical questions have been an ongoing quest not only from a philosophical or religious point of view but also from a scientific scenario. It is questions such as What is the origin of the elements? that nuclear physics research specifically addresses.

The current composition of the Universe is the result of the nucleosynthesis proceed from the initial material, namely H and ${}^4\text{He}$ nuclei created a few minutes after the Big-Bang, [Hoy46, Hoy54]. Nuclear reactions, together with other processes such as β decay are the mechanisms responsible of this synthesis, and they need to be understood in order to explain the evolution, structure and composition of the past, present and future Universe.

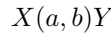
Specifically, this thesis focuses on studying the synthesis of ${}^7\text{Be}$ through the nuclear reaction ${}^3\text{He}(\alpha,\gamma){}^7\text{Be}$. The cross section of this reaction is required by the *Solar Standard Model (SSM)* that explains the evolution, behaviour and composition of the Sun. It is also an important input parameter for theoretical calculations explaining the cosmological origin of light elements in the early Universe due to the *Big-Bang Nucleosynthesis (BBN)*.

1.1 Nuclear astrophysics: some relevant basic concepts

In stars (or in astrophysical scenarios such as the Big-Bang) energy is released via the fusion of two atomic nuclei, i.e. through nuclear reactions. Nuclear reactions are usually denoted as:



where a is the projectile, X is the target, Y is the recoiling nucleus and b the ejectile of the reaction. Normally, a and b are light nuclei but occasionally they can be γ rays, which cases the reactions are called *nuclear photoeffect* and *radiative capture*, respectively. When the nuclear reactions are carried out in laboratories, a is usually accelerated as a beam and X is a stationary target. In the case of direct kinematics the projectile is lighter than the target while reactions in inverse kinematics are carried with beams heavier than targets. The nuclear reactions are also denoted in a compact way as:



This convention will be used in the following section, specifically to discuss (p, γ) or (α, n) astrophysical reactions involving the same type of one interacting nucleus and one reaction product. It should be pointed out that following the nuclear astrophysics convention of (α, γ) reactions, our reaction of interest will be denoted as ${}^3\text{He}(\alpha, \gamma){}^7\text{Be}$ independently that the beam is ${}^3\text{He}$ or ${}^4\text{He}$ (α).

The available energy in the above reactions, by the fact of converting some nuclear masses in others ($E = mc^2$), is known as the *Q-value* of the reaction and it is defined as:

$$Q = (m_a + m_X - m_b - m_Y) c^2 \quad (1.1)$$

If $Q < 0$, then the reaction is endothermic and only proceed upon providing an extra energy. If $Q > 0$ the reaction is exothermic and, in principle it could occur even at zero energy. In reality, exothermic reaction may not proceed at zero energy due to the existence of Coulomb and centrifugal barriers as well as the competing reaction channels (barriers and competing channels are also present in endothermic reactions). Therefore, there is a probability $\sigma(E)$ for the reaction to occur (the **cross section**) which is defined by:

$$\sigma(E) = \frac{N_R/t}{(N_X/A)(N_a/t)} \quad (1.2)$$

where N_R/t is the number of reactions per unit of time, N_X/A is the number of target nuclei per unit area and N_a/t is the number of incident beam particles per unit of time.

For charged particle induced reactions^a, apart from the nuclear force, the electrostatic repulsive force plays a determining role. The Coulomb barrier energy between interacting nuclei, E_C , is given by:

$$E_C = \frac{Z_a Z_X e^2}{R_n} \quad (1.3)$$

here Z_a and Z_X are the atomic number of the interacting nuclei, R_n is the square well radius, and e is the electron charge. Classically, if we consider no centrifugal barriers ($\ell=0$) and assuming the target at rest, the beam energy should be higher than E_c to overcome the Coulomb barrier and proceed to the reaction. The potential seen by a projectile when approaches a nucleus assuming no centrifugal barriers is shown in Figure 1.1. The reaction will take place if the projectile overcomes the Coulomb barrier and drop into the well potential.

^aAlso neutron induced reactions are relevant in nuclear astrophysics but they will not be discussed here

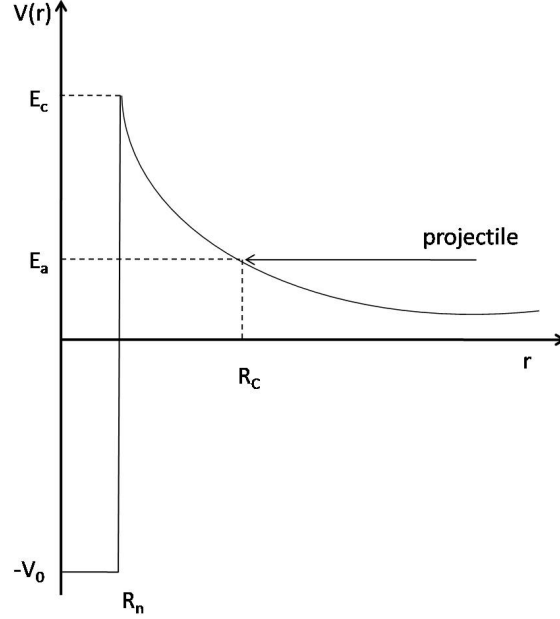


Figure 1.1: A schematic diagram of the potential seen by a projectile with incoming energy E_a in a nuclear reaction considering no centrifugal barriers ($\ell=0$, s -wave). The total potential is given by an attractive potential well for $r < R_n$. For $r > R_n$ it is given by the Coulomb potential. R_c is the radius at which the incident energy is equal to the Coulomb potential energy, $E_a = Z_a Z_X e^2 / R_c$.

Nevertheless, despite the fact that the energy is lower than the height of the well, quantum mechanics predicts a probability for penetrating the barrier by *tunnel effect*, or a reaction probability. The transmission coefficient, giving the probability for penetrating the Coulomb barrier for an s -wave (which is a likely scenario at astrophysical energies) can be given by [Ili07]:

$$P_{\ell=0} \approx \exp \left(-\frac{2}{\hbar} \sqrt{\frac{2m}{E}} Z_0 Z_1 e^2 \left[\frac{\pi}{2} - 2\sqrt{\frac{E}{E_C}} + \frac{1}{3} \left(\frac{E}{E_C} \right)^{3/2} \right] \right) \quad (1.4)$$

where E is the energy in the **centre of mass system** or relative energy. For the astrophysical energies of interest, which are well-below the Coulomb barrier, i.e. $E \ll E_C$, the $P_{\ell=0}$, (in the following P_0) can be approximated to:

$$P_0 \simeq \exp \left(-\frac{2\pi}{\hbar} \sqrt{\frac{m}{2E}} Z_0 Z_1 e^2 \right) \equiv e^{-2\pi\eta(E)} \quad (1.5)$$

known as **Gamow factor**. The Sommerfeld parameter, η , can be given by

$$\eta(E) = \frac{2\pi Z_a Z_X e^2}{h v} \quad (1.6)$$

where v is the relative velocity of the interacting nuclei and h is the Plank constant. Numerically, $2\pi\eta = 0.989534 Z_a Z_X \sqrt{\frac{1}{E} \frac{M_a M_X}{M_a + M_X}}$.

On the other hand, the cross section is also proportional to a geometrical factor^b $\pi/k^2 \propto 1/E$, being k the wave-number. Therefore, the reaction cross section, $\sigma(E)$, can be written as the product of three factors:

$$\sigma(E) = \frac{1}{E} S(E) e^{-2\pi\eta(E)} \quad (1.7)$$

^bIt can be proved that the total cross section for all reaction channels different from the elastic scattering is given by: $\sigma_\ell = \frac{\pi}{k^2} (2\ell + 1) (1 - |e^{2i\delta_\ell}|^2)$ [Ili07]

where the factor $S(E)$, is the **astrophysical S-factor** and E is the centre of mass energy. It is worth pointing out, that the S -factor contains all the information related to nuclear properties (effects of finite nuclear size, higher partial waves, anti-symmetrisation etc...). Moreover, the high and well-known energy dependence of the reaction cross section due to the Coulomb interaction is avoided in the astrophysical factor, $S(E)$, and this allows easier extrapolations of this factor to low energies. The situation is demonstrated in Figure 1.2 using the ${}^3\text{He}(\alpha,\gamma){}^7\text{Be}$ reaction. While the dependence of σ with E is doubly exponential, with the S -factor is nearly linear.

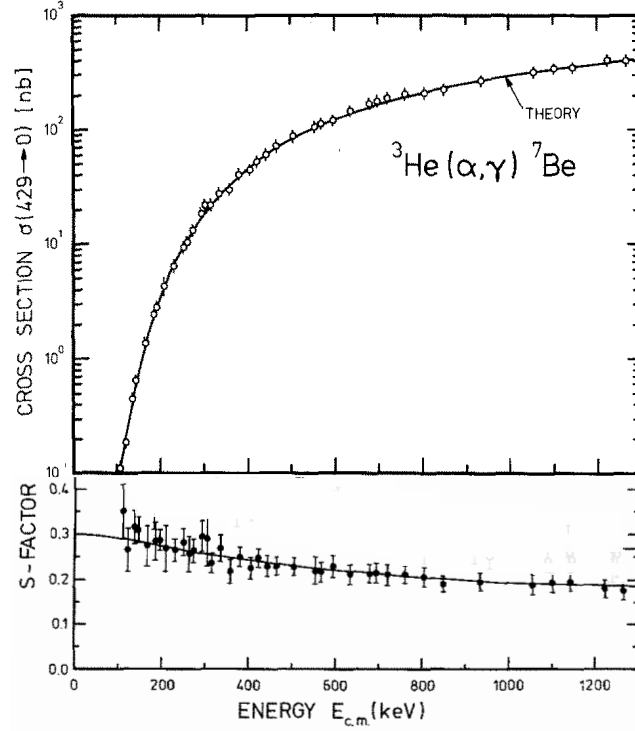


Figure 1.2: Energy dependence of the cross section and the S -factor for the ${}^3\text{He}(\alpha,\gamma){}^7\text{Be}$ reaction. While the cross section, in the upper panel, shows a doubly exponential dependence with energy, the S -factor in the lower panel, shows a smooth weak energy dependence. Figures are taken and adapted from [KBB82].

It should be also pointed out that the Gamow factor is an approximation of the s -wave Coulomb barrier penetration probability. However, even when there is a contribution from the other partial waves (p -waves, d -waves...), the expression 1.7 results also in a reduced energy dependence for the S -factor.

The **reaction rate** in astrophysical environments between the two interacting nuclei, a and X , (see expression 1.2) can now be rewritten as:

$$r_{aX} = N'_a N'_X v \sigma(v) \quad (1.8)$$

where $r_{aX} = N_R/(Vt)$ is the number of reactions per unit of volume and time, and $N'_a = N_a/V$, and $N'_X = N_X/V$ are the number of interacting nuclei per unit of volume. In the astrophysical environments as stellar plasmas, there is a relative velocity distribution for the interacting nuclei, $P(v)$. This kinetic energy distribution results from the thermal motion of the nuclei, hence the reactions are referred as *thermonuclear reactions*. The probability of finding a nucleus with a velocity $v+dv$ is given by $P(v)dv$ and the expression 1.8 is converted into:

$$r_{aX} = N'_a N'_X \int_0^{\infty} v P(v) \sigma(v) dv \equiv N'_a N'_X \langle v \sigma(v) \rangle. \quad (1.9)$$

Under the conditions of hydrostatic equilibrium of stellar plasmas, the velocities of the motion of the interacting nuclei are non-relativistic and the nuclei gas is non-degenerate. The relative velocity distribution of the interacting nuclei is given in most cases by a Maxwell-Boltzmann distribution:

$$P(v) = 4\pi v^2 \left(\frac{\mu}{2\pi k_B T} \right)^{3/2} e^{-\frac{\mu v^2}{2k_B T}} \quad (1.10)$$

here k_B is the Boltzmann constant, $\mu = m_a m_X / (m_a + m_X)$ is the reduced mass, T is the temperature and v the relative velocity. From expressions 1.7, 1.9 and 1.10 we now obtain

$$\langle \sigma v \rangle = \left(\frac{8}{\pi \mu} \right)^{1/2} \left(\frac{1}{k_B T} \right)^{3/2} \int_0^\infty S(E) e^{-\frac{E}{k_B T}} e^{-2\pi\eta} dE. \quad (1.11)$$

The highest energy dependence of the rate in the 1.11 integral is in the two exponential terms. The first one, related to the Maxwell-Boltzmann distribution of the nuclei energies (which have a maximum at $\frac{1}{2}k_B T$) goes to zero at high energies, and the second one related to the tunnelling probability through the barrier which goes to zero for low energies. Therefore, the energy at which the reaction probability is maximum can be obtained by convoluting the two functions. The resulting function is known as **Gamow Peak** and the energy at which the reaction rate maximises is known as the **Gamow Energy**.

The Gamow Peak for the ${}^3\text{He}(\alpha, \gamma){}^7\text{Be}$ reaction in the Sun is shown in Figure 1.3. The green curve shows the Maxwell Boltzmann distribution factor, $e^{-\frac{E}{k_B T}}$, for $T_{\text{sun}} \sim 1.55 \cdot 10^7$ K. The energy which maximise the probability for this reaction is $\frac{1}{2}k_B T \simeq 0.65 \text{ keV}$ and the probability drops for energies higher than this one. The red line shows the tunnel effect probability $e^{-2\pi\eta}$ (recall that this has been taken for s -waves and $E \ll E_C$ approximations) indicating that the higher the energy is the more likely to cross the barrier. The blue line shows the convolution of both curves, whose maximum of $\sim 22 \text{ keV}$ is the Gamow Energy for ${}^3\text{He}+{}^4\text{He}$ capture reaction.

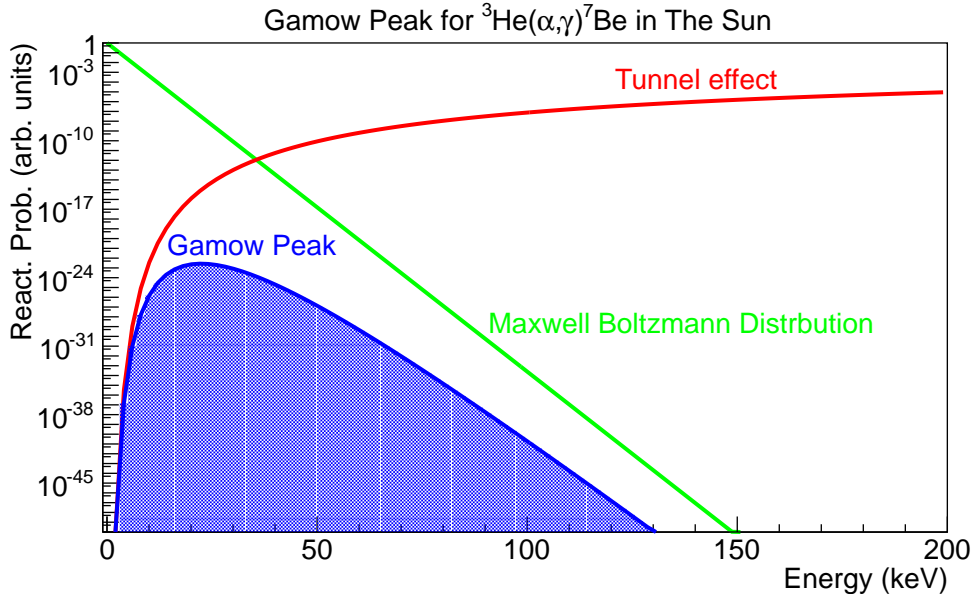


Figure 1.3: The Gamow Peak for the ${}^3\text{He}(\alpha, \gamma){}^7\text{Be}$ reaction in the Sun. The red line shows the probability of crossing the Coulomb barrier given by $e^{-2\pi\eta}$. The green line shows the Maxwell Boltzmann energy distribution of nuclei with temperature $T_{\text{sun}} \sim 1.55 \cdot 10^7$ K and the blue line shows the convoluted function resulting with the Gamow Peak. The maximum in the Gamow Peak is known as Gamow Energy, which in this case is $\sim 22 \text{ keV}$.

For a constant value of $S(E)$ respect to E , the Gamow Energy can be estimated by equalling the first derivative of the integrand with respect to E to zero. This calculation results in:

$$E_{\text{Gamow Energy}} = \left[\left(\frac{\pi}{\hbar} \right)^2 (Z_0 Z_1 e^2)^2 \left(\frac{\mu}{2} \right) (k_B T)^2 \right]^{1/3} \quad (1.12)$$

1.2 Nuclear Astrophysical Processes

Although in general it can be claimed that the Universe is rather static with little global activity, it is worth noting that there are some very active local scenarios, as stars or supernovae explosions, where nearly all existing nuclei are continuously being produced. And these are, indeed, the elements which will create new different astrophysical sites, as future galaxies or planets. Thinking for example of Earth, a lot of nuclear processes occurred in different time periods before producing such a big quantity of elements present in it. And not only different periods, but also different scenarios under different conditions were needed to explain the production of all the elements from the primordial H and ^4He that were created following the Big-Bang explosion.

Figure 1.4, adopted from [SR01], shows a part of the chart of nuclei. Here, nuclei, the processes by which they are usually produced and the corresponding astrophysical sites where they occur are colour coded (see caption for more details).

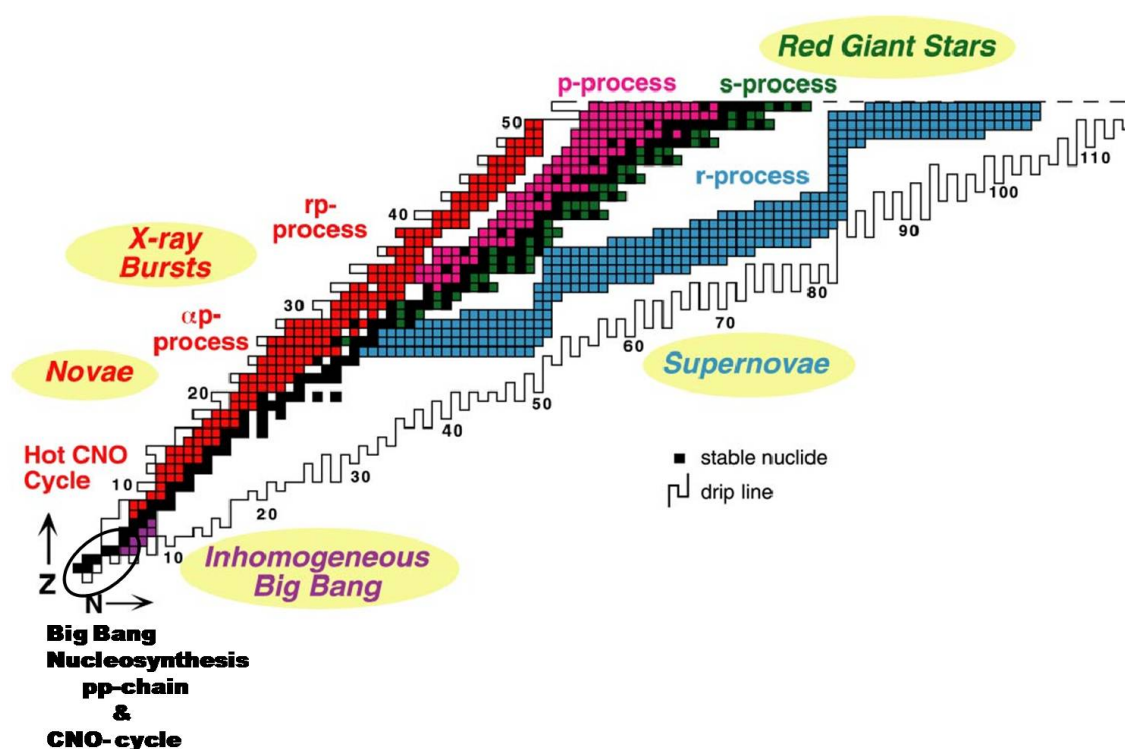


Figure 1.4: A diagram adapted from reference [SR01] where the nuclei produced in the same process are plotted with the same colour. The astrophysical scenarios in which the nuclei are created are also indicated with the same colour inside circles. The black circle, enclosing the nuclei produced in the Big-Bang Nucleosynthesis, pp-chain and CNO-cycle has been added to the original plot in order to show the names of processes creating the very light nuclei.

The primordial nucleosynthesis was the origin of the synthesis of light nuclei up to mass $A=7$. The main remaining nucleus is H , but also $^3,^4\text{He}$, D and small quantities of $^6,^7\text{Li}$. All other higher masses nuclei were created in negligible quantities. Later, stars are formed via gravitational attraction

and the hydrogen burning starts when the temperature inside rises up to $T \sim (10 - 15) \cdot 10^6 K$. In light stars, with masses smaller than eight solar masses, the pp-chain, triple- α reaction and CNO cycle are the main mechanisms fusing nuclei with masses no higher than ^{20}Ne . These processes (excluding the triple- α) together with the BBN, where our reaction plays a determining role, will be detailed in the next sections. The triple α -process, which also produce light nuclei, will be briefly described below.

The other processes shown in Figure 1.4 occur in higher-mass stars and stellar explosions. These processes are required to explain e.g. the abundance of high-mass elements in the Solar System. In the following a brief description of some of the processes is presented together with the triple- α process. For more details see for example [Rol88]:

triple- α

In light stars with a high quantity of α particles originated from the Big Bang, there is a small probability of trapping two α particles in the low-lying resonances in ^8Be . This small probability is large enough to allow for a third α particle to collide with the resonance producing a triple- α composite. This composite is an excited state in ^{12}C , which can either decay back to three α particles, or by γ emission to lower energy states in ^{12}C . The key point of this process is that there is a narrow 0^+ resonance in the $^8\text{Be} + \alpha = ^{12}\text{C}^*$ system at 287 keV above the 3α breakup threshold. This resonant state, known as the *Hoyle state*, is essential in order to explain the relative high abundance of ^{12}C in the Universe)

α -burning

After the pp-chain, CNO-cycle or triple- α process some residual nuclei, mainly oxygen and carbon, exist. In high-mass stars, the gravitational pressure is high enough to increase the temperature allowing the α particles to overcome the Coulomb barrier with the residual nuclei. Thus, a series of α -capture reactions can occur producing higher mass nuclei up to ^{56}Fe .

s-process

In Red Giants, some extra neutrons can be produced in (α, n) reactions during the α -burning. These neutrons will react, for example, with the iron seed nuclei produced in the α -burning stages via (n, γ) reactions. These reactions will be followed through the stable iron isotopes line until some unstable isotope is reached, then, because the (n, γ) is a much slower process (therefore is called s(slow)-process) than the β decay, the nucleus, will β -decay to the ($Z+1, N-1$) daughter nucleus. This nucleus can go through the (n, γ) process until another β^- unstable nucleus is produced and thus the nucleosynthesis proceeds. With this process, nuclei as heavy as uranium can be produced.

r-process

Although by the previous processes nearly all stable elements are produced, the abundances seen for example in the Solar System cannot be explained and additional processes and scenarios are needed. One of these scenarios are the Supernova explosions. In a Supernova explosion, the high temperatures and high neutron abundances allow for the (n, γ) reactions to reach more unstable isotopes as the reaction times are faster (rapid-process) than the β decay times. The (n, γ) reactions end either when the neutron drip line is reached (unbound nuclei) after which β -decays will follow until reaching a stable nuclei with the same mass or, where the closed-shell nuclei at $N=82, 126$ and 184 are found. In the latter case, the process times are comparable to β decay times. These nuclei are known as *waiting points*.

rp-process

The rp-process mainly occurs in binary systems involving neutron stars. In such binary system, hydrogen is exchanged between the two stars. As a result X-rays are produced with high flux, and thus these systems are known as *X-Ray bursters*. An increase in temperature leads to a series of (p, γ) reactions usually hindered by Coulomb barriers. The (p, γ) reactions will follow until either the proton drip line is reached, or the β decay times are fast enough to compete against the proton capture rate. After β -decays, (p, γ) reactions continue up to nuclei with $A \sim 100$ where the higher Coulomb barriers hinder the reaction.

p-process

In order to explain some neutron deficient nucleus abundances, processes other than those described above are needed. The p-process is thought to happen in the core collapse supernova explosion. A shock wave passing through the material initiate a sequence of (γ, n), (γ, p) and (γ, α) reactions on stable seed nuclei producing p-rich nuclei.

1.3 The Sun and the Solar Neutrino Problem

Pauli postulated in 1931 a new particle in order to justify the energy and momentum conservation in the β decay process, that afterwards was named as *neutrino- ν* (small neutral particle) by Fermi. Since then, due to the particle was postulated by the Standard Model as a massless neutral particle interacting weakly with matter, a lot of complex experiments have been carried out in order to directly detect this particle and study its properties.

As the Sun is the nearest star to us, it is the best studied. In the context of neutrino physics it is invaluable as for e.g. the Sun produce neutrinos acting as a factory. The *Solar Standard Model* (SSM) treats the processes happening in the Sun and models the astrophysical environments to predict neutrino fluxes.

Among all nuclear processes in the Sun, about 99% of energy is produced via a series of reactions, the so called *pp-chain*, whose overall effect is to convert four protons into one ^4He nucleus. The remaining 1% is created through the CNO cycle (Carbon-Nitrogen-Oxygen). The ^{12}C seed for the CNO cycle is produced by means of the triple- α process. Both the *pp-chain* and the CNO cycle are shown in Figure 1.5, where the originated neutrinos can be observed in bold. It must be pointed out that among the three different neutrino flavours, those produced in the *pp-chain* are electron neutrinos (ν_e).

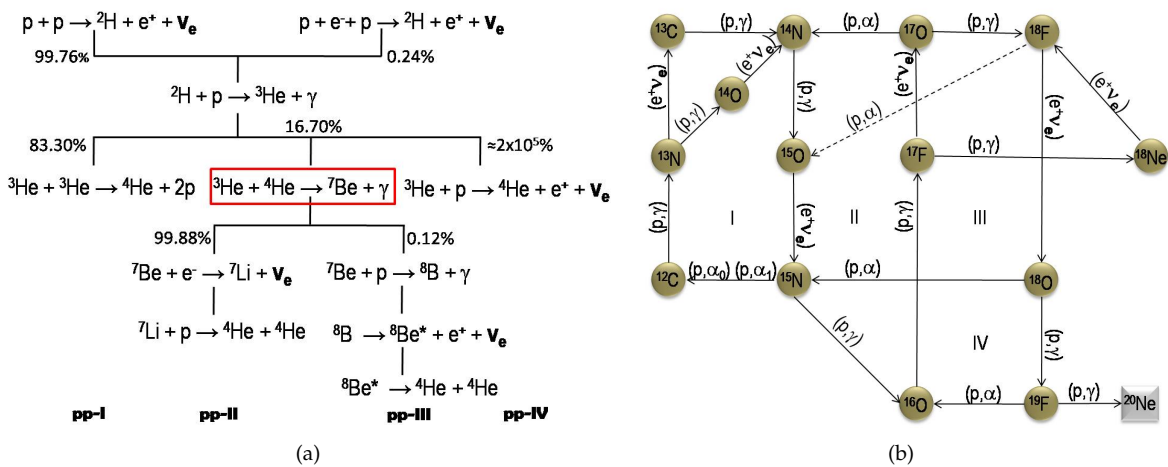


Figure 1.5: (a) The four reaction sub-chains in the *pp-chain* with branching percentages indicated. (b) The CNO cycle divided into the four CNO sub-cycles. The sub-cycle marked as I produces the most of the energy and significant solar neutrino flux among the CNO cycle.

From an experimental point of view the historical motivation for the detection of solar neutrinos was related to determine the possible neutrino mass and the likely oscillations between the three neutrino flavours. Furthermore, the detection of solar neutrinos is vital in probing the astrophysical conditions and verifying the hypothesis that the thermonuclear reactions are the solar energy source. Nowadays, the detection of solar neutrino fluxes is still ongoing with ever increasing accuracy and improved experimental techniques utilising complex set ups. A corroboration between these experimentally measured neutrino fluxes with the SSM estimations addresses several important questions in physics. The SSM estimations need the following inputs parameters (see for example [BHL82]):

- *pp-chain* and CNO cycle reactions **cross sections** (Figure 1.5)
- Solar constant
- Abundances for solar elements heavier than helium
- Opacities
- Equation of state
- Solar Age

The first set of solar neutrino experiments measured neutrino fluxes that are much lower than the value predicted by the SSM. This is the so-called *Solar Neutrino Problem*. Two different solutions were put forward, namely, either the experimental measurements were correct and thus the theory should be changed, or the neutrinos changed their characteristic, or decay, while they travel from the Sun to the Earth. This latter solution was based on the instability of neutrinos initially studied by Reines and collaborators [RSP80]

The initial experimental investigations aimed to detect the high energy solar neutrinos coming from the β^+ decay of ${}^8\text{B}$. The ${}^8\text{B}$ is created in the pp -chain from the reaction ${}^7\text{Be}(p,\gamma){}^8\text{B}$ and decays afterwards via the β^+ decay to ${}^8\text{Be}$ which breaks into two alpha particles. The solar model calculations in the sixties [BFI63, Sea64, PR64, Bah64b, Bah66, BCD67, BBS68] already established that the Sun emits a high solar neutrino flux from the ${}^8\text{B}$ decay as shown in Figure 1.6.

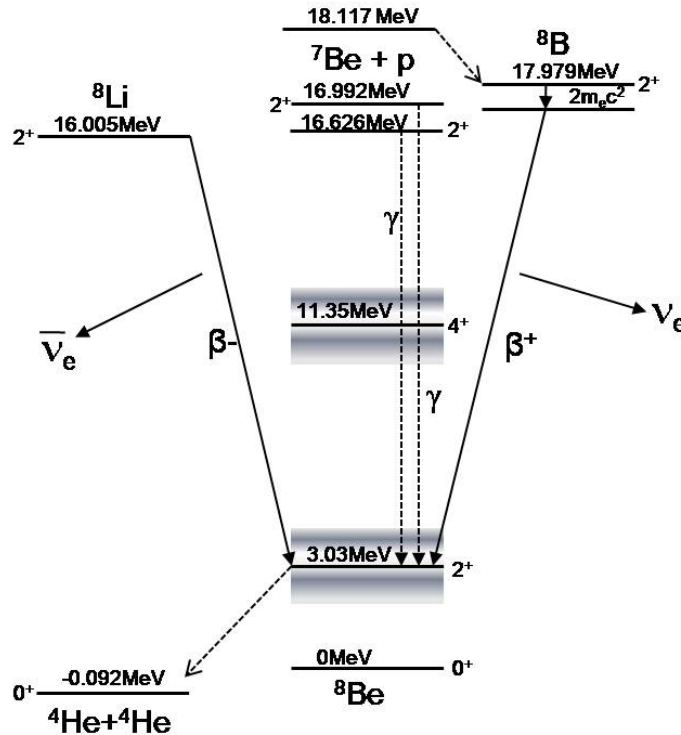


Figure 1.6: ${}^8\text{B}$ decay. This decay is the origin of the high energy neutrino flux in the Sun.

This decay emits the second highest energy neutrino among the solar neutrinos produced during the pp -chain. From an experimental point of view the detection of this neutrinos allows to select a high energy detection threshold avoiding thus the contamination produced by the cosmic radiation which plays an important role when detecting weak interacting particles like neutrinos.

In an attempt to detect the solar neutrinos from the ${}^8\text{B}$ decay, and based on the suggestions by John N. Bahcall that these high energy neutrino can be captured via the ${}^{37}\text{Cl}(\nu, e^-){}^{37}\text{Ar}$ reaction [Bah64a], Raymond Davids and collaborators devised an experiment. They used a big tank of C_2Cl_4 as target, the ${}^{37}\text{Ar}$ was extracted from the tank using a circulating ${}^4\text{He}$ gas system, which was guided to a proportional counter for observing their β^+ decay and thus estimate the solar neutrino flux. The setup was placed 4400 m underground in order to reduce the cosmic ray background due to muons, which can produce protons that subsequently could produce ${}^{37}\text{Ar}$ via the ${}^{37}\text{Cl}(p, n){}^{37}\text{Ar}$ reaction. This experiment yield a value of $2 \cdot 10^6 \text{ cm}^2 \text{ s}^{-1}$ for the neutrino flux from the ${}^8\text{B}$ decay [DJHH68], which was approximately three times lower than the theoretical estimations.

It is clear these days that the initial SSM calculations overestimated the neutrino flux due to the

lack of knowledge for e.g., ${}^3\text{He}({}^3\text{He},2\text{p}){}^4\text{He}$ reaction, that affects the origin of the high energy flux indirectly because it competes with the ${}^3\text{He}(\alpha,\gamma){}^7\text{Be}$ reaction (see Figure 1.5(a)). In particular, the rate for this reaction is five times higher than the predictions at this time.

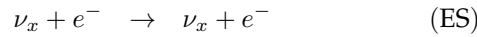
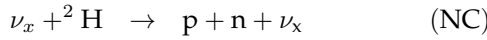
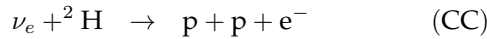
The uncertainties in most of the reactions, ${}^3\text{He}({}^3\text{He},2\text{p}){}^4\text{He}$, ${}^3\text{He}(\alpha,\gamma){}^7\text{Be}$ and ${}^7\text{Be}(\text{p},\gamma){}^8\text{B}$, were reduced in the sixties. In the following decades a lot of improvements were made in determining the cross sections for reactions responsible for direct and indirect solar neutrino production (see for example the review by Bahcall and Pinsonneault, [BP95]). On the other hand, new unexpected progress in the theoretical calculations based on the SSM made possible a new physics beyond the electro-weak standard model. However, the results from the experiments continued showing a discrepancy with the theoretical predictions in spite of the joined efforts to solve the problem.

During the 90's the big neutrino observatories continued detecting the solar neutrino fluxes from the ${}^8\text{B}$ decay. A comparison between the results obtained by Raimon-Davis [Dav94] using a chlorine detector and the Kamiokande collaboration [FHI96] using a Cherenkov image water detector in the IInd and IIIrd stages showed inconsistencies (in 2079 days of measurement Kamiokande collaboration observed 597 events against the 1213 expected), which pointed to the possibility that the neutrinos undergone oscillations between their flavours as they travelled from the centre of Sun to the detector.

The discrepancy could be solved with the suggestion by Bahcall and Bethe [BB90]. Based on the important calculation by Mikheyev-Smirnov-Wolfenstein [Mik86] (MSW effect) showing the mechanism by which a big fraction of the solar electric neutrinos ν_e^- would change to muonic neutrinos ν_μ when they travel from the centre of the Sun to the earth, Bahcall and Bethe proved that the measured spectra were in perfect agreement with the non-adiabatic solution of the MSW effect assuming a mass defect between the neutrinos of $\Delta m^2 = 1 \cdot 10^{-8} \cdot \sin^{-2} \Theta_{\nu}$ eV against the one predicted by Bethe of $6 \cdot 10^{-5}$ [Bet86].

Furthermore, in case of not considering neutrino oscillations, in order to interpret the results from gallium detectors GALLEX (GaLLium EXperiment [Kir98]) and SAGE (Soviet-American Gallium Experiment [Gav01]), no neutrinos coming from the ${}^7\text{Be}$ decay with energies bellow 4.5 MeV would be required. Nevertheless, it was known the existence of them ([AAB98] section VIII) and they have been detected for the first time using the BOREXINO detector at the Laboratori Nazionali dil Gran Sasso, [ABB08].

The success of the SNO (Sudbury Neutrinos Laboratory) experiment, [AAA02], revealed the neutrino oscillations from the direct detection of solar neutrinos, giving response to the deficit of neutrinos observed in the other experiments. The SNO experiment consists of a water Cherenkov detector placed 6100 m underground in Sudbury, Ontario (Canada) that is able to detect not only electric neutrinos but also mounic and taunic neutrinos using the reactions:



The first charge current (CC) reaction is only sensitive to electric neutrinos, while the neutral current (NC) and the elastic scattering (ES) are sensitive to all of the three e , μ and τ neutrino flavors. Taking into account that the thermonuclear fusion reaction in the Sun only produce electron neutrinos, the direct detection of the other two neutrinos flavors would demonstrate the neutrino oscillations. From the measured neutrino fluxes ($\phi_e = 1.76 \cdot 10^6 \text{cm}^{-2} \text{s}^{-1}$ and $\phi_{\mu,\tau} = 3.41 \cdot 10^6 \text{cm}^{-2} \text{s}^{-1}$) approximately a third corresponds to electron neutrinos and this rate clearly established the neutrino oscillations (see reference [AAA07] for the experiment specifications and detailed results).

On the other hand, in nuclear reactors neutron rich nuclei are created abundantly and decay afterwards by the β^- process emitting anti-neutrinos. Detections of these particles also proved the neutrinos oscillations without the need of a massive medium such as the Sun. The KamLAND (kamilka Liquid scintillator Antri-Neutrino Detector) studied the neutrino oscillations from the anti-neutrinos observations from reactors with an experimental setup which replaced to the Super-Kamiokande [FFI01] and reported the same evidence for the neutrino oscillations [AEE08].

The new investigations with the liquid organic scintillator target at BOREXINO detector, have been able to detect anti-neutrinos coming directly, possibly, from the Sun. A limit on the transition probability from solar neutrinos to anti-neutrinos of $1.3 \cdot 10^{-4}$ was reported [BBB11].

The solar neutrino spectrum from the SSM calculations is shown in the Figure 1.7.

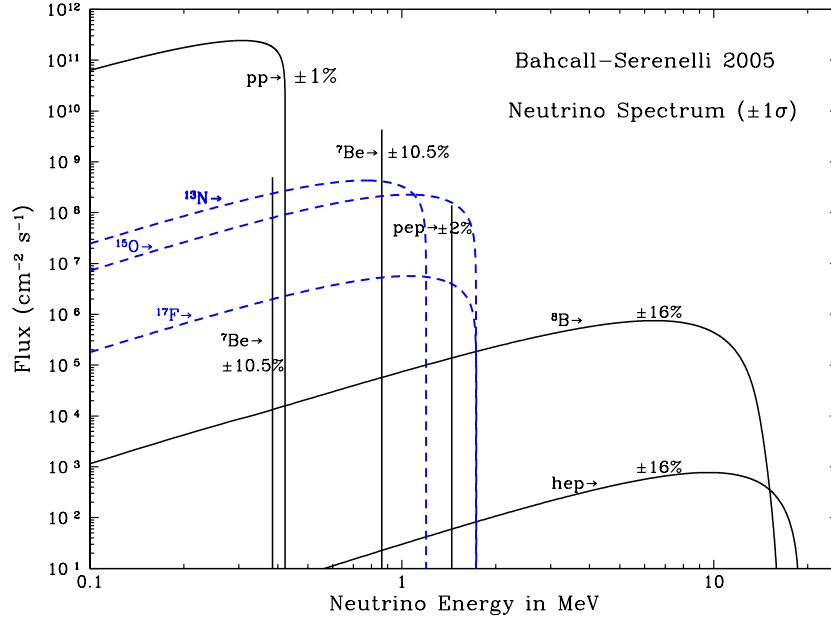


Figure 1.7: The solar neutrino spectrum calculated using the Standard Solar Model [BP95].

Although the main discrepancies between the estimations by SSM and direct observations seems to be understood by means of neutrino oscillations, the estimated error by the SSM for the solar neutrinos are not still low enough and the experimental uncertainties of the nuclear reactions cross sections, which are used as input parameters, need to be reduced. While the main neutrino flux in the low energy range is due to neutrinos emitted in the p+p reaction the high energy part of the spectrum is mainly produce by the ${}^8\text{B}$ β^+ -decay, and also influenced by the ${}^7\text{Be}$. Models estimate that the neutrino fluxes from the ${}^8\text{B}$ and ${}^7\text{Be}$ decays are directly proportional to the S-factor of the ${}^3\text{He}(\alpha, \gamma){}^7\text{Be}$ via $\phi_\nu({}^7\text{Be}) \propto S_{34}(0)^{0.86}$ and $\phi_\nu({}^8\text{B}) \propto S_{34}(0)^{0.81}$. Therefore, a precise determination of the cross section of this reaction is highly required. Indeed, the ${}^3\text{He}(\alpha, \gamma){}^7\text{Be}$ cross section is currently one with the largest experimental uncertainties among the nuclear input parameters. This is reflected in the uncertainties of the SSM predictions (cf. Figure 1.7). The nuclear rates also have a determining role in constraining the parameters governing the solar neutrino oscillations.

On the other hand, the solar Gamow Peak energy for the ${}^3\text{He}(\alpha, \gamma){}^7\text{Be}$ reaction is ≈ 22 keV, as can be seen in Figure 1.3, and the measurements at this energy are impossible with the current experimental devices. Thus, theoretical models are used to extrapolate the cross sections measured at higher energies, which essentially is the driving motivation for the present thesis work.

1.4 Big-Bang Nucleosynthesis and the Primordial ${}^7\text{Li}$ problem

Currently, the *Big-Bang Model* is the most successful cosmological theory as it can explain three important features: the expansion of the Universe, the cosmic microwave background radiation and the primordial nuclear abundances.

Approximately, 13.8 billion years have passed since the Big Bang Explosion resulting in the present expanding and cold ($T_0=2.73$ K) Universe. An artistic timeline of the expanding Universe is shown in Figure 1.8, where different eras as the Dark Ages or the Development of Galaxies and Planets are labelled.

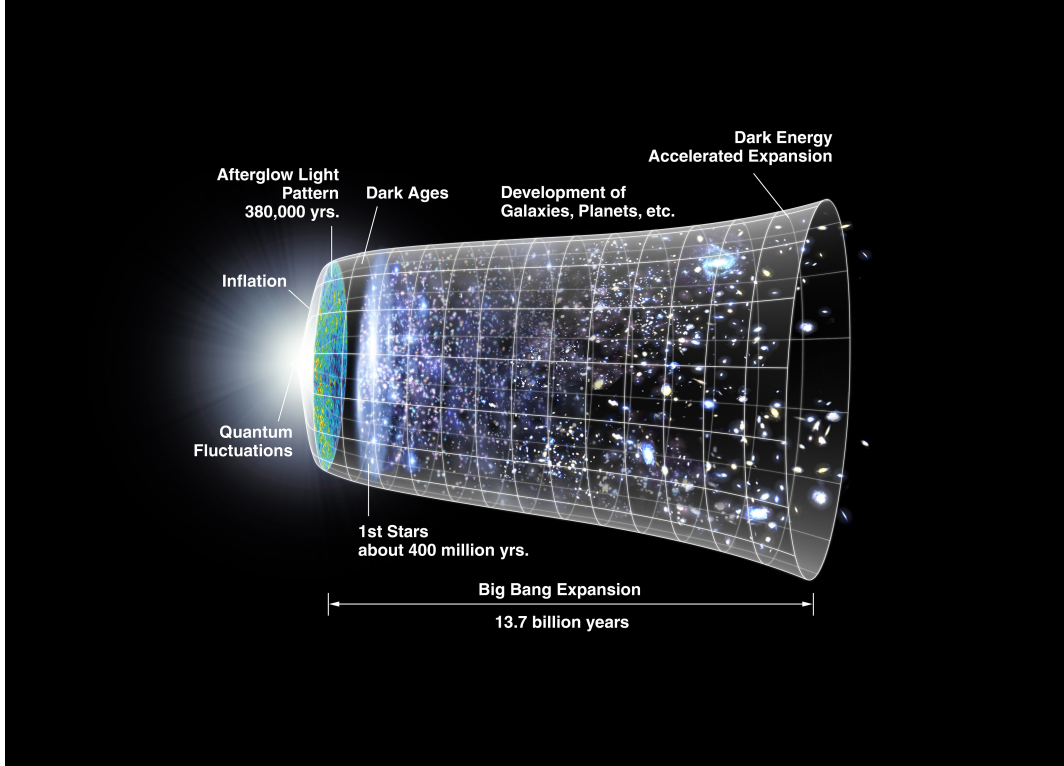


Figure 1.8: The figure taken from NASA shows an impression of the Universe expansion timeline, since the initial Big-Bang quantum fluctuations. Some of the eras such as the Dark Ages before the Galaxies were created are marked.

During the initial hot expansion the Universe was filled with relativistically moving particles interacting via weak interaction. Once the protons and neutrons had been created within $t \sim 10^{-6}$ s and following the Big Bang and the early times of the Universe, $t < 1$ s, the thermal energy was high enough (> 1293.3 keV) to convert free protons into free neutrons and vice-versa by weak interaction as well as the $e^- + e^+ \leftrightarrow \gamma + \gamma$ reaction. It was only after two seconds when the temperature was low enough to allow protons and neutrons to retain their identities. After ~ 200 s of cooling and expansion and with a temperature of ~ 0.9 GK the nuclear reactions could compete with the destruction of nuclei by photons.

In this framework and under the assumptions of an homogeneous and isotropic Universe, the Standard Big Bang Nucleosynthesis (SBBN) explains the production of the first elements during the time window between ~ 200 -1000 s following the Big Bang. The Standard Big Bang Nucleosynthesis is a vast field and it is out of the scope of this thesis to explain all the details. The main aspects of the model related to our ${}^3\text{He}(\alpha, \gamma){}^7\text{Be}$ reaction will be recalled, based on the details presented in [MM93, OSW00].

Primordial nucleosynthesis started via the $p(n, \gamma)d$ reaction (production of deuterium (d)), which is the seed for the rest of the reaction network. The main reaction network showing the production and destruction of the main primordial elements is shown in Figure 1.9. The most relevant remaining light nuclei are d , tritium (t), ${}^3\text{He}$, ${}^4\text{He}$, and ${}^7\text{Li}$; the gap at $A=8$ prevents the production of heavier nuclei with significant amounts. The aim of the SBBN is to determine how the mass flowed through the network for a temperature range of $1.2 \cdot 10^9 \geq T \geq 3 \cdot 10^8$ K. For the ${}^3\text{He}(\alpha, \gamma){}^7\text{Be}$ reaction, the relative

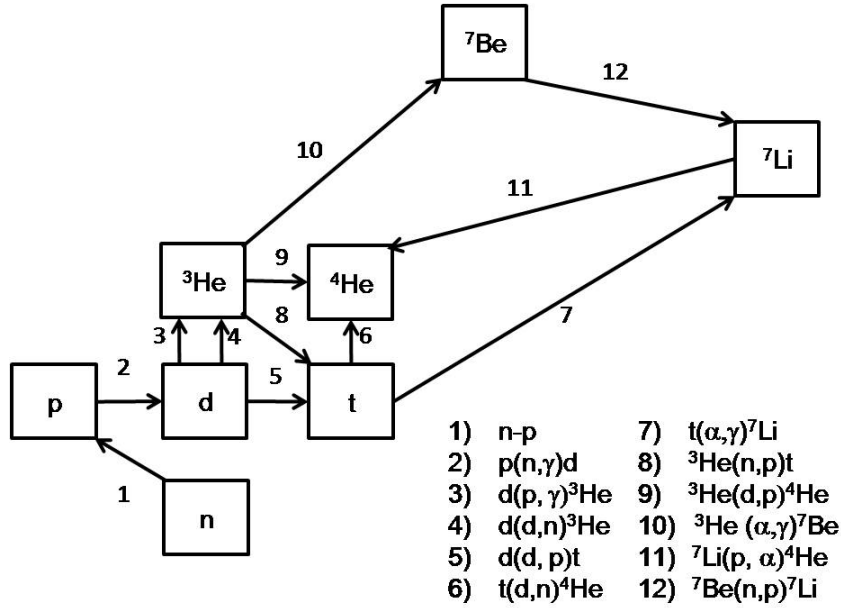


Figure 1.9: Main reaction network for the Big Bang Nucleosynthesis.

Gamow Peak energies corresponding to these temperatures are in the interval of $400 \geq E_{\text{CM}} \geq 180$ keV which are accessible in the laboratory. While the $p(n,\gamma)d$ cross section is based on theory (although the error associated is less than 1%), data exist for the others.

Historically, the BBN was a three free parameter theory, namely the baryon density, the neutron lifetime and the number of neutrino flavours. After obtaining knowledge of the number of neutrino flavors inferred from the LEP experiment at CERN, $N_\nu = 2.9840 \pm 0.0082$ and the neutron mean lifetime, $\tau_n = 885.7 \pm 0.8\text{s}$ [Gro08], it became one parameter theory. In this framework with the experimental cross sections as input model parameter, it was possible to estimate the expected abundances of the primordial elements as a function of the free parameter η (baryon/photon ratio). Figure 1.10 shows the SBBN estimations of the primordial abundances as a function of the baryon/photon density ratio, η . Therefore, from a comparison with the primordial abundances obtained from the direct observations of poor metal stars, one could infer η .

More recently, the Wilkinson Microwave Anisotropy Probe (WMAP) has measured with high sensitivity the Cosmic Microwave Background (CMB) spectrum originated from the acoustic oscillations when the electrons coupled to nuclei to form atoms $4 \cdot 10^5$ years after the Big Bang. The CMB is sensitive to the initial mass distribution (n_B) and thus the baryon to photon ratio can be derived precisely, quoting $\eta_{10} = 6.23 \pm 0.17$, where $\eta = n_B/n_\gamma = 10^{-10}\eta_{10}$ [KDN09]. n_γ is the photon density and is considered to be constant after that almost all positrons and electrons annihilated ~ 14 s after the Big-Bang. The WMAP value for η can now be used as input parameter in the SBBN and the calculated primordial abundances can be compared with the direct astronomical observations.

There is a good agreement of the abundances for d , ${}^3\text{He}$, and ${}^4\text{He}$, while the estimations of the amount of primordial ${}^7\text{Li}$ are approximately three times higher than those from observations. This is the so-called *Primordial ${}^7\text{Li}$ Problem*. Figure 1.11, from [CFO08], shows a comparison between the primordial elements abundances directly observed (in yellow) and those estimated in the SBBN model including five years of measurements by WMAP and the revision of the data for the ${}^3\text{He}(\alpha,\gamma){}^7\text{Be}$ reaction in [CD08] (in blue). Discrepancy by a factor of three can be observed for the ${}^7\text{Li}/\text{H}$ ratio between the estimations by the SBBN (blue) and the direct observations from poor metal stars (yellow).

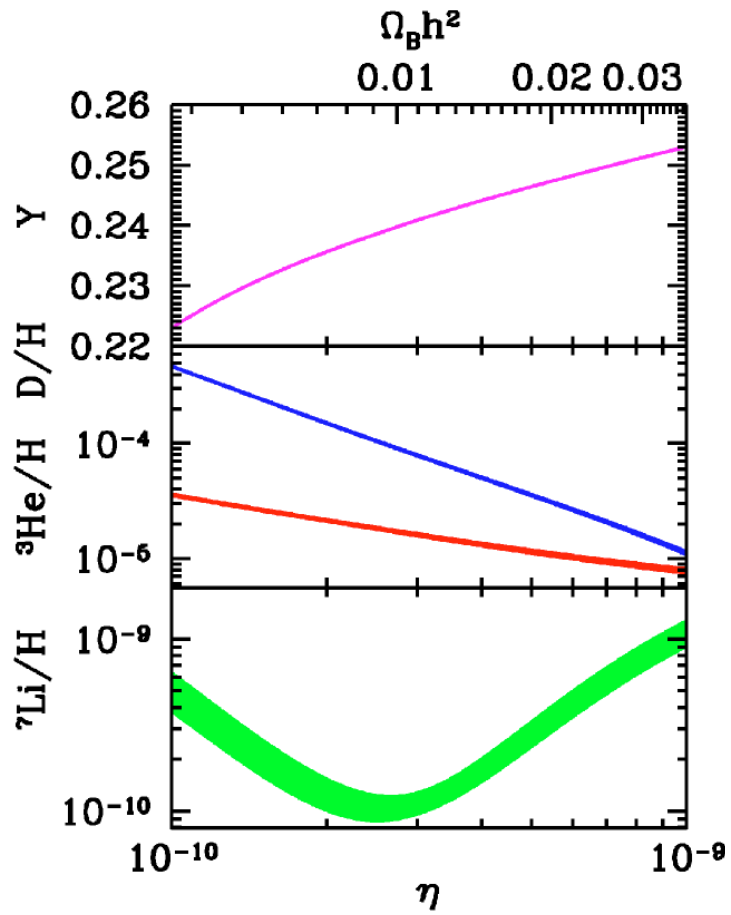


Figure 1.10: Primordial light element abundances as functions of the baryon/photon ratio (taken from [Cyb04]). The ${}^4\text{He}$ abundance is expressed as mass fraction Y , while the abundances for deuterium, ${}^3\text{He}$, and ${}^7\text{Li}$ are expressed as mole ratios.

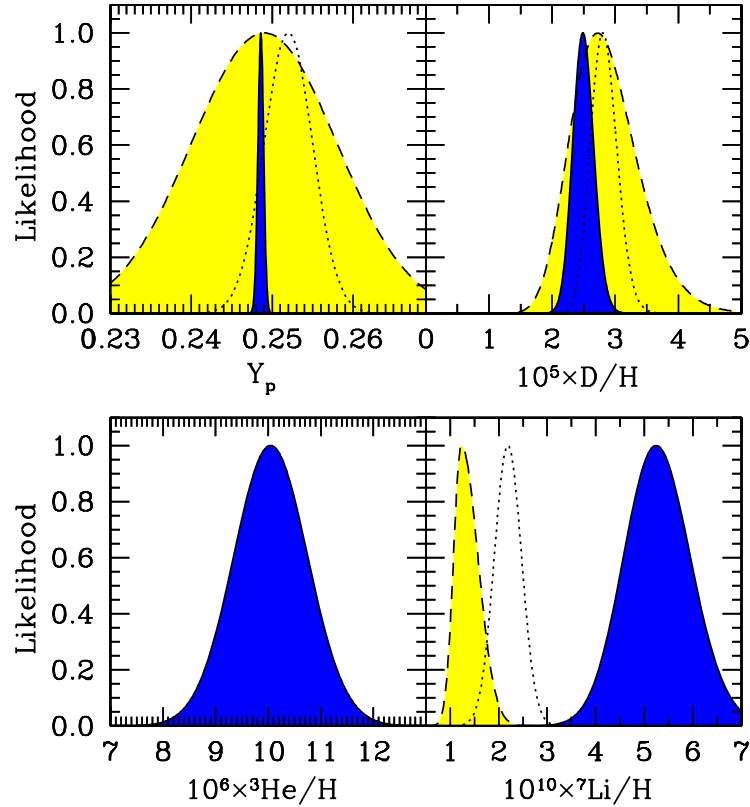


Figure 1.11: Calculated and observed likelihoods for ${}^4\text{He}$ (Y_p), D/H , ${}^3\text{He}/H$ and ${}^7\text{Li}/H$. The dark blue areas show the likelihood calculated with the SBBN results using the η parameter from WMAP observations. The observational likelihoods are shown in the yellow shaded region and dotted likelihood functions. For the ${}^7\text{Li}/H$, the shaded yellow area shows the value inferred from the observation of halo stars. The dotted function shows the determination from a globular cluster. Figure has been taken from [CFO08]

The origin of this discrepancy is still unknown. Different solutions have been suggested including physics beyond the Standard Model and the cosmological variation of the fine structure constant. The latter would suppose a variation in the deuterium binding energy and thus a decrease in the estimations for the ${}^7\text{Li}$ abundance. The reliability of the observed primordial abundances in poor metal stars is also under discussion as the current Universe conditions are far from those in the primordial conditions. Some other sources of systematic uncertainties could arise from a possible scenario that ${}^7\text{Li}$ would have been depleted if the outer layers of the stars were transported deep enough and ${}^7\text{Li}$ was mixed with the hot material inside the star.

Currently, information on accuracy levels of the reaction rates are not seen as solutions to the discrepancy. However, accurate information on the reaction rates is required to estimate the abundances precisely and thus constrain the discrepancy. The ${}^7\text{Li}$ is mainly produced by the ${}^3\text{He}(\alpha,\gamma){}^7\text{Be}$ and subsequent ${}^7\text{Be}(n,p){}^7\text{Li}$ reactions and destroyed by the large cross section of the ${}^7\text{Li}(p,\alpha){}^4\text{He}$ reaction (see Figure 1.9). Particularly, the ${}^7\text{Li}$ abundance is directly proportional to the ${}^3\text{He}(\alpha,\gamma){}^7\text{Be}$ reaction rate as ${}^7\text{Li}/H \propto S_{34}^{0.96}$ where S_{34} is the astrophysical S -factor of the reaction. A precise determination of the ${}^3\text{He}(\alpha,\gamma){}^7\text{Be}$ cross section will help to reduce the uncertainty in the model predictions and will constrain the underlying physics, eventually helping to solve the *Primordial ${}^7\text{Li}$ problem*. This effect is demonstrated for example in reference [CFO08] where a new data evaluation for the ${}^3\text{He}(\alpha,\gamma){}^7\text{Be}$ reaction shows an upward shift of 16% in central value of the ${}^7\text{Li}$ abundance.

Finally, it is also worth noting here that other new nuclear physics solutions are continuously searched but without success. For example, in reference [KD11] authors studied the 16.8 MeV state in ${}^9\text{B}$ and found that it is unable to enhance the ${}^7\text{Be}(d,p)$ reaction rate by the amount needed to resolve the cosmological lithium problem. Other examples are studied in [CGX12] where a complete network

of more than 400 reactions have been included in the BBN calculations, yet finding no solutions and discrepancy of the estimated primordial ${}^7\text{Li}$ is still persistent.

1.5 The ${}^3\text{He}(\alpha,\gamma){}^7\text{Be}$ Reaction: Experimental Previous Knowledge

Due to the relevance of the ${}^3\text{He}(\alpha,\gamma){}^7\text{Be}$ reaction in the SSN and the SBBN, the cross section has been studied experimentally using different techniques with ever-increasing accuracy. The decay scheme of the ${}^3\text{He}+{}^4\text{He}$ direct capture is shown in Figure 1.12. This radiative capture reaction creates a ${}^7\text{Be}$ nucleus and has a Q-value of 1.587(1) MeV. Prompt γ -rays with two different energies are emitted in the process corresponding to the population of the ground state (γ_0) or the first excited state (γ_1) in the ${}^7\text{Be}$. The latter de-excites via emission of a 429 keV γ -ray to the ground state (γ_2). The created ${}^7\text{Be}$ is an unstable nucleus. It decays via electron capture process to ${}^7\text{Li}$ with a half life of 53.24(4) d. The Q value of this process is 862 keV and with a well known branching ratio of 10.44(4)% the decay populates the first excited state in ${}^7\text{Li}$ at 478 keV from which a γ ray emanates (γ_3).

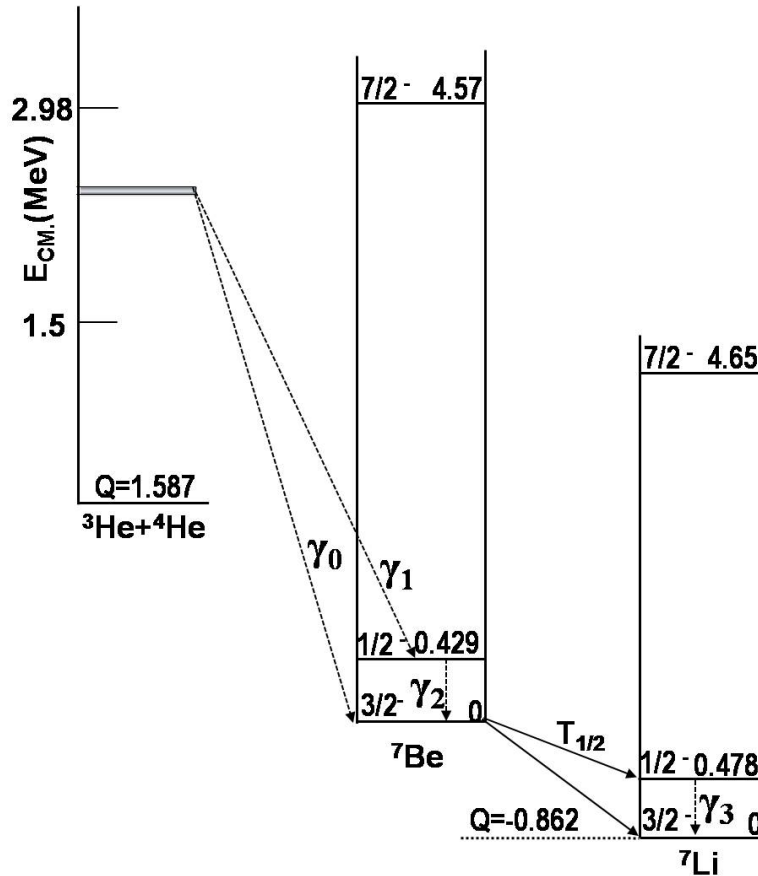


Figure 1.12: Decay scheme of ${}^3\text{He}+{}^4\text{He}$ direct capture state with the emission of prompt γ -rays. The ${}^7\text{Be}$ decay to ${}^7\text{Li}$ is also shown. The energies are displayed in MeV.

The three different techniques used for determining the cross section consist of measuring either, the prompt γ_0/γ_1 -rays of the reaction ("*Prompt Method*"), the ${}^7\text{Be}$ recoils ("*Direct Recoil Counting Method*") or the subsequent γ_3 rays from the de-excitations of the first excited state in ${}^7\text{Li}$ to its ground state ("*Activation Method*"). The first experiment performed in order to determine the cross section of the ${}^3\text{He}(\alpha,\gamma){}^7\text{Be}$ reaction was done by Holmgren and Jhonston in the late fifties [HJ59] using the *Prompt- γ Detection Method*. Measurements using the same method were carried out by

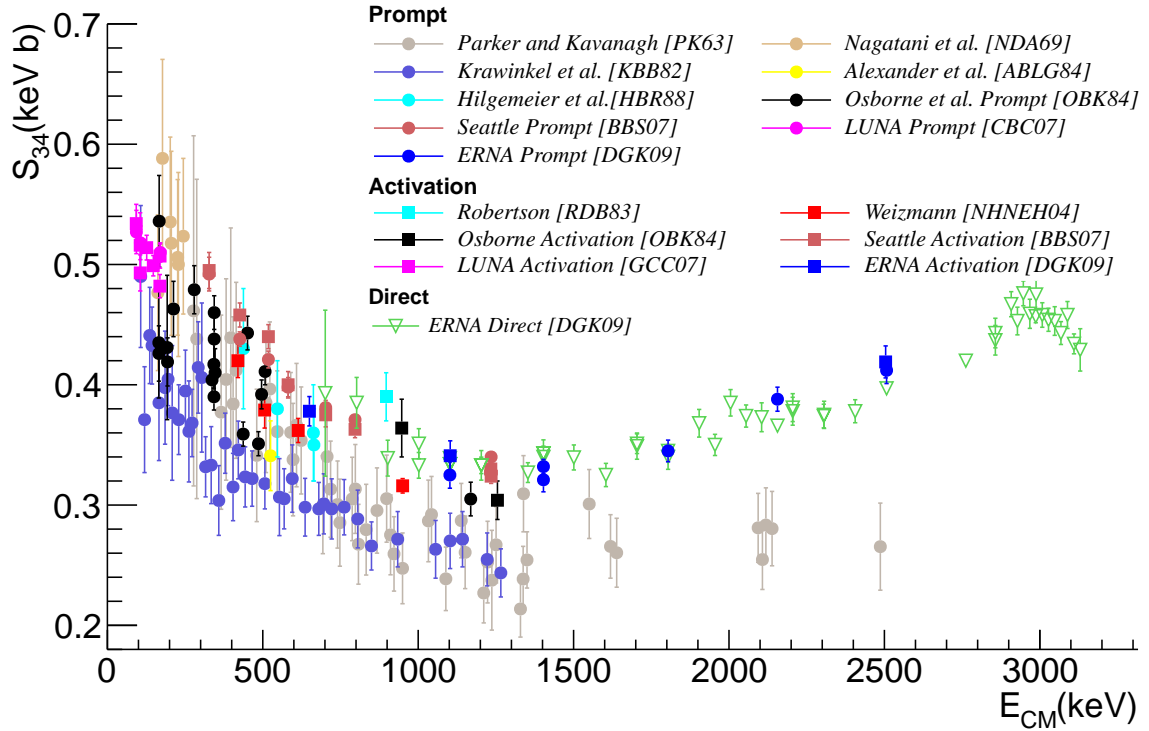


Figure 1.13: The available data of the astrophysical S -factors for the ${}^3\text{He}(\alpha,\gamma){}^7\text{Be}$ reaction (S_{34}) Data from measurements performed by the Prompt Method, Activation Method and Direct Recoil Counting Method are shown in circles, squares and triangles, respectively.

[PK63, NDA69, KBB82, ABLG84, HBR88], while in [RDB, VKSW83, NHNEH04] the *Activation Method* was the choice. Both methods were used simultaneously in the works presented in [OBK84, BBS07] and by the LUNA collaboration (Laboratory for Underground Nuclear Astrophysics) [CBC07]. The activation measurements performed at LUNA are also detailed in [BCC06] and [GCC07]. Recently, the *Direct Recoil Counting Method* was employed for the first time using the European Recoil separator for Nuclear Astrophysics (ERNA), [DGK09] where measurements using the *Prompt Method* and *Activation Method* were also performed simultaneously. At the same time of the work presented here two other measurements were carried out, one using the *Activation Method* [BGH13] and other using the *Prompt Method* [KUD13].

The centre of mass energy range covered in the mentioned experiments is between 93 and 3130 keV. Energies above 1200 keV were covered only by measurements [PK63] and [DGK09] and show a big discrepancy with each other. A summary of all experimental measurements performed before the work presented here is shown in Figure 1.13, except those from [HJ59]. The violet points from reference [KBB82] are increased by 40% as recommended in [HBR88] to account for the a wrong estimation of the target thickness. As can be seen, there is a big dispersion among the different set of measurements, especially, in the range span between 1200 keV and 2500 keV. Resolving this discrepancy is one of the motivations of this work.

The different set of measurements have used different theoretical models (which will be detailed in the next Chapter) to obtain the extrapolated $S_{34}(0)$ value. The $S_{34}(0)$ values are normally used in the astrophysical models and also for comparing the different experimental results. A comparison between the $S_{34}(0)$ values as extracted from the different experimental measurements is shown in Figure 1.14. Green circles show the $S_{34}(0)$ values obtained using the *Prompt Method*, in red squares are represented the $S_{34}(0)$ values obtained using the *Activation Method* and, in open black squares are the values obtained by combination of different methods (see caption for more details). As can be observed, the discrepancy among the different methods is significant.

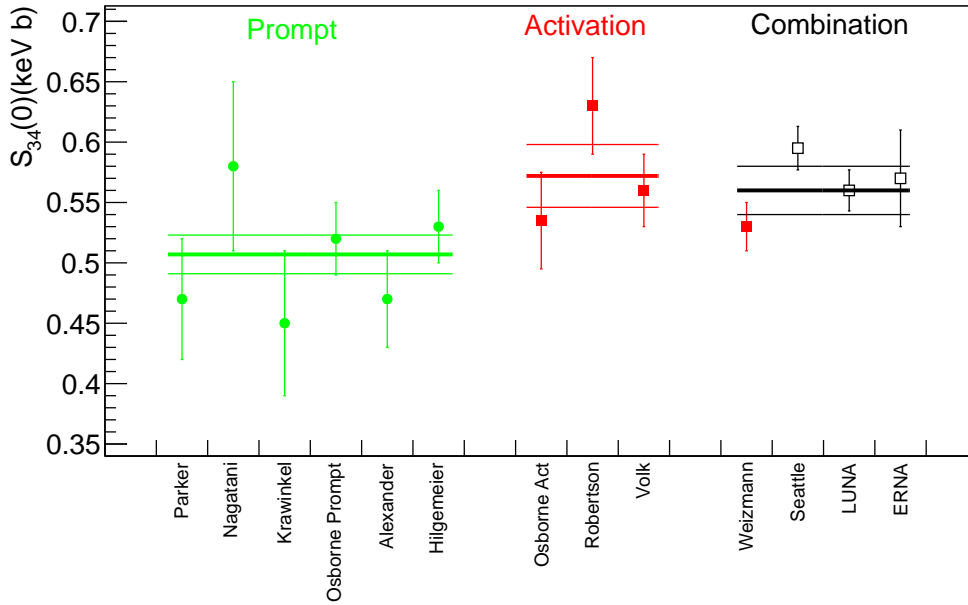


Figure 1.14: The $S_{34}(0)$ values obtained from different experiments carried out before the measurements presented here. Results obtained by using the Prompt Method (green circles), the Activation Method (red squares) and different complementary methods (open black squares) are shown: Seattle [BBS07] and LUNA [CBC07] used Activation and Prompt Methods at the same time while ERNA [DGK09] combined Activation, Prompt and Direct methods. The Nagatani value is the result from a reanalysis of data and the Kräwinkel values are normalised as specified in [HBR88]. The thick green line is the recommended value in [AAB98] based on the Prompt experiments at the time of the review, and the thin green lines are the associated errors. The red lines refer to the same for the Activation method. The black line is the recommended $S_{34}(0)$ value in the [AGR11] review for the evaluation of Weizmann, Seattle, LUNA and ERNA data. It should be noted that while the open squares for Seattle, LUNA and ERNA are obtained by a combination of the different methods used in each case, the evaluation [AGR11], takes into account only the activation measurements from Brown and LUNA, and direct counting measurements from ERNA.

In the 1998 evaluation by Adelberger et al. [AAB98], the weighted mean for the $S_{34}(0)$ values using the Prompt measurements at the time of the revision, was quoted to be 0.507 ± 0.016 keV b (green lines in Figure 1.14). For the Activation measurements, it was 0.572 ± 0.026 keV b (red lines in Figure 1.14). Two possible solutions for this apparent discrepancy between the two methods were discussed namely, a possible systematic error in one of these methods, for example ${}^7\text{Be}$ contamination in the Activation Method, or the presence of a non radiative channel (small monopole contribution -E0-) to which the Prompt Method would not be sensitive. The results in [BBS07] and [CBC07] and subsequently in [DGK09] ruled out the latter possibility by determining the cross sections using these two techniques, simultaneously. The studies in [SH03] conclude that the E0 pair emission, E0 resonance emission, E1 emission and internal conversion are negligible.

In the new 2011 review of modern physics [AGR11], the evaluation was only based on the most recent activation measurements [NHNEH04, BBS07, CBC07, DGK09] up to 1 MeV energy. This choice was justified by the fact that while the Activation measurements determine directly the total cross sections, the Prompt measurements must include a correction due to the γ anisotropy, but suffer from the fact that no angular distribution at the necessary level of precision are available. For example, while LUNA [CBC07] used the Tombrello and Parker angular distribution to correct [TP63a], Seattle [BBS07] and ERNA [DGK09] prompt data consider an isotropic angular distribution. Theoretical models of Kajino et al. [Kaj86] and Nollet [Nol01] (detailed in the next chapter) were used to fit the data and the recommended value for $S_{34}(0)$ was given as $0.56 \pm 0.02(\text{expt}) \pm 0.02(\text{theor})$ keV b (black lines in Figure 1.14). Due to the discrepancies above 1 MeV, new data in this energy region are recommended by the authors in order to constrain the theoretical models, strongly supporting the work presented here. Furthermore, prompt γ -ray distribution measurements in this energy range are also recommended

and thus one of the objectives of our measurements is to also obtain this information. In this context, it is worth pointing out that the prompt γ -ray angular distribution measured by [KBB82] up to 1.29 MeV were in agreement with the almost isotropic angular distribution in [TP63a].

Finally, measurements of the cross section identifying the population of the first excited state (σ_{429}) and the ground state ($\sigma_{g.s.}$) have been carried out by different authors [PK63, NDA69, KBB82, ABLG84, OBK82, BBS07, DGK09]. In Figure 1.15, where those cross sections are plotted by using the $\sigma_{429}/\sigma_{g.s.}$ ratio, it can be observed the discrepancies among the experimental data. New information of the $\sigma_{429}/\sigma_{g.s.}$ ratio would also help to resolve these discrepancies and constrain the theoretical models.

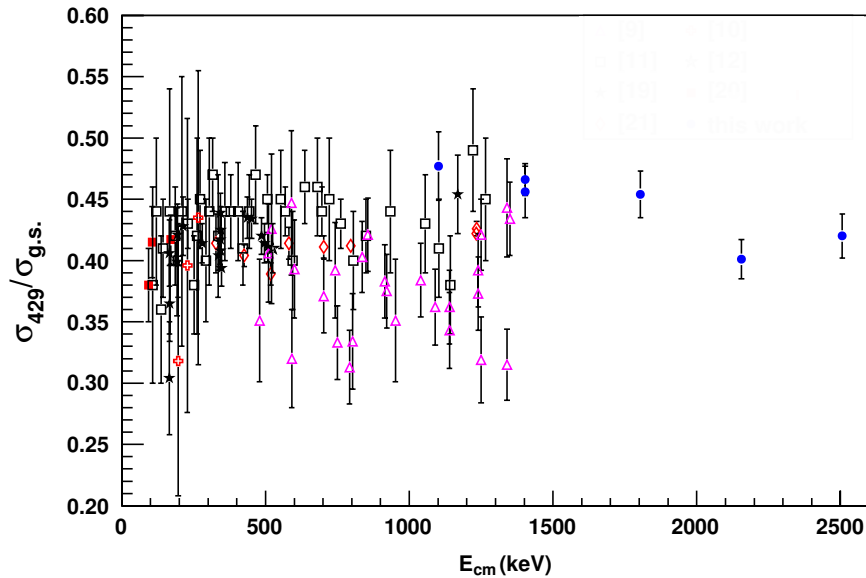


Figure 1.15: Ratio for the cross section of the ${}^3\text{He}(\alpha,\gamma){}^7\text{Be}$ reaction populating the first excited state (σ_{429}) and the ground state ($\sigma_{g.s.}$) Figure taken from [DGK09]. The blue dots are the values from [DGK09], open pink triangles from [PK63], red open crosses from [NDA69], open black squares from [KBB82], small black stars from [ABLG84], big black stars from [OBK82], red squares from [CBC07] and red diamonds from [BBS07].

1.6 Conclusion

The ${}^3\text{He}(\alpha,\gamma){}^7\text{Be}$ reaction plays a determining role in the *Big Bang Nucleosynthesis* and the *Standard Solar Model*. Specifically, the discrepancies among the existing S-factor data for the ${}^3\text{He}(\alpha,\gamma){}^7\text{Be}$ reaction have a direct influence in the estimations of the primordial ${}^7\text{Li}$ abundance and high energy solar neutrino flux. Both estimations demand precise measurements and low uncertainties of 3% in $S_{34}(0)$ value.

On the other hand, due to the experimental limitations it is not possible to determine the cross section of this reaction at very low energies and thus theoretical models (explained in the next Chapter) are used to extrapolate. Among the S-factors, values at medium energies play important roles as they help to constrain the theoretical models in obtaining an accurate extrapolated $S_{34}(0)$ value. Currently, the available two data sets for centre of mass energies above 1 MeV disagree with each other and new measurements are required in order to solve the discrepancy and better constrain the extrapolations. Moreover, no information about the prompt γ -ray angular distribution is available in this medium-high energy region which would also help to constrain the theoretical models. Furthermore, discrepancies in the ratio between the population of the ground state and first excited state in the ${}^7\text{Be}$ exists and also here new data would help to resolve the discrepancy. These observations motivated the present work, in which measurements to obtain the aforementioned data were carried out.

"A theory with mathematical beauty is more likely to be correct than an ugly one that fits some experimental data."

Paul Dirac

CHAPTER 2

THEORETICAL FORMALISM

Abstract: In this chapter some of the theoretical approaches used for explaining the ${}^3\text{He}(\alpha,\gamma){}^7\text{Be}$ radiative capture reaction will be discussed. The framework for this reaction and general theoretical procedures to determine radiative capture reaction cross sections will be given. Complementary, the phase shifts analysis will be detailed, which can be used to constrain the models.

Similarly to the usage of light and processes such as reflexion or refraction to determine the properties of light and interaction with matter, in Nuclear Physics beam of particles are used to study the properties of nuclei and nuclear interactions. One of the main methods used to determine those properties and understand the underlying physics is to carry out reactions between nuclei (nuclear reactions).

In the previous chapter, different existing experimental data for the astrophysical S-factor of the ${}^3\text{He}(\alpha,\gamma){}^7\text{Be}$ reaction have been presented. Existing significant discrepancies between different sets of measurements have been pointed out. Different theoretical models apparently reproduce the experimental results and provide some knowledge of the reaction mechanism and the structural properties of the partners. The models can be grouped as Potential Models, Microscopic Models and R-matrix analysis. Moreover, recent pioneer work using the ab-initio approach has been performed. A general overview of these models will be presented in this chapter.

Furthermore, the reliability of the models, rests on simultaneous explanation of the ${}^3\text{He}+{}^4\text{He}$ capture and the phase shift analysis of the ${}^3\text{He}+{}^4\text{He}$ elastic scattering data. Therefore, these aspects will also be briefly discussed.

2.1 Nuclear Reactions

In nuclear reactions, an interaction process between the reaction partnered nuclei generally is governed by the strong nuclear force, but in which the electromagnetic force may also play a determining role.

Nuclear reactions can be classified according to different criteria, e.g. according to their time scale:

- **Direct Reactions:** These are the faster and happen within $\sim 10^{-22}$ s with cross sections varying smoothly with the incident kinetic energy. Either a few nucleons on the surface or the nucleus as a whole participate in this process. Quantum mechanically, these reactions are modelled as *one step transitions* between the initial and final states. Examples for direct reactions are:
 - Elastic Reactions: Rutherford scattering process where the products in the outgoing final are the same as the nuclei in the incoming initial channel: $A(b,b)A$
 - Inelastic Reactions: Similar to the elastic scattering but one of the nuclei will remain excited: $A(b,b^*)A$ or $A(b,b)A^*$
 - Transfer Reactions^a: In this reactions nucleons are transferred either from the projectile to the target, referred as stripping reactions, or from the target to the projectile (pickup reactions)
 - Breakup Reactions: One of the two ejectile is broken in two or more fragments, e.g. $A(b, b=c+d)A$
 - Knockout Reactions: These reactions involve removal of a nucleon or cluster of nucleons from a nucleus, leaving one of the residual nuclei in its excited state.
 - Direct Capture Reactions: The two incident nuclei ($A+B$) capture each other. To form a composite state that lives long enough and avoid going back to the initial $A+B$ state, some energy must be released, either by direct emission of particles or by γ -radiation. The latter are called **radiative capture** reactions $-A(b,\gamma)C-$ and will be detailed in the next sections. The reverse process, $C(\gamma,b)A$, is called photo-disintegration:
- **Resonance Reactions:** These are longer lived configurations of nucleons. The resonances can be identified using the cross sections, as they have a peak structure when plotted against energy. The peak widths (Γ) are typically between 100 keV and 1 MeV. The incoming particles form a quasi-state, "the resonance state", which can live for a time between 10^{-19} and 10^{-21} s.
- **Compound Nucleus Reactions:** These involve all possible interactions between the nucleons in the two interacting nuclei. The two nuclei fuse creating an intermediate nucleus (where the interacting nuclei lose their identities) generally in an excited state which de-excites via emission of γ radiation by electromagnetic processes, or decays by particle evaporation or fission. The compound nucleus will live for a relatively long time.

2.2 Electromagnetic Transitions: Direct Radiative Capture Reactions

The electromagnetic transitions connect an initial wave function Ψ_i for a group of charged particles with energy E_i described by the Hamiltonian operator $H=H_0$ to a final wave function Ψ_f , for the charged particles plus electromagnetic radiation (photons), with energy E_f and described by the Hamiltonian $H=H_0+H_\gamma$. Here, H_γ is the electromagnetic operator and transition probability can in general be given by: $w_i \sim | \langle \Psi_f | H_\gamma | \Psi_i \rangle |^2$.

The electromagnetic transitions can be classified using the relative energies involved in the initial and final states as (cf. Figure 2.1):

^aTogether with Radiative Capture Reactions, Transfer Reactions are the most relevant in Nuclear Astrophysics

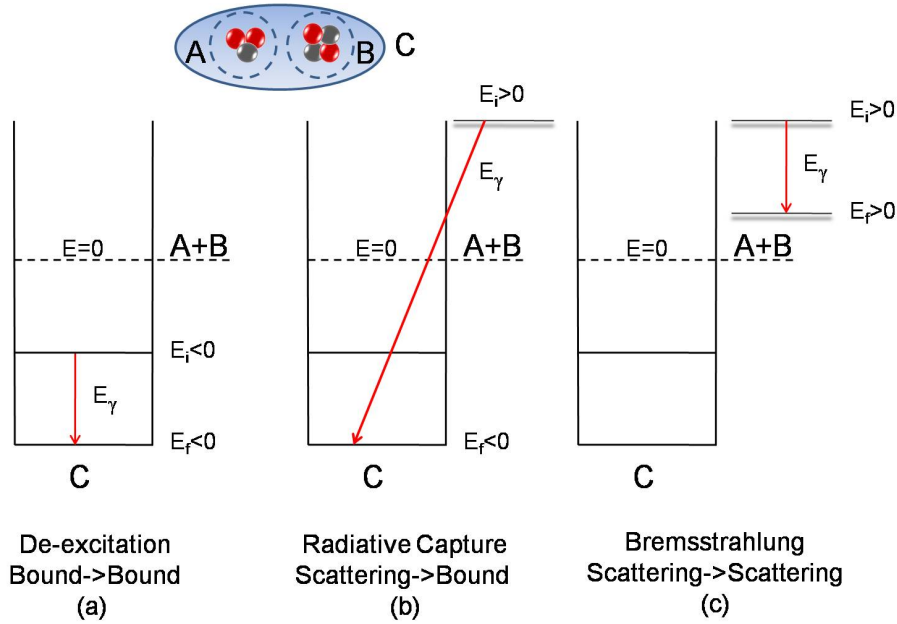


Figure 2.1: Electromagnetic transitions. (a) De-excitation between two bound states in a nucleus "C". (b) Radiative capture reaction from a scattering state (A+B nuclei) to a bound state (C nucleus). (c) Bremsstrahlung electromagnetic radiation from the transition between two scattering states.

- $E_i < 0$ and $E_f < 0$: The transition occurs from a bound state to a bound state by emitting a corresponding γ -ray (**De-excitation**). The initial and final states are characterised by spins and parities $J_i \pi_i$ and $J_f \pi_f$, respectively. The transition probability, given by $w_i \sim |\langle \Psi^{J_f \pi_f} | H_\gamma | \Psi^{J_i \pi_i} \rangle|^2$, provides the γ -width $\Gamma_\gamma = \hbar w$, which is related to the mean life $\tau = \hbar / \Gamma_\gamma$ of the state.
- $E_i > 0$ and $E_f < 0$: The transition occurs from a scattering state to a bound state by emitting the corresponding electromagnetic radiation. These are known as **Direct Radiative Capture Reactions**. The initial and final states are characterised by spins and parities $J_i \pi_i$ and $J_f \pi_f$, respectively. The initial scattering wave function, $\Psi(E)$ can be described as an expansion in partial waves, $\Psi(E) = \sum_{J_i} \Psi^{J_i \pi_i}(E)$ and the transition probability $w_i \sim |\langle \Psi^{J_f \pi_f} | H_\gamma | \Psi(E) \rangle|^2$ provides the capture cross section.
- $E_i > 0$ and $E_f > 0$: The transition occurs from a scattering state to a scattering state emitting the so-called **bremsstrahlung** radiation. This is a transition in the continuum.

Direct Radiative Capture Reactions

While in the fusion reactions all channels with mass higher than the projectile and target are available and statistical approaches are used, in the radiative capture only the electromagnetic channel is allowed. The cross section have a smooth variation with energy and γ emission is usually isotropic, characteristic of an electric dipole p to s transition, and no spin flip, (i.e. the spin is uncoupled from the orbit) [CD61]. Such processes are said to be external as the capture occurs by electromagnetic force at larger distances outside the range of the strong interaction. Therefore, in principle, the cross section is expected to be insensitive to structural details of the interacting nuclei.

Figure 2.2 shows a diagram of the ${}^3\text{He}(\alpha, \gamma)$ radiative direct capture reaction in the centre of mass system (see appendix B for the discussion about centre of mass system). The transitions can populate different bound states by emitting the corresponding electromagnetic radiation, which are known as prompt γ -rays^b. If an excited state is populated in a final nucleus a subsequent γ -ray connecting the two bound states is emitted. The corresponding wavelengths of the prompt γ -ray are

^bAlthough the electromagnetic radiation from direct radiative capture reaction is called γ -ray, these cannot be understood

~ 1500 fm that are much larger than the nuclear radii, justifying that the long wavelength approximation can be considered in the calculations.

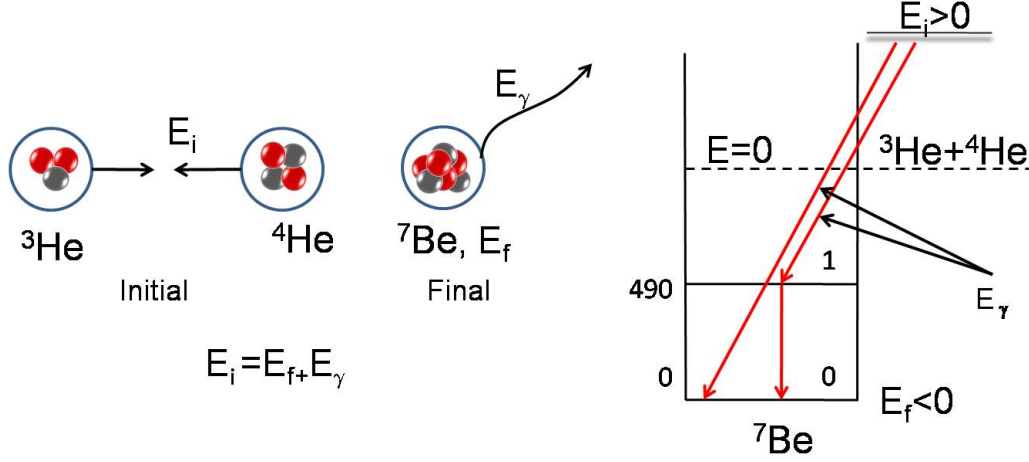


Figure 2.2: A schematic of ${}^3\text{He}(\alpha, \gamma){}^7\text{Be}$ Direct Radiative Capture Reaction in the centre of mass system (left). The direct radiative capture of the He nuclei can be described as electromagnetic transitions from a scattering state to a bound state (right). The initial scattering state with energy $E_i > 0$ connects with a final state in the ${}^7\text{Be}$ nucleus by populating the 1st excited and ground states and emitting the corresponding prompt γ -rays.

Due to the relatively small strength of the H_γ operator, perturbation theory can be applied for the electromagnetic transitions described above. The electromagnetic processes have lower probability compared to, for example, nuclear reactions governed by the strong force. Thus, the electromagnetic radiation widths Γ_γ are smaller compared to the particle emission widths (i.e. $\Gamma_\gamma/\Gamma_p < 1$).

The electromagnetic operator H_γ depends on the nuclear coordinates (nuclei or nucleons according to the model) and the photon properties (E_γ , emission angle Ω_γ ...) and can be expressed as:

$$H_\gamma \sim \sum_{\lambda\mu\sigma} k_\gamma^\lambda \mathcal{M}_\mu^{\sigma\lambda}(r_1, \dots, r_A) \mathcal{D}_{\mu q}^\lambda(\Omega_\gamma) \quad (2.1)$$

where σ is equal to E or M depending on the Electric or Magnetic transition character, λ is the order of the multipole, which in principle can take values between 1 to ∞ although in practice $\lambda = 1$ or 2, μ is an integer number between $-\lambda$ to $+\lambda$, $\mathcal{M}_\mu^{\sigma\lambda}$ is the multipole operator that depends on the nucleon coordinates r_i and, $\mathcal{D}_{\mu q}^\lambda(\Omega_\gamma)$ is the Wigner function depending on the photon emission angle (Ω_γ).

The electric operator is given by:

$$\mathcal{M}_\mu^{E\lambda} = e \sum_i \left(\frac{1}{2} - t_{iz} \right) r_i^\lambda Y_\lambda^\mu(\Omega_{ri}) \quad (2.2)$$

where t_{iz} is the isospin, taking values of $+1/2$ (neutrons) and $-1/2$ (protons), and $\mathbf{r}_i = (r_i, \Omega_i)$ is the nucleon space coordinate. On the other hand, the magnetic operator can be expressed by:

$$\mathcal{M}_\mu^{M\lambda} = \frac{\mu_N}{\hbar} \sum_i [\nabla(r^\lambda Y_\lambda^\mu(\Omega_r))]_{r=r_i} \cdot \left(\frac{2g_{li}}{\lambda+1} \mathbf{L}_i + g_{si} \mathbf{S}_i \right) \quad (2.3)$$

where \mathbf{S}_i and \mathbf{L}_i are the spin and orbital angular momenta of the nucleon i .

Therefore, integrating over Ω_γ , the transition probability is given by:

$$W_{J_i \pi_i \rightarrow J_f \pi_f} \sim \sum_{\lambda\sigma} \underbrace{k_\lambda^{2\lambda+1}}_{\text{Photon}} \underbrace{|\langle \Psi^{J_f \pi_f} || \mathcal{M}^{\sigma\lambda} || \Psi^{J_i \pi_i} \rangle|^2}_{\text{Nucleus}} \quad (2.4)$$

as the usual γ -rays in the sense of radiation emitted in the transition between two states

while the reduced transition probability can be expressed by:

$$B(\sigma\lambda, J_i\pi_i \rightarrow J_f\pi_f) = \frac{2J_f + 1}{2J_i + 1} |\langle \Psi^{J_f\pi_f} || \mathcal{M}^{\sigma\lambda} || \Psi^{J_i\pi_i} \rangle|^2 \quad (2.5)$$

and the width, Γ_γ , by:

$$\Gamma_\gamma(J_i\pi_i \rightarrow J_f\pi_f) = \hbar W_{J_i\pi_i \rightarrow J_f\pi_f} \quad (2.6)$$

Some of the properties of the electromagnetic transitions are :

- There is a hierarchy between the multipoles: $\frac{w(\sigma, \lambda+1)}{w(\sigma, \lambda)} \sim (k_\gamma R)^2 \ll 1 \implies E1 \gg E2 \approx M1 \gg E3 \approx M2, \dots$. Therefore, only a few multipoles (usually just one) are important for a given transition.
- The multipole order λ must satisfy: $|J_i - J_f| \leq \lambda \leq |J_i + J_f|$
- The transition parity is given by:
 - $\pi_i\pi_f = (-1)^\lambda$ for electric transitions
 - $\pi_i\pi_f = (-1)^{\lambda+1}$ for magnetic transitions
- There is no transition with $\lambda = 0$ and the $E1$ transitions are forbidden in $N=Z$ nuclei

In astrophysical reactions, energies are low, thus, the low total momentum $J_i=0$ has dominant contribution to the transition probability of the reaction rate.

2.3 Radiative Capture Cross Section in a Potential Model

For the radiative capture reactions, which are the most important in case that transfer reaction channels are closed, the cross sections for a given final state J_f can be written as (see expression 2.4):

$$\sigma(J_f, E) \sim \sum_{\lambda\sigma} k_\lambda^{2\lambda+1} |\langle \Psi^{J_f\pi_f} || \mathcal{M}^{\sigma\lambda} || \Psi^{J_i\pi_i} \rangle|^2. \quad (2.7)$$

This is a general definition valid for any of the theoretical calculations used to describe the radiative capture reactions. The electromagnetic operator $\mathcal{M}^{\sigma\lambda}$ was discussed in the previous sections, and the wave functions $\Psi^{J_i\pi_i}$ and $\Psi^{J_f\pi_f}$ are model specific. Here some general descriptions of the *potential models* will be given as an example.

In general, potential models (includes optical models, direct captures models...) are based on the descriptions of nuclear processes by a Schrödinger equation using local potentials in the entrance and exit channels. In the of Direct Capture Reactions, the direct capture model (DC) is used^c, where the calculations are simple due to the assumed structureless point-like nuclei and usage of potentials such as the Optical Models without any imaginary part and spin dependence.

If \mathbf{R}_{CM} is the position of the centre of mass, and \mathbf{r} is the relative coordinate between the two interacting nuclei, the position of each nuclei is given by:

$$\mathbf{r}_1 = R_{CM} - \frac{A_2}{A} \mathbf{r} \quad (2.8)$$

$$\mathbf{r}_2 = R_{CM} - \frac{A_1}{A} \mathbf{r} \quad (2.9)$$

The initial wave functions with E^{ℓ_i} scattering energy can be defined as:

$$\Psi^{\ell_i m_i}(\mathbf{r}) = \frac{1}{r} u_{\ell_i}(r) Y_{\ell_i}^{m_i}(\Omega) \quad (2.10)$$

^cAmong potential models, *optical models* are used for elastic scattering analysis and *distorted-wave Born approximation (DWBA)* are used for transfer reactions

while and the final wave function with final energy E^{ℓ_f} can be given as:

$$\Psi^{\ell_f m_f}(\mathbf{r}) = \frac{1}{r} u_{\ell_f}(r) Y_{\ell_f}^{m_f}(\Omega) \quad (2.11)$$

The radial functions $u(r)$ are obtained by solving the Schrödinger equation:

$$-\frac{\hbar^2}{2\mu} \left(\frac{d^2}{dr^2} - \frac{\ell(\ell+1)}{r^2} \right) u_{\ell} + V(r)u_{\ell} = E^{\ell} u_{\ell} \quad (2.12)$$

where the potentials $V(r)$ can be different in the initial and final states and the parameters are adjusted to reproduce properties such as **phase shifts** (details in next section), bound states energies etc...

Examples of the typical potentials used are:

$$V_{\text{Coul}}(R) = Z_p Z e^2 \begin{cases} \left(\frac{3}{2} - \frac{R^2}{2R_{\text{Coul}}^2} \right) \frac{1}{R_{\text{Coul}}} & \text{for } R \leq R_{\text{Coul}} \\ \frac{1}{R} & \text{for } R \geq R_{\text{Coul}} \end{cases} \quad (2.13)$$

for the Coulomb potential, where $R_{\text{Coul}} = r_{\text{Coul}} A^{1/3}$ is the radius of the nucleus considered as an sphere with uniformly distributed total charge of Ze . For the nuclear interaction the most commonly used potential is the "Woods-Saxon" shape:

$$V(R) = -\frac{V_r}{1 + e^{\frac{R-R_r}{a_r}}} \quad (2.14)$$

where V_r is the depth, a_r is the diffuseness, and R_r is the nuclear radius, which is commonly expressed by $R_r = 1.2 \cdot A^{1/3}$ for A the number of nucleons. With this ingredients, the radial functions are adjusted on $u_{\ell}(r) = F_J(kr) \cos \delta_J + G_J(kr) \sin \delta_J$ at large distances.

As example, the electric operator for two particles can be rearranged as:

$$\mathcal{M}_{\mu}^{E\lambda} = e (Z_1 |\mathbf{r}_1 - \mathbf{R}_{\text{CM}}|^{\lambda} Y_{\lambda}^{\mu}(\Omega_{r_1 - R_{\text{CM}}}) + Z_2 |\mathbf{r}_2 - \mathbf{R}_{\text{CM}}|^{\lambda} Y_{\lambda}^{\mu}(\Omega_{r_2 - R_{\text{CM}}})) \quad (2.15)$$

which provides

$$\mathcal{M}_{\mu}^{E\lambda} = e \underbrace{\left[Z_1 \left(-\frac{A_2}{A} \right)^{\lambda} + Z_2 \left(-\frac{A_1}{A} \right)^{\lambda} \right]}_{Z_{\text{eff}}} r^{\lambda} Y_{\lambda}^{\mu}(\Omega_r) = e Z_{\text{eff}} r^{\lambda} Y_{\lambda}^{\mu}(\Omega_r) \quad (2.16)$$

Thus, the matrix elements are expressed by

$$\langle \Psi^{J_f m_f} | \mathcal{M}_{\mu}^{E\lambda} | \Psi^{J_i m_i} \rangle = e Z_{\text{eff}} \langle Y_{J_f}^{m_f} | Y_{\lambda}^{\mu} | Y_{J_i}^{m_i} \rangle \int_0^{\infty} u_{J_i}(r) u_{J_f}(r) r^{\lambda} dr \quad (2.17)$$

and reduced matrix elements by:

$$\langle \Psi^{J_f} || \mathcal{M} || \Psi^{J_i} \rangle = e Z_{\text{eff}} \langle J_f 0 \lambda 0 | J_i 0 \rangle \cdot \left(\frac{(2J_i + 1)(2\lambda + 1)}{4\pi(2J_f + 1)} \right)^{1/2} \int_0^{\infty} u_{J_i}(r) u_{J_f}(r) r^{\lambda} dr \quad (2.18)$$

Therefore, for given values of J_i , J_f and λ , the integrated cross section result in:

$$\sigma_{\lambda}(E) = \frac{8\pi e^2}{k^2 \hbar c} Z_{\text{eff}}^2 k_{\gamma}^{2\lambda+1} F(\lambda, J_i, J_f) \left| \int_0^{\infty} u_{J_i}(r, E) u_{J_f}(r) r^{\lambda} dr \right|^2 \quad (2.19)$$

with:

$$F(\lambda, J_i, J_f) = \langle J_i \lambda 0 0 | J_i 0 \rangle (2J_i + 1) \frac{(\lambda + 1)(2\lambda + 1)}{\lambda(2\lambda + 1)^2} \quad (2.20)$$

$$k_{\gamma} = \frac{E - E_f}{\hbar c} \quad (2.21)$$

The normalisation procedure leads to obtain the radial wave functions:

$$u_J \mapsto F_j(kr)\cos\delta_J + G_J(kr)\sin\delta_J \quad (2.22)$$

for the initial continuum state, and

$$u_J \mapsto C\exp(-k_B r) \quad (2.23)$$

for the final bound state, and the total (integrated) cross section will given by:

$$\sigma(E) = \sum_{\lambda} \sigma_{\lambda}(E). \quad (2.24)$$

As there is no interference between the multiplicities, the differential cross sections can be given by:

$$\frac{d\sigma}{d\theta} = \left| \sum_{\lambda} a_{\lambda}(E) P_{\lambda}(\theta) \right|^2 \quad (2.25)$$

where $P_{\lambda}(\theta)$ are the Legendre polynomial. Thus, the angular distribution measurements are necessary to separate the multiplicities, although usually one of the multiplicities contributes dominantly dominant.

Apart from potential models, microscopic models based for example on *Resonating group methods* (RGM), are also used to describe the cross section of radiative capture reaction. RGM are fully microscopic in nature, which solve the seven-body problem (in case of $^3\text{He}(\alpha, \gamma)^7\text{Be}$) using nucleon-nucleon potentials with the parameters adjusted to reproduce the bound state and resonance properties. It is out of the scope of this thesis to describe this method here, details can be found in [Wee37, Whe37].

2.4 Phase-shifts Analysis: Elastic Scattering of ^3He and ^4He and its Relevance to $S_{34}(E)$ Data

In the previous section (see expression 2.12), it was already discussed that the parameters of the $V(r)$ potential used to describe our $^3\text{He}(\alpha, \gamma)^7\text{Be}$ reaction are adjusted to reproduce the phase shifts obtained from the ^3He - ^4He elastic scattering data. Moreover, different theoretical models describing the $^3\text{He}(\alpha, \gamma)^7\text{Be}$ reaction will be presented in the next section. Their reliability will be gauged by booking at their ability to reproduce the experimental phase shifts for the elastic channel of the $^3\text{He}+^4\text{He}$ reaction. Here, the meaning of phase shift and different phase shift analyses related to our reaction will be discussed.

Quantically, a mono-energetic beam of particles is represented by a plane wave, which suffers scattering upon passing through a region where influence a potential $V(r)$ created by a nucleus is present. In nuclear physics experiments performed to study elastic scattering reactions, the detectors are placed far away from the scattering centre, that is, in a region where particles do not significantly feel the presence of the potential anymore. Thus, one will be interested only in the asymptotic part of the scattered wave function, i.e. $r \rightarrow \infty$. Clearly, a detector placed in the asymptotic region will detect not only the plane waves, but also its scattered component. For the simple case of spherically symmetric potentials $V(r)$ the stationary part of the incident plane wave can be described as:

$$\Psi = e^{i\mathbf{k}\cdot\mathbf{r}} = e^{ikz} = e^{ikr\cos\theta} = \sum_{\ell=0}^{\infty} (2\ell+1) i^{\ell} j_{\ell}(kr) P_{\ell}(\cos\theta) \quad (2.26)$$

where $j_{\ell}(x)$ and $P_{\ell}(\cos\theta)$ are the Bessel functions and the Legendre polynomials, respectively. The outgoing wave functions far from the scattering centre can be expressed by:

$$\Psi \sim \underbrace{e^{ikz}}_{\text{incoming}} + f(\theta) \underbrace{\frac{e^{ikr}}{r}}_{\text{scattered}} \quad (2.27)$$

where the symbol \sim refers to the asymptotic value, and the θ dependence in the scattering amplitude function $f(\theta)$, accounts for the probabilities as a function of the angle with respect to the incoming beam. Therefore, the elastic scattering cross section is given by:

$$\frac{d\sigma^s}{d\Omega} = |f(\theta)|^2 \quad (2.28)$$

When the interactions are governed by central potentials $V(r)$, the solutions of the Schrödinger equation

$$\nabla^2\Psi + \frac{2m}{\hbar^2} [E - V(r)] \Psi = 0 \quad (2.29)$$

can be expressed as linear combinations of the separable radial and angular parts

$$\Psi = \sum_{\ell,m} a_{\ell m} \frac{u_{\ell}(r)}{r} Y_{\ell}^m(\theta, \phi) \quad (2.30)$$

where $u_{\ell}(r)$ is obtained from the radial Schrödinger equation:

$$\frac{d^2u}{dr^2} + \frac{2m}{\hbar^2} \left[E - V(r) - \frac{\hbar^2 \ell(\ell+1)}{2n r^2} \right] u = 0 \quad (2.31)$$

with the boundary condition $u_{\ell}(0) = 0$. The dependence of ϕ can be eliminated because of the symmetry in the scattering process of particles due to a central potential, and the wave function takes the form of:

$$\Psi = \sum_{\ell} a_{\ell} P_{\ell}(\cos\theta) \frac{u_{\ell}(r)}{kr} \quad (2.32)$$

On the other hand, at large distances from the origin the spherical Bessel functions reduce to a simple expression:

$$j_{\ell}(kr) \sim \frac{\sin(kr - \frac{\ell\pi}{2})}{kr} = \frac{e^{i(kr - \frac{\ell\pi}{2})} - e^{i(kr - \frac{\ell\pi}{2})}}{2ikr}, \quad (2.33)$$

therefore, by substituting in the expression 2.26 we have

$$e^{ikr\cos\theta} \sim \frac{1}{2i} \sum_{\ell=0}^{\infty} (2\ell+1) i^{\ell} P_{\ell}(\cos\theta) \left[\frac{e^{i(kr - \frac{\ell\pi}{2})} - e^{i(kr - \frac{\ell\pi}{2})}}{kr} \right] \quad (2.34)$$

which represents the asymptotic form of a plane wave. The first term in brackets corresponds to an outgoing spherical wave and the second to an incoming spherical wave. The asymptotic form of Ψ can be obtained if we observe that the presence of a potential cause a perturbation in the outgoing part of the plane wave, and such a perturbation can be represented for the elastic scattering by a unitary module function:

$$S_{\ell}(k) = e^{2i\delta_{\ell}} \quad (2.35)$$

We now have,

$$\Psi \sim \frac{1}{2i} \sum_{\ell=0}^{\infty} (2\ell+1) i^{\ell} P_{\ell}(\cos\theta) \left[\frac{S_{\ell}(k) e^{i(kr - \frac{\ell\pi}{2})} - e^{i(kr - \frac{\ell\pi}{2})}}{kr} \right] \quad (2.36)$$

and from a comparison with expression 2.32, the asymptotic form of $u_{\ell}(r)$ can be seen as

$$u_{\ell}(r) \sim \sin \left(kr - \frac{\ell\pi}{2} + \delta_{\ell} \right). \quad (2.37)$$

Thus, due to the effect of potential on the outgoing channel, $u(r)$ differs from the radial function of a free particle by the presence of the **phase shift** δ_{ℓ} . From expressions 2.27, 2.34 and 2.36 we have

$$f(\theta) = \frac{1}{k} \sum_{\ell=0}^{\infty} (2\ell+1) e^{i\delta_{\ell}} \sin\delta_{\ell} P_{\ell}(\cos\theta) \quad (2.38)$$

and integrating the expression 2.28 the total elastic scattering cross section takes the form of

$$\sigma^s = \frac{4\pi}{k^2} \sum_{\ell} (2\ell + 1) \sin^2 \delta_{\ell} \quad (2.39)$$

Therefore, for a given potential $V(r)$ between, e.g. two interacting nuclei as ^3He and ^4He , the evaluated phase shifts obtained by solving the equation 2.31 must reproduce the measured elastic scattering cross section. In other words, the potential $V(r)$ to be used in the theoretical capture model for our $^3\text{He}(\alpha, \gamma)^7\text{Be}$ reaction can be validated by using the $^3\text{He}+^4\text{He}$ elastic scattering data

The asymptotic wave functions of ^7Be bound states are well known. However, differences among models originate from differing s-wave phase shifts and from short-range contributions of the potentials. The latter are difficult to compute and can only be proved by capture reaction experiment above 1 MeV centre of mass energy. Concerning to the phase shifts, the most of the $^3\text{He}(\alpha, \gamma)^7\text{Be}$ studies are informed only by the phase shift analysis of Tombrello and Parker [TP63b]. They measured the elastic scattering of ^3He ions from ^4He target gas at incoming energies above 5.75 MeV. They obtained the excitation curves, i.e. cross section versus energy at a fixed angle, for eight different angles and the angular distributions at four different bombarding energies. Figure 2.3 shows an example of the excitation curves at three different angles (a) and the angular distributions (differential cross sections) at two different bombarding energies (b). In both cases the solid line represents the fit to the data using derived phase shifts.

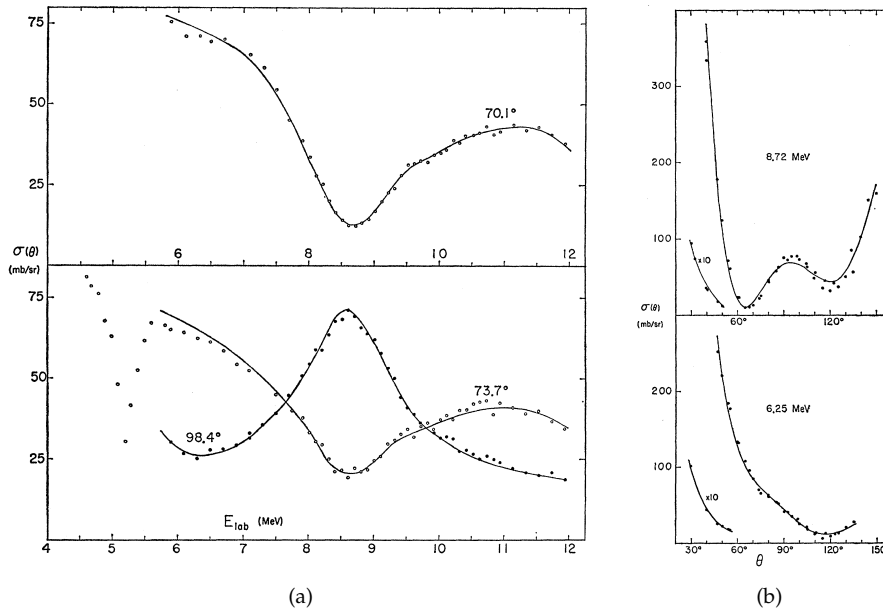


Figure 2.3: Results of the elastic scattering of ^3He from ^4He as shown in [TP63b]. The dots represent and solid lines represent data and calculation, respectively. (a) The excitation curves for 70.1° , 73.7° and 98.4° , where the dip (peak) at excitation energy of 8.7 MeV and forward (backward) angles corresponds to a new resonance predicted by the authors with the phase shifts analysis. (b) shows the scattering cross section for the bombarding energies of 8.72 and 6.25 MeV.

As it can be seen there is a good agreement between experimental data and the calculations from a phase shift analysis. It is worth pointing that the properties of the four lowest levels in the ^7Be level scheme could also be reproduced by their calculations.

A different phase shift fitting analysis has been done by Mohr et al. [MAK93, Moh09]. where strength parameters λ and λ_{LS} of the potential (obtained by folding procedure [SL72]):

$$V(r) = \lambda V_F(r) + \lambda_{LS} \frac{f m^2}{r} \frac{dV_F(r)}{dr} \vec{L} \cdot \vec{S} + V_C(r) \quad (2.40)$$

are adjusted to the measured phase shifts at energies relative higher compared to Spiger and Tombrello [ST67], Boykin et al. [BBH72] and Hardy et al. [HSB72]. The results are compared with the ${}^3\text{He}(\alpha,\gamma){}^7\text{Be}$ cross section data from ERNA [DGK09] and with the elastic scattering angular distributions measured at lower energies in [MAK93] and [BJP64] covering the same energy range. The results are shown in Figure 2.4, where (a) shows the ${}^3\text{He}+{}^4\text{He}$ elastic scattering angular distributions with the different curves representing different values of the λ and λ_{LS} parameters and (b) the same for the ${}^3\text{He}(\alpha,\gamma){}^7\text{Be}$ astrophysical S-Factor. The elastic scattering cross sections are reproduced with the black ($\lambda = 1.45$) or dash green line ($\lambda = 1.40$). This corresponds to the $L = 2$ elastic phase shift weak potential strength. However, the ${}^3\text{He}(\alpha,\gamma){}^7\text{Be}$ reaction cross section at high energy from ERNA [DGK09] can be described only with a significantly enhanced $L = 2$ potential ($\lambda \sim 1.60$).

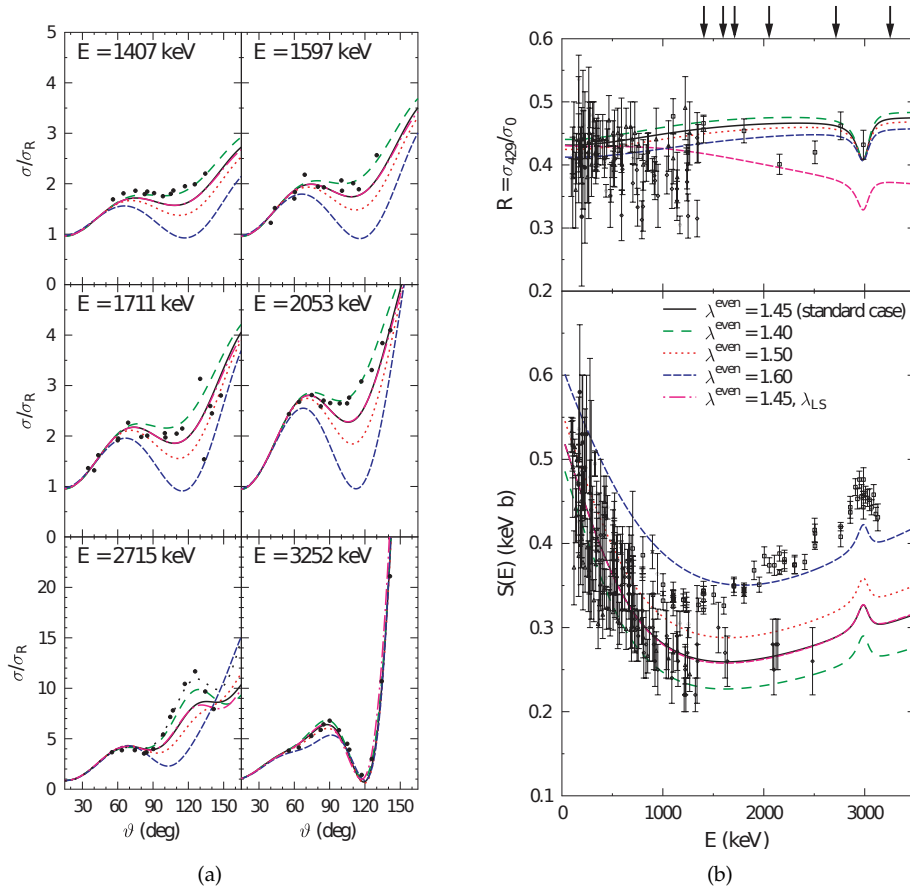


Figure 2.4: Direct Capture model calculation by P. Mohr [Moh09], where the potential parameters are obtained by phase shift analysis of the elastic scattering data. (a) The elastic scattering angular distribution of ${}^3\text{He}+{}^4\text{He}$. The points represent the experimental data from [MAK93, BJP64] and the different fits display different potential strengths (λ). (b) shows the astrophysical S-factor of the ${}^3\text{He}(\alpha,\gamma){}^7\text{Be}$ reaction. The colour of the fits are the same as those in (a).

Finally, it should be stressed that even though the phase shift analysis is a good constraining tool in validating the theoretical models, to date, most of the theoretical models rely on one experiment from the early 1960's without any error estimations [TP63b]. Although, the experimental data were extended to lower energies by Mohr et al. [MAK93], they do not include error estimations in the phase shifts analysis [AGR11].

2.5 Theoretical Descriptions of the ${}^3\text{He}(\alpha,\gamma){}^7\text{Be}$ Reaction

The reaction ${}^3\text{He}(\alpha,\gamma){}^7\text{Be}$ occurs via the radiative capture process. The ground state spins for ${}^4\text{He}$ and ${}^3\text{He}$ are 0^+ and $1/2^+$, respectively. As mentioned in the previous chapter, at low energies, the $\ell = 0$ relative orbital angular momentum of the pair of nuclei (i.e. s-wave channel) has dominant contribution to the reaction probability. For this channel, the total incoming angular momentum is $J_i = 1/2^+$. The ${}^7\text{Be}$ ground and first excited states have spins of $J_f=3/2^-$ and $J_f=1/2^-$, respectively. Therefore, in line with the properties of electromagnetic transitions described in section 2.2, the E1 transition from the S-wave channel dominates for this reaction both for the ground and the first excited states. Figure 2.5 shows calculated contributions of $\ell = 0, 1, 2$ and 3 partial waves and E1, E2 and M1 multipoles from reference [KIN81]. As can be seen the s-wave partial contribution from the E1 transitions are the dominant at low energies. As the energy is increased other partial wave contributions become significant ($\ell = 2$, d-wave).

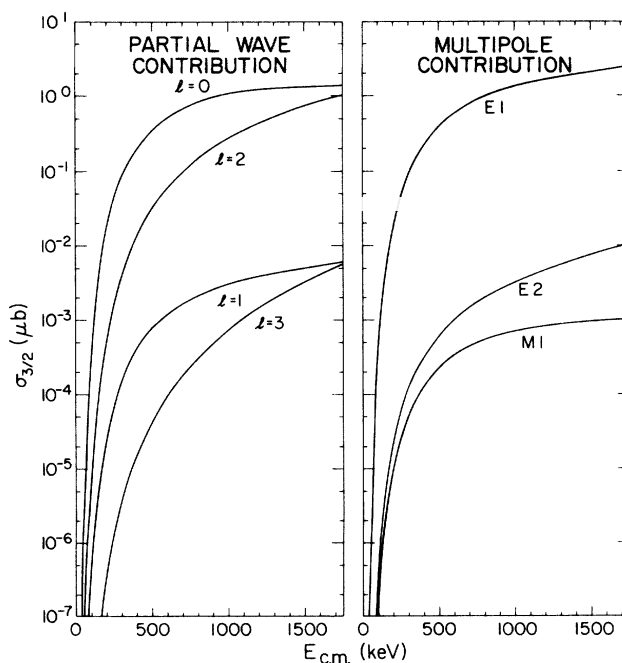


Figure 2.5: Different partial wave (s,p,d,f) and electromagnetic transition ($E1,E2,M1$) contributions leading to the ground state of ${}^7\text{Be}$ by the radiative capture reaction ${}^3\text{He}(\alpha,\gamma){}^7\text{Be}$. Figure is taken from [KIN81].

The initial calculations for this reaction were performed by Christy and Duck [CD61] and by Tombrello and Phillips [TP61]. The first experimental results for this reaction by Holmgren and Johnston [HJ59] were already explained in a quantitative way by assuming an extra-nuclear direct capture by electric dipole emission (E1) from the s-wave ($\ell = 0$) of the initial states to the final bound p-wave states ($1p_{3/2}, 1p_{1/2}$) that were assumed to be of two body form: ${}^3\text{He}+{}^4\text{He}$ cluster.

Several theoretical calculations followed in order to both reproduce the experimental data and achieve further insight into the physics mechanism of the reaction by, for example, considering different potential models. Differences arise, for example, from considering non-external contributions (nuclear effects) and initial-states phase-shifts (previous section). The ${}^3\text{He}+{}^4\text{He}$ cluster configuration has overlaps with the two bound states of ${}^7\text{Be}$ populated in our reaction. Therefore the Pauli principle requires radial nodes in these overlaps with a small (but non-zero) short-range contribution [AGR11]. Here, only an overview of the representative models highlighting the main qualitative features will be presented.

Tombrello and Parker use an external capture potential model and first order perturbation the-

ory. Only the asymptotic forms of the bound and scattering states wave functions are considered, neglecting the behaviour of the wave functions at short distances [TP63a]. The ^3He and ^4He nuclei are treated as point particles and the hard sphere scattering radius considered is determined by the phase shift analysis in [TP63b]. Also potential models with more realistic treatment of contributions from 2.8 to 7.0 fm distances are provided by Kim et al. [KIN81], Buck et al. [BBR85, BM88] and Mohr et al. [MAK93]. They use nucleus-nucleus potentials such as Wood-Saxon or folding potentials. The wave functions are calculated from potentials, which simultaneously describe the bound-state properties and phase shifts. Therefore, the energy behaviour of the astrophysical S-factors in this models is almost fixed by the spectroscopic factors considered in the models.

Other calculations are based on microscopic cluster model frameworks, where the system is described by antisymmetrized wave functions of two clusters using phenomenological nucleon-nucleon potentials. The relative motion of the clusters is solved using resonating group or generator coordinate methods. The energy dependence in this case, particularly the evaluation of Kajino et al. using microscopic cluster models and resonating group method (RGM) [KTA87] is similar to that determined using hard-sphere model by Tombrello and Parker. This RGM model, details can also be found in [KA84, Kaj86], also reproduces the phase shifts of Tombrello and Parker [TP63b] without employing any fitting procedure. The potential models have a justification in the resonating group work in the form of microscopic potential model of Langanke [Lan86]. This model, and those using RGM [KA84, KTA87] predicted the energy dependence of the isospin mirror reaction $^3\text{H}(\alpha,\gamma)^7\text{Li}$ reaction before this was experimentally measured by Brune et al. [BWR94] (see Figure 2.6(b)). However, some variations appear between different RGM models in that they employ different types of interaction. These differences depend on the diffuseness of the ^7Be ground state [Kaj86, CL00]. Moreover, large differences are observed in the astrophysical S-factor and phase shift values if the model space is expanded, for example when cluster states of $^6\text{Li}+p$ channel are added to the RGM wave functions [MH86, CL00]. Other microscopic approaches were due to Walliser et al. [WKT84] and Liu et al. [QKT81] while [DDK95] used a potential model approach.

Kenneth Nollet considers an accurate realistic nucleon-nucleon interaction to derive the wave functions employing a variational Monte Carlo technique [Nol01]. In this approach, the relative motion of the initial states is based on the potential used by Kim et al. [KIN81], and it accurately reproduces the s-wave shift of Tombrello and Parker [TP63b]. Other electromagnetic observables in ^7Li and ^7Be nuclei are in reasonable agreement with those from the microscopic calculations of Kajino [Kaj86]. Also, the energy dependence is the same as the seen in [Kaj86] while the absolute $S_{34}(0)$ value is 25% smaller.

Usage of spectroscopic factors by potential models can justify the fact of considering rescaling parameters in order to fit the experimental data and extrapolate to lower energies. Rescaled Microscopic models should be as accurate as potential models and more accurate than hard-sphere model [AGR11]. Some experimental data evaluations have been also carried out. Descouvemont et al. use R-matrix fit analysis (essentially reduced to a potential model) to determine the $S_{34}(0)$ [DAA04]. Cyburt and Davids, [CD08], evaluated the experimental modern data from Weizmann [NHNEH04], Seattle [BBS07], and LUNA [BCC06, GCC07, CBC07] using a minimal model-dependent approach. They based their work on the fact that the reaction is dominated by external capture and the S-factor exhibits subthreshold poles in low energy astrophysical range according to Mukhamedzhanov and Nunes [MN02]. The *Solar Fusion Cross Section II* evaluation [AGR11], uses rescaled theoretical models of Nollet [Nol01] and Kajino [Kaj86] (the energy dependence is the same) to fit the same modern data used in the evaluation of Cyburt and Davids, plus the ERNA data [DGK09] up to 1 MeV.

The first ab-initio calculations by Thomas Neff [Nef11] are based on a fully microscopic fermionic molecular dynamics (FMD) approach with a realistic interaction that reproduces the nucleon-nucleon scattering data. Specifically, this model uses the Argonne V18 Interaction which reproduces the deuteron properties and the nucleon-nucleon phase shifts. The known properties of the bound state such as the charge radii, quadrupole moments or energy could be well reproduced by the calculations. The calculated phase shifts in the s-wave and d-wave channels agree also fairly well with the experimental data in [ST67, BBH72]. To obtain the cross section of the $^3\text{He}(\alpha,\gamma)^7\text{Be}$ reaction only dipole transitions (E1) from the s- and d-waves are considered. There seems to be a significant contribution

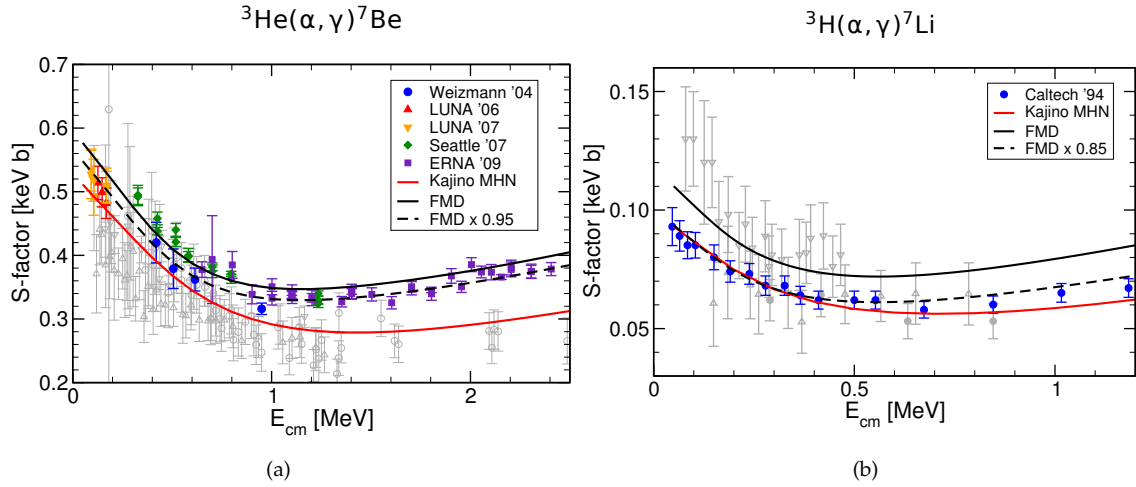


Figure 2.6: The black line shows the *ab-initio* astrophysical S -factor calculations for the reactions ${}^3\text{He}(\alpha,\gamma){}^7\text{Be}$ (a) and ${}^3\text{H}(\alpha,\gamma){}^7\text{Li}$ (b). The red line shows the calculations by Kajino [Kaj86].

of the internal part of the nuclei and therefore the reaction should not be considered purely external. The agreement with the modern data is remarkable up to 2.5 MeV (note that the Solar Fusion Cross Section II considered only up to 1 MeV) as it can be seen in Figure 2.6(a). However, for the isospin mirror ${}^3\text{H}(\alpha,\gamma){}^7\text{Li}$ reaction, even though the energy dependence is well described when comparing with the new experimental data of Brune et al. [BWR94], the absolute scale is off 15% (see Figure 2.6(b)). This should be further investigated. Modifications in theory may be required to reproduce both reactions if new experimental data are obtained for both reactions at medium energies.

Table 2.1 shows $S_{34}(0)$ values from for different evaluations and models highlighting the discrepancies among them.

Model/Evaluation	$S_{34}(0)$ (keV·b)
R-matrix [DAA04]	0.51 ± 0.04
Cyburst and Davids [CD08]	0.580 ± 0.043
Solar Fusion Cross Sections II [AGR11]	$0.56 \pm 0.02(\text{expt}) \pm 0.02(\text{theor})$
Ab-initio calculations [Nef11]	0.593

Table 2.1: $S_{34}(0)$ values from different theoretical models and evaluations. R-matrix and Cyburst and Davids use experimental data evaluation. Solar Fusion Cross Section II evaluation use the theoretical models of Kajino et al. [KTA87] and Nollet [Nol01] and the experimental data up to 1 MeV. Finally, the FMD *ab-initio* calculation do not utilise any data but directly gives obtain the $S_{34}(0)$.

In Figure 2.7 the most used theoretical calculations are plotted together with the modern experimental data. The theoretical curves are given without any normalisation. As mentioned earlier, the theoretical models could be normalised to fit the experimental data. Regardless the effect of normalisation, there is discrepancy in the energy dependence at high energy, and none of them completely reproduce the observed resonance corresponding to the $7/2^-$ state in ${}^7\text{Be}$. New experimental data in the range of 1-3 MeV will constrain the theoretical models and help understanding the importance of the non-external nuclear contributions.

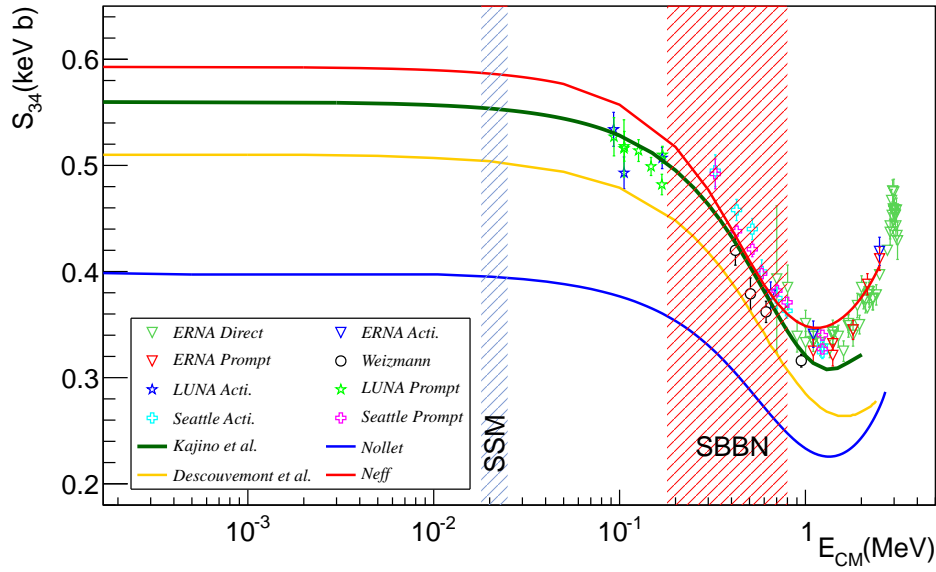


Figure 2.7: A comparison between the theoretical models from Kajino et al. [KTA87], Nollat [Nol01], Descouvemont et al. [DAA04] and Neff [Nef11], plotted together with the modern data from ERNA [DGK09], Weizmann [NHNEH04], LUNA [BCC06, CBC07, GCC07] and Seattle [BBS07]

2.6 Conclusion

In this chapter the ${}^3\text{He}(\alpha,\gamma){}^7\text{Be}$ has been described in terms of a nuclear reaction as an electromagnetic transition between an ${}^3\text{He}+{}^4\text{He}$ scattering state and a bound state in ${}^7\text{Be}$. The general formalism to obtain the cross section of such reactions has been described together with the phase shift analysis procedure for elastic channel. The main features of different theoretical models have been described. Differences between the theoretical models at medium-high energy are observed, not only in the absolute scale, factor but also in the energy dependence. New experimental in the range of $E_{\text{CM}}=1\text{-}3$ MeV will help us to constrain the theoretical models and to investigate the importance of the non-external nuclear contribution to the cross section. The importance of the phase shift analysis has also been demonstrated. Although it will be discussed in Chapter 6, it is worth mentioning here, that new experimental elastic scattering data would be also needed as most of the potentials and microscopic models rely on the phase analysis on one experiment in the 1960's.

"A theory is something nobody believes, except the person who made it. An experiment is something everybody believes, except the person who made it."

Albert Einstein

CHAPTER 3

EXPERIMENTAL TECHNIQUES

Abstract: In this Chapter the two experimental techniques used to determine the cross section of the ${}^3\text{He}(\alpha,\gamma){}^7\text{Be}$ reaction will be described. Firstly, experimental approaches used in previous works will be recalled. Later, the two main sections will detail the two complementary activation and direct recoil counting methods together with the setups used in our measurements to determine $\sigma(E)$ and evaluate the astrophysical S-factor. The observables and the error contributions as well as all the other necessary details to determine the cross section and the consistency checks for the two types of methodologies will be discussed.

In the previous Chapters motivation for obtaining the astrophysical S-factor for the ${}^3\text{He}(\alpha,\gamma){}^7\text{Be}$ reaction and the theoretical background have been detailed. Here, the experimental techniques used in order to determine the cross section, and thus the S-factor are described.

A well designed experimental setup with good control of the different settings is the key for successful measurements and reliable results with minimised uncertainties. Different approaches have already been used aiming to determine the accurate cross sections of this reaction at different energies. A few pros and cons of some of these methods will be presented in this Chapter.

In our case, two experiments using alternative and complementary techniques were performed in order to determine the cross section for the ${}^3\text{He}(\alpha,\gamma){}^7\text{Be}$ reaction at medium-high energies. The reason for selecting this energy range was discussed in the first Chapter and will be recalled here. In the first experiment, the *Activation Method* was chosen for simplicity allowing us a better control of the set up. For the second type of experiment, the *Direct Recoil Counting Method* was chosen employing the DRAGON spectrometer at TRIUMF. In contrast to the activation method this is a complicated setup and require extensive characterised tests. Information related to the prompt γ -ray angular distribution as well as the $\sigma_{429}/\sigma_{g.s.}$ ratio were also aimed for in this experiment.

3.1 The Reaction and the Methods for Cross Section Measurements

In Chapter 1 the important role of the ${}^3\text{He}(\alpha,\gamma){}^7\text{Be}$ reaction in the Sun and in the Big Bang Nucleosynthesis were discussed. A schematic picture of how the reaction takes place, for example in the Sun, can be seen in Figure 3.1. ${}^4\text{He}$ and ${}^3\text{He}$ nuclei approach each other and when the nuclei overcome the Coulomb and centrifugal barriers fusion occurs, creating a ${}^7\text{Be}$ nucleus and emitting a prompt γ ray. The ${}^7\text{Be}$ ions are unstable and decay to the first excited state at 478 keV in ${}^7\text{Li}^*$ by the electron capture process with a half life of 53.24(4) days and a branching ratio of 10.44(4)%. A γ ray of 478 keV is subsequently emitted by the de-excitation of the excited ${}^7\text{Li}^*$ to ground state.

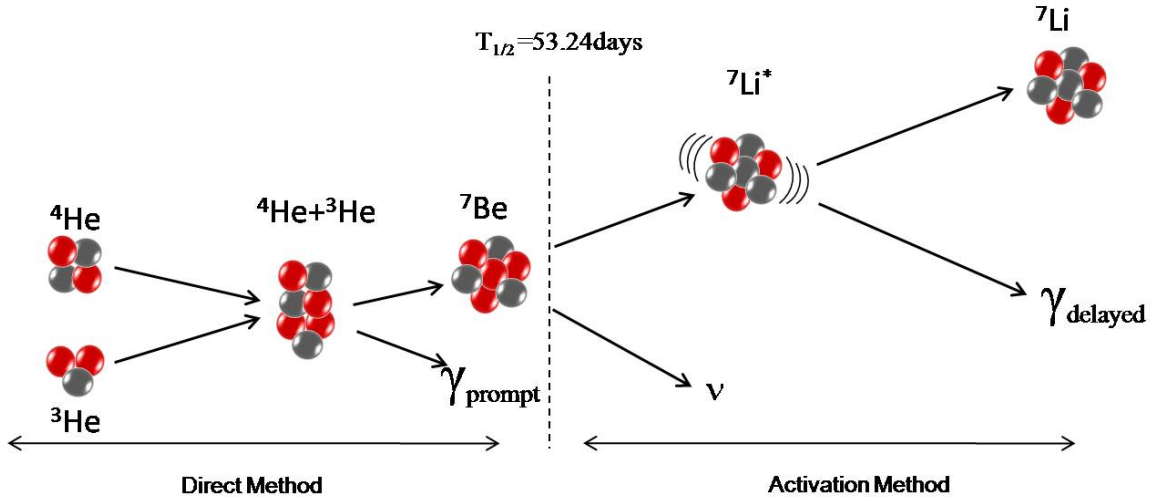


Figure 3.1: Diagram showing the ${}^3\text{He}$ capture on ${}^4\text{He}$, emission of the prompt γ -ray and the subsequent decay of the reaction product, ${}^7\text{Be}$. The ${}^7\text{Be}$ ions decay via electron capture producing ${}^7\text{Li}^*$ in its first excited state and emitting a neutrino with a branching ration of 10.44(4)%. The subsequent 478 keV γ -ray from ${}^7\text{Li}^*$ is also shown. In the lower part regions representing the two experimental methods used in the present work are also indicated.

A sketch of the decay scheme of the reaction is shown in Figure 1.12. Some information relevant for this reaction is specified in Table 3.1.

$Q_{{}^3\text{He}(\alpha,\gamma){}^7\text{Be}}$	1580(1) keV
$E({}^7\text{Be}_{1^{\text{st}}\text{state}}^*)$	429 keV
$T_{1/2}({}^7\text{Be})$	53.24(4) d
$Q_{{}^7\text{Be}(e^-, \nu){}^7\text{Li}}$	862 keV
B.R. (${}^7\text{Li}_{1^{\text{st}}\text{state}}^*$)	10.44(4)%
$E({}^7\text{Li}_{1^{\text{st}}\text{state}}^*)$	478 keV

Table 3.1: Some details of the ${}^3\text{He}(\alpha,\gamma){}^7\text{Be}$ reaction, ${}^7\text{Li}$ and ${}^7\text{Be}$ nuclei. "Q" represents the Q-value for the reaction and ${}^7\text{Be}$ decay. E corresponds to the energies for the different states in ${}^7\text{Li}$ and ${}^7\text{Be}$. $T_{1/2}$ is the half life of the ${}^7\text{Be}$ nucleus and B.R. is the branching ratio populating the first excited state in the ${}^7\text{Li}$.

The important parameter needed for the astrophysical models is the S-factor, given through the cross section $\sigma(E)$ as detailed in the expression 1.7. Therefore, the aim of our measurements is to determine the absolute cross section of the ${}^3\text{He}(\alpha,\gamma){}^7\text{Be}$ reaction and from there estimate the S-factor, which will be denoted as $S_{34}(E)$, where E is the centre of mass energy. In order to determine

$\sigma_{34}(E)$ by carrying out measurements in the laboratory one of the helium interacting isotopes must be accelerated as a beam and the other should be the target (recall that at atmospheric conditions the natural state of the helium is gaseous). Accurate determinations of an absolute cross sections need careful measurements of different observables. Taking a glance at the Figure 3.1, if one wants to determine the absolute cross section of the reaction, the number of total ${}^7\text{Be}$ produced ($Y_{7\text{Be}}$) and the total number of interacting nuclei ($N^{\circ}{}_{4\text{He}}, N^{\circ}{}_{3\text{He}}$) must be known. Therefore, the expression 1.2 for $\sigma(E)$ assumes the following form in this case

$$\sigma_{34}(E) = \frac{Y_{7\text{Be}}}{N^{\circ}{}_{4\text{He}} \cdot N^{\circ}{}_{3\text{He}}} \quad (3.1)$$

From a close look at Figure 3.1, it can be seen that there are three possible methods to obtain the cross section, namely:

- *Direct Recoil Counting Method:* The ${}^7\text{Be}$ recoils are detected directly.
- *Prompt γ -Detection Method:* The number of recoils are determined by detecting the prompt γ -rays.
- *Activation Method:* The recoils are collected and their total number is estimated by detecting the 478 keV γ -rays from the ${}^7\text{Li}^*$ de-excitation.

Apart from the three different experimental techniques already discussed, two other approaches can be found in the literature, namely *Accelerator Mass Spectrometry (AMS)* and the *Coulomb Breakup* techniques (see below).

Furthermore, even though the goal of the different techniques is the same, when determining the cross section differences appear also, for example, in how the total number of incoming beam particles are measured, whether kinematic is direct or inverse, in the detection systems, and in assumptions made e.g. in the prompt γ -ray distributions. An overview of all experiments using the three different techniques can be seen in the section 1.5. Here, some differences among the different setups will be briefly described, in particular, those performed at LUNA (Laboratory for Underground Nuclear Astrophysics) and ERNA (European Recoil separator for Nuclear Astrophysics).

LUNA SETUP

The Laboratory for Underground Nuclear Astrophysics [GAB94, Bro11] in Italy's Gran Sasso underground laboratory (LNGS) was designed for measuring low cross sections of nuclear astrophysics reactions. The ${}^3\text{He}(\alpha, \gamma){}^7\text{Be}$ cross section measurement was carried out using the 400 kV LUNA2 accelerator where the *Prompt γ -Detection* and *Activation Methods* covering a centre of mass energy range from 93 keV to 170 keV were used. The setup used is shown in Figure 3.2(a). A ${}^4\text{He}$ beam impinged onto a windowless differentially pumped ${}^3\text{He}$ gas target. The beam was stopped in a copper disk placed in front of the calorimeter which estimated the incoming number of beam particles. The ${}^7\text{Be}$ recoils were deposited in the same copper plate. A silicon detector monitored the ${}^3\text{He}$ gas density by detecting the double scattered beam particles with the gas and the carbon foil. In the *Prompt γ -Detection Method* the prompt γ -rays were detected in the shielded High Purity Germanium (HPGe) detector, while for the *Activation Method* the copper plates were removed and the subsequent γ -ray from the ${}^7\text{Li}$ de-excitation was detected with another germanium detector in a low-background environment.

ERNA SETUP

The European Recoil separator for Nuclear Astrophysics (ERNA) is located at the 4MV Dynamitron Tandem Laboratorium of the Ruhr-Universität Bochum, Germany. A general definition of recoil separators is given in section 3.3.1. A layout of the global ERNA setup is shown in Figure 3.2(b) and details can be found in [DDS08] and references therein. The three techniques mentioned above

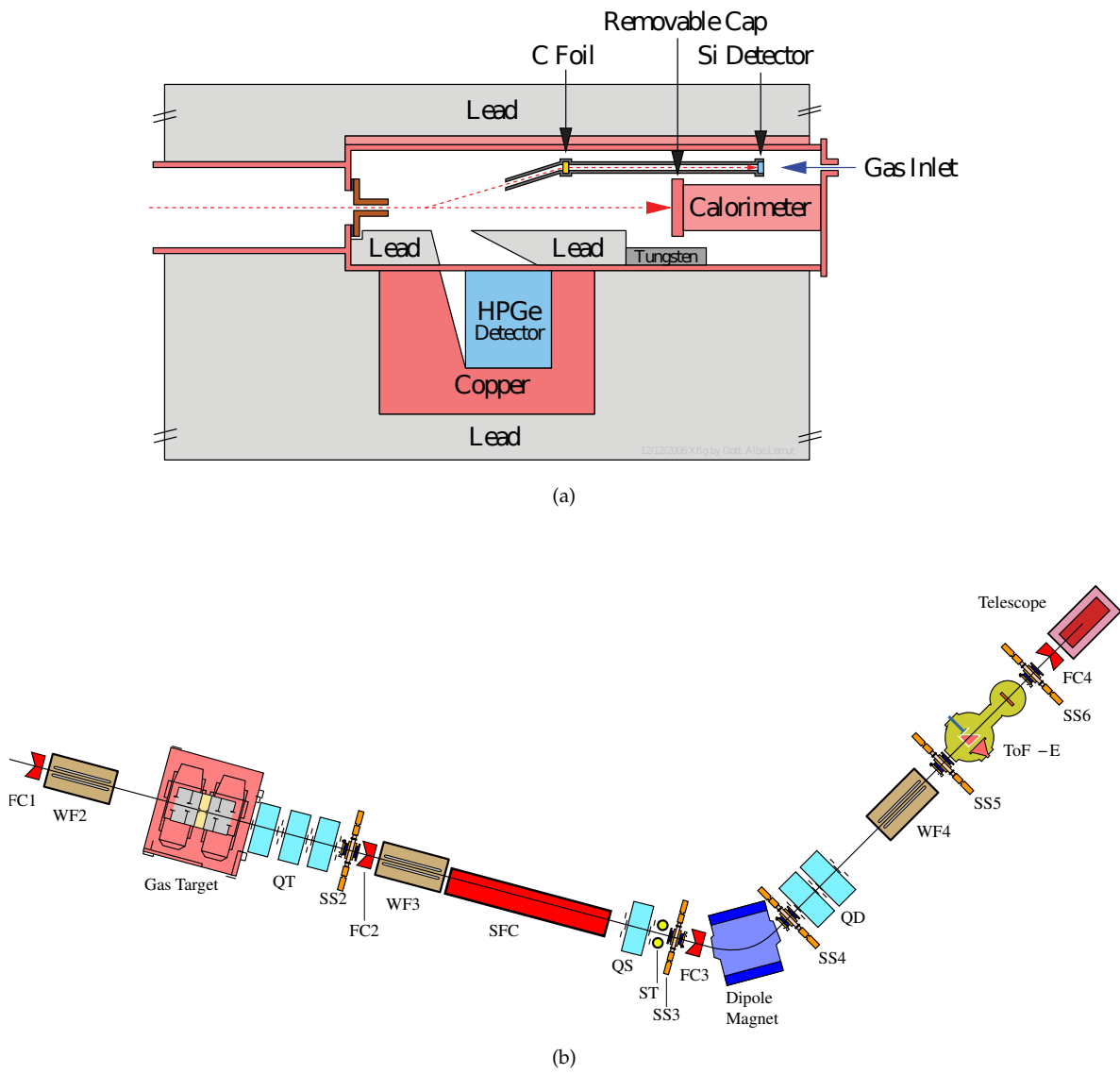


Figure 3.2: Examples of different experimental setups used for determining the cross section of the ${}^3\text{He}(\alpha,\gamma){}^7\text{Be}$ reaction. (a) LUNA setup sketch [CBC07]. (b) ERNA layout from [DDS08]

were used in the ERNA collaboration to determine the cross section of the ${}^3\text{He}(\alpha,\gamma){}^7\text{Be}$ reaction in the centre of mass energy region 700-3100 keV. A recirculating gas system was used to maintain a constant ${}^3\text{He}$ gas pressure in the target cell that was impinged by a ${}^4\text{He}$ beam. The number of the incoming beam particles were measured by using Faraday cups placed along the separator and the ${}^3\text{He}$ target density was scaled from previous measurements using a ${}^4\text{He}$ gas target. For the *Direct Recoil Counting Method* the ${}^7\text{Be}$ recoils were separated from the leaky beam by using various electric and magnetic elements of the separator. Eventually, the recoils were directly counted in a Gas Silicon Telescope placed at the end of the separator. In the *Prompt γ -Detection Method* the prompt γ -rays were detected using three NaI detectors placed close to the gas cell. Finally, in the *Activation Method*, a copper catcher was placed at 31 cm from the target cell where the ${}^7\text{Be}$ were deposited. The ${}^7\text{Be}$ activity was measured in the LNGS using the same setup than the one used in LUNA work.

The ${}^7\text{Be}$ recoils implanted in a catcher could also be counted using the *AMS technique*. In order to prove the reliability of the technique, a known quantity of ${}^7\text{Be}$ by using the reaction ${}^7\text{Li}(p,n){}^7\text{Be}$ was produced in the 3MeV Van de Graaff accelerator of the Weizmann Institute. Later, with the ${}^7\text{Be}$, BeO^- samples were prepared by adding a precisely determined quantity of ${}^9\text{Be}$. While the ratio ${}^7\text{Be}/{}^9\text{Be}$ chemically calculated was expected to be $4.4\cdot 10^{-13}$, the measured ratio with the AMS quoted $1.2\cdot 10^{-13}$. Several potential sources were suggested to explain this discrepancies and further investigation was planned according to [BBBH01]. However, there have been no such further measurements to date.

On the other hand, two indirect experiments were also tried in an attempt to reduce the uncertainties of the cross section of the ${}^3\text{He}(\alpha,\gamma){}^7\text{Be}$ reactions: ${}^7\text{Be}$ break up on ${}^{208}\text{Pb}$ target at 100 MeV/u at the National Superconducting Cyclotron Laboratory and on ${}^{12}\text{C}$ target at 25 MeV/u (*Coulomb Breakup* technique). The idea was to extract the $S_{34}(0)$ value from the indirect Coulomb breakup. In order to do so the nuclear and Coulomb effect must be clearly separated. As it was concluded in [SN04], it is not clear whether this method will help to improve the $S_{34}(0)$ as it is not possible to eliminate the nuclear contribution by just angular selection criterion. No further improvements on this method have been reported so far.

To summarise, different energy regions can be addressed using different facilities, techniques, and detectors. In the following subsections the energy region of our interest the techniques facilities employed to carry out our experiment will be reasoned out, [Nar13]. The details of the two experimental setups will then follow.

3.1.1 Energy range for the present work

As discussed in Chapter 1, a large scattered among the experimental $S_{34}(E)$ data is observed, this is particularly remarkable between the two data sets [PK63, DGK09], in the region $E_{\text{CM}} = 1$ to 3 MeV centre of mass energy (see Figure 3.3).

The experimental limitations to determine the cross sections at low energies have already been mentioned. The cross section decreases doubly exponentially with decreasing energy (see for example the upper panel in figure 1.2) and thus measuring the cross section of the ${}^3\text{He}(\alpha,\gamma){}^7\text{Be}$ reaction at the relevant energies corresponding to the SSM (Gamow Peak ~ 22 keV) results impossible. As a consequence, theoretical models are often used (Chapter 2) to get the $S_{34}(0)$ value. As can be observed in Figure 3.3, these theoretical models also show discrepancy between themselves in the same 1-3 MeV energy region.

Therefore, we have measured the cross section of the ${}^3\text{He}(\alpha,\gamma){}^7\text{Be}$ reaction in this centre of mass energy region from 0.8 to 3 MeV aiming to address the current discrepancies between the data sets ([PK63, DGK09]). Despite being far from the astrophysical interesting energy region, these measurements are crucial to constrain the theoretical extrapolations, which currently disagree not only in absolute value of the $S_{34}(0)$ but also in the energy dependence $S_{34}(E)$ curves (see Figure 3.3).

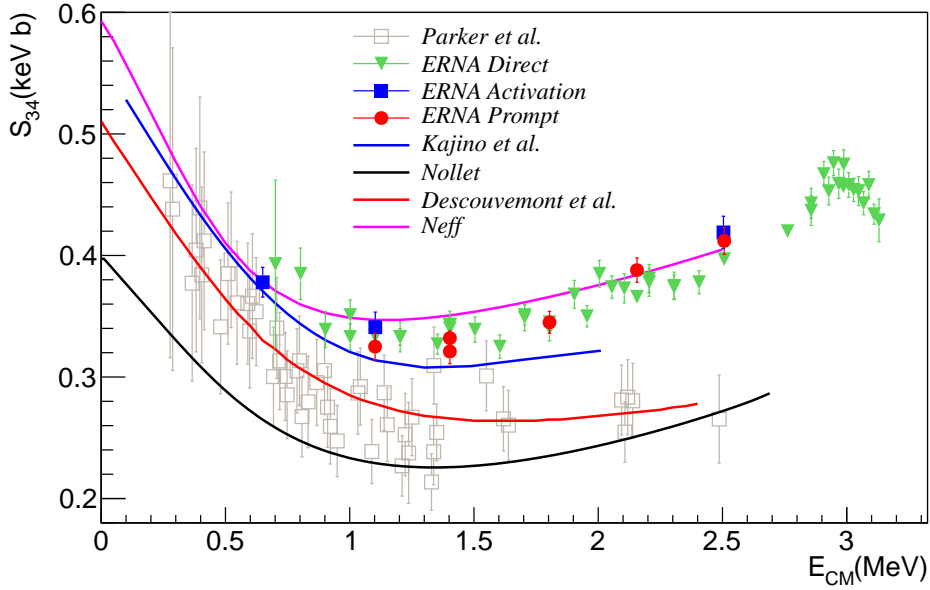


Figure 3.3: Comparison between the previous experimental values (points) of $S_{34}(E)$ from Parker et al. [PK63] and ERNA collaboration [DGK09], and theoretical models (lines) of Kajino et al. [KA84], Nollet [Nol01], Descouvemont et al. [DAA04] and Neff [Nef11] in the region of $E_{CM}= 1-3$ MeV.

3.1.2 Experimental methods: our choices

Among different approaches employed to determine the cross section of the ${}^3\text{He}(\alpha,\gamma){}^7\text{Be}$ reaction, the *Coulomb breakup* and the *AMS* are not suitable to obtain results with sufficient accuracy. In the *Prompt γ -Detection Method*, assumptions must be made about the prompt γ ray angular distributions. Moreover, HPGe detector are the best option in order clearly resolve and the prompt γ peaks; but low efficiency and usage of extended gas targets increase statistical uncertainties.

We thus decided to measure the cross section of the ${}^3\text{He}(\alpha,\gamma){}^7\text{Be}$ reaction by using the two different and complementary techniques: *Activation* and *Direct Recoil Counting* methods, [CGRB14].

3.1.3 Facilities and setups for the present work

After establishing the energy range of interest and the experimental methods of our choice, the facilities utilised for our measurements are introduced. The criteria for the choice of the laboratories include availability of stable (non radioactive) ion beam of ${}^3\text{He}$ or ${}^4\text{He}$ with well defined and stable (within a fraction of keVs) beam energies in the region of 2-7 MeV.

Nowadays, there are many particle accelerators facilities around the world. Among those devoted to nuclear physics and astrophysics many of them are dedicated mainly to produce radioactive ion beam (RIB facilities) such as ISOLDE at CERN (Geneva, Switzerland), IGISOL (Jyväskylä, Finland), GSI (Darmstadt, Germany) and RIKEN (Japan). There are also others including small scale accelerator facilities as CNA (Seville, Spain) which fulfil criteria for our measurements without the need of using a large scale accelerator.

On the other hand, in order to carry out an experiment using the *Direct Recoil Counting Method*, further arrangements are required. Due to the kinematic conditions of the reaction, the recoils are produced with momentum in forward direction following the beam path. In order to count the recoils, we need to separate and identify them from the beam particles. In principle one could use a detector such as double sided silicon strip detectors (DSSSD), ionisation chambers, or configuration of different detectors as telescopes which would allow an identification of particles based on their energies and masses. However, with the high beam currents usage in our case due to the low cross sections, such detectors could not be used as they would get damaged if particles with high rates hit them.

Taking into account the previous issues two different types of experiments were performed employing the *Activation* and *Direct Recoil Counting* techniques. The *Activation* experiment was performed using the tandem accelerator at the CMAM facility, in Madrid, Spain. We used the setup that was successfully used at the Weizmann Institute to determine the cross section of the same reaction in the centre of mass energy region 420-950 keV [NHNEH04]. For the *Direct Recoil Counting* experiment we used the DRAGON recoil separator at the TRIUMF laboratory in Vancouver, Canada. The separator has already been used for measuring several astrophysical reaction cross sections. The capture reaction studies in the present work has beam and target particles of similar mass which yields a recoil cone angle that is at the limits of the DRAGON separator acceptance. As we will see, it will however allow us to separate beam ions from recoils and together with simulations reliable cross sections measurements can be performed.

In the activation method a ${}^3\text{He}^+$ beam at nine different energies in the range of $E^{\text{beam}} = 2.1\text{--}5.3$ MeV and a ${}^4\text{He}$ gas target in conjunction were used. The ${}^7\text{Be}$ recoils produced were collected in a Cu catcher and the subsequent γ -rays from the de-excitation of the ${}^7\text{Li}$ were detected. Recall here that even the standard way to denote this reaction in this case would be ${}^4\text{He}({}^3\text{He},\gamma){}^7\text{Be}$ because the beam is ${}^3\text{He}$, I will follow the convention of the typical astrophysical (α,γ) reactions and I will denote it as ${}^3\text{He}(\alpha,\gamma){}^7\text{Be}$.

In the direct recoil counting method the target consisted of a windowless ${}^3\text{He}$ gas, and the beam was ${}^4\text{He}$. Four different beam energies between 3.5 and 6.5 MeV were used. In this case, the ${}^7\text{Be}$ recoils were directly counted in a double sided silicon strip detector (DSSSD) at the focal plane of the DRAGON separator.

3.2 Activation Method @ CMAM

The experiment was performed at CMAM (Centro de MicroAnálisis de Materiales) in Madrid [CMA]. CMAM houses an electrostatic linear tandemron accelerator and six beam lines. Figure 3.4 shows a layout of the accelerator hall and the beam lines. The *Nuclear Physics Line* was used to perform our measurements. This line was developed, designed and built by the Experimental Nuclear Physics Group at the Instituto de Estructura de la Materia (CSIC) -see [Sab03] for more details-. It is operating since the first experiment performed in April 2005 by the same group to study the excited states of ${}^{12}\text{C}$ using complete kinematic techniques [Alc06].

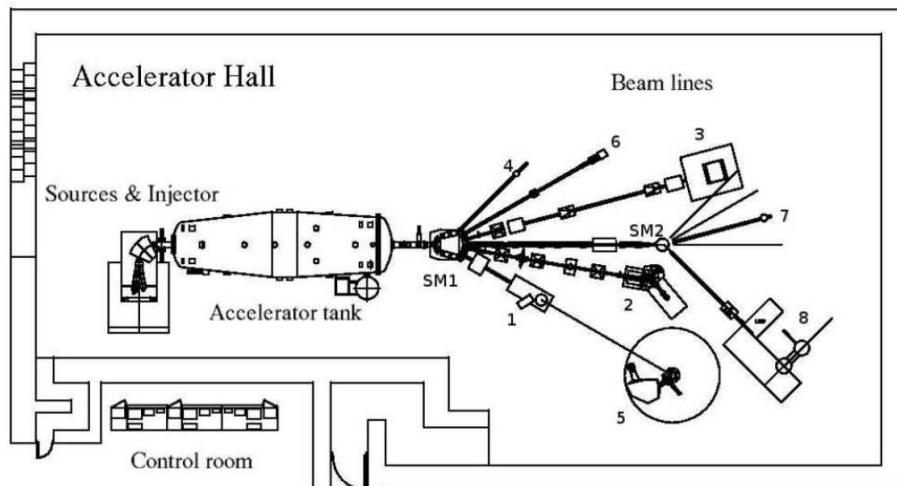


Figure 3.4: Layout of the CMAM accelerator hall (courtesy of [Pas04]). The magnet (SM1) switches the beam between several beam lines meant for: (1): Multi-purpose, (2): Time-of-Flight, (3): External micro-beam, (4) Environmental studies, (5) Magnetic spectrograph, (6) Nuclear Physics, (7) Ion-beam Modification of Material, and (8) Ultra-High Vacuum experiments. Our work took place in the Nuclear Physics Line.

At the CMAM accelerator, by the use of the Duoplasmatron or the Sputtering ion sources can nearly all elements be produced and accelerated. The Duoplasmatron ion source is mainly used to generate He ions and this was used in our experiment to produce ${}^3\text{He}^+$ ions in two discharge stages. The ions were then injected into a Lithium charge exchange canal producing the ${}^3\text{He}^-$ ions to be accelerated in the tandetron accelerator. A sketch of the ion source and the charge exchange canal are shown in Figure 3.5 and some details are given in the caption. The sputtering ion source is used for producing any other stable negative beam from solid sputter targets.

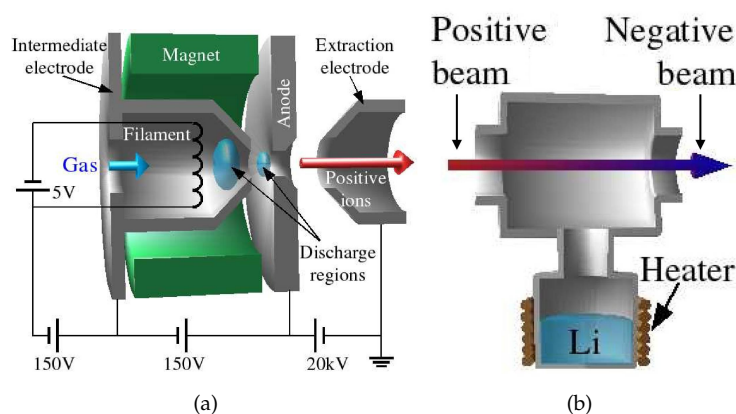


Figure 3.5: Sketch of the (a) Duoplasmatron ion source and (b) Lithium charge exchange canal (courtesy of [Alc10]). The He^+ ions are generated in two discharge stages in the ion source. A strong axial magnetic field confines the plasma into a small volume getting high plasma density. The He^+ ions flow through the anode aperture into the extraction region. They are then injected into a Lithium charge-exchange canal where they exchange electrons with Li vapour and get converted into ${}^3\text{He}^-$ ions.

The accelerator is a 5 MV coaxial high current tandetron using a Cockroft-Walton power supply system [GMH02]. The Cockroft-Walton system supplies beams highly stable in energy. This is a crucial requirement for this experiment because of the dependence of the cross section with energy, which demands not only a beam with precisely known energy but also constant energy throughout the runs. The maximum terminal voltage is 5 MV. The negative ions from the ion source are injected into the accelerator and are accelerated through a vacuum pipe towards the positive terminal placed at the centre of the accelerator. They cross a N_2 gas target, which strips the beam particles of atomic electrons producing positive beam ions. The ions with a charge state "q" are then repelled down to the end of the accelerator which is at ground potential. The final energy for the ions coming out of the accelerator is $E=V_T(q+1)$, where " V_T " is the terminal voltage.

3.2.1 Experimental setup

The experimental setup consisted mainly of a cylindrical reaction chamber placed at the end of the beam line. A schematic view of the reaction chamber is shown in Figure 3.6 and two photographs of the real setup are displayed in Figure 3.7. The reaction was produced by using a ${}^3\text{He}$ beam which impinged onto a ${}^4\text{He}$ gas target and the ${}^7\text{Be}$ ions created were collected in a 25 mm radius Cu catchers fixed in movable arm placed at the end of the chamber.

The ${}^4\text{He}$ gas target at pressures of ≈ 60 Torr was kept within the reaction chamber and was separated from the upstream beam line vacuum by a Ni foil window. A bypass system (see Figure 3.7(a)) was used in order to get pressures below 10^{-6} mbar in the chamber before filling it with the ${}^4\text{He}$ gas, guaranteeing no air contamination in the gas target. A constant ${}^4\text{He}$ gas flow of ≈ 1 litter/hour using a complex valves system ([Ten96]) was set in order not to overheat the target due to the beam intensity and to maintain the purity of the gas during the measurements. The pressure was monitored using a high precision pressure gauge, and the fluctuations were lower than 0.2%.

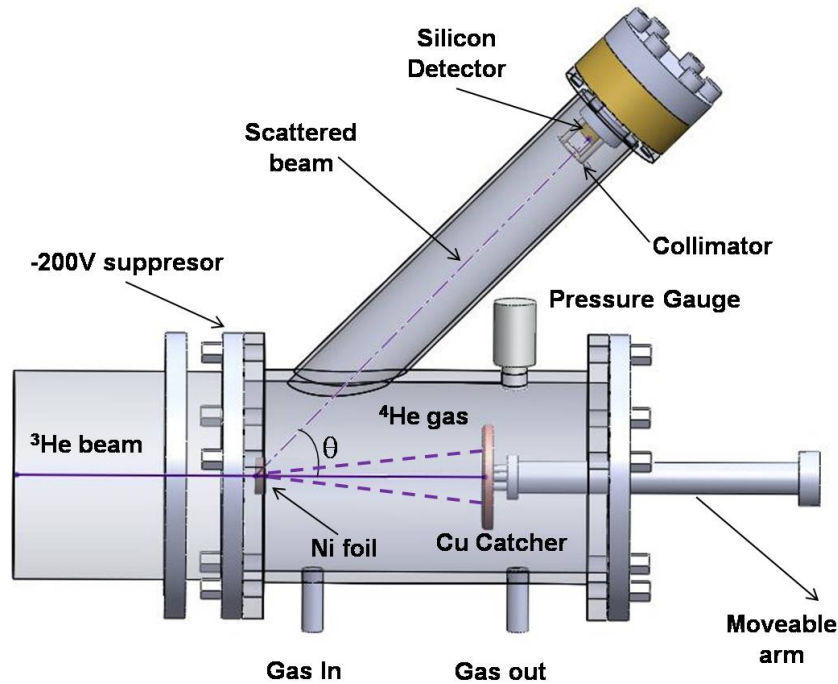


Figure 3.6: A Schematic view of various components that are part of the reaction chamber. The reaction was produced using a ^3He beam impinging onto a ^4He gas target that is "vacuum isolated" from the beam line using Ni foil. A Cu catcher placed on a movable arm at the end of the chamber was used to collect the ^7Be recoils. The subsequent γ -rays of the ^7Be were measured off-line using a specialised low background station. A silicon detector was placed at $\approx 45^\circ$ for monitoring the scattered beam from Ni foil. An electron suppressor kept at -200 V was placed before the Ni foil. See text for more details.

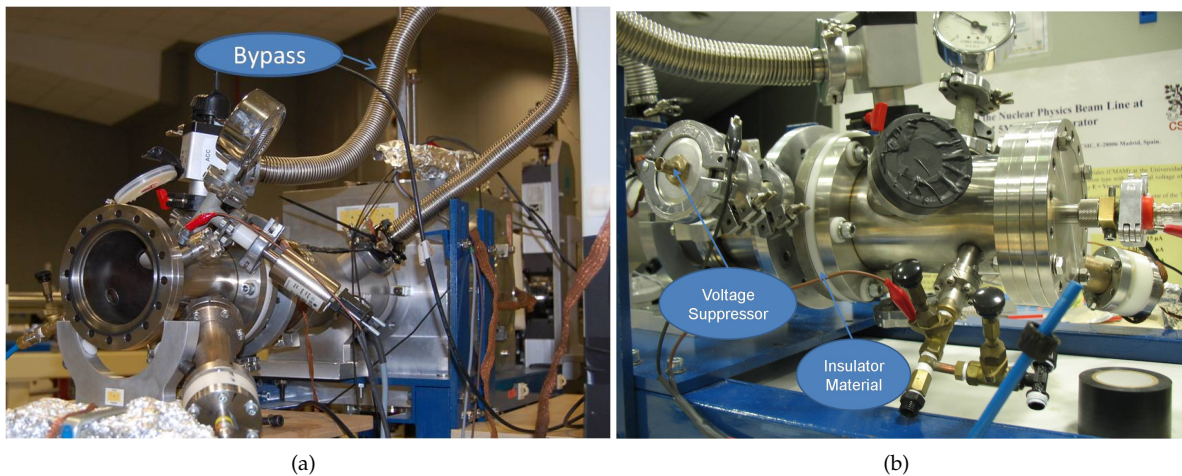


Figure 3.7: Photographs of the setup used installed at the Nuclear Physics Line at CMAM. (a) General view of the setup placed at the end of the line without the final closing flange. The bypass tube connecting the beam line and the chamber is marked. Before filling the reaction chamber with the ^4He gas, a pressure of $\approx 10^{-6}$ mbar was achieved inside the chamber using the turbo pumps in the beam line with the bypass open. The bypass was then closed and the chamber was filled with the ^4He gas target. (b) Closer view of the reaction chamber where the electron suppressor and the insulator plate are indicated. See Figure 3.6 for more details about the setup.

A collimated silicon detector placed at $\theta \approx 45^\circ$ with respect to the beam direction was used to estimate the number of incoming particles by monitoring the scattered beam from the Ni foil at the different energies. Details of how this silicon detector works can be found in appendix A.

The chamber was electrically isolated from the beam line. The elements such as Cu catcher and detector were electrically connected to the chamber and together they acted as a Faraday cup to monitor the incoming beam. An electron suppressor with an applied voltage of -200V was set before the Ni foil, avoiding an increased current due to the secondary electrons from the beam impact escaping from the Ni foil. The current was measured using a calibrated current NIM Digital Current Integrator (ORTEC module 439 [ORT]) whose output signal was displayed on a NIM scaler (CAEN module N1145 [CAE]), showing the current rate (incoming beam particles per second), and the accumulated current for each measurement.

The output signals of the silicon detector and the integrated charge signal were processed and saved using the electronic setup shown in Figure 3.8. When a ^3He ion hits the Si detector, it creates an electric signal proportional to the deposited energy. The signal usually has a low amplitude and must be amplified and processed before being digitised and saved. The detector output signal was doubled at the first stage of the processing (in the preamplifier) and they were processed separately. With the first chain ("energy chain") the information about the deposited energy is kept, while the second chain ("temporal chain") keeps temporal information of the signal, required to gate the energy signal in order to select the region of interest and to avoid making the DAQ system busy with noise. The caption in Figure 3.8 describes more details and the specifications of the modules can be read in appendix A.

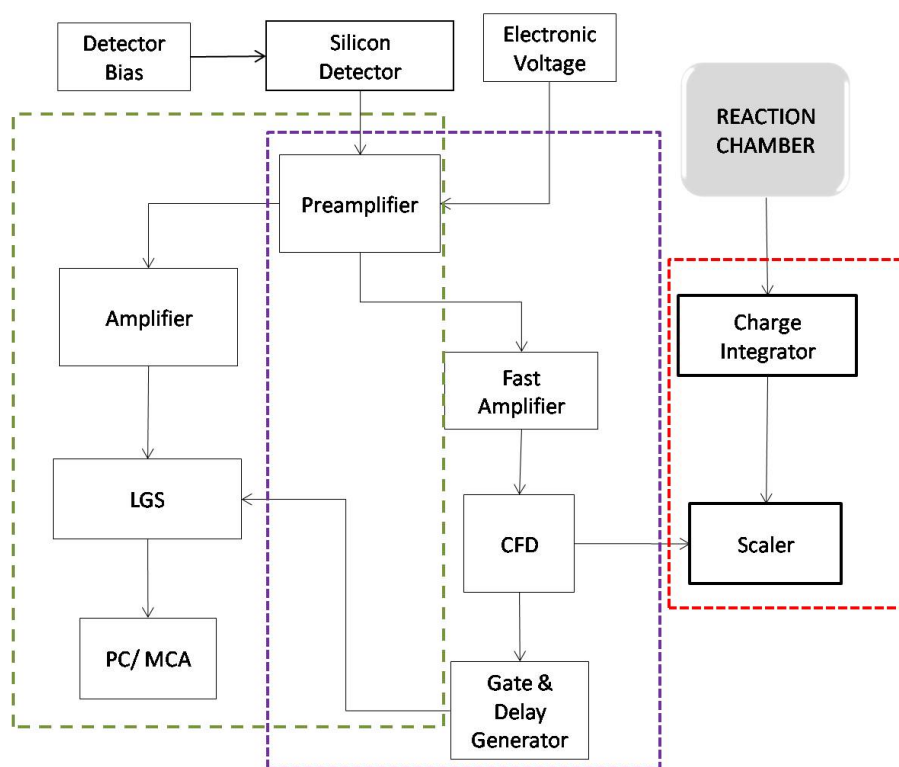


Figure 3.8: Diagram of the electronic used in the activation experiment at CMAM. The dash green line includes all modules used to obtain the energy spectrum in the silicon detector ("energy chain") and the violet one contain those modules used to filter the signals in order to discard electronic noisy and background signals ("temporal chain"). The red dash lines encloses the electronic modules used to integrate the electric charge in the chamber. The output signal from the detector is firstly pre-amplified. Two equal outputs signal comes out from the pre-amplifier, one to be process in the energy chain and the other in the temporal chain. LGS: Linear Gate Stretcher, MCA: Multichannel Analyzer, CFD: Constant Fraction Discriminator. Appendix A describe the specifications of the different modules.

3.2.2 Details of the measurements

The experiment was performed during two periods, in 2009 and 2011. Five measurements for different ^3He beam energies were used during each of these periods. In order to reduce the uncertainties every variable, i.e., constant pressure, target length or beam energy are kept under control and continuously monitored during the experiment. If the chamber is filled with the gas target and the catcher is placed in its position, as soon as the beam hits the target the ^7Be implantation starts. Therefore, all the tests were carried out with no gas in the chamber. If a catcher was present during test done with the target gas, then a new catcher was placed for the following production run, wasting scheduled beam time. The beam time utilisation is vital in this experiment because the cross section of this reaction is in the order of μb (based on the ERNA data [DGK09]) therefore, production time was optimised in order to minimise the statistical error contributions. In addition, as will be explained below, the catchers were sent to Israel and the γ activity from the Cu catchers was measured using a specialised low background γ counting setup.

In the 2009 experiment, each measurement was performed continuously and the target length was fixed at the beginning of each measurement. In the 2011 run it was not possible to run the accelerator overnight and each measurement was divided in two or three different days in order to optimise the ^7Be implantation, fixing the target length in the first day. In this case, after measuring during one day, the setup was remained without any changes except that the target was replaced with fresh supply next day.

Some details of the measurements performed with the activation experiment are shown in Table 3.2. For the measurements taken during the 2011 experiment an effective implantation time was calculated according to the procedure in reference [FM62].

$E_{^3\text{He}}$ (keV)	T_{IMP} (hr)	Year
2105.89 ± 2.23	10.2	2011
2306.28 ± 2.37	9.9	2009
2506.67 ± 2.51	11.6	2011
2807.26 ± 2.71	10.9	2011
3208.05 ± 2.99	8.6	2009
4009.63 ± 3.54	16.1	2011
4410.42 ± 3.82	8.1	2009
4811.20 ± 4.09	5.1	2009
4811.20 ± 4.09	6.7	2011
5312.19 ± 4.44	6.6	2011

Table 3.2: Details of the measurements performed in Madrid in 2009 and 2011 using the Activation Method. The ^3He incoming beam energies within the error given by the accelerator are shown in the second column, the third column shows the implantation time for each energy.

3.2.2.1 Experimental energy determination

The incoming beam energy is precisely estimated from the terminal voltage. In general, for a tandem accelerator, the energy of the beam, E^{beam} , is calculated from:

$$E^{\text{beam}} = E_{\text{ext}+(n+1)} \cdot V_T \quad (3.2)$$

where "E_{ext}" is the extraction energy of the beam from the source. For the case of ³He it is 18 V. Although according to the manufacture the error associated is ±2%, it has been observed even smaller. In any case, it is negligibly small when comparing with the total beam energy. "n" is the charge state of the ³He ion, which in our case was 1⁺ and "V_T" is the actual terminal voltage. There is a calibration factor that relates the nominal terminal voltage we introduce for setting the accelerator during the experiment, V_{nom}, and the actual terminal voltage:

$$V_T = A + B \cdot V_{nom} \quad (3.3)$$

where "A" and "B" are the relation coefficients, unique for every machine.

After the 2011 measurements, the accelerator was re-calibrated using, among others, the resonance reaction ²⁷Al(p,γ)²⁸Si at 992 keV. The measurements resulted in the coefficients values: A=4.4±0.4 kV and B=1.0173±0.0007.

The beam energies have been determined from the nominal terminal voltages considered during the 2009 and 2011 experiments. The errors associated with the beam energies are given by the uncertainties in the relation coefficients A and B. The energy values together with their errors are shown in the second column in Table 3.2.

3.2.2.2 Observables

As can be seen from expression 3.1, in order to determine the reaction cross section and subsequently the S-factor, the total number of incoming particles, the number of recoils produced in the reaction, and the target areal density must be known:

- Two methods were simultaneously used for determining the number of ³He incoming number of particles. As already mentioned, the chamber as a whole was also a Faraday cup and the accumulated charge in the chamber was measured as a number of *Pulses*, where each pulse corresponded to 10⁻¹⁰C. The number of incoming particles could thus be estimated by using the following expression:

$$N_{3He} = \frac{Pulses \cdot 10^{-10}C}{q \cdot e^-} \quad (3.4)$$

here, q is the charge state of the incoming beam, which in this case was 1⁺ and e⁻ is the electron charge in coulombs. The current can be obtained dividing the previous expression by the measurement time. The typical currents during our experiment were around 200nA.

The second method was used to cross check the results for the number of incoming particles. These could be estimated using the ³He beam particles scattered from the Ni foil and detected in the silicon detector. The Coulomb interaction between the beam particles and the Ni foil can be given by:

$$V_c = 1.44(MeV \cdot fm) \cdot \frac{q_1 \cdot q_2}{R_n} \quad (3.5)$$

here, q₁=2 and q₂=28, and considering at first order approximation $R_n \approx 1.23(A_1^{1/3} + A_2^{1/3})$, V_c ≈ 12 MeV (for a more realistic square-well radius $R_n \sim 8fm$ and thus V_c ≈ 9MeV). Thus, as the incoming beam energies are below this value, only Coulomb interaction plays a role and therefore detected particles at a given θ depends on the Rutherford cross section given by:

$$\frac{d\sigma}{d\Omega} = \left(\frac{zZe^2}{4\pi\epsilon_0} \right)^2 \left(\frac{1}{4T_a} \right) \frac{1}{\sin^4 \frac{\theta}{2}} \quad (3.6)$$

where z and Z are the atomic number of the beam and target ions respectively, T_a is the incoming beam energy and θ is the scattered output angle with respect to the beam direction. Thus, as the elastic scattering cross section is known, the total number of incoming particles can be determined from the number of particles detected in the silicon detector and the areal density of the Ni foil.

• Due to the low pressures in the reaction chamber, it can be assumed that the gas behaves as an ideal gas, thus the gas target areal density (N_t) is estimated using the expression:

$$N_t = 9.66 \cdot 10^{18} \frac{l \cdot P}{T_0 + T_C} (^4\text{He}/\text{cm}^2) \quad (3.7)$$

where l in cm is the length between the Ni foil and Cu catcher (for each measurement this length was kept constant by fixing the movable arm in which the Cu catcher was placed), P in Torr is the gas pressure, and T_0 and T_c in kelvin are the room temperature and the correction in temperature due to the beam heating respectively. The temperature corrections (T_C) are calculated assuming a linear dependence on the beam power from the values in [NHNEH04].

• The ^7Be recoils were deposited in the 50mm diameter Cu catchers kept 11-12 cm downstream from the Ni foil. In order not to underestimate the cross section we need to guarantee that all the recoils are implanted in the copper catcher:

The beam straggling was simulated using the TRIM code [SRI] for different beam energies and effective target lengths according to Table 5.3. In our simulations it was considered that the point-like mono energetic ^3He beam punch through $1.03 \mu\text{m}$ Ni foil (see section 3.2.4.4) plus half of gas length, based on the assumption that the reaction takes place at the centre of the target. The straggling for the maximum and minimum energies are shown in Figure 3.9. On the other hand, due to the kinematics of the reaction, the momentum of the ^7Be recoils is along the beam direction, therefore are forward focused. The straggling of the ^7Be recoils passing through half of the target length before reaching the Cu catcher have also been simulated with TRIM. The monoenergetic recoil energies considered in the simulation corresponds to the recoil ion create at the centre of the gas target and the prompt γ -ray emitted at 90° . Figure 3.10 shows the simulated straggling of the ^7Be nuclei for the maximum and minimum energies.

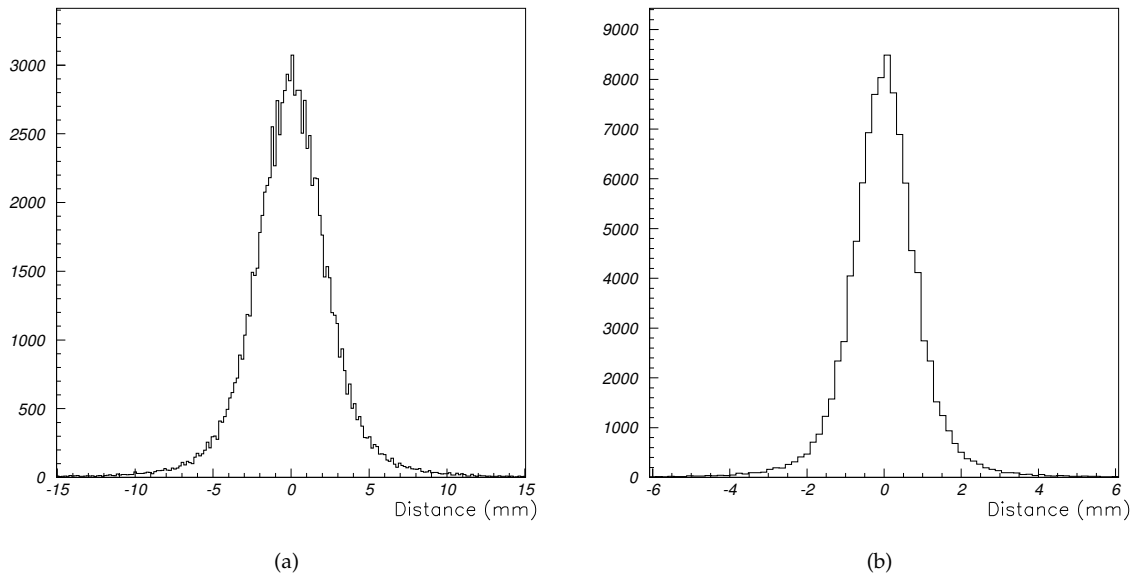


Figure 3.9: Mono-energetic point-like ^3He beam straggling distribution using 10^5 particles crossing the $1.03 \mu\text{m}$ of Ni foil plus half of the ^4He experimental target length. The simulations were run using TRIM code [SRI]. (a) Incoming beam energy of 2106 keV corresponding to the lowest energy measured and gas target length of $13.29/2=6.65$ cm. The FWHM of the distribution from a Gaussian fit results: 5.5 mm . (b) Same for 5312 keV incoming beam energy (highest energy measured) and same gas target length. The FWHM in this case results: 1.9 mm

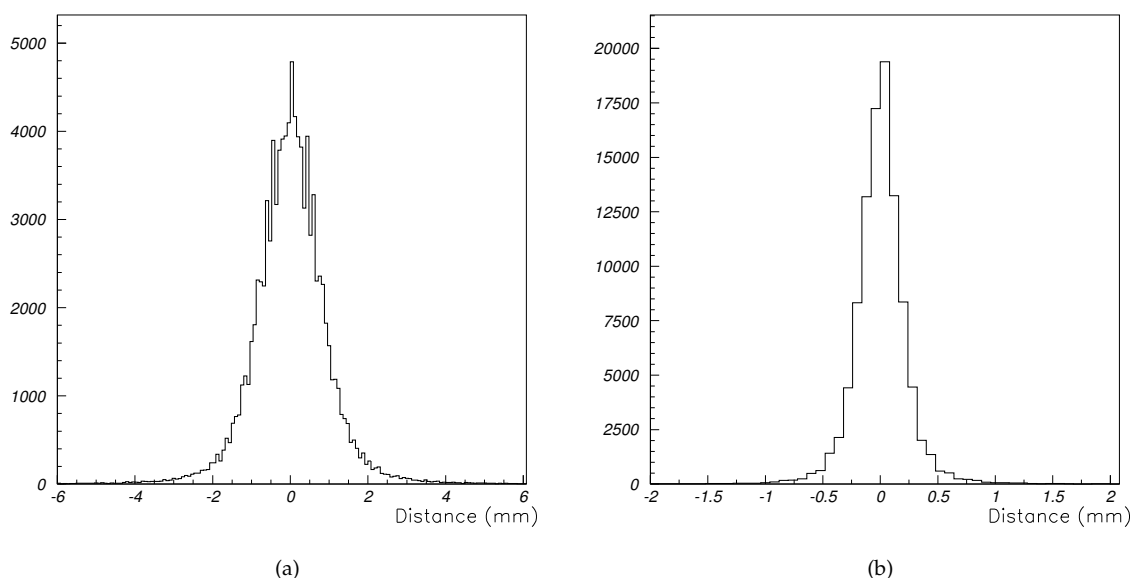


Figure 3.10: ${}^7\text{Be}$ recoil straggling distribution for 10^5 ions crossing half of the experimental target length. (a) Incoming energy of 585.5 keV corresponding to 1360 keV ${}^3\text{He}$ beam energy. The FWHM of the distribution from a Gaussian fit results in 1.9 mm. (b) Same for a ${}^7\text{Be}$ energy of 2112.1 keV corresponding to 4910 keV beam energy.

The beam optimisation was done at the beginning of every experiment. The final downstream flange of the chamber was replaced by another flange with a quartz viewer and a metal grid. The beam was monitored on the quartz using a camera. This assured a good overlap of the beam axis and the chamber axis so that the beam passed throughout the centre of the Ni foil and the ${}^3\text{He}$ gas target. Beam path also got an additional cross-check, namely this can be gauged by the level of agreement between the number of beam particles estimated using the chamber as a Faraday cup and the scattered beam detection in the Silicon detector. Two pictures of the beam showing both how it is centred in the Ni foil and the direction are shown in Figure 3.11.

From a beam spot size of 1-2 mm and a maximum ~ 5 mm straggling of the beam and ~ 2 mm for the recoils estimated by SRIM for the lowest energy, we can guarantee that all the recoils fall within a 20 mm on the 50 mm catcher.

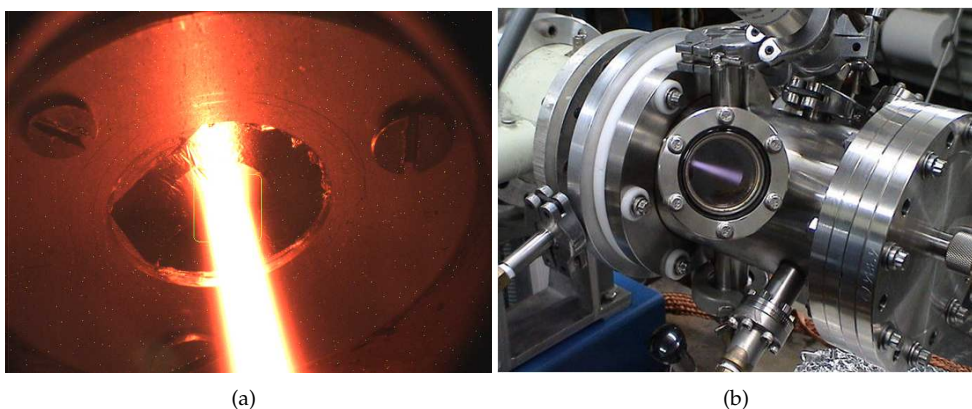


Figure 3.11: Photos taken during production runs as beam passing through the centre of the Ni foil (a) and the gas target (b). The violet colour is due to the light emission following ionisation of the target ions because upon the beam impact.

3.2.3 Setup for γ -activity measurements

One catcher was used for each measurement at a given energy. After the recoil implantation the delayed 478keV γ -activity from the catchers was measured off-line at the low-background detection station of Soreq Research Center, Yavne, Israel. A sketch of the station is shown in Figure 3.12.

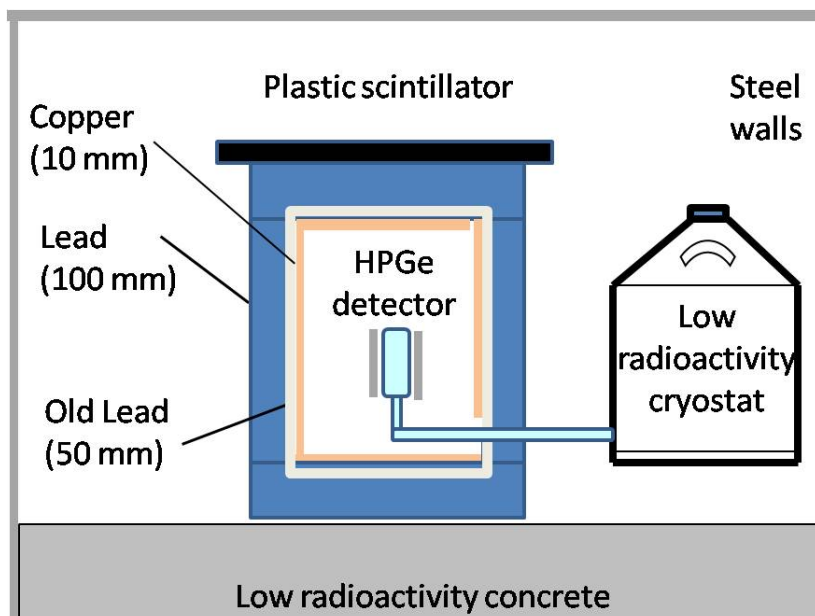


Figure 3.12: A sketch of the HPGe low background station at SOREQ. See text for more details.

The γ -rays were measured by an ap-type coaxial 70 mm diameter High-Purity-Germanium detector (HPGe, model 65-83, GEM series, ORTEC), having 70% relative efficiency and peak resolution of 1.7 keV at 1332 keV. The γ -rays were measured by placing the copper catchers at distance of 20 mm from the HPGe detector. This well-established arrangement with an optimised solid angle and precisely known efficiency correction of 1.3% for the ^7Be spatial distribution over the catchers had an effective shielding to suppress the ambient background. The passive part of the shielding is 50 mm of mercury, 10 mm of copper, lead of 150 mm thickness (50 mm are radiologically ultra-clean) and the active part is a plastic detector of dimensions $1000 \times 1000 \times 50 \text{ mm}^3$ (BC408 plastic scintillator by Saint Gobain) placed on top of the lead shield and operated in anti-coincidence (veto detector) with the HPGe detector in order to discard events from the cosmic rays. Two pictures of the complete station (a) and a catcher in the measurement position (b) can be seen in Figure 3.13.

The activity spectra were collected for durations between 3-10 days, to minimise the statistical uncertainty in γ counting. The absolute detection efficiency was $(4.36 \pm 0.10)\%$ or all catchers except for those at 4811 2807 and 2106 keV in 2011 which efficiency was $(3.79 \pm 0.11)\%$ relative error.

The signals from the HPGe and the scintillator detectors were amplified and then fed into the signal and gate inputs (correspondingly) of an ADC module (model 927 by ORTEC), which was connected to a PC via USB cable and the software MAESTRO-32 was used for spectral acquisition. Thus, the signal from the HPGe detector is gated in anti-coincidence with the scintillator detector reducing cosmic background. This assembly of the passive and active shielding provides a background radiation rate of 0.67 events/seconds over the energy range of 40-2800 keV.

The energy for the γ -ray to be detected from the ^7Be activity is 478 keV. In order to check possible background interfering in this energy region a spectrum was collected during 168 h without any Cu catcher, i.e. activity seen in the HpGe with the shield. The spectrum is shown in Figure 3.14.

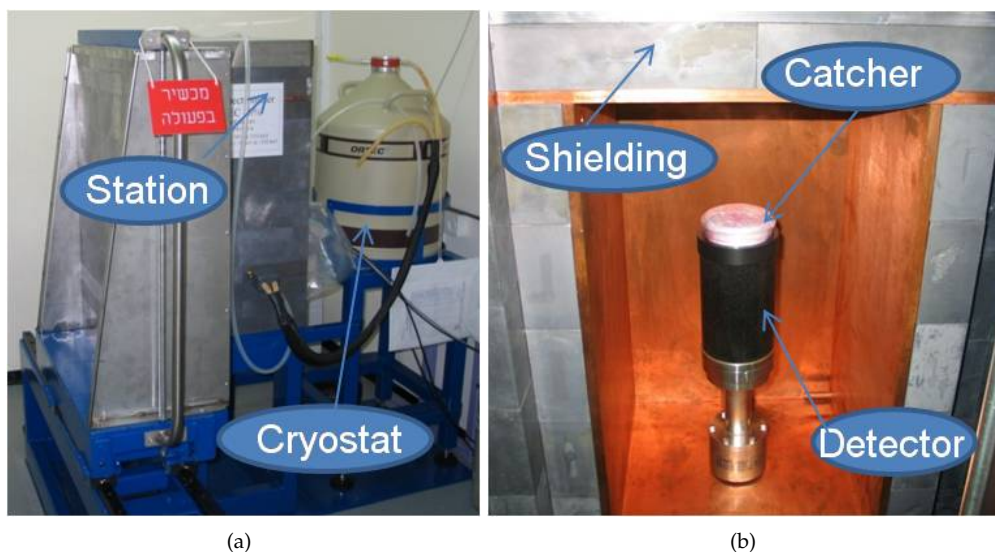


Figure 3.13: (a) Picture of the low background HPGe detector station paced in a basement in SOREQ centre. (b) Copper catcher in the position to be measured.

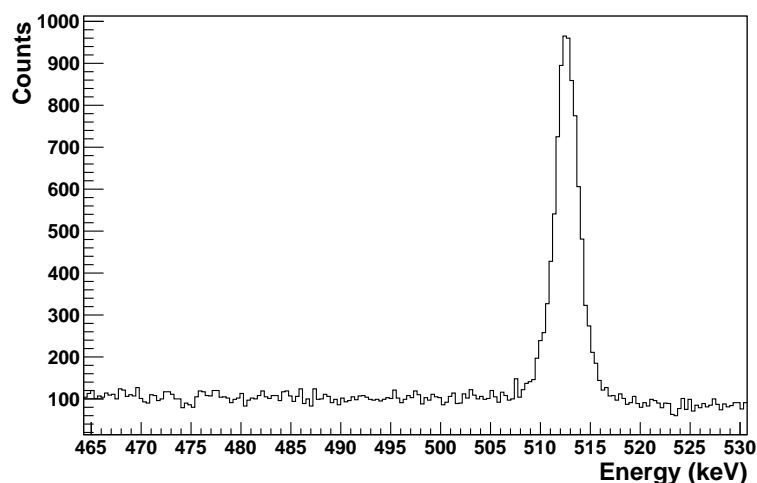


Figure 3.14: Background γ -activity detected in the HPGe in the low background station at SOREQ centre in the week preceding the Cu catcher measurements in 2009. The 511 keV peak is from the γ radiation coming from the e^-e^+ background annihilation. The positrons (e^+) are originated by pair production interaction of the γ -rays background with the surrounding materials.

As can be seen the spectrum does not show any interfering peak around 478 keV and, a 0.025 counts/s background rate in the 450-500 keV region with a bin size of 0.35 keV is observed. Exactly the same spectrum was obtained for a Cu catcher prepared with no target gas but the ^3He beam at an energy around 4 MeV. This confirms that there is no background contribution from the beam hitting the Cu catcher.

3.2.4 Additional measurements

In the following some of the complementary measurements performed that allowed better control of the experimental setup and the better estimations of the experimental errors.

3.2.4.1 Energy calibration of the silicon detector

In order to know the energy of the ^3He ions reaching the detector, energy calibration measurements for the silicon detector were performed. They were carried out at the beginning of each experiment using two standard alpha sources: ^{148}Gd , and a standard triple alpha source ($^{239}\text{Pu} + ^{241}\text{Am} + ^{244}\text{Cm}$). The energies of the alpha particles emitted by these sources are shown in Table 3.3.

α source	E_α (keV)	I_α (%)
^{148}Gd	3182.787(24)	100
	5156.59(14)	73.3(8)
^{239}Pu	5144.3(8)	15.1(8)
	5105.5(8)	11.5(8)
^{241}Am	5485.56(12)	84.5(10)
	5442.80(13)	13.0(6)
	5388.23(13)	1.6(2)
^{244}Cm	5804.82(5)	76.4(2)
	5762.70(3)	23.6(2)
	5664(3)	0.022(1)

Table 3.3: Energies and intensities for alpha particles from ^{148}Gd and triple alpha (^{239}Pu , ^{241}Am and ^{244}Cm) sources used for calibration [Lun].

For the calibration measurements the collimator in the chamber was replaced first by the ^{148}Gd source and then by triple alpha source. The pressures inside the chamber for the two measurement were below $\sim 10^{-6}$ mbar which guarantees no energy losses by the α particles before reaching the detector. The two calibration spectra are shown in Figure 3.15.

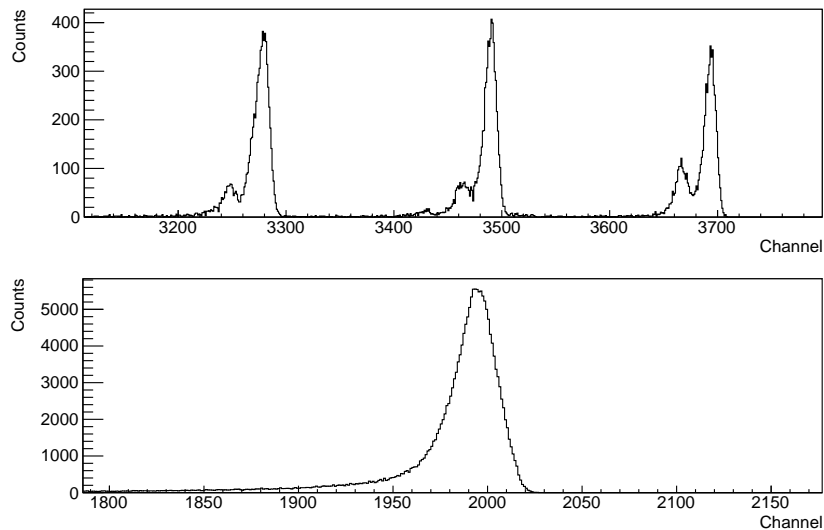


Figure 3.15: Triple alpha (top) and ^{148}Gd (bottom) source spectra as taken with the silicon detector during the 1000 and 300 s respectively

It is worth noting that for this experiment the energy resolution is not an important parameter. The aim of using the detector lies on determining the number of scattered beam particles reaching

detector, and knowing the energy calibration is just a way of cross check the scattered particles.

The procedure to calibrate the detector was to perform a regression analysis between the values of the centroid from the ^{148}Gd source and the highest intensity peaks from triple alpha source shown in Figure 3.15 and their nominal values in Table 3.3. The values used are shown in third and second columns in Table 3.4, respectively.

α source	E_α (keV)	Centroid (ch)	FWHM (keV)
^{148}Gd	3182.787(24)	1994 (1)	36.23
^{239}Pu	5156.59(14)	3280 (1)	23.06
^{241}Am	5485.56(12)	3491(1)	19.11
^{244}Cm	5804.82(5)	3694(1)	18.94

Table 3.4: Regression analysis values for the energy calibration of the silicon detector. Second column shows the nominal values of the energies considered and third column shows their corresponding centroids in channels taken from Figure 3.15. Fourth column shows the full width half maximum of the peak (FWHM) of the peak after calibration.

The regression analysis gives the relation between the histogram channel number and the alpha particles energies. In this case, this can be expressed by:

$$\text{Energy (keV)} = 109.4 (36) \cdot \text{channel} + 1.54 (1) \quad (3.8)$$

3.2.4.2 Radius of the collimator

In order to estimate the number of incoming beam ions from the scattered particles, it is necessary to know the solid angle covered by the detector i.e. to know exactly the area of the hole of the collimator. A small radius collimator was chosen to not cover a wide angle and thus better constrain the scattered particle solid angle. Due to the standard elements as caliper could not measure such small distances the radius was determined experimentally.

An alpha spectrum from a ^{148}Gd source placed before the collimator was taken during ~ 10 h together with a pulser of 10 Hz count rate in the system. Afterwards, another spectrum was collected by replacing the collimator with one of known $4 \pm 0.05\text{mm}$ diameter, i.e. larger diameter, during ~ 3 h. The unknown radius of the smallest collimator (R_s) is obtained from the expression below. In this expression the number of alpha particles detected in the collimator in both cases are normalised using the number of pulsers counts in order to account for the differences in the collection times for the two spectra:

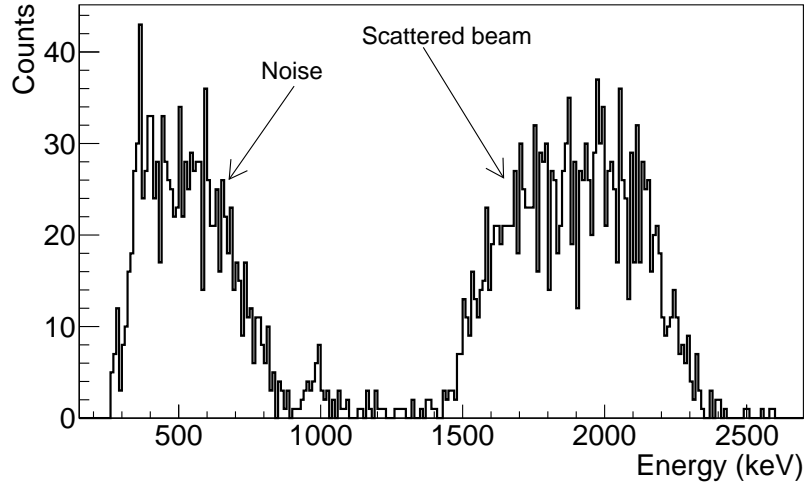
$$\frac{\pi R_s^2}{\pi R_b^2} = \frac{\text{Peak}_s / \text{Pulser}_s}{\text{Peak}_b / \text{Pulser}_b} \quad (3.9)$$

Here, the "s" subscript refers to the small unknown radius collimator and "b" subscript refers to the big known radius collimator. *Peak* and *Pulser* refer to the integration of the ^{148}Gd source peak and the pulser peak in the spectra respectively. The collimator radius was estimated to be: $R_s = 0.270 \pm 0.003\text{mm}$.

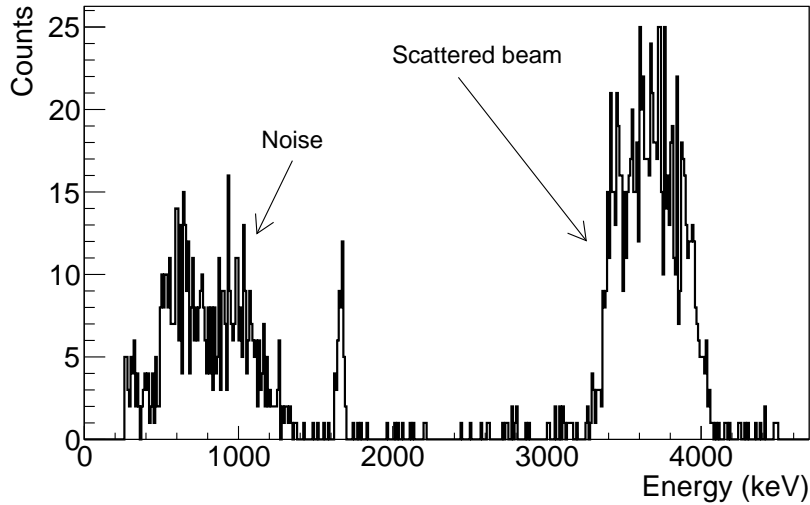
3.2.4.3 Aperture angle of the collimator

Continuing with the interest of determining the detector solid angle, the angle of the collimator respect to the Ni foil needs also to be known. To determine the collimated angle of the silicon detector with respect to the beam, the Ni foil (see Figure 3.6) was replaced by a C foil, and the same setup (also same small collimator) without any mechanical changes was used. In this case, a ^4He beam at

seven different energies (2, 2.5, 3, 3.5, 4, 4.5 and 5 MeV) impinged onto the chamber with no gas inside and pressures in the order of $\sim 10^{-6}$ mbar. The seven spectra for the scattered particles in the C foil detected with the silicon detector were saved. Two examples corresponding to the 3 MeV and 5 MeV incoming ${}^4\text{He}$ beam energies are shown in Figure 3.16. The wide energy spread in the peak is due to the C foil thickness and where the reaction takes place, at the entrance, middle or end of the foil.



(a)



(b)

Figure 3.16: Silicon spectra corresponding to 3 (a) and 5 (b) MeV ${}^4\text{He}$ beam particles scattered from a C foil. Peaks corresponding to noise and ${}^4\text{He}$ elastic scattered particles are marked. The energy spread is related to the thickness of the foil. The more deeper the scattering takes place in the C foil the higher is their energy in the detector.

The idea was to obtain the angle (ϑ) of the collimated detector by considering the particles scattered at the end of the C foil and taking into account the expression relating the energy of elastically scattered particles (E_1) and the incoming beam after subtracting for energy loss in the C foil (E_0)

$$\frac{E_1}{E_0} = \frac{1 + 2\rho\cos\Theta + \rho^2}{(1 + \rho)^2} \quad (3.10)$$

$E_{\alpha}^{incoming}$ (keV)	$E_{\alpha}^{detected}$ (keV)
2000	1528 ± 10
2500	1947 ± 15
3000	2376 ± 15
3500	2779 ± 20
4000	3244 ± 20
4500	3593 ± 15
5000	4052 ± 15

Table 3.5: Experimental input values for the program used in order to determine the collimated detector angle and the C foil thickness. For different incoming ^4He beam energies showed in the first column, the second column shows the energies of the detected scattered particles together with errors.

here ρ is the mass ratio between ion beam and target, and Θ is the output angle in the centre of mass system.

Unfortunately, the carbon foil thickness was not known to sufficient accuracy therefore, the energy at the end of the foil (E_0) cannot be calculated and thus the angle can not be directly obtained from expression 3.16. Moreover, the angle is very sensitive to minor changes, and with the low statistic the highest energy of the peaks cannot be obtained precisely. Instead, a program using MINUIT subroutine has been created. Two variables, angle and thickness are optimised simultaneously using the experimental values shown in Table 3.5. From the incoming energy, the program estimates the energy loss by interpolating the SRIM input values assuming a C foil thickness and estimates the angles utilising the expression 3.10. It gives the optimised values of C foil thickness and the silicon detector angle that fit best the scattered particle spectra. Finally, the angle is transformed to laboratory reference system using the expression:

$$\cos\vartheta = \frac{\cos\Theta + \rho}{\sqrt{1 + 2\rho\cos\Theta + \rho^2}} \quad (3.11)$$

here, ϑ is the the angle in the laboratory system. The resulting values for the thickness and ϑ are $(0.428 \pm 0.048)\mu\text{m}$ and $(44.9 \pm 0.4)^\circ$, respectively. The corresponding solid angle covered by the collimator placed before the detector is: $4.7 \cdot 10^{-6}\text{sr}$

3.2.4.4 Ni foil thickness

As already mentioned, the cross section of the reaction is dependent on the energy. In order to calculate the energy at which the capture reaction takes place, the energy-loss of the ^3He beam particles in the Ni foil must be taken into account and thus the Ni foil thickness must be known. The Ni foil thickness was determined experimentally using standard energy loss techniques with a setup which consisted of another silicon barrier detector and the standard triple alpha source inside a vacuum chamber. Firstly, the alpha source was placed in front of the detector for calibration following the same procedure used to calibrate the other detector (cf. section 3.2.4.1). This spectrum is shown in Figure 3.17.

The Ni foil, dismantled after the 2009 experiment, was then placed between the alpha source and the detector. The corresponding spectrum was saved. The same measurement with a 2 mm radius collimator between the source and the Ni foil was also performed. Finally, in order to check possible foil damages because of the beam impact, a measurement replacing the used Ni foil by a new unused Ni foil, with characteristics similar to that the used in the experiment, was also carried out. Various histograms corresponding to these measurement are shown in Figure 3.18. As can be seen all measurements performed agree for the energy of the alpha particles after crossing both the used and the new Ni foil. The black spectrum shows the total number of counts after adding all of them.

The Ni foil thickness was determined using the SRIM code and the energy loss by the alpha particles crossing the Ni foil, which are ~ 400 keV. The thickness resulted to be: $(1.03 \pm 0.02)\mu\text{m}$, which is close to the value given by the manufacture of $1\mu\text{m}$.

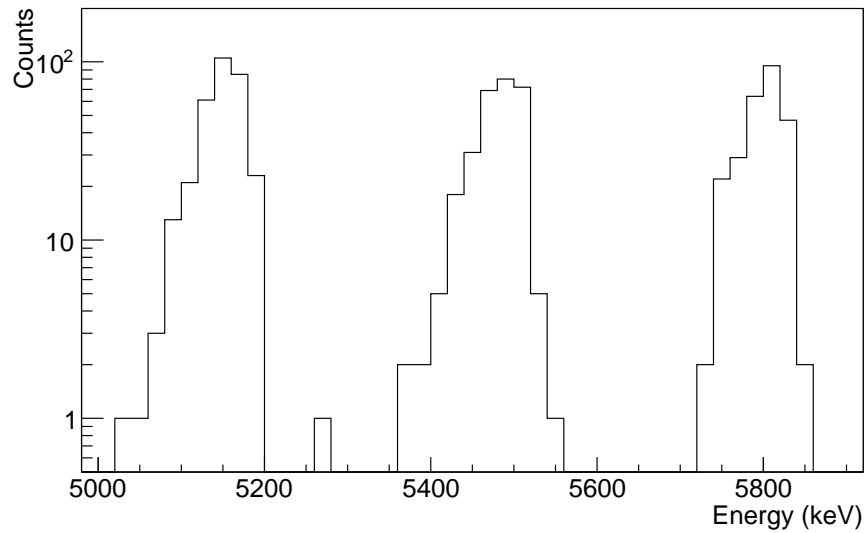


Figure 3.17: Energy spectra of alpha particles from a triple alpha source taken with the detector used to determine the Ni foil thickness.

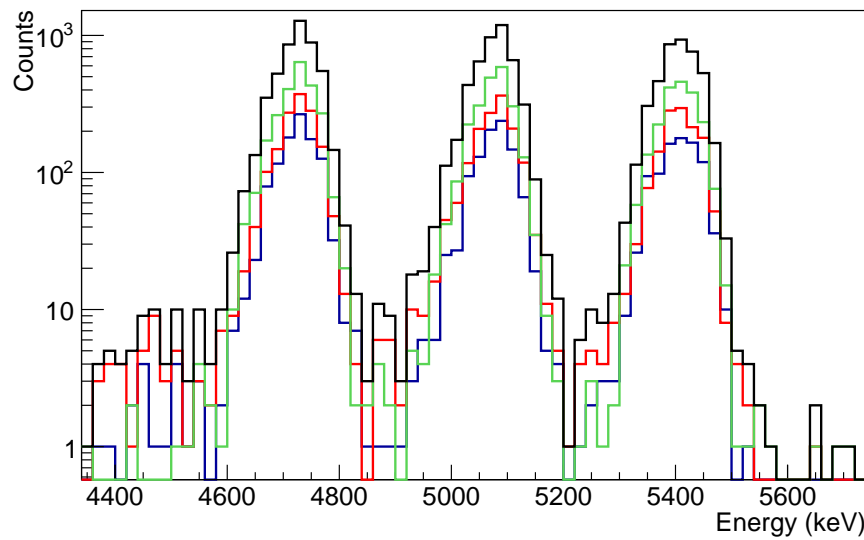


Figure 3.18: Energy spectra of alpha particles from a triple alpha source after crossing a Ni foil. In red the spectrum taken with the Ni foil used in the experiment with a 2 mm radius collimator between the source and the foil. The blue ones shows the same without collimator and the green spectrum shows the histogram taken with a new Ni foil. Black spectrum shows the sum of all of them, used for the energy lost calculations.

The following sections will describe the complementary experiment using the direct recoil counting method. The data analysis and the results of the activation experiment will be detailed in Chapter 5.

3.3 Direct Recoil Counting Method @ DRAGON

The experiment using the *Direct Recoil Counting Method* was performed at TRIUMF (TRI -from the three original founding members University of Brithish Columbia, University of Victoria, and Simon Fraser University-University Meson Facility) laboratory in Vancouver, Canada. The laboratory is dedicated to Nuclear Physics and Particle Physics research. The general layout of the laboratory is shown in Figure 3.19. It houses a main cyclotron of ~ 17.9 m diameter, which accelerate hydrogen ions, H^+ , in a magnetic field of 5600 Gauss producing primary beams with currents up to $\sim 100\mu A$ and energies up to 500 MeV. The proton beam is delivered to different beam lines depending upon the experiment to be performed. For nuclear physics experiments the proton beam is let to impinged on targets such as tantalum or UC_x in the target stations, producing radioactive secondary beams which after mass selection in a mass separator are guided to the two main facilities, ISAC-I (Isotope Separator and Accelerator) and ISAC-II.

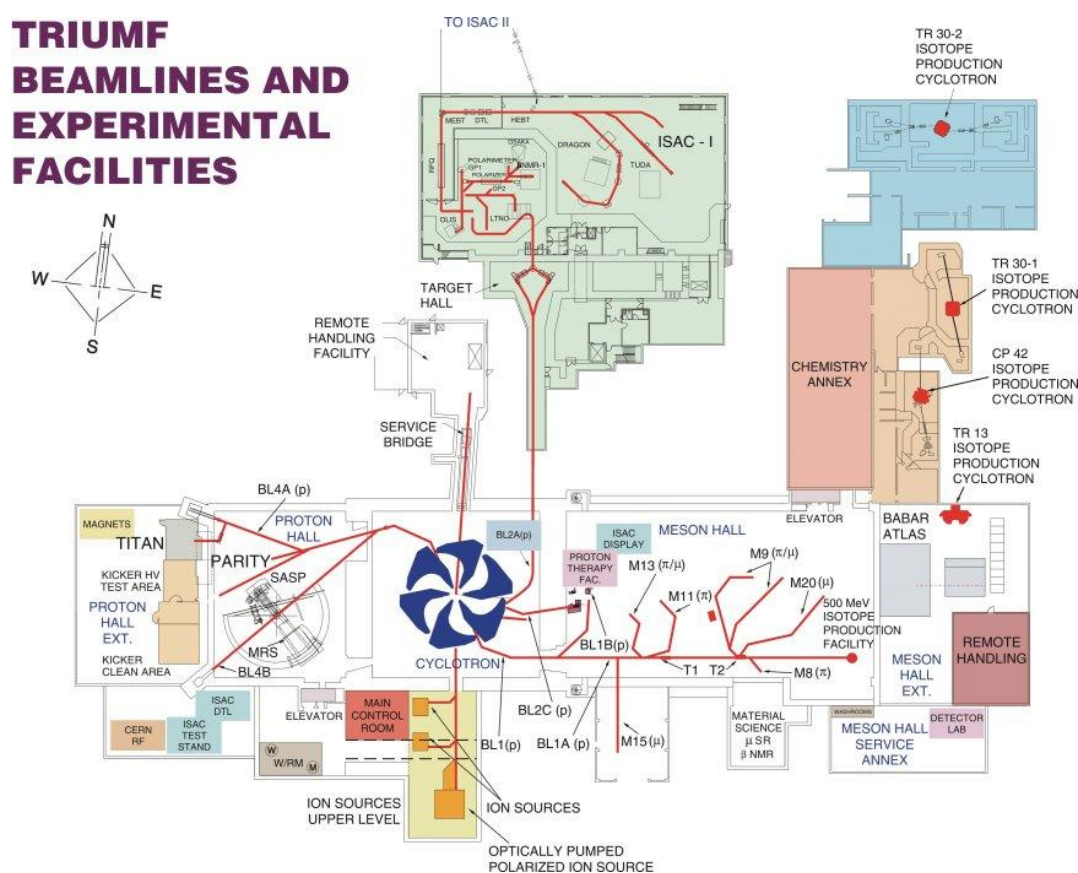


Figure 3.19: Layout of the TRIUMF laboratory with the cyclotron and some of the facilities as ISAC-I where our experiment was performed.

Furthermore, in the ISAC-I and ISAC-II facilities, apart from the radioactive beams, stable beams from the Off-Line Ion Source (OLIS) can be accelerated. As our beam in this case is 4He which can be obtained directly from a gas bottle we only needed to use OLIS. The OLIS facility can produce most of stable ions beams from $Z=1$ to $Z=87$. It consists of a high voltage terminal containing a *surface ionising source*, a *ECR-multi-charge ion source (Supernanogam)* and a *microwave cusp ion source*. For our experiments in September 2011 and August 2013, the Supernanogam source [JWG10] and the Microwave Ion source [JAC08] were used, respectively to produce the $^4He^+$ ion beams.

After the ion extraction from OLIS, the ions were accelerated in the ISAC-I facility. The first stage of acceleration happens in the radio-frequency quadrupole, where the ions can be accelerated

from 2 keV/u to 150 keV/u. The second stage of acceleration happens in a drift tube linac (DTL), which is divided into eight modules (five accelerating structures and three bunchers). The beam is firstly bunched in the DTL entrance by means of the medium energy beam transport buncher (MEBT) and can be further bunched in time from 4 ns to 1 ns by means of the high energy beam transport (HEBT) located downstream the DTL. After the DTL, the beam was guided to the DRAGON (Detector of Recoils And Gammas Of Nuclear Reactions) separator where the experiment was performed. A layout of the ISAC-I hall including the different accelerator stages and the DRAGON facility is shown in Figure 3.20.

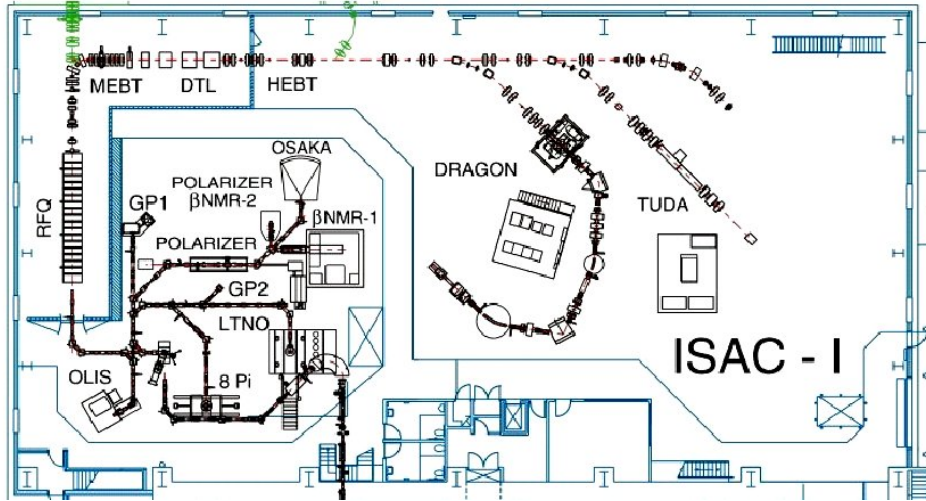


Figure 3.20: Layout of the ISAC-I hall with the different acceleration elements and DRAGON facility. The ${}^4\text{He}$ beam ions were produced in the Off-Line Ion Source (OLIS) and accelerated using the RFQ and DTL elements before reaching the DRAGON experimental area where the experiment was performed. Some other experimental set ups in the ISAC-I hall such as 8π or TUDA are also marked

3.3.1 DRAGON setup

In order to count ${}^7\text{Be}$ recoils directly, they must be separated from the unreacted beam particles before being counted in a detector. Recoil separators are devices which separate nuclear reaction products (recoils) leaving a target from the unreacted beam particles. In addition, some separators have the additional property that they can disperse the reaction products at the focal plane according to their mass/charge.

The recoil separators use electromagnetic elements such as electric dipoles, magnetic dipoles, Wien filters etc, to separate the recoils from the unreacted primary beam. In addition, magnetic quadrupoles are used to focus the ions, and magnetic sextupoles and octupoles are used to correct higher order aberrations. Because heavy ions are routinely used as beams, high vacuum is necessary in recoil separators in order to avoid losses due to multiple scattering or charge-changing collisions.

Usually, the yield of recoils is peaked near 0° , and thus the recoils are mixed in with primary beam particles that have not reacted as both leave the target. To obtain the maximum suppression of beam, the beam particles are blocked at an early stage of the separator. The dipole magnetic and electric fields are set to pass particles with energy E_o , mass M_o , and charge Q_o along the central trajectory, and the quadrupole lenses are set to focus the particles at the focal plane.

DRAGON, placed at TRIUMF's ISAC-I hall, is a recoil separator designed for measuring radiative capture reaction cross sections of astrophysical interest. DRAGON consist of four main components, a windowless recirculating gas target, a γ -detector array, an electromagnetic separator (EMS) and a heavy-ion recoil detection system [HBB03]. A diagram of the DRAGON facility with the main elements is shown in Figure 3.21 and the details of the different component will follow.

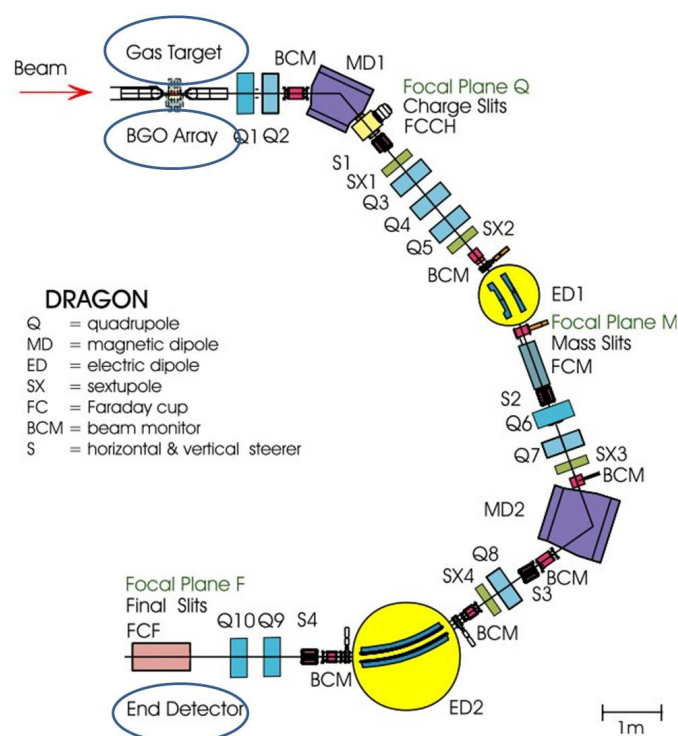


Figure 3.21: Diagram of the DRAGON facility taken from Ref. [EHB05]. Radioactive and stable beams enter the windowless gas target which is usually filled with either hydrogen or helium gas with pressures between 0.2 to 10 Torr. The recoils produced after the reaction emerge the target with different charge states and almost with the same momentum of the beam. The recoils are separated from the beam particles using the two magnetic dipoles, MD1 and MD2, and the two electrostatic dipoles, ED1 and ED2. Magnetic quadrupoles and sextupoles are used to focus the particles. Enclosed in circles are the three main components, Gas Target, BGO Array and End Detector.

In our experiment, a ^4He beam impinged onto the ^3He gas target kept in the target cell. Eventually, they fuse producing the ^7Be recoils and prompt γ -rays. The latter are detected in the BGO detectors surrounding the target. The recoils are forwarded focus and exit the target with different charge states together with the unreacted beam particles. The first quadrupoles (Q1 and Q2) focus both the unreacted and recoil beams after exiting the target and before they enter to rest of the separator. Then, the two magnetic and electric dipoles select the ^7Be recoils from the unreacted beam taken into account the different charge state and different kinetic energy between them. The ^7Be with the given charge state are then counted in the end detector.

3.3.1.1 Gas target

The ^3He gas target was enclosed inside a windowless cell with an effective length of ~ 11 cm, that was positioned inside an aluminium target box. A sketch of the cell position is shown in Figure 3.22. A photo of the Al target box attached to the beam line is displayed in Figure 3.23. A part of the BGO array and pumps together with pumping tubes can be also seen.

Inside the box and exiting the cell there are two "arms" which accommodate two collimated *Ion Implanted* semiconductor silicon detector to monitor the scattered beam and target particles. The entrance and exit apertures of the cell are circles holes of 3 and 4 mm radius, respectively. The box is connected to the beam line through a series of differentially pumped tubes.

Although a windowless gas target maximise the transmission of the recoils through the target, it requires a differential pumping system both upstream and downstream of the target to maintain the beam line vacuum. The eight turbo pumps, three upstream and five downstream maintain the vacuum out of the cell, e.g. 10^{-6} mbar was maintained at the entrance of the first quadrupole (Q1

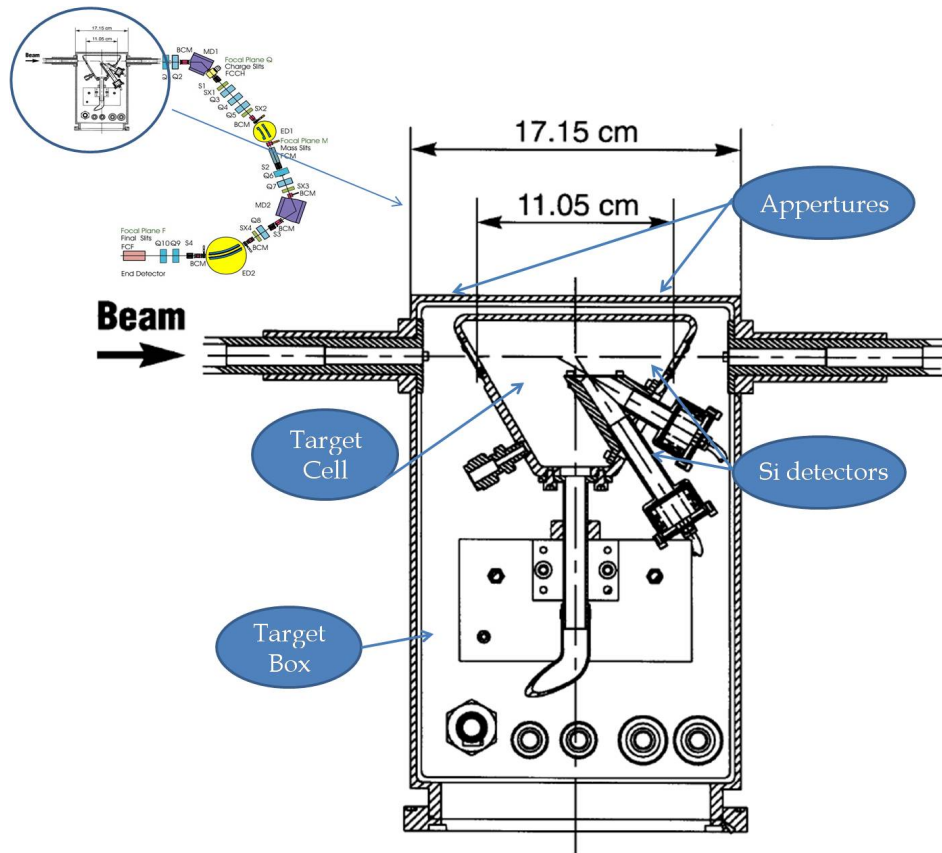


Figure 3.22: A schematic view of the target cell, from Ref. [LIB03]. The target cell is fixed to one of the lids of the target box (see Figure 3.23). To detect the scattered beam as well as target particles, two collimated silicon detectors were placed at 30° and 57° to with respect to the beam direction.

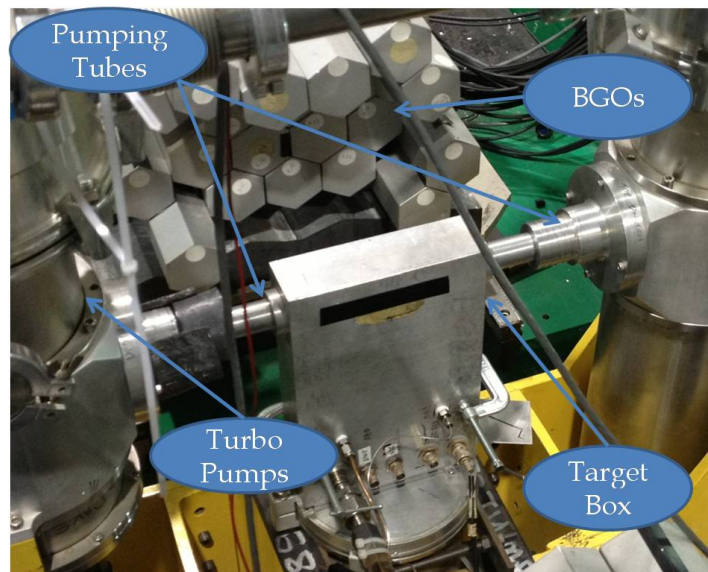
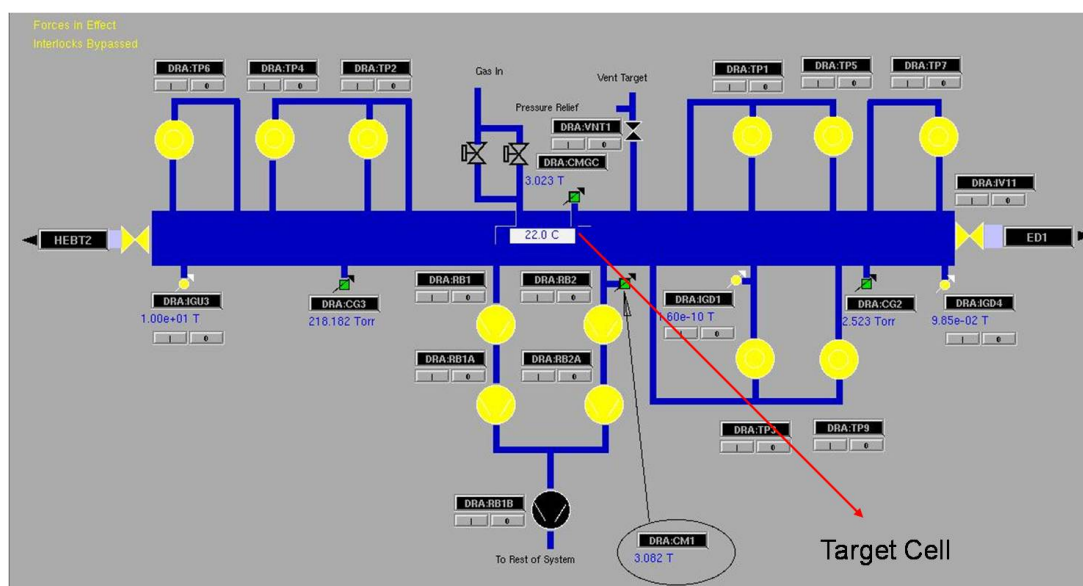


Figure 3.23: Real picture of the box and the pumping tubes connecting to the beam line. The face of the box showed is the one holding the target cell.

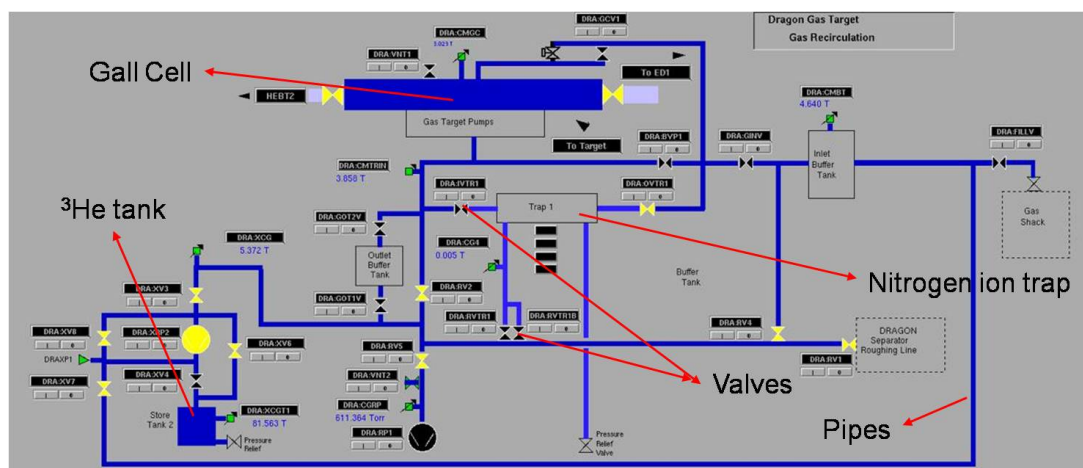
3. Experimental Techniques

in Figure 3.21). The ^3He gas pressure range during our experiment varied from 4.9 to 6 Torr and a recirculating gas system using a liquid nitrogen ion trap guaranteed a constant pressure and purity of gas target inside the cell during the time of each individual measurement.

The complexity of the system of the windowless gas target is illustrated in Figure 3.24, where (a) shows the pumping tubes and the gas box in blue, the AI box inside which the target cell can be also seen; the vacuum pumps (rootsblowers and turbo pumps) are also shown in yellow; (b) shows the recirculating gas system. All valves and pumps are computer controlled in order to achieve a target gas-profile with a nearly constant density across its effective length.



(a)



(b)

Figure 3.24: Screen shots of the DRAGON target gas system which can computer controlled remotely; (a) shows the target box and pumping tubes (blue rectangle) with the different pumps (in yellow) used to keep constant the gas pressure inside the cell. (b) shows the recirculating gas system. The ^3He gas tank and Nitrogen ion trap, several meters and valves are also marked.

It should be pointed out that this DRAGON experiment was the first of its type using ^3He gas target, therefore, accurate information of the density profile was obtained and will be detailed in the next section.

3.3.1.2 γ -detector array

In order to detect the prompt γ -rays from the reaction, a γ -detector array was surrounding the target box consisting of 30 Bismuth Germanate Oxide scintillation (BGO) detectors of 76 mm length in a close packed configuration (see Figure 3.25). The scintillator detectors have the property of luminescence, that is, they absorb the incoming radiation and re-emit it in the form of light. Therefore, the scintillators are coupled to a light sensing devices, photomultipliers, which absorb light from the scintillator and produce electrons via the photoelectric effect. The resulting signal can be then processed using standard methods [Leo87].

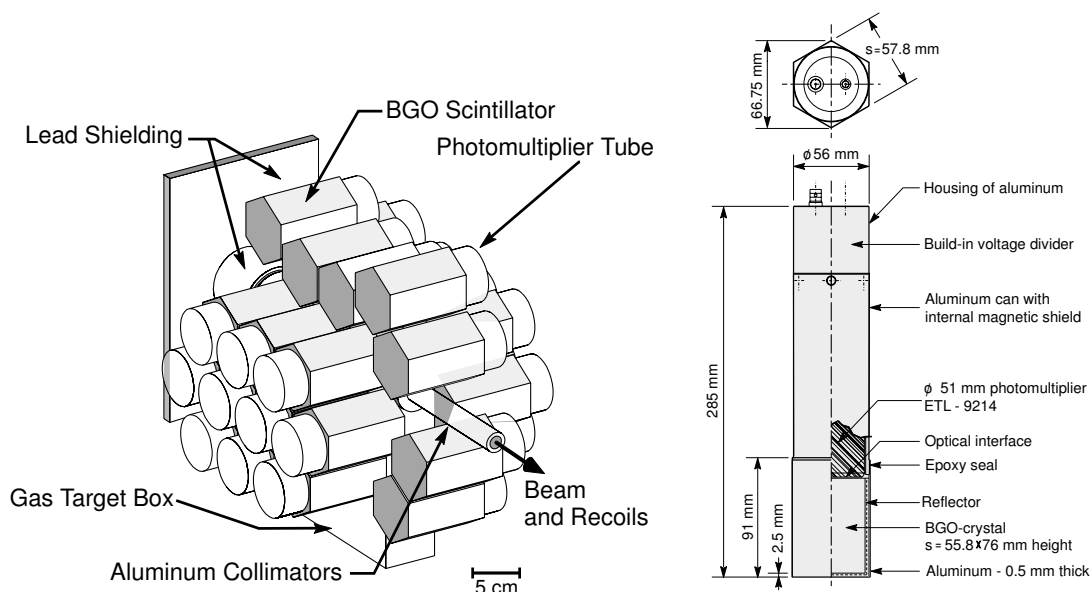


Figure 3.25: The BGO γ -ray detector array surrounding the target box. It consists of 30 individual hexagonal detectors coupled to cylindrical photomultiplier tubes [HBB03]

The DRAGON BGO detectors have a hexagonal shape coupled to a cylindrical 51 mm diameter photomultiplier tube (PMT). Monte Carlo simulations predict a γ -ray efficiency from (45-60)% for the energy range 1-10 MeV over the 11 cm target cell and a FWHM of 7% at 6.13 MeV [HBB03].

A typical BGO spectrum of our experiment is shown in red in Figure 3.26. In the same Figure, in blue is shown the spectrum obtained in coincidence with the ${}^7\text{Be}$ recoils detected in the DSSSD at the focal plane. A comparison between the two spectra reveals high background contribution in the BGO detectors. Remarkably high is the contribution from the de-excitation of ${}^{30}\text{Si}$ produced by beam induced reaction with the Al present in the beam line components. The two peaks in the blue spectrum show the γ -ray from the "direct capture state" (DC) de-excitation to the ground state (γ_0) and to the 429 keV first excited state (γ_1) in ${}^7\text{Be}$ (see caption for more details).

3.3.1.3 Electromagnetic separator

The ${}^7\text{Be}$ recoils produced in the gas target enter the EMS, where the recoils are separated from the ${}^4\text{He}$ beam particles. The latter are efficiently suppressed and only recoils reach the focal plane of the separator. The downstream pumping tubes and apertures limit the recoils accepted by the separator. This is influenced by where the reaction is produced through the target length. The separator was checked separately with dedicated test to confirm that the recoils created in an angular cone of around 20 mrad were accepted.

Both beam and recoils emerge with almost the same momentum and with different charge states. The magnetic and electric elements are tuned in order to obtain the optimum beam suppres-

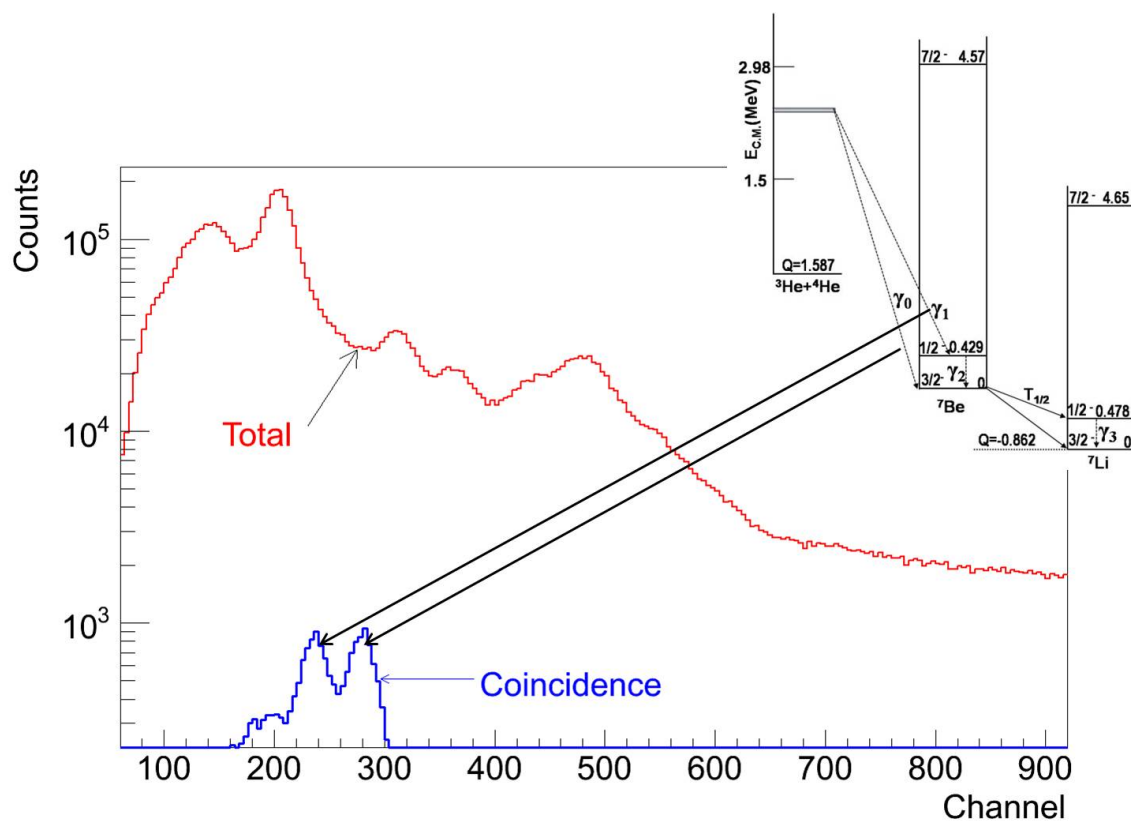


Figure 3.26: The total γ -ray spectrum is shown in red for the ${}^3\text{He}(\alpha,\gamma){}^7\text{Be}$ reaction at a ${}^4\text{He}$ beam energy of 3.521 MeV and ${}^3\text{He}$ target pressure of ~ 6 Torr. The highest energy peak is due to the de-excitation in the ${}^{30}\text{Si}$ produced by the beam induced reaction ${}^{27}\text{Al}({}^4\text{He},p){}^{30}\text{Si}$ possibly with the aluminium target box, pumping tubes and apertures. The same spectrum is shown in blue for coincidence events with the ${}^7\text{Be}$ recoils detected in the focal plane. The two peaks corresponds to γ rays from the de-excitation between the direct capture state to the first excited state and to the ground state in the ${}^7\text{Be}$ nuclei. The subsequent 429 keV γ_2 -ray is not seen because of the threshold set in the BGO due to the high background.

sion, recoil separation and acceptance. The first stage of the separation occurs in the first magnetic and electric dipoles (MD1 and ED1 in Figure 3.21). One of the charge states of the recoils is selected by MD1 and the particles are then separated by ED1 based on their kinetic energy. The magnetic dipole separates the particles based on their rigidity as:

$$B\rho = \frac{p}{q} \quad (3.12)$$

here B is the magnetic field, ρ is the gyroradius with respect to the beam direction, p is the momentum and q the charge state of the particle. As the momentum p for both beam and recoil are very similar, the gyroradius ρ is constant for the dipole, setting a magnetic field B in the dipole leads to a selection of one of the charge states. Slits strategically placed after MD1 allow only particles with the selected charge state going through the next step of the separator.

The field of the magnetic dipole is measured with a NMR probe located in the vacuum vessel. A recent calibration of NMR reading using the $^{24}\text{Mg}(p,\gamma)^{24}\text{Al}$ reaction at centre of mass energy of 0.22 MeV has confirmed the relationship:

$$\frac{E}{A} = k \left(\frac{qB}{A} \right)^2 \quad (3.13)$$

with $k=48.15(7)$ MeV/T² [HRF12]. Here, E , A and q are the kinetic energy, the mass in atomic units (u) and the charge state of the particle while B corresponds to the magnetic field. The next phase of separation occurs in first electric dipole (ED1 in Figure 3.21), which separates particles based on the kinetic energy per charge as:

$$\varepsilon\rho = \frac{pv}{q} \quad (3.14)$$

where ε is the electric field and v the velocity of the particle. As with MD1 a set of slits are strategically positioned at the ED1 focus to stop the unwanted particles.

A second magnetic dipole (MD2) and electric dipole (ED2) follow the first separation stage and allow further beam suppression. Magnetic quadrupoles and sextupoles are used to focus the particles. We used the standard procedure to set the separator for the ^7Be recoils (see section 3.3.2). For the two highest energies measured, the separator was tuned to detect $^7\text{Be}^{3+}$ because the beam suppression was estimated to be better. Due to the difficulties of getting low enough stable fields in the magnetic dipoles, we tuned the separator to detect $^7\text{Be}^{2+}$ for the two lowest energies.

3.3.1.4 Double-Sided Silicon Strip Detector (DSSSD) at the focal plane

Once the recoils have been separated from the beam particles, they reach the final focus at the end of the separator. Different detectors are used in DRAGON including a DSSSDs, MCP and *Ionisation Chambers*, to determine the final position energy and mass of the recoils.

In our experiment, the ^7Be recoils were implanted and detected in the DSSSD consisting of a silicon wafer with 16 front strips with respect to the recoils impact, and 16 orthogonal back strips which collect the charge (see Figure 3.27).

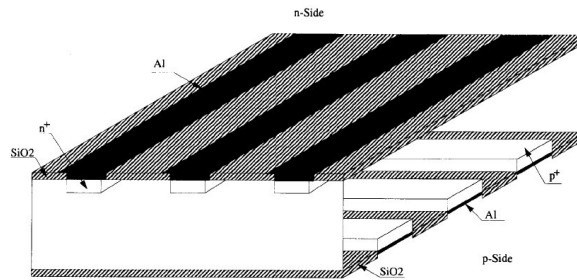


Figure 3.27: Diagram of a Double-Sided Silicon Strip Detector. The p and n sides and the $p+$ and $n+$ corresponding strips as well as the Al contacts are marked.

Each strip has 3 mm width providing an effective area of $256 \times 9 \text{ mm}^2$ over the 5 cm^2 detector surface. The gap between the strips is $120 \mu\text{m}$ due to which a $3.85 \pm 0.10\%$ of the incident ions on the detector's surface will not be detected with the correct energy at the detector (see reference [WHRD03]). Front strips are biased with voltage while back strips are kept at ground potential. When the ions hit the DSSSD, electron-hole pair are created in the silicon (see section A.1) and are guided to opposite strips inducing electric signals of opposite polarity on front and back sides. This allow us to determine the energy and to identify the position of the particle hitting the detector.

3.3.1.5 Electronic setup

As in the Madrid experiment, an electronic setup is required in order to process the electronic signals from the detectors before being digitised and saved. This setup requires more electronic devices compared to the Madrid experiment. Apart from the detectors already mentioned here, a BGO array, silicon detectors and DSSSD, other detection systems are likely to be used in DRAGON depending upon the kind of experiment performed (ionization chamber, Germanium detectors...). The electronic set-up is designed to process the signals produced in all of the detectors and a detailed explanation of the different modules and signals is beyond the scope of this thesis. Moreover, between our experiments in 2011 and 2013 the data acquisition system (DAQ) was changed. In both experiments the data were saved and displayed on-line using the TRIUMF-MIDAS (Multi Instance Data Acquisition System) system.

The signals processing are separated in two parts: one for the "head" of the DRAGON, which includes the γ -ray detectors, and another for the "tail" of the DRAGON, including the DSSSD (or ionisation chamber, depending on the experiment), MCPs, and also the silicon detectors.

In the old system used for the 2011 experiment an event on either the head or the tail side could activate the DAQ system and there was only one readout. Coincidence conditions between both sides were set entirely in the hardware. When there was an event trigger from either side, a time gate was opened up and a search for triggers in the other side was carried out during the time of the gate and thus acquiring the coincide events.

In the 2013 the DAQ system had been updated: it consisted of two separate and independent DAQ (two VME crates), one for the "head" and one for the "tail". Each crate was triggered and read out separately and was tagged with timestamps from a "master" clock that is part of the head electronics. In this case, the coincident events could be figured out in the analysis phase by looking at the timestamps. Any two events with triggers within $10 \mu\text{s}$ of each other are deemed a coincidence event. The energy and temporal electronic chains associated to each detector are similar to those shown in Figure 3.8 for the Madrid experiment, and a summary diagram of the trigger electronic system for the 2013 experiment is shown in Figure 3.28.

3.3.1.6 Faraday cups

Other elements playing an important role in our experiment are the Faraday cups. A series of Faraday cups placed across DRAGON separator are used for tuning. These are also important in determining the beam currents and some of the additional observables such as charge state distributions. In the following, the nomenclature of the DRAGON control program to describe their location across DRAGON (see Figure 3.21 to identify the location):

- FC4: located just before the gas target, it measures the incoming current
- FC1: located after the target and before MD1, it measures the transmission throughout the target.
- FCCH: located after the MD1 charge slits, it measures the current of a selected charge state.
- FCM: located after ED1, it measures the current after the selection of charge state and energy.
- FCF: located before the focal plane detector, it measures the current at the end of the separator.

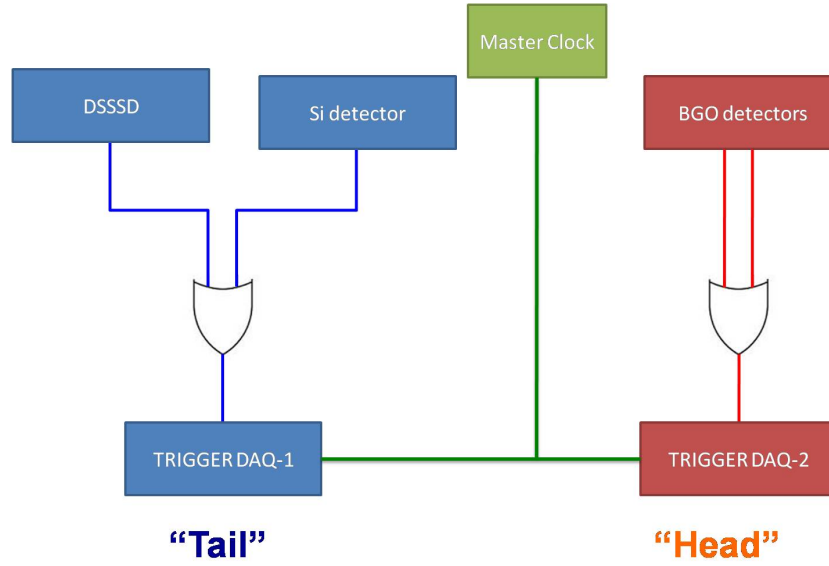


Figure 3.28: A sketch of the trigger electronic setup for the 2013 experiment using DRAGON.

3.3.2 Details of the measurements

The experiment was run in two different periods, in 2011 and 2013, carrying out studies at three and one incoming beam energies, respectively. Some of the corresponding parameters are shown in Table 3.6.

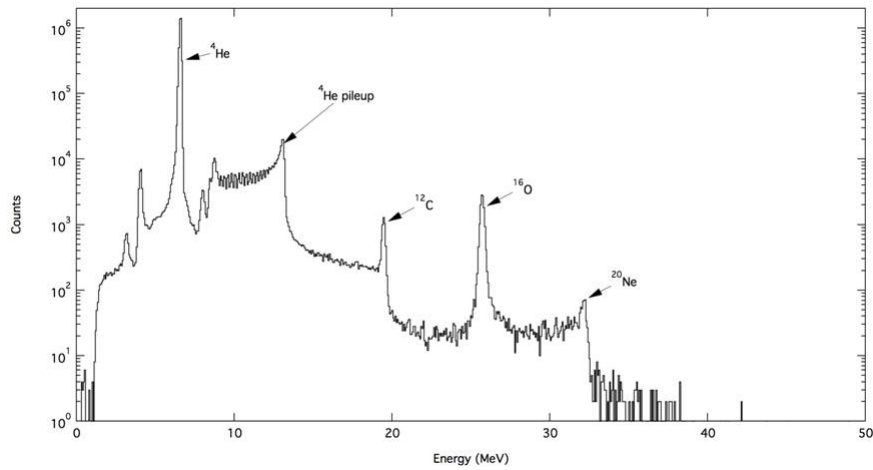
Run	$E_{^4\text{He}}$ (keV)	Time (hr)	^7Be Charge state	B (MD1) Gauss
2011	6553.88 ± 2.78	6.4	3+	2458.70
	5165.97 ± 2.19	14.1	3+	2186.61
	3521.61 ± 1.50	10.1	2+	2697.14
2013	4716.45 ± 2.00	4.2	2+	3102.419
2013 (Impl.)	4716.49 ± 2.00	27.8*	N/A	N/A

Table 3.6: Some relevant details for the measurements performed in 2011 and 2013. The ^4He incoming beam energies within the error given by the accelerator are shown in the second column, the third column shows the measurement time for each energy, the fourth column shows the ^7Be recoil charge state selected in the separator and the fifth one shows the averaged values for MD1 magnetic field $B(\text{MD1})$ at each energy. Errors in $B(\text{MD1})$ are negligible.

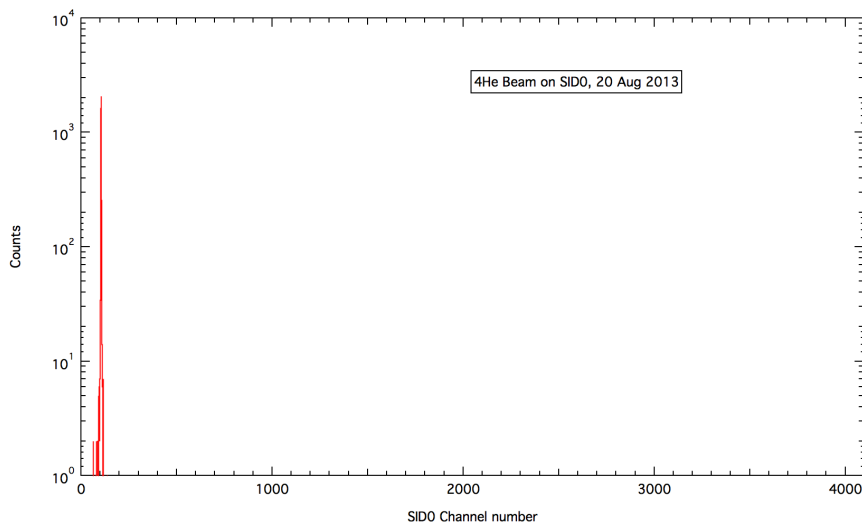
(*)Effective implementation time.

3.3.2.1 Beam purity

In 2011 the supernanogam was used while in 2013 it was the microwave ion source. In order to determine the beam purity, in both cases, a gold foil was placed after the DTL (see Figure 3.20) and a surface barrier silicon detector at 30° with respect to the beam axis detected the scattered beam ions. The on-line $^4\text{He}^+$ beam purity spectra taken with both sources are shown in Figure 3.29, from which the level of contaminants can be noted.



(a)



(b)

Figure 3.29: On-line $^4\text{He}^+$ beam purities. The spectra, of the beam scattered from a gold foil and detected in a surface silicon barrier detector placed at 30° after the DTL, corresponding to (a) the supernanogam ion source in the 2011 and (b) the microwave ion source used in the 2013 run. It should be noted that both spectra are in logarithmic scale. Therefore, the influence of the contaminants is negligible.

3.3.2.2 Tuning procedure for the separator

The separator must be tuned in order to optimise the transmissions for the recoils from the gas target to the DSSSD. It must be pointed out here that the ${}^7\text{Be}$ recoils exit the target with different charge states. The separator is tuned to accept one of the charge states using the standard procedure for DRAGON.

Following this procedure, we tuned the separator to achieve optimum transmission for an attenuated ${}^4\text{He}$ beam through the ${}^3\text{He}$ gas target. The first stage consists of centring the beam in the target cell. A charge-couple device (CCD) camera is mounted on MD1 facing the gas cell. It is used for online monitoring the light from the ionisation of the gas particles due to the beam passing. This allowed us to centre the beam from ISAC-I in the target cell. A picture taken with the CCD camera during one of our measurement is shown in Figure 3.30. The inner and outer yellow circles represents the entrance and exit apertures of the target cell.

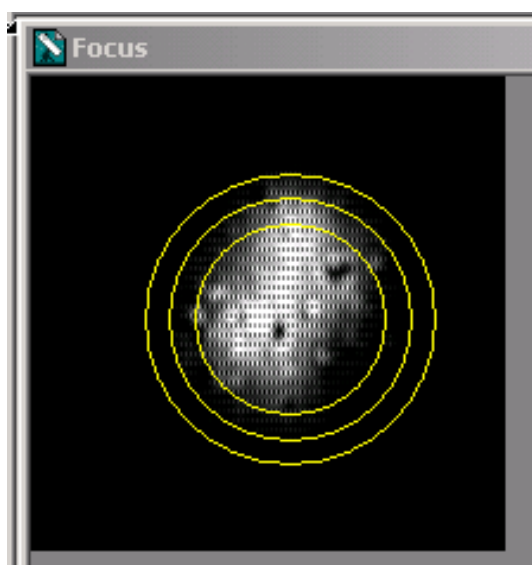


Figure 3.30: On-line CCD camera image of the light produced upon the ${}^4\text{He}$ beam impact on a ~ 6 torr ${}^3\text{He}$ gas target.

Next, the beam is tuned step by step, through the different elements, along which several devices such as slits and beam profile monitors steeres and Faraday cups have been installed to optimise the transmission to the the DSSSD. Controlled adjustments of the magnetic fields, electric fields, and all devices along the separator could be made with the Experimental Physics and Industrial Control System (EPICS). EPICS is a set of software tools which allows real time adjustments to the interfaced equipment [EPI]. Figure 3.31 shows the EPICS control software for half of the first separation stage. Different elements can be observed (see caption for the details). Finally, once the attenuated beam reaches the final Faraday cup, the mass and charge is changed to select the ${}^7\text{Be}$ recoils using EPICS control system. Here, the separator settings were automatically scaled, which we refer to changing to "recoils mode". The change to recoils using EPICS does not take into account the differences in energy losses of beam and recoils in the gas target.

In our reaction, the most symmetric studied ever at DRAGON, the energy differences between the recoils created upstream and downstream are not negligible, in contrast to the typical reactions studied using DRAGON, e.g. (p,γ) reactions with heavier beam compared to ${}^3\text{He}$. This very important aspect will influence the acceptance of the separator that is tuned to select one energy (above all in the electric dipoles). In the 2011, the standard procedure to change from attenuated beam to recoil mode was employed. On the other hand in the 2013 experiment a different manual procedure was used. It consisted of tuning the attenuated beam and changing the magnetic field manually utilising the expression 3.13. For the latter the energy of the recoils created at the centre of the gas target minus the

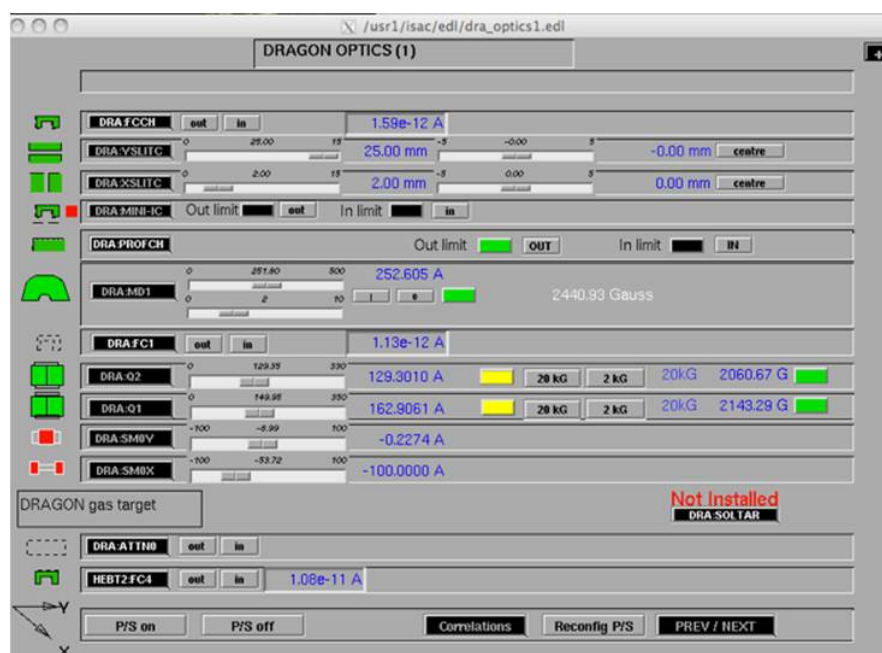


Figure 3.31: EPICS control system for half of the first separation stage of DRAGON. The controlled elements are: FC4 (HEBT2:FC4), the gas target, quadrupoles (Q1,Q2), FC1 (DRA:FC1), the first magnetic dipole (DRA:MD1), slits (DRA:XSLITC and DRA:SLITC) and FFCH (DRA:FFCCH).

energy loss in half of the gas effective length was considered. This procedure favours the selection of the recoils created at the centre of the target. This is in contrast to the standard method where recoils created at the end of the gas target were favoured. As it will be discussed in the next chapter, these differences in procedures will have a strong influence on the acceptance of the recoils.

3.3.2.3 2011 measurements

Three beam energies were considered during the 2011 measurements (see Table 3.6). In principle, the separator should be tuned to select the 3^+ charge state (${}^7\text{Be}^{3+}$) based on our beam suppression studies (details in section 3.3.3.2). However, for the lowest energy measured, MD1 and MD2 could not bend and did not allow us to select the ${}^7\text{Be}^{3+}$ recoils. Therefore, the separator was tuned to select ${}^7\text{Be}^{2+}$ recoils. Some measurements were taken for the ${}^7\text{Be}^{3+}$ settings for the lowest energy, they will not be presented here, because the acceptance of the separator cannot be determined without knowing properly the MD1 and MD2 magnetic fields.

Two examples of the DSSSD spectra showing ${}^7\text{Be}^{3+}$ and ${}^7\text{Be}^{2+}$ recoils are presented in Figure 3.32. It can be noted that for the 3^+ charge state there is not peak corresponding to unreacted beam components close to the recoil peak as expected from the beam suppression studies. In contrast, for the ${}^7\text{Be}^{2+}$, the unreacted beam appears close to the recoil peak. Thus, we could not completely separate the recoils from the unreacted beam.

3.3.2.4 2013 measurements

In 2013 measurements, another measurement was performed using $E_{4\text{He}}^{\text{beam}} = 4717(2)$ keV (see Table 3.6). Based on the experience from the 2011 measurements, two issues were complementary treated in order to better understand our knowledge of DRAGON for this reaction: the likely unreacted beam contribution in the recoil peak seen for the 2^+ charge state during the 2011 measurements, and try to reduce the dependence of the transmission of the recoils throughout DRAGON.

- The MD1 and MD2 could not select the 3^+ charge state (${}^7\text{Be}^{3+}$) for this measurement, thus

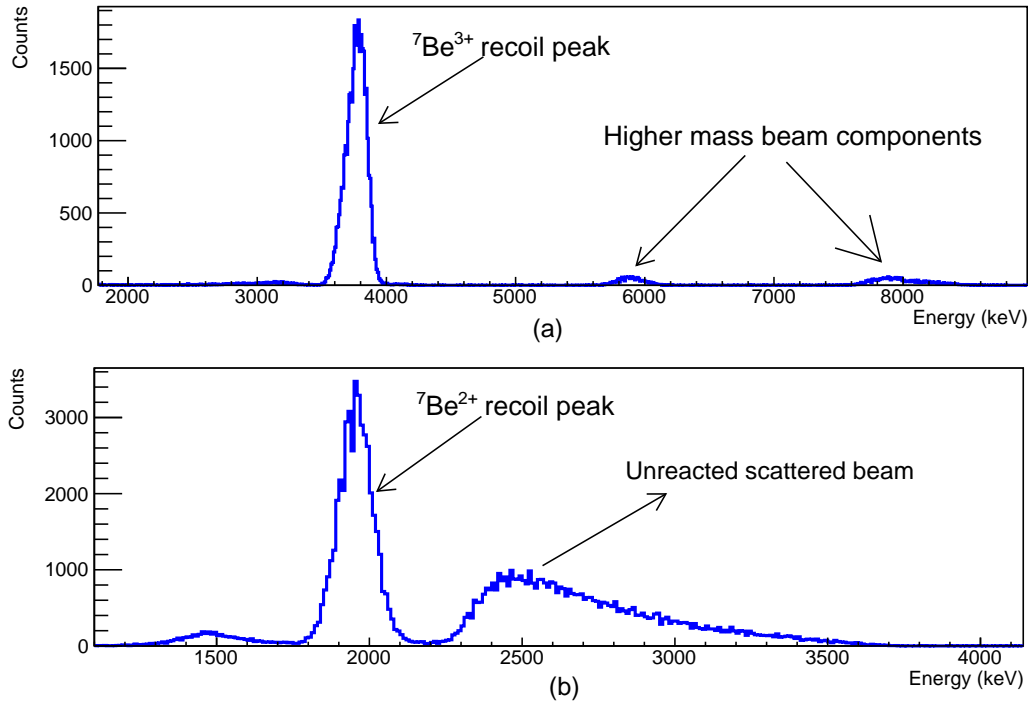


Figure 3.32: The histograms show ${}^7\text{Be}$ recoils detected in any of the 16 front strip of the DSSS. Here, (a) and (b) corresponds to the beam energies of 5166.01 keV and 3521.64 keV and the charge states of 3^+ and 2^+ , respectively.

the separator was tuned to accept the ${}^7\text{Be}^{2+}$ recoils. Figure 3.33 again present the problem due to the selection of the 2^+ charge state, namely, the contribution of the unreacted beam to the recoil peak in the proximity. The DRAGON Micro-Channel Plate Detectors (MCP) placed before the DSSSD were used during some of the measurement to gauge this effect from the leaky beam.

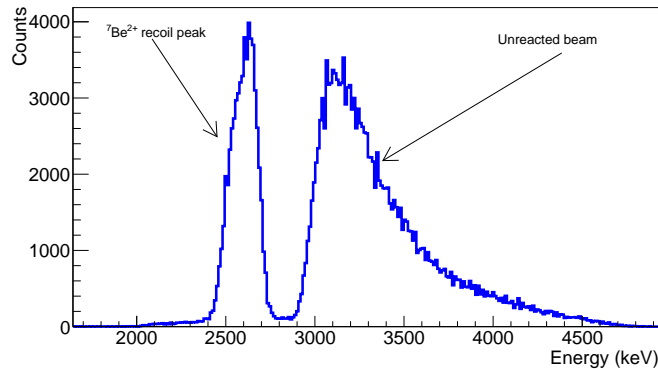


Figure 3.33: DSSSD spectrum for the ${}^7\text{Be}^{2+}$ recoils taken during the 2013 run, with $E_{\text{He}}^{\text{beam}} = 4717(2)$ keV

The DRAGON MCP consists of two microchannel plates in the chevron configuration, one behind the other [Lam01]. Ions crossing the devices deposit a small amount of energy. Secondary electrons escape the foil and are accelerated by a first grid and a second deflects them toward the MCP, where they are detected. The time of flight between the two different plates allow us to identify the mass of the ions. This allowed us to distinguish between mass 4 and mass 7 corresponding to the leaky beam and recoil. Figure 3.34 shows where the MCP are located at DRAGON.

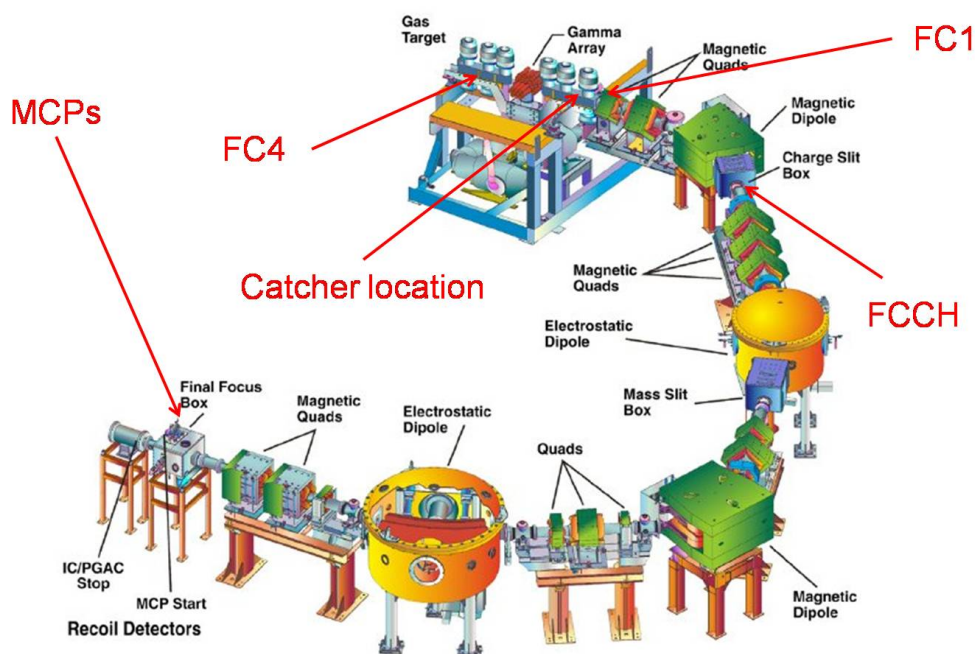


Figure 3.34: DRAGON layout where the location of some devices are labelled in red

The MCP's were placed in and out of the beam path, using a manual drive. It is important to move them as the recoil losses in MCP's could not be accurately estimated. Therefore, the measurements taken with the MCP's in the beam path are not used to determine our reaction cross section. Nevertheless, measurements have been useful to analyse the effects of the leaky beam.

•As will be discussed in the next Chapter, one of the key information required is the DRAGON acceptance of the recoils from this reaction, that is, the fraction of the recoils which can reach the end detector without being stopped throughout the separator. Therefore, the separator was tuned manually in this case and simulation work is the key in this respect.

We also performed an additional cross-check by carrying out a complementary measurement at the same beam energy and gas target condition using the *activity* method at DRAGON ("implantation mode"). For thus we placed a Cu catcher 85 cm downstream of the gas target, i.e. before the first sextupole of the separator (see Figure 3.34) and therefore the recoils do not cross the entire separator before getting implanted.

As the implantation runs were only carried out during the nights, with breaks during the days an effective implantation time has been determined in the same way as for the Madrid experiment following the procedure of reference [FM62].

3.3.2.5 Data taking

In the recoil mode (in 2011 and 2013), the information from different detectors was saved in files which can be individually treated or added off-line. Unless there were some problems during the experiment, each file was automatically closed and saved each 60 minutes, and a new file started. At the beginning of each file, a set of readings with Faraday cups FC4,FC1,FC4,FCCH,FC4 were automatically taken and save for determining the beam currents. Pressure and temperature in the target cell were saved automatically every five minutes, together with electric and magnetic fields in the electric and magnetic dipoles, respectively. See Table 3.6 for some details.

For the implantation mode (in 2013) the recoils were implanted in the Cu catcher and the cell temperature as well as the pressure were also saved each five minutes. None of the magnetic or electric fields were recorded as the separator was not used in this mode. A new file with the information related to the scattered beam in the silicon detectors and the BGO array was opened every hour, after

recording the the FC4 reading. This FC4 reading allowed us to determine the total number of beam particles in the implantation mode. The FC1 and FCCH were placed downstream after Cu catcher and thus were not relevant, see Figure 3.34.

3.3.2.6 Experimental determination of the beam energy

The cross section of the ${}^3\text{He}(\alpha,\gamma){}^7\text{Be}$ reaction is energy dependent. Therefore precise information of the incoming beam energy is required. Typical differences of a few keV were seen in previous experiments between the beam energy provided by the ISAC team and the one determined within the DRAGON setup. We used the standard procedure with DRAGON, based on the magnetic fields measured with the NMR probe placed in the first magnetic dipole, MD1.

As MD1 is not capable of bending ${}^4\text{He}^{1+}$, the beam was converted to the ${}^4\text{He}^{2+}$ ion in the target cell filled with ${}^3\text{He}$ gas at different pressures [MN67, AMHM65]. The ${}^4\text{He}^{2+}$ ions passed through MD1 and the magnetic field "B" was set so that the ions were centred in the 2mm wide charge slits after MD1 (S1 in Figure 3.21). An analysis of the magnetic field versus the ${}^3\text{He}$ gas pressure was used to obtain the magnetic field with no target gas, which corresponded to the incoming beam energy. The kinetic energy is then obtained from the expression 3.13. An example of the extrapolation procedure to zero pressure (no gas condition) is shown Figure 3.35; in this case the magnetic field for no gas inside the cell is 2705 Gauss, and the corresponding beam energy is 3.521 MeV.

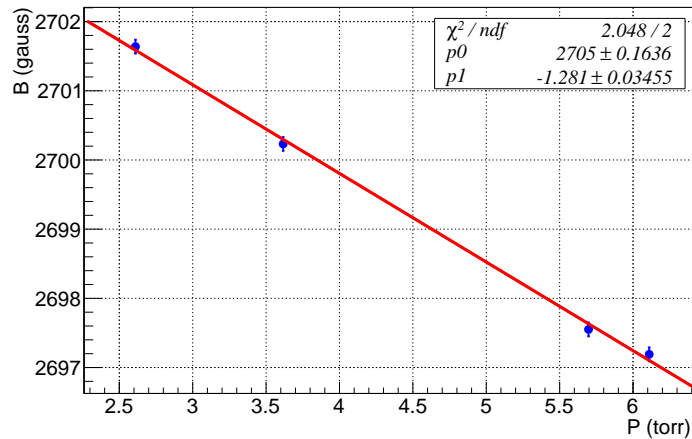


Figure 3.35: Example of magnetic field values in MD1 for an ${}^4\text{He}^{1+}$ beam after crossing a ${}^3\text{He}$ gas target at different pressures for the beam energy of ~ 3.5 MeV given by ISAC. The fields were read out once the beam was centred in the 2 mm width slits placed after MD1. The offset from the fit, 2704.93 Gauss, gives the extrapolated magnetic field value for the incoming beam without any gas in the target cell. The beam energy can be calculated by using the expression 3.13 where $A=4.00154$ and $q=2$. For the case of this graph the beam energy at 0 Torr pressure is 3.521 MeV.

The associated beam energy dispersion is reported to be 0.1% FWHM at 1.5A MeV by ISAC-I website [GUI]. Therefore, the spread in the kinetic energy can be given by:

$$\Delta E = E \frac{0.1\%}{2\sqrt{2\ln 2}} \quad (3.15)$$

The four beam energies used in the experiment are listed in Table 3.6 within their errors.

3.3.2.7 Observables

As in the case of Madrid experiments, the three main observables to determine the ${}^3\text{He}(\alpha,\gamma){}^7\text{Be}$ reaction cross section are: the total incoming ${}^4\text{He}$ beam particles, the total number of ${}^7\text{Be}$ recoils produced on the ${}^3\text{He}$ gas target areal density:

• For this experiment the number of beam particles have been determined from the combination of two observables, namely, the scattered ions detected in the two silicon detectors placed at 30° and 57° and the currents measured by Faraday cups. Examples spectra taken with the collimated silicon detectors placed at 30° (a) and 57° (b) are shown in Figure 3.36 for the case of ^4He beam at 5166 keV and a ^3He gas target at the pressure of ~ 6 torr. At this energy, two peaks originated from the scattered beam and the scattered target particles can be separated in the 30° detector, but they are merged in the case of the 57°.

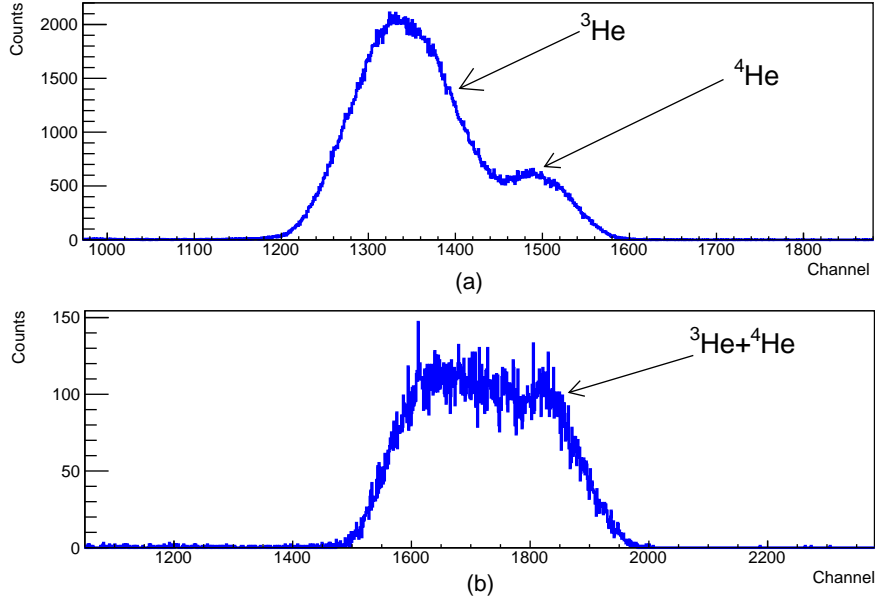


Figure 3.36: Collimated ion implanted silicon detector spectra at (a) 30° and (b) 57°, taken for an incident ^4He beam at $E_{\text{beam}} 5166$ keV impinging onto a ~ 6 torr ^3He gas target.

The scattering of ^3He by ^4He has been studied by, for example, R.J. Spieger and T.A Tombrello [ST67] showing (i) an energy dependence different from that given in 3.6 for the Rutherford scattered beam particles from the Ni foil and, (ii) the large energy dependence of the cross section for the elastic scattering channel. For each energy, we determine a normalisation factor between incoming particles measured via the Faraday cup readings and the total scattered particles in the silicon detector (^3He and ^4He peaks integrated together) and utilised them to determine the total number of incoming particles. It is worth noting that the correspondence between laboratory and centre of mass angles is different at each energy and thus the centre of mass angle subtended by the detector is different for the different energies.

• The total number of ^7Be recoils is derived from the total counts in the recoil peak of the DSSSD spectra i.e. (Y_{DSSSD}). This yield corresponds to those ^7Be recoils with a particular charge state that managed to go through the separator, hit in the active area of the DSSSD and be accepted by the DAQ. Therefore, the total number of recoils produced, can be given by:

$$Y_{^7\text{Be}} = \frac{Y_{\text{DSSSD}}}{t_{\ell} \cdot q_f \cdot \epsilon_{\text{DRAGON}} \cdot \epsilon_{\text{DSSSD}}} \quad (3.16)$$

here, t_{ℓ} , q_f , ϵ_{DRAGON} and ϵ_{DSSSD} refers to DAQ livetime, charge state fraction of the recoils for the selected charge in the separator, the recoil acceptance of DRAGON for this reaction and the DSSSD detection efficiency, respectively.

• The gas target areal density is calculated using equation 3.7. In this case the pressure, P and total temperature, T_0 will be the average of all the values recorded each 5 minutes during the experiment. The temperature correction due to the beam heating of the target in this case is negligible.

The effective target length, l , is considered 12.3 ± 0.5 cm. This value is based on the effective length determined with the energy losses of the ^{12}C beam used for the target density profile measurements (section 3.3.3.4) and from previous measurements performed using different ion beams and targets.

3.3.3 Additional measurements

Some complementary and important measurements are required in order to extract the cross section from our measurements [NSD12]. As mentioned in the previous section, MD1 and MD2 separate particles based on their charge states (see expression 3.12) and only the recoils with the chosen charge state get through these dipoles. Therefore, we need to estimate the $^7\text{Be}^{1+,2+,3+,4+}$ charge state fractions at the exit of the target in order to know the total number of ^7Be recoils produced in the capture reaction. On the other hand, in the energy range of interest, it can be safely assumed that the probability for the reaction to occur is the same throughout the effective gas target length. Therefore, the acceptance of the separator is influenced by the origin of the recoils and thus experimental determination of the target density profile (TDP) is required. The details of the charge state distribution (CSD) and TDP measurements together with the DSSSD calibration and beam suppression measurements are given in the following subsections.

3.3.3.1 DSSSD calibration

The objective of our experiment is to determine the cross section of the $^3\text{He}(\alpha,\gamma)^7\text{Be}$ reaction. Therefore, a clean identification of the ^7Be recoil is the key requirement, but a reasonable knowledge of their energies should be extracted. In fact, we can calculate the recoil energy rather well from the known beam energy and the effective target length. Moreover, we can precisely determine the ^7Be recoil energy accepted by the separator by using the expression 3.13 and the MD1 magnetic field value.

In this context, it is sufficient, but required to have the peak corresponding to a given ^7Be energy aligned between the spectra for the various DSSSD strips. These spectra can then be added in order to obtain the correct total number of the recoils.

Firstly, the linearity behaviour for all 32 strips was studied using a pulser at voltages of 0.5, 1, 1.5, 2 and 2.5 V. An example for one of the strips can be seen in Figure 3.37 where an analysis regression between the nominal voltage and the channel in the histogram is shown. The offset, $p0$, from the fit (25.5 for the example in Figure 3.37) is the value corresponding to no particle hitting the detector (0 voltage.)

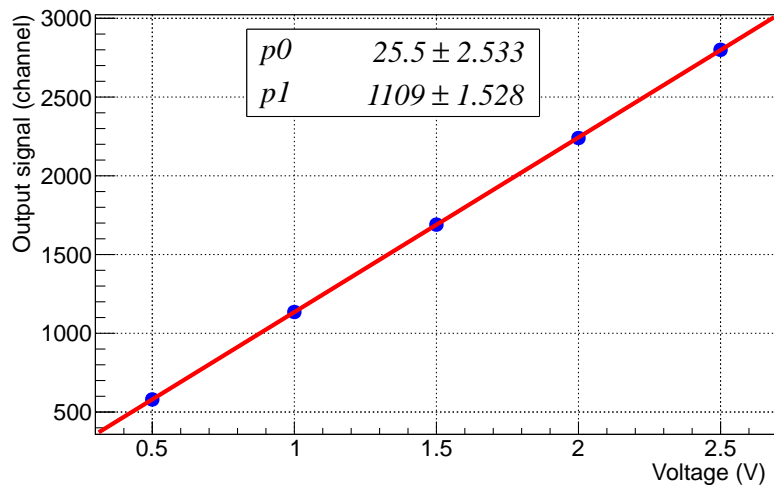


Figure 3.37: Linearity check for the vertical strip. "X" and "Y" axes show the pulser voltage and the corresponding channel in the DSSSD histogram. $p0$ and $p1$ gives offset and slope for the linear fit, respectively. As can be seen, a clear linearity behaviour is present for this strip.

Complementary, a calibration measurement was then performed by placing a standard triple alpha source in front of the DSSSD. As in the case of Madrid experiment a linear regression between the channel numbers and the values for the energy deposited in the DSSSD was done for each strip. The deposited energy for the alpha particles was slightly different from the standard triple alpha energies given in Table 3.3. These differences essentially come from the energy losses in the aluminium dead layer with effective thickness of $0.5 \mu\text{m}$. The energy losses in the dead layer was estimated using the SRIM code [SRI]. Apart from the triple alpha energies, the offsets such as this presented in Figure 3.37 were used in the calibration process.

The comparison for the energy matching for the strips before and after energy calibration in keV is shown in Figure 3.38. As can be seen, there is good energy matching for the alpha particle peaks among all strips after calibration.

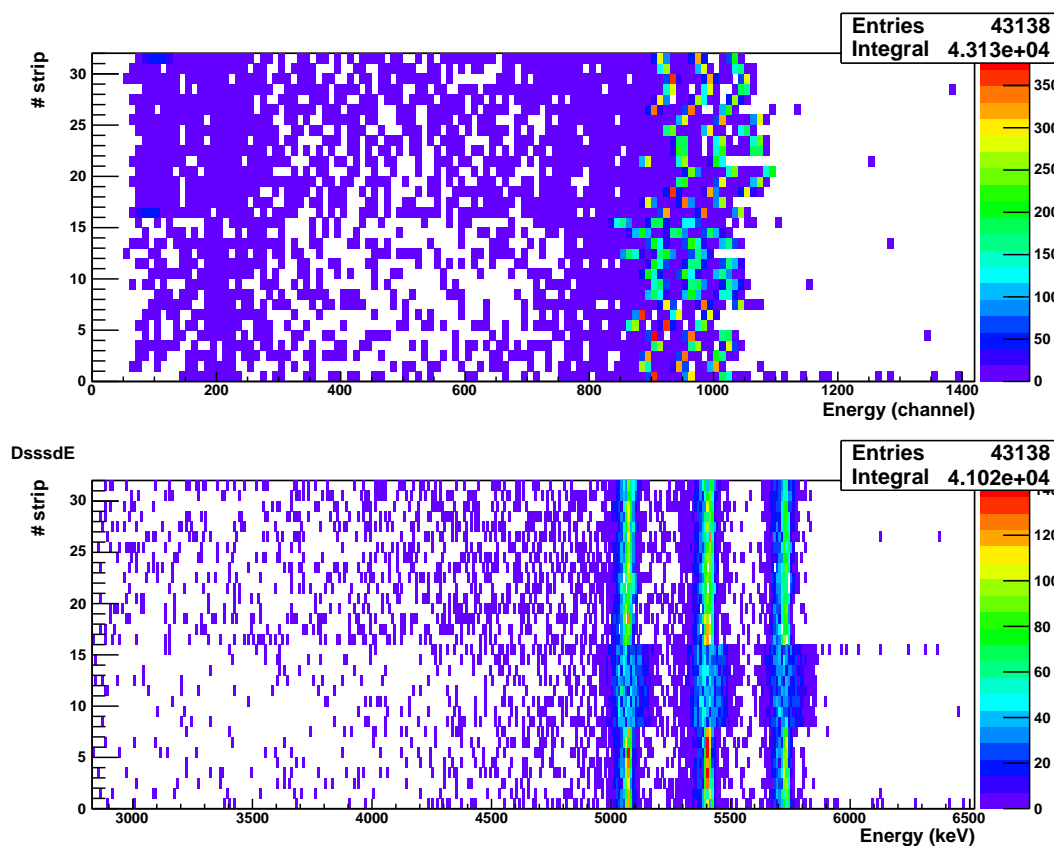


Figure 3.38: The DSSSD strip number versus energy, before (upper) and after (lower) energy calibration. The energy is shown in keV. A good match for the alpha energy peaks among the different strips can be seen.

3.3.3.2 Beam suppression

In contrast to other reactions studied using DRAGON e.g. (p,γ) reactions using higher mass beams, the relative mass difference between the α beam particles and ${}^7\text{Be}$ recoils is large. This is advantageous as DRAGON settings for the beam and recoils are very different, allowing a good beam suppression. In addition, for the case of 3^+ charge state of the ${}^7\text{Be}$ recoils the beam suppression is even higher because there is no 3^+ charge state for the beam. Indeed, we performed separate tests to quantify the beam suppression for our reaction [SSA13].

The three overlaid spectra shown in Figure 3.39 were taken in order to study the ${}^4\text{He}$ beam contribution to the ${}^7\text{Be}^{3+}$ recoils at $E^{\text{beam}} \sim 6.5 \text{ MeV}$. The red histogram, collected for 31345 s represents an attenuated 6.542 MeV ${}^4\text{He}$ beam detected in the DSSSD, when DRAGON was tuned to

the recoils and with no target gas in the cell. The events in channels between 1000 and 1100, represent events from the beam and scattered by a foil in the microchannel plate detector placed before the DSSSD. The ${}^7\text{Be}^{3+}$ recoils spectrum in the black histogram was taken with ~ 7 Torr gas inside the target cell, $1.95(6) \times 10^{16}$ incoming beam particles and the separator tuned to $A/q=7/3$ and 3.741 MeV energy. The latter corresponds to the recoil energy. Also a background spectrum with no beam taken during 20967 s (~ 6 h) is shown in blue.

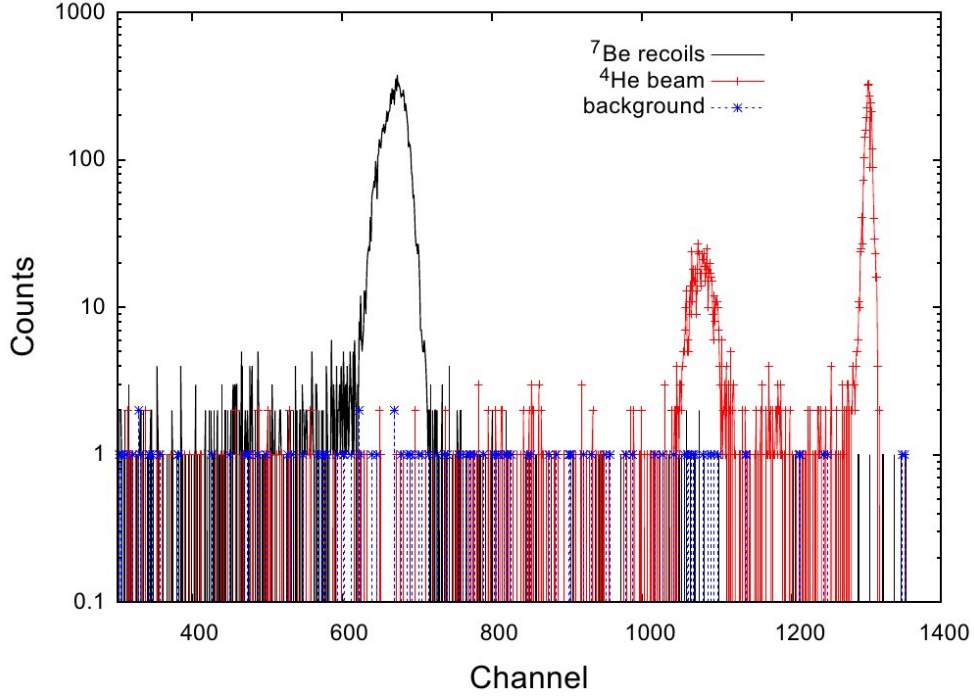


Figure 3.39: Spectra taken reference [SSA13] highlighting the beam suppression for our reaction. The attenuated 6.542 MeV beam energy spectrum is shown as red histogram. The recoils spectrum and the background spectra are shown in black and blue respectively (see text for more details).

The expected number of events in a considered range of channels for the background and recoils spectra are given by $\nu_b = R_b \Delta t_b$ and $\nu_s = (R_b + R_s) \Delta t_s$, respectively. Here R_b is the background event rate and R_s is the scattered ${}^4\text{He}$ event rate. Two constrains $\nu_s \geq 1.50\nu_b$ based on the duration of the runs and, $R_b \geq 0$ are also present. The probability of having i background counts and j beam scattered counts is given by: $P_{ij} = \binom{\nu_b^i}{i!} \exp(-\nu_b) \cdot \binom{\nu_s^j}{j!} \exp(-\nu_s)$ for an expectation values $[\nu_b, \nu_s]$. The limiting probability is given by the data, $P_0 = P_{ij}[i = N_b, j = N_s]$ being N_b and N_s the number of background events and the scattered beam events in the region of interest. The 90% confident intervals are define for all $[\nu_b, \nu_s]$ that satisfy the conditional sum:

$$\sum_{ij|P_{ij} \geq P_0} P_{ij} \leq 0.90. \quad (3.17)$$

Two ranges of channels were considered: 770-1320 and 300-400. From the study in this two ranges, the integrated beam suppression from channels 300 to 1320 is $> 1.2 \cdot 10^{14}$ in terms of the total number of incident ions divided by the number of transmitted ions at 90% CL.

The beam suppression has been determined for the ${}^7\text{Be}^{3+}$ recoils at $E^{\text{beam}} = 6.542$ MeV, which is the highest energy in our experiment. As already mention, for the $E^{\text{beam}} = 3.521$ and 4.716 MeV the separator was tuned to 2^+ charge state instead of 3^+ charge state due to the limitations of the separator in bending the ${}^7\text{Be}^{3+}$ recoils at those energies. The contributions of the leaky beam in the recoil energy region for the ${}^7\text{Be}^{2+}$ recoils at these energies were measured using the MCP's.

3.3.3.3 Charge state distributions

The ${}^7\text{Be}$ recoils produced along the length of the target interchange electrons with ${}^3\text{He}$ gas atoms. Therefore, a distribution of the ${}^7\text{Be}^{+1}$, ${}^7\text{Be}^{+2}$, ${}^7\text{Be}^{+3}$ and ${}^7\text{Be}^{+4}$ ions is present at the exit of the target cell. During the experiment DRAGON was set to select either the 3^+ or 2^+ charge states, therefore the fraction of these particular charge states (F_q) must be known in order to determine absolute cross sections as this determines the overall detection efficiency of our setup for ${}^7\text{Be}$ recoil detection.

Once the ions pass through minimum effective gas thickness needed for F_q to reach an equilibrium, this charge fraction stays constant upon encountering further gas atoms. Previous ${}^{16}\text{O}$ and ${}^{24}\text{Mg}$ F_q measurements using DRAGON are shown Figure in 3.40 [LIB03]. As can be seen after some critical gas thickness the charge state equilibrium is reached.

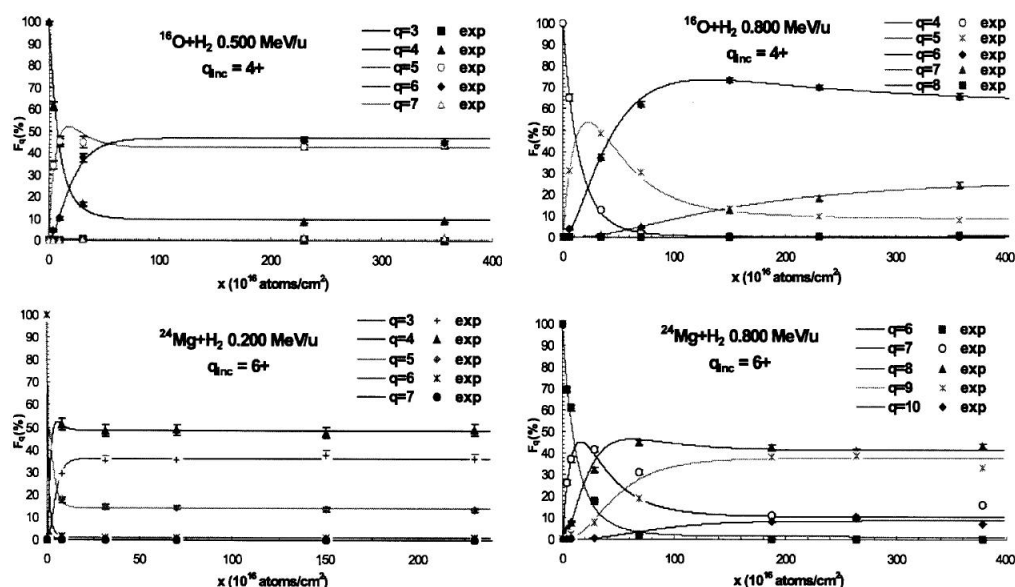


Figure 3.40: Fractional charge states measured using DRAGON taken from reference [LIB03]. The charge state fractions for the ${}^{16}\text{O}$ and ${}^{24}\text{Mg}$ ions are plotted as a function of the incoming energy and incident beam charge state. As can be observed, the charge state fraction do not change after a critical thickness.

Some arguments are given in the paper based on the results for charge state fraction using DRAGON, which fit the Gaussian distribution well (see Figure 3.41).

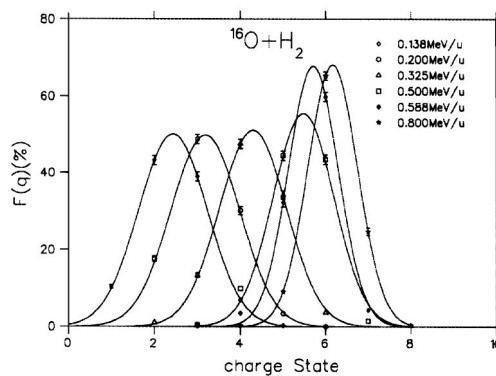


Figure 3.41: Figure taken from [LIB03] shows equilibrium charge state distributions for a ${}^{16}\text{O}$ beam at different energies impinging onto a ${}^2\text{H}$ target. The charge state fractions are fitted using Gaussian functions.

Therefore an average equilibrium distribution can be given semi-empirically by [Bet72]:

$$\bar{q} = Z_p \left[1 - \exp \left(-\frac{A}{Z_p^\gamma} \sqrt{\frac{E}{E'}} + B \right) \right] \quad (3.18)$$

where A , B and γ are free parameters, Z_p is the atomic number of the projectile with energy E (MeV/u) and $E' = 0.067635$ MeV/u. Although some values for A , B and γ parameters are determined in reference [LIB03] these can not be used in our analysis as these semi-empirical expressions are not general and depend on each experiment itself. However, some observations can be made. For a given incident beam element, the charge state equilibrium is independent of the initial charge state or isotope. The cross section of capture and loss of electrons for an ion beam depends on the velocity of the projectiles, atomic number of the ion beam and nuclear charge of the target atoms.

Based on these qualitative observations we performed measurements in order to determine the charge state distribution of the ${}^7\text{Be}$ recoils. We used a ${}^9\text{Be}^{2+}$ beam at three different incoming energies onto a ${}^3\text{He}$ gas target at different pressures. The charge state fractions (F_q) are determined by obtaining the ratio between the incoming ${}^9\text{Be}^{2+}$ beam current measured using FC4 Faraday cup placed before the gas target, and the number of ${}^9\text{Be}^q$ ions (being $q = 2^+, 3^+$ or 4^+) measured in FCCH. This cup is located downstream MD1, the magnetic field value of which selects charge state of interest. Therefore, we have

$$F_q = \frac{N_{{}^9\text{Be}^q}}{N_{{}^9\text{Be}^{2+}_{\text{incoming}}}} = \frac{I_{\text{FCCH}} \cdot T / (q \cdot e^-)}{I_{\text{FC4}} / (2 \cdot e^-)} \quad (3.19)$$

here, I 's represent currents measured in the Faraday cups in ampere, e^- is the electron charge and q is the selected ${}^9\text{Be}$ charge state in MD1. The transmission, T , throughout the gas target was estimated by the ratio between the currents measured in FC4 and FC1 (placed just before Q1) without gas in the target cell.

Using a computer program called "Rosumn" Faraday cup readings were taken in the following order FC4-FC1-FC4-FCCH-FC4. Each of these cup measurements takes 30 seconds. If there is gas inside the target cell, FC1 readings cannot be used for determining the transmissions due to the mixture of different charge states at that point. Therefore FC1 were considered with no gas target inside.

The charge state fractions measured using the ${}^9\text{Be}^{2+}$ ion beam and ${}^3\text{He}$ gas target are shown in the Table 3.7. The FC4 reading was considered as the average of the three FC4 measurements taken during every cup reading sequence. In chapter 5, a typical 30 seconds Faraday cup reading and how the information is extracted will be shown. For $E_{{}^9\text{Be}}^{\text{beam}} = 533.78$ keV/u and 420.54 keV/u, the charge state distributions were measured using two different pressures in order to prove that the charge state equilibrium is reached for a gas pressure >1 Torr. Figure 3.42 shows the example case of $E_{{}^9\text{Be}}^{\text{beam}} = 533.78$ keV/u. As can be seen the charge state equilibrium is reached. This means that all ${}^7\text{Be}$ recoils created via the ${}^3\text{He}(\alpha, \gamma){}^7\text{Be}$ reaction which pass through the gas of 1 Torr of effective pressure will exit the target with the same charge state distribution. Thus, the charge state selection in MD1 will affect in the same way independently of where they were created and we can infer the total number of recoils produced from just detecting one charge state and taking into account the charge state fraction (F_q) in Table 3.7.

$E^{incoming}/u$ (^9Be) (keV)	Transmission (%)	P (Torr)	q	F_q (%)		
533.91	95	0.95	2	12.08 ± 2.17		
			3	59.78 ± 1.85		
			4	27.97 ± 0.91		
		5.25	2	10.80 ± 2.32		
			3	59.05 ± 1.87		
			4	29.15 ± 1.21		
420.64	96	5.3	2	22.88 ± 3.78		
			3	61.87 ± 2.55		
			4	12.59 ± 1.73		
		1.1	2	23.42 ± 4.06		
			3	60.07 ± 3.05		
			4	13.28 ± 2.18		
		284.09	92	5.31	2	52.30 ± 3.33
					3	37.91 ± 2.37
					4	1.82 ± 0.98

Table 3.7: Charge state distributions (CSD) for a $^9\text{Be}^{2+}$ beam onto ^3He gas target. ^9Be electric charge after passing through the gas target is shown in the fourth column. The charge fractions in the fifth column were measured using three different incoming beam energies shown in the first column and determined as explained in section 3.3.2.6. For the first two energies, the CSD was measured at two different pressures shown in the third column in order to show that the charge state equilibrium was reached at 1 Torr. The transmission between FC4 and FC1 placed before and after the target box, respectively is indicated in the second column and it was measured with no gas inside the target cell.

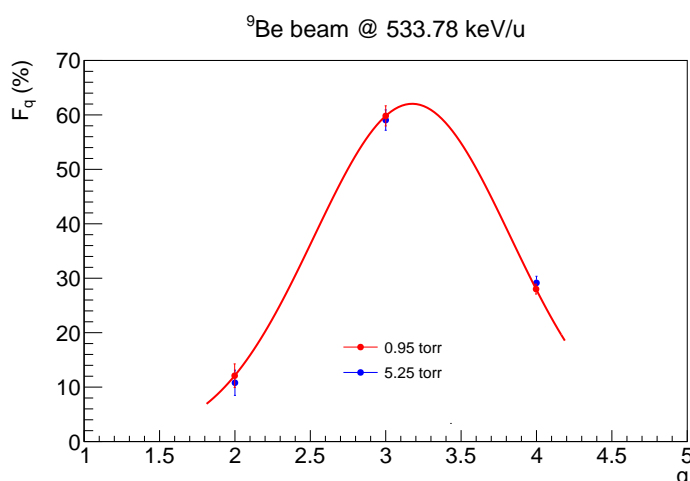


Figure 3.42: Charge state distribution for a $^9\text{Be}^{2+}$ beam with incoming energy of 533.78 keV/u onto a ^3He gas target at two different pressures, 0.95 and 5.25 torr. The values for the charge state fractions (F_q) for the different charges (q) are the same within the errors for the two values of ^3He gas pressure. This means that the charge state equilibrium is reached at and above the target gas pressure of 0.95 Torr.

3.3.3.4 Target density profile

Kinematic calculations (see appendix B) for the ${}^3\text{He}(\alpha,\gamma){}^7\text{Be}$ reaction show that the maximum recoil cone angle is ~ 20 mrad, which nearly corresponds to the separator geometrical acceptance. Moreover, a distinctive feature is that in our range of energy this is a non-resonant reaction. Thus, the probability of the reaction to occur is the same throughout the effective target length. This is in contrast to the most of reactions studied at DRAGON, which are usually resonant reactions. These two facts, namely, i) mass symmetry in the incoming reaction channel leading to large cone angle, and ii) the position for ${}^7\text{Be}$ production anywhere in the target, limit the recoil acceptance of the separator.

If some other effects are considered as the ${}^4\text{He}$ beam and ${}^7\text{Be}$ recoil straggling in the material along their path, variation on the beam direction, or the fact that the beam is not point-like, the recoil cone angle can be seen increased to 22 mrad [Ree12], which is above the 20 mrad of geometrical acceptance. It should be noted that in this case we assumed that the reaction takes place upstream the target centre. Such effects will be treated in the next chapter using simulations for estimating the DRAGON ${}^7\text{Be}$ recoil acceptance reaction where the true target density profile must be included.

The target density profile (TDP) was experimentally determined using the ${}^3\text{He}({}^{12}\text{C}, {}^{14}\text{N}\gamma)\text{p}$ resonant reaction. Moreover, this was the first time using a ${}^3\text{He}$ gas target in DRAGON, and this measurements served as cross checks on the previously measured effective target length using ${}^2\text{H}$ and ${}^4\text{He}$ targets.

The experiment was performed using a ${}^{12}\text{C}^{2+}$ ion beam impinging onto a ~ 6 torr ${}^3\text{He}$ gas in the target cell. Half of the BGO detector array surrounding the gas box was removed from surroundings and a single lead shielding BGO detector was used to detect the γ -rays from the reaction ${}^{12}\text{C}+{}^3\text{He}$. The shielded detector was placed on top of a movable platform, which allowed us to move it along the length of the gas box. Figure 3.43 shows two photographs of the shielded BGO detector in front of the target box as it was used during the experiment.

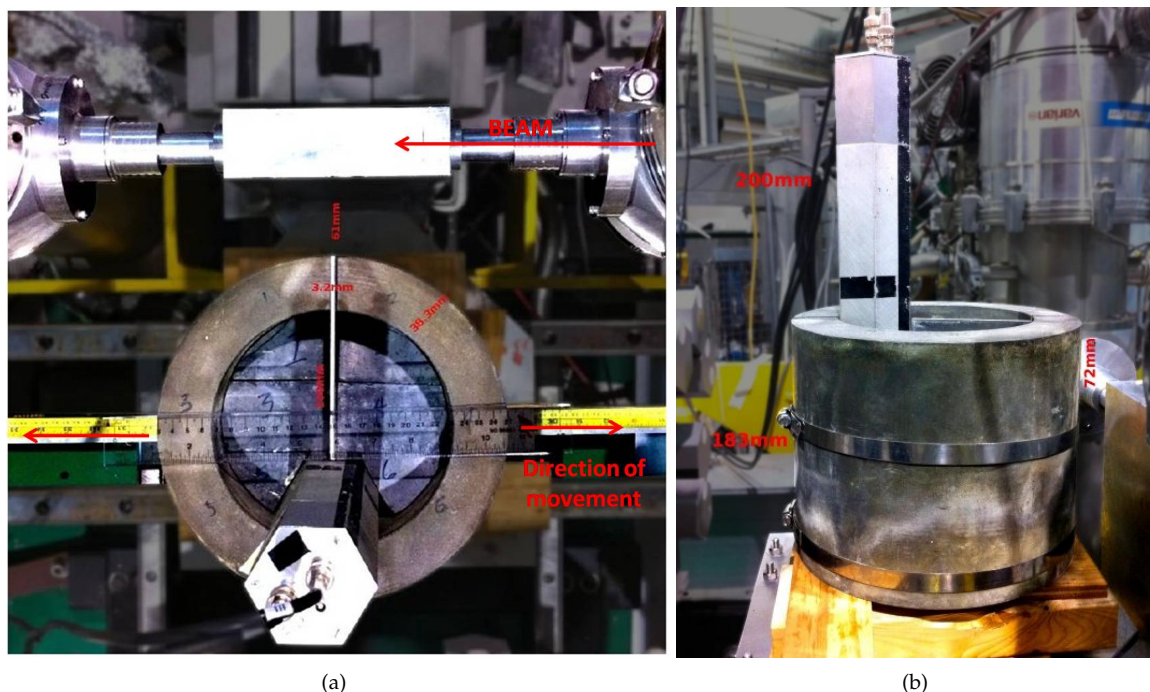


Figure 3.43: Setup used for the measurements of the target density profile. (a) An upper view of the set up is shown together with the target cell and the shielded BGO detector placed in front. The 3.2 mm length is the slit in the shielding through which the γ -ray from the reaction in the cell are viewed by BGO. (b) A side view of the set up is shown here.

Based on the results from reference [KBR64], in which the ${}^3\text{He}({}^{12}\text{C}, {}^{14}\text{N}\gamma)\text{p}$ reaction was studied using direct kinematics, i.e. ${}^3\text{He}$ beam onto a ${}^{12}\text{C}$ target, there is a known broad resonance centered at 2.99 MeV beam energy for the ${}^{12}\text{C}({}^3\text{He}, {}^{14}\text{N}\gamma)\text{p}$ (6.44 MeV state in ${}^{14}\text{N}$) reaction. This was observed by the detection of the 6.44 MeV γ rays at this particular 2.99 MeV energy and not above (3.46 MeV) or below (2.62 MeV) the energy. This broad resonance was chosen in order to have a low energy dependence across the target length. The goal of our measurements was to populate the same resonance state using inverse kinematics (we need to use the ${}^3\text{He}$ as target due to our interest of determining the TDP for ${}^3\text{He}$) and detect the 6.44 MeV γ -ray. The target density profile could be determined by comparing the number of γ -rays detected by the BGO collimated using a 3.2 mm slit placed at different positions across the target box (see Figure 3.43(a)).

A part of the energy level diagram relevant for the reaction with $\text{p}+{}^{14}\text{N}$ in the exit channel is shown in Figure 3.44. Some other open reaction channels e.g. ${}^3\text{He}({}^{12}\text{C}, {}^{11}\text{C})\alpha$ are not denoted. By selecting the optimum ${}^{12}\text{C}$ beam energy, the 14.46 MeV state in ${}^{15}\text{O}$ is populated. This state decays by proton emission populating the 6.44 MeV state in ${}^{14}\text{N}$, which de-excites by the emission of one of the four possible γ -rays with the relative intensity shown in the figure. The incoming beam energy of 12.088 MeV for our measurements was determined using the same procedure described in section 3.3.2.6, using MD1 tuned to select the 5+ charge state of ${}^{12}\text{C}$.

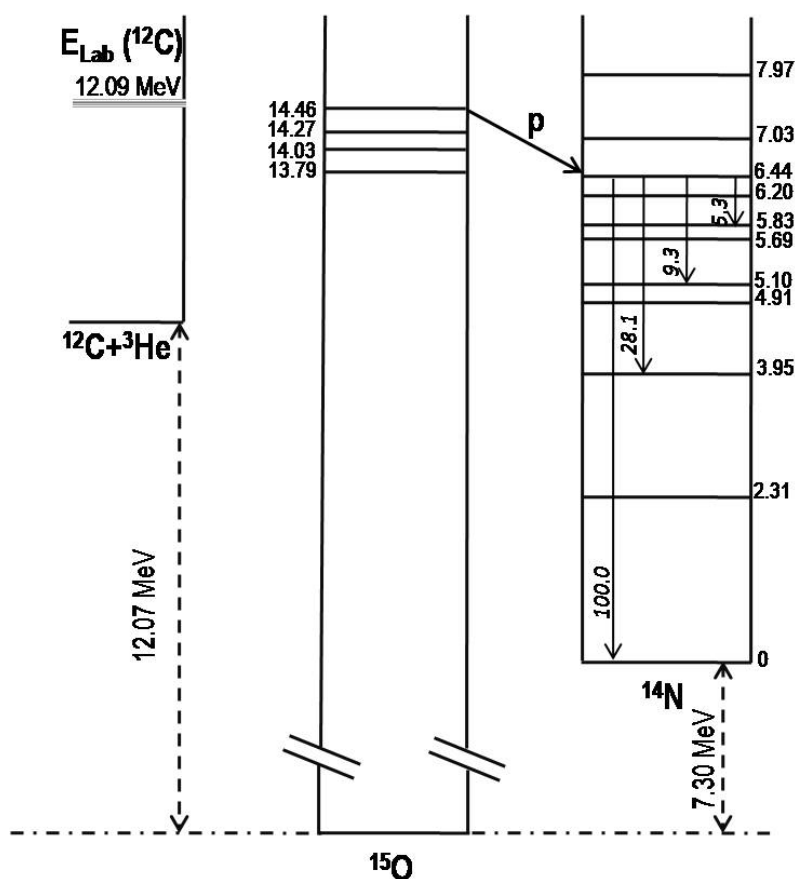


Figure 3.44: A relevant part of the energy level diagram for the ${}^{12}\text{C}+{}^3\text{He}$ reaction showing the excited states in ${}^{14}\text{N}$ and ${}^{15}\text{O}$ nuclei that play important role in our analysis. The levels are marked with their energies in MeV (from [Nuc]). All the γ -rays from the 6.44 MeV state in ${}^{14}\text{N}$, to the ground, 3.95, 5.10 and 5.83 MeV states, are also shown with their relative intensity written down in italic. Using a 12.09 MeV ${}^{12}\text{C}$ beam, we populated the 14.46 MeV state in ${}^{15}\text{O}$, which decays mainly via proton emission to the 6.44 MeV state in ${}^{14}\text{N}$. Some other channels are opened for this energy, such as ${}^3\text{He}({}^{12}\text{C}, {}^{11}\text{C})\alpha$, but they are not shown in the figure, these are irrelevant for TDP determination.

In order to check the $^{12}\text{C}^{2+}$ beam purity, the beam was scattered using a gold foil located just after the DTL. Figure 3.45 shows an on-line calibrated spectrum of the Rutherford scattered particles detected in a silicon surface barrier detector kept at 30° with respect to the beam taken during a short measurement. The yield in the peaks implies that ^{18}O contaminant is present at a level of 0.5% in the beam.

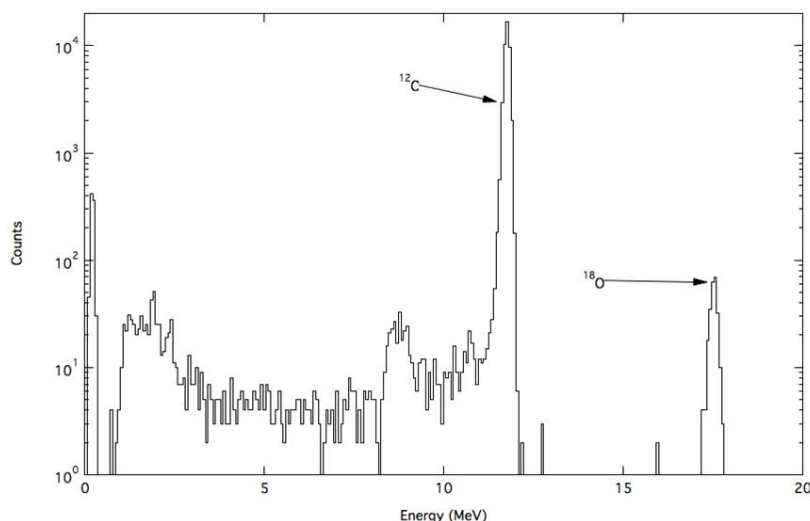


Figure 3.45: An on-line spectrum of ^{12}C beam scattered from a gold foil placed after the DTL (see text for details).

An example BGO spectrum showing the γ -rays from the $^3\text{He}(^{12}\text{C}, ^{14}\text{N}\gamma)\text{p}$ reaction is shown in Figure 3.46, for the BGO placed at the centre of the target cell. The measurements were performed covering a range between -11 cm upstream and 9 cm downstream with respect to this position. It should also be noted that the distance between the beam line and BGO detector was kept constant as we moved the shielded BGO along the target box.

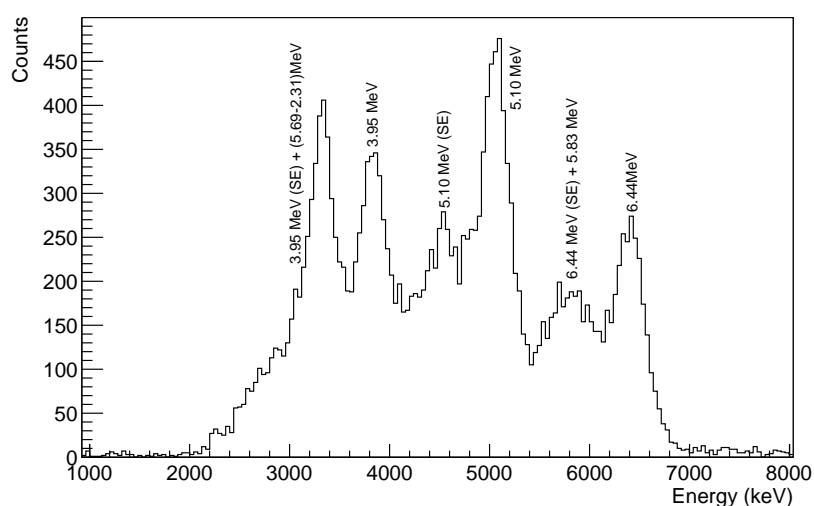


Figure 3.46: BGO spectrum for the $^3\text{He}(^{12}\text{C}, ^{14}\text{N}\gamma)\text{p}$ reaction with the BGO detector viewing the centre of the gas cell. The main peaks are labelled with their energy in MeV. SE refers to the single escape peak of the related energy.

The TDP is related to the yield of the 6.44 MeV γ -peak in each of the BGO position. The yield for each position is given by:

$$Yield = \frac{BGO^{6.44\gamma} / Livetime \cdot 8.02 \cdot 10^{-8}}{SB0 \cdot P} \quad (3.20)$$

where $BGO^{6.44\gamma}$ is the 6.44 MeV integrated peak, $livetime$ is the correction due to dead time of the acquisition system, P is the pressure in the target cell included as the correction related to the different number of ^3He gas particles for each run and, $SB0$ is the normalisation factor related to the ^{12}C beam particles for each run.

During each measurement, for different BGO positions, the scattered beam ions with the gas were detected in the ion implanted silicon detector mounted on the arm of the gas cell at 30° (see Figure 3.22). Figure 3.47 shows a calibrated spectrum of scattered particles detected in the silicon detector for a ^{12}C beam at 12.09 MeV impinging onto the ^3He gas target at 5.9 torr.

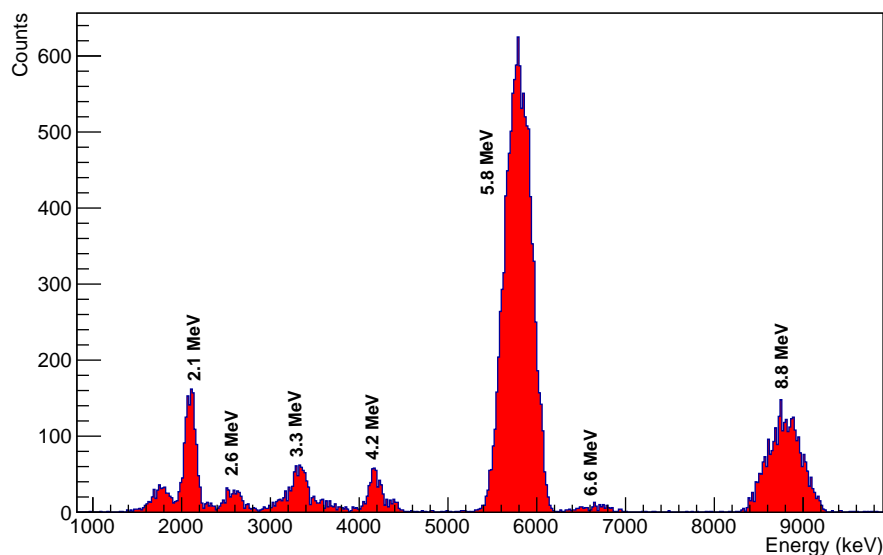


Figure 3.47: A scattered particles spectrum detected with the silicon detector placed a 30° with respect to the beam for a 12.088 MeV ^{12}C beam impinging onto the ^3He target at 6 torr. Some of the peaks are labeled with their corresponding energy, see text for the details of the peak particles origin. The peak of interest for the the TDP measurements is the 5.8 MeV corresponding to the scattered ^3He from ^{12}C .

Energies corresponding to the peaks and their origin are:

- 8.8 MeV: α particles from the $^3\text{He}(^{12}\text{C}, ^{11}\text{C})\alpha$ reaction
- 6.6 MeV: ^3He elastic scattered from the ^{18}O beam component
- 5.8 MeV: ^3He elastic scattered from ^{12}C
- 2.1 MeV: protons for the $^3\text{He}(^{12}\text{C}, ^{14}\text{N}^*)\text{p}$ reaction

In order to normalise the yield with the number of incoming ^{12}C beam particles, $SB0$ factor in expression 3.20 is considered as the 5.8 MeV peak integration. Thirty seven measurements were taken for different BGO positions between -11 cm downstream and 9 cm upstream with respect to the target cell. The average time taken for each of the measurements was ~ 2500 s with a livetime of $\sim 99\%$. The gas pressure for each run has been calculated as the average of the pressure readings saved each five minutes during the measurements. $BGO^{6.44\gamma}$ is the area under the 6.44 MeV peak, which is deduced by fitting the 6.44 and 5.83 MeV peaks in Figure 3.26 to two Gaussian distributions simultaneously.

A background spectrum was subtracted for all BGO spectra, however, no influence was seen in the 6.44 MeV peak region.

Figure 3.48 shows the target density profile obtained using the expression 3.20. It is worth noting that there are two unwanted features in the profile which should be corrected. These are, (i) the asymmetry of the profile between the downstream and upstreams ends of the target cell and, in the region corresponding to the target cell, between ~ -50 mm and ~ 50 mm (see Figure 3.22); the profile is not flat as would be expected for our recirculating gas system and a slope is evident, and (ii) the yield is non-zero in the extremes, i.e. at $+100$ mm. The latter would mean that there is gas far away from the centre of the target cell, which would alter the acceptance significantly.

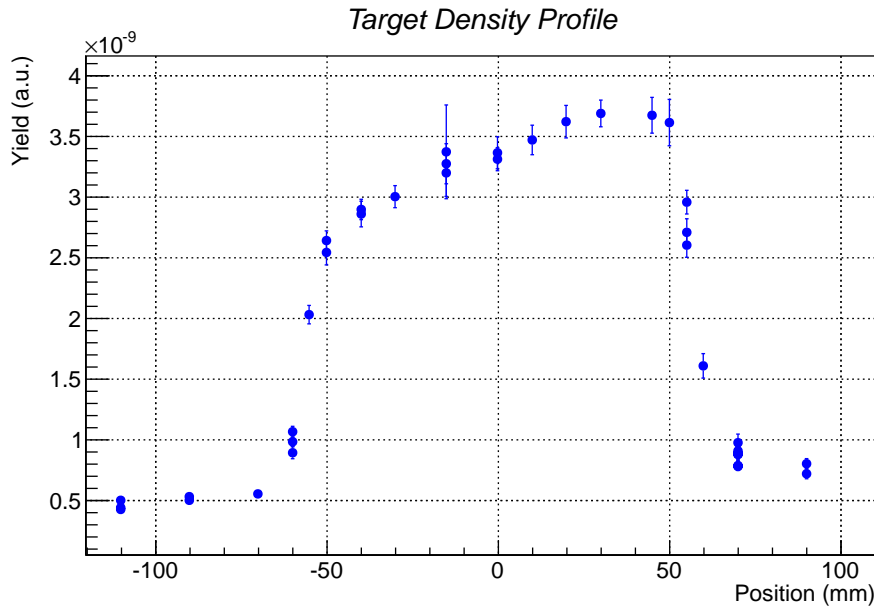


Figure 3.48: The measured target density profile obtained using the expression 3.20. The X axis shows the different positions of the BGO detector parallel to the beam axis.

In order to correct for the asymmetry and the sloped-profile in the gas cell, we considered the energy loss by the beam throughout the gas target and the energy dependence of the resonance reaction. The ^{12}C beam energies at the entrance and exit of the target are 12.09 and 11.96 MeV, respectively. The latter is extracted directly from the MD1 reading (3452.92 G) tuned for the $^{12}\text{C}^{+5}$ beam, after crossing the ^3He gas target at 5.8 Torr pressure. On the other hand, the resonance reaction populates an unstable excited state of ^{15}O , the decay of which has the Breit-Wigner distribution:

$$w(E) \propto \frac{(\Gamma/2)^2}{(E - E_0)^2 + (\Gamma/2)^2} \quad (3.21)$$

here, Γ is the level width and is inversely proportional to the lifetime. The values of $E_0 = 14.46$ MeV and $\Gamma = 100$ keV are taken from [Nuc]. Figure 3.49 shows in blue a representation of the Breit-Wigner expression for the population of the 14.46 MeV state in ^{15}O using a ^{12}C beam on a ^3He target. E_0 and Γ have been converted to consider a ^{12}C beam and the proportional factor has been considered as $w(E_0) = 1$ for simplicity for our purposes. In red is shown the beam energy region between 11.96 and 12.09 MeV representing the extremes of the target cell, and it can be observed the probability for the decay varies significantly. Thus, a correction factor in the expression 3.20 has been included in order to account for this variation.

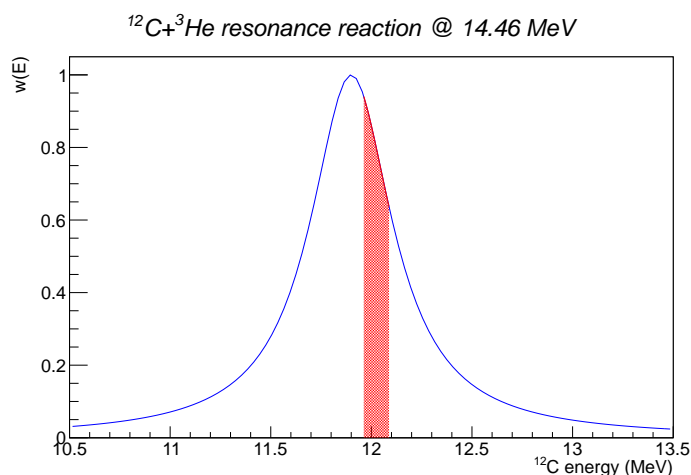


Figure 3.49: The blue curve shows the probability decay ($w(E)$) of the $^{12}\text{C}+^3\text{He}$ resonance corresponding to the 14.46 MeV state in the ^{15}O . The "x"-axis shows the energy of a ^{12}C beam. The shaded region in red, represents the beam energy loss in the gas cell.

Assuming an effective length of ~ 12.3 cm estimated from the energy loss (12.08-11.96 MeV) by the beam crossing the 5.8 Torr of ^3He gas and the SRIM code [SRI], the beam energy at each position (E_p) has been determined by linear extrapolation. Considering E_p , the expression 3.20 has been multiplied at each position by the factor $w(E_p)$. This account for the difference in probabilities of the reaction to occur due to the variation of the beam energy across the target cell.

The new TDP, corrected for different reaction probabilities at each position, is shown in Figure 3.50. Clearly this profile does not have a slope with the target cell and is rather symmetric outside, in line with our expectation for our configuration of the cell and the differentially pumping system.

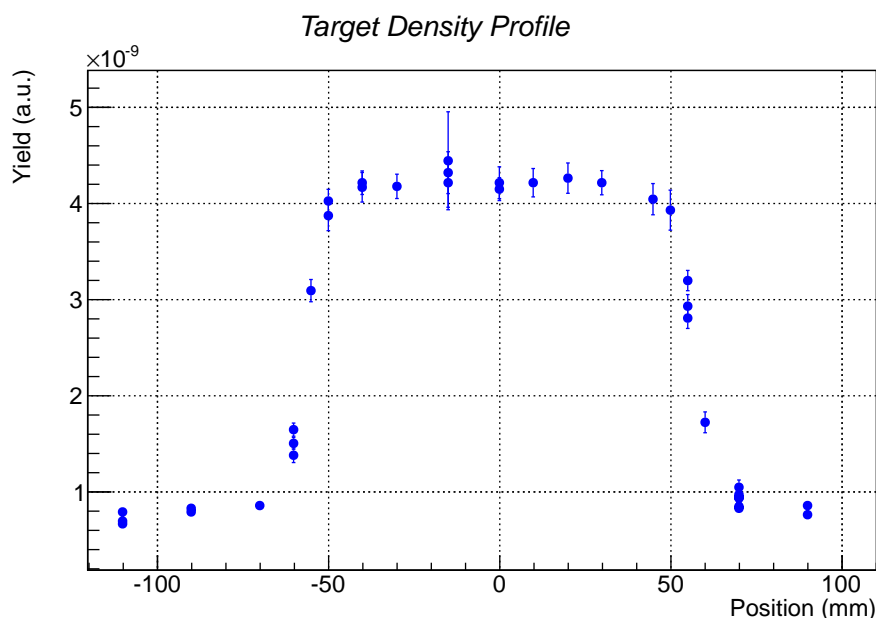


Figure 3.50: A corrected target density profile obtained after considering the different beam energy at each position and the variations in the probability of the resonance reaction to occur. For each position in the x-axis, the y-axis shows the yield calculated using the expression 3.20 multiplied by the $w(E_p)$ factor where E_p is the energy at each position.

As can be observed in Figure 3.50 the non-zero γ -yield is still persistent but now symmetric at both extremes. This is against the expectations from the differentially pumped system with our particular arrangements, which creates a profile with a rapid decrease in pressure at the extremes of the cell, beyond which the pressure should go to zero rapidly, and thus no reactions should occur. Therefore, we claim that the non-zero γ -yield effect is due to the non 100% shielding of the BGO and a constant background should be subtracted from the whole profile.

In order to probe this argument let us compare the situation at two different positions of the BGO detector, the extreme at $z=-11$ cm and the centre at $z=0$ cm. The ratio between the yields at this positions is 0.17 and Figure 3.51 shows the two cases considered.

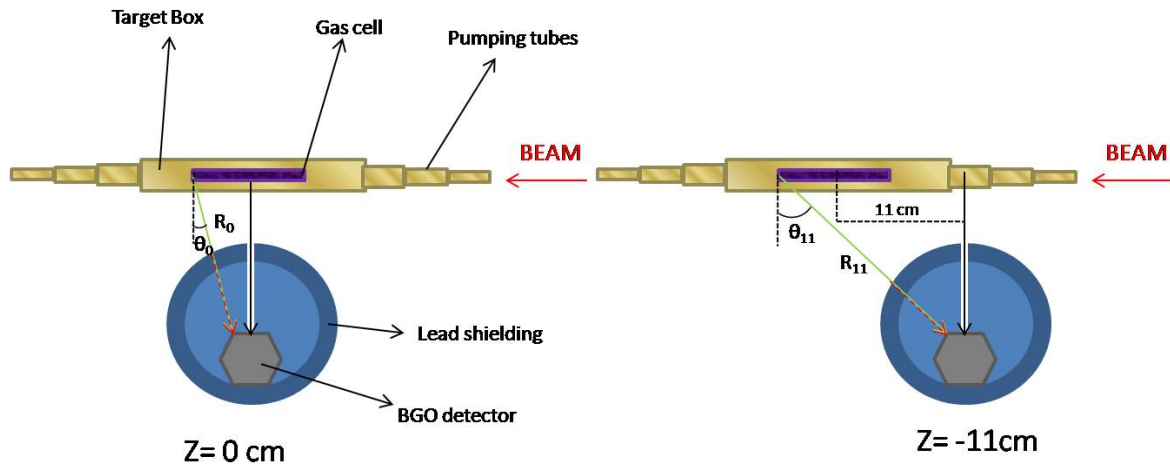


Figure 3.51: The two different BGO detector positions ($z=0$ and $z=-11$ cm) used to analyse the effect of the shielding and subtended solid angle by the BGO. In green are shown the γ rays created at the exit of the target cell, and in red the part of the rays inside the shielding.

In these two positions, the γ -rays produced at the left extreme of the gas cell can in principle go through the shielding along the green lines, where R_0 and R_{11} indicate the distances to reach the detector. For these two scenarios, the subtended solid angles and the γ attenuation through the shield need to be considered. The ratio between the two solid angles can be given by: $d\Omega_{z=-11}/d\Omega_{z=0} = \frac{\cos\theta_{11} \cdot R_0}{\cos\theta_0 \cdot R_{11}} = 0.55$ based on the measured distances. Now, the relative γ intensity at some distance in a material can be expressed as: $I/I_0 = e^{-\mu \cdot x}$, where μ is the linear attenuation coefficient and I_0 and I are the γ intensities before and after crossing a " x " distance in the material, respectively. Taking into account that $\mu_{(lead)} = 0.505/cm$ and the different distances crossed by the beam through the lead (red dashed line in Figure 3.51), the ratio $e_{z=0}^{-\mu \cdot s} / e_{z=-11}^{-\mu \cdot s}$ results in 0.57. Thus, although the solid angle is smaller for further distances it gets compensated by the γ attenuation effects and a constant yield at first order approximation could be expected for all measurements at the different positions. It should be noted that we had a reasonable assumption that γ -rays are emitted isotropically based on the symmetry seen in the extremes of our target density profile.

In principle, a Montecarlo simulation could be determined the effect of the shielding, taking into account effects such as the non equal probability of producing the reaction at the different positions in the target or corrections for the Doppler effect of the different γ -rays, etc... However, the present method already constitutes a very good estimation, therefore we will consider a constant "yield background" which is assumed to be the yield value at $z=-11$ cm. In Figure 3.52, the blue points show the final experimental target density profile with the first order "background yield" subtraction correction.

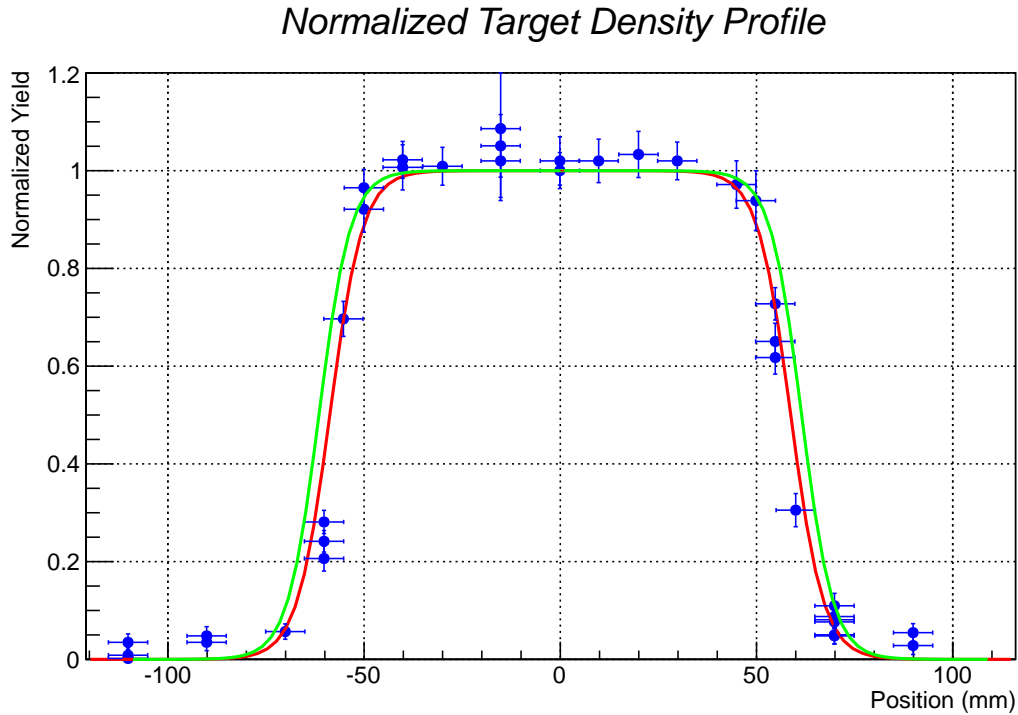


Figure 3.52: Final normalized target density profile. The blue points shows the normalised yield corrected with the energy dependence given by the expression 3.21 and after subtraction of a constant background. The red fit shows the "best" fit to the points with a Fermi function obtained using ROOT program and the green curve shows the same fit constraining that the effective length is 12.3 cm.

The red and green curves in Figure 3.52 show two fits to the data points using the Fermi function given by [Hut02]:

$$\text{Yield}^{\text{Norm}} = \frac{1}{1 + e^{(|z|-R)/a}} \quad (3.22)$$

where R and a are the two free parameters. The red curve shows the "best" fit to the data point using the ROOT package [ROO] and the green curve shows the fit constraining that the effective length is 12.3 cm. This length is obtained from the energy losses of the ^{12}C passing through the ^3He gas target and estimated from the MD1 magnetic fields. In the next chapter, influences due to of different slopes and effective lengths in the profile will be discussed.

3.4 Conclusion

Two experimental techniques have been used to determine the cross section of the $^3\text{He}(\alpha, \gamma)^7\text{Be}$ reaction in the range of E_{CM} 1-3 MeV. The details of the two experiments and setups have been given in this chapter.

The *Activation Method* was performed at CMAM using a tandemron accelerator. The reaction was produced using a ^3He beam at nine different energies on a ^4He gas target. The total number of ^7Be recoils produced are deduced by measuring the γ activity arising from the de-excitation of the ^7Li produced by the electron capture decay of the ^7Be . The γ measurements were performed using the SOREQ low background HPGe detector station. The analysis of the data will be presented in the next chapter. The careful control and good knowledge of various parameters such as the solid angle subtended by the silicon detector, the Ni foil thickness or silicon detector energy calibrations have been discussed in this chapter.

The *Direct Recoil Counting Method* was performed using the DRAGON spectrometer at TRIUMF. The reaction was carried out using inverse kinematics, i.e. ${}^4\text{He}$ beam at four different energies on a ${}^3\text{He}$ gas target. One measurement using the *Activation Method* was also performed at one of the energies at which data was already obtained in direct recoil counting method. The total number of recoils produced are inferred by detecting one of the charge states in a DSSSD placed at the focal plane at the end of the separator. The necessary charge state distribution measurements were carried out using a ${}^9\text{Be}$ beam. An important parameter for this experiment is the recoil acceptance of the separator because the recoil cone angle of the reaction, when effects such as straggling are included, is above the geometrical acceptance of the separator. The density profile of the windowless gas target is also a crucial parameter that was determined experimentally and used in the simulations to determine the acceptance of the separator (see next chapter). Other details concerning the beam energy determination, DSSSD calibration, separator tuning have also been discussed. The analysis of the data will be presented in chapter 5.

"We cannot solve our problems
with the same thinking we used
when we created them".

Albert Einstein

CHAPTER 4

GEANT SIMULATIONS OF DRAGON

Abstract: In this Chapter the simulations performed in order to obtain the acceptance of the DRAGON separator for the recoils created in our ${}^3\text{He}(\alpha,\gamma){}^7\text{Be}$ reaction are discussed. Firstly, different input parameters considered in order to define the experimental conditions are detailed. Then, the results from the simulations carried out for the different beam energies and finally, the estimated uncertainties in the acceptance from the simulations due to the possible changes in the input parameters are presented.

In the previous Chapter the two experimental techniques used in this work to determine the astrophysical S-factor were detailed. Additional essential measurements were also presented there. Some of these measurements are needed in order to get the astrophysical S-factor precisely, e.g. the experimental determination of the collimated silicon detector angle in Madrid experiment, and some of them were even necessary in order to determine the absolute cross section, e.g. the charge state distribution using the DRAGON separator.

On the other hand, simulating experimental conditions using GEANT codes have become common in designing experiments as well as understanding measured quantities. In the case of Madrid experiment, thanks to the simplicity and good experimental knowledge and control of the parameters of the setup, no detailed simulations were necessary. By contrast, the DRAGON setup needed extensive simulations as the separator acceptance is such that there is a scope for losing ${}^7\text{Be}$ recoils between the production points in the target and the detection in the DSSSD.

The loss of these recoils depends on various parameters, an experimental control of which is very difficult, if not impossible. Therefore, we resorted to simulations to obtain additional information on the acceptance of the setup to obtain the final results from TRIUMF work. It is worth pointing out that the acceptance of the DRAGON separator has high influence on the $S_{34}(E)$ data. The influence of possible variations in many parameters, such as the beam spot size or the magnetic fields in the dipoles must be precisely studied as they can change the acceptance significantly. Therefore, an extended discussion about the transmissions of the ${}^7\text{Be}$ recoils generated via the ${}^3\text{He}(\alpha,\gamma)$ reaction will be presented in this chapter.

4.1 Introduction

As it has been already mentioned throughout this text, one of the main concerns to be taken into account for studying the ${}^3\text{He}(\alpha,\gamma){}^7\text{Be}$ reaction at DRAGON is the separator acceptance or transmission for the recoils produced in this reaction (ϵ_{DRAGON}). **For a given charge state** the acceptance is defined as the ratio of the recoils detected in the DSSSD and the total recoils created in the gas target ($\epsilon_{\text{DRAGON}} = \frac{7\text{Be}^{\text{DSSSD}}}{7\text{Be}^{\text{produced}}}$). In order to estimate the DRAGON acceptance for our reaction, the GEANT 3-DRAGON simulation code has been adapted to recreate our experimental conditions and obtain ϵ_{DRAGON} parameter.

GEANT (GEometry And Tracking) 3 is a FORTRAN software which allows the construction of different geometrical setups, the interaction between particles and the tracking of particles in different media and electromagnetic fields using Monte Carlo techniques [GEA]. Any GEANT simulation consists of three main stages: initialisation, event processing and termination. In the three stages the user can incorporate his own codes. In the first stage the user defines the different geometrical volumes of the setup and the materials, the sensitive volumes are specified. During the processing phase the events are firstly created, the kinematics is defined and the particle's path through the different volumes is tracked, interactions with the different media are simulated and secondary events, such as likely γ rays, are tracked. The response of the detectors to the particle hits is also considered at this stage. During the termination phase the statistical information is computed. The information is saved event by event as ntuples in files (files with one row an n-columns of information per event) and are also histogrammed into frequency distributions by the software package HBOOK [HBO]. A detailed information about the GEANT structure can be found in reference [GEA].

The GEANT 3-DRAGON code was designed using the version 3.2.1 of GEANT and it consists of two main geometrical parts. The first includes the target box and cell, BGOs and pumping tubes placed before the first quadrupole (Q1 in Figure 4.1(b)). The second part concerns the separator and includes all the components after the first quadrupole. The magnetic and electrostatic elements of the separator are scaled (i.e. magnetic and electric field are set to let the recoils go through) to the corresponding recoils in the reaction by using an input RAYTRACE file read at the initialisation stage. Figure 4.1 shows the two main geometrical areas discussed in the context of the simulation, (a) the target region and (b) the separator.

This code has previously been used and tested for other reactions studied with DRAGON for example the ${}^{17}\text{O}(\alpha,\gamma){}^{21}\text{Ne}$ or ${}^{12}\text{C}(\alpha,\gamma){}^{16}\text{O}$ reactions [MBH06]. The code has been adapted in order to determine the overall acceptance of the ${}^3\text{He}(\alpha,\gamma){}^7\text{Be}$ reaction.

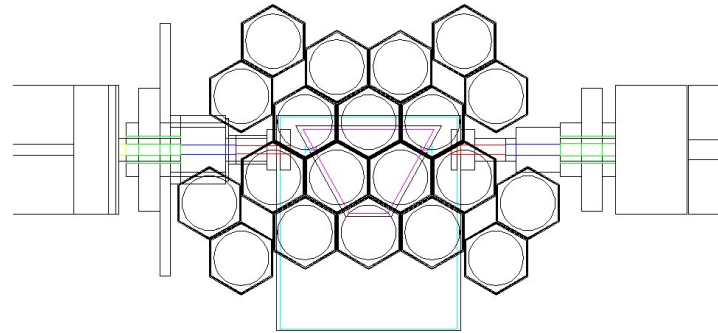
4.2 Input Parameters for the Code

To estimate the acceptance of DRAGON for a given reaction, the experimental conditions must be recreated as closely as possible in the simulations. In contrast to the previous reactions studied, the angular emission recoil cone angle of our reaction is above the geometrical acceptance of the separator, thus all input parameters can play a determining role in the transmission of the recoils through the separator. The following subsections describe the realistic input parameters used in the simulations.

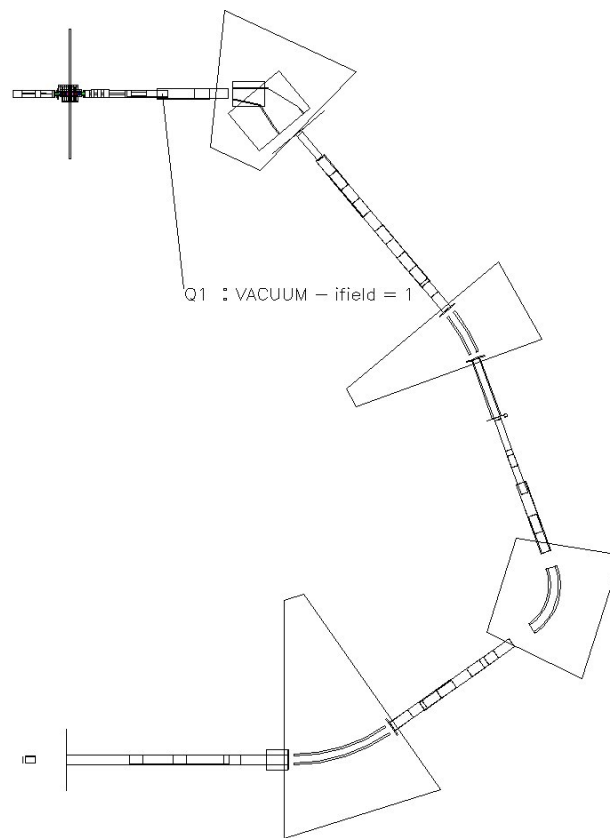
4.2.1 The gas target

As the gas target is kept in a windowless cell differentially pumped, it is important to include accurate knowledge of the density profile as this will determine the probability for the ${}^7\text{Be}$ production and their acceptance by the separator. The target density profile was studied using the ${}^3\text{He}({}^{12}\text{C}, {}^{14}\text{N}\gamma)\text{p}$ reaction, and the details and results are explained in section 3.3.3.4. As whatever volume defined with GEANT 3 can only be filled with one material, i.e. gas with a constant pressure and temperature, the target density profile (TDP) function shown in Figure 3.52 must be adapted to our defined GEANT volumes.

Figure 4.2 from GEANT simulations shows volumes with different colours for the target cell where most of the gas is contained, and for the pumping tubes where there could be residual gas.



(a)



(b)

Figure 4.1: Two geometrical areas from the GEANT 3-DRAGON simulation. (a) Target side with the target box, target cell pumping tubes and BGOs and (b) separator.

The target cell, target box, downstream aperture and pumping tubes are labelled, followed by the materials which they are filled in (e.g. "CELG: Gas target", where the volume "CELG" refers to the target cell which is filled with a material called "Gas Target"). Some volumes, like the cell apertures have been split into two pieces (XAPG and XAP2) in order to let two different materials to be used.

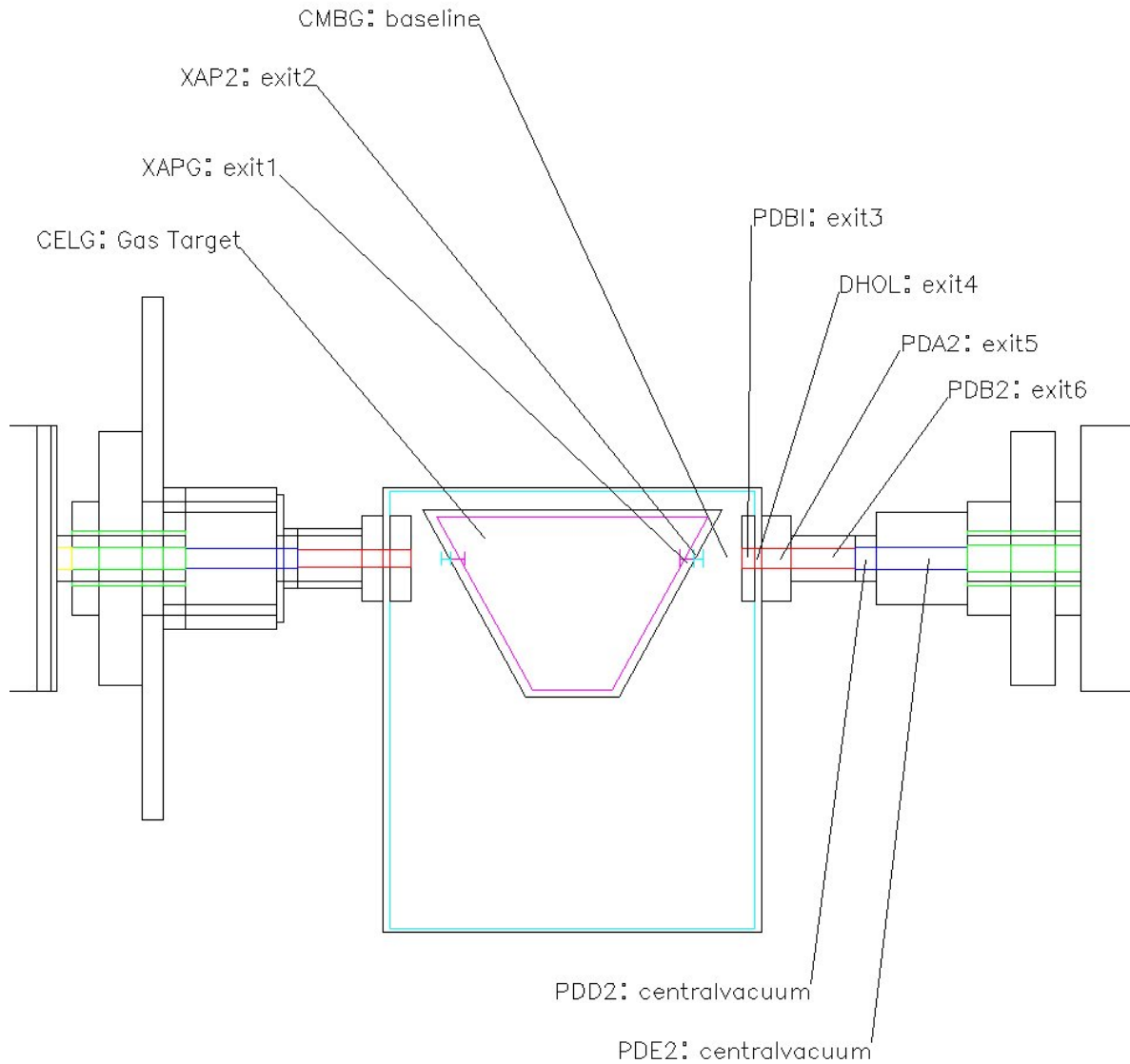


Figure 4.2: Some of the target volumes defined in GEANT 3-DRAGON. The target box (CMBG), target cell (CELG), exiting aperture (XAPG,XAP2) and downstream pumping tubes (PDI,DHOL,PDA2,PDB2,PDD2,PDE2) are indicated. The volumes are followed by the different defined materials.

A central ^4He gas target material for the target cell is defined for every energy using the experimental target pressures and temperatures shown in Table 5.7. This material is named as "Gas target". The other materials are defined with a fraction of the density of the "Gas Target". In order to determine this fraction, the measured TDP has been fitted to a step-function as shown in Figure 4.3. The density of a given material is obtained by multiplying the "Gas Target" density by the coefficient (Coeff) from the fit.

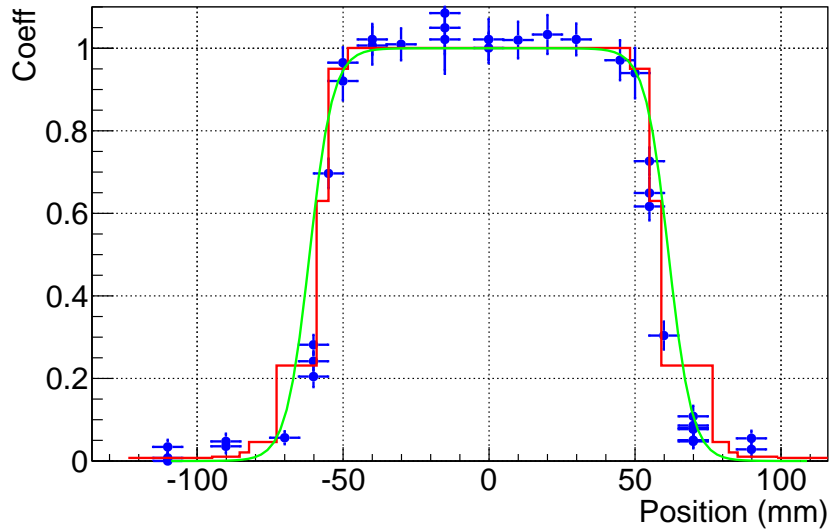


Figure 4.3: Same TDP as the shown in Figure 3.52 where a step function in red is included. Every step represents a different volume in GEANT like defined in Figure 4.2. The corresponding coefficient (Coeff) shows the density ratio respect to the "Gas Target" material in the cell.

Changes in the step function and the influence this has on the acceptance will be studied in section 4.5 in order to determine the uncertainty associated to the transmissions.

4.2.2 The beam energy

The ^4He mean beam energies (Table 3.6) are given as input parameters to the program. The program creates a Gaussian distribution with the given mean value and with a FWHM of 0.1% according to ISAC-I specifications. For each beam particle (event), the energy is then randomly selected from the distribution and the corresponding momentum vector is calculated. Figure 4.4 shows an example of 10^5 simulated particles with 3521.6 MeV mean beam energy.

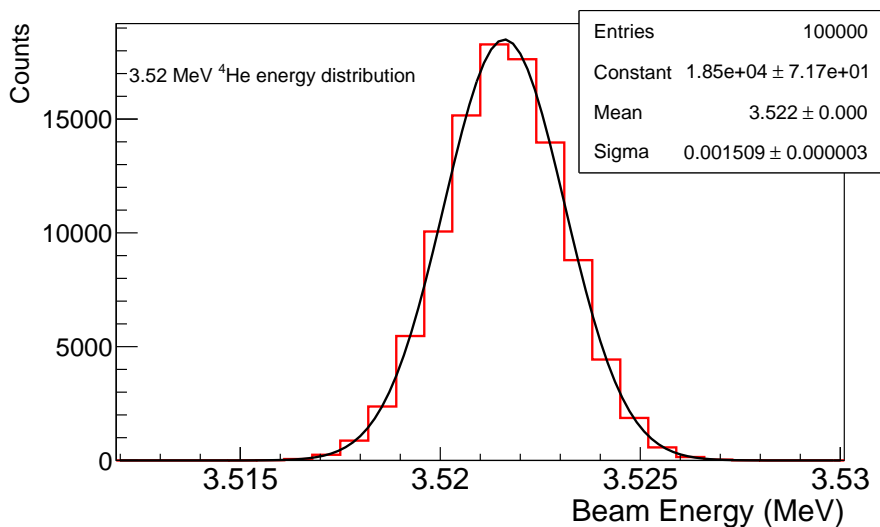


Figure 4.4: Simulated energy distribution for 10^5 ^4He beam particles at the mean energy of 3521.6 keV. The black curve represents a Gaussian fit whose parameters are given in the box

4.2.3 The beam spot size and divergence

It is needed to take into account the finite spot size and divergence of the beam as these will have influence on the separator acceptance. The simulated beam spot size is based on the experimental transmissions of the beam through the gas target. The beam transmissions are calculated for the runs of each energy as the ratio of the FC1 and FC4 readings and a mean value is calculated by averaging those values.

This areal transmissions represent to two dimensional Gaussian "cut off" at the 6 mm diameter entrance aperture compared to the full Gaussian integrated over x and y to infinity. This gives us the widths $\sigma_{x/y}$ of both X and Y Gaussian distributions, i.e. the beam stop size. Then, the emittance in the angular direction can be determined from the ISAC equations and so the beam divergence. According to ISAC-I values the normalised emittance for 2rms is 0.2 μm thus:

$$\text{Emittance} = \frac{0.2}{\beta\gamma} \quad (4.1)$$

$$2\Delta\theta_{x/y} = \frac{\text{Emittance}}{2\sigma_{x/y}} \quad (4.2)$$

where $\beta = \frac{v}{c}$, $\gamma = \frac{1}{\sqrt{1-\frac{v^2}{c^2}}}$ and $\Delta\theta_{x/y}$ is the divergence Gaussian width in the X/Y axis. Table 4.1 shows the experimental transmissions, $\sigma_{x/y}$ and $\Delta\theta_{x/y}$ for the four experimental beam energies.

$\sim E_{\text{He}}$ (MeV)	Transmission (%)	$\sigma_{x/y}$ (mm)	$\Delta\theta_{x/y}$ (mrad)
6.5	89.30±1.68	1.41868(*)	0.562
5.2	96.97±1.29	1.13444	0.836
4.7	94.09±1.51	1.26132	0.783
3.5	93.91±2.95	1.26807	0.911

Table 4.1: Beam characteristics for the four beam energies studied. The experimental transmissions for the ${}^4\text{He}$ beam are shown in the second column. From the transmissions the beam particle standard deviations in the X and Y directions are estimated and are shown in the third column. The standard deviations of the divergence beam distribution are shown in the fourth column.

(*)The real value considered in the simulations is 1.50 mm as it reproduces more fairly the 89.30% experimental transmission.

In GEANT, the $\sigma_{x/y}$ values are introduced in the input files, the program determines the $\Delta\theta_{x/y}$ divergence standard deviations from the nominal mean beam energies and ISAC equations. For each event GEANT selects randomly the offset in the X and Y direction from the Gaussian distributions of standard deviation $\sigma_{x/y}$ and the divergence from the Gaussian distributions of $\Delta\theta_{x/y}$ standard deviations. Figure 4.5 shows an example of the simulated beam spot and X-divergence for the 3.522 MeV beam energy.

Changes in the beam spot and divergence due to the errors in the transmissions will also be studied in section 4.5.

4.2.4 The reaction probability and reaction location

For a given energy another parameter that determines the transmission of DRAGON is where the reaction occur in the gas target. In our beam energy range, even after including the energy loss in the target (<20 keV), no resonances are present and thus the cross section can be assumed to be constant. For example, a distribution shown in Figure 4.6 (top) is assumed for $\sigma_{34}(E_{\text{CM}})$ for the case

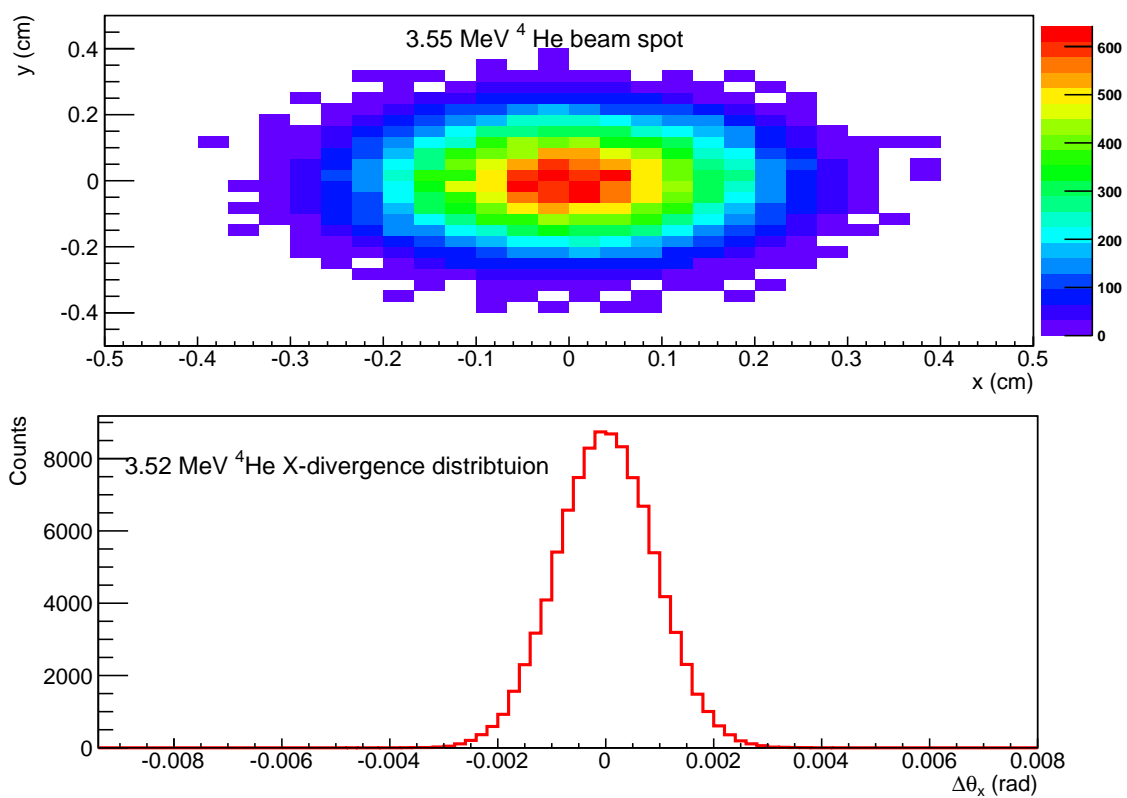


Figure 4.5: Simulated 10^5 ^4He beam particles at ~ 3.52 MeV. (a) shows the beam spot and (b) the X-divergence of the beam.

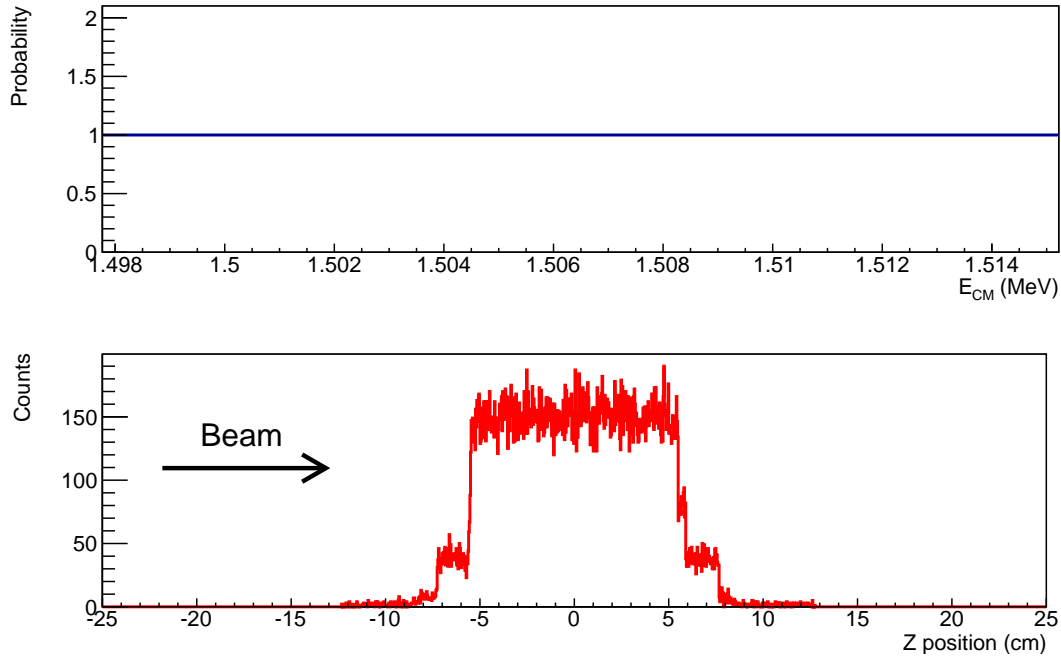


Figure 4.6: Reaction probability for 10^5 beam particles for the case of $E_{CM} \sim 1.5$ MeV (beam energy ~ 3.5). (a) shows the reaction probability $\equiv 1$ for the E_{CM} across the target length. For each event, GEANT code selects a random "goal-energy" from this distribution. In case that the centre of mass energy at any point equals the random energy the reaction will occur. (b) shows where the 55383 reactions are produced throughout the gas target being $z=0$ cm placed at the centre of the 1cell.

of the beam energy of ~ 3.5 MeV (corresponding $E_{CM} \sim 1.5$ MeV). GEANT uses this input function as a probability distribution between the outgoing and incoming centre of mass energy region. For each event, a "goal-energy" is randomly selected from the distribution. In case that during the beam tracking the centre of mass energy at any point is equal to the random "goal-energy" the reaction will be produced and the ${}^7\text{Be}$ recoil created. Clearly, the probability for the ${}^7\text{Be}$ production depends only on the target density profile, therefore as shown in Figure 4.6 (bottom) the production profile of ${}^7\text{Be}$ recoils follows the TDP.

4.2.5 The S_1/S_0 branching ratio and the γ -rays angular distribution

The ${}^7\text{Be}$ recoil angle and the prompt- γ ray emission angle depend on each other in the capture reaction. Moreover two different capture γ rays corresponding to decay to the ground state (γ_0) or the first excited state (γ_1) are present. For the latter, a 429 keV- γ ray is subsequently emanated from the de-excitation of the first excited state to the ground state in ${}^7\text{Be}$. Therefore assumptions related to prompt- γ ray angular distributions as well as to the ratio between the population of the first excited and ground state (S_1/S_0) must be made.

As initial first order approximation, the values for (S_1/S_0) has been determined from a linear extrapolation of Figure 4.7 taken from reference [CD08], while changes in this ratio will be studied in the section 4.5. For each reaction GEANT will create a prompt γ_1 or γ_0 and corresponding ${}^7\text{Be}$ state with relative ratios (S_1/S_0) shown in Table 4.2.

Concerning the angular γ -rays distribution, isotropic angular distributions for both γ_0 and γ_1 are assumed based on the results in reference [DGK09]. In GEANT 3-DRAGON this is done by introducing a uniform distribution for the values of $\cos(\Theta)$, where Θ is the centre of mass polar angle in the spherical coordinate system. The 429 keV γ ray distribution is always isotropic as it comes from a $1/2$ spin state.

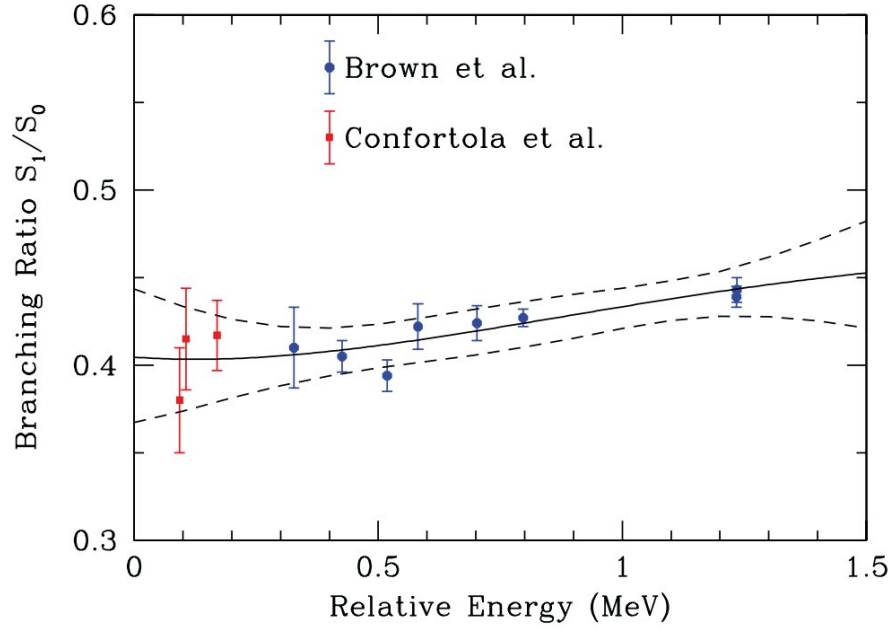


Figure 4.7: The S_1/S_0 branching ratio. A fit to the data (solid line) as calculated by Cyburt and Davids [CD08], where the data are taken from [BBS07, CBC07]. For the simulations a linear extrapolation of the fit up to 2.8 MeV centre of mass energy has been carried out in order to determine the S_1/S_0 branching ratio.

$\sim E_{\text{He}}$ (MeV)	E_{CM} (MeV)	S_1/S_0
6.5	2.81	0.5077
5.2	5.16	0.4829
4.7	2.02	0.4755
3.5	1.51	0.4545

Table 4.2: The S_1/S_0 branching ratios considered in the simulations.

4.2.6 The separator settings

One of the most determining parameter for the DRAGON acceptance is the separator settings. Therefore the electrostatic and magnetic fields used for the simulations play a key role.

As already explained, the experimental procedure constitutes in tuning the separator for the optimal transmission of the beam through the gas target and centre the beam throughout the different elements of the separator, the separator is then rescaled to the charge and mass of the recoils. This procedure is essential as the low recoil yield does not allow the actual adjustments for the separator settings in optimising recoil transmissions. An important issue to be considered here is that the potential energy loss differences between beam and recoil in the gas target are not taken into account by the rescaling program in automatic manner. This will have influence on the mean accepted recoil energy (\bar{E}) and thus on the overall acceptance. Indeed, during the 2011 run the separator was automatically tuned to the recoils following the usual procedure. Clearly this was not optimal. In the 2013 experiment an improvement was made by tuning the separator manually to obtain optimal transmission for the energy of the recoils created at the centre of the target taking into account the energy losses before exiting the target, in contrast to the automatic optimisation procedure used in the 2011 runs.

In GEANT simulations, the settings of the separator are usually adjusted based on parameters of the reaction. The code determines the scaling values of the magnetic and electric fields from the kinetic energy and momentum of the recoils created at the centre of the target after crossing half of the target length, eventually obtaining the optimal settings for the separator. Nevertheless, in order to guarantee the consistency between the experimental and GEANT settings, the tuning energies in GEANT have been manually set to those corresponding to the experimental ones. Table 4.3 gives the experimental tuning energies (column three) used in the simulations, that corresponds to the MD1 magnetic fields during the experiment (Table 3.6) and calculated using the expression 3.13. The fourth column shows the mean energies at the exit of the gas target of the recoils that are created at the centre. The fifth column shows the relative difference between them.

Run	$\sim E_{4\text{He}}$ (MeV)	$E_{7\text{Be}}^{\text{tuning}}$ (keV)	$\bar{E}_{7\text{Be}}^{\text{simu}}$ (keV)	Relative Difference $\frac{ E_{7\text{Be}}^{\text{tuning}} - E_{7\text{Be}}^{\text{theor}} }{E_{7\text{Be}}^{\text{theor}}} (\%)$
	6.5	3734.51	3696.02	1.04
2011	5.2	2940.21	2898.33	1.44
	3.5	1997.32	1955.01	2.16
2013	4.7	2642.67	2647.71	0.20

Table 4.3: Experimental ${}^7\text{Be}$ energies used in the simulations for the tuned conditions. While the MD1 values during the 2011 campaign were automatically determined by the program by scaling the setting for the beam, for the 2013 measurements the MD1 value was set manually for the energy corresponding to the recoils created at the centre of the target.

As can be observed, for the 2011 measurements, when the separator was tuned automatically to "recoils mode", the relative differences between the real tuning energy $E_{7\text{Be}}^{\text{tuning}}$ and $\bar{E}_{7\text{Be}}^{\text{simu}}$, which would maximise the transmissions of the recoils created at the centre, are relatively high. For the 2013 measurement, the separator was tuned manually and therefore, the relative difference energy for this case is remarkably smaller compared to the measurements in 2011, maximising the transmission of the recoils created in the centre of the gas target.

Looking at the relative difference between the 2011 energies in Table 4.3, the trend is consistence with the stopping power of a ${}^7\text{Be}$ nucleus crossing a ${}^3\text{He}$ gas target. Figure 4.8 shows the stopping power of ${}^7\text{Be}$ ions in ${}^3\text{He}$ gas target calculated using the SRIM code[SRI]. It can be observed that in the range of interest, i.e. $\sim 2000 - \sim 3700$ keV for the ${}^7\text{Be}$ recoils, the higher the energy is the lower is

the amount of energy loss. Therefore, for the highest energy the relative difference between the mean energy and the automatically separator tune energy must be lower as seen in Table 4.3.

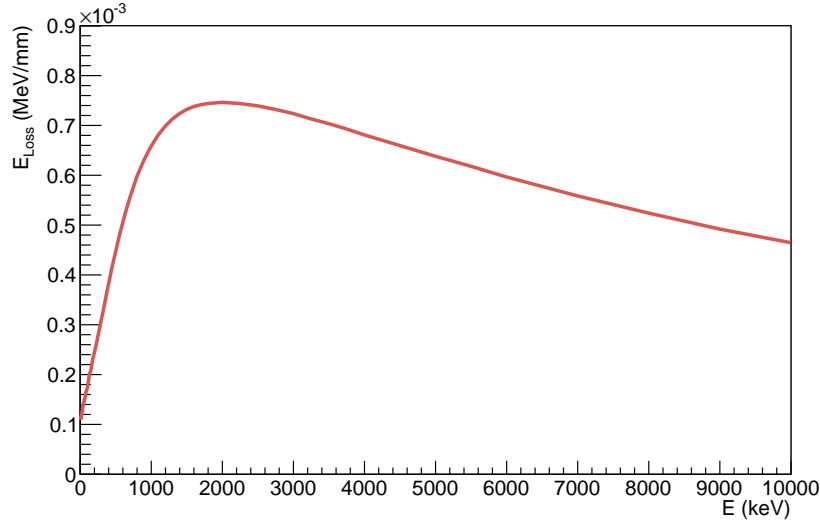


Figure 4.8: Stopping power for ${}^7\text{Be}$ recoils crossing a $9.327 \cdot 10^{-7} \text{ g/cm}^3$ density ${}^3\text{He}$ gas target.

4.3 First Simulations and Analysis

Taking into account the conditions and parameters defined above, the recoil transmissions through the separator for each energy are calculated as the ratio between the recoils reaching the end detector and the total recoils created in the gas target. From now on, unless otherwise specified, simulation will be carried out assuming 10^5 beam particles.

Figure 4.9 shows some output spectra from the first series of simulations with the given input parameters. In the left column are shown the kinematics curves representing the output recoil angle after emitting the γ -ray versus the kinetic energy. In blue are shown the recoils reaching the DSSSD and in green those loosed throughout the separator, i.e. do not reach the focal plane. The second and third column shows the projections of the previous spectra where in red are the total recoils created in blue the detected ones and in green those stopped before reaching the DSSSD. As can be observed the acceptance-dependence is stronger on the recoil energy compare to the angle (e.g. for the highest energy, the second column shows the different energy between detected recoils (blue) and not-detected (green), while this effect in not seen for the angles in the third column).

In the second column, it can be seen that for the first three histograms corresponding to beam energies of 6.5, 5.2, and 3.5 MeV of 2011 measurements, the recoils created with the higher energies are more likely to be detected. These correspond mostly with those recoils created at the end of the gas target according to Figure 4.10, which represent the positions where the recoils are created. This is in concordance with that during the 2011 run the separator was tuned automatically from the beam tuning without taking into account the different energy losses between recoils and beam particles. For the last case, 4.7 MeV energy, the separator was tuned manually setting the magnetic field to the exiting recoil energy of the recoil created at the centre of the gas target and as can be observed the detected histogram is more symmetric on the detected energy.

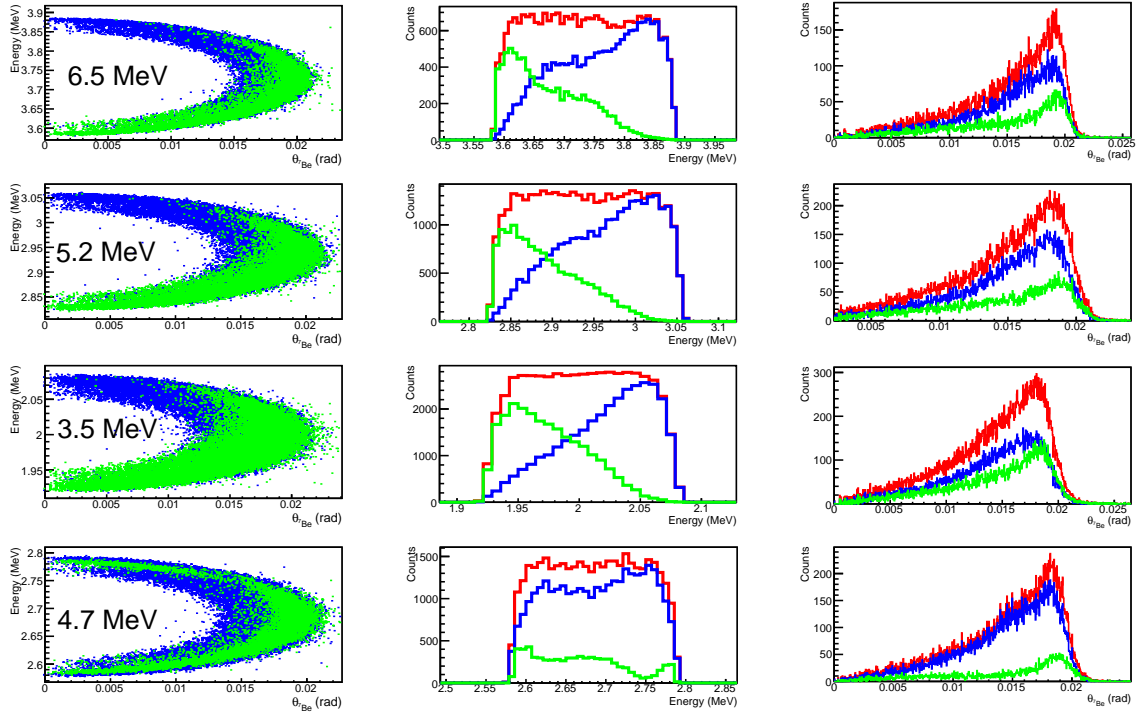


Figure 4.9: Outputs for 10^5 beam particles simulated at the different beam energies. The left column shows the kinematics curves and the middle and right columns show the projections for the recoil energy and the output recoil angle. In red are shown all recoils created for each energy, in blue those reaching the end detector and in green those stopped throughout the separator. As can be seen from the second and third columns, when the separator is optimized for the recoils created at the centre of the gas target, the acceptance is optimal and the area under the green curve corresponding to the recoils stopped within the separator is minimal.

The first results for the acceptance at the different beam energies are shown in Table 4.4.

Run	E_{He} (keV)	${}^7\text{Be}$ recoils created	${}^7\text{Be}$ recoils detected	Transmission (%)
	6553.88	26365	17617	66.8 ± 0.6
2011	5165.97	34790	26374	66.3 ± 0.5
	3521.61	55535	32282	58.1 ± 0.4
2013	4716.45	38842	31863	82.0 ± 0.6

Table 4.4: DRAGON transmission for the ${}^3\text{He}(\alpha,\gamma){}^7\text{Be}$ reaction. Only statistical errors are shown here.

Specific knowledge of the DRAGON's transmission efficiency for the ${}^3\text{He}(\alpha,\gamma){}^7\text{Be}$ is gained by examining where in the separator the recoils are stopped. The location of different components where recoils stop are labelled in the schematic DRAGON layout shown in Figure 4.11, and Figure 4.12 shows the fraction of the recoils stopped by the given components. It can clearly be seen that the majority of the recoils are stopped at the charge slits for all energy cases being the relative percentage small for the 4.7 MeV (2013 experiment with manually separator tuning), in agreement with the effect discussed above.

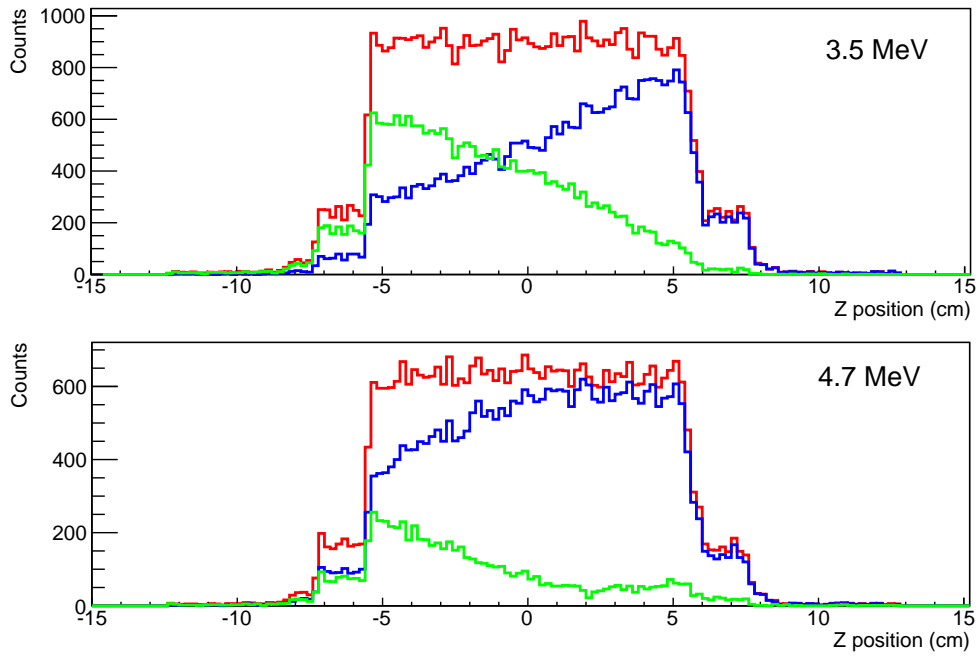


Figure 4.10: Positions of the recoils created in the gas target. The colors have the same meaning than Figure 4.9. The top panel shows the ~ 3.5 MeV beam energy case and the bottom panel the ~ 4.7 MeV

Figure 4.11: Layout of DRAGON. The red labels point at different components where the recoils are stopped

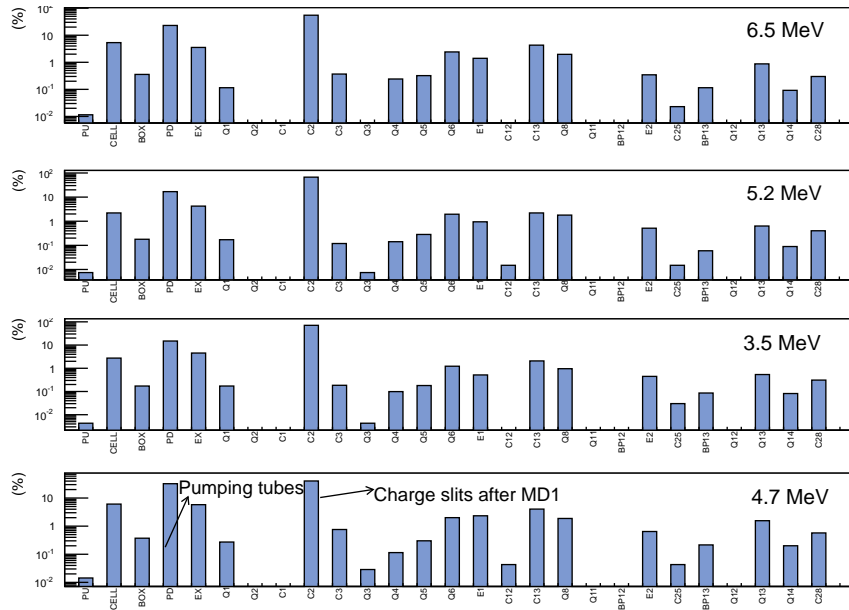


Figure 4.12: Percentage of the recoils stopped in the different volumes throughout the separator. PU refers to the pumping tubes upstream the target box, PD refers to the first pumping tubes downstream the target cell (up to ~ 15 cm) and EX indicates the different tubes up to the first quadrupole (from 15 to ~ 85 cm). The other volumes are labeled in Figure 4.11.

4.3.1 Tests on the DRAGON recoil energy selection procedure

The transmissions shown in Table 4.4 are much lower than the originally predicted, above all for the 2011 run. This should be in line with the discussion above the tuning energies used. In order to further examine the effect of the automatic settings for the 2011 runs, 20000 beam particles have been simulated tuning the energy to the recoils created at the centre of the target cell. The results, displayed in Table 4.5, show a big improvement in the transmission when the mean ${}^7\text{Be}$ energy is used to tune the separator.

Run	$E_{4\text{He}}$ MeV	$\bar{E}_{7\text{Be}}^{\text{simu}}$ keV	$E_{7\text{Be}}^{\text{tuning}}$ keV	Transmission %	Difference %
	~ 6.5	3696.02	3696.02	78.9 ± 1.6	15.3
2011	~ 5.2	2898.33	2898.33	81.1 ± 1.3	18.2
	~ 3.5	1955.01	1955.01	75.7 ± 1.6	23.5

Table 4.5: Simulated transmissions for the tuning energies matching mean exiting recoil energy. The transmission differences with the results in Table 4.4 are also shown.

This proves that the difference in ${}^7\text{Be}$ energy due to the energy loss in the target plays an important role in the transmissions of the recoils throughout the separator for the ${}^3\text{He}(\alpha, \gamma){}^7\text{Be}$ reaction. For the case that the tuning energy is the same as that of the ${}^7\text{Be}$ mean energy at the exit for the recoils created at the centre of the gas cell, the differences with the real tuned energies are shown in the sixth column. As expected, for the highest energy the difference is less significant because the energy losses are smaller.

At this stage, I would like to reiterate the fact that DRAGON should be tuned to the recoils created at the centre of the target, which was also concluded in Figure 4.9. The corresponding kinematics

curves, displayed in Figure 4.13(a), do not show the previous asymmetries in the energy acceptance and even for the highest energy the percentage of recoils stopped in charge slits shown in Figure 4.13(b) are not dominant ones anymore. Therefore, it is evident again that the limiting factor determining the transmission is the kinetic energy of the recoils.

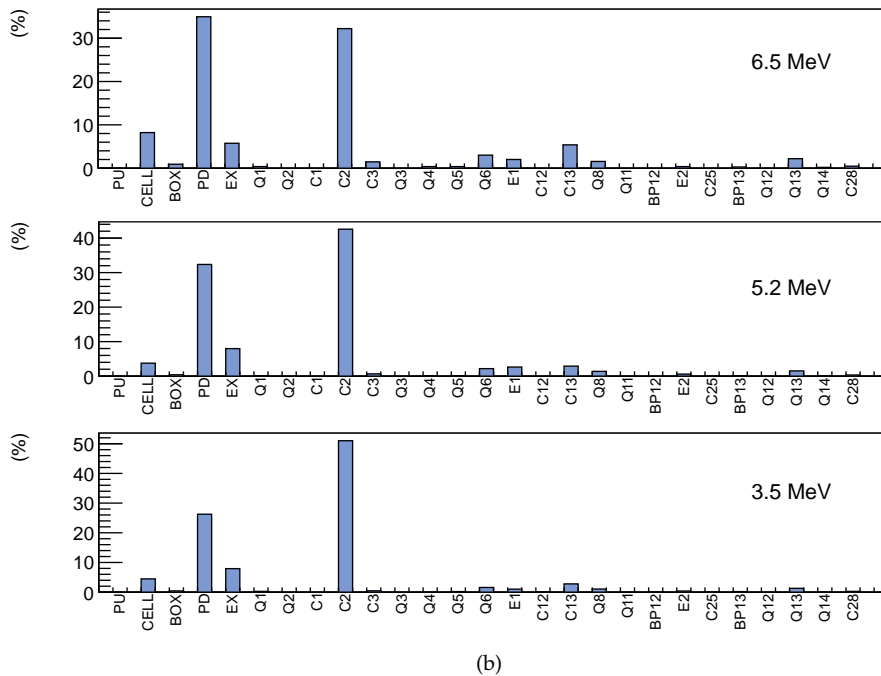
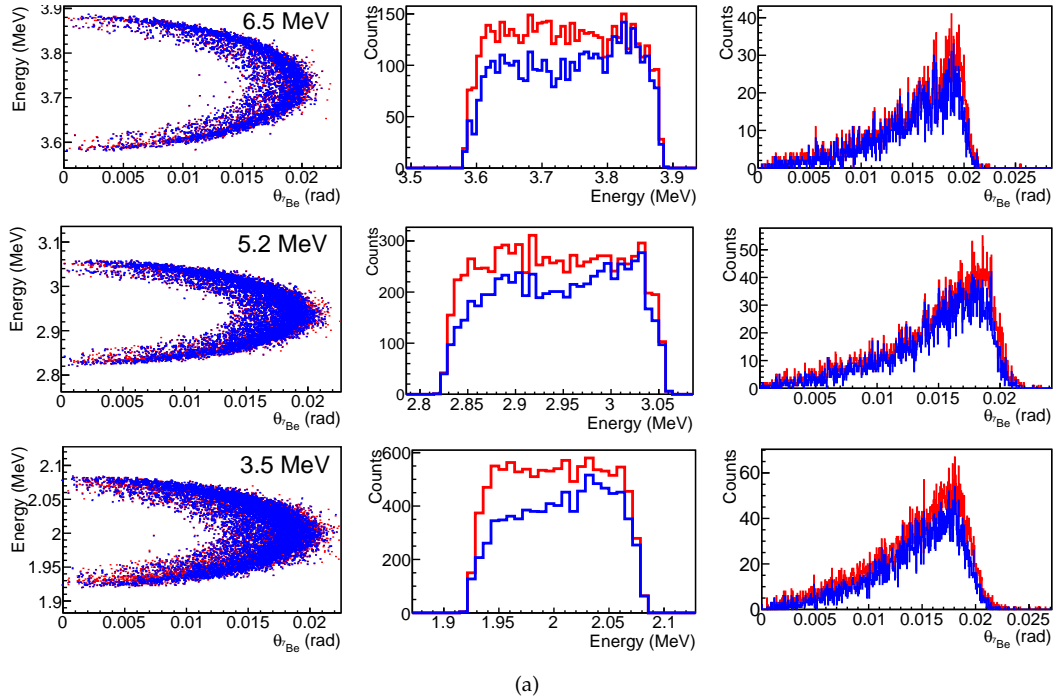


Figure 4.13: Simulation outputs when the tuned separator energy is set to the mean exiting recoil energy. (a) show the kinematics curves and projections being in this case in red the recoils created and blue the detected ones; (b) shows the percentage recoils stopped in the different volumes

4.4 Final Simulations using the Measured Tubes Displacements

As can be observed from the previous plots (e.g. Figure 4.12) some of the recoils are stopped in the exiting pumping tubes before the first magnetic quadrupole Q1 ($z=85$ cm). For this reason a careful determination of a likely displacement of the tubes was done using a theodolite [Vuj01]. Some displacements were observed in both vertical and horizontal direction at different positions as shown in Figure 4.14.

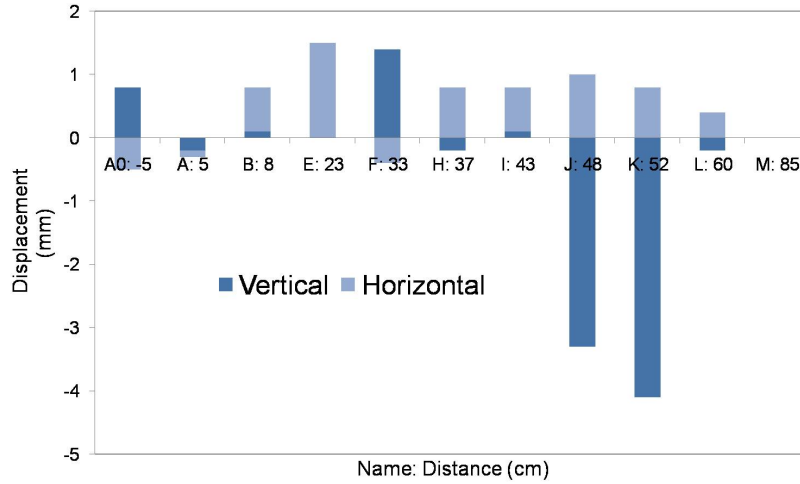


Figure 4.14: Horizontal and vertical DRAGON tubes displacements measured using a theodolite. Each pumping tube is labelled with a letter in order to be identified followed by the end distance of the tube in cm.

The displacements have been introduced in the code in order to extract the correct values for transmissions. It should be pointed out that the two first displacements corresponding to the entrance and exiting cell apertures (at -5 and 5 cm of the centre of the target, respectively) were a consequence of the setup for the 2013 experiment so these two are added only to the 4.7 MeV simulation. A new series of simulations were performed for each energy with the new geometry including the displacements of the tubes. The others parameters such as γ ray angular distributions or tuning energies are the same as before. Table 4.6 shows the results of the transmissions in the fifth column while in the sixth column display the relative differences when comparing with transmissions shown in Table 4.4.

Run	$\sim E_{4\text{He}}$ (MeV)	${}^7\text{Be}$ recoils created	${}^7\text{Be}$ recoils detected	Transmission (%)	Relative Difference (%)
	6.5	25931	14873	57.3±0.6	14.1±1.2
2011	5.2	39694	22907	57.7±0.5	12.9±1.0
	3.5	55383	28392	51.3±0.3	11.8±0.9
2013	4.7	38554	27627	71.7±0.6	12.6±0.9

Table 4.6: DRAGON transmissions after considering the displacements of the pumping tubes shown in Figure 4.14. The last column shows the relative differences with the results shown in Table 4.4.

As can be seen, the higher the energy, the higher the effect of the displacements; this is in line with the fact that output recoil angles are slowly increasing with energy (see Appendix B for the

kinematics of this reaction). Figure 4.15 shows in black the maximum recoil angle for our centre of mass energies while the red dots just indicates the trend. Therefore the effect of the tube displacements will also increase with energy.

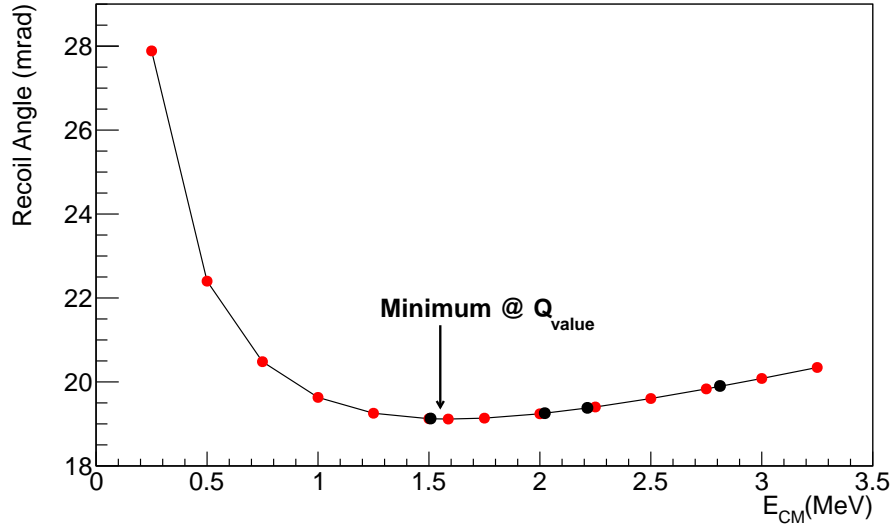


Figure 4.15: Maximum output recoil angle distribution for different centre of mass energies. In black are shown the centre of mass energies corresponding to our beam energies

The effect of each pumping tube displacement can be observed for example in Figure 4.16. Here, the number of recoils stopped in the different volumes are displayed for the 3.5 MeV energy. The number of stopped recoils before Q1 are increased from 5199 for no displacements (a) to 10420 with displacement (b).

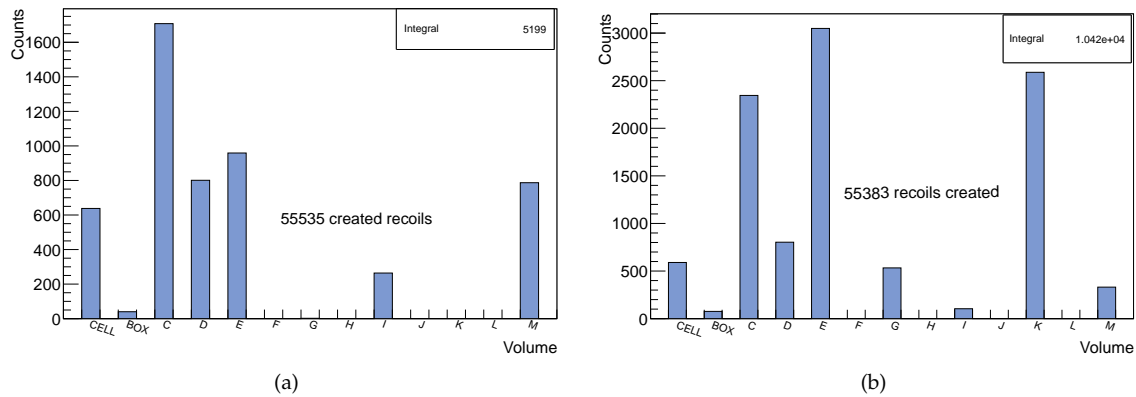


Figure 4.16: Simulated recoils stopped in the DRAGON pumping tubes for the 3.5 MeV beam energy. The volumes are named according to Figure 4.14. (a) with no displacements and (b) with the displacements shown in Figure 4.14

Clearly, the displacement of the volume labeled as "K", placed just before the first quadrupole Q1, has a crucial effect on the acceptance. As can be seen the displacement of volumes "E" and "C" are also significant. The new kinematics curves after considering the effect of the tubes displacements are shown in Figure 4.17.

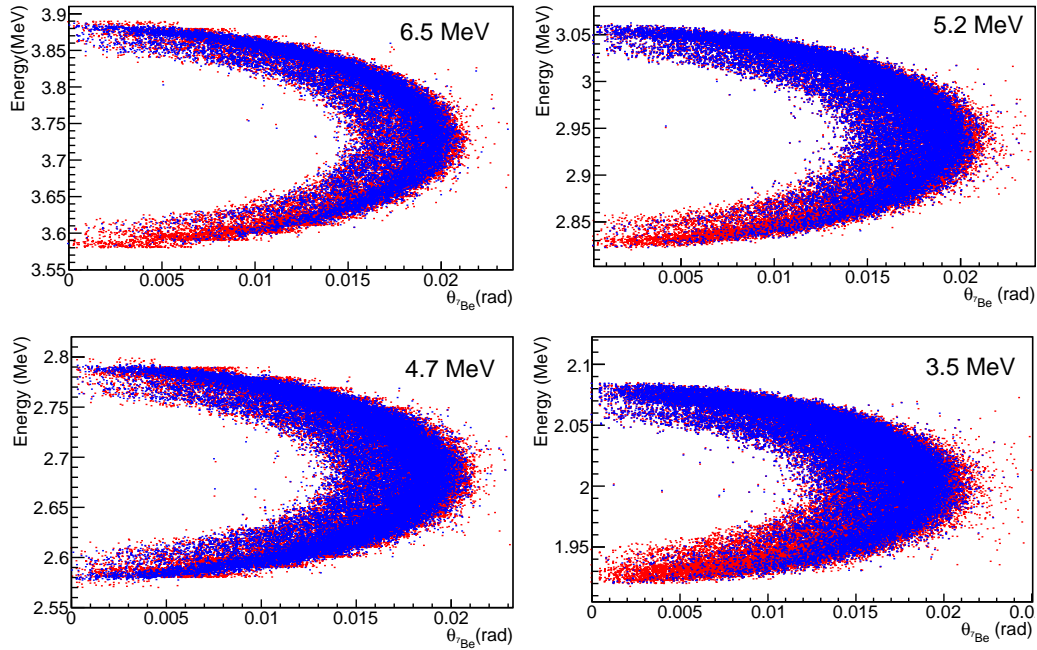


Figure 4.17: Kinematics curves after introducing the pumping tubes displacements. The red dots show the recoils produced and the blue ones corresponds to those detected in the DSSSD

Unless otherwise specified, the transmissions values ϵ_{DRAGON} shown in Table 4.6 which also include the effect of the displacements pumping tubes will be considered as the final transmissions of DRAGON for our reaction.

4.4.1 The DSSSD and the BGO spectra: simulations and data

Here, several tests will be discussed to determine the reliability of the simulations. Figure 4.18 shows a comparison between the simulated (in red) and real (in blue) DSSSD spectra for the ~ 3.5 MeV and ~ 5.2 MeV beam energy cases. For the 3.5 MeV case, the slightly differences between the two spectra are due to two effects. Firstly, for the DSSSD calibration a $0.5\mu\text{m}$ dead layer has been considered to calibrate the detector however, this is not accurate enough and moreover, the triple alpha energies used to calibrate the detector are not close to this recoil energy. This implies an offset in the calibrated DSSSD energy. Secondly, the real DSSSD resolution is not consider in the simulation, which would increase the width of the simulated recoil peak.

An example comparing the experimental and simulated DSSSD hit-maps is displayed in Figure 4.19, where in the left column are shown the simulated hit-maps for the ~ 5.2 and ~ 3.5 MeV beam energy cases and on the right side the corresponding simulated hit-maps. While for the 3.5 MeV case the recoil spots are more or less centre in the DSSSD in both the simulated and experimental hit-maps, for the 5.2 MeV different recoil spot displacements can be observed. In order to account for these differences different input parameters are varied and the resulting effects is considered to determine uncertainties in the transmissions shown in Table 4.6.

For the BGO detectors, two examples of spectra comparing the simulations and experimental data are shown in Figure 4.20. Both, experimental and simulated spectra display the energy of the BGO whose recorded energy for the given event is the maximum among the thirty BGO detectors. Only the events that are in coincidence with recoils have been considered in both experimental and simulated histograms, i.e. a recoil is detected simultaneously in the DSSSD. As it was discussed in Chapter 3, it is not possible to identify the prompt γ -rays peak in the total single BGO spectra (without coincide with the DSSSD) due to the high background contamination including some beam induced background (see Figure 3.26).

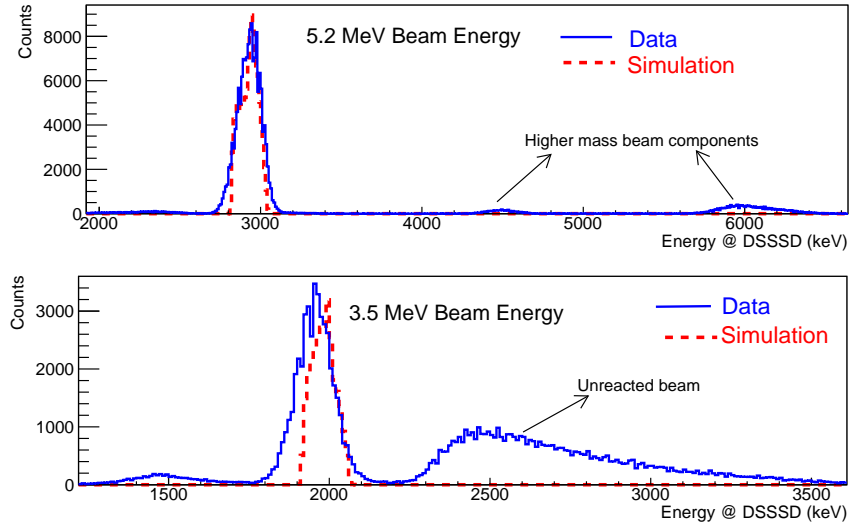


Figure 4.18: Comparison between the simulated DSSSD spectra (red dash line) with the measurements (in blue) for beam energy of 5.2 MeV (top) and 3.5 MeV (bottom) The highest peaks show the recoiling ${}^7\text{Be}$ nucleus in the DSSSD.

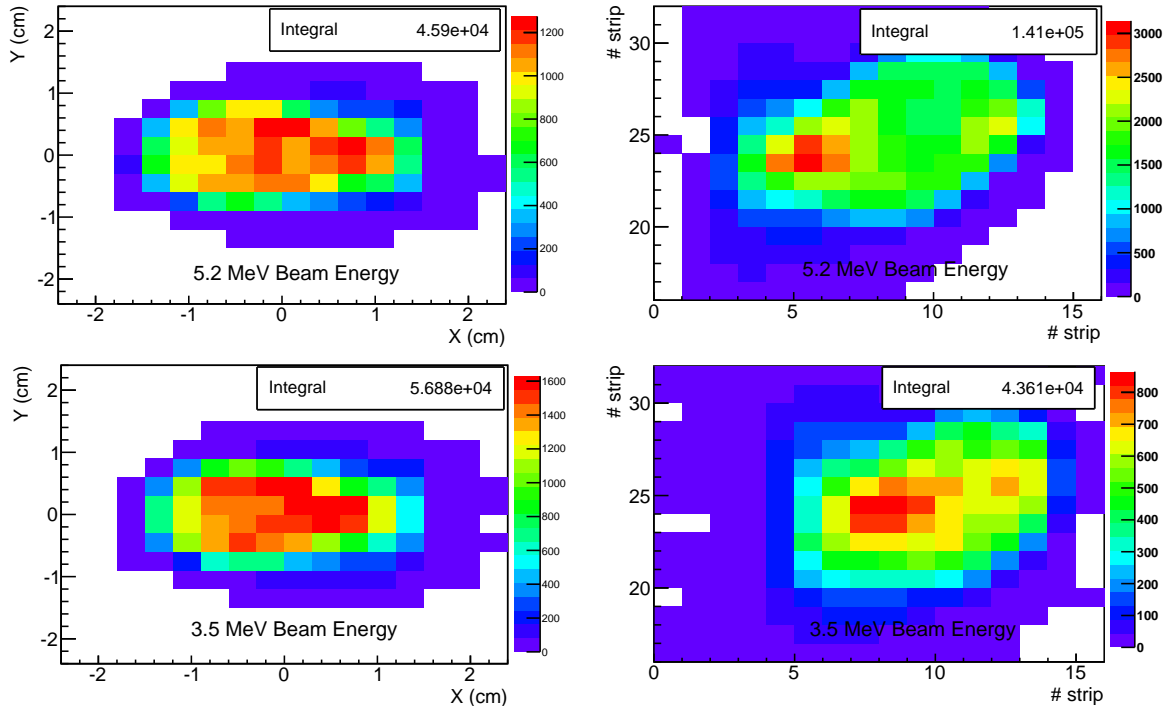


Figure 4.19: DSSSD hit-maps for beam energies of ~ 5.2 MeV and ~ 3.5 MeV. For simulations (left) X and Y are shown in cm and from measurements (right) with the X and Y axis indicates the strip number. In order to increase the statistics for the hit-maps in these plots 2-10⁵ beam particles were simulated for these cases. The apparent difference between simulation and measurements could be due to the lack of precise knowledge of all DRAGON parameters or the exact DSSSD position and eventual angle.

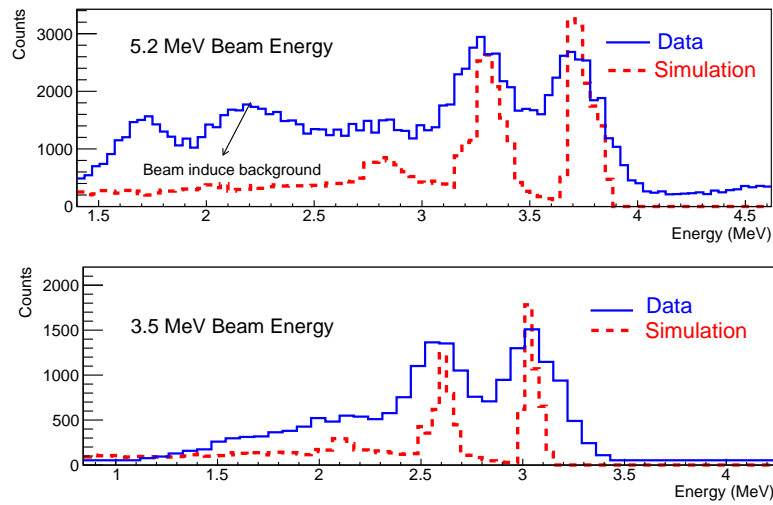


Figure 4.20: Comparison between the simulated BGO spectra (in red) and the experimental (in blue) in coincide with the ${}^7\text{Be}$ recoils. The two highest energy peaks corresponds to the γ rays from the de-excitation of the capture state to the ground and first excited state. It must be pointed out that for the 5.2 MeV the real simulated spectrum has been multiplied by four in order to have comparative number of counts in the γ peaks comparing to the experimental one.

The peak width differ between the simulated and experimental spectra as the real resolutions of the BGO detectors are not included in the simulations. The relative intensity of the two peaks seems to be different between experimental data and simulations, this is due to the assumed S_1/S_0 ratio in the simulations and further analysis on that will be performed in the following sections.

The BGO hit-maps patterns have been simulated independently for each γ peak that are selected by placing the corresponding energy gates (see Figure 4.21 for the 3.5 MeV case)

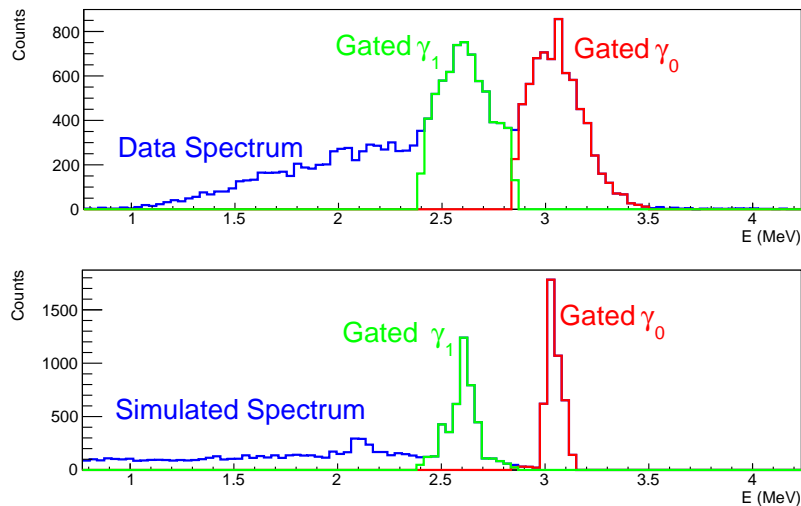


Figure 4.21: For the 3.5 MeV beam energy case are shown the gates performed in the experimental data spectrum (top panel) and the simulated one (bottom panel).

Figures 4.22 and 4.23 shows the BGO hit-maps for the γ_0 and γ_1 rays at the different beam energies that are obtained by placing the corresponding energy gates. The simulated spectra have been artificially scaled in order to have the same number of counts as that of the counts in the experimental ones.

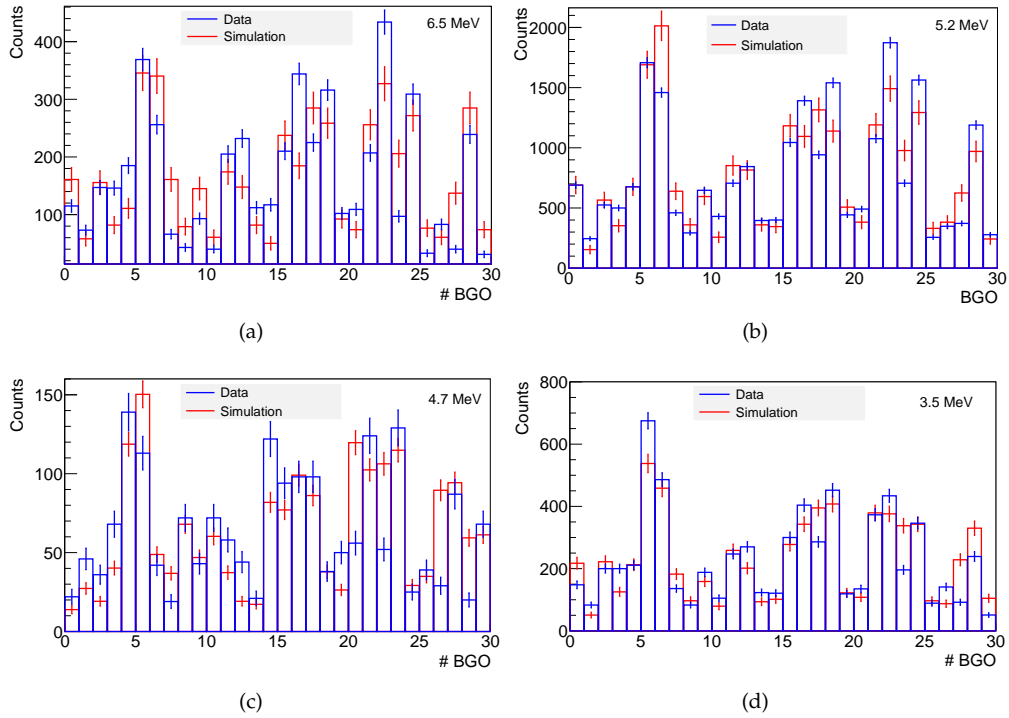


Figure 4.22: BGO hit-maps corresponding to γ_0 . The simulated histograms are normalized to the total number of hits in the experimental data. Each panel is tagged with E^{beam} .

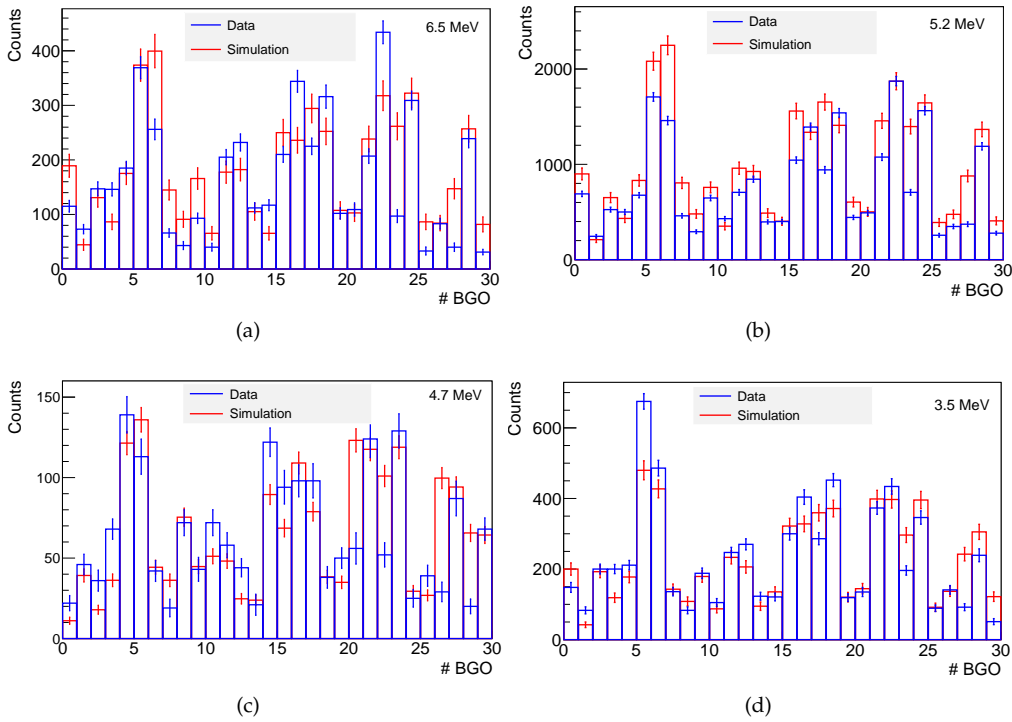


Figure 4.23: BGO hit-maps for corresponding γ_1 . The simulated histograms are normalized to the total number of hits in the experimental data. Each panel is tagged with E^{beam} .

Further investigations of the influence of the γ angular distribution assumptions will be made in the following section. In order to quantify the dispersion between simulated and experimental data, I will use $\chi^2_{\nu-1}$ value defined as:

$$\chi^2_{\nu-1} = \left(\sum_{i=1}^{30} \frac{(N_i^{\text{data}} - N_i^{\text{simu}})^2}{\sigma_{N_i^{\text{data}}}^2 - \sigma_{N_i^{\text{simu}}}^2} \right) / 29 \quad (4.3)$$

$$(4.4)$$

where N_i^{data} and N_i^{simu} are the number of γ -counts in a given BGO detector and $\sigma_{N_i^{\text{data}}}$ and $\sigma_{N_i^{\text{simu}}}$ are the associated errors respectively. The results are shown in Table 4.7.

$E_{\text{He}} \text{ (MeV)}$	~ 6.5	~ 5.2	~ 4.7	~ 3.5
$\chi^2_{\nu-1}(\gamma_0)$	7.5	5.3	1.1	6.7
$\chi^2_{\nu-1}(\gamma_1)$	8.2	11.1	6.4	5.6

Table 4.7: χ^2 as defined in expression 4.3 for the comparison of the simulated and experimental BGO hit-map.

4.5 Simulations for Estimating Uncertainties in ϵ_{DRAGON}

In the previous section some discrepancies have been observed when comparing the simulated and experimental data. Furthermore, differences between the simulated mean recoil energies and those used for setting up the DRAGON separator have been observed. These are originated because DRAGON program considers only the change in mass of the nuclei without taking into account difference in energy loss between beam and recoils. An analysis of the output mean energy shows agreement with those calculated using SRIM, which suggests that the ${}^7\text{Be}$ recoils loses approximately seven times more energy than an alpha particle crossing the same distance for a given energy. Indeed, it has been proved that the transmissions increase notably by considering the mean energy to scale DRAGON. However, the mass and energy range of the reactions partners is one in which energy loss is poorly described by theory [Ili07].

Therefore, with a better understanding of the results from the original series of simulations, a number of additional tests have been carried out to determine the DRAGON's sensitivity to several parameters. The central values of the transmissions are those shown in Table 4.6 and their sensitivity to the parameters are considered when determining the uncertainties. In the following, only information differing from what already presented will be detailed and it will always be considered that the number of beam particles simulated are 10^5 .

4.5.1 Gas target density profile

The density profile of the windowless gas target was determined experimentally using the method explained in 3.3.3.4. In the simulation a step function fit of the experimental data was used (Figure 4.3). In order to account for both the uncertainties in the experimental data and those related to the fit, variations in the width and steepness of the profile are considered as possible sources of systematic error in the results of the transmissions.

Effective length of the gas target

In order to estimate the error in the transmission related to the target length, the actual effective target length of 12.3 is varied ~ -0.5 cm, according to the red fit in Figure 3.52. The new step function is shown in violet in Figure 4.24.

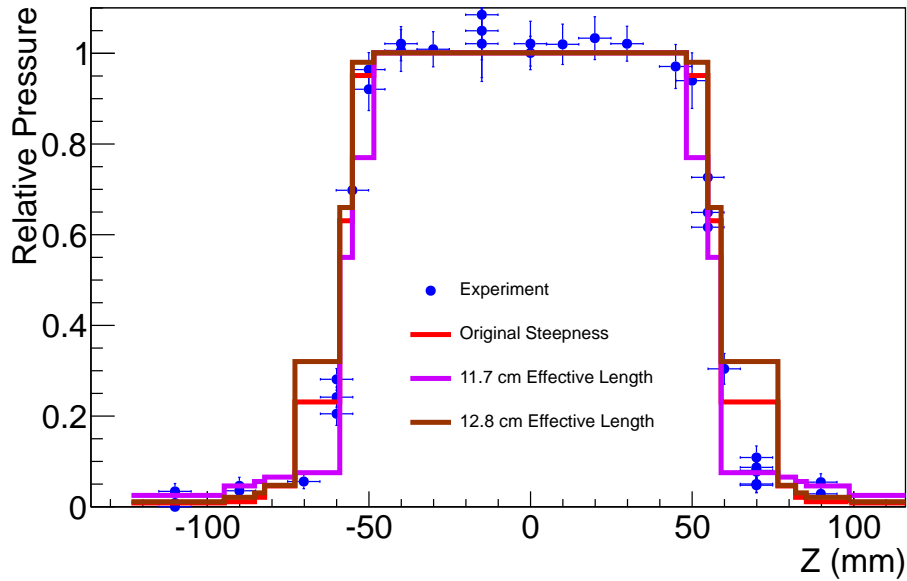


Figure 4.24: Step target density profiles for the original 12.3 cm (red) 11.75 cm (violet) and 12.8 cm (brown) effective lengths compared the experiments (blue dots).

The results are shown in Table 4.8 where in the last column are indicated the relative differences to the final transmissions in Table 4.6.

Run	E_{He} (MeV)	${}^7\text{Be}$ recoils created	${}^7\text{Be}$ recoils detected	Transmission (%)	Relative Difference (%)
	~ 6.5	25383	14624	57.6 ± 0.6	$+0.45 \pm 1.47$
2011	~ 5.2	38825	22710	58.5 ± 0.5	$+1.36 \pm 1.19$
	~ 3.5	54010	28191	52.2 ± 0.4	$+1.82 \pm 1.05$
2013	~ 4.7	36921	26625	72.1 ± 0.6	$+0.64 \pm 1.13$

Table 4.8: DRAGON transmissions when the effective length is 11.75 cm (see Figure 4.24). The column titled "relative difference" displays the difference in transmission values between the transmissions in Table 4.6 and the simulations done here.

As observed, reduce the effective length of the gas target does not have a large effect on the transmission. As expected, the maximum relative difference is for the the lowest energies because the energy losses (i.e. the gas quantities) play a more determining role for lower energies.

Even though the effect of considering a change in the effective length does not play a very influential role, the opposite case in which the width of the profile is increased must be investigate. The corresponding step function is shown in brown in Figure 4.24 and the transmissions are displayed in Table 4.9.

Run	E_{He} (MeV)	${}^7\text{Be}$ recoils created	${}^7\text{Be}$ recoils detected	Transmission (%)	Relative Difference (%)
	~ 6.5	14784	26691	55.4 ± 0.6	-3.43 ± 1.15
2011	~ 5.2	23532	41397	56.8 ± 0.5	-1.50 ± 0.89
	~ 3.5	28745	56660	50.7 ± 0.4	-1.04 ± 0.77
2013	~ 4.7	27945	39466	70.8 ± 0.6	-1.19 ± 0.89

Table 4.9: DRAGON transmissions when the effective length is 12.8 cm (see Figure 4.24). The column titled "relative difference" displays the difference in transmission values between the transmissions in Table 4.6 and the simulations done here.

In this case, for the three lowest energies the relative differences are similar to the ones obtained in Table 4.8 for the 11.7 cm effective length. However, a significant relative difference is observed for the highest energy. A possible explanation to this, could be in line with the highest influence of the tube displacements for the higher energy (see Table 4.6).

Steepness of the gas profile

Although from the previous analysis it is not expected a high effect from changing slightly the target density profile, it is necessary to examine the effect of modifying the steepness of the step function by considering that the pressure decrease more rapidly and thus the pressure is higher in the extremes. The new step function is displayed in violet in Figure 4.25 where it can be observed that in the two first steps out of the centre (cell apertures) the pressure decrease more rapidly than in the original one (red).

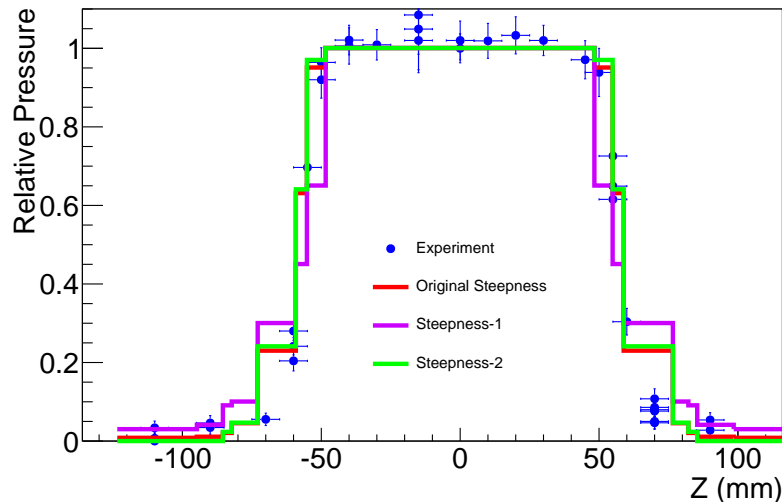


Figure 4.25: New step functions in violet (and green) where the pressure decreases (increases) more rapidly than in the original one (red).

The transmissions obtained with the modified step function are displayed in Table 4.10. As expected, the relative differences are negative because the proportion of the gas further upstream is higher and as expected from Figure 4.10 the recoils create further upstream are more likely to be stopped. The relative differences are similar to those obtained by changing the effective target length in Table 4.9.

Run	$E_{4\text{He}}$ (MeV)	${}^7\text{Be}$ recoils created	${}^7\text{Be}$ recoils detected	Transmission (%)	Relative Difference (%)
	~ 6.5	26575	14758	55.5 ± 0.6	-3.18 ± 1.15
2011	~ 5.2	40612	23092	56.9 ± 0.5	-1.47 ± 0.90
	~ 3.5	56766	28561	50.3 ± 0.4	-1.85 ± 0.76
2013	~ 4.7	39263	27914	71.1 ± 0.6	-0.79 ± 0.89

Table 4.10: DRAGON transmissions when profile step is changed to those in violet in Figure 4.24. The column titled "relative difference" displays the difference in transmission values between the transmissions in Table 4.6 and the simulations done here.

The same study has been made considering that the pressures decreases smother in the cell apertures. The step function is shown in green in Figure 4.25 and the corresponding transmissions are given in the Table 4.11. The relative differences are also smaller due to the proportion of gas downstream is lower.

Run	$E_{4\text{He}}$ (MeV)	${}^7\text{Be}$ recoils created	${}^7\text{Be}$ recoils detected	Transmission (%)	Relative Difference (%)
	~ 6.5	14687	26184	56.1 ± 0.6	-2.20 ± 1.17
2011	~ 5.2	22995	39870	57.7 ± 0.5	-0.06 ± 0.92
	~ 3.5	28298	55244	51.2 ± 0.4	-0.08 ± 0.78
2013	~ 4.7	27409	38322	71.5 ± 0.6	-0.19 ± 0.91

Table 4.11: DRAGON transmissions when profile step is changed to this shown in green in Figure 4.24. The column titled "relative difference" displays the difference in transmission values between the transmissions in Table 4.6 and the simulations done here.

The final error contributions associated to the target density profile are given in Table 4.12. The introduced uncertainties are smaller than 2% except for the highest energy where in line with the observed effect of the tube displacement, the introduced uncertainties are considerable higher.

Run	$E_{4\text{He}}$ (MeV)	Original Transmission (%)	Uncertainty associated to the effective length	Uncertainty associated to the steepness
	~ 6.5	57.3 ± 0.6	$+0.3$ -2.0	-1.8 -1.3
2011	~ 5.2	57.7 ± 0.5	$+0.8$ -0.9	-0.8 $+0.0$
	~ 3.5	51.3 ± 0.3	$+0.9$ -0.5	-1.0 $+0.0$
2013	~ 4.7	71.7 ± 0.6	$+0.5$ -0.9	-0.6 -0.1

Table 4.12: Systematics errors introduced to the final transmission efficiencies due to the assumptions made on the target density profile. For the given energy, the fourth column gives error for considering a 11.7 cm effective length (top) and 12.8 cm (bottom). For the fifth column shows the error from a rapid pressure decrease in the apertures (up) and a smother pressure decrease (bottom).

4.5.2 Beam offset

The beam from ISAC facility can vary in transverse emittance and in central location. During the experiment the central location of the beam is monitored with the CCD camera inside an alignment port of the first magnetic dipole. However, there is a possibility that the beam can drift in the transverse directions to the beam direction during a period of time. Thus, the next step will be to analyze the effect on the transmission of transverse offset beam displacements of ± 1 mm in both x and y directions.

X-axis

The transmissions obtained by considering ± 1 mm displacements in the x directions are given in Table 4.13.

Run	$E_{4\text{He}}$ (MeV)	Transmission +1mm-X(%)	Relative Difference (%)	Transmission -1mm-X(%)	Relative Difference (%)
	~ 6.5	57.6 ± 0.6	$+0.36 \pm 1.48$	54.6 ± 0.6	-4.87 ± 1.18
2011	~ 5.2	58.9 ± 0.5	$+2.05 \pm 1.20$	54.4 ± 0.5	-5.65 ± 0.90
	~ 3.5	51.9 ± 0.4	$+1.28 \pm 1.06$	49.3 ± 0.4	-3.86 ± 0.78
2013	~ 4.7	73.9 ± 0.6	$+3.07 \pm 1.18$	66.7 ± 0.5	-6.93 ± 0.86

Table 4.13: DRAGON transmissions with beam displacements of ± 1 mm in the x direction. Columns titled with Relative Difference show the difference with the transmissions shown in Table 4.6

A significant difference is observed respect to the simulations shown in Table 4.6. According to the results, a displacement in the negative direction produces even higher change in the transmission than in the positive one. The relative differences are higher for the 2013 run and Figure 4.26 shows that pumping tubes downstream are the responsible for the significant increase in the number of stopped recoils for a displacement of -1 mm in the x direction.

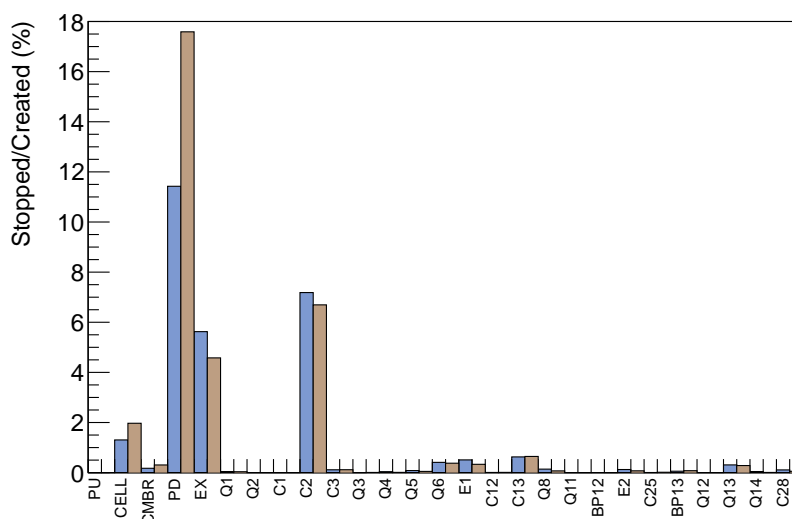


Figure 4.26: For the 4.7 MeV the blue bars show the volumes where the recoils are stopped without any beam offset (Table 4.6) and in brown where the recoils stop with a -1 mm displacement in the x axis. The numbers are give as ratios of number of recoils stopped in a given volume and the total number of recoils created.

Y-axis

The same type of analysis have been performed in order to see the influence of a displacement in the y direction. The results for both +1 mm and -1 mm offsets are displayed in Table 4.14.

Run	$E_{4\text{He}}$ (MeV)	Transmission +1mm-Y(%)	Relative Difference (%)	Transmission -1mm-Y(%)	Relative Difference (%)
2011	~ 6.5	55.2 ± 0.6	-3.83 ± 1.19	56.5 ± 0.6	-1.55 ± 1.20
	~ 5.2	55.2 ± 0.5	-4.35 ± 0.91	56.7 ± 0.5	-1.81 ± 0.92
	~ 3.5	49.3 ± 0.4	-3.91 ± 0.78	50.6 ± 0.4	-1.23 ± 0.79
2013	~ 4.7	68.2 ± 0.6	-4.85 ± 0.89	70.6 ± 0.6	-1.45 ± 0.92

Table 4.14: DRAGON transmissions with beam displacements of ± 1 mm in the y direction. Columns titled with Relative Difference show the difference with the transmissions shown in Table 4.6

In this case a significant decrease in the transmission is observed independently of a positive or negative displacement in the y direction beam clearly higher when the displacement is in the positive direction.

The uncertainties introduced to the final transmissions as consequence of the location in the x and y axis are summarized in Table 4.15.

Run	$E_{4\text{He}}$ (MeV)	Original Transmission (%)	Uncertainty associated to x -axis displacement	Uncertainty associated to y -axis displacement
2011	~ 6.5	57.3 ± 0.6	$+0.2$ -2.8	-2.2 -0.9
	~ 5.2	57.7 ± 0.5	$+1.2$ -3.3	-2.5 -1.0
	~ 3.5	51.3 ± 0.3	$+0.7$ -2.0	-2.0 -0.6
2013	~ 4.7	71.7 ± 0.6	$+2.2$ -5.0	-3.5 -1.0

Table 4.15: Error introduced to the mean transmission efficiencies from the uncertainty in the beam location along with the x and y axes.

4.5.3 Beam emittance

As described in section 4.2.3 the beam emittance is introduced in GEANT by defining a Gaussian beam spot distribution obtained from the experimental beam transmissions and Gaussian divergence distribution calculated from the normalised beam emittance from ISAC-I. In order to account for the effects of changes in the beam emittance on transmissions efficiencies, some parameters are varied within respectively estimate errors.

Beam transmission

Here the $\sigma \uparrow$ and $\sigma \downarrow$ corresponds to the changed beam transmission by ± 3 units with respect to those given in Table 4.1. The values of $\Delta\theta_{x/y}$ are changed accordingly. Table 4.16 shows the values considered for the modified $\sigma_{x/y}$ together with the transmissions and relative differences respect to the values in Table 4.6. The associated uncertainties to the transmissions are shown in Table 4.17.

Run	$E_{4\text{He}}$ (MeV)	$\sigma_{x/y} \uparrow$ (mm)	Transmission (%)	R. Difference (%)	$\sigma_{x/y} \downarrow$ (mm)	Transmission (%)	R. Difference (%)
	~ 6.5	1.60	56.5 ± 0.6	-1.47 ± 1.20	1.40	57.2 ± 0.6	-0.32 ± 1.16
2011	~ 5.2	1.26	56.9 ± 0.5	-1.34 ± 0.92	0.75	60.3 ± 0.5	-4.51 ± 1.21
	~ 3.5	1.37	50.5 ± 0.4	-1.41 ± 0.79	1.14	52.0 ± 0.4	1.34 ± 1.04
2013	~ 4.7	1.36	70.4 ± 0.6	-1.80 ± 0.90	1.13	71.9 ± 0.6	0.30 ± 1.11

Table 4.16: DRAGON transmissions when there is an increase ($\sigma_{x/y} \uparrow$)/decrease ($\sigma_{x/y} \downarrow$) in the beam transmission. Columns titled with Relative Difference show the difference with the transmissions shown in Table 4.6

Beam divergence offset

Following the systematic procedure so far, in which an offset has been introduced in the beam spot, and the beam spot distribution and beam divergence were changed simultaneously to fit different transmissions, the next step is to study the influence of a likely offset in the beam divergence itself. For that, a ± 0.5 mrad offset have been introduced in both $\Delta\theta_x$ and $\Delta\theta_y$. In the program the particles are randomly selected with the divergence detailed in the section 4.2.3, and after that 0.5mrad are added to the divergence in the selected direction for each event (see Figure 4.27).

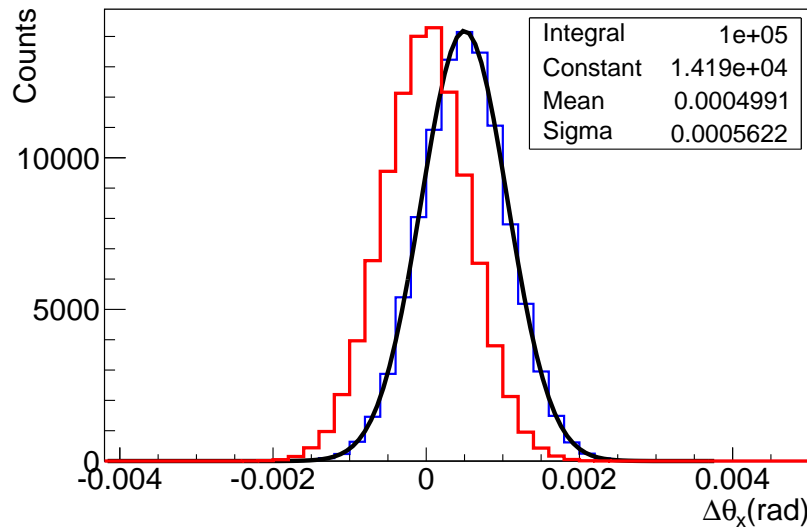


Figure 4.27: An offset of +0.5 mrad in divergence in the x direction, $\Delta\theta_x$, for the 6.5 MeV beam energy. Red histogram corresponds to the original x divergence distribution $\Delta\theta_x = 0.56$ mrad. Events are randomly selected from this distribution. Latter a displacement of 0.5 mrad is added to this event (blue distribution). The black curve shows a fit to the distribution, and the parameters show the same width (0.56 mrad) but a displacement of 0.499 mrad.

The errors introduced in the transmissions due to the offsets in the beam divergences are displayed in Table 4.17.

Run	$E_{4\text{He}}$ (MeV)	Original Trans. (%)	Uncertainty from beam transmission	Uncertainty from $\Delta\theta_x$ displacement	Uncertainty from $\Delta\theta_y$ displacement
2011	~ 6.5	57.3 ± 0.6	-0.2 -0.8	-1.1 -1.0	-0.8 -0.8
	~ 5.2	57.7 ± 0.5	$+2.6$ -0.8	$+0.0$ $+0.1$	$+0.0$ $+0.3$
	~ 3.5	51.3 ± 0.3	$+0.7$ -0.7	-0.6 -0.1	-0.2 $+0.4$
2013	~ 4.7	71.7 ± 0.6	$+0.2$ -1.3	-0.3 -0.3	-1.2 $+0.1$

Table 4.17: Error introduced to the final transmission efficiencies from the uncertainty in the beam divergence along the x and y axis. The top values shown the uncertainty when the offsets is in the positive direction ($+0.5$ mrad) and the bottom ones the relative to -0.5 mrad.

4.5.4 Beam energy

The next parameter to be examined is the ^4He beam energy from the ISAC-I facility. To account for the uncertainties in the central beam energy, the simulation were run considering central energies $\pm 0.17\%$ of the original simulations, considering the same Gaussian widths ([HRF12]). Table 4.18 shows in the second column the new simulated beam energies (higher and lower) and in the fourth column the associated uncertainties obtained.

Run	$E_{4\text{He}}$ (keV)	Original Transmission (%)	Uncertainty associated to mean beam energy
2011	6586 6521	57.3 ± 0.6	$+1.3$ -3.1
	5192 5140	57.7 ± 0.5	$+1.8$ -1.6
	3539 3504	51.3 ± 0.3	$+1.8$ -1.7
2013	4704 4693	71.7 ± 0.6	$+0.4$ -0.9

Table 4.18: Error introduced to the final transmission efficiencies from the uncertainty in the mean beam energies. The new beam energies are shown in the second column where the top value represents 0.25% increase from the original values and in the bottom a 0.25% decrease. The associated uncertainties are shown in the fourth column.

As can be observed a variation in the mean energy results in a relative big change in the recoil transmissions. These is not an unexpected result because as it was presented above the the energy plays the more determining role in the DRAGON transmission.

An increase in the beam energy leads to an increase in the recoil in energy and a mean output energy closer to the valued that the separator was tuned for, thus an increase in the transmission. For the 2013 run, the tuning energy was set manually closer to the real mean output energy, thus an increasing of the tuning energy does not have a big effect in the transmission . A decrease in the beam energy leads to a decrease in the transmission because of the same reasons.

4.5.5 The branching ratio S_1/S_0

The next investigation is to check the influence of the S_1/S_0 ratio for the population of the first excited and ground states of the ^7Be recoils. The values adopted so far are those shown in Table 4.2 based on the extrapolations in reference [CD08]. However, the simulated BGO spectra (see Figure

4.20) shows that the relative ratio of the γ_1/γ_0 (being γ_1 and γ_0 the areas under the corresponding γ peaks) is different when comparing to the experimental data.

In order to double check the influence in the DRAGON transmission on the assumptions made about the S_1/S_0 ratio and try to reproduce the experimental γ_1/γ_0 ratio, a first series of simulations have been performed. Based on the relative same area of the γ_0 and γ_1 experimental peaks, the first assumption is to employ a S_1/S_0 ratio equal to 1. The transmissions obtained are shown in the third column in Table 4.19. While the relative differences shown in the fourth column are similar to that obtained by varying other parameters as divergence, the relative S_1/S_0 ratio are clearly larger than those obtained with the experimental data (see Figure 4.28). This effect is due to the contribution from the escape peak corresponding to the γ_0 rays (γ_0 -511 keV) to the γ_1 peak.

Run	$E_{4\text{He}}$ (MeV)	Transmission ($S_1/S_0=1$) (%)	R. Difference (%)	S_1/S_0	Transmission (%)	R. Difference (%)
	~ 6.5	58.4 ± 0.6	1.74 ± 1.47	0.393	56.0 ± 0.6	-2.42 ± 1.17
2011	~ 5.2	59.6 ± 0.5	3.35 ± 1.21	0.495	58.0 ± 0.5	$+0.55 \pm 1.18$
	~ 3.5	53.0 ± 0.4	3.32 ± 1.06	0.420	51.3 ± 0.4	$+0.04 \pm 1.03$
2013	~ 4.7	73.5 ± 0.6	2.58 ± 1.14	0.423	70.8 ± 0.6	-1.14 ± 0.9

Table 4.19: Transmissions obtained with different S_1/S_0 ratios. In the third column are shown the transmissions associated with $S_1/S_0=1$. In the 6th column the transmissions with the S_1/S_0 ratios displayed in the four column are shown. The relative differences are calculated with respect to the transmissions in Table 4.6.

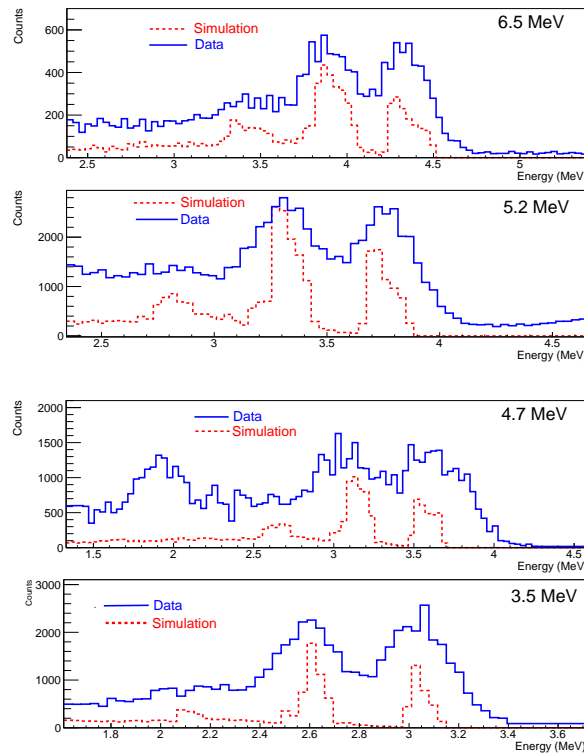


Figure 4.28: BGO spectra comparison between the experimental data and simulation with $S_1/S_0=1$. Both simulated and experimental spectra are shown in coincide with a ${}^7\text{Be}$ in the DSSSD.

Further simulations have been carried out to get closer values to the experimental γ_1/γ_0 data. The final ratio which better reproduce the experimental values are shown in fifth column in Table 4.19. The associated transmissions and relative differences are shown in columns seventh and eighth, respectively. In order to be conservative the maximum errors among the different tested S_1/S_0 will be considered and are given in Table 4.20. A comparison between data and the simulated ones for the S_1/S_0 ration are also shown in the same Table.

Run	$E_{4\text{He}}$ (MeV)	Original Transmission	Uncertainty from S_1/S_0	γ_1/γ_0 Experimental	γ_1/γ_0 simulation(*)
2011	~ 6.5	57.3 ± 0.6	$^{+1.0}_{-1.7}$	1.09 ± 0.02	1.13 ± 0.03
	~ 5.2	57.7 ± 0.5	$^{+1.9}_{-0.8}$	1.25 ± 0.01	1.26 ± 0.03
	~ 3.5	51.3 ± 0.3	$^{+1.7}_{-0.3}$	0.99 ± 0.02	1.03 ± 0.02
2013	~ 4.7	71.7 ± 0.6	$^{+1.8}_{-1.4}$	1.02 ± 0.03	1.01 ± 0.02

Table 4.20: γ_1/γ_0 experimental and simulated ratios. It is worth noting that the peak intensities are taken from the γ spectra in coincidence with recoils in the DSSSD.

(*)Corresponding to simulations with the S_1/S_0 ratios shown in the fifth column in Table 4.19.

4.5.6 γ -rays angular distributions

So far in the simulations the prompt γ -ray angular distributions emitted in the ${}^3\text{He}(\alpha,\gamma){}^7\text{Be}$ reaction are considered isotropic. This assumption would be experimentally justified at energies below $E_{\text{CM}}=1.23$ MeV [DGG09, BBS07]. However, our energies have been carried out at energies above $E_{\text{CM}}=1.23$ MeV. Therefore error contribution from γ anisotropy should be considered, for which the simulations have been done. For that, the γ angular distribution from reference [TP63a] has been considered. They calculated the prompt γ rays of the ${}^3\text{He}(\alpha,\gamma){}^7\text{Be}$ reaction using the ${}^3\text{He}+{}^4\text{He}$ scattering phase shift and expressed the differential cross section as a function of the angular momentum of the final state of ${}^7\text{Be}$ (ground state or first excited state) as:

$$\frac{d\sigma}{d\Omega} = \sigma_0(J_f)[1 + a_1(J_f)\cos\Theta + a_2(J_f)\cos^2\Theta + a_3(J_f)\cos^3\Theta + a_4(J_f)\cos^4\Theta] \quad (4.5)$$

where J_f is the angular momentum of the ${}^7\text{Be}$ final state, Θ is the polar angle of the gamma ray in the centre of mass system with respect to the beam axis, and a_1, a_2, a_3 and a_4 are energy dependent coefficients and vary depending on the final state populated in the ${}^7\text{Be}$. For our beam energies, the coefficients for both ground state and first excited state have been extracted from their energy dependent coefficient plots, and the differential cross section are given by:

$$\begin{aligned}
 6.5 \text{ MeV: } \frac{d\sigma}{d\Omega} &= \begin{cases} \sigma_0(J_f)[1 - 0.66\cos\Theta - 0.034\cos^2\Theta + 0.51\cos^3\Theta - 0.043\cos^4\Theta, \text{ for ground state} \\ \sigma_0(J_f)[1 - 0.09\cos\Theta - 0.2\cos^2\Theta + 0.03\cos^3\Theta + 0.0\cos^4\Theta, \text{ for first state} \end{cases} \\
 5.2 \text{ MeV: } \frac{d\sigma}{d\Omega} &= \begin{cases} \sigma_0(J_f)[1 - 0.226\cos\Theta - 0.02\cos^2\Theta - 0.02\cos^3\Theta + 0.017\cos^4\Theta, \text{ for ground state} \\ \sigma_0(J_f)[1 - 0.034\cos\Theta - 0.08\cos^2\Theta - 0.03\cos^3\Theta + 0.0\cos^4\Theta, \text{ for first state} \end{cases} \\
 4.7 \text{ MeV: } \frac{d\sigma}{d\Omega} &= \begin{cases} \sigma_0(J_f)[1 - 0.173\cos\Theta + 0.025\cos^2\Theta + 0.00\cos^3\Theta + 0.017\cos^4\Theta, \text{ for ground state} \\ \sigma_0(J_f)[1 - 0.033\cos\Theta - 0.02\cos^2\Theta - 0.02\cos^3\Theta + 0.0\cos^4\Theta, \text{ for first state} \end{cases} \\
 3.5 \text{ MeV: } \frac{d\sigma}{d\Omega} &= \begin{cases} \sigma_0(J_f)[1 - 0.036\cos\Theta + 0.109\cos^2\Theta - 0.047\cos^3\Theta + 0.017\cos^4\Theta, \text{ for ground state} \\ \sigma_0(J_f)[1 - 0.066\cos\Theta + 0.097\cos^2\Theta - 0.047\cos^3\Theta + 0.0\cos^4\Theta, \text{ for first state} \end{cases}
 \end{aligned}$$

Using these expressions, the relative probabilities for the direction of the γ rays are introduced in the simulations as function of $\cos\Theta$. Thus, the relative probabilities of the direction of the γ rays are randomly selected from those shown in Figure 4.29.

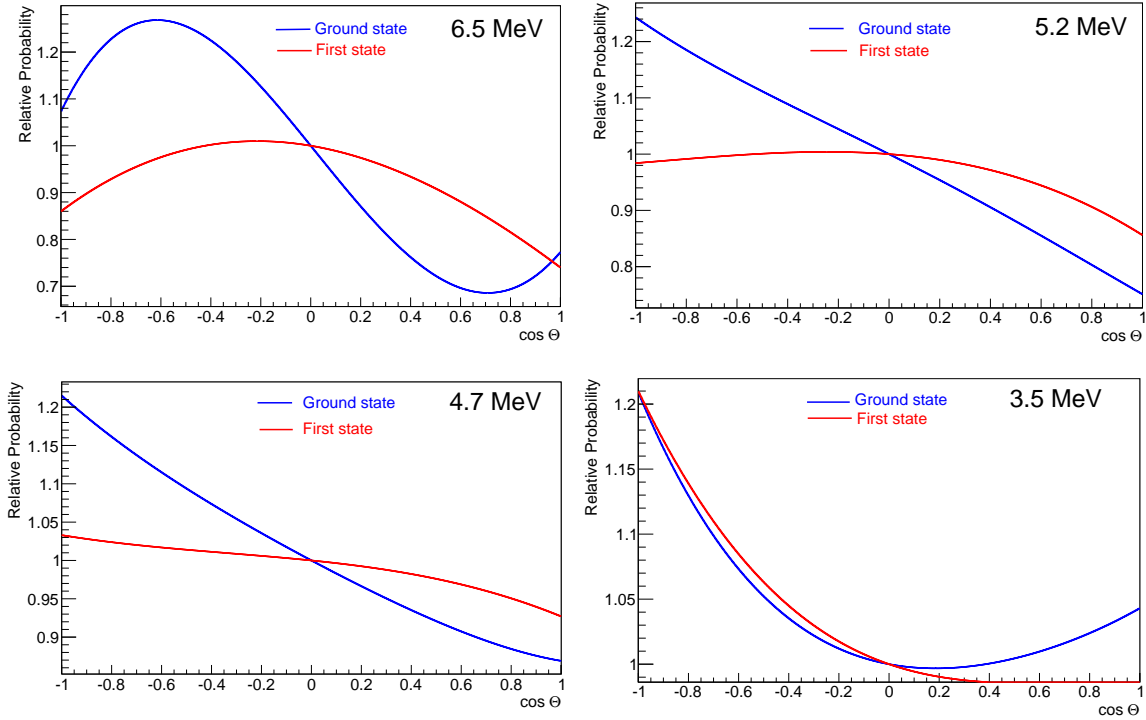


Figure 4.29: Relative probabilities for the direction of the prompt γ rays populating the ground state (blue) and the first excited state (red) at $E^{\text{beam}}=6.5, 5.2, 4.7$ and 3.5 MeV that are introduced in the GEANT 3 code.

The transmissions obtained with Tombrello and Parker's distributions are shown in Table 4.21 together with the relative differences comparing to those in Table 4.6 and also associated uncertainties to the original transmissions.

Run	E_{He} (MeV)	Transmission (%)	R. Difference (%)	Uncertainty from Angular Distribution
	~ 6.5	58.9 ± 0.6	2.71 ± 1.49	± 1.6
2011	~ 5.2	60.6 ± 0.5	5.07 ± 1.22	± 2.9
	~ 3.5	52.4 ± 0.3	2.20 ± 1.05	± 1.1
2013	~ 4.7	72.1 ± 0.6	0.62 ± 1.12	± 0.4

Table 4.21: DRAGON transmissions for the ${}^3\text{He}(\alpha,\gamma){}^7\text{Be}$ reaction when the gamma angular distribution is the calculated for Trombello and Parker in reference [TP63a].

In order to compare with the isotropic distribution Table 4.22 shows the $\chi^2_{\nu-1}$ values calculated using the expression 4.3.

$\sim E_{4\text{He}}$ (MeV)	6.5	5.2	4.7	3.5
$\chi^2_{\nu-1}(\gamma_0)$	5.7	7.7	7.0	5.5
$\chi^2_{\nu-1}(\gamma_1)$	10.3	8.2	5.5	4.7

Table 4.22: χ^2 as defined in expression 4.3 for the comparison of BGO hit-map between simulation and experimental data when the Tombrello and Parker distribution are assumed in the simulations

Observing the Tables 4.7 and 4.22 for the two angular distribution we believe that with intense simulations will be able to reduce the χ^2 by varying from a_0 to a_4 . For now, the changes observed in varying the angular distribution will be consider as an error introduced in the final transmissions.

4.6 ϵ_{DRAGON} Values and Uncertainties

The total systematic error contribution to the acceptance must be calculated from the estimated uncertainties. Conservative values of the uncertainties in each parameter previously described were used so that any correlation between variables could be account for. To calculate the total systematic errors introduced in the transmissions, both positive and negative contributions were treated independently. Therefore the total positive systematic error is given by:

$$\text{Error}_{\text{sys}}^+ = \sqrt{\sum_{i=1}^n (x_i^+)^2} \quad (4.6)$$

being the x_i^+ the positive uncertainties associated to the different experimental parameters tested in the simulations. In the same way, the total negative error is given by:

$$\text{Error}_{\text{sys}}^- = \sqrt{\sum_{i=1}^n (x_i^-)^2} \quad (4.7)$$

The final values of the transmissions and associated statistical and systematic errors are shown in Table 4.23, while a list with all tested parameters and their associated systematic uncertainty contributions to the transmission is given in Table 4.24.

Run	$E_{4\text{He}}$ (keV)	Transmission (%)	Statistical Error	Systematic Error
	6553.88	57.3	± 0.6	$+2.7$ -3.8
2011	5165.97	57.7	± 0.5	$+5.4$ -6.1
	3521.61	51.3	± 0.3	$+3.6$ -4.4
2013	4716.45	71.7	± 0.6	$+3.0$ -6.8

Table 4.23: Final DRAGON transmissions ϵ_{DRAGON} and associated statistical and systematic errors.

Parameter	Run	E_{He} (MeV)	Systematic Error (%)
TDP Effective Length	2011	~ 6.5	+0.3 -2.0
		~ 5.2	+0.8 -0.9
		~ 3.5	+0.9 -0.5
	2013	~ 4.7	+0.5 -0.9
TDP Steepness	2011	~ 6.5	-1.8 -1.3
		~ 5.2	-0.8 +0.0
		~ 3.5	-1.0 +0.0
	2013	~ 4.7	-0.6 -0.1
x Beam Offset	2011	~ 6.5	+0.2 -2.8
		~ 5.2	+1.2 -3.3
		~ 3.5	+0.7 -2.0
	2013	~ 4.7	+2.2 -5.0
y Beam Offset	2011	~ 6.5	-2.2 -0.9
		~ 5.2	-2.5 -1.0
		~ 3.5	-2.0 -0.6
	2013	~ 4.7	-3.5 -1.0
Beam Transmission	2011	~ 6.5	-0.2 -0.8
		~ 5.2	+2.6 -0.8
		~ 3.5	+0.7 -0.7
	2013	~ 4.7	+0.2 -1.3
$\Delta\theta_x$ Beam Offset	2011	~ 6.5	-1.1 -1.0
		~ 5.2	+0.0 +0.1
		~ 3.5	-0.6 -0.1
	2013	~ 4.7	-0.3 -0.3
$\Delta\theta_y$ Beam Offset	2011	~ 6.5	-0.8 -0.8
		~ 5.2	+0.0 +0.3
		~ 3.5	-0.2 +0.4
	2013	~ 4.7	-1.2 +0.1
Beam Energy	2011	~ 6.5	+1.3 -3.1
		~ 5.2	+1.8 -1.6
		~ 3.5	+1.8 -1.7
	2013	~ 4.7	+0.4 -0.9
S_1/S_0	2011	~ 6.5	+1.0 -1.7
		~ 5.2	+1.9 -0.8
		~ 3.5	+1.7 -0.3
	2013	~ 4.7	+1.8 -1.4
γ Angular Distribution	2011	~ 6.5	+1.6 -1.6
		~ 5.2	+2.9 -2.9
		~ 3.5	+1.1 -1.1
	2013	~ 4.7	+0.4 -0.4

Table 4.24: Experimental parameter tested in the transmissions simulations and their systematic errors.

"Physicists like to think that all you have to do is say, these are the conditions, now what happens next?"

Richard P. Feynman

CHAPTER 5

ANALYSIS AND RESULTS

Abstract: *In this chapter the analysis techniques, calculations and procedures to treat the data from the two experiments are detailed and the final results are presented in two main parts corresponding to the two experiments. The chapter starts with the Activation Experiment and follows with Direct Recoil Counting Experiment, focusing on the different observables and final results for the S-factor of the ${}^3\text{He}(\alpha,\gamma){}^7\text{Be}$ reaction at the energies of our investigations.*

Experiments are the keys to determine properties such as nuclear radius, spin and parities or cross sections. Following an experiment the more tricky task of data analysis starts which is crucial in obtaining meaningful results. Eventually, this allows for progress in understanding various processes, e.g. the formation of primordial elements in the Universe.

Different nuclear physics experiments are performed in order to obtain the same information, usually in order to reduce errors in the measurements and to provide consistent results that makes possible to understand the underlying physics. In addition, the development of new systems, such as detectors and advanced electronics take place benefiting the society and improving the results.

Experiments related to measure the cross section of astrophysical reactions aim at precise measurements. Theoretical models are used to extrapolate the experimental values down to the astrophysical relevant energies that are unreachable with current experimental systems. Therefore, constraining models using different measurements and complementary methods are required. This demands fool-proof analysis procedures that provides a very good understanding of all possible sources of errors in data that allows for reliable extraction of the observables.

It should be noted here that this is a high precision measurement where each parameter of the experiment has to be treated with specific care and thus I dedicate this chapter to data treatment.

5.1 Analysis I: Measurements using the Activation Method

Based on the expression 1.7, the astrophysical S-factor for the ${}^3\text{He}(\alpha,\gamma){}^7\text{Be}$ reaction, $S_{34}(E)$ is expressed by:

$$S_{34}(E) = \sigma_{34}(E) \cdot E \cdot e^{2\pi\eta(E)} \quad (5.1)$$

where E is the centre of mass energy (E_{CM}) and σ_{34} the cross section.

The reaction centre of mass energy is given in this case by (see appendix B):

$$E_{\text{CM}} = \frac{m_{4\text{He}}^{\text{T}}}{m_{4\text{He}}^{\text{T}} + m_{3\text{He}}^{\text{B}}} \cdot E^{\text{beam}} \quad (5.2)$$

where the different m are the nuclear masses in atomic units. In the following T will refer to the Target and B to the Beam. E^{beam} is the beam energy at the moment that the reaction happens.

The reaction cross section is given as:

$$\sigma_{34} = \frac{Y_{7\text{Be}}}{N_{4\text{He}}^{\circ\text{T}} \cdot N_{3\text{He}}^{\circ\text{B}}} \quad (5.3)$$

where $Y_{7\text{Be}}$, $N_{4\text{He}}^{\circ\text{T}}$ and $N_{3\text{He}}^{\circ\text{B}}$ are the total yield of recoils produced, the areal gas target density and the total number of incoming beam particles, respectively. In the diagram of the *activation* set up shown in Figure 5.1 the different observables required for determining the cross sections are indicated.

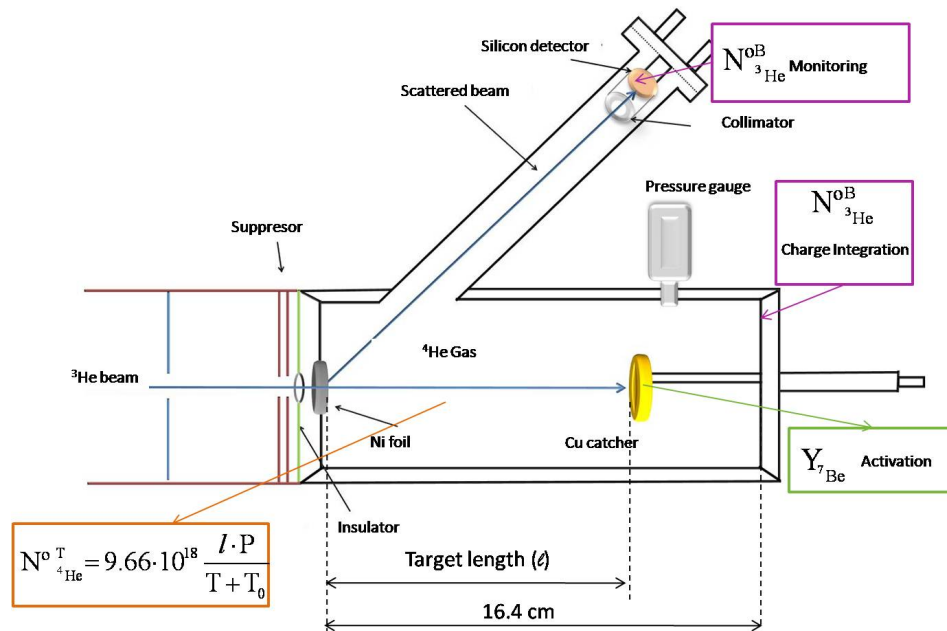


Figure 5.1: Scheme of the experimental set up used for the activation method in Madrid. The positions at which the different observables for determining the cross sections are indicated: the ${}^7\text{Be}$ yield from the deposited recoils in the Cu catcher, the ${}^4\text{He}$ gas target areal density from assuming an ideal gas behaviour and the ${}^3\text{He}$ beam from the charge integration and the silicon detector monitoring the scattered beam.

In the following, details of the analysis performed in order to obtain the beam particles, target density parameters, number of recoils produced and reaction centre of mass energy are presented.

5.1.1 The number of ^3He beam particles: $N^{\circ B}_{^3\text{He}}$

The number of incoming beam particles are determined by using two methods simultaneously: by measuring the incoming current using the target chamber as Farady cup and by counting the scattered beam particles into a collimated silicon detector position at 44.9° .

During the experiment, every 30 minutes the accumulated number of pulses corresponding to the integrated electric charge in the chamber and the online scattered peak integration in the silicon detector were noted down. This allowed us to have control over the beam stability during the measurements. Aiming to the same offline beam stability checks, the silicon spectrum was periodically saved as a new file and cleared, and the same was done with the scaler information. As an example, the comparison of different files taken for the ~ 2.5 MeV beam energy is shown in Figure 5.2. The charge integration method consisted of obtaining the number of particles using the expression 3.4. In the case of the silicon spectra, the scattered beam peak is integrated and the number of incoming particles is estimated using the expression 3.6.

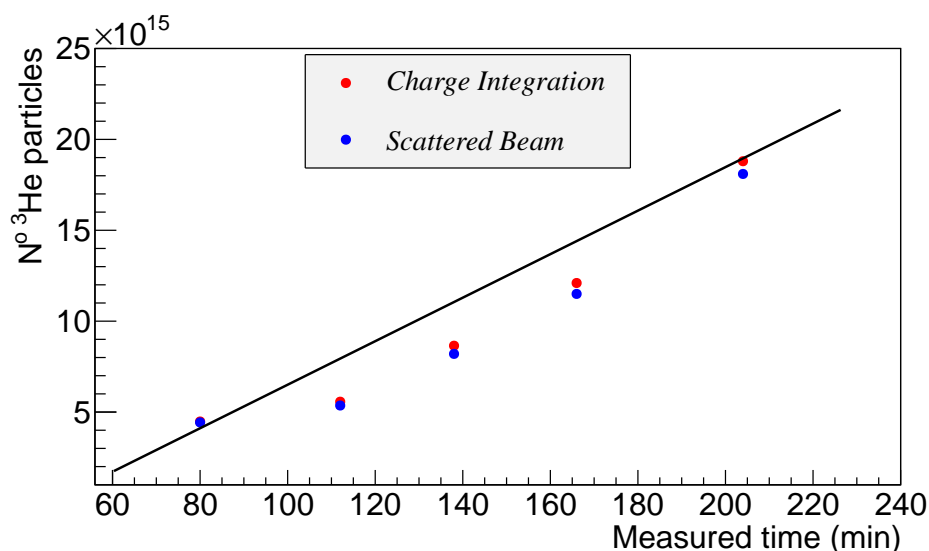


Figure 5.2: Comparison of the calculated number beam particles for different files taken for a ^3He beam at ~ 2.5 MeV impinging onto a ^4He gas target at ~ 60 Torr. The estimated number of beam particles (y axis) are shown as a function of the time for each measurement (x axis). The red and blue points dots correspond to methods using the charge integration and particles scattered from the Ni foil, respectively.

As can be seen there is an excellent agreement between both methods for all files. The fluctuations in the number of beam particles, apart from the time of each file, is due to the oscillations in the beam current during the experiment. Nevertheless, this does not have influence in the estimations of the total number of beam particles, because even though the current be higher or lower there is always agreement between the two methods. The same kind of agreement has been observed for all energies.

Thus, for each energy, the total number of beam particles with the scattered beam method have been obtained by adding off line the individual spectra (see for example Figure 5.3), integrating the elastic scattered peak and applying the expression 3.6 assuming a kinetic energy corresponding to the beam energy at the centre of the Ni foil. A cross-check using the LISE++ code[LIS] has also been done. In this case, the number of particles have been obtained by averaging the number of particles obtained by assuming that the reaction takes place at the beginning, centre and end of the foil.

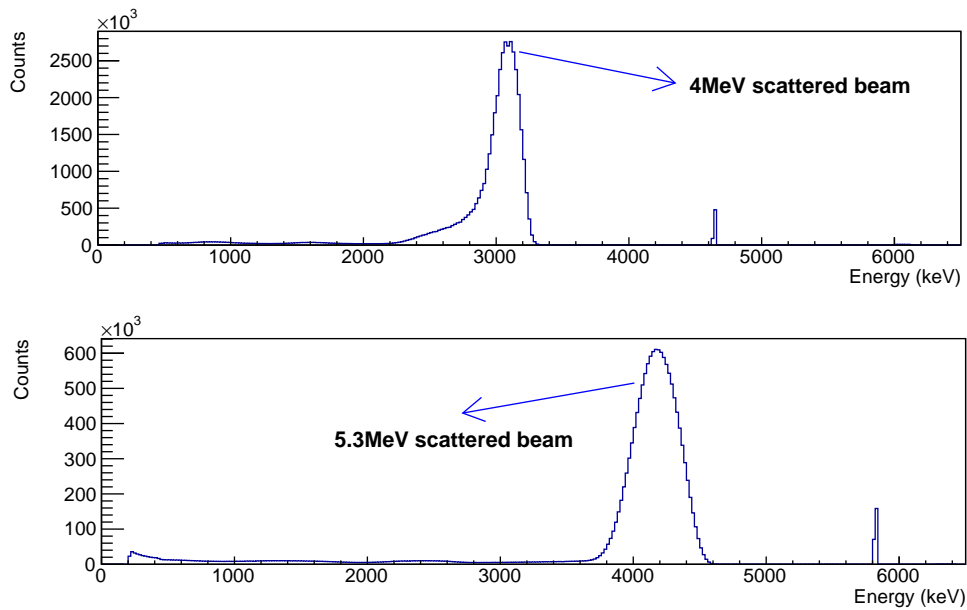


Figure 5.3: Spectra taken with the silicon detector for ^3He beam impinging onto a ^4He gas target. For ~ 4 MeV beam energy and ~ 60 Torr target pressure (top), and for 5.3 MeV in and ~ 50.8 Torr (bottom). The most intense peaks corresponds to the scattered beam with the Ni foil window.

For the charge integration method the number of pulses associated with each file have been added and the current is estimated using the expression 3.4 where one pulse corresponds to 10^{-10}C . The total number of beam particles for all energies are shown in Figure 5.4 for both charge integration and scattered beam particles and the values within the errors are shown in Table 5.6. Perfect agreement between the two methods can be observed.

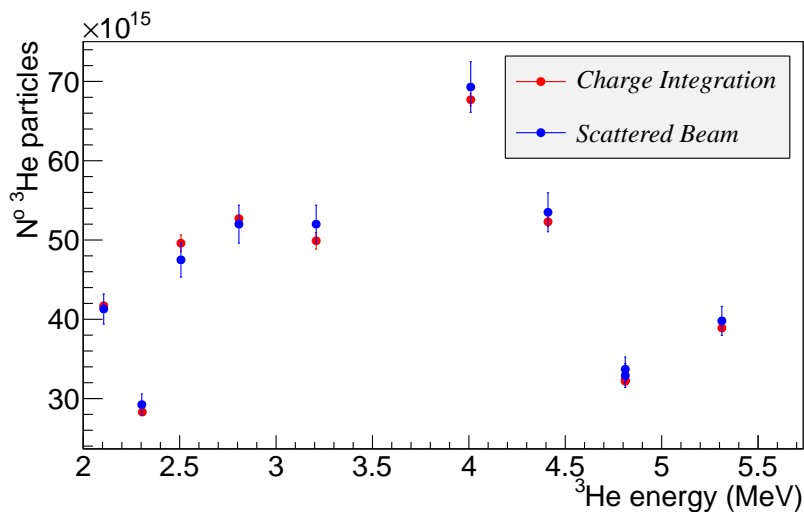


Figure 5.4: Total number of ^3He beam particles for different energies measured at CMAM. In red color are shown the number of particles estimated from the electric charge deposited in the chamber, and in blue color the estimated using the beam particles scattered from the Ni foil window.

5.1.1.1 Error estimations

Taking into account all sources of errors as shown in Table 5.1, a 4.6% relative error has been estimated for the number of beam particles using the scattered particles for all energies by standard error propagation.

Parameter value	Error Contribution
Collimator radius (0.27±0.03) mm	2.22%
Distance Ni foil-collimator (22.13±0.11) cm	0.99%
Collimator angle (44.9±0.4)°	3.38%
Ni foil thickness (1.03±0.02) μm	1.94%
Error Beam Energy (0.02-0.003)MeV	0.18%
Error Particles Detected (√Particles)	0.02%

Table 5.1: Error contribution from different parameters to the number of beam particles obtained using the scattered beam in the silicon detector.

For the case of the charge integration method the errors have been estimated by considering the relative difference between the number of beam particles calculated with both methods divided by two:

$$\text{Relative Error (\%)} = \left(1 - \frac{N_{3\text{He}}^{\text{Scattering}}}{N_{3\text{He}}^{\text{Integration}}} \right) * 100/2 \quad (5.4)$$

The errors associated to the number of particles estimated with the charge integration method oscillate between 0.42%-2.12%.

5.1.2 The ^4He gas target areal density: $N^{\text{oT}}_{4\text{He}}$

The number of ^4He gas particles per square centimeter is given by the expression 3.7 ($N_t = 9.66 \cdot 10^{18} \frac{\ell \cdot P}{T_0 + T_C}$). Here, ℓ , P and $T+T_0$ are the target length in cm, the pressure in Torr, and the gas temperature in kelvin, respectively.

Target length

The distance between the Ni foil and the front face of each Cu catcher (see Figure 5.1), i.e. ℓ , was determined at the beginning and the end of each run by measuring with a caliper the distance between the front face of the Cu catcher and the inner face of the final chamber flange and subtracting it from the 16.4 cm distance between the Ni foil and the end of the chamber. The errors associated to ℓ are obtained by propagating the caliper error (0.005 cm) for all measurements performed.

Target pressure

With a continuous gas flow the pressure was controlled inside the chamber, was continuously monitored and the value was noted each 30 minutes, approximately. The difference between maximum and minimum pressure for all runs was always lower than 2%, and lower than 0.16% for all runs in 2011. The associated errors have been determined from the error in the pressure gauge, considered

as 0.10 Torr, and the standard deviation of the pressures readings. An example of pressure stability is shown in Figure 5.5 where the red dots are the ^4He gas pressures when the ^3He beam impinged onto the gas with an energy of 4010 keV. The blue line shows the average pressure and the marked blue region indicates the error associated to the average.

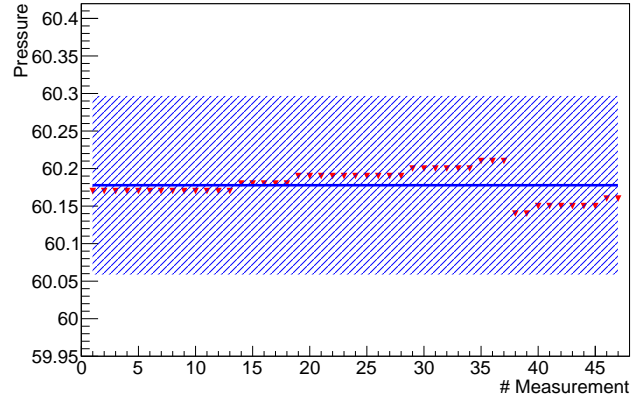


Figure 5.5: An example of the pressure stability in the activation experiment. The red dots gives the ^4He gas pressure readings performed during the measurement with the ^3He beam at an energy 4010 keV. The blue line indicates the average pressure and the shaded region represents the associated error.

Temperature

The gas temperature inside the chamber has been considered as the accelerator hall room temperature (T_0) plus the rising temperature due to the beam heating (T_C). The room temperature at the accelerator hall is 22.5°C and it was known to be very stable, indeed an automatic alarm goes off when a difference of $\pm 1.5^\circ\text{C}$ is observed, considered as the error for T_0 . As our setup is the same as the used in [NHNEH04] to determine the cross section of the same reaction at lower energies, T_C has been estimated by extrapolating the values reported there.

They measured the temperature correction (T_C) by using the resonance reaction $^{10}\text{B}(\alpha,p)^{13}\text{C}$ with a solid ^{10}B placed in the Cu catcher position and a 1.518 MeV α beam energy, populating the 12.70 MeV state in ^{14}N [AL55]. Subsequently the state decays by different channels emitting particles as shown in Table 5.2. For example, with a cross section of 42 mb the 12.7 MeV state in $^{14}\text{N}^*$ decays by emitting a proton, p_3 , and populating the 3.85 MeV state in $^{13}\text{C}^*$. Subsequent γ -rays are emitted due to the de-excitation of the $^{13}\text{C}^*$ nucleus.

E_α (MeV \pm keV)	$\Gamma_{\text{c.m.}}$ (keV)	$^{14}\text{N}^*$ (MeV)	Outgoing Particle (x)	σ_x (mb)	Γ_x (keV)
1518 ± 4	14 ± 4	12.7	α		1.7
			p_0	4.7	0.62
			p_1	1.3	0.17
			p_2	5.3	0.70
			p_3	42	5.6
			d	7.0	0.93
			n	32	4.3

Table 5.2: Resonance in $^{10}\text{B}+\alpha$ at 1.518 MeV taken from [AL55]. Here, p_0, p_1, p_2 and p_3 corresponds to the ground state and the 3.09, 3.68 and 3.85 MeV states of ^{13}C . γ -rays are subsequently emitted by de-excitation of the excited states in the $^{13}\text{C}^*$ nucleus.

Year	$E_{3\text{He}}$ (keV)	T_0+T_C (*) (K)	Pressure (P) (Torr)	Target Length (l) (cm)
	2306.28 ± 2.37	300.28 ± 2.25	54.68 ± 0.07	13.29 ± 0.02
	3208.05 ± 2.99	309.26 ± 2.19	63.77 ± 0.08	13.29 ± 0.02
2009	4410.42 ± 3.82	316.56 ± 9.83	50.66 ± 0.01	10.82 ± 0.02
	4811.20 ± 4.09	318.49 ± 7.92	50.83 ± 0.03	10.92 ± 0.02
	5312.19 ± 4.44	319.09 ± 2.25	56.68 ± 0.07	13.29 ± 0.02
	2105.89 ± 2.23	301.64 ± 2.11	60.14 ± 0.01	12.47 ± 0.02
	2506.67 ± 2.51	303.22 ± 2.20	60.16 ± 0.01	11.64 ± 0.02
2011	2807.26 ± 2.71	305.44 ± 2.15	60.08 ± 0.01	12.00 ± 0.02
	4009.63 ± 3.54	307.81 ± 2.45	60.18 ± 0.01	13.11 ± 0.02
	4811.20 ± 4.09	312.71 ± 3.63	51.16 ± 0.01	11.09 ± 0.02

Table 5.3: Values of the T_0+T_C , P and L parameters considered to determine the areal target density. See text for more details.

(*) The values shown here include the T_C calculated using the beam currents from the charge integration.

Basically, the procedure at the Weizmann Institute consisted of using a NaI detector placed close to the target chamber at 90° with the beam direction. The chamber was filled with ^4He gas target at different pressures. The energy of the ^4He beam was increased for each pressure in order to maximize the γ -ray NaI detector spectrum from the de-excitation of the 3.85 MeV state in the ^{13}C . The temperature correction is calculated from the energy lost in the gas target as the difference between the incoming energy and the resonance energy. For a beam power of 1 W (500 nA current of 2 MeV beam) they report a temperature correction of $T_C=17$ K.

The beam power for our measurements is given by:

$$\text{Beam Power} = \frac{N_{3\text{He}}^0 \cdot E(\text{MeV}) \cdot 10^6 \cdot e^-}{T_{\text{IMP}}} \quad (5.5)$$

and the temperature correction is determined using a linear dependence of T_C with the beam power from the values given in Ref. [NHNEH04]. The associated errors to T_C are given by the fluctuations in the beam current between the different files for each energy (i.e. see Figure 5.2). The total error associated with the temperature is given by 1.5° plus the error due to T_C . It is worth noting that the temperature corrections T_C 's have been calculated using the beam currents from the two methods used (charge integration and elastic scattering) being the differences between the values the same compared to the currents estimated with both in these methods (see Figure 5.2).

The values for pressure P , temperature ($T_0 + T_C$) and target length l are shown in Table 5.3. The results for the gas target areal density are shown in Table 5.6. The errors in the target density are calculated by standard error propagation from the errors in P , $T_0 + T_C$ and l shown in Table 5.3.

5.1.3 The ^7Be recoils produced in the Activation Method: $Y_{^7\text{Be}}$

The ^7Be recoils were implanted in the copper catcher. The delayed 478 keV γ -activity from the catchers was measured off-line by placing them at a distance of 20 mm from a HPGe detector at the low-background detection station at Soreq Research Center (see Figure 3.12). This well-established arrangement with an optimised solid angle had an effective shielding to suppress the ambient background.

Figure 5.6 shows in the upper panel the total spectrum of the ^7Be catcher at ~ 4 MeV beam energy and in the lower panel a zoom view of the energy region of interest (478 keV) in blue for

~ 4 MeV and in red for ~ 2.5 MeV. These spectra were collected for durations of 241.1 and 168.0 hours respectively, to minimize the statistical uncertainty in counting.

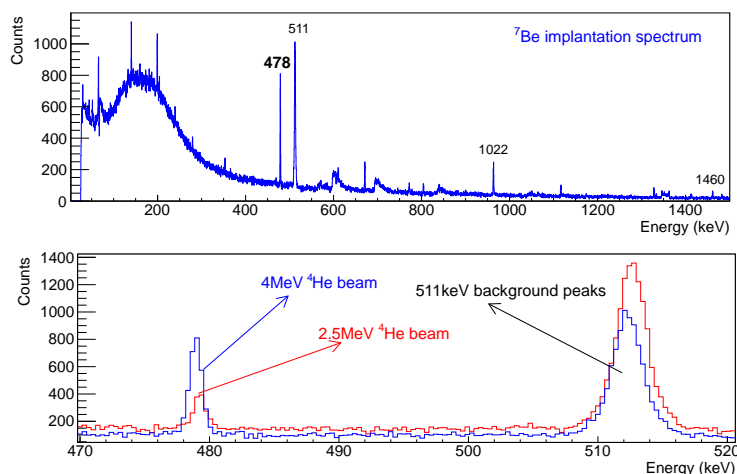


Figure 5.6: Spectra for the γ -rays from the catchers having implanted ${}^7\text{Be}$. In the upper panel a total spectrum for the ${}^7\text{Be}$ catcher at ~ 4 MeV beam energy is shown. Some of the peak energies are labelled. In the lower panel a zoom view for the region of interest is shown for 4 MeV beam energy (blue) and ~ 2.5 MeV (red).

For comparison, Figure 5.7 shows the count rate spectra for the ~ 2.5 and ~ 4 MeV together with the count rate spectrum for the background measurement shown in Figure 3.14. Apart from not observing any interfering between the 478 keV and the 511 keV peaks, the height of the 511.0 keV peak in the background is equal to the heights of this peak in the ${}^7\text{Be}$ catchers and the baselines of the three spectra are the same. This is a clear indication that the catchers do not contain annihilation γ -rays of 511.0 keV.

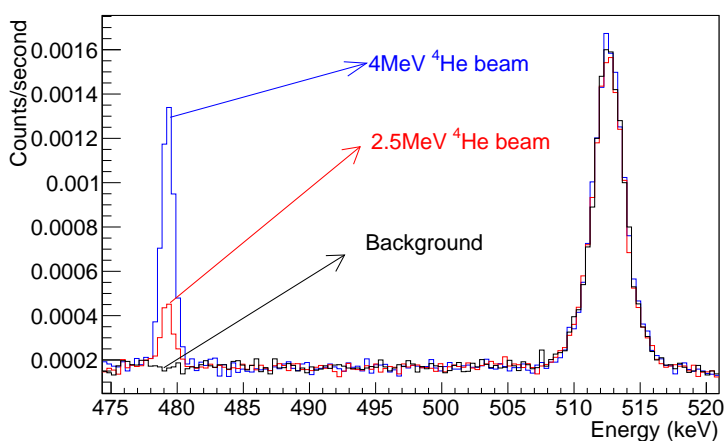


Figure 5.7: Spectra showing the γ count rates for the catchers prepared with ~ 2.5 and ~ 4 MeV ${}^4\text{He}$ beams in red and blue colors respectively. In black color the γ count rate for the background spectrum. Note that the levels of the Compton continuum bases are equal, as well as the heights of the 511.0 keV peaks.

5.1.3.1 478 keV peak integration

In order to determine the net number of counts under the 478 keV peak, we have used the procedure followed in reference [NEHY07]. In the case of non symmetric 478 keV peak, the peak is

divided in three regions, a central top region with g counts and two regions with G_1 and G_2 counts in the left and right sides, respectively. Two extra regions, one in the left side with B_1 number of counts and one in the right side with B_2 are considered in order to estimate the background under the peak (see Figure 5.8 for the case of non symmetric peak where the top channel is just one channel).

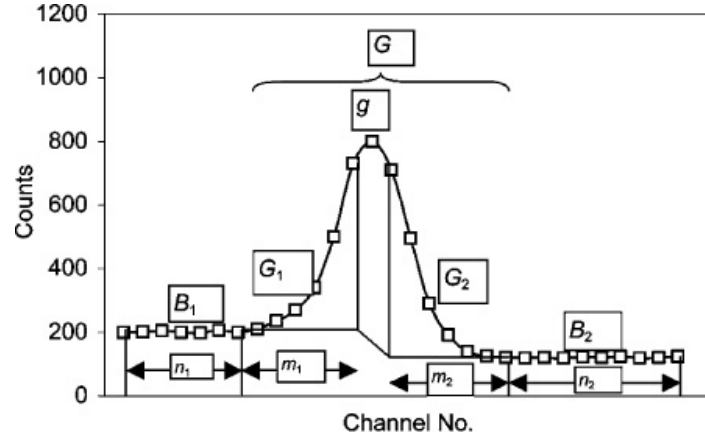


Figure 5.8: Peak regions defined in order to determine the net area under the 478 keV peak. The widths are n_1 , m_1 , n_2 and m_2 and the number of counts of the different regions are B_1, G_1, G_2 and B_2 respectively. g indicates the counts under the single top channel. Figure taken from [NEHY07].

The total number of counts under the peak is given by: $G=G_1+G_2+g$, and the baseline to be subtracted assuming that the top region is just one channel is [NEHY07]:

$$B = \frac{m_1+0.5}{n_1} B_1 + \frac{m_2+0.5}{n_2} B_2 \quad (5.6)$$

Thus, the net number of count under the peak is given by: $N=G-B$ and the associated uncertainty is

$$\sigma(N) = [G + \sigma^2(B)]^{0.5} \quad (5.7)$$

with the $\sigma^2(B)$ the variance of the baseline:

$$\sigma^2(B) = \left(\frac{m_1+0.5}{n_1}\right)^2 B_1 + \left(\frac{m_2+0.5}{n_2}\right)^2 B_2 \quad (5.8)$$

In case of getting a symmetric peak, i.e. two channels with the highest number of counts, $g=0$ and 0.5 must be removed in expression 5.8. Table 5.4 shows the net number of counts N under the 478 keV peak for the different energies within their statistical errors.

5.1.3.2 Determination of the total number of ${}^7\text{Be}$ recoils produced

After obtaining the number of net counts under the 478 keV γ peak (N) the next step is to determine the total number of ${}^7\text{Be}$ recoil produced for each beam energy.

Being N the number of counts in the 478 keV γ peak measured during the decay time T_d , ε_A the absolute efficiency of the HPGe detector used, and $B.R.$ the branching ratio populating the first excited state in the ${}^7\text{Li}$ (see Figure 1.12), we can establish the total number of decayed ${}^7\text{Be}$ nuclei (N_{DEC}) during the time T_d by:

$$N_{\text{DEC}} = \frac{N}{\varepsilon_A \cdot B.R.} \quad (5.9)$$

A γ detection efficiency of 0.0436 ± 0.0010 (systematic uncertainty $\pm 2.29\%$) was obtained experimentally using a ^7Be point source placed at the same 2 cm distance from the HPGe detector and different transverse directions.

On the other hand, denoting by N_A and N_0 to the number of ^7Be nuclei in the catcher at the end and at the beginning of the decay measurement at SOREQ, respectively and T_d to the decay time, we can establish by the *Universal Law of Radioactive Decay*.

$$N_A(T_d) = N_0 \cdot e^{-\lambda \cdot T_d} \quad (5.10)$$

Thus:

$$N_0 - N_A(T_d) = N_{\text{DEC}} \quad (5.11)$$

$$N_0 = \frac{N_{\text{DEC}}}{1 - e^{-\lambda \cdot T_d}} \quad (5.12)$$

where λ is decay constant expressed by $\lambda = \frac{\ln 2}{t_{1/2}}$. The half life $t_{1/2}$ of the ^7Be hosted in a copper material is 53.353(50). More details can be found in reference [NEHY07] for the measurement of the decay rate of ^7Be in Cu.

Being T_l the lost time since the implantation at CMAM finishes until the measurement of the decay starts, it can stated that:

$$N_0 = N_{\text{IMP}} \cdot e^{-\lambda \cdot T_l} \rightarrow \quad (5.13)$$

$$N_{\text{IMP}} = N_0 \cdot e^{+\lambda \cdot T_l} \quad (5.14)$$

where N_{IMP} is the number of ^7Be nuclei at the time implantation finishes.

Moreover, due to the fact that the ^7Be recoils are unbound nuclei, in order to determine the total number of ^7Be produced we need to take into account the production of the recoils as well as their decay. Generally we can assume that for a given time implantation time t , the number of ^7Be nuclei present in the catcher is denoted by:

$$dN_1(t) = R \cdot dt - \lambda \cdot N_1 \cdot dt \quad (5.15)$$

being R the reaction rate for the formation of the ^7Be nuclei, expressed by:

$$R = N_b \cdot \sigma \cdot I \quad (5.16)$$

where N_b is the number of nuclei in the target, σ is the cross section and I the incident nuclei. Integrating the equation 5.15, the number of ^7Be nuclei for a given time $N_1(t)$ is given by:

$$N_1(t) = \frac{R}{\lambda} \cdot (1 - e^{-\lambda \cdot t}) \quad (5.17)$$

and thus, clearing R up:

$$R = \frac{N_1(t) \cdot \lambda}{1 - e^{-\lambda \cdot t}} \quad (5.18)$$

Denoting as T_{IMP} to the implantation time (see Table 3.2), the reaction rate R during the experiment is:

$$R = \frac{N_{\text{IMP}} \cdot \lambda}{1 - e^{-\lambda \cdot T_{\text{IMP}}}} \quad (5.19)$$

where N_{IMP} is the number of nuclei in the catcher at end of the implantation as shown in equation 5.14. Therefore, the total number of ${}^7\text{Be}$ nuclei produced will be given by:

$$N_{7\text{Be}} = R \cdot T_{\text{IMP}} \quad (5.20)$$

The values for the implantation times are shown in Table 3.2, while the net counts under the 478 keV peak, the decay times T_d the lost times T_l are shown in Table 5.4.

Year	$E_{3\text{He}}$ (keV)	N (counts)	T_d (d)	T_l (d)
	2306.28 ± 2.37	399 ± 77	0.411	19.848
	3208.05 ± 2.99	1094.8 ± 82.2	0.356	36.843
2009	4410.42 ± 3.82	541.97 ± 52.6	0.336	48.845
	4811.20 ± 4.09	845.72 ± 80.3	0.213	30.567
	5312.19 ± 4.44	1938.8 ± 84.0	0.274	16.225
	2105.89 ± 2.23	538.0 ± 78.1	0.426	29.398
	2506.67 ± 2.51	934.9 ± 64.4	0.485	22.792
2011	2807.26 ± 2.71	911.0 ± 72.5	0.452	23.573
	4009.63 ± 3.54	2488.0 ± 66.1	0.673	16.965
	4811.20 ± 4.09	1487.3 ± 86.6	0.279	13.795

Table 5.4: Variables for the determination of the number of ${}^7\text{Be}$ recoils produced during the experiment. For the different energies shown in the second column the third column shows the net number of counts under the 478 keV γ peak. The fourth column shows the decay time and the fifth column the lost time since implantation finishes until the decay time starts. The implantation times are shown in Table 3.2.

5.1.3.3 Error contributions

The errors associated to the total number of ${}^7\text{Be}$ recoils are composed by statistical and systematic contributions. The relative (percentage) statistical errors for the produced ${}^7\text{Be}$ recoils are the same as those given for the net number of counts under the 478 keV peak as defined by the expression 5.7. A 2.33% systematic contribution is quoted based on the uncertainties of the different parameters shown in Table 5.5

Parameter value	Error Contribution
$T_{1/2}$ (53.353 \pm 0.05) days	0.18%
B.R. 1 st state in ${}^7\text{Li}$ (10.44 \pm 0.04)%	0.38%
HPGe efficiency (4.36 \pm 0.10)%	2.29% (*)

Table 5.5: Systematic contribution to the number of ${}^7\text{Be}$ recoils.

(*) For the catchers implanted with beam energies of ~ 2.10 , ~ 2.8 and ~ 3.8 MeV the HPGe detector was replaced with another one with $\varepsilon = (3.79 \pm 0.001)\%$ and thus an error contribution of 2.90%.

5.1.4 Estimation of the reaction energy at the centre of mass system

In order to estimate the astrophysical S-factor as defined in the expression 1.7 the energy of the reaction in the centre of mass system is required. In reference [NHNEH04] where the same setup was used, the authors compare E_{CM} calculated assuming that the reaction takes place at the centre of the target and \bar{E}_{CM} by the effect of considering a target of finite energy width (ΔE_T). For $E_{\text{CM}}=420$ keV they compute only a difference of 0.3 keV (0.1%); in our case, where the energies are even higher this difference is even lower. Thus, we can consider that on average the reaction occurs at the centre of the gas target including a negligible error and therefore, the expression 5.2 becomes:

$$E_{\text{CM}} = \frac{m_{^4\text{He}}}{m_{^4\text{He}} + m_{^3\text{He}}} \cdot \left(E^{\text{beam}} - \Delta E_{\text{Ni}} - \frac{\Delta E_{^4\text{He}}}{2} \right) \quad (5.21)$$

where $m_{^4\text{He}}$ and $m_{^3\text{He}}$ are the target and beam nuclei masses in mass units respectively. E^{beam} is the incoming beam energy as shown in Table 5.4 and ΔE_{Ni} and $\Delta E_{^4\text{He}}$ are the energy losses in the Ni foil and the whole gas target length respectively.

The energy lost by the beam when crossing the Ni foil and half of the gas length, $\Delta E_{\text{Ni}} + \frac{\Delta E_{^4\text{He}}}{2}$, is obtained by using the TRIM code [SRI] and simulating 10^5 ^3He beam particles at the corresponding energies. The ^3He nuclei impinge onto a target composed of two layers: 1) $1.03\mu\text{m}$ of solid Ni foil and 2) ^4He gas target with densities calculated using the pressures and temperatures shown in Table 5.3 and the lengths are half of those shown in the same table. An example for the simulated output energy spectrum using a ~ 4 MeV beam energy and the corresponding target layers is displayed in Figure 5.9.

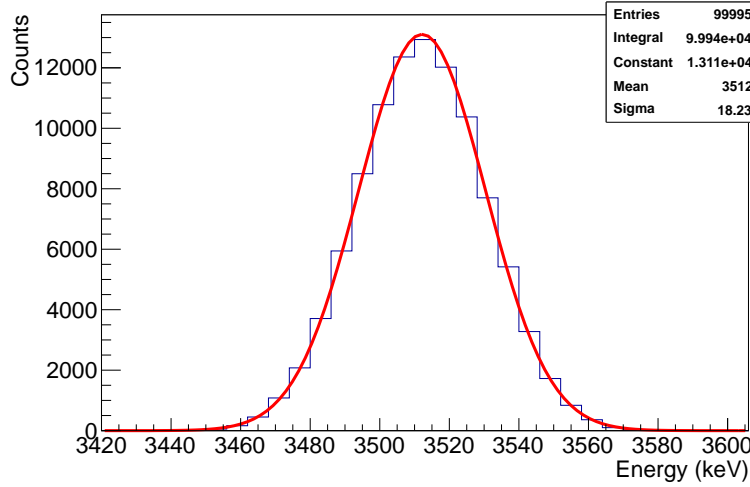


Figure 5.9: Energy spectrum from a TRIM simulation for a ^3He beam at 4009.63 keV crossing a $1.03\mu\text{m}$ Ni foil and a 60.18 Torr ^4He gas at 307.81 K and 6.55 cm length. The red curve shows a Gaussian fit to the spectrum and the numbers enclosed in the box show the parameters from the fit.

The output energies are fitted to Gaussian functions and the mean of the fit (3512 keV for the example in Figure 5.9) represents the beam energies at the centre of the target that is, all the terms enclosed in the brackets in expression 5.21. The centre of mass energy are then calculated by multiplying this mean energy by $\frac{m_{^4\text{He}}}{m_{^4\text{He}} + m_{^3\text{He}}}$.

The uncertainty associated to the centre of mass energy has been estimated by:

$$\Delta E_{\text{CM}} = \frac{m_{^4\text{He}}}{m_{^4\text{He}} + m_{^3\text{He}}} \cdot \Delta E \quad (5.22)$$

where ΔE is the error associated to the energy at the centre of the target, calculated by adding to the beam energy uncertainty (Table 3.2) the σ value from the Gaussian fit.

5.2 Astrophysical S-factors I: Measurements using the Activation Method

The results for the Activation experiment performed at CMAM are shown in the last two columns in Table 5.6. For the different beam energies displayed in the first column, the second column shows the corresponding centre of mass energies calculated as detailed above. The third column shows the number of beam particles estimated using the charge integration. The fourth and fifth columns show the total number of target and recoils nuclei for each energy. The cross section are shown in the sixth column and the astrophysical S-factors for the different energies calculated by using the expression 5.1 are shown in the seventh column. The uncertainties of the different parameters are shown between brackets. The errors for the cross section and astrophysical factor have been obtained by standard error propagation. For the values of $N_{3\text{He}}^{\text{beam}}$ and $N_{4\text{He}}^{\text{target}}$ the uncertainties refer the systematic contribution while the statistical contributions are negligible. For the case of $N_{7\text{Be}}^{\text{recoils}}$, $\sigma_{34}(E)$ and $S_{34}(E)$ the uncertainties are divided into statistical (first) and systematic (second) contributions.

$E_{3\text{He}}$ (keV)	E_{CM} (keV)	$N_{3\text{He}}^{\text{beam}}$ ($\cdot 10^{16}$)	$N_{4\text{He}}^{\text{target}}$ ($\cdot 10^{19}/\text{cm}^2$)	$N_{7\text{Be}}^{\text{recoils}}$ ($\cdot 10^6$)	$\sigma_{34}(E)$ (μb)	$S_{34}(E)$ (keV \cdot b)
2306.28 \pm 2.37	915.78 \pm 12.21	2.83(5)	2.34(2)	1.31(25)(3)	1.98(38)(6)	0.411(79)(15)
3208.05 \pm 2.99	1498.91 \pm 12.56	4.99(10)	2.65(2)	4.05(30)(9)	3.06(23)(10)	0.318(24)(11)
4410.42 \pm 3.82	2267.71 \pm 12.47	5.23(6)	1.67(5)	4.74(46)(11)	5.43(53)(22)	0.386(37)(16)
4811.20 \pm 4.09	2511.12 \pm 12.62	3.22(3)	1.68(4)	3.19(30)(7)	5.88(56)(21)	0.391(37)(14)
5312.19 \pm 4.44	2804.10 \pm 12.82	3.89(4)	2.28(2)	6.05(26)(14)	6.82(29)(19)	0.424(18)(12)
2105.89 \pm 2.23	777.17 \pm 12.70	4.17(2)	2.40(2)	1.49(22)(4)	1.49(22)(4)	0.418(61)(18)
2506.67 \pm 2.51	1054.15 \pm 12.31	4.96(10)	2.23(2)	2.26(16)(5)	2.05(14)(6)	0.339(23)(12)
2807.26 \pm 2.71	1249.64 \pm 12.41	5.27(4)	2.28(2)	3.61(29)(11)	3.00(24)(9)	0.390(31)(13)
4009.63 \pm 3.54	2006.95 \pm 12.31	6.77(8)	2.78(2)	7.87(21)(18)	4.70(12)(13)	0.367(10)(10)
4811.20 \pm 4.09	2510.00 \pm 12.62	3.23(7)	1.45(2)	3.88(23)(14)	6.85(40)(26)	0.455(27)(17)

Table 5.6: Results for the activation experiment. The first column shows the different beam energies used in the experiment. The second column shows the corresponding centre of mass energies taking into account the energy lost in the Ni foil and gas target. The third, fourth and fifth columns show the total number of particles in the beam, target and recoils respectively. The sixth and seventh column shows the cross section and astrophysical factor for the ${}^3\text{He}(\alpha,\gamma){}^7\text{Be}$ reaction. The uncertainties for each value are shown between brackets. When only one contribution it refers to the systematic error, and in case of two contributions the first one refers to the statistical uncertainty and the second one to the systematic error. Recall that the energies in $S_{34}(E)$ are E_{CM} .

The $S_{34}(E)$ values are plotted in Figure 5.10 together with the results from [DGK09, PK63]. The errors displayed in the plot are the statistical uncertainties as it is usually done by convention. Just by eye, it can be seen that our results follow the trend of ERNA data [DGK09] better than the Parker's [PK63]. Among all the points, the two at ~ 2 and ~ 2.5 MeV centre of mass energies are specially relevant. Due to their low uncertainty, they clearly show a complete agreement with ERNA and are rather discrepant comparing with Parker values. Also of special interest is the point at around ~ 1 MeV. The same activation and counting setups were used in [NHNEH04] where a measurement at the same energy was performed. An agreement within the experimental errors between these points strongly supports the reliability of the new set of measurements.

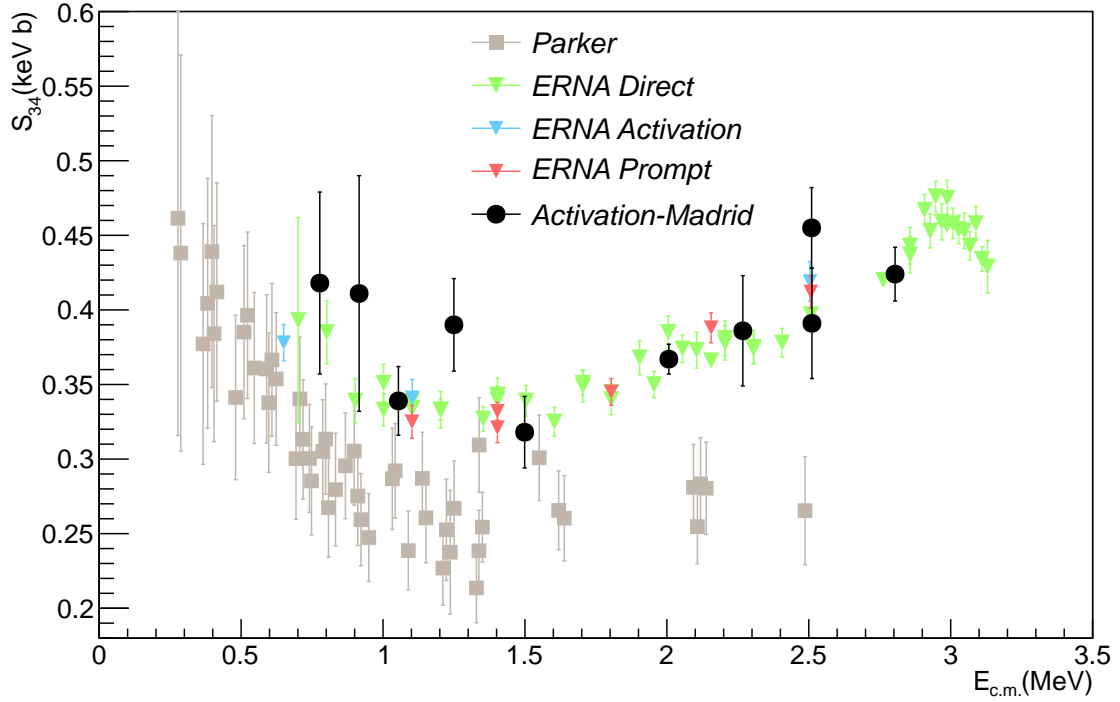


Figure 5.10: Astrophysical S -factor for the ${}^3\text{He}(\alpha,\gamma){}^7\text{Be}$ reaction using the activation method in Madrid (black dots). For comparison with previous results, with triangles and squares are shown the results from [DGK09] and [PK63] respectively.

In the next chapter a detailed quantitative analysis comparing our results with both Parker and ERNA is done as well as a comparison with the different theoretical models

5.3 Analysis II: Measurements using the Direct Recoil Counting Method

As in the *Activation Experiment* the astrophysical factor for the *Direct Detection Experiment* is given by the expression 5.1. In this case, the reaction was done using inverse kinematics, that is a ${}^4\text{He}$ beam impinging onto a ${}^3\text{He}$ target, and thus the cross section and centre of mass energy are given by:

$$\sigma_{34} = \frac{Y_{7\text{Be}}}{N_{4\text{He}}^{\text{oB}} \cdot N_{3\text{He}}^{\text{oT}}} \quad (5.23)$$

and

$$E_{\text{CM}} = \frac{m_{3\text{He}}^{\text{T}}}{m_{4\text{He}}^{\text{B}} + m_{3\text{He}}^{\text{T}}} \cdot E^{\text{beam}} \quad (5.24)$$

respectively. Where, in this case the $N_{4\text{He}}^{\text{oB}}$ is total number of beam particles, $N_{3\text{He}}^{\text{oT}}$ is the gas target areal density, and $Y_{7\text{Be}}$ is the total number of recoils produced. $Y_{7\text{Be}}$ is estimated based on the recoils detected in the final DSSSD placed at the focal plane of the accelerator (Y_{DSSSD}).

The locations marked in Figure 5.11 indicate where the observables require to determine σ_{34} are determined. In the following sections the detailed data analysis of these quantities are outlined.

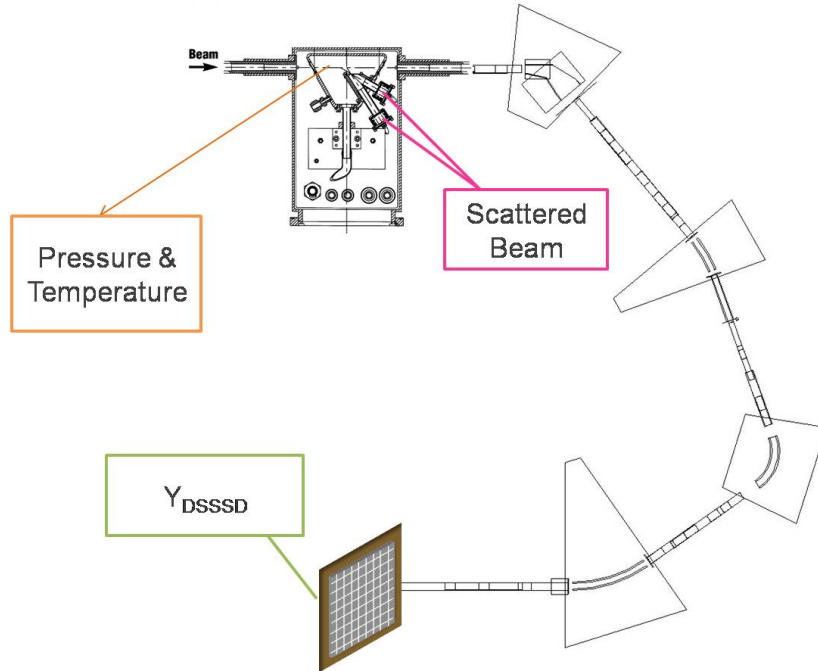


Figure 5.11: Experimental set up diagram for the Direct Recoil counting method at TRIUMF. The different observable required to extract σ_{34} are indicated. Note that this schematic is not to the scale.

5.3.1 Estimation of the reaction energy at the centre of mass system

In the same way than as in *Activation Method* experiment, we can assume that on average the reaction is produced at the centre of the gas target and thus the averaged centre of mass energy will be given by:

$$E_{CM} = \frac{m_{^3\text{He}}}{m_{^4\text{He}} + m_{^3\text{He}}} \cdot \left(E^{\text{beam}} - \frac{\Delta E_{^4\text{He}}}{2} \right) \quad (5.25)$$

where $\Delta E_{^4\text{He}}$ is the energy loss of the beam in the gas target that has been determined by simulating 10^5 particles using the TRIM code [SRI] following the same procedure as in section 5.1.4. The associated error are estimated from standard error propagation of the beam energies (Table 3.6) and error from the mean value of the energy loss from TRIM. Table 5.7 shows in the second column the calculated centre of mass energy for every beam energy.

$E_{^4\text{He}}$ (keV)	E_{CM} (keV)	Temperature (T) (K)	Pressure (P) (Torr)
6553.88	2813.57 ± 1.80	297.11 ± 1.97	5.73 ± 0.120
5165.97	2216.55 ± 1.68	297.64 ± 1.99	5.96 ± 0.21
4716.45	2023.73 ± 1.42	301.55 ± 1.61	5.02 ± 0.19
3521.61	1508.91 ± 1.29	297.30 ± 2.03	5.96 ± 0.17

Table 5.7: Beam energies, the corresponding center of mass energy at the center of the target cell, the average target pressure and temperature of the gas in the beam path are shown in columns 1, 2, 3 and 4 respectively.

5.3.2 The ^3He gas target areal density: $N^{\circ T}_{^3\text{He}}$

The gas target areal density is determined by the expression $N_t = 9.66 \cdot 10^{18} \frac{\ell \cdot P}{T_0 + T_C}$. In this case, the beam heating is negligible i.e. $T_C = 0$.

Pressure and temperature were recorded every five minutes during the runs. An averaged pressure and temperature is calculated for every run and a final pressure and temperature for every energy is calculated by averaging the values of all considered runs. The errors associated to the final pressure and temperature are obtained as the standard deviation of the values for the different runs plus a systematic error of 0.1 Torr for pressure and 1 K for temperature [GBB04]. An example is shown in Figure 5.12 for the pressure and temperature of the runs taken with ~ 5.2 MeV beam energy.

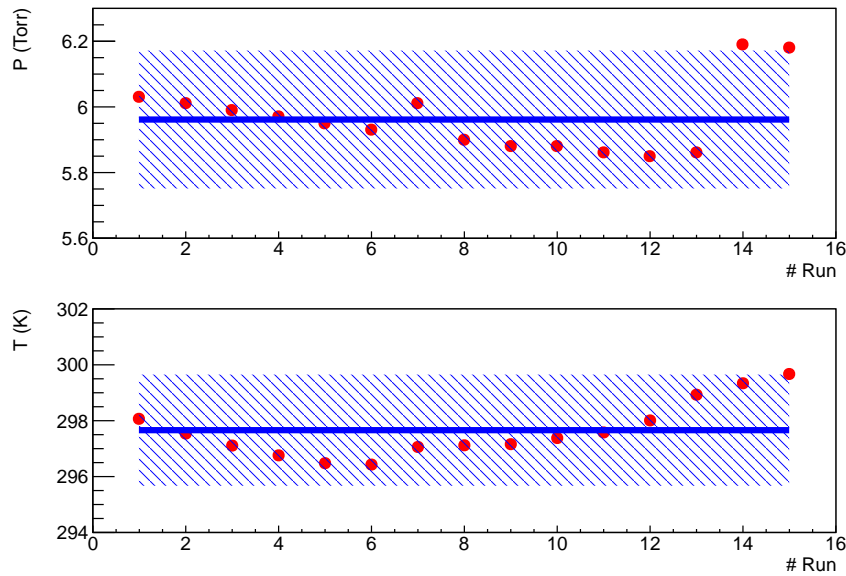


Figure 5.12: Gas target pressure (top panel) and temperature (bottom panel) for the ~ 5.2 MeV beam energy case. Each red dot corresponds to average values for a give run. The blue line gives the average value of all of the runs for this given energy. The marked regions show the final errors.

The red dots indicates the parameter values for different runs, while the blue lines show the final pressure and temperature values calculated as the average of the runs. The marked regions indicate the uncertainties. Table 5.7 shows the averaged pressures and temperatures for different beam energies.

The effective length of the gas target (ℓ) has been estimated as 12.3 ± 0.5 cm. This is based on two methods; firstly using the energy lost by the ^{12}C beam in the ^3He gas target. This measurement were performed to determine the target density profile and the details can be found in section 3.3.3.4. Secondly, using the available systematic from previous experiments where reactions with heavier ions impinging onto ^4He gas target were studied. In the latter case effective lengths were estimated by the beam energy losses.

5.3.3 The number of ^4He beam particles: $N^{\circ B}_{^4\text{He}}$

The number of beam particles are calculated by relating the scattered beam particles detected in the silicon detectors at 30° (Si-30) and 57° (Si-57) from the Faraday cup readings made at the beginning of each run every 60 minutes. Due to the fact that the DAQ system was changed between our measurements in 2011 and in 2013, two different approaches were used in order to extract the number of beam particles as explained in the following.

The 2011 measurement

The number of beam particles is obtained from the scattered particles detected the silicon detector and the Farady cup readings. The typical spectrum measured in the silicon detector was already shown in Figure 3.36. Complementary to the total spectrum, the information of the number of events per second detected in the silicon detector was also saved, this is the so called trigger rate (or scaler). Some examples of the trigger rate for each of the three energies in the Si-30 detector are shown in Figure 5.13. The x -axis represents the time, where every channel corresponds to two seconds and the y -axis corresponds to the number of triggers. Blue (upper panel) and red (lower panel) spectra correspond to the typical runs with constant and with varying trigger rates.

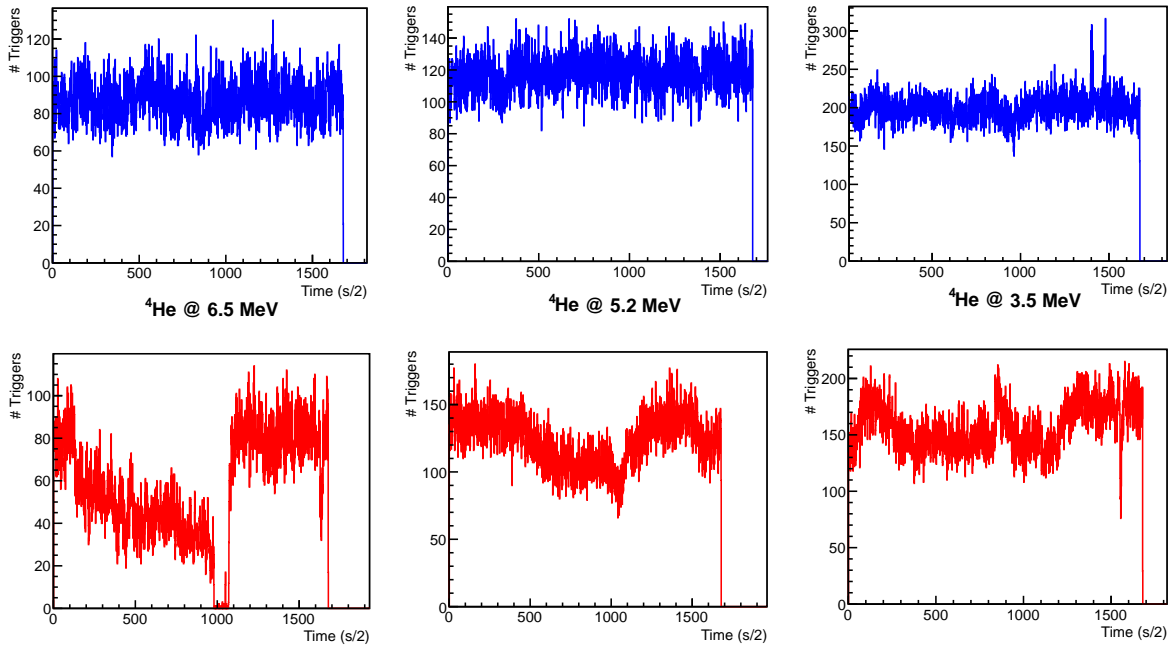


Figure 5.13: 30° silicon detector trigger rates for the different energies measured in the 2011 campaign. For each energy two histograms are plotted. Blue and red runs correspond to nearly constant and largely varying trigger rate conditions, respectively.

The procedure followed is to obtain an average final normalisation factor (R^F) among those runs with a constant trigger rate (**optimums run**), which essentially means that a constant current throughout the whole run is assumed. Then, this normalisation factor is applied to all the runs to get the number of beam particles. The normalisation factor for an optimum run is defined by:

$$R^{\text{run}} = \frac{\text{FC1}}{1.602 \cdot 10^{-19} \cdot q} \frac{\text{Time} \cdot \text{Livetime}}{\text{Si-30}} \cdot P \cdot T \quad (5.26)$$

This is the ratio of the number of scattered particles detected in the silicon detector and particles measured with the FC1 at the beginning of each run. Here, "FC1" is the reading of the Faraday cup 1 in ampere, $q=2$ is the beam charge state after crossing the target. "Si-30" is the integration of the total silicon spectrum for each run, "Time" is the time for each run and "Livetime" takes into account the effect of the dead time of the acquisition system. "P" and "T" are the pressure and temperature and are introduced in order to take into account the different number of target particles between different runs.

FC1 readings of of beam current

The current readings were taken automatically at the beginning of each run by using FC4, FC1, FC4, FCCH and FC4 in that sequence. Each measurement took 30 s, approximately. An example for a complete FC1 reading is shown in red in Figure 5.14. The increased and drop current in the extremes corresponds to the time when the cup is moved in and out, respectively. Therefore, only the central values are considered (see inset in Figure 5.14).

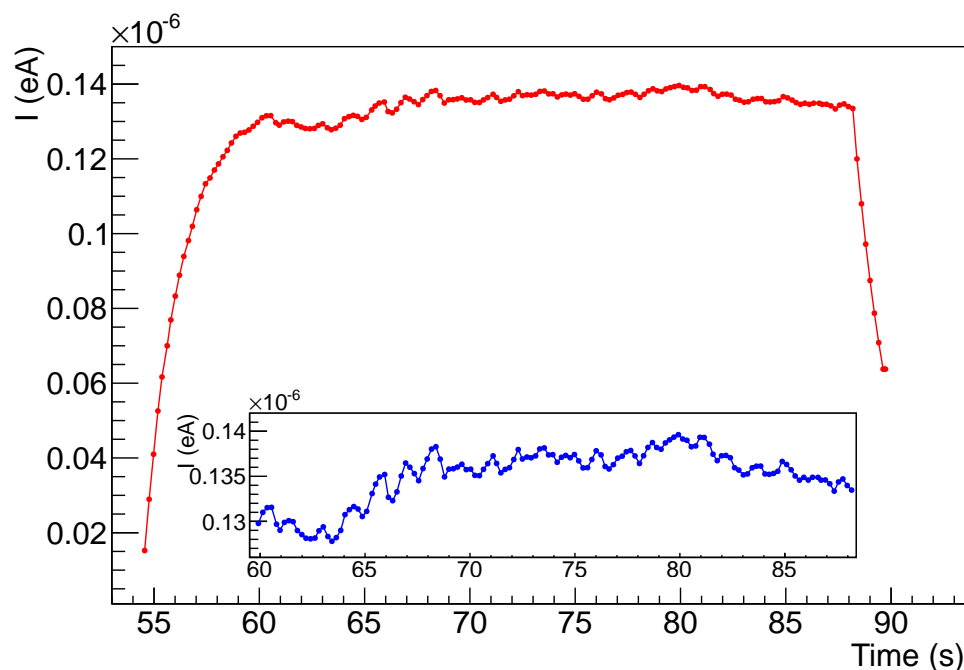


Figure 5.14: Example for FC1 reading for an optimum run. In red a total spectrum for a FC1 reading. The current increase and decrease in the extremes is related to the voltage turned on and off respectively. The inset shows a closer view of the central region considered in order to extract the averaged value of FC1.

The average of all central values of each measurement (i.e. blue points in Figure 5.14 inset) is used as FC1 in the expression 5.26. The error associated to FC1 is the standard deviation of the considered central values.

Integration of the peak in Si-30 spectra

The choice of considering the 30° detector instead of the 57° is based on the statistics. For each of the beam energies measured, Figure 5.15 shows the spectra for the silicon detector at 30° (Si-30) in the upper panel and for the detector at 57° (Si-57) in the lower one. The spectra show the scattered ^4He beam in the ^3He gas target at the pressures and temperatures indicated in the figure. The statistics in the scattered peak for Si-30 is considerably bigger than in the Si-57 and, due to the kinematics, the higher the energy is the bigger the $\frac{\text{Si-30}}{\text{Si-57}}$ ratio is.

As can be seen in the silicon spectra at 30°, and was already discussed in section 3.3.2.7, the double peak is due to the scattered ^4He beam by the ^3He target and vice-versa. The two peaks are clearly separated for the higher energy, while for the lower the energy it is the more difficult to separate both contributions. For this reason, in order to estimate the Si-30 factor in expression 5.26 the procedure consists of integrating the contribution of both peaks in the optimum files. Figure 5.16 shows an example for the Si-30 spectrum of an optimum run corresponding to ~ 6.5 MeV beam energy with $1.378 \cdot 10^4$ counts under the two peaks filled with red colour. The associated uncertainty to Si-30 is the square root of the value.

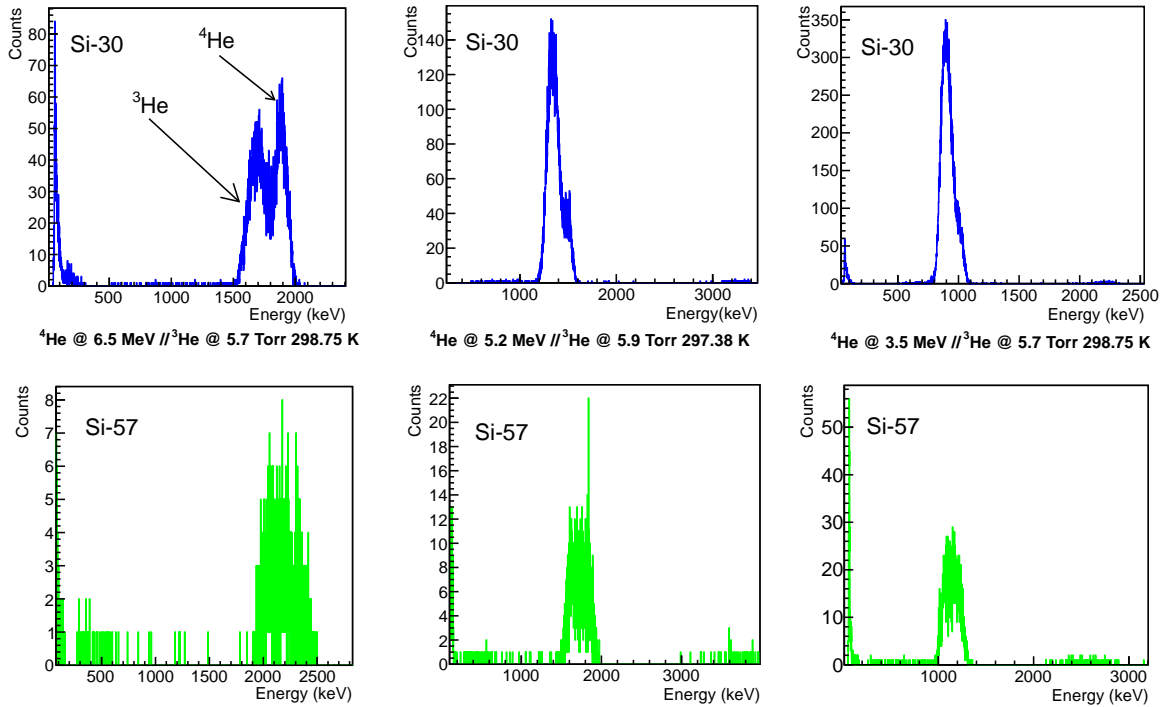


Figure 5.15: Typical spectra in blue and green for Si-30 and Si-57, respectively, corresponding to the measurements of different energies carried out in 2011.

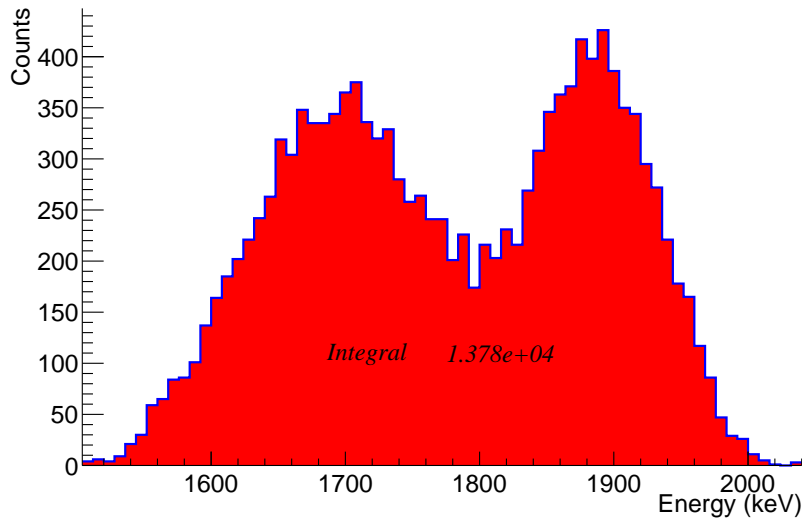


Figure 5.16: The spectra show the scattered particles in the 30° silicon detector for the ^4He beam energy of ~ 6.5 MeV. The integral gives the number of counts under the two peaks corresponding to Si-30 in expression 5.26.

It must be pointed out that for the highest energy case, where the two peaks can be clearly separated. Thus, the R^{run} normalization factors could be calculated replacing Si-30 by just the integration of the scattered ^4He beam peak contribution. Final results do not depend, on whether we use total spectrum or just the ^4He scattered peak.

Time and DAQ livetime

The measurement *time* of each run was saved during the experiment in the MIDAS system.

The livetime is calculated by dividing the total number of events recorded (acquired triggers) in the "tail" of DRAGON, by the total number of events received in the tail (total triggers), these include those events which could not be recorded due to the DAQ system was busy processing other events: ($\text{Lifetime} = \frac{\text{Acq. Trig}}{\text{Total Trig}}$). Considering the square root of the total and acquired triggers as the uncertainties of "Acq. Trig" and "Total Trig" respectively, an associated error to the Lifetime has been estimated by using standard error propagation.

Pressure and temperatures of the target

The pressure and temperature for every run is calculated as the average of the values saved every five minutes. The associated errors are calculated considering the standard deviation of the data plus a systematic error of 0.1 Torr for pressure and 1 K for temperature. Figure 5.17

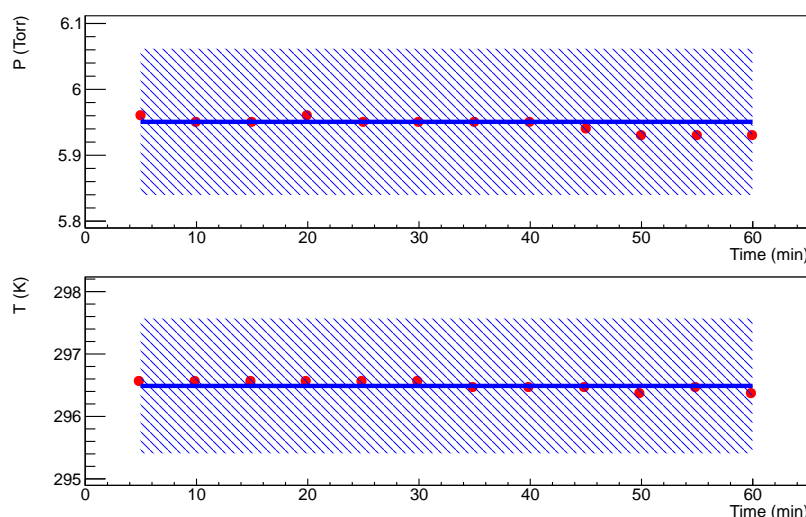


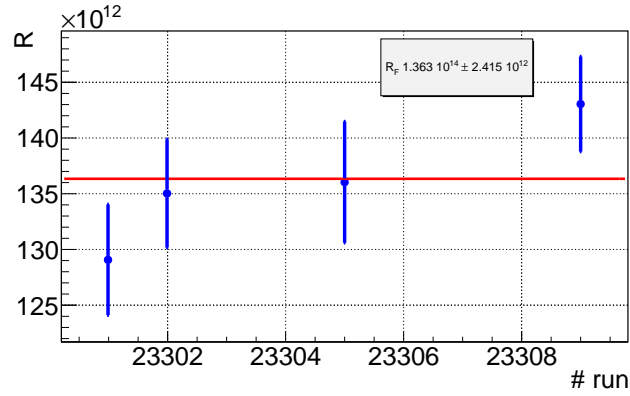
Figure 5.17: Gas target pressure (top panel) and temperature (bottom panel) for an optimum run of ~ 5.2 MeV beam energy. Each red dot corresponds to one of the value recorded every five minutes. The blue line gives average value for the given optimum run. The marked regions show the error considered in order to determine R^{run} .

After all variables are determined, the normalisation R^{run} factors are obtained for the optimum run for each energy. The uncertainties associated with the R^{run} factors are calculated using standard error propagation from the errors of every variable (FC1, Si-30, Lifetime, P and T). The final normalisation factors (R^{F}) for every energy are then calculated by the weighed average of all the corresponding R^{run} factors. Figure 5.18 shows the normalisation factors for the three energies. The blue dots are the normalisation factors for the optimum runs (R^{run}) and the red lines show the final R^{F} factors for the three energies.

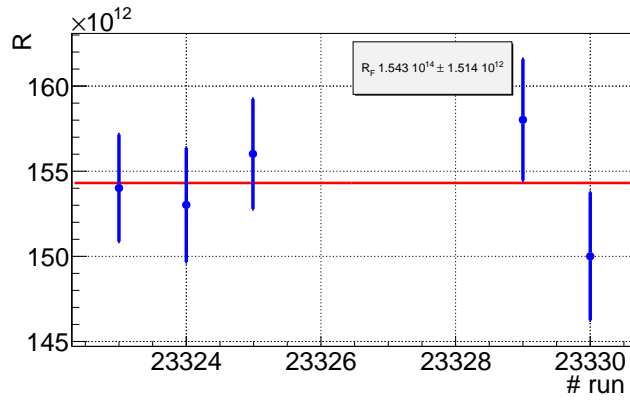
The number of incoming beam particles can then be calculated for any run, including optimum and no optimum runs, by using:

$$N_{4\text{He}}^{\text{B}} = \frac{R^{\text{F}} \cdot \text{Si-30}}{\text{Livetime} \cdot P \cdot T} \quad (5.27)$$

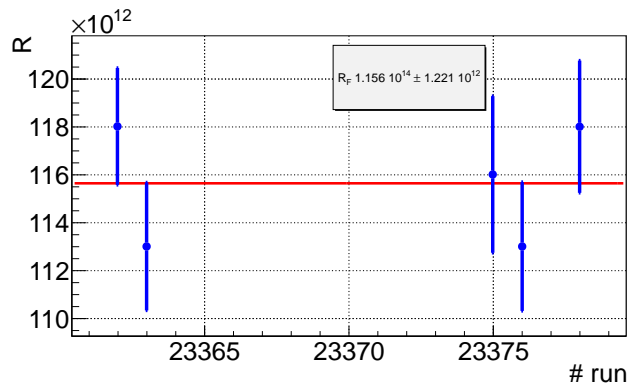
where Si-30, P and T are calculated for any given run using the procedure explained above for the optimum runs. The associated errors in the number of beam particles are calculated by using standard error propagation for the expression 5.27, where the uncertainty for R^{F} are the ones shown in Figure



(a)



(b)



(c)

Figure 5.18: Normalisation R factors for the 2011 measurements at energies of ~ 6.5 MeV (a), ~ 5.2 MeV (b) and ~ 3.5 MeV (c). The blue dots represent the normalisation factor for the runs, those with a nearly constant trigger rate. The red lines give the weighed averaged R_F .

5.18 and the uncertainties in P, T, Livetime and Si-30 are the explained above. The total number of beam particles for every energy is obtained by adding $N_{4\text{He}}^{r\text{B}}$ for all the runs.

The 2013 measurements

In the upgraded 2013 DAQ system, timestamps are recorded for every saved event including for those in the silicon spectrum. Therefore, the Si-30 events taken with the same duration than the Faraday cup measurement, could be used to estimate the normalisation factor.

Furthermore, it was already mentioned that during the 2013 measurements, the *Activation Method* was also used with the same beam energy as the direct count recoil measurement (~ 4.7 MeV) and target conditions. Therefore, the normalisation factor are the same in both cases and thus all optimum runs can be taken into account in order to obtain a final R^F factor.

One difference between the *Direct Recoil Counting Method* (direct runs) and the *Activation Method* (implantation runs) at TRIUMF must be considered here: FC1 is placed after the copper catcher position, therefore just FC4 readings were performed during the implantation runs (see Figure 3.34). Thus, the two R^{run} factors are defined differently for 2013 run as

$$R_{\text{direct}}^{\text{run}} = \frac{\text{FC1}}{1.602 \cdot 10^{-19} \cdot 2} \frac{60 \cdot \text{Livetime}}{(\text{Si-30})^{60\text{s}}} \cdot P \cdot T \quad (5.28)$$

for the direct runs and

$$R_{\text{activ}}^{\text{run}} = \frac{\text{FC4} \cdot \text{Trans}}{1.602 \cdot 10^{-19} \cdot 2} \frac{60 \cdot \text{Livetime}}{(\text{Si-30})^{60\text{s}}} \cdot P \cdot T \quad (5.29)$$

for the implantation runs. "P", "T" and "Livetime" are same as before and are determined as in the 2011 experiment. "Trans" is the beam transmission through the target, which is the ratio between the FC4 and FC1 readings in the direct measurements, and has been estimated to be 94.09%. Finally, $(\text{Si-30})^{60\text{s}}$ is the total number of scattered events during the first 60 seconds of the run with in the peak in the spectrum corresponding to the 30° silicon detector (see example in Figure 5.19).

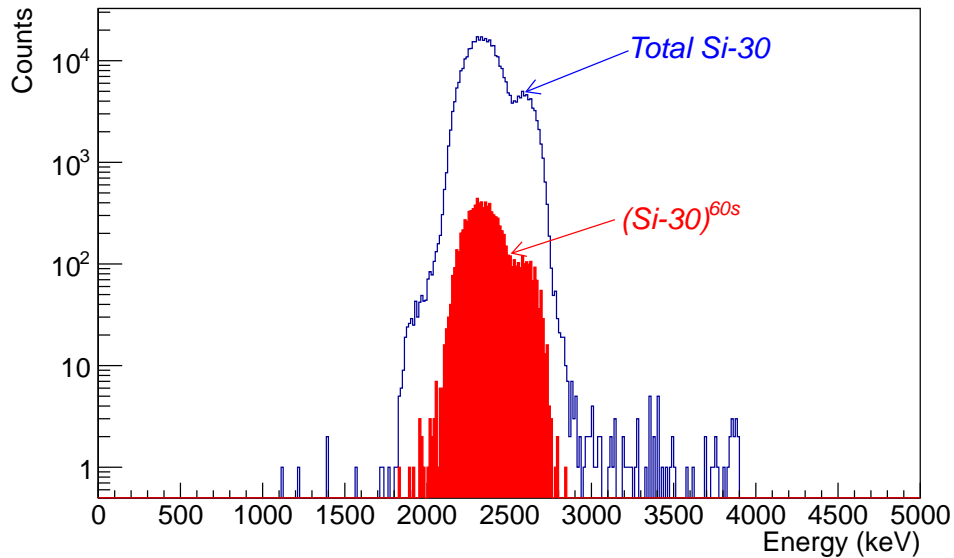


Figure 5.19: In blue the total 30° silicon spectrum for a 60 minutes run. In red the part of the spectrum taken during the first 60 s of the run. The integral under the red curve is the $(\text{Si-30})^{60\text{s}}$ for the expressions 5.28 and 5.29 as part of normalization procedure.

Figure 5.20 shows in blue the normalization R^{run} factors for the optimum runs for the 2013 experiment and the red line shows the final R^F factor.

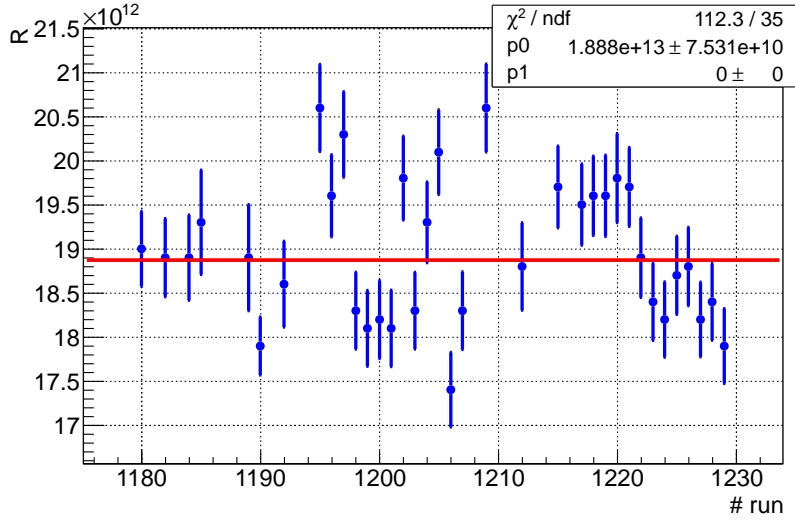


Figure 5.20: The blue dots show the normalization factors for the optimum runs in the 2013 measurements. The red line corresponding to the weighed average of the blue dots gives $1.888 \cdot 10^{13} \pm 7.531 \cdot 10^{10}$ for the R^F factor.

The total number of beam particles for every run is then estimated by using the expression 5.27 with $R^F = 1.888 \cdot 10^{13} \pm 7.531 \cdot 10^{10}$.

5.3.4 The ${}^7\text{Be}$ recoils produced in the direct recoil counting method: $Y_{7\text{Be}}$

The expression 3.16 establishes how to determine the total number of recoils for the *Direct Recoil Counting Method* at TRIUMF. In the previous Chapter it was discussed how to obtain the acceptance of DARGON. In the following the analysis performed in order to extract the other variables required to estimate $Y_{7\text{Be}}$.

5.3.4.1 Total counts in the focal plane DSSSD: Y_{DSSSD}

The separator was tuned to select a specific charge state for the ${}^7\text{Be}$ recoils, that were transmitted through the separator and detected at the final DSSSD at the focal plane of the separator (Y_{DSSSD}). Table 5.8 shows for the different incoming beam energies the selected charge state and the ${}^7\text{Be}$ recoil energy, obtained from the magnetic fields in MD1.

$E_{4\text{He}}$ (MeV)	${}^7\text{Be}$ Charge state	$E_{7\text{Be}}$ (keV)	Y_{DSSSD} (Counts)
~ 6.5	3+	3733.38	33465
~ 5.2	3+	2933.33	141707
~ 4.7	2+	2642.69	52668
~ 3.5	2+	1996.72	44135

Table 5.8: Details of the charge state and energy of the ${}^7\text{Be}$ recoils for the different ${}^4\text{He}$ incoming beam energies. The last column shows the total number of recoils detected in the DSSSD.

In order to obtain the parameter Y_{DSSSD} , the events in the DSSSD are treated event by event. First of all the calibration equation for the hit strip (see section 3.3.3.1) is applied to the energy channel corresponding to the hit. The result is the value of the deposited energy in the active area of the

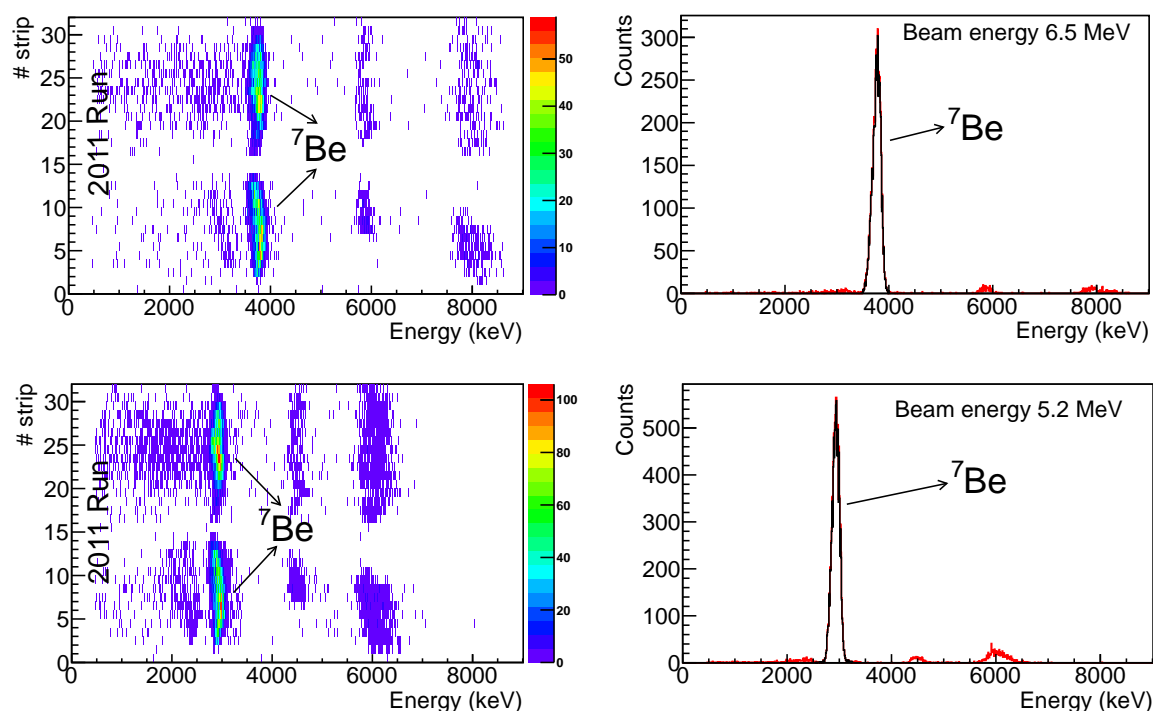


Figure 5.21: For the two highest energies studied the left side show the two dimensional spectra for the ${}^7\text{Be}$ recoils in the DSSSD strips. In right side are shown in red the projections histograms for the strips 1 to 15. In black are shown the coincide front-back events in the selected energy region.

detector. Then, the energy loss in dead layer is calculated based on the deposited energy and the values from SRIM code assuming an ${}^7\text{Be}$ crossing a $0.5\mu\text{m}$ effective aluminum layer. The energy loss is added to the deposited energy and thus the final incoming recoil energy is obtained.

For the different beam energies studied, Figures 5.21 and 5.22 show on the left side the energy versus strip number two dimensional histograms for given runs. The recoil peaks are identified in both the front strips, 0-15, and the back side strips, 16-31. On the right side are shown in red the projections in the x -axis from strips 0-15, that is, all events in the front strips for the given run. Superimposed, the spectra in black correspond to those events in the selected energy region of the recoil peak which have a corresponding hit in the back side in the same energy region (front-back coincidence events). Figure 5.21 shows the two highest energies studied where the ${}^7\text{Be}$ charge state was 3^+ . As can be seen there is not any unreacted beam contribution in the recoil peak as it was expected from the beam suppression studies detailed in the section 3.3.3.2. However, for the two lowest energies, where the recoil charge state selected was 2^+ , the unreacted beam particles reaching the DSSSD could interfere with the proper ${}^7\text{Be}$ recoil peak as can be seen in Figure 5.22.

In order to study a likely contribution of the unreacted beam in the recoil peak for the cases with 2^+ charge state, the MCP device (see section 3.3.2) was placed before the DSSSD and some runs were taken during the 2013 measurements. As the beam and recoils ions travel with different velocities, the time for crossing the two MCPs is different. Thus, the idea is to compare the time of flight of the ions between the two MCPs with the DSSSD spectra. The histogram in Figure 5.23 (upper panel) shows for all runs taken with the MCP the energy in the DSSSD versus the time amplitude converter (TAC) from the signals from the MCPs. As can be seen the ${}^7\text{Be}$ recoils are clearly identified and separated from the beam particles. Therefore, the energy region considered for the recoils selection in the DSSSD spectra for the 2^+ cases shown in black in the right side spectra in Figures 5.21 is justified.

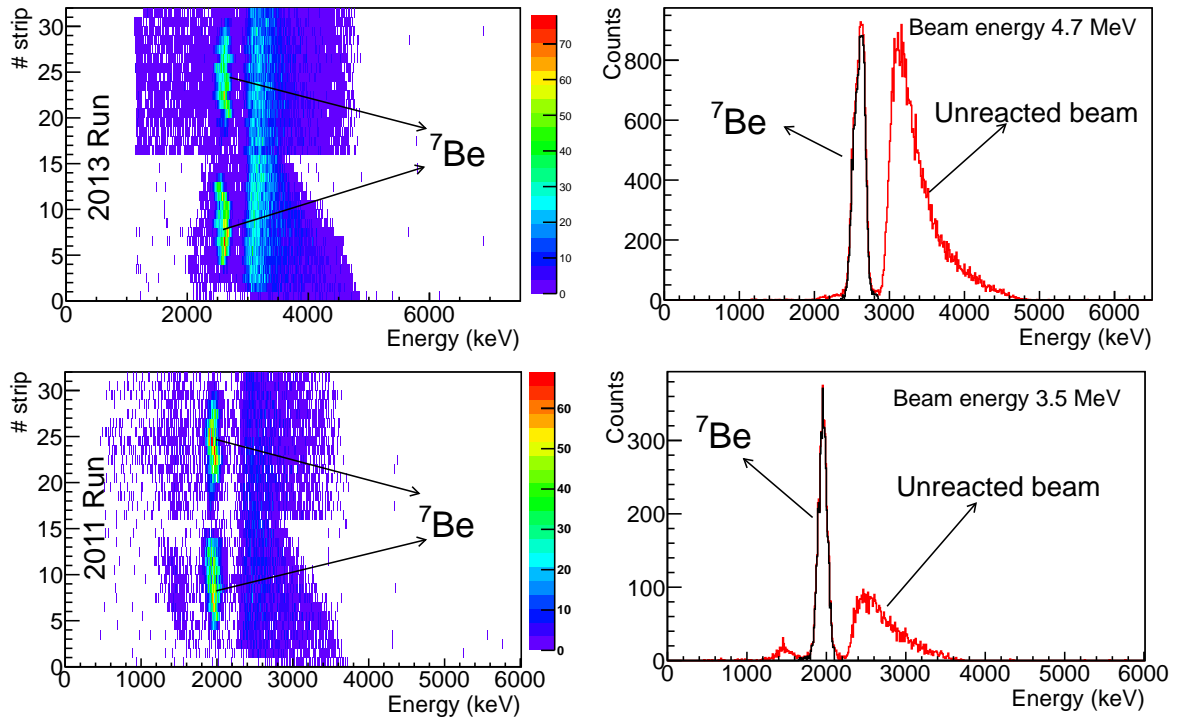


Figure 5.22: For the two lowest energies studies are shown the same spectra than the displayed in Figure 5.21 for the two highest energies.

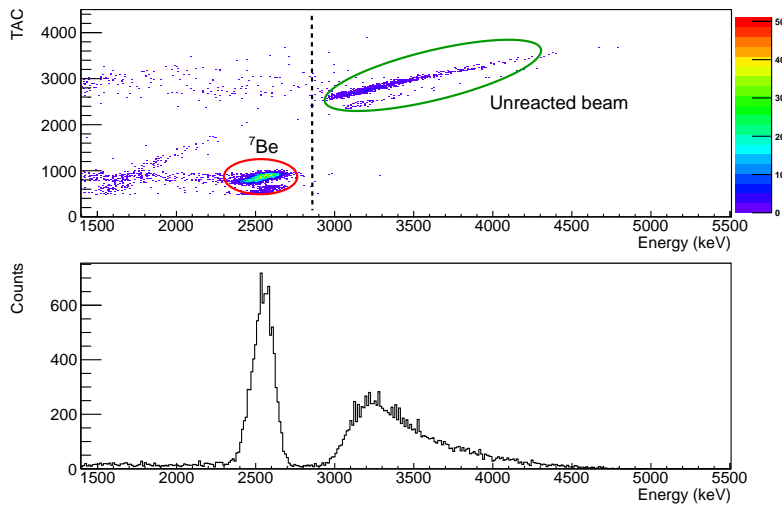


Figure 5.23: Upper panel shows DSSSD energy versus MCP-TAC histogram. The red circle encloses the ${}^7\text{Be}$ recoils which are clearly separated from the unreacted beam particles enclosed in the green circle. Lower panel shows the projection in the x-axis of the upper histogram.

It must be pointed out that those run where the MCP was used are not considered in to determine the final cross section, due to the fact that some of the recoils are stopped in the MCPs strips resulting in systematic errors. Also in the lower panel in Figure 5.23 can be observed that when the MCPs are in the separation between beam and recoils peaks is even better due to the different energy losses through the MCP. However, the energy losses are small and the separation can be extrapolated to the case of MCPs are out.

The number of ${}^7\text{Be}$ recoil has been determined for every run individually by demanding in the energy region of recoils in the DSSSD strips front-back coincidence. Next, the final number of recoils, Y_{DSSSD} , can be obtained by adding all individuals runs. The values of Y_{DSSSD} for the different energies are shown in the fourth column in Table 5.8 and only the statistical uncertainty is considered for Y_{DSSSD} .

5.3.4.2 Experimental efficiencies: t_ℓ , ϵ_{DSSSD} and q_f

The DAQ livetime (t_ℓ) is determined for every run by dividing the acquired triggers and the total triggers in the "tail" of DRAGON ($t_\ell = \frac{\text{Acq. Triggers}}{\text{Total Triggers}}$). For the mean value of t_ℓ for every energy, the acquired and total triggers for all runs have been added and a final value obtained in the same way. A negligible error is estimated using statistical error propagation for the acquired and total triggers. The second column in Table 5.9 shows the t_ℓ for different energies of our interest.

$E_{4\text{He}}$ (MeV)	t_ℓ (%)	ϵ_{DSSSD} (%)	q_f (%)
~ 6.5	84.12	96.15 ± 0.10	(3+)59.05 ± 1.87
~ 5.2	92.34	96.15 ± 0.10	(3+)61.87 ± 2.55
~ 4.7	94.18	96.15 ± 0.10	(2+)29.31 ± 3.81
~ 3.5	98.64	96.15 ± 0.10	(2+)52.30 ± 3.33

Table 5.9: $t_\ell, \epsilon_{\text{DSSSD}}$, and q_f for the different energies.

An efficiency of $\epsilon_{\text{DSSSD}} = 96.15 \pm 0.10\%$ value has been considered for the DSSSD based on the results in reference [WHRD03]. The loss of efficiency is coming from the insulating gap between the neighboring strips. When a charged particle hit the gap, it creates a reduced pulse height in the strips in comparison to a particle entering through a proper strip. The authors determined experimentally the effective gap width by using an ${}^{241}\text{Am}$ α source and a $180 \mu\text{m}$ slit and compared it with the strips width. The results showed that $(3.85 \pm 0.10)\%$ of α particles incident on the detector will have reduced pulse height.

The values for the charge state distribution, i.e. q_f , are based on the CSD measurements detailed in section 3.3.3.3 which only depend on the velocity, atomic number of the incident ion and the mass of the target. In order to obtain q_f , velocities (energies per nucleon) of the incoming ${}^9\text{Be}$ beam in the CSD measurements must be matched with the velocities of the ${}^7\text{Be}$ recoils when they are created. Table 5.10 shows the calculated recoils energies distributions for the recoils created at the entrance, center or end of the gas target depending on the different γ emission angles. The beam energy losses for the reaction at center and end of the target have been estimated using the SRIM code. In bold are shown the central energies per nucleon corresponding to the recoils created when the reaction takes place at the centre of the gas target and the γ emission angle is 90° . For the ~ 6.5 , ~ 5.2 and ~ 3.5 MeV beam energies the central recoil energies are similar within the errors to the ${}^9\text{Be}$ energies shown in Table 3.7 for the q_f measurements. Therefore, for these three energies the q_f values shown in Table 5.8 are the same as the charge state distribution results in Table 3.7. For the ~ 4.7 MeV energy the 2^+ charge state distributions have been interpolated to the 383.30 keV/u energy. Figure 5.24 shows the values for the distribution of the 2^+ charge state for the different energies. The points have been fitted to a second order polynomial ($\text{CSD}(2^+) = p_0 + \text{Energy} \cdot p_1 + \text{Energy}^2 \cdot p_2$) whose values are displayed in the plot.

E^{beam} (^4He) (keV)	ENTRANCE (keV/u)	MIDDLE (keV/u)	END (keV/u)	θ_γ ($^\circ$)
6553.94	511.55	511.08	510.61	0
	533.49	532.99	532.50	90
	553.39	553.47	552.96	180
5165.97	403.67	403.08	402.49	0
	420.45	419.83	419.22	90
	436.25	435.61	434.97	180
4716.45	368.65	368.12	367.60	0
	383.85	383.30	382.75	90
	398.20	397.63	397.06	180
3521.61	275.35	274.56	273.77	0
	286.57	285.76	284.93	90
	297.26	296.41	295.56	180

Table 5.10: For the different incoming beam energies shown in the first column, the third fourth and fifth columns show the energies per nucleon of the recoils depending on where the reaction takes place (entrance middle or end of the gas target). For each scenario three different energies are shown depending on the γ output angles (0° , 90° , and 180°)

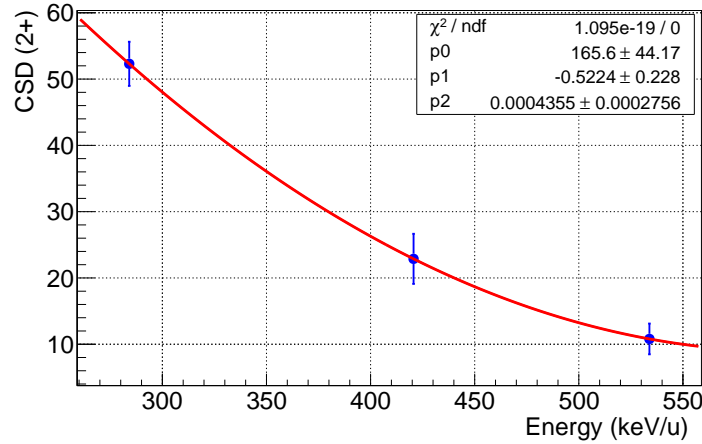


Figure 5.24: 2^+ Charge state distribution interpolation. The blue dots indicate the values of the CSD for the 2^+ shown in Table 3.7, and the red line shows a second order polynomial fit to the values. The values from the fit are shown in the plot.

The charge state distribution for the 383.30 keV/u energy estimated from the fit is shown in Table 5.9. A detailed description of the associated uncertainties to the q_f values is given in appendix B.

5.3.5 The ^7Be recoils produced in the activation method @ TRIUMF

The procedure followed to determine the number of implanted recoils is the same as in the Madrid experiment. The activated Cu catcher was measured at the same low background HPGe station in Israel (see Figure 3.12) where the gamma spectrum activity was taken during 12 days and it is shown in Figure 5.25.

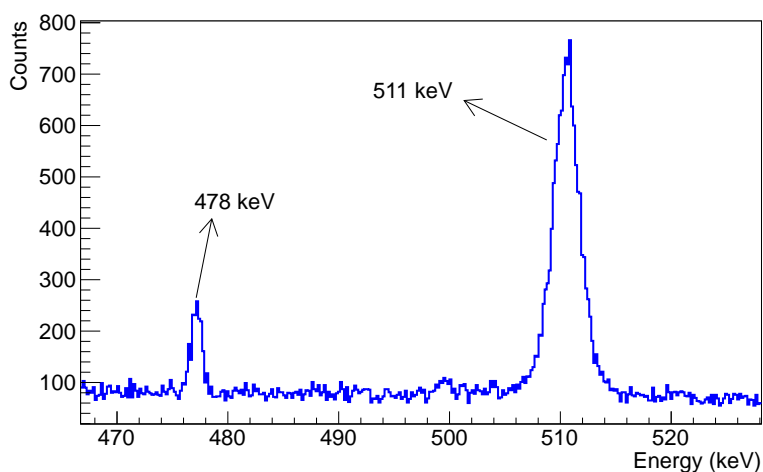


Figure 5.25: Gamma Activity spectrum from the activation measurement at TRIUMF. The 478 keV peak from the de-excitation of the ${}^7\text{Li}$ as well as the 511 keV background peaks are marked.

The number of γ counts under the 478 keV peak is determined as detailed in section 5.1.3.1 and the procedure followed to estimate the total number of ${}^7\text{Be}$ nuclei produced is the one explained in section 5.1.3.2.

Two extra correction factors must be considered in this activation measurement comparing to the Madrid experiment. Firstly, the Cu catcher is placed further away from the target cell compared to the Madrid experiment, ~ 85 cm downstream (see Figure 3.34), and therefore, the recoil spot is increased. Figure 5.26 shows the recoil spot at 85 cm as obtained from the GEANT 3 simulations. The efficiency of the HpGe detector for this recoil spot has been obtained by performing GEANT 4 simulations, which have been verified for the activation experiment in Madrid. The efficiency results in 0.0393 ± 0.0012 (3% systematic error).

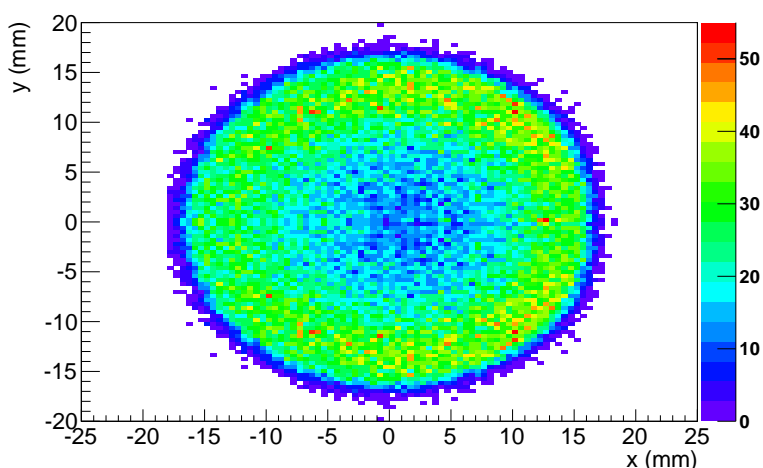


Figure 5.26: Recoil spot at 85 cm obtained from the simulations for activation method at TRIUMF

Secondly, not all recoils created reach the Cu catcher, being some of them stopped in target cell, target box and pumping tubes before 85 cm. According to the final series of the simulations at $E_{\text{beam}} \sim 4.7$ MeV (fourth row in Table 4.6) from the 28.3% total stopped recoils throughout the separator 18.5% are stopped before 85 cm.

Table 5.11 shows the values considered to determine the total number of ${}^7\text{Be}$ produced.

Parameter	Value
Implantation time	1.16
T_{IMP} (d)	
Decay time	12.0
T_d (d)	
Lost time	24.5
T_l (s)	
HPGe efficiency	3.93%
ϵ_A	
478 keV γ s	1113
N	
Recoils stopped pumping tubes	18.5%

Table 5.11: Parameters for activation measurement at TRIUMF in order to estimate the total number of ${}^7\text{Be}$ recoils produced as defined in section 5.1.3.2. The extra factor "Recoils stopped pumping tubes" includes the correction due to all the recoils stopped before reaching the Cu catcher as estimated from the GEANT simulations.

5.4 Astrophysical S-factors II: Measurements using Direct Recoil Counting Method

The results for all observables together with the cross sections and astrophysical S-factors for the direct detection method experiment are displayed in Table 5.12. The errors for all observables and σ_{34} and $S_{34}(E)$ are shown between brackets and a detailed description of how they are obtained is given in Appendix B.

Run	$\sim E_{4\text{He}}$ (MeV)	E_{CM} (keV)	$N_{4\text{He}}^{\text{beam}}$ ($\cdot 10^{16}$)	$N_{3\text{He}}^{\text{target}}$ ($\cdot 10^{18}$ cm^2)	$N_{7\text{Be}}^{\text{recoils}}$ ($\cdot 10^5$)	$\sigma_{34}(E)$ μb	$S_{34}(E)$ (keV \cdot b)
	6.5	2813.6 \pm 1.8	0.84(1)	2.29(11)	1.22(1)($^{+6}_{-14}$)	6.59(8)($^{+44}_{-80}$)	0.393(5)($^{+27}_{-49}$)
2011	5.2	2216.6 \pm 1.7	3.25(2)	2.38(13)	4.47(4)($^{+43}_{-47}$)	6.06(5)($^{+63}_{-79}$)	0.419(4)($^{+46}_{-50}$)
	3.5	1508.9 \pm 1.3	2.09(1)	2.38(12)	1.74(1)($^{+15}_{-17}$)	3.51(3)($^{+35}_{-38}$)	0.359(3)($^{+36}_{-40}$)
2013	4.7	2023.7 \pm 1.4	3.03(3)	1.98(11)	2.77(3)($^{+38}_{-44}$)	4.62(4)($^{+68}_{-79}$)	0.359(3)($^{+53}_{-61}$)
(Impl)	4.7	2023.7 \pm 1.4	26.5(1)	1.94(10)	28.8(20)(29)	6.22(44)(72)	0.484(34)(56)

Table 5.12: Results for the direct experiment. The second column shows the different beam energies used in the experiment. The third column shows the corresponding centre of mass energies taking into account the energy losses. The fourth, fifth and sixth columns show the total number of particles in the beam, target and recoils respectively. The seventh and eighth column show the cross section and astrophysical factor for the ${}^3\text{He}(\alpha,\gamma){}^7\text{Be}$ reaction. The uncertainties for each value are shown between brackets. When only one contribution it refers to the systematic error, and in case of two contributions the first one refers to the statistical uncertainty and the second one to the systematic error (positive and negative systematic uncertainties contributions are separated in some cases).

The results are displayed together with our Madrid results and literature data in Figure 5.27. As conventional, the errors displayed in the plot are only the statistical errors and as can be observed, the associated errors for the direct method at TRIUMF are negligible.

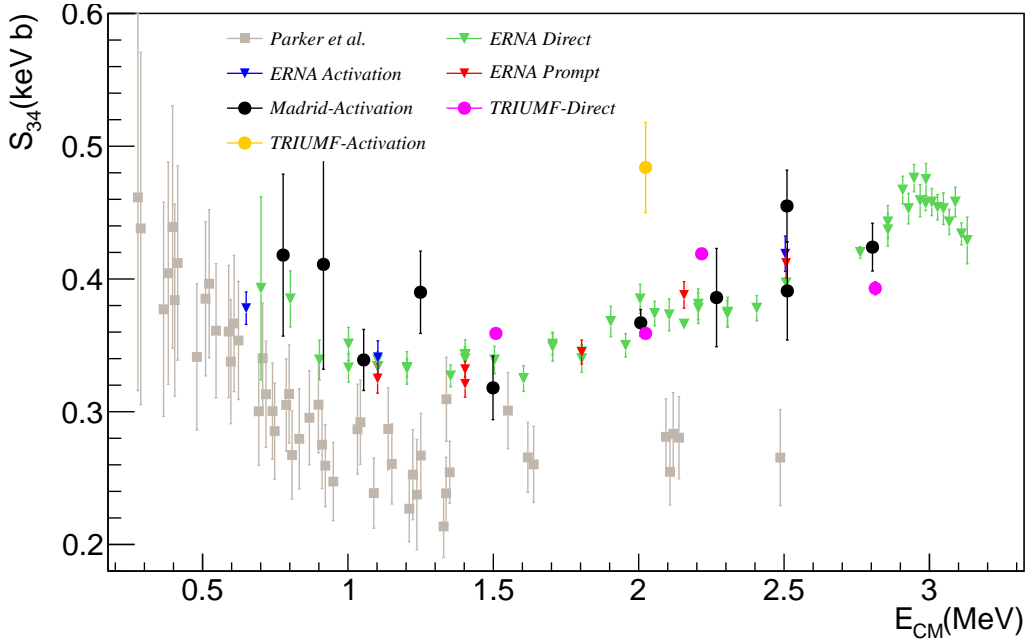


Figure 5.27: Astrophysical S -factor for the ${}^3\text{He}(\alpha,\gamma){}^7\text{Be}$ reaction using the direct counting method (violet dots) and the activation method (yellow dot) at TRIUMF. For comparison with previous results, with triangles and squares are shown the results from [DGK09] and [PK63] respectively and our results in Madrid with black dots.

At first glance can be seen that the astrophysical S -factors agree with the Madrid experiment as well as with ERNA and disagree with Parker ones. In the next chapter the comparison between our result and with previous ones will be studied in more detailed.

5.5 Conclusion

The results and analysis techniques used to deduce the observables required to determine the astrophysical S -factor have been detailed for the two experiment.

For the activation experiment in Madrid, the two techniques used to determine the number of ${}^3\text{He}$ beam particles have been compared. The pressure stability of the ${}^4\text{He}$ gas target has been shown in order to detail how the number of target particles are estimated. The detailed analysis performed in order to measure the ${}^7\text{Be}$ activity in the Cu catcher as well as the inferred number of recoils produced is also given. The results, shown together with previous measurement in the same energy range, agree with the measurement performed using the ERNA separator [DGK09] and disagree with those in reference [PK63].

For the direct counting recoil experiment, the number of ${}^4\text{He}$ beam particles were determined using the scattered beam particles with the gas target. Due to the upgrading of the acquisition system between the 2011 and 2013 measurements, the methods used to estimate the number of beam particles are shown separately for the two runs. The number of target particles are determine very precisely due to the continuous monitoring of pressure and temperature during the measurements. The effective target length is based on the experimental target density profile measurements detailed in chapter 3, and previous experiments with DRAGON. For the number of ${}^7\text{Be}$ recoils created, the detailed description for obtaining the number of recoils reaching the DSSSD is given. Corrections due to the charge state selection in the separator, livetime, and detector efficiency is reported. Furthermore, the simulation analysis performed in order to get the acceptance of DRAGON for the ${}^3\text{He}(\alpha,\gamma){}^7\text{Be}$ reaction is explained in detail. The activation measurement perform at DRAGON in order to cross check the direct counting measurements is also explained. The results are in agreement with the experiment performed in Madrid.

"Your theory is crazy, but it's not
crazy enough to be true."

Niels Bohr

CHAPTER 6

DISCUSSION AND FUTURE WORK

Abstract: *In this chapter the results for the astrophysical S-factors obtained from the two complementary experiments are compared to the literature data and calculations from theoretical models. A discussion about the results and future projects will also be presented.*

As it has been discussed in the previous chapters, several experiments have been performed since the first measurements of Holmégren and Johnston [HJ59] aiming to determine the astrophysical S-factor of the ${}^3\text{He}(\alpha,\gamma){}^7\text{Be}$ and ${}^3\text{H}(\alpha,\gamma){}^7\text{Li}$ reactions. Prior to the measurements presented, there were only two set of data in the E_{CM} range from 1 to 3 MeV. The results presented here are in the same energy range, allowing for a quantitative comparison with previous works.

Large discrepancies are seen in the experimental results as well as when comparing with the theoretical models. Only the new ab-initio calculation [Nef11] and those in [Moh09] extended the astrophysical S-factor calculations to medium energies, which is important not only to constrain the extrapolations down to the astrophysical energies, but also for understanding the influence of the non-external contribution to the reaction. The results presented here are also compared to the different theoretical models.

Finally, some work can still be done related to this reaction aiming for example to constrain the theoretical models and to get a lower uncertainty in the $S_{34}(0)$ value. Future possible experiments and studies to be performed by our collaboration will also be discussed in this chapter.

6.1 Summary of the S-factor Results

The new experimental results of the astrophysical S-factor for the ${}^3\text{He}(\alpha,\gamma){}^7\text{Be}$ reaction have been obtained using two experimental techniques, the *activation method* using a tandem accelerator in Madrid, and *direct recoil counting method* using the DRAGON spectrometer in Vancouver. These results are summarised in Table 6.1. where the last column shows the total error calculated as:

$$\Delta S(E)^{\text{Total}} = \sqrt{(\Delta S(E)^{\text{stat}})^2 + (\Delta S(E)^{\text{syst}})^2} \quad (6.1)$$

For the TRIUMF experiment the systematic uncertainties are calculated as the average between the positive (+) and negative (-) values.

E_{CM} (keV)	S(E) (keV·b)	$\Delta S(E)^{\text{stat}}$ (keV·b)	$\Delta S(E)^{\text{syst}}$ (keV·b)	$\Delta S(E)^{\text{total}}$ (keV·b)
777.2	0.418	0.061	0.018	0.063
915.8	0.411	0.079	0.015	0.081
1054.2	0.339	0.023	0.012	0.026
1249.6	0.390	0.031	0.013	0.034
1498.9	0.318	0.024	0.011	0.026
2007.0	0.367	0.010	0.010	0.014
2267.7	0.386	0.037	0.016	0.041
2510.0	0.455	0.027	0.017	0.032
2511.1	0.391	0.037	0.014	0.040
2804.1	0.424	0.018	0.012	0.022
1508.9	0.359	0.003	+0.036 -0.040	0.038
2023.7	0.359	0.003	+0.053 -0.061	0.057
2216.5	0.419	0.004	+0.046 -0.050	0.048
2813.6	0.393	0.005	+0.027 -0.049	0.039
2023.8	0.484	0.034	0.056	0.065

Table 6.1: Astrophysical S-factors obtained in the Madrid experiment (top part of the table), and at TRIUMF (bottom values). In the TRIUMF experiment, the thin line separates the direct counting measurements and the activation measurement. The last column shows the total error contribution.

Around the time of the measurements performed by our collaboration, two new measurements were performed by other groups. The ATOMKI group has determined the astrophysical S-factor at five E_{CM} between 1.5 to 2.5 MeV using the activation technique [BGH13]. The results, in the same energy region as that of our measurement show the same tendency discarding the low values and flat energy dependence of Parker and Kavanagh [PK63]. The Notre Dame group has determined the S-factor in the energy range of $E_{\text{CM}}=0.303\text{-}1.45$ MeV and performed new R-matrix analysis. [KUD13]. These results, together with our measurements and the measurements from Weizmann [NHNEH04], LUNA [BCC06, GCC07, CBC07], Seattle [BBS07] and ERNA [DGK09] groups are presented together in Figure 6.1. Moreover, the older data from Parker and Kavanagh [PK63] are displayed in the figure as they are in the same E_{CM} range. Traditionally, only statistical uncertainties are used when plotting the astrophysical S-factor. However, in Figure 6.1 total errors (ΔE^{total}) are used in order to compare different sets experimental data.

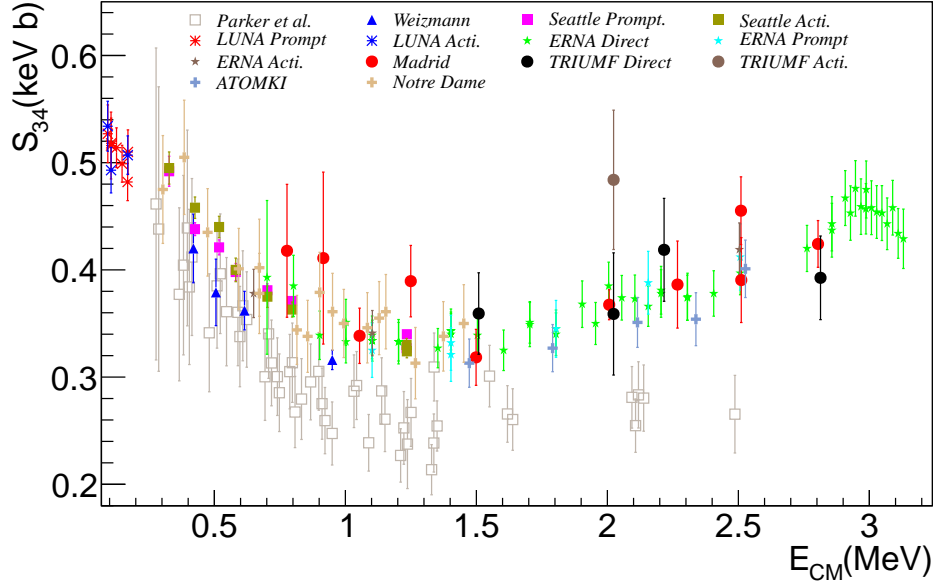


Figure 6.1: Astrophysical S -factors including both systematic and statistical uncertainties. Our data, (in circles) are shown together with the other new measurements (from 2004 on) of: Weizmann [NHNEH04], Seattle [BBS07], LUNA [CBC07], ERNA [DGK09], ATOMKI [BGH13], Notre Dame [KUD13], and the old measurements from Parker et al. [PK63], as they cover the same E_{CM} than our measurement. See text for more details.

It should be noticed that in the case of Madrid experiment the statistical uncertainties give the major contribution to the error bars while for the TRIUMF experiment the systematic uncertainties associated with DRAGON acceptance have the larger influence (see Table C.1). However, in some of the cases these uncertainties should be taken as an upper limit. For example, in the acceptance uncertainties, some of the most influencing parameters are the beam offsets in both x and y directions (see Table 4.24), which are considered to be around 1 mm. However the probability of having such a displacement during a lengthy run is small as beam position is controlled continuously with a CCD camera.

The direct counting measurement around $E_{CM} \sim 2$ MeV (2013 run) has the highest error contribution from the charge state fraction q_f . This is because no measurement of the charge state distribution corresponding to the recoils produced at this energy were yet performed.

6.2 Comparison with Previous Experimental Data and Discussion

The agreement of our results with the different experimental data sets has been quantified by using the chi-square method, i.e. by evaluating:

$$\chi^2_\nu = \left(\sum_i \frac{(S_A^i - S_B^i)^2}{(\Delta S_A^i)^2 + (\Delta S_B^i)^2} \right) / (\nu - 1) \quad (6.2)$$

where S_A and S_B are the astrophysical S -factors at a given E_{CM} from our experiment and from one of the data sets from the literature, respectively. ΔS_A^2 and ΔS_B^2 are the corresponding total errors and ν are the number of points considered.

The S_A and S_B values must be compared at the same E_{CM} . Therefore, the S_B values are calculated as the average of the values so that the corresponding average of the E_{CM} is less than 25 keV comparing with our E_{CM} values. In order to deduce the astrophysical S -factor at around 2.8 MeV in the case of Parker and Kavanagh, an extrapolation of the data was necessary. 1 As can be observed the agreement with the ERNA data is considerably better (0.75 and 0.54 for Madrid and TRIUMF data)

	Parker and Kavanagh	ERNA direct	ATOMKI
Madrid	7.40 ($\nu = 10$)	0.75 ($\nu = 10$)	1.55 ($\nu = 4$)
TRIUMF direct	5.98 ($\nu = 4$)	0.54 ($\nu = 4$)	1.40 ($\nu = 3$)

Table 6.2: χ^2_ν values calculated using expression 6.2. Here, S_A are our astrophysical S -factors and S_B are those from Parker and Kavanagh [PK63], of ERNA [DGK09] or ATOMKI [BGH13]. The ν values give the number of data points considered in each case.

compared to that with the Parker and Kavanagh data (7.40 and 5.98). A good agreement when comparing with the new ATOMKI data (1.55 and 1.40) can be also seen. The absolute S -factor from the ATOMKI data are slightly smaller than those from the ERNA although they agree fairly well within the error bars.

A χ^2 value of 0.54 is obtained when comparing *activation* data from Madrid and *recoil counting* data from TRIUMF efforts ($\nu = 4$). This good agreement using two independent experimental setups and techniques justify discard the old data from Parker and Kavanagh, providing that the improvements in the detection systems and analysis techniques makes it worth while to redo old measurements. Parker and Kavanagh used the prompt method by employing cylindrical NaI(Tl) scintillators to detect the prompt γ -rays produced on a ^4He beam capture on a ^3He gas target. The discrepancy seen could be due to a contaminated target gas. This speculation is based on the fact that the ^3He gas target was replaced by ^4He between the measurements in order to perform background measurements, which could have left residual ^4He component in the ^3He target gas.

6.3 Comparison with Theoretical Models and Discussion

Different theoretical models available for describing the $^3\text{He}(\alpha,\gamma)^7\text{Be}$ reaction were discussed in chapter 2. Figure 6.2 displays some of the different calculations together with our experimental data. Two different features can be analysed when comparing with the theoretical calculations, namely the absolute scale and energy dependence.

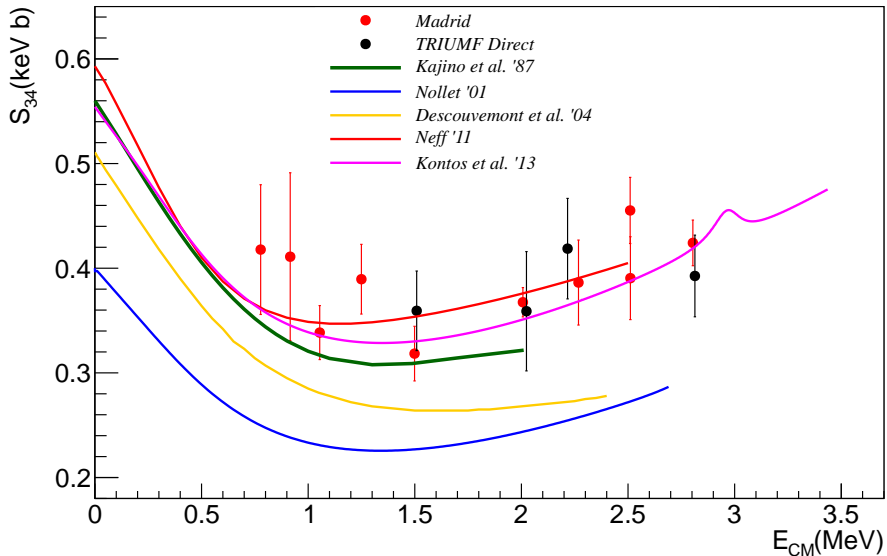


Figure 6.2: A comparison between theoretical calculations from Kajino et al.'87 [KTA87], Nollet'01 [Nol01], Descouvemont et al.'04 [DAA04], Neff'11 [Nef11], and Kontos et al.'13 [KUD13], with the activation data from Madrid and the counting data from TRIUMF. The error bars include both systematic and statistical contributions.

As can be observed the ab-initio calculation by Neff reproduce our data reasonably well for both absolute and energy dependence without any normalisation factor. However, this model can not explain the data for the isospin mirror reaction and these calculations should be treated with some caution. The recent R-matrix analysis from Kontos et al. [KUD13] is also shown in Figure 6.2. This analysis fits all the new published data (123 experimental data points) including those three points with the lowest error bars from our Madrid experiment and the ${}^3\text{He}(\alpha,\alpha){}^3\text{He}$ elastic scattering data from [BJP64, MAK93]. It can be seen that this model reproduce also the absolute and energy dependence of our data.

It is clear from Figure 6.2 that the other theoretical models do not reproduce the absolute scale. However, based on the discussion in chapter 2, and that presented in *Solar Fusion Cross Sections II* evaluation [AGR11], the theoretical calculations can be normalised to the experimental data. Therefore, in order to compare both the energy dependence and the absolute scale, normalisation factors \mathcal{N} have been obtained by minimising the χ^2 defined as:

$$\chi_{\mathcal{N}}^2 = \sum_{i=1}^{14} \frac{(\mathcal{N}S_{\text{model}}^i - S_{\text{expe}}^i)^2}{(\Delta S_{\text{expe}}^i)^2} / (\nu - 1) \quad (6.3)$$

A program using MINUIT subroutine was written for this purpose. In order to consider all our 14 data points calculations have been extrapolated up to energies of ~ 2.8 MeV. It should be clear that these extrapolations are made by considering the energy trends observed in Figure 6.2, without any physics considerations as this is used only to compare the energy dependence of our data and the calculations. Table 6.3 shows the \mathcal{N} -factors for the different models obtained using the subroutine. The extrapolated values down to zero energy $S_{34}(0)$, obtained from the normalised model calculations plotted in Figure 6.3, are also given. where the normalised models are plotted.

	Kajino et al.	Nollet	Descouvemont et al.	Neff	Kontos et al.
\mathcal{N}	1.174 ± 0.002	1.504 ± 0.003	1.374 ± 0.003	0.998 ± 0.002	1.045 ± 0.002
$S_{34}(0)$	0.656	0.601	0.702	0.592	0.577
$\chi_{\mathcal{N}}^2$	0.99	0.73	1.01	0.69	0.71

Table 6.3: The \mathcal{N} -factors defined in expression 6.3 for the representative models and S -factors extrapolated to zero energy $S_{34}(0)$.

The $\chi_{\mathcal{N}}^2$ values in the last row indicate the goodness of different models fits to our experimental data, i.e. how well the representative theoretical models reproduce the energy dependence seen in our results. All values are around one and therefore, we can say that after normalisation all models reproduce the energy dependence in our energy region. However, they quote very different $S_{34}(0)$ values. This highlight different energy dependence in lower E_{CM} range for these models.

It is worth noting that the Kontos et al. R-matrix analysis already includes in their fit our three points with lowest errors [CGNB12]. Indeed, they used a 0.976 normalisation factor to our three points in order to get an optimal fit to all the given experimental data. According to all the results presented in this thesis work, this normalisation factor should be increased. On the other hand they used also ERNA data, which also constrain the normalisation factor. The ab-initio calculation by Neff reproduce our results rather well without any normalisation factor ($0.998 \pm 0.002 \sim 1$).

The normalised theoretical models are plotted together with all the modern data in Figure 6.4. As can be seen the neither Kajino nor Descouvemont model can reproduce the energy dependence of our data and the Weizmann and low energy data from LUNA (violet and red stars points) at the same time. The same argument can be observed from Nollet calculations, although the energy dependence is better reproduced. Therefore we argue that the Neff ab-initio and the Kontos et al. R-matrix fit are the once best reproducing the energy dependence over the range. For Neff calculations, the difference between the $S_{34}(0)=0.593$ keV b before and the 0.592 keV b value after the normalisation are negligible. However, for kontos et al. $S_{34}(0)=0.554$ keV b and a 7% difference is observed after normalisation

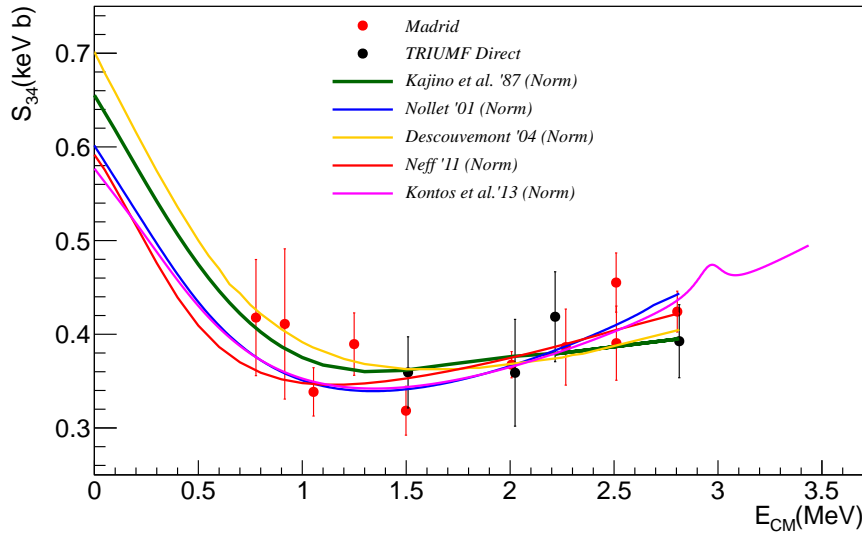


Figure 6.3: Theoretical models normalised with the \mathcal{N} -factors in Table 6.3.

($S_{34}(0)=0.577\pm 0.001$ keV b). It is worth pointing that among the new experimental data in literature only those from LUNA are measured in the lowest energy region, which are constraining the energy dependence at this energy. New astrophysical S-factors in the range of $E_{\text{CM}}=100\text{-}300$ keV by using, for example, the *direct counting recoil technique* are recommended in order to better validate the present situation.

The agreement between the Weizmann [NHNEH04] and the current Madrid work experiments at around 1 MeV, which were performed using the same setup, supports the reliability of the other points in the activation setup. However, none of the representative models can explain both results in a fully consistent manner. For example, an analysis of the Weizmann data and our three points at ~ 1 , ~ 2 and ~ 2.8 MeV from Madrid experiment using Neff model gives $\chi^2 \sim 18$ (of which ~ 14 comes from the data point at 950 keV). This is evident in Figure 6.4, where the blue triangle is away from the red curve by more than 2σ .

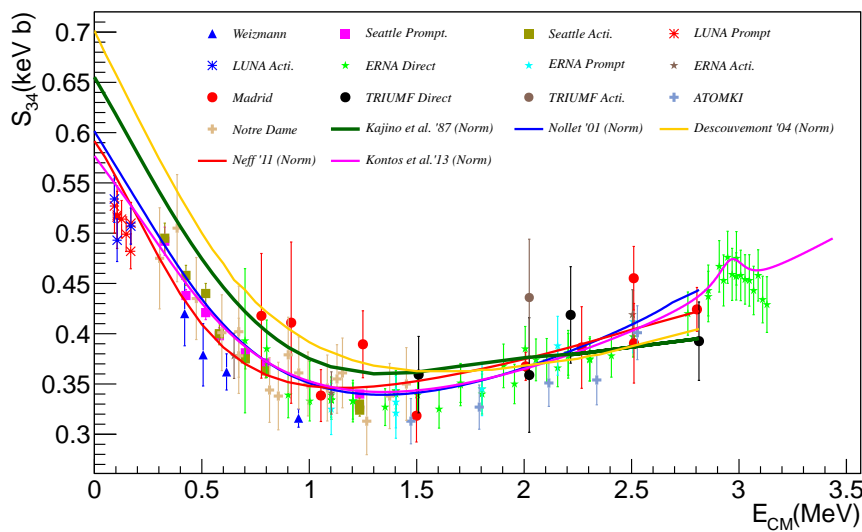


Figure 6.4: The modern experimental data for the ${}^3\text{He}(\alpha, \gamma){}^7\text{Be}$ reaction together with the theoretical calculations normalised to our experimental results.

6.4 S_1/S_0 Ratio and γ -rays Angular Distributions

For TRIUMF experiment, the S_1/S_0 ratios, i.e. the ratios given the probability of first excited state in ${}^7\text{Be}$ getting populated by the direct capture state relative to the ground state, are obtained by fitting the simulated intensities of the two gamma peaks ($\gamma_{429}/\gamma_{g.s.}$) with those from experimental spectra. It is worth noting that in both cases the γ spectra are taken in coincidence with recoils detected in the focal plane DSSSD detector (see section 4.5.5). The resulting S_1/S_0 ratios are shown in Table 4.19 and in Figure 6.5 together with the previous modern data. As can be seen, we have determined the branching ratio at the highest E_{CM} so far, that points to a energy independent nature of S_1/S_0 in the entire range between 1 and 3 MeV.

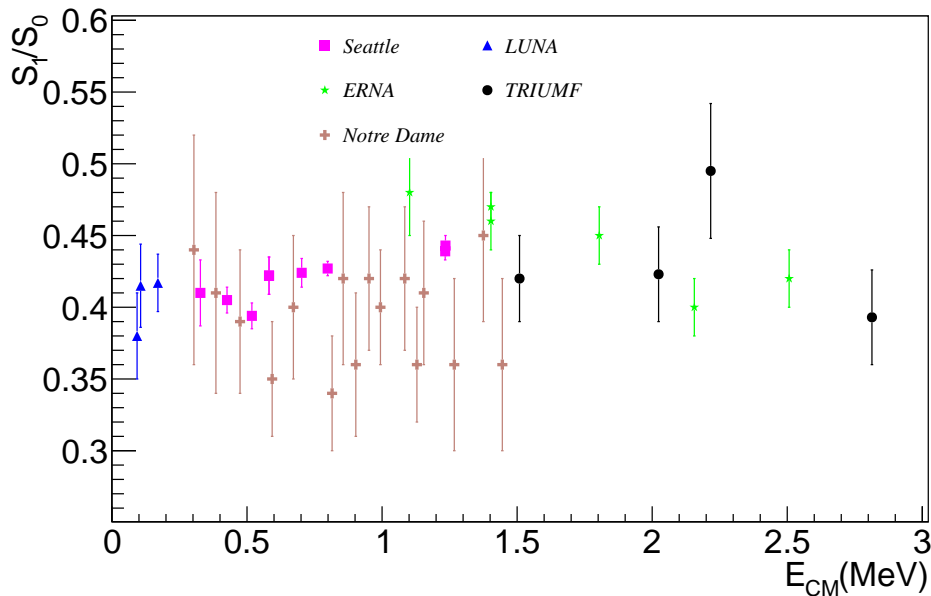


Figure 6.5: S_1/S_0 ratios obtained using the prompt- γ spectra by the BGO surrounding the gas target in our TRIUMF experiment (black dots). For a comparison, existing data are also shown.

These results should be treated with caution as the branching ratios in the simulations are obtained assuming an isotropic γ -ray emission. The recoil angle and thus the acceptance depends on the angular distribution of the emitted γ -ray therefore, different γ -ray distributions for the two γ -rays would imply different corresponding acceptances and S_1/S_0 ratios would be different. Therefore, the simulations we considered the evaluated S_1/S_0 values from [CD08], and the variations in S_1/S_0 have been taken as potential uncertainties in the astrophysical factors. However, the changes in the acceptance due to the variations in the γ -ray angular distributions (see section 4.5.6) are within the systematic errors when varying other parameters. Therefore, we can consider the branching ratios obtained assuming isotropic angular distributions and assume the systematic uncertainties in the acceptance. Thus, in our error bars in Figure 6.5 are displayed both statistical contributions and the systematic contributions.

In order to get further insight in the angular distribution, a comparison of the experimental and simulated BGO hit-maps assuming both isotropic angular distribution and those from Parker and Tombrello [PK63] was performed (see Tables 4.7 and 4.22). No big changes are observed, but our astrophysical factors had the corresponding uncertainty contributions. A systematic variation of the angular distributions coefficients would lead to better agreement between the experimental and the simulated BGO-hit maps. The resulting γ -angular distribution coefficients would constrain the theoretical models. But, on the other hand, we could not use all γ -events due to the background in the BGO detectors, i.e. we can consider only those in coincidence with ${}^7\text{Be}$ recoils. This fact would introduce an error from the acceptance in the obtained coefficients. A new experiment aiming to

precisely determine the angular distribution i.e. constraining the coefficients in expression 4.5, is planned by our collaboration.

6.5 Impact on Astrophysics

The $S_{34}(0)$ value, obtained using the FMD model calculations, [Nef11] and Kontos et al. R-matrix fit [KUD13] have a direct influence on the predictions of the Big-Bang Nucleosynthesis and of the Standard Solar Model.

- In order to evaluate and compare the impact on the standard solar model, we consider the value for $S_{34}(0)=0.56$ keV b recommended in the revision *Solar Fusion Cross Section II* [AGR11]. Our value of 0.577 keV b considering the renormalization of Kontos et al. is $\sim 3\%$ larger and translates to a $\sim 2.61\%$ and $\sim 2.45\%$ increase in the solar neutrino fluxes from ${}^7\text{Be}$ ($\phi_\nu({}^7\text{Be})$) and ${}^8\text{B}$ ($\phi_\nu({}^8\text{B})$) calculated from the expressions in [CD08]. The R-matrix fit from Kontos et al. including three of our points from Madrid experiment estimates $S_{34}(0)=0.554$ keV b and therefore, practically no such deviations in the neutrino fluxes are estimated.

The changes are higher if we consider the normalised value from Neff model [Nef11] of 0.592. This value is very close to the one obtained without any normalisation (0.593) and therefore we can consider this model as the one that best reproduce our results. On the other hand it should be recalled that this model is based on ab-initio calculation thus, without considering any of the experimental data it can reproduce both phase shifts and capture reaction cross sections. The increase of 5.89% in the $S_{34}(0)$ value compared to that from [AGR11] translates into an 5.05% and 4.75% in $\phi_\nu({}^7\text{Be})$ and $\phi_\nu({}^8\text{B})$, respectively.

- Concerning to the BBN it was already discussed that the solution to the ${}^7\text{Li}$ problem will not be solved by means of the ${}^3\text{He}(\alpha,\gamma){}^7\text{Be}$ reaction. However, the recommended $S_{34}(0)$ values have a direct impact on the estimations of the primordial ${}^7\text{Li}$ abundance. A calculation of a new primordial ${}^7\text{Li}$ abundance is out the scope of this work, however a qualitative analysis can be done. According to [DGK09], a primordial ${}^7\text{Li}$ abundance of ${}^7\text{Li}/\text{H}=(5.4\pm 0.3) 10^{-10}$ is obtained with $S_{34}(0)=0.57$ keV b. This abundance is factor 3 or more larger than the observational values. In our case the $S_{34}(0)$ is a 3.86% larger than that considered in [DGK09] and therefore, the corresponding primordial ${}^7\text{Li}$ abundance results to become even larger than the current value, thus worsening the problem (see for example [CFO08]).

6.6 Future work

The present situation of the ${}^3\text{He}(\alpha,\gamma){}^7\text{Be}$ reaction is far from being settled from neither theoretical nor experimental data. The situation at around $E_{\text{CM}} \sim 1$ MeV is worth pointing where the theoretical models start to deviate. A lot of experimental points around this energy agree between themselves when the uncertainties are taken into account. However, the Neff calculation, which better reproduce the S-factor at higher energies, deviates from the precise data of Weizmann at 950 keV by $\sim 4\sigma$. Moreover, this model cannot reproduce the absolute scale of the S-factor for the ${}^3\text{H}(\alpha,\gamma){}^7\text{Li}$ reaction. On the other hand, the experimental data of this reaction were obtained more than 20 years ago. Therefore new experimental information is required in order to constrain the theoretical models and thus the S_{34} extrapolation to zero energy. Our collaboration plans to develop new experiments in order to constrain the the experimental information of the ${}^3\text{He}(\alpha,\gamma){}^7\text{Be}$ reaction.

One of our aims is to determine the experimental cross section of the ${}^3\text{H}(\alpha,\gamma){}^7\text{Li}$ **mirror reaction** using ${}^3\text{H}$ implanted targets [WRH00], as none of the calculations can simultaneously reproduce the energy dependence and absolute value of both this reaction and the ${}^3\text{He}(\alpha,\gamma){}^7\text{Be}$ reaction. Moreover, the previous experiments studying this reaction were done using ${}^3\text{H}$ targets of only $1\mu\text{g}/\text{cm}^2$. This measurements would give more accurate results due to the higher number of target atoms with no target deterioration.

One of our other objectives is to determine the prompt γ -rays angular distributions for both ${}^3\text{He}(\alpha,\gamma){}^7\text{Be}$ and ${}^3\text{H}(\alpha,\gamma){}^7\text{Li}$ reactions. For that we plan to use Germanium detectors from arrays such as TIGRESS at TRIUMF [SAA05]. This measurements will also aim to determine the absolute cross section of both reactions by using the prompt γ technique, not used so far by our collaboration. This measurements will help us determining different partial wave (s,d, et...) contributions to this cross section and constrain theoretical extrapolations to give more accurate extrapolated $S_{34}(0)$ values.

Finally, we plan to measure the ${}^3\text{He}(\alpha,\alpha){}^3\text{He}$ elastic scattering. In chapter 2, it was discussed how potential models cannot simultaneously reproduce the phase shifts and capture cross section [Moh09], considering only the dominated extranuclear/direct capture. On the other hand, FMD model reproduces the phase shifts as well as the reaction rates but fails to explain the results for the ${}^3\text{H}+\alpha$ channel. Also, accurate data are needed for energies above $E_{\text{CM}} \sim 2$ MeV that should be compared with the calculations including the ${}^6\text{Li}+\text{p}$ break up channel, opened up at this energy. We aim to achieve $\sim 5\%$ accuracy by using a chamber placed at DRAGON target chamber, which has ports for particle detection at angles of 30, 50, 60, 70, 90, 100, 120, 130, 135 and 140 degrees with respect to the beam.

All of this, apart from a likely elastic scattering measurements of ${}^3\text{H}(\alpha,\alpha){}^3\text{H}$ with implanted targets using for example TUDA set up will lead us to consistent comparison with the calculations for both these reaction and constrain the errors in the theoretical extrapolated $S_{34}(0)$ factor.

6.7 Conclusion

In this chapter the main results and conclusions of the work in this thesis have been discussed. The experimental results obtained in both the Madrid and TRIUMF experiments have been compared with previous experimental works in the same energy region, solving the discrepancies among them and discarding those old results from Parker and Kavanagh [PK63]. Later, our results have been compared with different theoretical models, calculating the normalisation factor required to obtain good fits to our astrophysical S-factors. The ab-initio FMD model calculations by Neff [Nef11] reproduces our measurements rather well. Therefore, the adopted value of 0.593 ± 0.02 keV b is adopted as recommended value for $S_{34}(0)$. The impact on astrophysics of this adopted value has been discussed and finally the future work to be done by our collaboration have been briefly mentioned.

"Science does not know its debt to imagination"

Ralph Waldo Emerson

CHAPTER 7

CONCLUSIONS

The ${}^3\text{He}(\alpha,\gamma){}^7\text{Be}$ reaction rate is an input parameter and therefore has a determining role in the estimations of the solar neutrino flux by the SSM and the prediction of primordial ${}^7\text{Li}$ abundance predictions by the BBN. Large discrepancies are seen in the rate or S-factor for this reaction among the different data sets and theoretical calculations, specially in the range of $E_{\text{CM}}=1-3$ MeV. In this region, contributions from the non-external capture is expected, but a clear picture is missing due to the limited experimental and theoretical works.

Driven by these primary, nevertheless, very broad interest, this reaction has been studied in this thesis work, by employing two complementary experimental techniques: the *activation method* using a 5 MV tandem accelerator at CMAM laboratory in Madrid, and the *direct recoil counting method* using the DRAGON separator at TRIMF, Vancouver.

Some important outcomes are;

- Two experimental set-ups have been completely characterised in order to study the ${}^3\text{He}(\alpha,\gamma){}^7\text{Be}$ reaction
- Ten new $S_{34}(E)$ values with low systematic uncertainty have been obtained in the range of $E_{\text{CM}}=1-3$ MeV using the *activation* technique and by employing a very well controlled ${}^7\text{Be}$ production and a γ -counting setups
- Three of the measurements using the *activation* technique has special relevance due to the low statistical uncertainty and with good accuracy
- The density profile of the ${}^3\text{He}$ gas target in the DRAGON cell has been measured for the first time and can be used for future experiments at the DRAGON separator
- The charge state distribution of Be nuclei after crossing ${}^3\text{He}$ target gas have been determined for the first time, using target pressures between 1 to 6 Torr, that indicate charge state equilibrium at 1 Torr
- A very high suppression of incident beam has been measured when ${}^7\text{Be}$ recoils from the ${}^3\text{He}(\alpha,\gamma){}^7\text{Be}$ are selected by DRAGON separator

- The GEANT-3 DRAGON code has been modified and adapted to perform extensive simulations, including a new specific prompt γ -ray angular distributions which will be used for the design of future experiments
- Several tests have been performed in order to constrain the angular distribution of the prompt γ -rays. The variation of the angular distributions have been introduced as potential uncertainties in the acceptance and intense simulations with the adapted GEANT-3 code could lead to a better constrain in the coefficients of the γ -ray angular distribution
- Four new data points for the S_1/S_0 branching ratios have been determined. This includes the point corresponding to 2.8 MeV that, is the highest energy at which such data has been obtained so far
- Four new $S_{34}(E)$ values have been determined with the lowest statistical uncertainty measured so far using the *direct recoil counting* technique
- A good agreement is seen between the two data sets obtained using two independent techniques
- The results obtained in this thesis clearly agree with those from ERNA collaboration [DGK09] and fully disagree with Parker et al.'s work [PK63], in the same energy region
- Our data show very good agreement with the ab-initio FMD calculations [Nef11]
- Based on our experimental results and the ab-initio calculations we recommend a value of $S_{34}(0)=0.593$ keV b1
- From the description of our results and other experimental sets further data are yet required in a wide energy range using different techniques for a comparison of the results and consistent data evaluations
- None of the current theoretical calculations can describe simultaneously the two mirror reactions ${}^3\text{He}(\alpha,\gamma){}^7\text{Be}$ and ${}^3\text{H}(\alpha,\gamma){}^7\text{Li}$. New measurements of the mirror reaction are strongly suggested as well as elastic scattering data of the ${}^3\text{He}(\alpha,\alpha){}^3\text{He}$ reaction in order to constrain the theoretical potentials
- Due to the discrepancies between the theoretical models of the s- and p-wave contributions to the $S_{34}(E)$ factor, precise angular distributions of the prompt γ -rays are also recommended.

"It has become appallingly obvious that our technology has exceeded our humanity"

Albert Einstein

APPENDIX *A*

SILICON DETECTOR AND ELECTRONIC MODULES

Abstract: *In this appendix the general details of semiconductor detectors and in particular of this used in the Activation experiment will be briefly described. As an example of the typical electronic modules used in Nuclear Physics experiments, those used in the activation experiment in Madrid will be also detailed.*

A.1 The Silicon Detector used in Activation Experiment

In the activation experiment performed at CMAM laboratory in Madrid, a semiconductor detector was used to detect the scattered ionised ^3He beam ions.

For semiconductor materials, the energy gap between the valence and conduction bands is $\sim 1\text{eV}$. This is smaller compared to that for insulators ($\sim 5\text{eV}$) and allows creation from electron-hole pairs (electrons from the valence band are excited to the conduction band) when a charged particle crosses the material [Kno00]. At non zero temperature a small number of electrons gain enough thermal energy and get elevated to the conduction band, creating the corresponding hole. Both the hole and the electron take part in random thermal motion. To control this movement of charge, some small quantities of doped elements, with 3 (p-type semiconductor) or 5 (n-type semiconductor) valence electrons are added to the semiconductor material. When a p-type and n-type are joined, the electrons from n-type material spread through the p-type material and neutralise with the holes there, creating a depletion region (active area). An electric field is created in the depletion zone due to the effective positive charge remained in the n-type material and negative charge in the p-type. When a charged particle go through the depletion zone the created electron-holes pairs move in opposite directions following the electric field, creating an electric signal whose amplitude is proportional to the incoming energy. In practice, a reverse bias is applied to the detector in order to enlarge the active area and to increase the electric field strength for efficient charge collection. The drawback in the process is that some amount of leakage current is created.

For the activation experiment a surface silicon barrier detector reversed biased with +120V was used (see Figure A.1). These types of detectors consist of a p-type thin layer material on top of a n-type

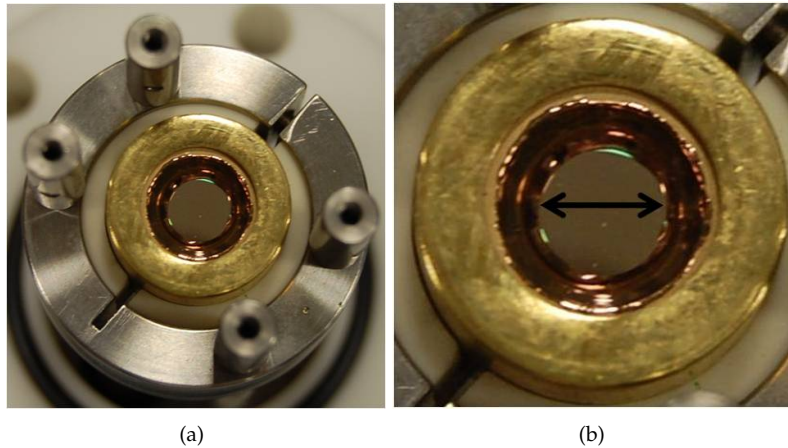


Figure A.1: (a) A photo of for the silicon surface barrier detector in the holder used in the activation experiment performed at CMAM laboratory in Madrid. (b) A schematic of the p-material, gold layer and the depletion zone that is extended due to the reverse biased.

doped silicon and an evaporated gold layer on the front surface acting as electric contact. For more details about semiconductor detectors see Chapter 11 in reference [Kno00].

A.1.1 Electronic modules

Section 3.2.1 describes both electronic chains used to process the electronic signal of the silicon detector and the integrated electric charge in the chamber. A diagram showing the processing of the different chains using electronic modules is displayed in Figure 3.8. In the following some details of the modules will be given:

Preamplifier:

The main purpose of the preamplifier is to amplify the low amplitude signals from the detector introducing minimal amount of noise and avoiding capacitance effects. The preamplifier is therefore placed as close to the detector as possible. The preamplifier used in this experiment is of *charge sensitive* type and it integrates the whole charge from the detector pulse in a capacitor removing the detector capacitance dependence. Therefore, the output voltage signal depends only on the charge and the capacitance of the capacitor. The module used in the experiment was MPR-I manufactured by MESYTEC [MES].

Amplifier:

Before being digitized, the signal must be further amplified and shaped in the amplifier. Shaping the pulse e.g. as a Gaussian function is important for different reasons: the output pulse from the preamplifier has a long tail, from 40 μs to hundreds of μs then, a new signal from the detector may come during this time. In order to avoid the overlapping between different signals this tail must be eliminated by integrating the pulse in the amplifier for an appropriate time, which corresponds to the shaping time of 1 μs for this experiment. The model used in this experiment was: *Dual Amplifier-855* manufactured by ORTEC [ORT].

Time Filter Amplifier (TFA):

This is a type of amplifier in which the pulse is shaped optimizing the pulse/noise ratio and preserving the temporal information of the signal. In this case this TFA was used to amplifies the signal to be used in the *coincidence setup*.

Constant Fraction Discriminator (CFD):

The CFD is designed to provide a timing signal corresponding to the original signal with an amplitude above a threshold relevant to the experiment. A CFD eliminates those pulses coming from the electronic noise and keeps the pulses from the detector. The signals above the threshold are transformed to one volt digital signal to be used in the rest of the *coincidence setup*. In this experiment the

threshold was set in order to avoid the electronic noise and the background radiation.

Gate and Delay Generator:

A gate and delay generator module generates a logic output signal during a period in the order of μs . The temporal gate is generated when the module receives a logic signal, in this case from the CFD. The output width of the signal is set by looking at the signal in the oscilloscope together with the signal from the amplifier and fitting the width to the same as that from the amplifier. The output gate is sent to the Linear Gate and Stretcher together with the signal from the amplifier in order to select just the “good” events to be digitised (those selected by the threshold in the CFD).

Linear Gate and Stretcher (LGS):

The module 542 manufactured by ORTEC is useful to select or discard pulses according to coincidences and temporal conditions, that is the hardware coincide is carried out. The module has two inputs, the output signal from the amplifier and the temporal gate from the *Gate and Delay Generator*. During the experiment it was used to select the coincidence pulses coming from the energy chain and those from the temporal chain where just the events above the threshold in the CFD were considered.

Multichannel Analyzer (MCA):

An MCA consist of a device which classifies and counts events in real time. The classification can be made based on different parameters of the incoming pulse (one pulse per event). Once the pulses are classified they will be accumulated together in some channels, where each channel stores events with the same characteristics. Most common MCAs classification is based on the height of the incoming pulse, *pulse height*, which in our case is proportional to the deposited energy in the detector. Once the pulses are classified in the MCA, they are saved as histograms. For this experiment the software MAESTRO®-32 version 6 developed by ORTEC ([ORT]) was used together with a multichannel buffer plate (MCB) in a computer. After the direct digitization of the output signal from LGS, the software showed the spectra online and the data were saved in ASCII format.

Charge Integrator and Scaler

A charge integrator (ORTEC-439 [ORT]) and a scaler (1145-QUAD CALER AND PRESENT COUNTER TIME [CAE]) were used to monitor and determine the beam intensity. Using the accelerator electrical ground as zero voltage, a BNC cable connected directly the reaction chamber to the charge integrator (all the appropriate elements in the chamber were electrically connected and together they acted as a Faraday Cup). The output of the integrator, as a number of pulses, (10^{-10} C/pulse) was sent to the Scaler module, where the number of pulses per second and the accumulated number of pulses for each run were displayed. The accumulated number and the count rate pulses were manually recorded each half an hour to monitor the beam stability. At the end of each measurement the number of pulses was saved.

"Never memorize something that
you can look up"

Albert Einstein

APPENDIX \mathcal{B}

KINEMATICS

Abstract: In this appendix some general expressions useful to understand the kinematics related to the capture reactions $A+B \rightarrow C+\gamma$ will be given. Firstly, the transformation between laboratory and centre of mass coordinate systems will be presented and after that the reaction kinematics will be presented.

B.1 From Laboratory to Centre of Mass System

The nuclear reactions are observed in a reference frame which is at rest in the Laboratory (*Laboratory System*). However, from a theoretical point of view the movement of the centre of mass of nuclei does not play a role in the reaction itself. Therefore, it is more convenient to use a frame in which the centre of mass of the nuclei is at rest (*Centre of Mass System*).

Figure B.1 shows the velocities involved in a radiative capture reaction in both *Laboratory* and *Centre of Mass* systems. The target is considered to be at rest in the laboratory system. In the following, variables without the prime symbol, ' , will correspond laboratory system and those with "" to the centre of mass system.

Utilising the definition of the centre of mass system, before the collision, we have it can stated that:

$$|\vec{p}'_1| = |\vec{p}'_2| \quad (\text{B.1})$$

$$\vec{V}'_1 = \vec{V}_1 - \vec{V}_{CM} \quad (\text{B.2})$$

$$\vec{V}'_2 = -\vec{V}_{CM} \quad (\text{B.3})$$

here \vec{V}_{CM} is the velocity of the centre of mass in the laboratory system and 1 and 2 represent the projectile/beam and target, respectively. After working out some algebra, we have

$$\vec{V}_{CM} = \left(\frac{m_1}{m_1 + m_2} \right) \vec{V}_1 \quad (\text{B.4})$$

$$= \left(\frac{m_1}{m_1 + m_2} \right) \sqrt{\frac{2E_1}{m_1}} \quad (\text{B.5})$$

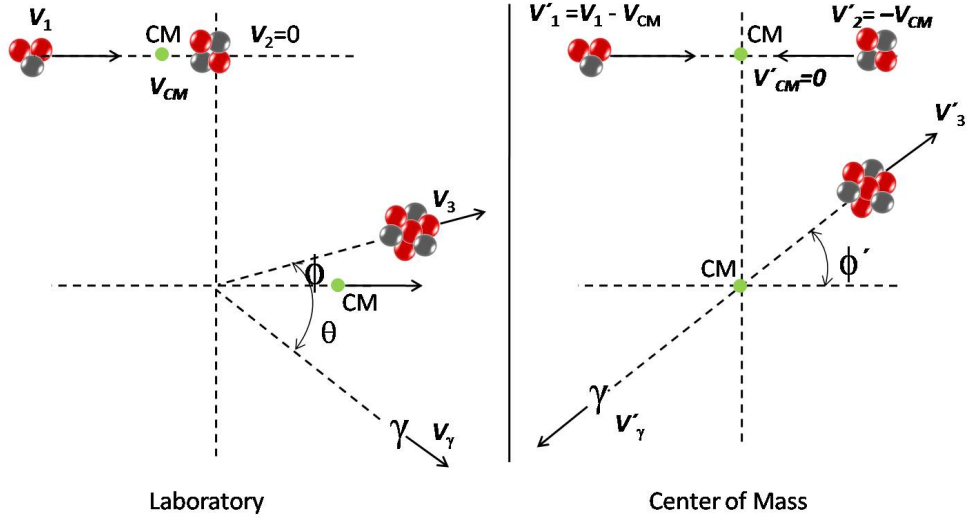


Figure B.1: Velocities involved in a capture reaction $1(2,\gamma)3$ given in the laboratory system (left) and centre of mass system (right). Top and bottom shows the situation before and after the reaction takes place, respectively. The target, 2, is at rest in the laboratory system, 1 is the incoming beam, and the green dot indicates the centre of mass position.

where the m_1 and m_2 are the masses of the interacting nuclei, the velocities of which in the centre of mass system are given by:

$$\vec{V}'_1 = \left(\frac{m_2}{m_1 + m_2} \right) \vec{V}_1 \quad (\text{B.6})$$

and

$$\vec{V}'_2 = \left(\frac{m_1}{m_1 + m_2} \right) \vec{V}_1. \quad (\text{B.7})$$

The kinetic energy in the centre of mass system is then given by

$$T' = T'_1 + T'_2 = \frac{1}{2} m_1 V_1'^2 + \frac{1}{2} m_2 V_2'^2 \quad (\text{B.8})$$

which, utilising B.6 and B.7 becomes

$$T' = \frac{m_2}{m_2 + m_1} T_1. \quad (\text{B.9})$$

Here, T_1 is the kinetic energy of the incoming beam (particle 1 in Figure B.1) in the laboratory system. The T' energy, that is, a $\frac{m_2}{m_2+m_1}$ fraction of the beam energy, is the real available energy for the nuclear reaction. Therefore, What is the rest of beam energy used for?

In order to understand where the remaining energy is utilised, let's take a look to the kinetic energy in the laboratory system and perform some algebra:

$$\begin{aligned} T &= \frac{1}{2} V_1^2 m_1 = \frac{1}{2} V_1^2 m_1 \left(\frac{m_2 + m_1}{m_2 + m_1} \right) = \frac{1}{2} V_1^2 \left(\frac{m_2 m_1 + m_1^2}{m_2 + m_1} \right) \\ &= \frac{1}{2} V_1^2 \left(\frac{m_2 m_1}{m_2 + m_1} + \frac{m_1^2}{m_2 + m_1} \right) = \frac{1}{2} V_1^2 m_1 \left(\frac{m_2}{m_2 + m_1} \right) + \frac{1}{2} V_1^2 \left(\frac{m_1^2}{m_2 + m_1} \right) \end{aligned}$$

and taking into account the expressions B.4 and B.9 it becomes

$$T = T' + T_{\text{CM}}. \quad (\text{B.10})$$

Here, T_{CM} is the kinetic energy of the centre of mass point in the laboratory system ($T_{\text{CM}} = \frac{1}{2}(m_1 + m_2)V_{\text{CM}}^2$). Therefore, from the total initial kinetic energy (T), only part is available in the nuclear reaction (T') while the rest is spent on the movement of the centre of mass. This will be transferred to the movement of the nucleus and γ radiation in the exit channel but do not participate in the reaction itself.

Conventionally, the kinetic energy in the centre of mass system before the collision is named as E_{CM} as it is the available total energy for the reaction, and in this form it has been called through this thesis. Also the E_{rel} is used in literature indicating that this is the *relative* energy of the interacting nuclei in the laboratory system.

Now, let us consider the situation after the collision. In the same way as before the collision, $V'_{\text{CM}}=0$ after the collision and then,

$$|\vec{p}'_3| = |\vec{p}'_4| \quad (\text{B.11})$$

The kinetic energy in the centre of mass system after the collision (E_{CM}^f) is given by

$$E_{\text{CM}}^f = E_{\text{CM}} + Q \quad (\text{B.12})$$

being Q the Q-value of the reaction (see expression 1.1).

Finally, the relation between the laboratory and centre mass angle of the emitted photon can be given by,

$$\cos\theta = \frac{\cos\theta' + \beta}{1 + \cos\theta'}, \quad (\text{B.13})$$

where the relativistic parameter β is defined as

$$\beta = \frac{\sqrt{T_1(T_1 + 2m_1c^2)}}{m_2c^2 + m_1c^2 + T_1} \quad (\text{B.14})$$

B.2 Kinematics for Capture Reactions in the Laboratory System

In order to obtain the kinematics expression for the radiative capture reactions, let us assume that the target nucleus 2 to be stationary in the laboratory system (Figure B.1 left). Conservation of energy and linear momentum yields the equations:

$$m_1c^2 + T_1 + m_2c^2 = m_3c^2 + T_3 + E_\gamma \quad (\text{B.15})$$

$$\sqrt{2m_1E_1} = \sqrt{2m_2T_2}\cos(\phi) + \frac{E_\gamma}{c}\cos(\theta) \quad (\text{B.16})$$

$$0 = \sqrt{2m_2T_2}\sin(\phi) + \frac{E_\gamma}{c}\sin(\theta). \quad (\text{B.17})$$

$$(\text{B.18})$$

Here, E_γ , ϕ and θ are the photon energy, and the recoil and γ -ray emission angles, respectively. After performing some algebra and eliminating T_2 and ϕ and solving for the energy of the emitted photon, we have

$$E_\gamma = Q + \frac{m_2}{m_3}T_1 + E_\gamma \frac{V_2}{c} \cos\theta - \frac{E_\gamma^2}{2m_2c^2} = Q + \frac{m_2}{m_3}T_1 + \Delta E_{\text{Dopp}} - \Delta E_{\text{rec}}. \quad (\text{B.19})$$

Therefore, the photon energy is given by the sum of four terms: (i) the Q-value, $Q = (m_1 + m_2 - m_3)c^2 = T_3 + E_\gamma - E_1$, (ii) the bombarding energy in the centre of mass system, (iii) the *Doppler shift* due to the photon is emitted by a nucleus at a speed of $V_3=V_1(m_1/m_3)$; and (iv) the recoil shift which

is caused by the energy shift on the recoiling nucleus. The numerical expressions for the two last terms are given by:

$$\Delta E_{\text{Dopp}} = 4.63367 \cdot 10^{-2} \frac{\sqrt{M_1 T_1}}{M_3} E_\gamma \cos\theta \quad (\text{B.20})$$

$$\Delta E_{\text{rec}} = 5.36772 \cdot 10^{-4} \frac{E_\gamma}{M_3} \quad (\text{B.21})$$

where, all energies are in units of MeV and the rest masses are in units of u. These two terms represent relatively small corrections.

The expression B.19 shows E_γ both on left and right hand side. When a precision of $\sim \text{keV}$ is sufficient, we have the approximated relationship $E_\gamma \approx Q + T_1(m_2)/m_3$, where the masses are given by integer u unit masses. To achieve better accuracy, the masses in B.19 should be replaced by: $m_i + E_i/(2c^2)$ and the exact relativistic expression for the photon energy is then given by:

$$E_\gamma = \frac{Q(m_1 c^2 + m_2 c^2 + m_3 c^2)/2 + m_3 c^2 T_1}{m_1 c^2 + m_3 c^2 + T_1 - \cos\theta \sqrt{T_1(2m_1 c^2 + T_1)}} \quad (\text{B.22})$$

where E_γ denotes the photon energy for the ground state transition. Thus, the recoiling nucleus kinetic energy in the laboratory system is given by

$$T_3 = Q - E_\gamma + T_1 \quad (\text{B.23})$$

On the other hand, the relation between the emission angles for the photon (θ) and recoil (ϕ) is given by

$$\phi = \arctan \left(\frac{\sin\theta}{E_\gamma^{-1} \sqrt{2m_1 c^2 T_1} - \cos\theta} \right) \quad (\text{B.24})$$

The maximum recoil angle, ϕ_{max} , is obtained when the photon is emitted perpendicular to the incident beam direction $\theta = 90^\circ$, which is given by,

$$\phi_{\text{max}} = \arctan \left(\frac{E_\gamma}{\sqrt{2m_1 c^2 T_1}} \right) \quad (\text{B.25})$$

Therefore, the recoils are emitted in forward direction into a cone of half-angle ϕ_{max} .

If an excited state in nucleus 3 is populated, then the Q-value in the above expressions must be replaced by $Q=Q_0-E_{ex}$ where Q_0 corresponds to the ground state.

B.3 From Kinetic Energy to Momentum

In the previous section, it has been derived how to obtain the kinetic energy of the recoiling nucleus in the laboratory system (expression B.23). Here, the relation between the kinetic energy and the momentum will be given. The equations relating the total relativistic energy E_3 , the kinetic energy T_3 and the momentum p_3 of a particle with mass m_3 are given by:

$$T_3 = E_3 - m_3 c^2 \quad (\text{B.26})$$

$$E_3^2 = p_3^2 c^2 + m_3^2 c^4 \quad (\text{B.27})$$

and with some rearrangement,

$$E_3 = T_3^2 + m_3^2 c^4 + 2T_3 m_3 c^2 \quad (\text{B.28})$$

and substituting for E_3 , we have

$$p_3^2 c^2 = T_3^2 + 2m_3 c^2 T_3. \quad (\text{B.29})$$

As we often use the energy expressed as MeV/u, we can define

$$T_3(\text{MeV}) = \tilde{T}_3 \cdot A \quad (\text{B.30})$$

where A is the mass number, and \tilde{T}_3 is the energy per nucleon in [MeV/u]. Noting that

$$m = A \cdot A_m \quad (\text{B.31})$$

with $A_m = 931.494 \text{ MeV}/c^2$ and inserting the two previous equations in equation B.29, we have

$$p_3 = A \sqrt{\tilde{T}_3(\tilde{T}_3 + 2A_m)} \quad \text{MeV}/c. \quad (\text{B.32})$$

"An expert is a person who has made all the mistakes that can be made in a very narrow field"

Niels Bohr

APPENDIX C

ERRORS

***Abstract:** In this appendix some procedures followed to obtain systematic and statistical error in parameters such as number of beam particles, target particles, cross section or astrophysical S-factors will be discussed. Some general concepts will be used to demonstrate how errors are extracted for the observables in this thesis and their propagation are discussed.*

In the following sections, some expressions will be given without any proof, and the reader is referred to [Tay82] and [RBKR03] for more details and extended discussion.

C.1 Systematic and Statistical Uncertainties

Systematic uncertainties are those which can not be revealed by repeating the measurements as they are related to the inaccuracies in the knowledge of various parameters. On the other hand, the statistical uncertainties will arise from overall statistical fluctuations in the measured observables over a finite amount of time and not from the lack of precision in the measuring instruments.

Statistical uncertainties are usually related to count events in a detector. Let us assume that we repeat an experiment where we count in a detector the alpha particles emitted by a standard source under the same conditions and times. The distribution of the results of the number of counts will follow a Poisson Distribution whose standard deviation (σ), is determine by:

$$\sigma = \sqrt{\mu} \tag{C.1}$$

here, σ is for a single measurement of the distribution. Therefore, in our case, where we usually do one measurement, we consider σ as the statistical uncertainty associated with the measurement.

On the other hand, **systematic uncertainties** will be related to the measurement equipment or technique, how well calibrated the system is or how stable the experimental conditions are. These uncertainties are highly important as the accuracy (how close the result of our experiment is to the

true value) of our experiment is related to how well we can control and understand the systematic uncertainties. Errors of this type have to be carefully estimated with a good understanding of the setup. Therefore, a careful characterisation of the setup to understand and minimize all possible systematic uncertainties plays an crucial role in an experiment.

C.2 Statistical Treatment of Data

The random errors, i.e. errors than can be revealed by repeating the measurements, can be treated statistically as they are considered as fluctuations in observations that yield different results each time we do the experiment. Therefore, for N measurements of a quantity x_i , the best value is given by the mean value \bar{x} , defined by:

$$\bar{x} = \frac{\sum_{i=1}^N x_i}{N} \quad (\text{C.2})$$

while the average uncertainty associated to each measurement is given by the standard deviation, defined by:

$$\sigma_x \equiv \sqrt{\frac{1}{N-1} \sum (x_i - \bar{x})^2} \quad (\text{C.3})$$

which we can adopt as the uncertainty associated to a single measurements. It could be demonstrated by performing a single measurement that we would find a probability of 68.27% , that our result will be within σ_x of the correct valued. On the other hand, it can be proved the uncertainty \bar{x} value is given by the standard deviation of the mean ($\sigma_{\bar{x}}$):

$$\sigma_{\bar{x}} = \frac{\sigma_x}{\sqrt{N}} \quad (\text{C.4})$$

C.2.1 The Normal Distribution

In order to perform statistical analyses of an experiment, several measurements are required. The distribution from the measurements are usually as histograms (x-y plots), where x -axis shows the data values and y -axis shows the number of times this measurement results in that value. The X -axis is usually divided in bins, the corresponding y -value gives the number of times the result takes a value within that range.

Typically, Normal Distribution or Gaussian Distributions are seen when fluctuations in measurements are affected only by randoms errors. After sufficient number of measurements the number of times the data takes a value above and below the "true" value will be the same. Thus, it will result in a distribution centred on the "true" X -value^a and, the larger the deviation from the "true" X -value is, the smaller the frequency it is obtained with. This normal distributions can be expressed as:

$$G(x) = \frac{N}{2\sqrt{2\pi}} e^{-(x-X)^2/2\sigma^2} \quad (\text{C.5})$$

where X is the central or "true" value, x is the value corresponding to a given measurement, σ is the width of the distribution and N is the normalization constant. An example of a Gaussian distribution with $N=1$, $\sigma=1$, and $X=0$ is shown in Figure C.1.

^aThere is no measurement which can exactly determine the correct value of any continuous variable. Thus, the true value here is the one which occurs with the highest frequency.

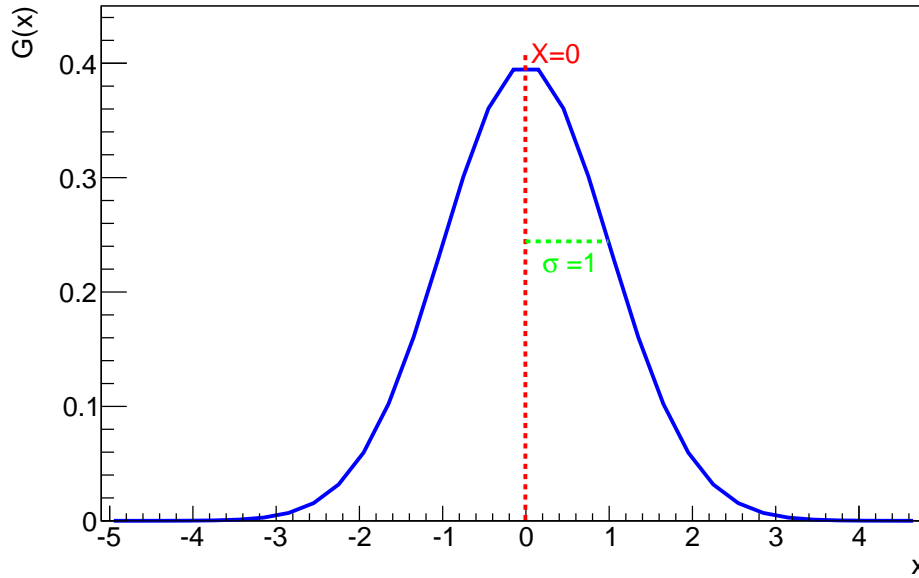


Figure C.1: Gaussian distribution with $N=1$, $\sigma = 1$, and $X=0$.

It can be proved that the Gaussian function width σ , is the standard deviation of the distribution (σ_x):

$$\sigma = \sigma_x \quad (\text{C.6})$$

with the same meaning and effect as σ_x defined in C.3 . Therefore, σ can be considered as the error to a single measurement.

It is worth mentioning that, when systematic errors are added to the random errors all values get shifted in one direction and the distribution will have a new "true" X -value shifted in the same direction.

C.3 The χ^2 Testing Method

The χ^2 testing procedure is the standard analysis to compare the results between different measurements, or between a given set of measurements and a given theory. If we make n measurements, χ^2 is usually defined as:

$$\chi^2 = \sum_{k=1}^n \left(\frac{\text{observed value} - \text{expected value}}{\text{Error}} \right)^2 = \sum_{k=1}^n \frac{(O_k - E_k)^2}{\sigma^2} \quad (\text{C.7})$$

where O_k is the measured value with a standard deviation of σ and E_k is the expected value. Often, the *reduced* χ^2 value denoted by $\bar{\chi}^2$ and defined as:

$$\bar{\chi}^2 = \chi^2/d \quad (\text{C.8})$$

is also used, where d is the number of degrees of freedom. If the value of $\bar{\chi}^2$ is around one, then the agreement between the compared values should be considered as good and if $\bar{\chi}^2$ is much larger than one then the two sets of compared values should be seen as in disagreement.

C.4 Least-squares Fits and Errors

Measurements and data analysis usually take advantage of the mathematical relationship between different variables. For example, the study in Figure 3.35, where a linear relationship is seen

between the magnetic field required to bend the ^4He beam and the pressure in the gas target. The analytical method of finding the best fit line is called *linear regression* or *least-squares fit*. Let us consider a measurement where two observables assume a linear relationship, $y_i = Ax_i + B$. The best functional fit to data, can then be given by the A and B values, which minimize the value of χ^2 , i.e.

$$\chi^2 = \sum_{i=1}^N \frac{(y_i - A - Bx_i)^2}{\sigma_{y_i}^2}. \quad (\text{C.9})$$

Minimizing χ^2 with respect to the parameters A and B , we have:

$$A = \frac{\sum_{i=1}^N w_i x_i^2 \sum_{i=1}^N w_i y_i - \sum_{i=1}^N w_i x_i \sum_{i=1}^N w_i x_i y_i}{\Delta} \quad (\text{C.10})$$

$$B = \frac{\sum_{i=1}^N w_i \sum_{i=1}^N w_i x_i y_i - \sum_{i=1}^N w_i x_i \sum_{i=1}^N w_i y_i}{\Delta} \quad (\text{C.11})$$

$$\Delta = \sum_{i=1}^N w_i \sum_{i=1}^N w_i x_i^2 - \left(\sum_{i=1}^N w_i x_i \right)^2 \quad (\text{C.12})$$

where $w_i = 1/\sigma_i^2$ introduce the weight factors for each of measurement. The errors associated to A and B are given by:

$$\sigma_A = \sqrt{\frac{\sum_{i=1}^N w_i x_i^2}{\Delta}} \quad (\text{C.13})$$

$$\sigma_B = \sqrt{\frac{\sum_{i=1}^N w_i}{\Delta}} \quad (\text{C.14})$$

The same method can be generalised for y which is expected to be a higher order polynomial in x : $y = A + Bx + \dots + Hx^n$, although the algebra becomes complex.

C.5 Error Propagation

Often measured values of a variable depends on one or more other measured variables. The relevant example from our experiment, namely, the cross section depends on the number of recoils, beam and target particles. Therefore, we should estimate the propagation of uncertainties from several measured variables (u, v, \dots) to determine the uncertainty in whatever variable x which depends on u, v, \dots . The general expression relating the variance σ_x^2 (square of the standard deviation) of the dependent variable x to the variances of u, v, \dots is given by:

$$\sigma_x^2 \approx \sigma_u^2 \left(\frac{\partial x}{\partial u} \right)^2 + \sigma_v^2 \left(\frac{\partial x}{\partial v} \right)^2 + \dots \quad (\text{C.15})$$

C.6 Error in TRIUMF Experiment

In this section, how the errors are obtained for different variables in our experiment performed at TRIUMF are detailed. The systematic and statistical uncertainties are treated separately. The final systematic (statistical) errors in the cross section or S-factor are obtained by standard error propagation with expression C.15 of the systematic (statistical) uncertainties in the observable that the cross section depend on, namely, numbers of ^3He target particles, ^4He beam particles and ^7Be recoils.

C.6.1 Errors contributions to the number of ^3He target particles

NO statistical errors are considered in the number of target particles. Taking into account the expression $N_t = 9.66 \cdot 10^{18} \frac{\ell \cdot P}{T}$, the systematic uncertainty in to N_t is obtained from standard error propagation of the uncertainties:

- $\Delta\ell = 0.5$ cm, from previous experiments and TDP measurements.
- $\Delta P = (0.1 + \sigma_P)$ Torr and $\Delta T = (1 + \sigma_T)$ k: The final values for pressure and temperature are taken as the average value of the corresponding values recorded each five minutes. However, it is worth noting here that as the pressure and temperature change during the run the average value of the "true" readings do not have the same meaning as in expression C.2 where it is assumed that the "true" value is the same and the deviations are coming from random errors. Therefore, the standard deviations of a single measurement (σ_T and σ_P) are considered as errors, instead of the standard deviation of the mean. The 0.1 Torr and 1 K systematics contributions are taken from reference [GBB04].

C.6.2 Error contributions to the number of ^4He Beam Particles

The number of beam particles in our measurements is given by (cf. section 5.3.3):

$$N_{^4\text{He}}^{\text{ob}} = \frac{R^F \cdot \text{Si-30}}{\text{Livetime} \cdot P \cdot T} \quad (\text{C.16})$$

The statistical error is obtained by standard error propagation of the statistical uncertainty associated to the Si-30 variable (area of the peak in the silicon detector) which is given by the expression C.1:

$$\sigma_{\text{Si-30}} = \sqrt{\text{Si-30}} \quad (\text{C.17})$$

The final statistical errors in N_4^{ob} are smaller than 0.5 %.

The systematic error arises from the systematic uncertainty in P and T calculated as detailed in section C.6.2 and from the systematic uncertainty in R_F from the fits shown, for example, in Figure 5.18.

C.6.3 Error contributions to the number of ^7Be recoils

The total number of ^7Be produced is given by (cf. section 3.3.2.7):

$$Y_{^7\text{Be}} = \frac{Y_{\text{DSSSD}}}{t_\ell \cdot q_f \cdot \epsilon_{\text{DRAGON}} \cdot \epsilon_{\text{DSSSD}}} \quad (\text{C.18})$$

The statistical error in the $Y_{^7\text{Be}}$ can be obtained by propagating i) the error in Y_{DSSSD} i.e. the ^7Be nuclei detected in the DSSSD, which is given by:

$$\sigma_{Y_{\text{DSSSD}}} = \sqrt{Y_{\text{DSSSD}}} \quad (\text{C.19})$$

and ii) the statistical uncertainty associated with ϵ_{DRAGON} shown in Table 4.23.

The systematic errors propagated are:

- 0.10% error associated with ϵ_{DSSSD} .
- The systematic uncertainty associated with ϵ_{DRAGON} shown in table 4.23.
- The error in t_ℓ calculated from the total and acquired triggers.

- The errors in q_f are obtained from the CSD distribution measurements.

The two facts, namely the CSD are energy dependent, and the recoils are created with a distribution in energy (see Table 5.10) have been also taken into account. Figure C.21 shows the charge state fractions within their errors at different energies for both the 2^+ (left) and 3^+ (right) charge states of ^9Be . Enclosed in circles are the values considered in the data analysis (see Table 3.6) and the green dots are values for the "highest" and "lowest" recoil energies for different sets of S_{34} capture data at different E_{CM} . As can be seen, for the four cases the charge state fractions associated to the "highest" and "lowest" recoil energies, (i.e. the limits indicated by the green points) are always within the error bars of the mean values. This, added to the fact that most of the recoils are created along with a 90° γ emission (assuming isotropic prompt γ -ray angular distributions), which should have the mean CSD values, makes us argue that the uncertainty in q_f to be the same as that for the mean values.

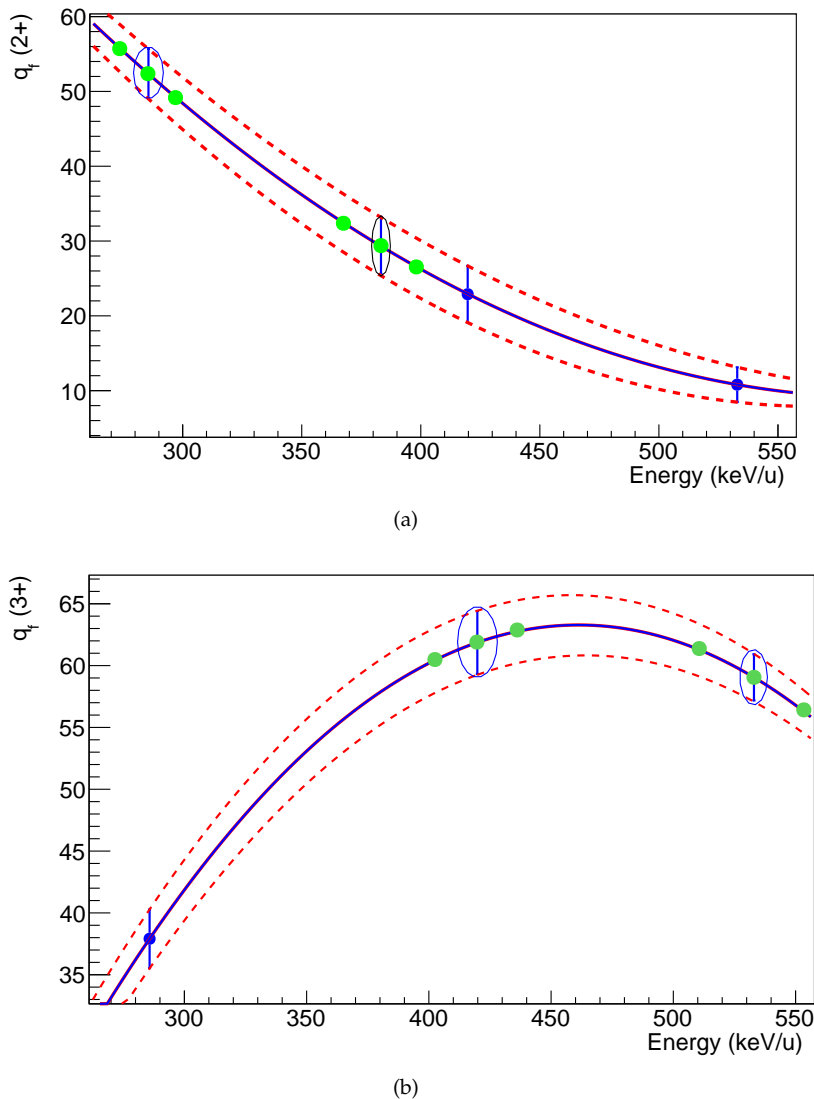


Figure C.2: Charge state fractions for 2^+ and 3^+ for the different recoils energies. Enclosed in circles are the mean values of the different q_f used corresponding to the energy of the recoil created at the center of the gas target with the prompt γ -ray emitted at 90° . The green dots indicates for the maximum and minimum recoils energies the charge state fraction obtained by extrapolation of the measured values.

C.6.4 Error contributions to the $S_{34}(E)$ factor

Different error contributions to the astrophysical factors obtained from the direct counting experiment at TRIUMF are shown in Table C.1 (systematics) and C.2 (statistical).

$E_{4\text{He}}$ MeV	$\Delta S_{34}^{\text{sy}t}$ (%)	ΔE (%)	$\Delta^4\text{He}$ (%)	$\Delta^3\text{He}$ (%)	$\Delta\ell$ (%)	(%) $\Delta P, \Delta T$ (%)	(%)Be (%)	Δq_f (%)	$\Delta\epsilon_{\text{DRAGON}}$ (%)	$\Delta t_\ell, \Delta\epsilon_{\text{DSSSD}}$ (%)
~ 6.5	$\begin{smallmatrix} +6.96 \\ -12.57 \end{smallmatrix}$	0.03	1.23	4.62:	4.07	2.19	$\begin{smallmatrix} +5.06 \\ -11.62 \end{smallmatrix}$	3.17	$\begin{smallmatrix} +3.94 \\ -11.18 \end{smallmatrix}$	0.26
~ 5.2	$\begin{smallmatrix} +10.98 \\ -11.91 \end{smallmatrix}$	0.06	0.60	5.40:	4.07	3.56	$\begin{smallmatrix} +9.53 \\ -10.59 \end{smallmatrix}$	4.12	$\begin{smallmatrix} +8.60 \\ -9.76 \end{smallmatrix}$	0.12
~ 3.5	$\begin{smallmatrix} +10.04 \\ -11.00 \end{smallmatrix}$	0.09	0.45	4.97:	4.07	2.87	$\begin{smallmatrix} +8.71 \\ -9.80 \end{smallmatrix}$	6.37	$\begin{smallmatrix} +5.94 \\ -7.45 \end{smallmatrix}$	0.22
~ 4.7	$\begin{smallmatrix} 14.80 \\ 17.02 \end{smallmatrix}$	0.06	0.98	5.64:	4.07	3.92	$\begin{smallmatrix} +13.65 \\ -16.03 \end{smallmatrix}$	13.0	$\begin{smallmatrix} +4.15 \\ -9.37 \end{smallmatrix}$	0.12

Table C.1: Systematic errors contributions to the astrophysical S -factor from the Direct Recoil Counting experiment at TRIUMF. The second column shows the total systematic uncertainties, while the columns titled as ΔE , $\Delta^4\text{He}$, $\Delta^3\text{He}$ and $\Delta^7\text{Be}$ show individual contributions from the energy, number of beam particles, number of target particles, and number of recoils to $\Delta S_{34}^{\text{sy}t}$, respectively. The columns titled as $\Delta\ell$, ΔP , ΔT give error contributions from the target length, pressure and temperature, respectively to the systematic uncertainty in the number of $\Delta^3\text{He}$ target particles. The columns titled as Δq_f and $\Delta\epsilon_{\text{DRAGON}}$, give contributions from the measured charge state fractions and DRAGON efficiencies, respectively to the systematic uncertainty in the number of ^7Be recoils.

Run	$E_{4\text{He}}$ MeV	$\Delta S_{34}^{\text{stat}}$ (%)	$\Delta^4\text{He}$ (%)	$\Delta^7\text{Be}$ (%)	$\Delta\epsilon_{\text{DRAGON}}$ (%)	ΔY_{DSSSD} (%)
2011	~ 6.5	1.24	0.37	1.18	1.05	0.55
	~ 5.2	0.92	0.17	0.91	0.87	0.27
	~ 3.5	0.77	0.17	0.75	0.59	0.48
2013	~ 4.7	0.95	0.07	0.94	0.84	0.44

Table C.2: Systematic error contributions for the astrophysical S -factor from Direct Recoil Counting experiment at TRIUMF. The third column shows the total statistical uncertainties. The columns titled as $\Delta^4\text{He}$, and $\Delta^7\text{Be}$ show the contributions from number of beam particles and number of recoils to $\Delta S_{34}^{\text{stat}}$ respectively. The columns titled as $\Delta\epsilon_{\text{DRAGON}}$ and ΔY_{DSSSD} , give individuals contributions from DRAGON efficiency and the ^7Be counts in the DSSSD to the statistical uncertainty in the number of ^7Be recoils,

SPANISH SUMMARY/RESUMEN EN CASTELLANO

Abstract: *El trabajo presentado en esta tesis versa sobre el estudio de la sección eficaz de la reacción nuclear de interés astrofísico ${}^3\text{He}(\alpha,\gamma){}^7\text{Be}$. En este apéndice se presentará, en castellano, un amplio resumen del trabajo presentado. En primer lugar se motivará el trabajo desarrollado. Seguidamente se detallarán las técnicas experimentales utilizadas para determinar la sección eficaz de la reacción así como el análisis y los resultados. Por último, se discutirán los resultados obtenidos y su impacto.*

D.1 Estudios sobre la Reacción ${}^3\text{He}(\alpha,\gamma){}^7\text{Be}$: Motivación

La sección eficaz de la reacción nuclear ${}^3\text{He}(\alpha,\gamma){}^7\text{Be}$ juega un papel relevante en dos escenarios astrofísicos importantes: las predicciones de la abundancia del ${}^7\text{Li}$ primordial en el universo a través de la *Nucleosíntesis Estándar del Big-Bang* (SBBN por sus siglas en inglés), y las estimaciones del flujo de neutrinos solares procedentes de las desintegraciones del ${}^8\text{B}$ y ${}^7\text{Be}$ a través del *Modelo Solar Estándar* (SSM por sus siglas in inglés).

Desde los primeros estudios llevados a cabo por Holmgren y Johnston [HJ59], intensos esfuerzos se han llevado a cabo tanto experimental como teóricamente con el objetivo de determinar la sección eficaz de dicha reacción de forma precisa. Actualmente, el estudio de esta reacción sigue siendo objeto de investigaciones con el objetivo de extraer el factor astrofísico $S_{34}(E)$ con una incertidumbre reducida.

D.1.1 La nucleosíntesis del Big-Bang y el problema del ${}^7\text{Li}$ primordial

Actualmente la teoría del Big-Bang es el modelo cosmológico más aceptado debido a que explica tres aspectos importantes: la expansión del Universo, la radiación de fondo microondas y la nucleosíntesis primordial.

En el marco de la teoría del Big-Bang y del modelo estándar de partículas, la SBBN explica la producción de los primeros elementos en el universo entre los 200 y 1000 s después de la explosión

del Big-Bang. La Figura D.1 muestra la cadena principal de reacciones involucradas en la producción de los elementos primordiales. Ésta comenzó con la reacción $p(n, \gamma)d$, la cual generó el deuterio d , semilla para la producción del resto de elementos. Los principales elementos remanentes de esa nucleosíntesis primordial fueron, d , tritio (t), ${}^3\text{He}$, ${}^4\text{He}$ y ${}^7\text{Li}$; la inexistencia de núcleos estables con $A=8$ evitó la presencia de isótopos primordiales más pesados en abundancias relevantes. Para las condiciones de temperaturas durante la SBBN, el intervalo de energías del pico de Gamow para la reacción ${}^3\text{He}(\alpha, \gamma){}^7\text{Be}$ es $400 \geq E_{\text{CM}} \geq 180$ keV, las cuales son accesibles en los laboratorios.

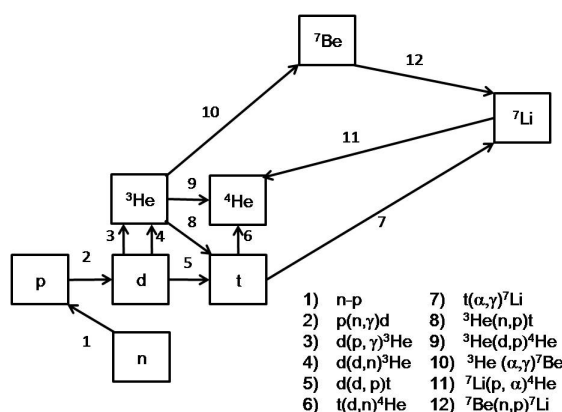


Figure D.1: Cadena de las principales reacciones involucradas de la Nucleosíntesis del Big Bang.

La Figura D.2 muestra una comparativa de las estimaciones de las abundancias calculadas con la SBBN y los valores inferidos de la observación directa.

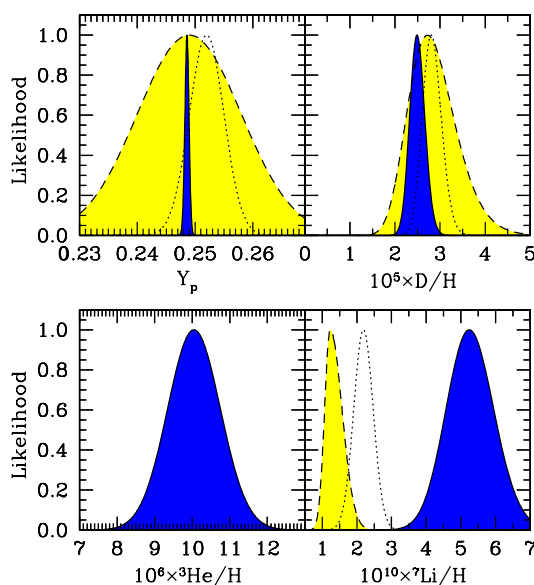


Figure D.2: Probabilidades calculadas y observadas para la abundancia de los elementos primordiales ${}^4\text{He}$ (Y_p), D/H , ${}^3\text{He}/H$ y ${}^7\text{Li}/H$. Las regiones en azul muestran las probabilidades estimadas con el SBBN. Las regiones en amarillo y las punteadas muestran las probabilidades obtenidas a partir de la observación directa de diferentes emplazamientos astrofísicos. Para la abundancia del ${}^7\text{Li}$, (${}^7\text{Li}/H$), la región amarilla muestra los valores inferidos a partir de la observación de estrellas con halo y la función punteada muestra la determinación mediante la observación de clusters globulares de estrellas. La Figura ha sido obtenida de [CFO08]

Como puede observarse las abundancias estimadas de los elementos primordiales de d , ${}^3\text{He}$ y ${}^4\text{He}$ están en acuerdo con aquellos valores inferidos de las observaciones astrofísicas directas. Sin

embargo, las estimaciones sobre la abundancia del ${}^7\text{Li}$ primordial son aproximadamente tres veces superiores a las observadas. Éste es el conocido como *Problema del ${}^7\text{Li}$ primordial*.

El origen de esta discrepancia es aún desconocido. Diferentes soluciones han sido sugeridas incluyendo física más allá del modelo estándar. También se ha discutido ampliamente si la discrepancia puede ser debida a una mala estimación en las tasas de reacciones nucleares implicadas. El ${}^7\text{Li}$ es producido principalmente a través de la reacción ${}^3\text{He}(\alpha,\gamma){}^7\text{Be}$ y posterior ${}^7\text{Be}(n,p){}^7\text{Li}$ y destruido mediante ${}^7\text{Li}(p,\alpha){}^4\text{He}$. En concreto, ${}^7\text{Li}/\text{H} \propto S_{34}^{0.96}$ donde S_{34} es el factor astrofísico de nuestra reacción de interés. A pesar de que actualmente no se cree que una determinación precisa de la tasa de reacción de ${}^3\text{He}(\alpha,\gamma){}^7\text{Be}$ vaya a resolver el *problema*, reducirá la incertidumbre en los modelos. Por ejemplo, la evaluación de nuevos datos de la sección eficaz de dicha reacción, [CFO08], mostró un desplazamiento de un 16% en el valor central de la abundancia del ${}^7\text{Li}$ primordial.

D.1.2 El sol y el problema de los neutrinos solares

Como la estrella más cercana, el Sol, es la estrella más estudiada. Las condiciones presentes allí hacen del Sol un emplazamiento perfecto para la producción de numerosos procesos nucleares. El origen de estos procesos, desde un punto de vista de nucleosíntesis estelar, es explicado por el *Modelo Solar Estándar*.

La Figura D.3 muestra las principales reacciones nucleares en el Sol agrupadas en la cadena protón-protón, en la cual se genera el 99% de la energía solar, y el ciclo CNO que supone el 1% restante.

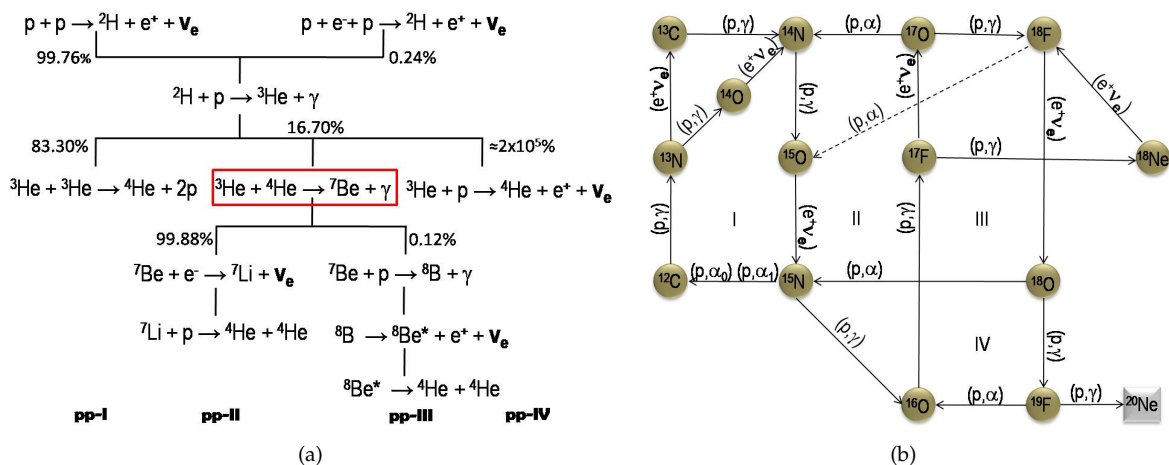


Figure D.3: Principales reacciones nucleares en el Sol agrupadas en (a) cadena protón-protón, y (b) ciclo CNO.

Entre otros observables, el SSM predice el flujo de neutrinos solares. Históricamente, las estimaciones de SSM predecían una producción de neutrinos solares de alta energía de aproximadamente el triple comparadas con las detecciones directas en la Tierra. Estas grandes discrepancias fueron parcialmente resueltas mediante la postulación y posterior comprobación de las *oscilaciones de neutrinos*. Actualmente, las estimaciones del flujo de neutrinos solares por el SSM, mostradas en la Figura D.4, no son lo suficientemente precisas. Concretamente, el flujo de neutrinos de alta energía procedente de la desintegración del ${}^7\text{Be}$ y ${}^8\text{B}$ es directamente proporcional al factor astrofísico de nuestra reacción en la forma: $\phi_\nu({}^7\text{Be}) \propto S_{34}(0)^{0.86}$ y $\phi_\nu({}^8\text{B}) \propto S_{34}(0)^{0.81}$, respectivamente [CD08]. Por tanto una determinación precisa de la tasa de reacción es determinante para reducir la incertidumbre asociada al flujo de neutrinos. Concretamente, de la incertidumbre asociada a los parámetros nucleares de entrada del SSM, la sección eficaz de la reacción ${}^3\text{He}(\alpha,\gamma){}^7\text{Be}$ es la de segunda mayor influencia.

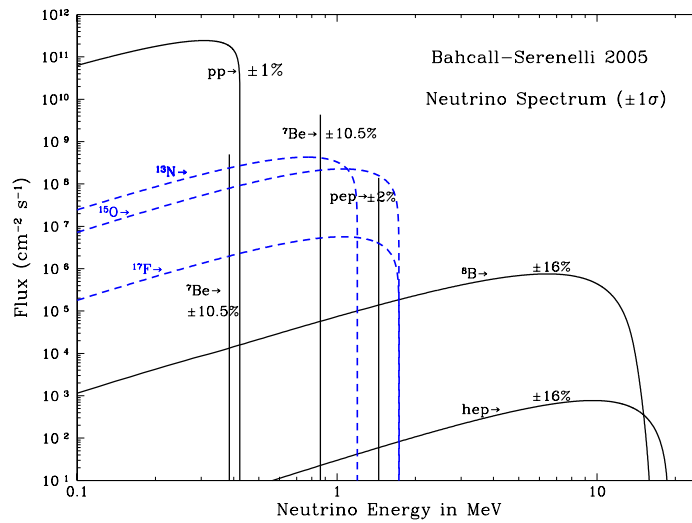


Figure D.4: Espectro de neutrinos solares estimado por el SSS [BP95].

D.1.3 Estudios experimentales previos

Dada la importancia de la reacción ${}^3\text{He}(\alpha,\gamma){}^7\text{Be}$ en el SSM y BBN, la sección eficaz de esta reacción se ha determinado experimentalmente utilizando cada vez técnicas con mayor precisión. La Figure D.5 muestra un esquema de como se produce la reacción reacción y la posterior desintegración del ${}^7\text{Be}$.

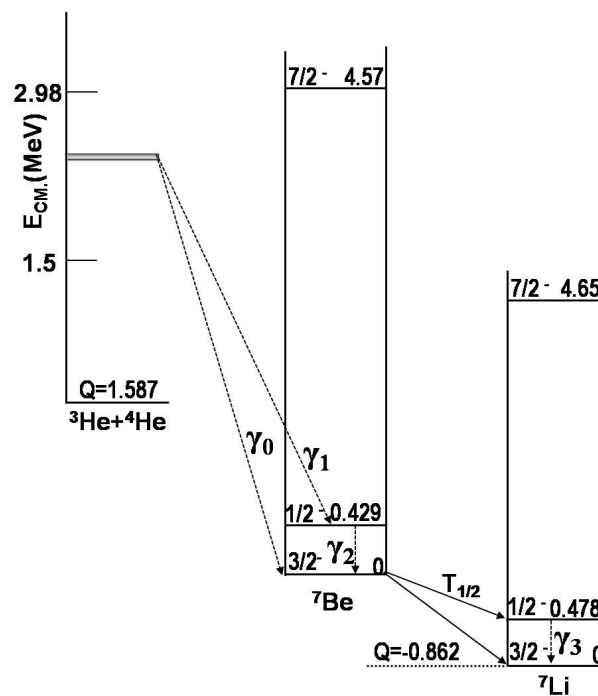


Figure D.5: Esquema de la reacción ${}^3\text{He}(\alpha,\gamma){}^7\text{Be}$ con la emisión de la radiación gamma directa y la posterior desintegración del ${}^7\text{Be}$. Las energías están expresadas en MeV.

La **captura radiativa** del ${}^3\text{He}$ y ${}^4\text{He}$ forma un núcleo de ${}^7\text{Be}$ siendo el valor-Q de la reacción 1.587(1) MeV. En el proceso de fusión se emite un rayo γ con dos energías disponibles dependiendo de que se pueble el estado fundamental (γ_0) o el primer estado excitado (γ_1) en el ${}^7\text{Be}$. En el último caso la desexcitación del estado se produce mediante la emisión de un rayo γ de 429 keV quedando el ${}^7\text{Be}$ en el estado fundamental. El ${}^7\text{Be}$ formado es un núcleo inestable que decae mediante el proceso de captura electrónica con una vida media de 53.24(4) días. El valor-Q de la reacción es 862 keV y con una tasa de 10.44% la desintegración puebla el primer estado excitado del ${}^7\text{Li}$ a 478 keV, el cual se desexcita emitiendo un rayo γ (γ_3) de esa energía.

En función del producto de reacción detectado, tres técnicas experimentales diferentes son usadas para determinar la sección eficaz de la reacción. En el *Método de Activación* se detecta la radiación gamma procedente de la desexcitación del ${}^7\text{Li}$ tras la colección los núcleos de ${}^7\text{Be}$ producidos. En el *Método de Detección Directa* los núcleos de ${}^7\text{Be}$ son contados directamente. En el *Método de Radiación- γ Directa* se detecta la radiación γ directa producida en la reacción. La Figura D.6 muestra los datos existentes del factor astrofísico previos a la investigación presentada aquí agrupados en función de la técnica utilizada.

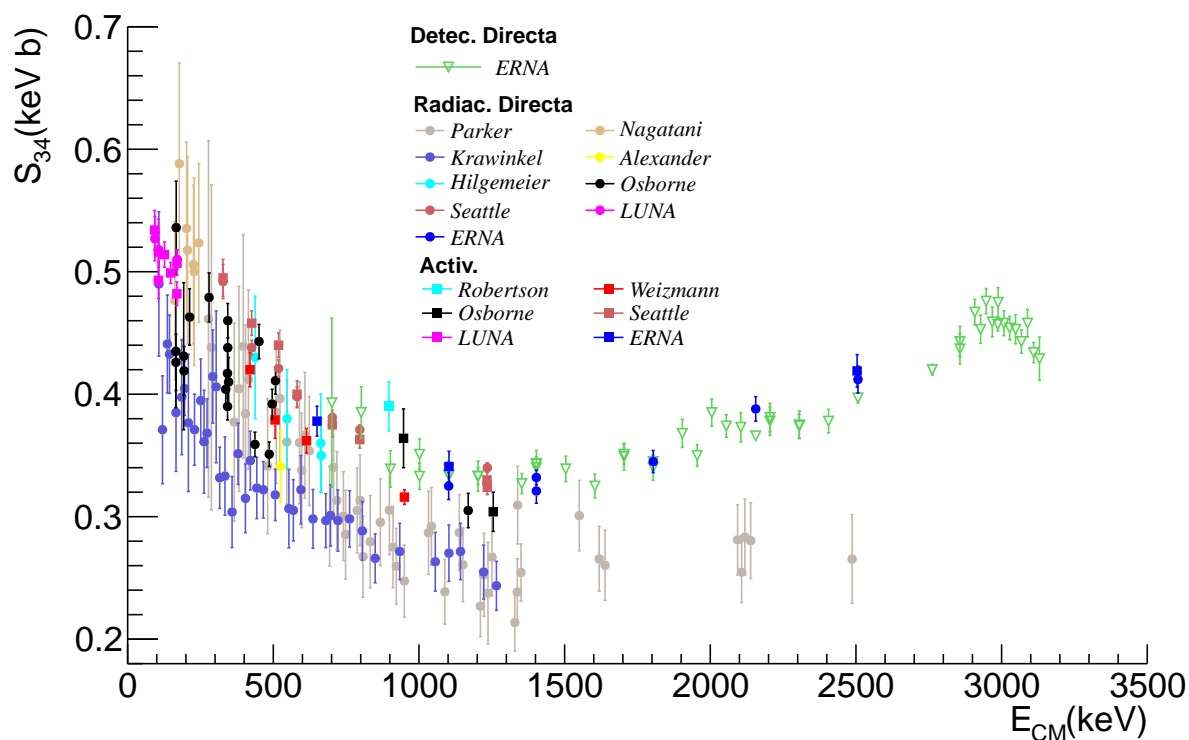


Figure D.6: Valores del factor-S astrofísico para la reacción ${}^3\text{He}(\alpha,\gamma){}^7\text{Be}$ (S_{34}). Los datos obtenidos utilizando el Método de Radiación- γ Directa, Método de Activación y el Método de Detección Directa se muestran en círculos, cuadrados y triángulos, respectivamente.

El rango de energías cubierto en los experimentos previos está entre 93 y 3130 keV. Solo las medidas de Parker y Tombrello [PK63] y la colaboración ERNA [DGK09] realizaron medidas a energías superiores a 1200 keV, las cuales muestran una gran discrepancia entre ellas. Resolver esta discrepancia es uno de los objetivos del trabajo presentado en esta tesis.

Los datos experimentales utilizan diferentes modelos teóricos para obtener el valor del factor $S_{34}(0)$. Una comparativa entre los diferentes valores del factor $S_{34}(0)$ obtenidos mediante las diferentes técnicas experimentales se muestra en la Figura D.7. Como puede observarse existe una gran discrepancia entre los diferentes valores.

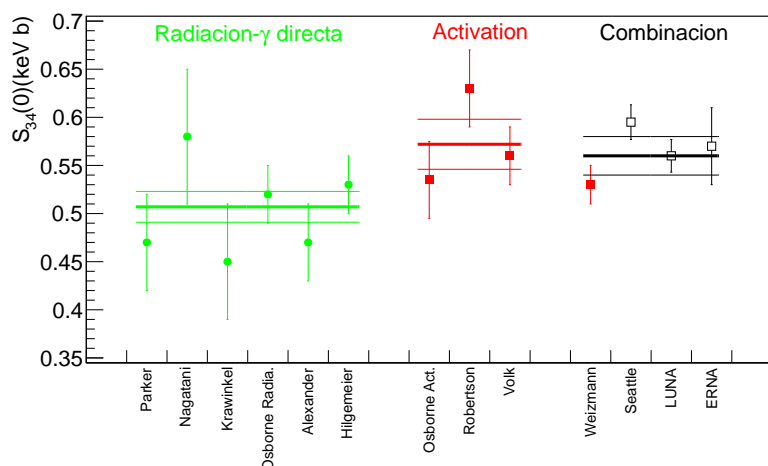


Figure D.7: Valores del factor $S_{34}(0)$ obtenidos a partir de las diferentes medidas experimentales previas al trabajo presentado en esta tesis. Los resultados fueron obtenidos mediante el método de radiación γ directa (círculos verdes), método de activación (cuadros rojos) y métodos complementarios simultáneamente (cuadros abiertos): Seattle [BBS07] and LUNA [CBC07] utilizaron el método de activación y detección directa de la radiación γ simultáneamente, mientras que la colaboración ERNA [DGK09] convinó los tres métodos. La línea gruesa de color verde es el valor recomendado en [AAB98] basándose en los experimentos de detección de radiación gamma directa al tiempo que se publicó la revisión, y la líneas verdes delgadas muestran el error considerado. The líneas rojas tiene el mismo significado para el método de activación. La línea negra es el valor recomendado de $S_{34}(0)$ en la revisión en [AGR11] basados en la evaluación de los datos de Weizmann, Seattle, LUNA y ERNA. Debería notarse que mientras que los cuadros abiertos para Seattle, LUNA y ERNA son obtenidos por combinación de diferentes métodos, la evaluación solo tiene en cuenta las medidas de activación de Seattle y LUNA y las de detección directa de ERNA.

D.1.4 Modelos teóricos

La reacción ${}^3\text{He}(\alpha, \gamma){}^7\text{Be}$ es un tipo de reacción nuclear directa de las conocidas como *captura radiativa*. Estas son transiciones electromagnéticas entre un estado de "dispersión" inicial y un estado ligado final mediante la correspondiente emisión de radiación electromagnética. Diferentes cálculos teóricos han sido llevados a cabo intentado reproducir los datos experimentales y entender el mecanismo de reacción. Los cálculos pueden ser agrupados en *modelos potenciales*, [KIN81, BBR85, MAK93] y en *modelos microscópicos* [QKT81, KA84] además de aquellos que utilizan análisis de matriz-R [DAA04], o las evaluaciones en [CFO08] y [AGR11], que utiliza los modelos de [Nol01] y [Kaj86]. Recientemente, los primeros cálculos ab-initio utilizando la aproximación de dinámica molecular fermiónica, realizados sin tener en cuenta medidas experimentales [Nef11], son los primeros en reproducir los datos de la colaboración ERNA a energías intermedias.

Modelo/Evaluación	$S_{34}(0)$ (keV·b)
Matriz-R [DAA04]	0.51 ± 0.04
Cyburty y Davids [CD08]	0.580 ± 0.043
Solar Fusion Cross Sections II [AGR11]	$0.56 \pm 0.02(\text{expt}) \pm 0.02(\text{theor})$
Cálculos Ab-initio [Nef11]	0.593

Table D.1: Valores de $S_{34}(0)$ obtenidos con diferentes cálculos teóricos. Matriz-R y Cyburty y Davids utilizan la evaluación de datos experimentales. La evaluación Solar Fusion Cross Section II utiliza los modelos de Kajino et al. [KTA87] y Nollé [Nol01] y los datos experimentales más recientes hasta 1 MeV. Por último, lo cálculos ab-initio no utilizan ninguno de los datos experimentales y obtienen directamente el valor de $S_{34}(0)$.

La Tabla D.1 muestra los valores del factor $S_{34}(0)$ según los diferentes cálculos, evidenciando la discrepancia entre los diferentes modelos teóricos. La Figura D.8 muestra diferentes cálculos conjuntamente con los datos obtenidos a partir de los datos de Weizmann en el año 2004 [NHNEH04]. Como puede observarse, no solo el valor del factor $S_{34}(0)$ es diferente entre los modelos teóricos, además, obviando el factor normalización, la dependencia del factor astrofísico con la energía es diferente, sobre ζ todo a partir de 1 MeV. Nuevos datos a energías intermedias son necesarios puesto que limitarán la dependencia del factor astrofísico con la energía y por tanto las extrapolaciones a energías de interés astrofísico.

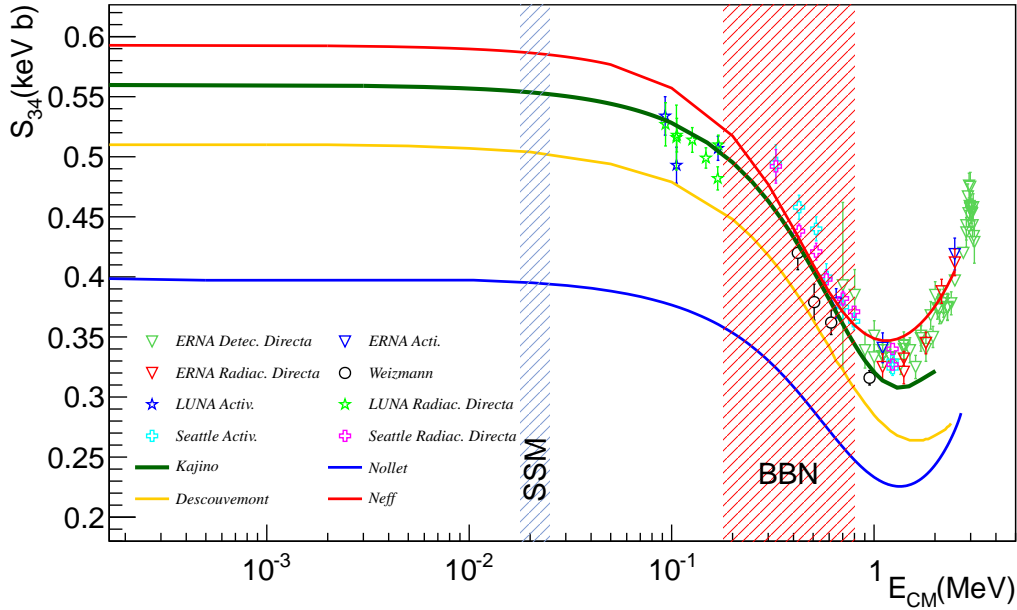


Figure D.8: Comparación de los diferentes modelos teóricos de Kajino et al. [KTA87], Nolllet [Nol01], Descouvemont et al. [DAA04] y Neff [Nef11], junto con los datos experimentales de ERNA [DGK09], Weizman [NHNEH04], LUNA [BCC06, CBC07, GCC07] y Seattle [BBS07]

Es importante notar que los cálculos ab-initio [Nef11], que reproducen los resultados de ERNA [DGK09], a pesar de reproducir la dependencia con la energía de la reacción espejo ${}^3\text{H}(\alpha, \gamma){}^7\text{Li}$ discrepan en un 15% en el valor absoluto al comparar con los resultados experimentales de Brune et al. [BWR94].

D.2 Técnicas Experimentales

De entre las tres técnicas experimentales enumeradas en la sección anterior hemos utilizado el método de activación y el método de detección directa para determinar la sección eficaz de la reacción ${}^3\text{He}(\alpha, \gamma){}^7\text{Be}$ en el rango $E_{\text{CM}}=1-3$ MeV. Debido a las limitaciones experimentales la sección eficaz no se puede determinar a las bajas energías astrofísicas, por ejemplo a los 22 keV correspondientes al pico de Gamow en el Sol, por tanto, los modelos teóricos son utilizados para extraer el factor $S_{34}(0)$ a partir de valores determinados a energías superiores. Medidas experimentales en el rango $E_{\text{CM}}=1-3$ MeV son especialmente relevantes puesto que ayudarán a resolver la discrepancia entre los datos existentes en este rango [PK63], [DGK09] y facilitarán la extrapolación a energías de interés astrofísico.

Actualmente existen muchas instalaciones con aceleradores de partículas en todo el mundo. De las dedicadas a física nuclear y astrofísica, algunas están especialmente enfocadas a la producción de haces de iones radiactivos como ISOLDE en el CERN, GSI o RIKEN. Existen también algunas otras que incluyen aceleradores de menor escala como por ejemplo el CNA en Sevilla, las cuales satisfacen las necesidades de energía y estabilidad necesarias en nuestros experimentos.

Por otra parte, para realizar el experimento usando el *método de detección directa*, algunos requerimientos adicionales son necesarios. Debido a la cinemática de la reacción los núcleos de ${}^7\text{Be}$ son producidos hacia delante siguiendo prácticamente la misma dirección del haz. Por tanto, los iones de ${}^7\text{Be}$ tienen que ser separados e identificados de las partículas del haz antes de ser "contados". En principio se podría utilizar un detector que permita la identificación de partículas como un DSSSD o cámaras de ionización, pero debido a las altas intensidades necesarias en estos experimentos el detector dejaría de ser eficiente al incidir tantas partículas sobre él puesto que se deterioraría.

Basándose en la discusión anterior el experimento de *activación* se ha realizado utilizando el acelerador tandem en el Centro de Microanálisis de Materiales de Madrid, España. Para el experimento de *detección directa* se ha utilizado el separador DRAGON en la instalación TRIUMF, en Vancouver, Canadá

D.2.1 Método de activación

En el experimento llevado a cabo en el CMAM se utilizó un haz de ${}^3\text{He}$ que incidía sobre un blanco gaseoso de ${}^4\text{He}$ el cual estaba almacenado en una cámara de reacción. La Figura D.9 muestra un esquema del montaje experimental. El ${}^7\text{Be}$ formado se depositaba en una placa de cobre situada al final de la cámara y su desintegración era medida posteriormente en una estación de bajo fondo constituida por un detector de germanio de alta pureza. Se utilizaron diez energías incidentes diferentes, cinco medidas en el 2009 y cinco en el 2011. Para cada energía, la sección eficaz de la reacción nuclear (σ_{34}) viene dada en este caso por:

$$\sigma_{34}(E) = \frac{N_{7\text{Be}}}{N_{3\text{He}}^{\text{haz}} \cdot N_{4\text{He}}^{\text{blanco}}} \quad (\text{D.1})$$

donde $N_{7\text{Be}}$, $N_{3\text{He}}^{\text{haz}}$ y $N_{4\text{He}}^{\text{blanco}}$ son el número de núcleos de ${}^7\text{Be}$ producidos, el número de partículas incidentes y la densidad superficial del blanco, respectivamente.

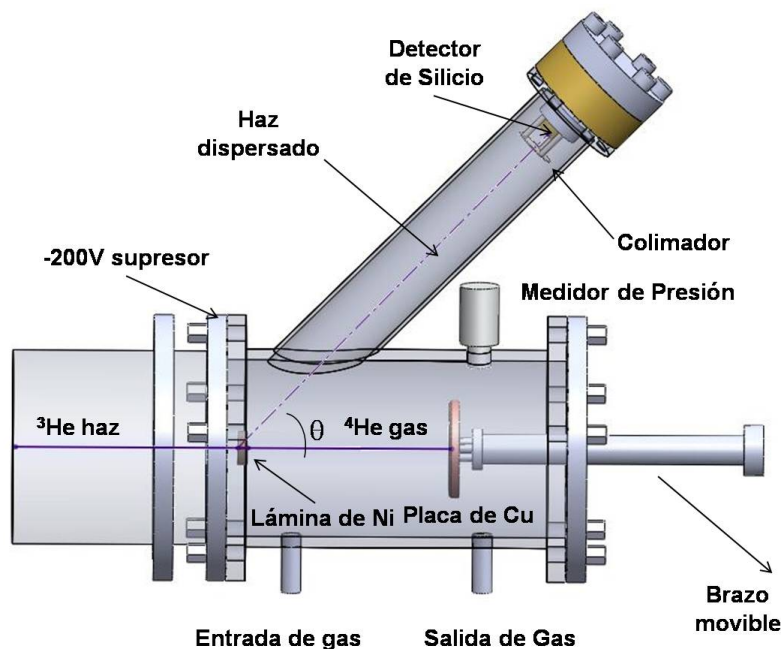


Figure D.9: Diagrama del montaje experimental. Un haz de ${}^3\text{He}$ incidía sobre el haz de ${}^4\text{He}$ encerrado en la cámara y separado de la línea de vacío mediante una lámina de níquel. Un detector de silicio situado a 45° se utilizó para monitorizar el haz dispersado con la lámina de Ni. En la placa de cobre, situada sobre un brazo móvil al final de la cámara, se depositaban los núcleos de ${}^7\text{Be}$ generados. Un supresor de electrones a -200V colocado delante de la lámina de Niquel evitaba que los electrones de la lámina de Ni saliesen repelidos por el impacto del haz.

Para determinar el número de partículas incidentes $N_{\text{He}}^{\text{haz}}$ se utilizaron dos métodos simultáneamente. Por una parte la cámara actuaba en sí misma como una taza de Faraday. Todos los elementos de la cámara estaban conectados eléctricamente y separados de la línea experimental mediante material aislante y por tanto la carga depositada en la cámara era medida. Por otra parte el haz dispersado elásticamente con la lámina de Ni era monitorizado en el detector de silicio, y el número de partículas incidentes es determinado teniendo en cuenta la expresión de dispersión Rutherford.

Debido a las bajas presiones utilizadas durante el experimento (≈ 60 Torr) se puede considerar que el gas se comporta como un gas ideal y por tanto se puede estimar la densidad superficial del mismo mediante la expresión:

$$N_{\text{blanco}} = 9.66 \cdot 10^{18} \frac{\ell \cdot P}{T_0 + T_C} \quad (\text{at/cm}^2) \quad (\text{D.2})$$

donde ℓ en cm es la longitud del blanco, P en Torr es la presión del gas, T_0 en Kelvin es la temperatura ambiente igual a $22.5 \pm 1.5^\circ\text{C}$ y T_C es el aumento de temperatura en el gas debido al impacto del haz. El valor de ℓ se corresponde con la distancia entre la lámina de Ni y la placa de Cu. La placa de cobre era fijada al principio de cada medida y la distancia era determinada tanto al principio como al final de la medida. La presión fue monitorizada durante todo el experimento y el valor efectivo fue determinado como la media entre los valores obtenidos para cada medida. La corrección T_C ha sido obtenida mediante extrapolación lineal de los valores experimentales obtenidos con el mismo montaje utilizado en el Instituto Weizmann para determinar la sección eficaz de la misma reacción a energías más bajas [NHNEH04].

El ${}^7\text{Be}$ creado se depositaba en una placa de cobre por la propia cinemática de la reacción. Se utilizó una placa de cobre para cada energía, las cuales fueron enviadas al Centro de Investigaciones Nucleares SOREQ donde disponen de una instalación de bajo fondo especializada en la detección de radiación γ . Allí se medía la radiación γ procedente de la desexcitación del primer estado excitado del ${}^7\text{Li}$ generado tras la desintegración del ${}^7\text{Be}$. Un esquema del dispositivo experimental se muestra en la Figura D.10, el cual se compone principalmente de un detector de germanio de alta pureza (HpGe) apantallado por diferentes capas de plomo, hormigón etc...y un plástico centellador usado en anti-coincidencia para reducir la radiación cósmica de fondo.

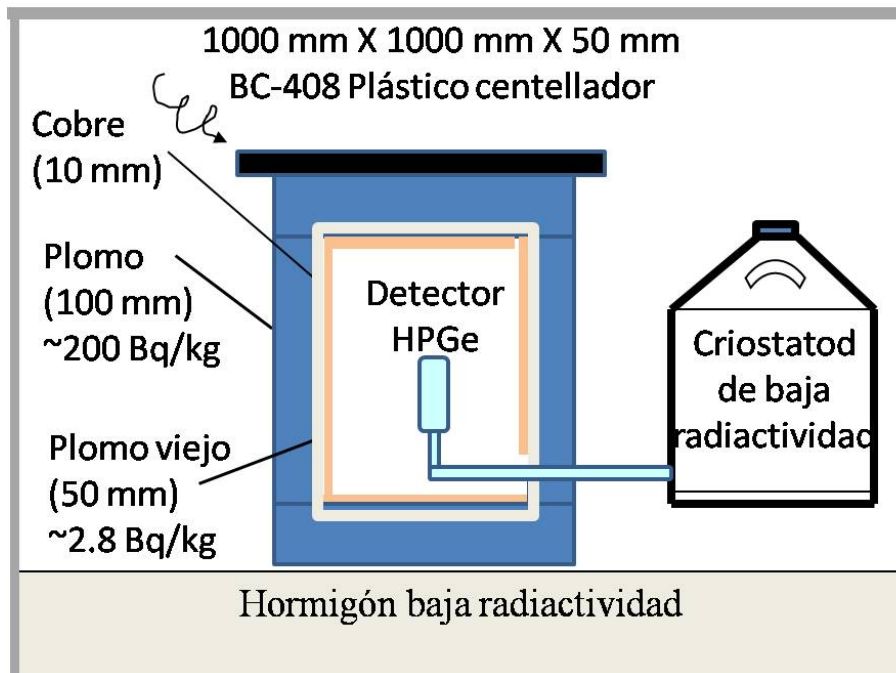


Figure D.10: Diagrama de la instalación de bajo fondo en SOREQ.

D.2.2 Método de detección directa

Para el experimento realizado mediante la técnica de detección directa del ${}^7\text{Be}$ utilizamos el separador DRAGON en TRIUMF [HBB03]. Se determinó la sección eficaz de la reacción a cuatro energías diferentes utilizando un haz de ${}^4\text{He}$ que incidía sobre un blanco gaseoso de ${}^3\text{He}$. Un diagrama del separador se muestra en la Figura D.11. DRAGON consta de cuatro elementos principales: un blanco gaseoso sin ventana el cual se mantiene en la cámara de reacción mediante un complejo sistema de bombas de vacío; una matriz de detectores centelleadores BGO que rodean al blanco; el separador, compuesto por dipolos cuadrupolos y sextupolos eléctricos y magnéticos; y un sistema de detección situado en el plano focal del separador, que en nuestro caso fue un detector de silicio de bandas (DSSSD).

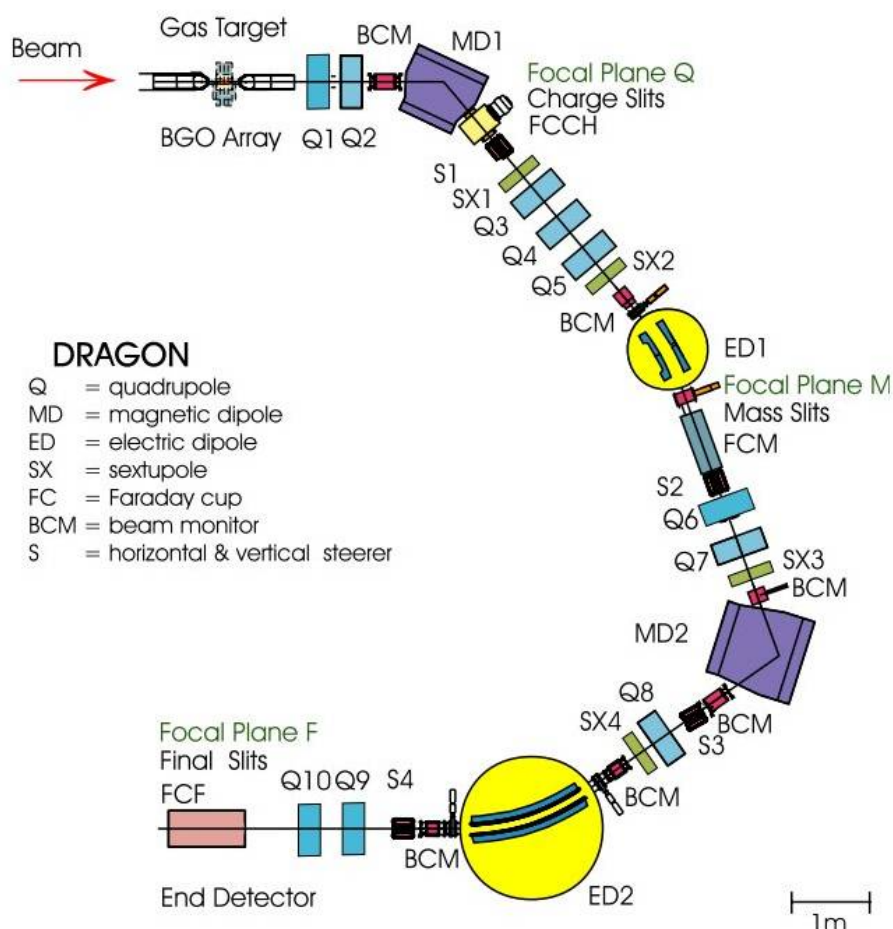


Figure D.11: Diagrama del separador DRAGON. Los haces de partículas estables o radiactivas inciden en el blanco gaseoso sin ventana, habitualmente hidrógeno o helio a presiones que oscilan de 0.2 a 10 Torr. Los iones procedentes de las reacciones (p,γ) o (α,γ) salen del blanco con diferentes estados de carga y casi el mismo momento que el haz incidente. Dichos iones son separados de las partículas del haz mediante dos dipolos magnéticos (MD1 y MD2) y dos dipolos eléctricos (ED1 y ED2). Cuadrupolos y Sextupolos magnéticos son utilizados para focalizar las partículas. Un DSSSD se localiza al final del separador donde se detectan los núcleos procedentes de la reacción.

En este experimento los iones de ${}^7\text{Be}$ generados se separaban de las partículas del haz utilizando los diferentes elementos del separador y eran detectados en el DSSSD situado en el plano focal. La radiación γ procedente de la reacción también era medida en los detectores BGO.

En este caso la sección eficaz de la reacción viene dada por:

$$\sigma_{34}(E) = \frac{N_{7\text{Be}}}{N_{3\text{He}}^{\text{blanco}} \cdot N_{4\text{He}}^{\text{haz}}} \quad (\text{D.3})$$

donde, el número total de iones de ${}^7\text{Be}$ producidos, $N_{7\text{Be}}$, se obtiene a partir de los detectados en el DSSSD. El número de partículas en el haz, $N_{4\text{He}}^{\text{haz}}$, se obtiene a partir de las partículas dispersadas y detectadas en dos detectores de silicio situados en la cámara de reacción a 30° y 57° con respecto a la dirección del haz. Por último, debido a las bajas presiones, ~ 6 Torr, la densidad superficial del blanco gaseoso se obtiene considerando la expresión D.2 donde $T_C=0$ en este caso.

Este sistema experimental es más complejo que el de activación y requiere de medidas adicionales para obtener la sección eficaz total de nuestra reacción.

Por una parte los iones de ${}^7\text{Be}$ emergen del blanco con diferentes estados de carga (${}^7\text{Be}^{4+,3+,2+,1+}$) mientras que solo uno es seleccionado en el separador. Por tanto es necesario conocer la proporción de iones generados con el estado de carga seleccionado en el separador. Para eso utilizamos un haz de ${}^9\text{Be}$ sobre un blanco gaseoso de ${}^3\text{He}$ y determinamos la fracción de iones que salían con cada estado de carga utilizando las tazas de Faraday situadas a lo largo del separador. Por otra parte se determinó el perfil de densidad del haz puesto que se trata de un blanco sin ventana con bombeo diferencial. Para ello utilizamos la reacción de resonancia ${}^3\text{He}({}^{12}\text{C}, {}^{14}\text{N})\text{p}$ con un detector BGO. La radiación γ procedente de la reacción era medida con el detector a diferentes distancias respecto al centro de la cámara y desplazándolo en paralelo a la línea de haz. Mediante la comparativa de la radiación γ detectada en las diferentes posiciones se determina el perfil de densidad del blanco. La Figura D.12 muestra el resultado.

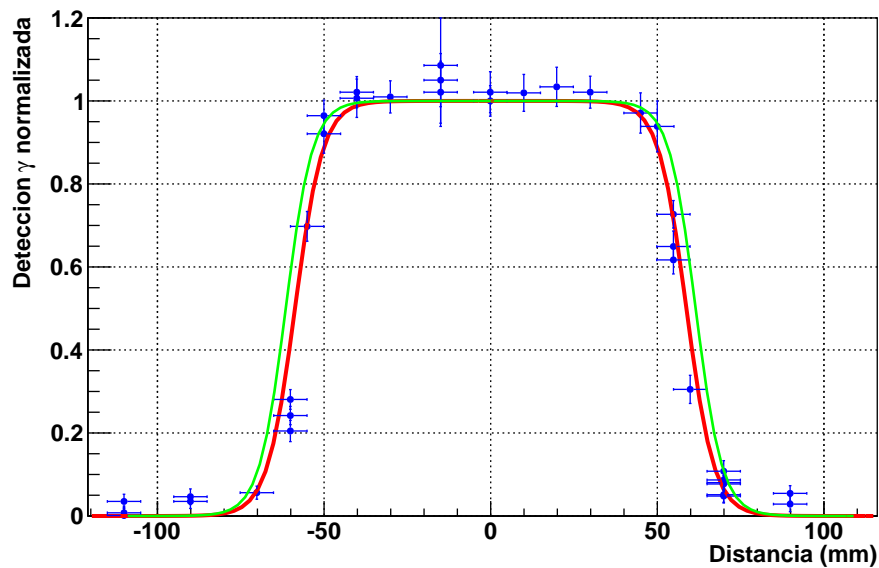


Figure D.12: Perfil de densidad del haz normalizado. Los puntos azules muestran la producción normalizada determinada experimentalmente, y las curvas rojas y verdes muestran dos de los ajustes realizados a los puntos experimentales utilizando la función de Fermi.

D.3 Simulaciones del Separador DRAGON

Otro de los parámetros determinantes para el estudio de esta reacción es la aceptación de DRAGON, es decir, la fracción de los iones creados que alcanzan el final del separador y no chocan con los elementos del mismo. Los cálculos cinemáticos de esta reacción muestran que el máximo

ángulo de salida de los núcleos de ${}^7\text{Be}$ puede llegar hasta ~ 20 mrad el cual, teniendo en cuenta la dispersión del haz y de los propios iones generados, puede verse incrementado hasta por ~ 2 mrad. Estos ángulos están al límite de la aceptación geométrica del separador y por tanto este efecto debe de ser estudiado en detalle para conocer la fracción de iones que se paran a lo largo del mismo. Para ello el código DRAGON-GEANT3 se ha modificado adaptándolo a nuestro experimento. En este código los diferentes elementos están diseñados acorde al separador real y los parámetros de entrada han sido modificados reproduciendo a las condiciones experimentales durante nuestra medidas. Algunos de los factores considerados son los siguientes:

- El blanco gaseoso utilizado sigue el mismo perfil que el determinado experimentalmente y mostrado en la Figura D.12. Para ello, puesto que GEANT no permite que el material de un volumen definido cambie, se han ajustado los datos experimentales a una función escalón donde cada escalón coincide con cada uno de los volúmenes de GEANT.
- La energía central del haz, E^{central} , se ha fijado según la determinada experimentalmente. Para cada evento simulado el programa determina aleatoriamente la energía de una distribución Gaussiana centrada en E^{central} y con anchura $\text{FWHM}=0.1\%E$, siguiendo las especificaciones del acelerador.
- El tamaño del haz y la divergencia simuladas se han calculado basándose en los parámetros de transmisión del haz a través del blanco medidos durante el experimento.
- La probabilidad de que la reacción tenga lugar es la misma a lo largo de todo el blanco puesto que la energía perdida en el mismo es muy pequeña. Por tanto, la distribución de reacciones producidas sigue el perfil de densidad del gas.
- La distribución angular de la radiación gamma emitida se considera isotrópica [DGK09]
- La probabilidad de que la reacción se produzca poblando el primer estado excitado o el estado fundamental se introdujo basándose en los cálculos en [CD08]
- Los parámetros del separador fueron introducidos basándose en los ajustes reales durante el experimento.
- El posible mal alineamiento de los elementos del separador situados antes del primer cuadrupolo fue medido utilizando un teodolito y los valores fueron introducidos en las simulaciones.

Los valores de transmisión (o aceptación) obtenidos de las simulaciones de 10^5 partículas incidentes para las diferentes energía del haz están mostrados en la Tabla 4.6

Año	$\sim E_{4\text{He}}$ (MeV)	${}^7\text{Be}$ creados	${}^7\text{Be}$ detectados	Transmisión
2011	6.5	25931	14873	57.3±0.6
	5.2	39694	22907	57.7±0.5
	3.5	55383	28392	51.3±0.3
2013	4.7	38554	27627	71.7±0.6

Table D.2: Trasmisiones de DRAGON. Para cada una de las energías del haz mostradas en la segunda columna, se han simulado 10^5 iones de ${}^4\text{He}$ incidentes. La tercera columna muestra el número de reacciones producidas o iones ${}^7\text{Be}$ generados mientras que en la cuarta columna se indica el número de esos que consiguió atravesar todo el separador y depositarse en el DSSSD. La última columna muestra la transmisión con el error estadístico asociado.

D.3.1 Error sistemático de la transmisión

Las potenciales variaciones de las condiciones experimentales durante las medidas experimentales se han tenido en cuenta como errores sistemáticos asociados a la transmisión. Para cuantificarlos se han realizado simulaciones en las que se han variado los diferentes parámetros de entrada acorde a los posibles cambios que se hubiesen podido ocasionar durante las medidas. La Tabla D.4 muestra en la primera columna los diferentes parámetros testeados y en la última columna el error sistemático asociado a la transmisión. Por último la Tabla D.3 muestra los valores finales de la transmisión así como los errores estadísticos y sistemáticos asociados. El valor final del error sistemático se ha obtenido mediante la suma cuadrática de cada una de las contribuciones mostradas en la Tabla D.4.

Año	$E_{4\text{He}}$ (keV)	Transmisión (%)	Error Estadístico	Error Sistemático
	6553.88	57.3	± 0.6	$+2.7$ -3.8
2011	5165.97	57.7	± 0.5	$+5.4$ -6.1
	3521.61	51.3	± 0.3	$+3.6$ -4.4
2013	4716.45	71.7	± 0.6	$+3.0$ -6.8

Table D.3: Transmisiones de DRAGON y errores estadísticos y sistemáticos asociados.

D.4 Análisis y Resultados

El objetivo de nuestros experimentos es determinar el factor astrofísico de la reacción ${}^3\text{He}(\alpha, \gamma){}^7\text{Be}$ expresado por:

$$S_{34}(E) = \sigma_{34}(E) \cdot E \cdot e^{2\pi\eta E} \quad (\text{D.4})$$

donde E es la energía en el sistema centro de masas. Por lo tanto, para cada uno de los dos experimentos se debe determinar, la energía en el sistema centro de masas y la sección eficaz de la reacción. Para la sección eficaz, el número de iones incidentes, la densidad superficial del blanco y el número de iones ${}^7\text{Be}$ producidos deben ser estimados. A continuación se detalla como son extraídos cada uno de los parámetros en los dos experimentos.

D.4.1 Método de activación

La energía de la reacción en el sistema centro de masas viene dada por

$$E_{\text{CM}} = \frac{m_{4\text{He}}}{m_{4\text{He}} + m_{3\text{He}}} \cdot \left(E^{\text{haz}} - \Delta E_{\text{Ni}} - \frac{\Delta E_{4\text{He}}}{2} \right) \quad (\text{D.5})$$

donde las "m" son las masas de los correspondientes iones, E^{haz} es la energía del haz calculada a partir de la tensión del terminal del acelerador tandem y ΔE_{Ni} y $\Delta E_{4\text{He}}$ son las energías perdidas por el haz al atravesar la lámina de níquel y el gas, respectivamente. Estas se han determinado utilizando el código SRIM [SRI].

El número de partículas incidentes se ha calculado a partir de las partículas dispersadas con la lámina de níquel y detectadas en el detector de silicio, y mediante la integración de carga. La Figura D.13 muestra el número de partículas calculadas utilizando los dos métodos para las diferentes energías incidentes. Como puede observarse hay un perfecto acuerdo entre las partículas determinadas utilizando los dos métodos.

Parámetro	Año	E_{He}^4 (MeV)	Error Sistemático (%)
Longitud Efectiva del Blanco	2011	~6.5	+0.3 -2.0
		~5.2	+0.8 -0.9
		~3.5	+0.9 -0.5
	2013	~4.7	+0.5 -0.9
Perfil del Blanco	2011	~6.5	-1.8 -1.3
		~5.2	-0.8 +0.0
		~3.5	-1.0 +0.0
	2013	~4.7	-0.6 -0.1
Desplazamiento del Haz (eje- x)	2011	~6.5	+0.2 -2.8
		~5.2	+1.2 -3.3
		~3.5	+0.7 -2.0
	2013	~4.7	+2.2 -5.0
Desplazamiento del Haz eje- y	2011	~6.5	-2.2 -0.9
		~5.2	-2.5 -1.0
		~3.5	-2.0 -0.6
	2013	~4.7	-3.5 -1.0
Transmisión del Haz	2011	~6.5	-0.2 -0.8
		~5.2	+2.6 -0.8
		~3.5	+0.7 -0.7
	2013	~4.7	+0.2 -1.3
Divergencia del Haz (eje- x)	2011	~6.5	-1.1 -1.0
		~5.2	+0.0 +0.1
		~3.5	-0.6 -0.1
	2013	~4.7	-0.3 -0.3
Divergencia del Haz (eje- y)	2011	~6.5	-0.8 -0.8
		~5.2	+0.0 +0.3
		~3.5	-0.2 +0.4
	2013	~4.7	-1.2 +0.1
Energía del Haz	2011	~6.5	+1.3 -3.1
		~5.2	+1.8 -1.6
		~3.5	+1.8 -1.7
	2013	~4.7	+0.4 -0.9
S_1/S_0	2011	~6.5	+1.0 -1.7
		~5.2	+1.9 -0.8
		~3.5	+1.7 -0.3
	2013	~4.7	+1.8 -1.4
Distribución angular γ	2011	~6.5	+1.6 -1.6
		~5.2	+2.9 -2.9
		~3.5	+1.1 -1.1
	2013	~4.7	+0.4 -0.4

Table D.4: Parámetros analizados para evaluar la transmisión de DRAGON y el error sistemático asociado.

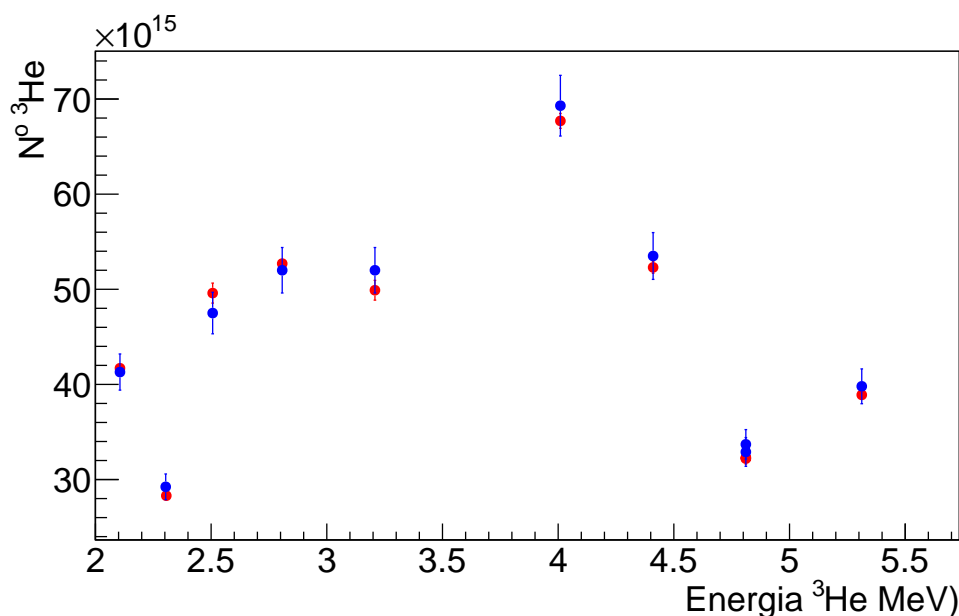


Figure D.13: Número total de partículas del haz incidente para las diferentes energías del haz medidas en el CMAM. En rojo se muestra el número de partículas estimadas mediante la integración de carga y en azul mediante la dispersión elástica del haz con la lámina de Ni.

Para determinar la densidad superficial del blanco la presión se controló durante todo el experimento y los valores se anotaron frecuentemente. Para cada energía, la presión se calcula considerando la media entre los valores tomados y el error asociado se determinó como la desviación típica de los valores más 0.1 Torr de error instrumental. Un ejemplo de la estabilidad de la presión y por tanto de la densidad superficial del blanco gaseoso para la energía del haz de 4010 keV se muestra en la Figura D.14.

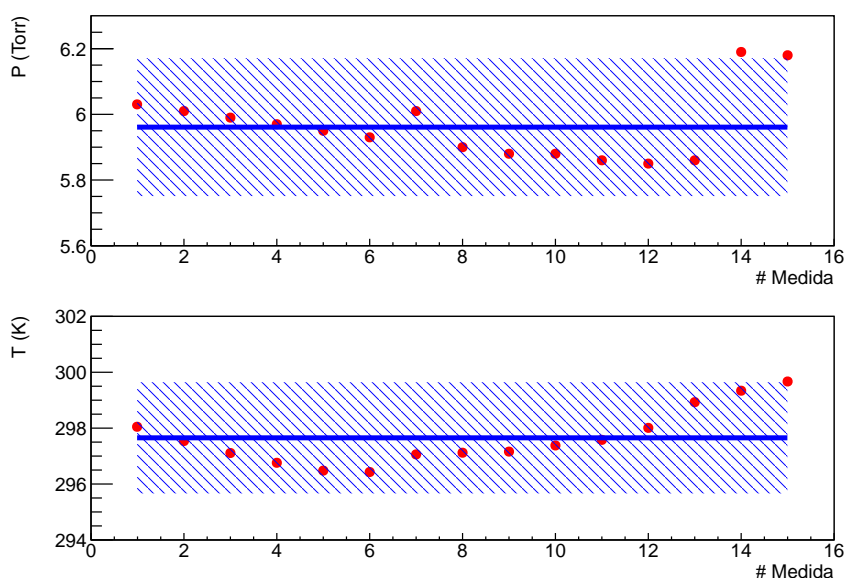


Figure D.14: Estabilidad de la presión para el método de activación siendo la energía del haz 4010 keV. Los puntos rojos muestran las medidas experimentales de la presión del ^4He gaseoso, la línea azul muestra el valor medio considerado y la zona rayada muestra el error asociado al valor medio.

El número de iones de ${}^7\text{Be}$ producidos se recolectó en las placas de cobre. La radiación γ retardada procedente de la desexcitación del primer estado excitado del ${}^7\text{Li}$ fue medida utilizando la estación de bajo fondo. La Figura D.15 muestra un ejemplo de uno de los espectros adquiridos. En el panel superior se muestra un espectro completo para la energía de haz de 4010 keV y en el panel inferior se muestra la región en torno a 478 keV donde se pueden identificar los picos de interés claramente separados del pico a 511 keV. El procedimiento seguido para la obtención del número de cuentas en el pico de interés es el detallado en [NEHY07]. A partir del número de cuentas en el pico, el número total de iones producido se calcula teniendo en cuenta la ley de desintegración radiactiva así como los tiempos transcurridos durante la implantación, entre la implantación y el comienzo de medida del espectro y el tiempo de obtención del espectro.

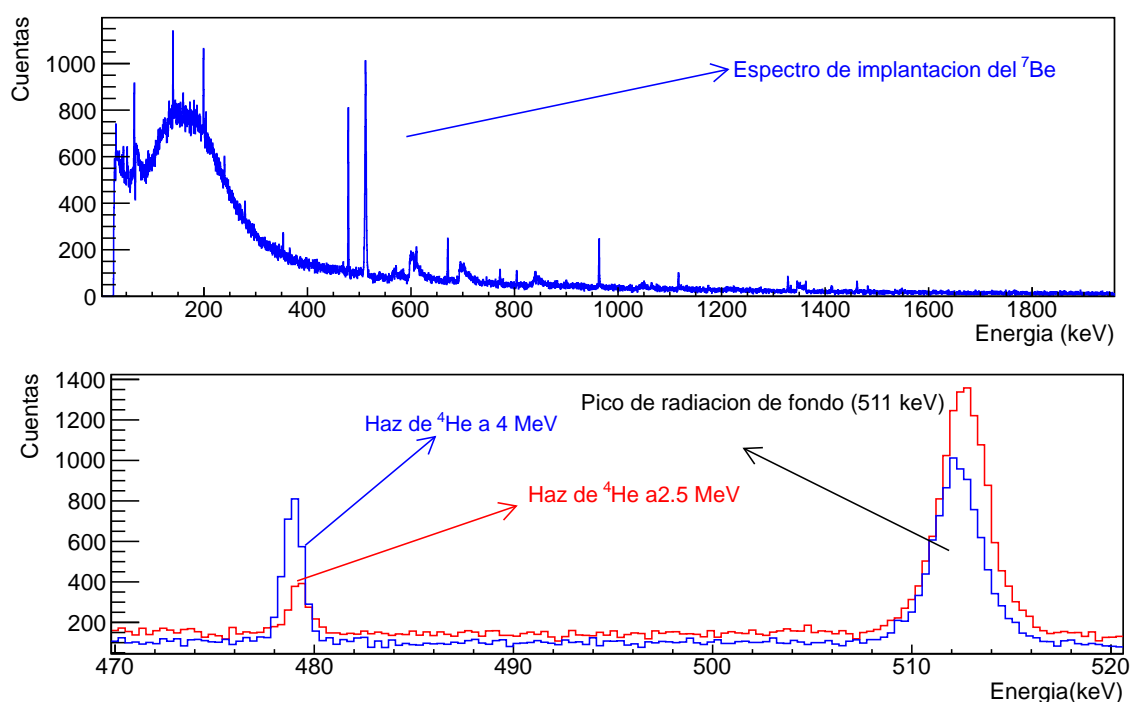


Figure D.15: Espectros de radiación γ de los núcleos ${}^7\text{Be}$ implantados en las placas de cobre. En el panel superior se muestra el espectro total de ${}^7\text{Be}$ cuando la energía del haz era 4 MeV. In la parte inferior la región de interés para las energías del haz de 4 MeV (azul) y 2.5 MeV (rojo).

La Tabla D.5 muestra los valores de los diferentes parámetros obtenidos con el método de activación. Para las diferentes energías de haz mostradas en la primera columna, la segunda columna muestra la energía en el sistema centro de masas correspondiente. La tercera, cuarta y quinta columna muestran el número de iones en el haz, la densidad superficial de blanco gaseoso y el número de núcleos de ${}^7\text{Be}$ generados en cada caso, respectivamente. Las columnas sexta y séptima muestran el valor de la sección eficaz y el factor astrofísico para las diferentes energías. Las incertidumbres asociadas a cada valor están mostradas entre paréntesis. Los errores obtenidos para la sección eficaz han sido determinados mediante propagación de errores estándar. Para, $N_{{}^3\text{He}}^{\text{haz}}$ y $N_{{}^4\text{He}}^{\text{blanco}}$ los errores se refieren a la contribución sistemática, mientras que para $N_{{}^7\text{Be}}$, $\sigma_{34}(E)$ y $S_{34}(E)$ las contribuciones están separadas en estadísticas (primeras) y sistemáticas (segundas).

Los factores $S_{34}(E)$ se representan en la Figura D.18 junto con los resultados obtenidos en el experimento de detección directa y otros valores en la literatura.

$E_{^3\text{He}}$ (keV)	E_{CM} (keV)	$N_{^3\text{He}}^{\text{haz}}$ ($\cdot 10^{16}$)	$N_{^4\text{He}}^{\text{blanco}}$ ($\cdot 10^{19}/\text{cm}^2$)	$N_{^7\text{Be}}$ ($\cdot 10^6$)	$\sigma_{34}(E)$ (μb)	$S_{34}(E)$ (keV \cdot b)
2306.28 \pm 2.37	915.78 \pm 1.39	2.83(5)	2.34(2)	1.31(25)(3)	1.98(38)(6)	0.411(79)(12)
3208.05 \pm 2.99	1498.91 \pm 1.74	4.99(10)	2.65(2)	4.05(30)(9)	3.06(23)(10)	0.318(24)(10)
4410.42 \pm 3.82	2267.71 \pm 2.21	5.23(6)	1.67(5)	4.74(46)(11)	5.43(53)(22)	0.386(37)(16)
4811.20 \pm 4.09	2511.12 \pm 2.37	3.22(3)	1.68(4)	3.19(30)(7)	5.88(56)(21)	0.391(37)(14)
5312.19 \pm 4.44	2804.10 \pm 2.57	3.89(4)	2.28(2)	6.05(26)(14)	6.82(29)(19)	0.424(18)(12)
2105.89 \pm 2.23	777.17 \pm 1.31	4.17(2)	2.40(2)	1.49(22)(4)	1.49(22)(4)	0.418(61)(13)
2506.67 \pm 2.51	1054.15 \pm 1.47	4.96(10)	2.23(2)	2.26(16)(5)	2.05(14)(6)	0.339(23)(11)
2807.26 \pm 2.71	1249.64 \pm 1.58	5.27(4)	2.28(2)	3.61(29)(11)	3.00(24)(9)	0.390(31)(12)
4009.63 \pm 3.54	2006.95 \pm 2.06	6.77(8)	2.78(2)	7.87(21)(18)	4.70(12)(13)	0.367(10)(10)
4811.20 \pm 4.09	2510.00 \pm 2.37	3.23(7)	1.45(2)	3.88(23)(14)	6.85(40)(26)	0.455(27)(17)

Table D.5: Resultados para el experimento de activación. La primera columna muestra las energías del haz. La segunda columna muestra la energía correspondiente en el sistema centro de masas teniendo en cuenta las energías perdidas en la lámina de Ni y el blanco gaseoso. La columna tercera cuarta y quinta muestran el número de partículas en el haz, en el blanco gaseoso y de núcleos de ^7Be producidos respectivamente. Las columnas sexta y séptima muestran la sección eficaz y el factor astrofísico de la reacción $^3\text{He}(\alpha,\gamma)^7\text{Be}$ respectivamente. Las incertidumbres asociadas a cada valor se muestran entre paréntesis. En caso de que solo exista una incertidumbre se refiere a la contribución sistemática y en caso de que haya dos la primera es la estadística y la segunda es la sistemática.

D.4.2 Método de detección directa

En el caso del método de detección directa la energía de la reacción en el sistema centro de masas viene dada por :

$$E_{\text{CM}} = \frac{m_{^3\text{He}}}{m_{^3\text{He}} + m_{^4\text{He}}} \cdot \left(E^{\text{haz}} - \frac{\Delta E_{^3\text{He}}}{2} \right) \quad (\text{D.6})$$

El número de partículas en el haz se determina a partir de las partículas dispersadas y detectadas en los detectores de silicio situados a 30° y 57° en la cámara de reacción y las tazas de Faraday situadas a lo largo del separador. Se han elegido para cada energía las medidas en las que la corriente es estable, y se define para ellas el factor de normalización como:

$$R^{\text{run}} = \frac{\text{FC1}}{1.602 \cdot 10^{-19} \cdot q} \frac{\text{Time} \cdot \text{Livetime}}{\text{Si-30}} \cdot P \cdot T \quad (\text{D.7})$$

dond FC1 es la lectura de la taza de Faraday situada tras el blanco gaseoso, $q=2$ es la carga del haz tras atravesar el blanco, Time es el tiempo de cada medida, Livetime es la corrección debida al tiempo muerto del sistema de adquisición y Si-30 es el número de partículas dispersadas en el detector de silicio a 30° . P y T son la presión y temperatura del gas respectivamente. A continuación se promedian los factores R^{run} y se obtiene el factor promedio R^{F} para cada energía. El número de partículas totales para cada energía viene dado por la suma para medida dada por:

$$N_{^4\text{He}}^{\text{Beam}} = \frac{R^{\text{F}} \cdot \text{Si-30}}{\text{Livetime} \cdot P \cdot T} \quad (\text{D.8})$$

La densidad superficial de partículas en el blanco gaseoso se determina mediante la expresión D.2 para lo que se monitorizó la presión y temperatura durante todo el experimento. La Figura D.16

muestra un ejemplo de la estabilidad de presión y temperatura para el caso de la energía del haz ~ 5.2 MeV.

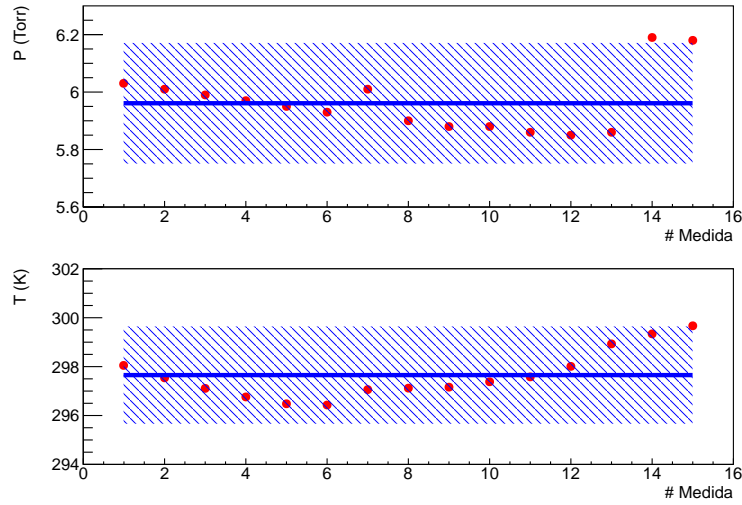


Figure D.16: Presión (panel superior) y temperatura (panel inferior) del blanco gaseoso para una medida con energía del haz de ~ 5.2 MeV. Los puntos rojos muestran las diferentes lecturas cada cinco minutos. La línea azul muestra la media de todas las medidas y la zona sombreada el error asociado.

El número total de núcleos de ${}^7\text{Be}$ producidos ($Y_{\tau\text{Be}}$) viene dado por la expresión:

$$Y_{\tau\text{Be}} = \frac{Y_{\text{DSSSD}}}{t_{\ell} \cdot q_f \cdot \epsilon_{\text{DRAGON}} \cdot \epsilon_{\text{DSSSD}}} \quad (\text{D.9})$$

donde Y_{DSSSD} es el número de iones detectados en el DSSSD, t_{ℓ} es el tiempo real en que el sistema de adquisición está procesando datos, q_f es la fracción de núcleos que abandonan el blanco con el estado de carga seleccionada y determinado mediante las medidas de distribución de estado de carga, ϵ_{DRAGON} es la transmisión o aceptación determinada con las simulaciones (ver Tabla D.3) y ϵ_{DSSSD} es la eficiencia de detección del DSSSD. La Figura D.17 muestra un ejemplo de los histogramas obtenidos con el DSSSD para las energías del haz de 6.5 MeV (panel superior) y 5.2 MeV (panel inferior) y la Tabla D.6 muestra los valores obtenidos para los diferentes parámetros necesarios para obtener el valor de $Y_{\tau\text{Be}}$.

$E_{4\text{He}}$ (MeV)	t_{ℓ} (%)	ϵ_{DSSSD} (%)	q_f (%)	Y_{DSSSD}
~ 6.5	84.12	96.15 ± 0.10	(3+) 59.05 ± 1.87	33465
~ 5.2	92.34	96.15 ± 0.10	(3+) 61.87 ± 2.55	141707
~ 4.7	94.18	96.15 ± 0.10	(2+) 29.31 ± 3.81	52668
~ 3.5	98.64	96.15 ± 0.10	(2+) 52.30 ± 3.33	44135

Table D.6: $t_{\ell}, \epsilon_{\text{DSSSD}}, q_f$ y Y_{DSSSD} para las diferentes energías

Los valores de la energía en el sistema centro de masas, $N_{4\text{He}}^{\text{haz}}$, $N_{3\text{He}}^{\text{blanco}}$ y $Y_{\tau\text{Be}}$ así como la secciones eficaces y factores astrofísicos de la reacción ${}^3\text{He}(\alpha, \gamma){}^7\text{Be}$ se detallan en la Tabla D.7. Los factores astrofísicos $S_{34}(E)$ para las diferentes energías se muestran en la Figura D.18 junto con aquellos obtenidos en el experimento de activación y algunos de los valores en la literatura.

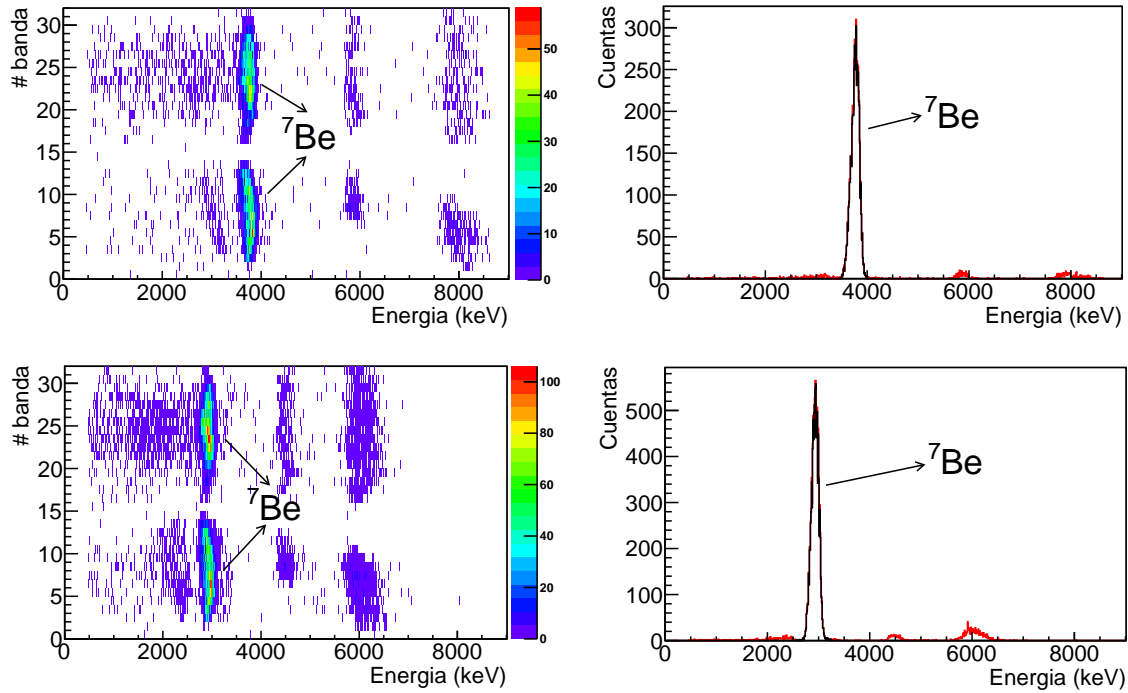


Figure D.17: Para las dos máximas energías, ~ 6.5 y ~ 5.2 MeV, a la izquierda se muestran los espectros 2D de los núcleos de ${}^7\text{Be}$ en las diferentes bandas del DSSSD. En la parte de la derecha están mostradas en rojo las proyecciones de las bandas 1-15. En negro se muestran los sucesos en coincidencia entre la parte delantera y trasera en el rango de energía seleccionado.

Año	$\sim E_{{}^4\text{He}}$ (MeV)	E_{CM} (keV)	$N_{{}^4\text{He}}^{\text{haz}}$ ($\cdot 10^{16}$)	$N_{{}^3\text{He}}^{\text{blanco}}$ ($\cdot 10^{18}$ $\frac{1}{\text{cm}^2}$)	$Y_{{}^7\text{Be}}$ ($\cdot 10^5$)	$\sigma_{34}(E)$ μb	$S_{34}(E)$ (keV \cdot b)
	6.5	2813.6 ± 1.8	0.84(1)	2.29(11)	$1.22(1)_{(-14)}^{(+6)}$	$6.59(8)_{(-80)}^{(+44)}$	$0.393(5)_{(-49)}^{(+27)}$
2011	5.2	2216.6 ± 1.7	3.25(2)	2.38(13)	$4.47(4)_{(-47)}^{(+43)}$	$6.06(5)_{(-79)}^{(+63)}$	$0.419(4)_{(-50)}^{(+46)}$
	3.5	1508.9 ± 1.3	2.09(1)	2.38(12)	$1.74(1)_{(-17)}^{(+15)}$	$3.51(3)_{(-38)}^{(+35)}$	$0.359(3)_{(-40)}^{(+36)}$
2013	4.7	2023.7 ± 1.4	3.03(3)	1.98(11)	$2.77(3)_{(-44)}^{(+38)}$	$4.62(4)_{(-79)}^{(+68)}$	$0.359(3)_{(-61)}^{(+53)}$
(Impl)	4.7	2023.7 ± 1.4	26.5(1)	1.94(10)	28.8(20)(29)	5.61(40)(64)	0.484(34)(56)

Table D.7: Resultados para el experimento de detección directa. La segunda columna muestra las diferentes energías del haz utilizada. En la tercera columna se muestran las energías en el sistema centro de masas correspondientes. La cuarta, quinta y sexta columnas muestran el número de partículas en el haz, el blanco y núcleos de ${}^7\text{Be}$ generados. Las columnas séptima y octava muestran los valores de la sección eficaz y el factor astrofísico de la reacción ${}^3\text{He}(\alpha, \gamma){}^7\text{Be}$. Las incertidumbres asociadas a cada valor se muestran entre paréntesis. En caso de que solo exista una incertidumbre se refiere a la contribución sistemática y en caso de que haya dos la primera es la estadística y la segunda es la sistemática. La última línea muestra los resultados obtenidos para una medida de activación realizada en TRIUMF utilizando la misma técnica que en el experimento de Madrid.

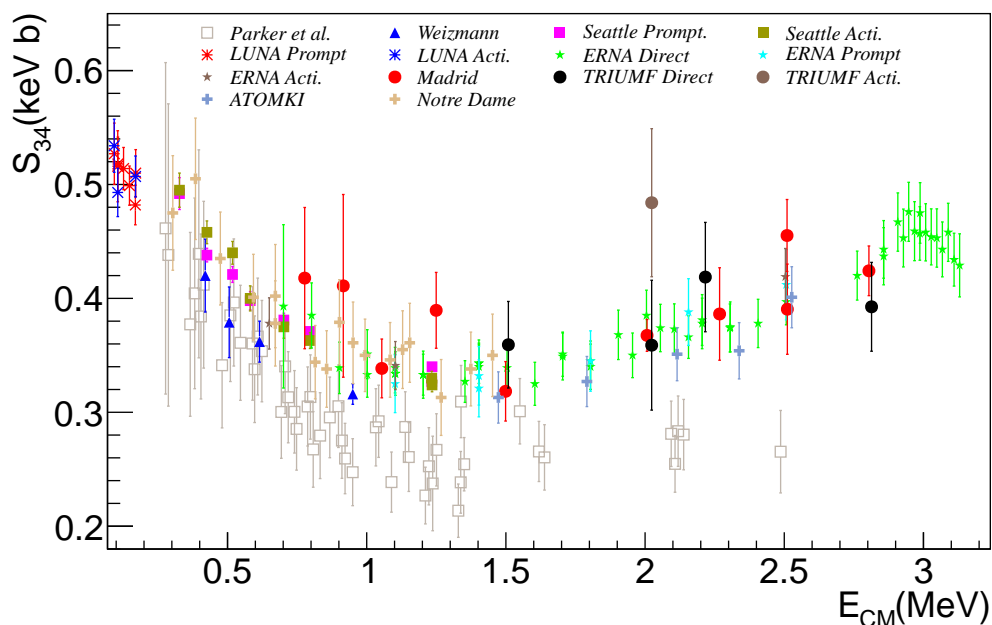


Figure D.18: Valores astrofísicos de la reacción ${}^3\text{He}(\alpha,\gamma){}^7\text{Be}$ obtenidos utilizando el método de detección directa (puntos negros) y método de activación (puntos rojos). Como comparativa se muestran los datos de ERNA [DGK09], Parker [PK63], LUNA [GCC07, BCC06], Weizmann [NHNEH04], Seattle [BBS07] y ATOMKI [BGH13].

D.5 Discusión

Los valores obtenidos para el factor $S_{34}(E)$ se han comparado con diferentes valores experimentales mediante el método de χ^2 . La Tabla D.8 muestra los valores obtenidos. Como puede comprobarse nuestros resultados resuelven completamente la discrepancia entre los valores de Parker y Kavanagh y ERNA, pudiendo descartar los primeros. Los datos de ATOMKI, obtenidos al mismo tiempo que los presentados en este trabajo concuerdan también con nuestro resultados.

	Parker and Kavanagh	ERNA	ATOMKI
Madrid	7.43 ($\nu = 10$)	0.76 ($\nu = 10$)	1.55 ($\nu = 4$)
TRIUMF direct	5.98 ($\nu = 4$)	0.54 ($\nu = 4$)	1.40 ($\nu = 3$)

Table D.8: Valores de χ^2_ν calculados utilizando la expresión 6.2. Nuestros datos de Madrid y TRIUMF conjuntamente se comparan con los datos de Parker and Kavanagh [PK63], of ERNA [DGK09] y ATOMKI [BGH13]. Los valores ν values dan el número de datos comparados en cada caso.

Los resultados obtenidos también se han comparado con los diferentes modelos teóricos. La Figura D.19 muestran los dos cálculos teóricos que mejor reproducen todos los valores obtenidos a partir de las medidas en Weizmann en 2004 conjuntamente con nuestros resultados. Estos modelos son los cálculos ab-initio realizados por Neff [Nef11] y los cálculos de matriz-R realizados por Kontos et al. [KUD13]. Los cálculos teóricos se encuentran normalizados con un factor 1.045 para Kontos y 0.998 para Neff debido a que con esa normalización los modelos reproducen mejor nuestros valores.

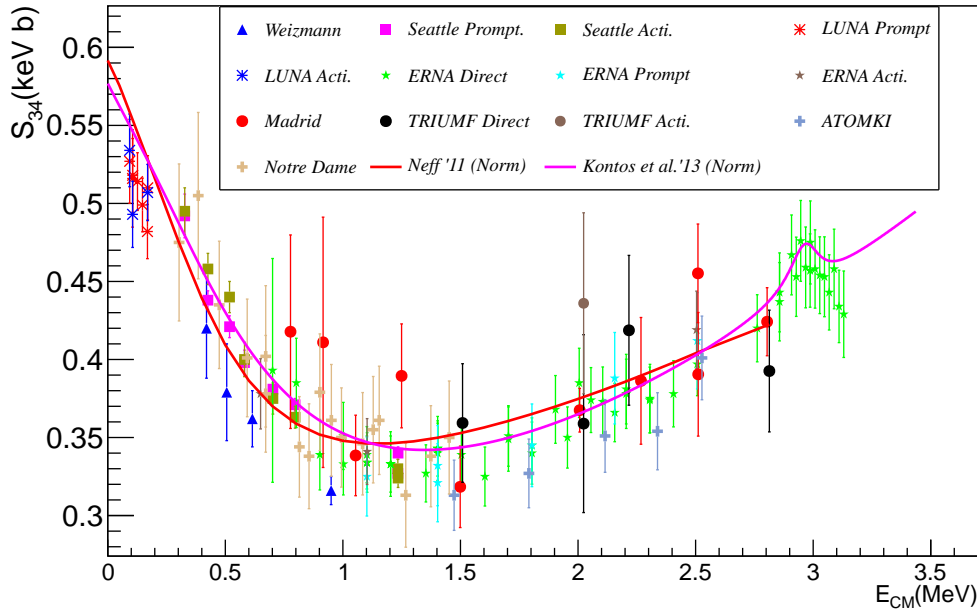


Figure D.19: Los valores experimentales del factor $S_{34}(E)$ se muestran conjuntamente con los cálculos teóricos de Neff [Nef11] y Kontos et al. [KUD13] normalizados para reproducir nuestros resultados.

D.5.1 Impacto en astrofísica

Los valores de $S_{34}(0)$ estimados a través de los modelos de Neff y Kontos tienen influencia directa en las predicciones del SBBN y el SSM.

Con el objetivo de comparar el impacto en el SSM, utilizamos como referencia el valor de $S_{34}(0)=0.56$ keV b sugerido en la revisión *Solar Fusion Cross Section II* [AGR11]. Nuestro valor de 0.577 keV b considerando la renormalización del ajuste de matriz-R por Kontos et al. es $\sim 3\%$ mayor, lo cual se traslada en un aumento de 2.61% y 2.45% en el flujo de neutrinos procedente de la desintegración del ${}^7\text{Be}$ ($\phi_\nu({}^7\text{Be})$) y ${}^8\text{B}$ ($\phi_\nu({}^8\text{B})$) respectivamente. El análisis de matriz-R de Kontos et al. sin incluir normalización que considera tres de nuestros valores obtenidos en el experimento de activación en Madrid, estima $S_{34}(0)=0.554$ keV b y por tanto sin desviaciones del flujo de neutrinos respecto al valor en [AGR11].

Los cambios son superiores si consideramos el valor normalizado de los cálculos de Neff [Nef11] de $S_{34}(E)=0.592$ keV b. Este valor es muy cercano al obtenido sin considerar factor de normalización de 0.593 keV b, y por tanto podemos considerar este último como el mejor reproduciendo nuestros resultados. Además, se debe mencionar que estos son cálculos ab-initio y por tanto no consideran ninguno de los valores experimentales. El incremento de 5.89% en $S_{34}(0)$ se traduce en aumento de 5.05% y 4.75% en $\phi_\nu({}^7\text{Be})$ y $\phi_\nu({}^8\text{B})$ respectivamente.

La estimación cuantitativa de la abundancia del ${}^7\text{Li}$ primordial basado en nuestros resultados está fuera del alcance de este trabajo, sin embargo un análisis cualitativo puede ser realizado. De acuerdo a los cálculos en [DGK09], la abundancia del ${}^7\text{Li}$ primordial es ${}^7\text{Li}/\text{H}=(5.4\pm 0.3) \cdot 10^{-10}$ cuando $S_{34}(0)=0.57$ keV b. En nuestro caso $S_{34}(0)$ es un 3.86% superior, por tanto la abundancia del ${}^7\text{Li}$ primordial se ve incrementada, empeorando por tanto el problema.

D.5.2 Conclusiones

Algunas de las principales conclusiones obtenidas en esta tesis son:

- Dos montajes experimentales han sido completamente caracterizados para estudiar la reacción ${}^3\text{He}(\alpha,\gamma){}^7\text{Be}$.

- Diez nuevos valores del factor $S_{34}(E)$ con bajo error estadístico han sido obtenidos en el rango $E_{CM}=1-3$ MeV utilizando el *método de activación*
- El perfil de densidad del gas del separador de DRAGON, así como la distribución de estado de carga de los iones y la supresión del haz para esta reacción han sido medidas experimentalmente
- El código de simulaciones GEANT3-DRAGON se ha modificado y adaptado para reproducir los parámetros experimentales del durante nuestras medidas.
- Cuatro nuevos valores del factor $S_{34}(E)$ con bajo error estadístico se han obtenido mediante el *método de detección directa*
- La comparación entre nuestros datos, obtenidos diferentes técnicas, muestra buen acuerdo entre ellos.
- Los resultados obtenidos en esta tesis están en acuerdo con los de la colaboración ERNA [DGK09] y discrepan de los de Parker y Kavanagh [PK63]
- Nuestros datos muestran acuerdo con los cálculos ab-initio de Neff [Nef11]
- Un valor de $S_{34}(0)=0.593$ keV b es recomendado in este trabajo basado en nuestros resultados y los cálculos ab-initio

"We build too many walls and not
enough bridges"

Isacc Newton

APPENDIX \mathcal{E}

ENGLISH SUMMARY

Abstract: *This thesis focuses on the study of the cross section of the astrophysical relevant ${}^3\text{He}(\alpha, \gamma){}^7\text{Be}$ reaction. In this appendix, a summary of the work covering the motivation behind these measurements, the experimental techniques employed, analysis procedures used and the outcomes are presented.*

E.1 Motivation

The cross section of the nuclear reaction ${}^3\text{He}(\alpha, \gamma){}^7\text{Be}$ plays a determining role in i) the estimations of the primordial ${}^7\text{Li}$ abundance by the Standard Big-Bang Nucleosynthesis (SBBN) and ii) the predictions of the solar neutrino fluxes from the ${}^7\text{Be}$ and ${}^8\text{B}$ decay by the Standard Solar Model (SSM). Figure E.1 shows the calculated and abundances of the primordial light elements. As can be observed, there is a high discrepancy between primordial ${}^7\text{Li}$ abundance inferred from direct observations and those calculated using the SBBN. The primordial ${}^7\text{Li}$ could be produced by the ${}^3\text{He}(\alpha, \gamma){}^7\text{Be}$ and subsequent ${}^7\text{Be}(p, \gamma){}^7\text{Li}$ reactions within the SBBN modelling, therefore a precise determination of the reaction rate is required to provide accurate input.

The solar neutrino calculations using the SSM are shown in Figure E.2. A comparison with the direct neutrino detections reveal that higher accuracies in the calculations e.g. of neutrinos fluxes from the ${}^7\text{Be}$ and ${}^8\text{B}$ decay are required. These neutrinos are originated from the pp-chain II and pp-chain III, which are opened by the ${}^3\text{He}(\alpha, \gamma){}^7\text{Be}$ reaction. Therefore, a high precision data of this reaction rate is required in these estimations.

Due to the experimental limitations, determination of the rate of this reaction at the astrophysical energies (Gamow peak in the Sun ~ 22 keV) is impossible. Instead, theoretical models are used to extrapolate the astrophysical factor ($S_{34}(E) = E \cdot \sigma_{34}(E) e^{2\pi\eta(E)}$) where E is the energy in the centre of mass system down to zero energy.

Figure E.3 shows a compilation of data (a) and representative calculations (b) of the S-factors. As can be observed there is high discrepancy among the data sets and calculations. This discrepancy is extremely large in the range of $E_{\text{CM}} = 1-3$ MeV, between the experimental data from the ERNA collaboration [DGK09] and the Parker and Tombrello [PK63] and among the theoretical models.

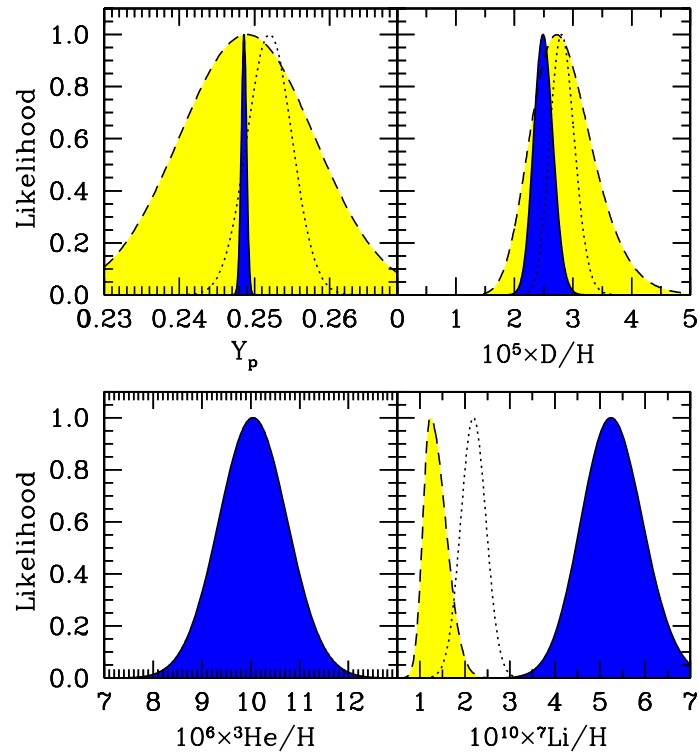


Figure E.1: Calculated and observed likelihoods for ${}^4\text{He}$ (Y_p), D/H , ${}^3\text{He}/H$ and ${}^7\text{Li}/H$. The dark blue areas show the likelihood calculated with the SBBN results using the η parameter from the Wilkinson Microwave Anisotropy Probe (WMAP) observations. The observational likelihoods are shown in the yellow shaded region and dotted likelihood functions. For the ${}^7\text{Li}/H$, the shaded yellow area shows the value inferred from the observation of halo stars. The dotted function shows the determination from a globular cluster. Figure has been taken from [CFO08]

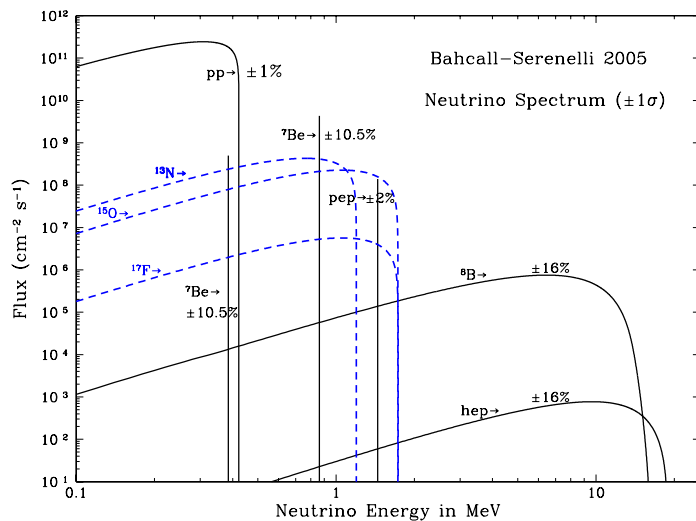
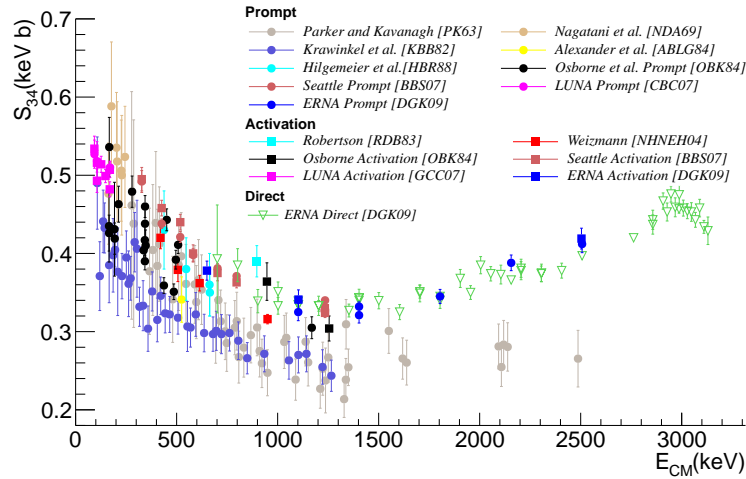
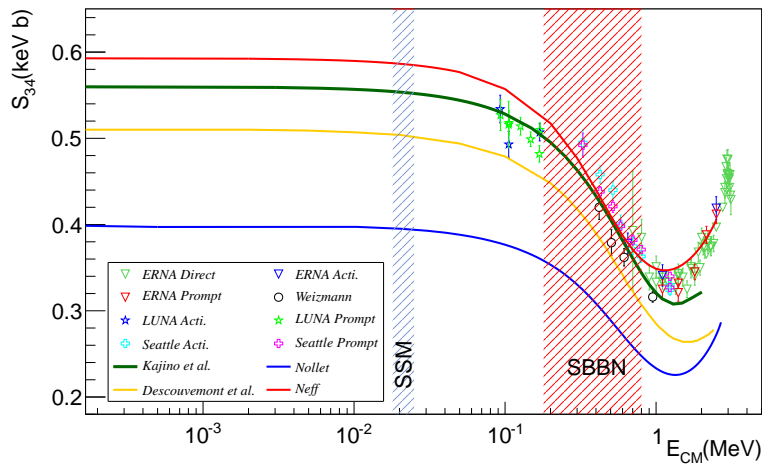


Figure E.2: The solar neutrino spectra calculated using the Standard Solar Model [BP95].



(a)



(b)

Figure E.3: (a) The available data of the astrophysical S -factors for the ${}^3\text{He}(\alpha, \gamma){}^7\text{Be}$ reaction (S_{34}). Data from measurements performed using the Prompt, Method and Direct Recoil Counting methods are shown in circles, squares and triangles, respectively. (b) A comparison between the theoretical models from Kajino et al. [KTA87], Nollet [Nol01], Descouvemont et al. [DAA04] and Neff [Nef11], plotted together with the modern data from ERNA [DGK09], Weizmann [NHNEH04], LUNA [BCC06, CBC07, GCC07] and Seattle [BBS07]. The energy regions of the interest for SSM and SBBN models are marked by blue and red shaded areas.

Aiming to fix the energy dependence of the S -factor and to constrain the theoretical models, required to extrapolate to astrophysical energies, we have measured the cross section of the reaction in the window $E_{\text{CM}}=1\text{-}3\text{MeV}$ using two complementary techniques.

E.2 Experimental Techniques and Results

The decay scheme of the ${}^3\text{He}+{}^4\text{He}$ direct capture state is shown in Figure 1.12. This radiative capture reaction creates a ${}^7\text{Be}$ nucleus and has a Q -value of 1.587(1) MeV. Prompt γ -rays with two different energies are emitted in the process corresponding to the population of the ground state (γ_0) or the first excited state (γ_1) in the ${}^7\text{Be}$. The latter de-excites via emission of a 429 keV γ -ray to the ground state (γ_2). The created ${}^7\text{Be}$ is an unstable nucleus. It decays via electron capture process to ${}^7\text{Li}$ with a half life of 53.24(4) d. The Q value of this process is 862 keV and with a well known branching

ratio of 10.44(4)% the decay populates the first excited state in ${}^7\text{Li}$ at 478 keV from which a γ ray emanates (γ_3).

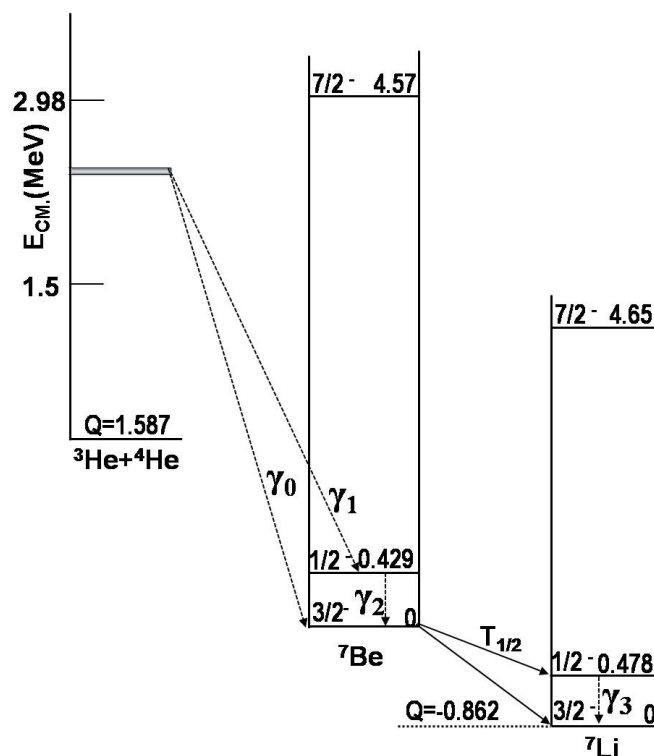


Figure E.4: Decay scheme of ${}^3\text{He}+{}^4\text{He}$ direct capture state with the emission of prompt γ -rays. The ${}^7\text{Be}$ decay to ${}^7\text{Li}$ is also shown. The energies are displayed in MeV.

Three different experimental techniques are therefore available to determine the cross section, namely, via the detection of the (i) prompt γ_0/γ_1 -rays of the reaction ("*Prompt Method*"), (ii) the ${}^7\text{Be}$ recoils ("*Direct Recoil Counting Method*") and (iii) the subsequent γ_3 rays from the de-excitations of the first excited state in ${}^7\text{Li}$ to its ground state, ("*Activation Method*").

We have performed measurements using the *Activation Method* at the Centro de Microanálisis de Materiales de Madrid (CMAM) and the *Direct Recoil Counting Method* utilising the DRAGON separator at TRIUMF laboratory in Vancouver.

E.2.1 Measurements using the activation method

The *activation method* setup is shown in Figure E.5. A ${}^3\text{He}$ beam impinged onto a ${}^4\text{He}$ gas target kept inside a reaction chamber using a Ni foil window. The ${}^7\text{Be}$ recoils were deposited in a Cu catcher placed at the end of the chamber. The subsequent delayed γ -activity was measured using a specialised low background HpGe detector station at the SOREQ centre in Israel (see Figure E.6). The number of incoming beam particles were determined by integrating the electric charge collected by the chamber, which was acting as a Faraday cup. This was cross-checked by detecting the beam which was elastically scattered from a Ni foil and entering into a silicon detector placed at 45° . Due to the low pressures in the chamber (~ 60 Torr), the areal target density was obtained by considering an ideal gas expression with a correction in the temperature due to the beam heating

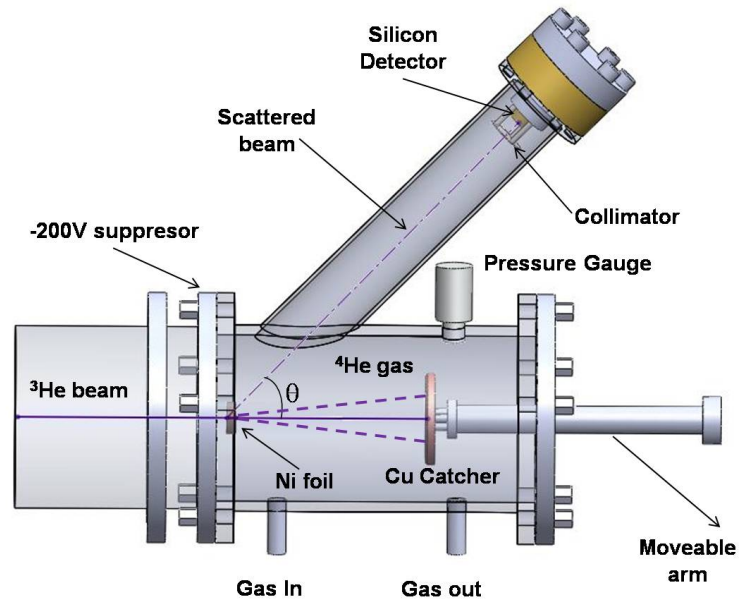


Figure E.5: A Schematic view of various components that are part of the reaction chamber. A ^3He beam impinged onto a ^4He gas target that is "vacuum isolated" from the beam line using Ni foil. A silicon detector was placed at $\approx 45^\circ$ for monitoring the scattered beam from a Ni foil. A Cu catcher placed on a moveable arm at the end of the chamber was used to collect the ^7Be recoils. An electron suppressor with -200 V was placed before the Ni foil. See text for more details.

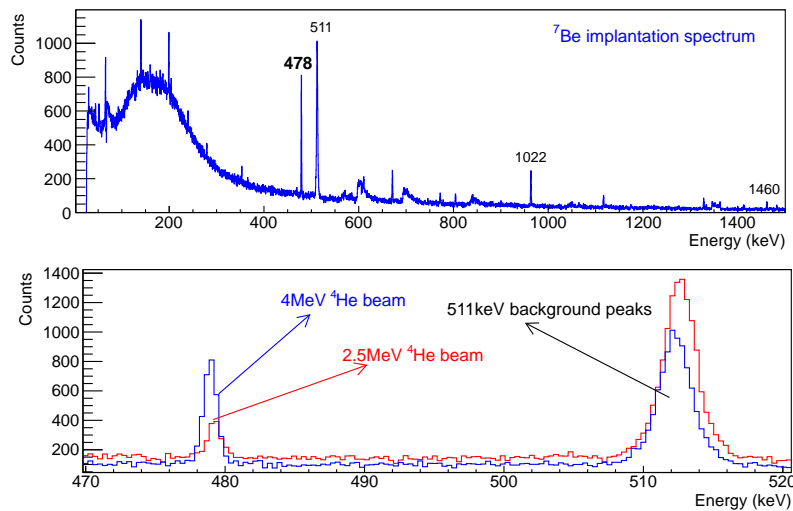


Figure E.6: Spectra for the γ -rays from the catchers having implanted ^7Be . In the upper panel a total spectrum for the ^7Be catcher at ~ 4 MeV beam energy is shown. Some of the peak energies are labelled. In the lower panel a zoom view for the region of interest is shown for beam energies of 4 MeV (blue) and ~ 2.5 MeV (red).

The values of various the parameters corresponding to our measurements using *activation method* as well as the results for the cross section and astrophysical $S_{34}(E)$ factors are shown in Table E.1.

$E_{^3\text{He}}$ (keV)	E_{CM} (keV)	$N_{^3\text{He}}^{\text{beam}}$ ($\cdot 10^{16}$)	$N_{^4\text{He}}^{\text{target}}$ ($\cdot 10^{19}/\text{cm}^2$)	$N_{^7\text{Be}}^{\text{recoils}}$ ($\cdot 10^6$)	$\sigma_{34}(E)$ μb	$S_{34}(E)$ (keV \cdot b)
2306.28 \pm 2.37	915.78 \pm 1.39	2.83(5)	2.34(2)	1.31(25)(3)	1.98(38)(6)	0.411(79)(12)
3208.05 \pm 2.99	1498.91 \pm 1.74	4.99(10)	2.65(2)	4.05(30)(9)	3.06(23)(10)	0.318(24)(10)
4410.42 \pm 3.82	2267.71 \pm 2.21	5.23(6)	1.67(5)	4.74(46)(11)	5.43(53)(22)	0.386(37)(16)
4811.20 \pm 4.09	2511.12 \pm 2.37	3.22(3)	1.68(4)	3.19(30)(7)	5.88(56)(21)	0.391(37)(14)
5312.19 \pm 4.44	2804.10 \pm 2.57	3.89(4)	2.28(2)	6.05(26)(14)	6.82(29)(19)	0.424(18)(12)
2105.89 \pm 2.23	777.17 \pm 1.31	4.17(2)	2.40(2)	1.49(22)(4)	1.49(22)(4)	0.418(61)(13)
2506.67 \pm 2.51	1054.15 \pm 1.47	4.96(10)	2.23(2)	2.26(16)(5)	2.05(14)(6)	0.339(23)(11)
2807.26 \pm 2.71	1249.64 \pm 1.58	5.27(4)	2.28(2)	3.61(29)(11)	3.00(24)(9)	0.390(31)(12)
4009.63 \pm 3.54	2006.95 \pm 2.06	6.77(8)	2.78(2)	7.87(21)(18)	4.70(12)(13)	0.367(10)(10)
4811.20 \pm 4.09	2510.00 \pm 2.37	3.23(7)	1.45(2)	3.88(23)(14)	6.85(40)(26)	0.455(27)(17)

Table E.1: Results for the activation experiment. Column 1: beam energies used in the experiment. Column 2: shows the corresponding centre of mass energies taking into account the energy losses in the Ni foil and gas target. Columns 3,4 and 5 show the total number of particles in the beam, target and recoils, respectively. Column 6 and 7 show the cross section and astrophysical factor for the $^3\text{He}(\alpha,\gamma)^7\text{Be}$ reaction. The uncertainties are shown between brackets. When only one contribution it refers to the systematic error, and in case of two contributions the first one refers to the statistical uncertainty and the second one to the systematic error.

E.2.2 Measurements using the direct recoil counting method

For the *direct recoil counting method*, we used the setup at the DRAGON separator (Figure E.7), designed to determine the reaction rate of astrophysical nuclear reactions. It consists of four main components: a recirculating windowless gas target, a BGO array surrounding the target, the separator composed by electric and magnetic dipoles, quadrupoles and sextupoles; and a final detection system placed at the focal plane of the separator, which in our case consisted of a DSSSD detector. We used a ^4He beam impinging onto a ^3He gas target and the ^7Be recoils were detected in the DSSSD.

As in the case of the activation experiment, the areal target density was obtained by considering an ideal gas behaviour (the pressures in this experiment were ~ 6 Torr). In order to estimate the effective length of the differentially pumped windowless gas target, we used the $^3\text{He}(^{12}\text{C}, ^{14}\text{N}\gamma)\text{p}$ resonance reaction. The γ -rays were detected in a BGO detector placed close to the target cell at different positions parallel to the beam line. The normalised experimental target density profile (TDP) is shown in Figure E.8. The number of beam particles were estimated using the Faraday cups along the separator and two silicon detectors placed inside the target chamber at 30° and 57° with respect to the beam axis.

The total number of ^7Be recoils were obtained using the expression E.1:

$$Y_{^7\text{Be}} = \frac{Y_{\text{DSSSD}}}{t_\ell \cdot q_f \cdot \epsilon_{\text{DRAGON}} \cdot \epsilon_{\text{DSSSD}}} \quad (\text{E.1})$$

where Y_{DSSSD} are the number of recoils detected in the DSSSD (see Figure E.9), t_ℓ and ϵ_{DSSSD} are the livetime and detector efficiency, respectively, and q_f and ϵ_{DRAGON} are the fraction of the recoils exiting the gas target with the selected charge state in the separator, and the acceptance of the separator for the corresponding energy.

The determined values for the different parameters in expression E.1 are shown in Table E.2.

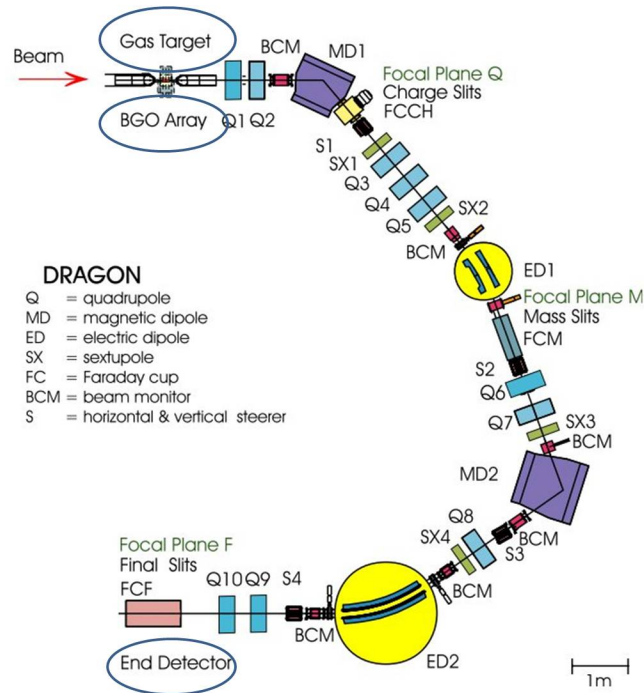


Figure E.7: Diagram of the DRAGON facility taken from Ref. [EHB05]. The ^4He stable beam enters the ^3He windowless gas target, with pressures ~ 5 Torr. The ^7Be recoils produced after the reaction emerge the target with different charge states and almost with the same momentum of the beam. The recoils are separated from the beam particles using the two magnetic dipoles, MD1 and MD2, and the two electrostatic dipoles, ED1 and ED2. Magnetic quadrupoles and sextupoles are used to focus the particles. Enclosed in circles are the three main components, Gas Target, BGO Array and End Detector.

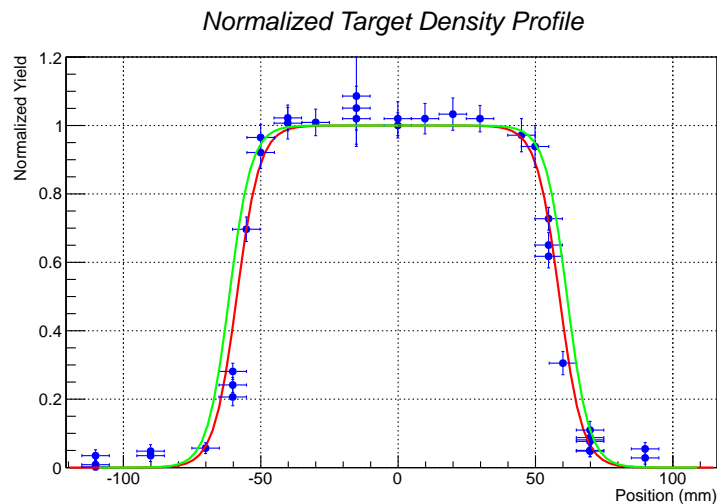


Figure E.8: Final normalised target density profile. The blue points show the normalised yield corrected with the energy dependence given by the expression 3.21 and after subtraction of a constant background. The red fit shows the "best" fit to the points with a Fermi function obtained using ROOT program and the green curve shows the same fit constraining the effective length to 12.3 cm.

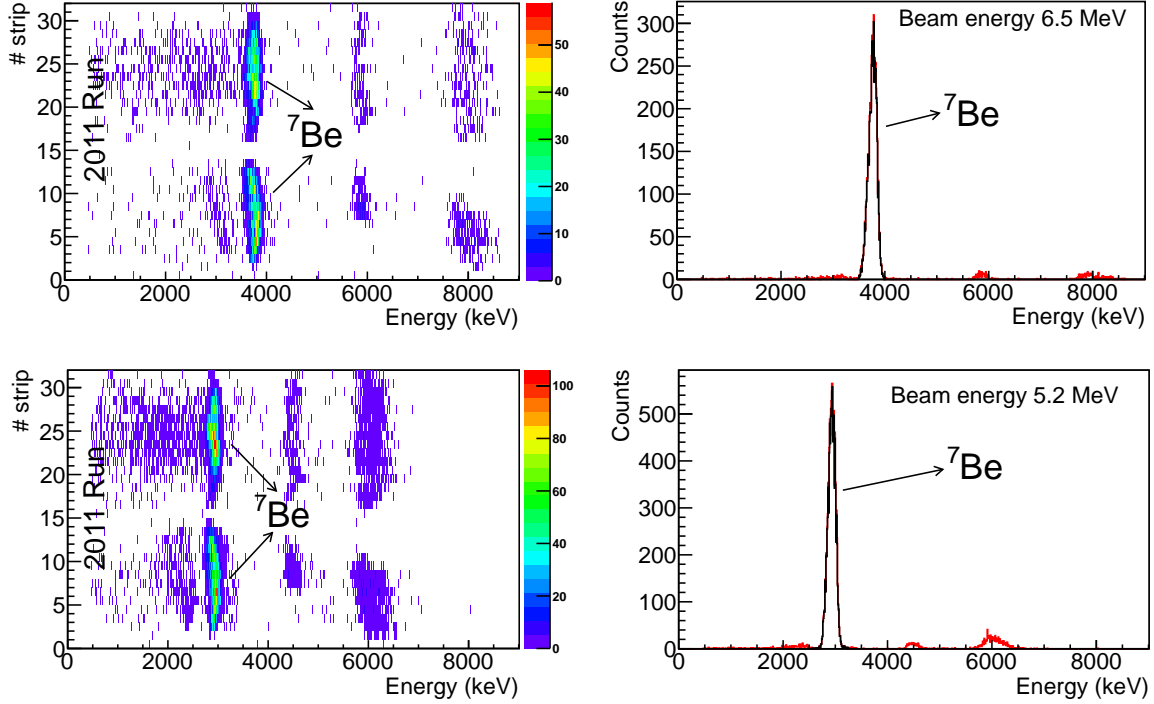


Figure E.9: (Left) Two dimensional spectra for the ${}^7\text{Be}$ recoils detected in the DSSSD strips for beam energies of 6.5 (up) and 5.2 MeV (down). (Right) Projections histograms for the strips 1 to 15 (red). Events in the selected energy region and detected simultaneously in the back and front strips are also shown (black).

$E_4\text{He}$ (MeV)	t_ℓ (%)	ϵ_{DSSSD} (%)	q_f (%)	Y_{DSSSD}	ϵ_{DRAGON}
~ 6.5	84.12	96.15 ± 0.10	(3+)59.05 ± 1.87	33465	57.3(± 0.6) $^{(+2.7)}_{(-3.8)}$
~ 5.2	92.34	96.15 ± 0.10	(3+)61.87 ± 2.55	141707	57.7(± 0.5) $^{(+5.4)}_{(-6.1)}$
~ 4.7	94.18	96.15 ± 0.10	(2+)29.31 ± 3.81	52668	71.7(± 0.6) $^{(+3.0)}_{(-6.8)}$
~ 3.5	98.64	96.15 ± 0.10	(2+)52.30 ± 3.33	44135	51.3(± 0.3) $^{(+3.6)}_{(-4.4)}$

Table E.2: Parameters values for determining $Y_{{}^7\text{Be}}$. The q_f shows the selected charge state between brackets and the corresponding charge state fraction. Y_{DSSSD} indicates the number of recoils detected simultaneously in the front and back strips of the DSSSD. The uncertainties in ϵ_{DRAGON} are given from statistical (first) and systematic (second) contributions.

As the charge state fraction of ions passing through gas target do not depend on the ion mass, the charge state distributions of the ${}^7\text{Be}$ recoils were experimentally determined by using a ${}^9\text{Be}$ and a ${}^3\text{He}$ target. The ${}^9\text{Be}$ velocities were chosen according to the velocities of the ${}^7\text{Be}$ recoils created in the reaction, and different gas target pressures were used. Our results showed that charge state equilibrium have been reached even at 1 Torr.

The acceptance of DRAGON was obtained by performing GEANT3 simulations for the reactions taking place in the gas target and the ${}^7\text{Be}$ recoils separation process. The real experimental conditions, such as beam transmission, beam energy, beam spot size, target density profile and separator tuning settings were used as input parameters in the simulations. Further simulations were run where the possible changes of these parameters during the experiment were taken into account and

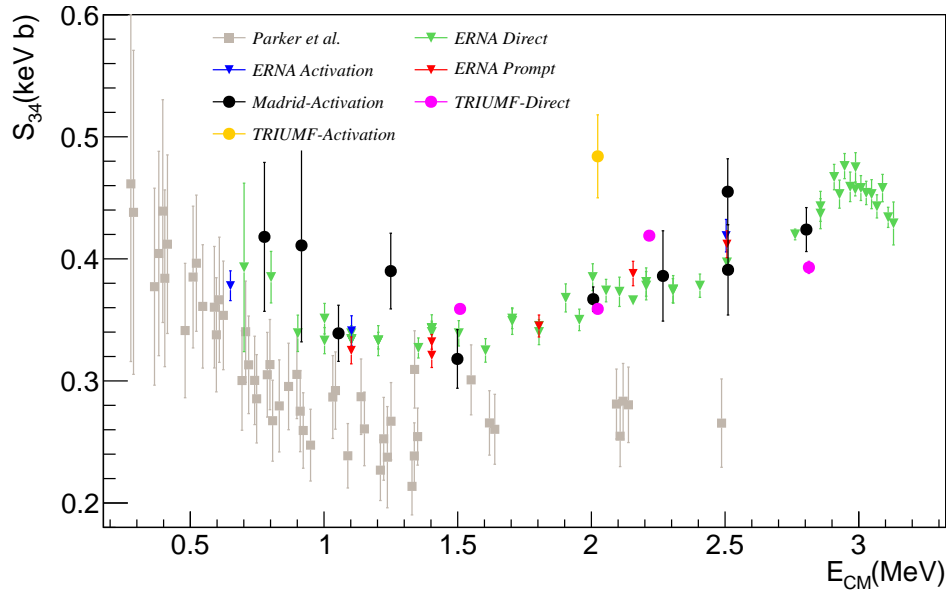


Figure E.10: Astrophysical S -factor for the ${}^3\text{He}(\alpha,\gamma){}^7\text{Be}$ reaction using the direct counting method (violet dots) and the activation method (yellow dot) at TRIUMF. For comparison our Madrid data (black dots) and the results from [DGK09] (triangles) and [PK63] (squares) are also shown.

the results were used to estimate systematic uncertainties.

The values of various parameters corresponding to our measurements obtained using the *direct recoil counting method* as well as the results for the cross section and astrophysical $S_{34}(E)$ factors are shown in Table E.3. The values are plotted in Figure E.10, where only the statistical uncertainties are shown.

Run	$\sim E_{4\text{He}}$ (MeV)	E_{CM} (keV)	$N_{4\text{He}}^{\text{beam}}$ ($\cdot 10^{16}$)	$N_{3\text{He}}^{\text{target}}$ ($\cdot 10^{18}$ $\frac{1}{\text{cm}^2}$)	$N_{7\text{Be}}^{\text{recoils}}$ ($\cdot 10^5$)	$\sigma_{34}(E)$ μb	$S_{34}(E)$ (keV·b)
	6.5	2813.6 ± 1.8	0.84(1)	2.29(11)	$1.22(1)_{(-14)}^{(+6)}$	$6.59(8)_{(-80)}^{(+44)}$	$0.393(5)_{(-49)}^{(+27)}$
2011	5.2	2216.6 ± 1.7	3.25(2)	2.38(13)	$4.47(4)_{(-47)}^{(+43)}$	$6.06(5)_{(-79)}^{(+63)}$	$0.419(4)_{(-50)}^{(+46)}$
	3.5	1508.9 ± 1.3	2.09(1)	2.38(12)	$1.74(1)_{(-17)}^{(+15)}$	$3.51(3)_{(-38)}^{(+35)}$	$0.359(3)_{(-40)}^{(+36)}$
2013	4.7	2023.7 ± 1.4	3.03(3)	1.98(11)	$2.77(3)_{(-44)}^{(+38)}$	$4.62(4)_{(-79)}^{(+68)}$	$0.359(3)_{(-61)}^{(+53)}$
(Impl)	4.7	2023.7 ± 1.4	26.5(1)	1.94(10)	$28.8(20)(29)$	$5.61(40)(64)$	$0.484(34)(56)$

Table E.3: Results for the direct experiment. Column 2: Beam energies used in the experiment. Column 3: corresponding centre of mass energies taking into account the energy losses. Column 4, 5 and 6 show the total number of particles in the beam, target and recoils respectively. Column 7 and 8 show the cross section and astrophysical factor for the ${}^3\text{He}(\alpha,\gamma){}^7\text{Be}$ reaction. The uncertainties are shown between brackets. When only one contribution it refers to the systematic error, and in case of two contributions the first one refers to the statistical uncertainty and the second one to the systematic error (positive and negative systematic uncertainties contributions are separated in some cases).

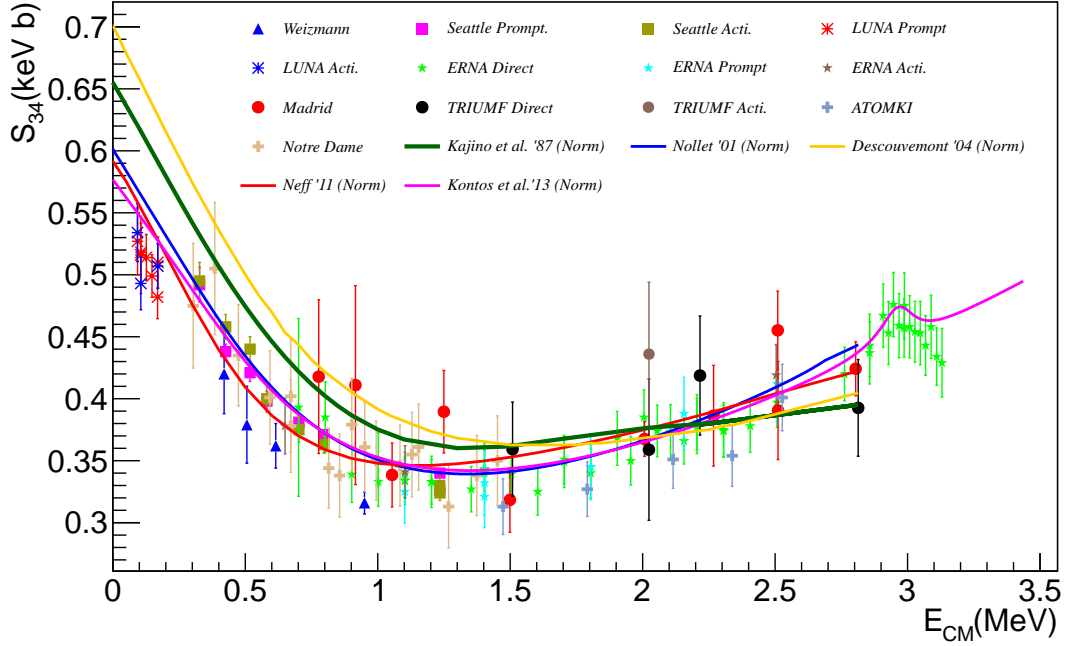


Figure E.11: The modern experimental data for the ${}^3\text{He}(\alpha,\gamma){}^7\text{Be}$ reaction together with the theoretical calculations normalised to our experimental results.

E.3 Discussion and Conclusions

The $S_{34}(E)$ results have been compared with the experimental values available in literature by using the χ^2 method. As can be seen from Table E.4 our results agree with the work from ERNA collaboration. The ATOMKI data, obtained around the time of this thesis also agree with our results. We therefore conclude that the energy dependence seen in the new data should be considered and the one observed by Parker and Kavanagh should be discarded.

	Parker and Kavanagh	ERNA direct	ATOMKI
Madrid	7.43 ($\nu = 10$)	0.76 ($\nu = 10$)	1.55 ($\nu = 4$)
TRIUMF direct	5.98 ($\nu = 4$)	0.54 ($\nu = 4$)	1.40 ($\nu = 3$)

Table E.4: χ^2_ν values calculated using expression 6.2. Here, S_A are our astrophysical S -factors and S_B are those from Parker and Kavanagh [PK63], of ERNA [DGK09] or ATOMKI [BGH13]. The ν values give the number of data points considered in each case.

The results were also compared with some of the available calculations. Figure E.11 shows the two theoretical calculations, namely, the ab-initio calculation by Neff [Nef11] and the R-matrix analysis by Kontos et al. [KUD13], these show good agreement with our results and all the new experimental data taken after the measurements at Weizmann in 2004. In order to reproduce our results, the calculated S_{34} curves from the works of Neff and Kontos et al. have been normalised with 0.998 and 1.045 factors, respectively.

E.3.1 Impact on astrophysics

In the present work, $S_{34}(0)$ values have been obtained by extrapolating our data using the FMD model calculations, [Nef11] and Kontos et al. R-matrix fit [KUD13]. Influence of our results on the

predictions of the Big-Bang Nucleosynthesis and of the Standard Solar Model can thus be investigated.

In order to compare the impact on the standard solar model, we consider the value for $S_{34}(0)=0.56$ keV b recommended in the revision *Solar Fusion Cross Section II* [AGR11]. Our value of 0.577 keV b considering the renormalisation of Kontos et al. R-matrix fit is $\sim 3\%$ larger and translates to a $\sim 2.61\%$ and $\sim 2.45\%$ increase in the solar neutrino fluxes from ${}^7\text{Be}$ ($\phi_\nu({}^7\text{Be})$) and ${}^8\text{B}$ ($\phi_\nu({}^8\text{B})$) calculated from the expressions in [CD08]. The R-matrix fit from Kontos et al. including three of our points from Madrid experiment, without considering our normalisation correction, estimates $S_{34}(0)=0.554$ keV b and therefore, practically no such deviations in the neutrino fluxes are estimated.

The changes are even higher if we consider the normalised value from Neff model [Nef11] of 0.592. This value is very close to the obtained without any normalisation consideration of 0.593 and therefore we can consider this model as the one best reproducing our results. On the other hand it should be recalled that this model is based on ab-initio calculation thus, without considering any of the experimental data it can reproduce both phase shifts and capture reaction cross sections. The increase of 5.89% in the $S_{34}(0)$ value compared to that from [AGR11] translates into an 5.05% and 4.75% in $\phi_\nu({}^7\text{Be})$ and $\phi_\nu({}^8\text{B})$, respectively.

As was already discussed, it is unlikely that the solution to the observed discrepancy between SBBN calculations and the observations of ${}^7\text{Li}$ abundances will be found by improving the knowledge of the ${}^3\text{He}(\alpha,\gamma){}^7\text{Be}$ reaction alone. Nevertheless, the recommended $S_{34}(0)$ values have a direct impact on the estimations of the primordial ${}^7\text{Li}$ abundance. A calculation of the new primordial ${}^7\text{Li}$ abundance is out the scope of this work, however a qualitative analysis can be done. According to [DGK09], a primordial ${}^7\text{Li}$ abundance of ${}^7\text{Li}/\text{H}=(5.4\pm 0.3) 10^{-10}$ is obtained using $S_{34}(0)=0.57$ keV b. This abundance is factor 3 larger than the observational values. In our case the $S_{34}(0)$ is a 3.86% larger than that considered in [DGK09]. Therefore, the corresponding primordial ${}^7\text{Li}$ abundance results to become even larger, thus worsening the problem (see for example [CFO08]).

E.3.2 Conclusions

The main outcomes from this work are:

- Two experimental set-ups have been completely characterised in order to study the ${}^3\text{He}(\alpha,\gamma){}^7\text{Be}$ reaction
- Ten new $S_{34}(E)$ values with low systematic uncertainty have been obtained in the range of $E_{\text{CM}}=1-3$ MeV using the *activation* technique and by employing a very well controlled ${}^7\text{Be}$ production and the γ -counting setups
- Three of the measurements using the *activation* technique has special relevance due to the low statistical uncertainty and with good accuracy
- The density profile of the ${}^3\text{He}$ gas target in the DRAGON cell has been measured for the first time and can be used for future experiments at the DRAGON separator
- The charge state distribution of Be nuclei after crossing ${}^3\text{He}$ target gas have been determined for the first time, using target pressures between 1 to 6 Torr, that indicate charge state equilibrium at 1 Torr
- A very high suppression of incident beam has been measured when ${}^7\text{Be}$ recoils from the ${}^3\text{He}(\alpha,\gamma){}^7\text{Be}$ are selected by DRAGON separator
- The GEANT-3 DRAGON code has been modified and adapted to perform extensive simulations, including a new specific prompt γ -ray angular distributions which will be used for the design of future experiments
- Several tests have been performed in order to constrain the angular distribution of the prompt γ -rays. The variation of the angular distributions have been introduced as potential uncertainties in the acceptance and intense simulations with the adapted GEANT-3 code could lead to a better constrain in the coefficients of the γ -ray angular distribution

- Four new data points for the S_1/S_0 branching ratios have been determined. This includes the point corresponding to 2.8 MeV that, is the highest energy at which such data has been obtained so far
- Four new $S_{34}(E)$ values have been determined with the lowest statistical uncertainty measured so far using the *direct recoil counting* technique
- A good agreement is seen between the two data sets obtained using two independent techniques
- The results obtained in this thesis clearly agree with those from ERNA collaboration [DGK09] and fully disagree with Parker et al.'s work [PK63], in the same energy region
- Our data show very good agreement with the ab-initio FMD calculations [Nef11]
- Based on our experimental results and the ab-initio calculations we recommend a value of $S_{34}(0)=0.593$ keV b

BIBLIOGRAPHY

- [AAA02] Q. Ahmad, R. Allen, T. Andersen, J. D. Anglin, J. Barton, E. Beier, M. Bercovitch, J. Bigu, S. Biller, R. Black, I. Blevis, R. Boardman, J. Boger, E. Bonvin, M. Boulay, M. Bowler, T. Bowles, S. Brice, M. Browne, T. Bullard, G. Bühler, J. Cameron, Y. Chan, H. Chen, M. Chen, X. Chen, B. Cleveland, E. Clifford, J. Cowan, D. Cowen, G. Cox, X. Dai, F. Dalnoki-Veress, W. Davidson, P. Doe, G. Doucas, M. Dragowsky, C. Duba, F. Duncan, M. Dunford, J. Dunmore, E. Earle, S. Elliott, H. Evans, G. Ewan, J. Farine, H. Fergani, A. Ferraris, R. Ford, J. Formaggio, M. Fowler, K. Frame, E. Frank, W. Frati, N. Gagnon, J. Germani, S. Gil, K. Graham, D. Grant, R. Hahn, A. Hallin, E. Hallman, A. Hamer, A. Hamian, W. Handler, R. Haq, C. Hargrove, P. Harvey, R. Hazama, K. Heeger, W. Heintzelman, J. Heise, R. Helmer, J. Hepburn, H. Heron, J. Hewett, A. Hime, M. Howe, J. Hykawy, M. Isaac, P. Jagam, N. Jelley, C. Jillings, G. Jonkmans, K. Kazkaz, P. Keener, J. Klein, A. Knox, R. Komar, R. Kouzes, T. Kutter, C. Kyba, J. Law, I. Lawson, M. Lay, H. Lee, K. Lesko, J. Leslie, I. Levine, W. Locke, S. Luoma, J. Lyon, S. Majerus, H. Mak, J. Maneira, J. Manor, A. Marino, N. McCauley, A. McDonald, D. McDonald, K. McFarlane, G. McGregor, R. Meijer Drees, C. Mifflin, G. Miller, G. Milton, B. Moffat, M. Moorhead, C. Nally, M. Neubauer, F. Newcomer, H. Ng, A. Noble, E. Norman, V. Novikov, M. O'Neill, C. Okada, R. Ollerhead, M. Omori, J. Orrell, S. Oser, A. Poon, T. Radcliffe, A. Roberge, B. Robertson, R. Robertson, S. Rosendahl, J. Rowley, V. Rusu, E. Saettler, K. Schaffer, M. Schwendener, A. Schülke, H. Seifert, M. Shatkay, J. Simpson, C. Sims, D. Sinclair, P. Skensved, A. Smith, M. Smith, T. Spreitzer, N. Starinsky, T. Steiger, R. Stokstad, L. Stonehill, R. Storey, B. Sur, R. Tafirout, N. Tagg, N. Tanner, R. Taplin, M. Thorman, P. Thornewell, P. Trent, Y. Tserkovnyak, R. Van Berg, R. Van De Water, C. Virtue, C. Waltham, J.-X. Wang, D. Wark, N. West, J. Wilhelmy, J. Wilkerson, J. Wilson, P. Wittich, J. Wouters, and M. Yeh, *Direct Evidence for Neutrino Flavor Transformation from Neutral-Current Interactions in the Sudbury Neutrino Observatory*, *Physical Review Letters* **89**, no. 1, 011301 (2002).
- [AAA07] B. Aharmim, Q. Ahmad, S. Ahmed, R. Allen, T. Andersen, J. Anglin, G. Bühler, J. Barton, E. Beier, M. Bercovitch, M. Bergevin, J. Bigu, S. Biller, R. Black, I. Blevis, R. Boardman, J. Boger, E. Bonvin, M. Boulay, M. Bowler, T. Bowles, S. Brice, M. Browne, T. Bullard, T. Burritt, J. Cameron, Y. Chan, H. Chen, M. Chen, X. Chen, B. Cleveland, J. Cowan, D. Cowen, G. Cox, C. Currat, X. Dai, F. Dalnoki-Veress, W. Davidson, H. Deng, M. DiMarco, P. Doe, G. Doucas, M. Dragowsky, C. Duba, F. Duncan, M. Dunford, J. Dunmore, E. Earle, S. Elliott, H. Evans, G. Ewan, J. Farine, H. Fergani, A. Ferraris, F. Fleurot, R. Ford, J. Formaggio, M. Fowler, K. Frame, E. Frank, W. Frati, N. Gagnon, J. Ger-

mani, S. Gil, A. Goldschmidt, J. Goon, K. Graham, D. Grant, E. Guillian, R. Hahn, A. Hallin, E. Hallman, A. Hamer, A. Hamian, W. Handler, R. Haq, C. Hargrove, P. Harvey, R. Hazama, K. Heeger, W. Heintzelman, J. Heise, R. Helmer, R. Henning, J. Hepburn, H. Heron, J. Hewett, A. Hime, C. Howard, M. Howe, M. Huang, J. Hykaway, M. Isaac, P. Jagam, B. Jamieson, N. Jelley, C. Jillings, G. Jonkmans, K. Kazkaz, P. Keener, K. Kirch, J. Klein, A. Knox, R. Komar, L. Kormos, M. Kos, R. Kouzes, A. Krüger, C. Kraus, C. Krauss, T. Kutter, C. Kyba, H. Labranche, R. Lange, J. Law, I. Lawson, M. Lay, H. Lee, K. Lesko, J. Leslie, I. Levine, J. Loach, W. Locke, S. Luoma, J. Lyon, R. MacLellan, S. Majerus, H. Mak, J. Maneira, A. Marino, R. Martin, N. McCauley, A. McDonald, D. McDonald, K. McFarlane, S. McGee, G. McGregor, R. Drees, H. Mes, C. Miffllin, K. Miknaitis, M. Miller, G. Milton, B. Moffat, B. Monreal, M. Moorhead, B. Morrisette, C. Nally, M. Neubauer, F. Newcomer, H. Ng, B. Nickel, A. Noble, E. Norman, V. Novikov, N. Oblath, C. Okada, H. O’Keeffe, R. Ollerhead, M. Omori, J. Orrell, S. Oser, R. Ott, S. Peeters, A. Poon, G. Prior, S. Reitzner, K. Rielage, A. Roberge, B. Robertson, R. Robertson, S. Rosendahl, J. Rowley, V. Rusu, E. Saettler, A. Schülke, M. Schwendener, J. Secrest, H. Seifert, M. Shatkay, J. Simpson, C. Sims, D. Sinclair, P. Skensved, A. Smith, M. Smith, N. Starinsky, T. Steiger, R. Stokstad, L. Stonehill, R. Storey, B. Sur, R. Tafirout, N. Tagg, Y. Takeuchi, N. Tanner, R. Taplin, M. Thorman, P. Thornewell, N. Tolich, P. Trent, Y. Tserkovnyak, T. Tsui, C. Tunnell, R. Berg, R. Water, C. Virtue, T. Walker, B. Wall, C. Waltham, H. Tseung, J.-X. Wang, D. Wark, J. Wendland, N. West, J. Wilhelmy, J. Wilkerson, J. Wilson, P. Wittich, J. Wouters, A. Wright, M. Yeh, and K. Zuber, *Determination of the ν_e and total ^8B solar neutrino fluxes using the Sudbury Neutrino Observatory Phase I data set*, *Physical Review C* **75**, 045502 (2007).

[AAB98] E.G. Adelberger, Sam M. Austin, John N. Bahcall, A.B. Balantekin, Gilles Bogaert, Lowell S. Brown, L. Buchmann, F. Edward Cecil, Arthur E. Champagne, Ludwig De Braeckeleer, Charles A. Duba, S. Elliott, S. Freedman, M. Gai, G. Goldring, Christopher R. Gould, Andrei Gruzinov, Wick C. Haxton, K. Heeger, Ernest Henley, Calvin W. Johnson, Marc Kamionkowski, Ralph Kavanagh, Steven E. Koonin, Kuniharu Kubodera, Karlhei Laganke, T. Motobayashi, Vijay Pandharipande, Parker P.D., R. Robertson, Claus Rolfs, R. F. Sawyer, N. Shaviv, T. D. Shoppa, K. Snover, Erik Swanson, Robert E. Tribble, Sylvaine Turck-Chièze, and J. Wilkerson, *Solar fusion cross sections*, *Reviews of Modern Physics* **70**, 1265 (1998).

[ABB08] C. Arpesella, H. Back, M. Balata, G. Bellini, J. Benziger, S. Bonetti, A. Brigatti, B. Caccianiga, L. Cadonati, F. Calaprice, C. Carraro, G. Cecchet, A. Chavarria, M. Chen, F. Dalnoki-Veress, D. D’Angelo, A. De Bari, A. De Bellefon, H. De Kerret, A. Derbin, M. Deutsch, A. di Credico, G. di Pietro, R. Eisenstein, F. Elisei, A. Etenko, R. Fernholz, K. Fomenko, R. Ford, D. Franco, B. Freudiger, C. Galbiati, F. Gatti, S. Gazzana, M. Giammarchi, D. Giugni, M. Goeger-Neff, T. Goldbrunner, A. Goretti, C. Grieb, C. Hagner, W. Hampel, E. Harding, S. Hardy, F. Hartman, T. Hertrich, G. Heusser, Aldo Ianni, Andrea Ianni, M. Joyce, J. Kiko, T. Kirsten, V. Kobychiev, G. Korga, G. Korschinek, D. Kryn, V. Lagomarsino, P. Lamarche, M. Laubenstein, C. Lendvai, M. Leung, T. Lewke, E. Litvinovich, B. Loer, P. Lombardi, L. Ludhova, I. Machulin, S. Malvezzi, S. Manecki, J. Maneira, W. Maneschg, I. Manno, D. Manuzio, G. Manuzio, A. Martemianov, F. Masetti, U. Mazucato, K. McCarty, D. McKinsey, Q. Meindl, E. Meroni, L. Miramonti, M. Misiaszek, D. Montanari, M. Monzani, V. Muratova, P. Musico, H. Neder, A. Nelson, L. Niedermeier, L. Oberauer, M. Obolensky, M. Orsini, F. Ortica, M. Pallavicini, L. Papp, S. Parmeggiano, L. Perasso, A. Pocar, R. Raghavan, G. Ranucci, W. Rau, A. Razeto, E. Resconi, P. Risso, A. Romani, D. Rountree, A. Sabelnikov, R. Saldanha, C. Salvo, D. Schimizzi, S. Schönert, T. Shutt, H. Simgen, M. Skorokhvatov, O. Smirnov, A. Sonnenschein, A. Sotnikov, S. Sukhotin, Y. Suvorov, R. Tartaglia, G. Testera, D. Vignaud, S. Vitale, R. Vogelaar, F. von Feilitzsch, R. von Hentig, T. von Hentig, M. Wojcik, M. Wurm,

- O. Zaimidoroga, S. Zavatarelli, and G. Zuzel, *Direct Measurement of the ${}^7\text{Be}$ Solar Neutrino Flux with 192 Days of Borexino Data*, *Physical Review Letters* **101**, 091302 (2008).
- [ABLG84] T.K. Alexander, G.C. Ball, W.N. Lennard, and H. Geissel, *Measurement of the absolute cross section of the ${}^3\text{He}({}^4\text{He},\gamma){}^7\text{Be}$ reaction at $E_{\text{cm}}=525$ keV*, *Nuclear Physics A* **427**, 526–544 (1984).
- [AEE08] S. Abe, T. Ebihara, S. Enomoto, K. Furuno, Y. Gando, K. Ichimura, H. Ikeda, K. Inoue, Y. Kibe, Y. Kishimoto, M. Koga, A. Kozlov, Y. Minekawa, T. Mitsui, K. Nakajima, K. Nakamura, M. Nakamura, K. Owada, I. Shimizu, Y. Shimizu, J. Shirai, F. Suekane, A. Suzuki, Y. Takemoto, K. Tamae, A. Terashima, H. Watanabe, E. Yonezawa, S. Yoshida, J. Busenitz, T. Classen, C. Grant, G. Keefer, D. Leonard, D. McKee, A. Piepke, M. Decowski, J. Detwiler, S. Freedman, B. Fujikawa, F. Gray, E. Guardincerri, L. Hsu, R. Kadel, C. Lendvai, K.-B. Luk, H. Murayama, T. O'Donnell, H. Steiner, L. Winslow, D. Dwyer, C. Jillings, C. Mauger, R. McKeown, P. Vogel, C. Zhang, B. Berger, C. Lane, J. Marić, T. Miletić, M. Batygov, J. Learned, S. Matsuno, S. Pakvasa, J. Foster, G. Horton-Smith, A. Tang, S. Dazeley, K. Downum, G. Gratta, K. Tolich, W. Bugg, Y. Efremenko, Y. Kamyshev, O. Perevozchikov, H. Karwowski, D. Markoff, W. Tornow, K. Heeger, F. Piquemal, and J.-S. Ricol, *Precision Measurement of Neutrino Oscillation Parameters with KamLAND*, *Physical Review Letters* **100**, 221803 (2008).
- [AGR11] E.G. Adelberger, A. García, R.G. Hamish Robertson, K. A. Snover, A.B. Balantekin, K. Heeger, M.J. Ramsey-Musolf, D. Bemmerer, A. Jughans, C.A. Bertulani, J.W. Chen, H. Constantini, P. Prati, M. Couder, E. Uberseder, M. Wiescher, R. Cyburt, B. Davids, S.J. Freedman, M. Gai, D. Gazit, L. Gialanella, G. Imbriani, U. Greife, M. Hass, W.C. Haxton, T. Itahashi, K. Kubodera, K. Langanke, D. Leitner, M. Letner, P. Vetter, L. Winslow, L.E. Marcucci, T. Motobayashi, A. Mukhamedzhanov, R.E. Tribble, Kenneth M. Nollet, F.M. Nunes, T.S. Park, P.D. Parker, R. Schiavilla, E.C. Simpson, C. Spitaleri, F. Strieder, H.P. Trautvetter, K. Suemmerer, and S. Typel, *Solar fusion cross sections . II . The pp chain and CNO cycles*, *Reviews of Modern Physics* **83**, 195–245 (2011).
- [AL55] F. Ajzenberg and T. Lauritsen, *Energy Levels of Light Nuclei. V*, *Reviews of Modern Physics* **27**, no. 1, 77 (1955).
- [Alc06] M. Alcorta, *Study of excited states of ${}^{12}\text{C}$ in full kinematics*, Master's thesis, Universidad de Huelva, 2006.
- [Alc10] M. Alcorta, *Nuclear structure of ${}^{12}\text{C}$ from 3-body break-up studies by light ion reactions in complete kinematics*, Ph.D. thesis, Universidad Complutense de Madrid, 2010.
- [AMHM65] J.C. Armstrong, J.V. Mullendore, W.R. Harris, and J.B. Marion, *Equilibrium charge-state fractions of 0.2 to 6.5 MeV helium ions in carbon*, *Proceedings of the Physical Society* **186**, 1283 (1965).
- [Bah64a] John N. Bahcall, *Solar Neutrino Cross Sections and Nuclear Beta Decay*, *Physical Review* **135**, no. 1B, 137–146 (1964).
- [Bah64b] John N. Bahcall, *Solare Neutrinos. I. Theoretical*, *Physical Review Letters* **12**, 300 (1964).
- [Bah66] John N. Bahcall, *Solar Neutrino*, *Physical Review Letters* **17**, no. 7, 398–401 (1966).
- [BB90] John N. Bahcall and H.A. Bethe, *A solution of the Solar-Neutrino Problem*, *Physical Review Letters* **65**, 2233 (1990).
- [BBB11] G. Bellini, J. Benziger, S. Bonetti, M. Buizza Avanzini, B. Caccianiga, L. Cadonati, F. Calaprice, C. Carraro, a. Chavarria, and a. Chepurinov, *Study of solar and other unknown anti-neutrino fluxes with Borexino at LNGS*, *Physics Letters B* **696**, 191–196 (2011).

BIBLIOGRAPHY

- [BBBH01] C. Bordeanu, D. Berkovits, E. Boaretto, and M. Hass, *Towards a measurement of $\sigma(^3\text{He}(^4\text{He},\gamma)^7\text{Be})$ with Accelerator Mass Spectrometry (AMS)*, *Progress in Particle and Nuclear Physics* **46**, 97–98 (2001).
- [BBH72] W.R. Boykin, S.D. Baker, and D.M. Hardy, *SCATTERING OF ^3He AND ^4He FROM POLARIZED ^3He BETWEEN 4 AND 10 MeV*, 241–249 (1972).
- [BBR85] Brian Buck, Richard A. Baldock, and J. Alberto Rubio, *Cluster model of $A = 7$ nuclei and the astrophysical S factor for $^3\text{He}(\alpha,\gamma)^7\text{Be}$ at zero energy*, *Journal of Physics G: Nuclear and Particle Physics* **11**, L11–L16 (1985).
- [BBS68] John N. Bahcall, Neta A. Bahcall, and Giora Shaviv, *Present status of the theoretical predictions for the ^{36}Cl solar-neutrino experiment*, *Physical Review Letters* **20**, no. 21, 1209–1212 (1968).
- [BBS07] T. Brown, C. Bordeanu, K. Snover, D. Storm, D. Melconian, A. Sallaska, S. Sjue, and S. Triambak, *$^3\text{He}+^4\text{He} \rightarrow ^7\text{Be}$ astrophysical S factor*, *Physical Review C* **76**, 055801 (2007).
- [BCC06] D. Bemmerer, F. Confortola, H. Costantini, A. Formicola, Gy. Gyürky, R. Bonetti, C. Brogini, P. Corvisiero, Z. Elekes, Zs. Fülöp, G. Gervino, A. Guglielmetti, C. Gustavino, G. Imbriani, M. Junker, M. Laubenstein, A. Lemut, B. Limata, V. Lozza, M. Marta, R. Menegazzo, P. Prati, V. Roca, C. Rolfs, C. Rossi Alvarez, E. Somorjai, O. Straniero, F. Strieder, F. Terrasi, and H. Trautvetter, *Activation Measurement of the $^3\text{He}(\alpha,\gamma)^7\text{Be}$ Cross Section at Low Energy*, *Physical Review Letters* **97**, 122502 (2006).
- [BCD67] John N. Bahcall, M. Cooper, and P. Demarque, *Dependence of the ^8B Solar Neutrino Flux on Heavy Element Composition*, *Astrophysical Journal*, no. 150, 723–724 (1967).
- [Bet72] Hans-Dieter Betz, *Charge States and Charge-Changing Cross sections of fast heavy ions penetrating through gaseous and solid media*, *Reviews of Modern Physics* **44**, no. 3, 465–539 (1972).
- [Bet86] H.A. Bethe, *Possible Explanation of the Solar-Neutrino Puzzle*, *Physical Review Letters* **56**, 1305 (1986).
- [BFI63] J.N. Bahcall, William A. Fowler, I. Iben, Jr., and R.L. Sears, *Solar Neutrino Flux*, *Astrophysics Journal* **137**, 344 (1963).
- [BGH13] C. Bordeanu, Gy. Gyürky, Z. Halász, T. Szücs, G.G. Kiss, Z. Elekes, J. Farkas, Zs. Fülöp, and E. Somorjai, *Activation measurement of the $^3\text{He}(\alpha,\gamma)^7\text{Be}$ reaction cross section at high energies*, *Nuclear Physics A* **908**, 1–11 (2013).
- [BHL82] John N. Bahcall, Walter F. Huebner, Stephen H. Lubow, Peter D. Parker, and Roger K. Ulrich, *Standar solar models and the uncertainties in predicted capture rates of solar neutrinos*, *Review of Modern Physics* **54**, 767–800 (1982).
- [BJP64] A. C. L. Barnard, C. M. Jones, and G. C. Phillips, *The Scattering of ^3He by ^4He* , *Nuclear Physics* **50**, 629–640 (1964).
- [BM88] B. Buck and A.C. Merchant, *Cluster model of $A = 7$ nuclei revisited , and the astrophysical at zero energy S factors for $^3\text{He}(\alpha,\gamma)^7\text{Be}$ and $^3\text{H}(\alpha,\gamma)^7\text{Li}$* , *Journal of Physics G: Nuclear and Particle Physics* **14**, L211–L216 (1988).
- [BP95] John N. Bahcall and M. Pinsonneault, *Solar models with helium and heavy-element diffusion*, *Reviews of Modern Physics* **67**, 781 (1995).
- [Bro11] C. Brogini, *Twenty years of LUNA*, *Progress in Particle and Nuclear Physics* **66**, 293–297 (2011).

- [BWR94] C. R. Brune, R. Kavanagh W., and C. Rolfs, ${}^3\text{H}(\alpha,\gamma){}^7\text{Li}$ reaction at low energy, *Physical Review C* **50**, no. 4, 2205 (1994).
- [CAE] CAEN S.p.A., <http://www.caen.it>.
- [CBC07] F. Confortola, D. Bemmerer, H. Costantini, A. Formicola, Gy. Gyürky, P. Bezzon, R. Bonetti, C. Brogгинi, P. Corvisiero, Z. Elekes, Zs. Fülöp, G. Gervino, A. Guglielmetti, C. Gustavino, G. Imbriani, M. Junker, M. Laubenstein, A. Lemut, B. Limata, V. Lozza, M. Marta, R. Menegazzo, P. Prati, V. Roca, C. Rolfs, C. Rossi Alvarez, E. Somorjai, O. Straniero, F. Strieder, F. Terrasi, and H. Trautvetter, *Astrophysical S factor of the ${}^3\text{He}(\alpha,\gamma){}^7\text{Be}$ reaction measured at low energy via detection of prompt and delayed γ rays*, *Physical Review C* **75**, 065803 (2007).
- [CD61] R.F. Christy and Ian Duck, *Gamma Rays from an Extranuclear Direct Capture Process*, *Nuclear Physics*, no. 24, 89–101 (1961).
- [CD08] R. H. Cyburt and B. Davids, *Evaluation of modern ${}^3\text{He}(\alpha,\gamma){}^7\text{Be}$ data*, *Physical Review C* **78**, 064614 (2008).
- [CFO08] Richard H. Cyburt, Brian D. Fields, and Keith A. Olive, *An update on the big bang nucleosynthesis prediction for ${}^7\text{Li}$: the problem worsens*, *Journal of Cosmology and Astroparticle Physics* **11**, 012 (2008).
- [CGNB12] M. Carmona-Gallardo, B. S. Nara Singh, M. J. G. Borge, J. A. Briz, M. Cubero, B. R. Fulton, H. Fynbo, N. Gordillo, M. Hass, G. Haquin, A. Maira, E. Nácher, Y. Nir-El, V. Kumar, J. McGrath, A. Muñoz Martín, A. Perea, V. Pesudo, G. Ribeiro, J. Sánchez del Rio, O. Tengblad, R. Yaniv, and Z. Yungreis, *New measurement of the ${}^3\text{He}(\alpha,\gamma){}^7\text{Be}$ cross section at medium energies*, *Physical Review C* **86**, 032801(R) (2012).
- [CGRB14] M. Carmona-Gallardo, A. Rojas, M. J. G. Borge, B. Davids, B. R. Fulton, M. Hass, B. S. Nara Singh, C. Ruiz, and O Tengblad, *${}^3\text{He}(\alpha,\gamma){}^7\text{Be}$ cross section measured using complementary techniques*, *European Physics Journal Web of Conferences* **66**, 07003 (2014).
- [CGX12] Alain Coc, Stéphane Goriely, Yi Xu, Matthias Saimpert, and Elisabeth Vangioni, *Standard Big Bang Nucleosynthesis Up To CNO With an Improved Extended Nuclear Network*, *The Astrophysical Journal* **744:158**, (18pp) (2012).
- [CL00] A. Csótó and K. Langanke, *Study of the ${}^3\text{He}({}^4\text{He},\gamma){}^7\text{Be}$ and ${}^3\text{H}({}^4\text{He},\gamma){}^7\text{Li}$ Reactions in an Extended Two-Cluster Model*, *Few-Body Systems* **29**, 121–130 (2000).
- [CMA] CMAM, Centro de Microanálisis de Madrid, Universidad Autónoma, Madrid, <http://www.cmam.uam.es/en>.
- [Cyb04] R. Cyburt, *Primordial nucleosynthesis for the new cosmology: Determining uncertainties 1and examining concordance*, *Physical Review D* **70**, 023505 (2004).
- [DAA04] Pierre Descouvemont, Abderrahim Adahchour, C. Angulo, Alain Coc, and Elisabeth Vangioni-Flam, *Compilation and R-matrix analysis of Big Bang nuclear reaction rates*, *Atomic Data and Nuclear Data Tables* **88**, no. 1, 203–236 (2004).
- [Dav94] Raymond Davis, *A review of the homestake solar neutrino experiment*, *Progress in Particle and Nuclear Physics* **32**, 13–32 (1994).
- [DDK95] S.B. Dubovichenko and A.V. Dzhazairov-Kakhramanov, *Phy.At. Nucl.* **58**, 579 (1995).
- [DDS08] A. Di Leva, M. De Cesare, D. Schurmann, N. De Cesare, A. D 'Onofrio, L Gialanella, R. Kunz, G. Imbriani, A. Ordine, V. Roca, D. Rogalla, C. Rolfs, M. Romano, E. Somorjai, F. Strieder, and F. Terrasi, *Recoil separator ERNA: Measurement of ${}^3\text{He}(\alpha,\gamma){}^7\text{Be}$* , *Nuclear Instruments and Methods in Physics Research Section A: Accelerators, Spectrometers, Detectors and Associated Equipment* **595**, 381–390 (2008).

BIBLIOGRAPHY

- [DGK09] A. Di Leva, L. Gialanella, R. Kunz, D. Rogalla, D. Schürmann, F. Strieder, M. De Cesare, N. De Cesare, A. D’Onofrio, Z. Fülöp, G. Gyürky, G. Imbriani, G. Mangano, A. Ordine, V. Roca, C. Rolfs, M. Romano, E. Somorjai, and F. Terrasi, *Erratum: Stellar and Primordial Nucleosynthesis of ${}^7\text{Be}$: Measurement of ${}^3\text{He}(\alpha, \gamma){}^7\text{Be}$* [*Phys. Rev. Lett.* **102**, 232502 (2009)], *Physical Review Letters* **103**, 159903 (2009).
- [DJHH68] Raymond Davis, Jr., Don S. Harmer, and Kenneth C Hoffman, *Search for neutrinos from the sun*, *Physical Review Letters* **20**, 1205 (1968).
- [EHB05] S. Engel, D. Hutcheon, S. Bishop, L. Buchmann, J. Caggiano, M.L. Chatterjee, A.A. Chen, J. D’Auria, D. Gigliotti, U. Greife, D. Hunter, A. Hussein, C. C. Jewett, A. M. Laird, M. Lamey, W. Liu, A. Olin, D. Ottewell, J. Pearson, C. Ruiz, G. Ruprecht, M. Trinczek, C. Vockenhuber, and C. Wrede, *Commissioning the DRAGON facility at ISAC*, *Nuclear Instruments and Methods in Physics Research Section A: Accelerators, Spectrometers, Detectors and Associated Equipment* **553**, 491–500 (2005).
- [EPI] EPICS, Experimental Physics and Industrial Control System, available program in: <http://www.aps.anl.gov/epics/index.php>.
- [FFI01] S. Fukuda, Y. Fukuda, M. Ishitsuka, Y. Itow, T. Kajita, J. Kameda, K. Kaneyuki, K. Kobayashi, Y. Koshio, M. Miura, S. Moriyama, M. Nakahata, S. Nakayama, A. Okada, N. Sakurai, M. Shiozawa, Y. Suzuki, H. Takeuchi, Y. Takeuchi, T. Toshito, Y. Totsuka, S. Yamada, S. Desai, M. Earl, E. Kearns, M. Messier, K. Scholberg, J. Stone, L. Sulak, C. Walter, M. Goldhaber, T. Barszczak, D. Casper, W. Gajewski, W. Kropp, S. Mine, D. Liu, L. Price, M. Smy, H. Sobel, M. Vagins, K. Ganzer, W. Keig, R. Ellsworth, S. Tasaka, A. Kibayashi, J. Learned, S. Matsuno, D. Takemori, Y. Hayato, T. Ishii, T. Kobayashi, K. Nakamura, Y. Obayashi, Y. Oyama, A. Sakai, M. Sakuda, M. Kohama, A. Suzuki, T. Inagaki, T. Nakaya, K. Nishikawa, T. Haines, E. Blaufuss, S. Dazeley, K. Lee, R. Svoboda, J. Goodman, G. Guillian, G. Sullivan, D. Turcan, A. Habig, J. Hill, C. Jung, K. Martens, M. Malek, C. Mauger, C. McGrew, E. Sharkey, B. Viren, C. Yanagisawa, C. Mitsuda, K. Miyano, C. Saji, T. Shibata, Y. Kajiyama, Y. Nagashima, K. Nitta, M. Takita, M. Yoshida, H. Kim, S. Kim, J. Yoo, H. Okazawa, T. Ishizuka, M. Etoh, Y. Gando, T. Hasegawa, K. Inoue, K. Ishihara, T. Maruyama, J. Shirai, M. Koshihara, Y. Hatakeyama, Y. Ichikawa, M. Koike, K. Nishijima, H. Fujiyasu, H. Ishino, M. Morii, Y. Watanabe, U. Golebiewska, D. Kielczewska, S. Boyd, A. Stachyra, R. Wilkes, and K. Young, *Solar ${}^8\text{B}$ and *hep* Neutrino Measurements from 1258 Days of Super-Kamiokande Data*, *Physical Review Letters* **86**, no. 25, 5651–5655 (2001).
- [FHI96] Y. Fukuda, T. Hayakawa, K. Inoue, K. Ishihara, H. Ishino, S. Jounkou, T. Kajita, S. Kasuga, Y. Koshio, T. Kumita, K. Matsumoto, M. Nakahata, K. Nakamura, K. Okumura, A. Sakai, M. Shiozawa, J. Suzuki, Y. Suzuki, T. Tomoeda, Y. Totsuka, K. S. Hirata, K. Kihara, Y. Oyama, M. Koshihara, K. Nishijima, T. Horiuchi, K. Fujita, S. Hatakeyama, M. Koga, T. Maruyama, A. Suzuki, M. Mori, T. Kajimura, T. Suda, A. T. Suzuki, T. Ishizuka, K. Miyano, H. Okazawa, T. Hara, Y. Nagashima, M. Takita, and T. Yamaguchi, *Solar Neutrino Data Covering Solar Cycle 22*, *Physical Review Letters* **77**, no. 9, 1683–1686 (1996).
- [FM62] J. Flegenhimer and Y. Marcus, *Specific activity after intermittent irradiation*, *Nucleonics* **20**, no. 5, 75–78 (1962).
- [GAB94] U. Greife, C. Arpesella, C. A. Barnes, F. Bartolucci, E. Bellotti, C. Broggin, P. Corvisiero, G. Fiorentini, A. Fubini, F. Gorris, C. Gustavino, M. Junker, R. W. Kavanagh, A. Lanza, P. Prati, P. Quarati, W. S. Rodney, C. Rolfs, H. P. Trytvetter, and D. Zahnow, *Laboratory for Underground Nuclear Astrophysics (LUNA)*, *Nuclear Instruments and Methods in Physics Research Section A: Accelerators, Spectrometers, Detectors and Associated Equipment* **350**, 327–337 (1994).
- [Gav01] V.N. Gavrin, *Solar neutrino results from SAGE*, *Nuclear Physics B* **91**, 36–43 (2001).

- [GBB04] U. Greife, S. Bishop, L. Buchmann, M.L. Chatterjee, A.A. Chen, J.M. D’Auria, S. Engel, D. Gigliotti, D Hunter, D.A. Hutcheon, A. Hussein, C.C. Jewett, A.M. Laird, M. Lamey, W. Liu, A. Olin, D. Ottewell, J. Rogers, and C. Wrede, *Energy loss around the stopping power maximum of Ne, Mg and Na ions in hydrogen gas*, Nuclear Instruments and Methods in Physics Research Section B: Beam Interactions with Materials and Atoms **217**, no. 1, 1–6 (2004).
- [GCC07] Gy. Gyürky, F. Confortola, H. Costantini, A. Formicola, D. Bemmerer, R. Bonetti, C. Brogini, P. Corvisiero, Z. Elekes, Zs. Fülöp, G. Gervino, A. Guglielmetti, C. Gustavino, G. Imbriani, M. Junker, M. Laubenstein, A. Lemut, B. Limata, V. Lozza, M. Marta, R. Menegazzo, P. Prati, V. Roca, C. Rolfs, C. Rossi Alvarez, E. Somorjai, O. Straniero, F. Strieder, F. Terrasi, and H. Trautvetter, *$^3\text{He}(\alpha,\gamma)^7\text{Be}$ cross section at low energies*, Physical Review C **75**, 035805 (2007).
- [GEA] GEANT, CERN Application Software Group. Geant detector description and simulation tool, CERN program library, April 1995.
- [GMH02] A Gottdang, D.J.W. Mous, and R.G. Haitsma, *The novel HVEE 5 MV Tandetron™*, Nuclear Instruments and Methods in Physics Research Section B: Beam Interactions with Materials and Atoms **190**, 177–182 (2002).
- [Gro08] Particle Data Group, Phys. Lett. B **667**, 1 (2008).
- [GUI] TRIUMF: GUIDE FOR EXPERIMENTERS, Available in: <http://www.triumf.info/wiki/exp-prog/index.php>.
- [HBB03] D.A. Hutcheon, S. Bishop, L. Buchmann, M.L. Chatterjee, A.A. Chen, J.M. D’Auria, S. Engel, D. Gigliotti, U. Greife, D. Hunter, A. Hussein, C.C. Jewett, N. Khan, M. Lamey, A.M. Laird, W. Liu, A. Olin, D. Ottewell, J.G. Rogers, G. Roy, H. Sprenger, and C. Wrede, *The DRAGON facility for nuclear astrophysics at TRIUMF-ISAC: design, construction and operation*, Nuclear Instruments and Methods in Physics Research Section A: Accelerators, Spectrometers, Detectors and Associated Equipment **498**, 190–210 (2003).
- [HBO] HBOOK, CERN Application Software Group. HBOOK - Statistical Analysis and Histogramming, CERN program library long writeup w5013, January 1995.
- [HBR88] M. Hilgemeier, H.W. Becker, C. Rolfs, H.P. Trautvetter, and J.W. Hammer, *Absolute Cross Section of the $^3\text{He}(\alpha,\gamma)^7\text{Li}$ reaction*, Zeitschrift für Physik A: Atoms and Nuclei **329**, 243–254 (1988).
- [HJ59] H. D. Holmgren and R. L. Johnston, *$^3\text{H}(\alpha,\gamma)^7\text{Li}$ and $^3\text{He}(\alpha,\gamma)^7\text{Be}$* , Physical Review **113**, no. 6, 1156–1158 (1959).
- [Hoy46] F. Hoyle, *The synthesis of the elements from hydrogen*, Astrophysical J. Suppl. **5**, 343 (1946).
- [Hoy54] F. Hoyle, *On nuclear reactions occurring in very hot stars. I. The synthesis of elements from carbon to nickel*, Astrophysical J. Suppl. **1**, 121 (1954).
- [HRF12] D.A. Hutcheon, C. Ruiz, J. Fallis, J.M. D’Auria, B. Davids, U. Hager, L. Martin, D.F. Ottewell, S. Reeve, and A. Rojas, *Measurement of radiative capture resonance energies with an extended gas target*, Nuclear Instruments and Methods in Physics Research Section A: Accelerators, Spectrometers, Detectors and Associated Equipment **689**, 70–74 (2012).
- [HSB72] D. M. Hardy, R. J. Spiger, S. D. Baker, Y.S. Chen, and T.A. Tombrello, *SCATTERING OF ^3He AND ^4He FROM POLARIZED ^3He BETWEEN 7 AND 18 MeV*, Nuclear Physics A **195**, 250–256 (1972).
- [Hut02] D.A. Hutcheon, *The gas target density profile*, DRAGON Technical Note.
- [Ili07] Christian. Iliadis, *Nuclear Physics of Stars*, WILEY-VCH Verlag GmbH & Co., 2007.

BIBLIOGRAPHY

- [JAC08] K. Jayamanna, F. Ames, G. Cojocaru, R. Baartman, P. Bricault, R. Dube, R. Laxdal, M. Marchetto, M. MacDonald, P. Schmor, G. Wight, and D. Yuan, *Off-line ion source terminal for ISAC at TRIUMF*, *The Review of scientific instruments* **79**, 02C711 (2008).
- [JWG10] K. Jayamanna, G. Wight, D. Gallop, R. Dube, V. Jovicic, C. Laforge, M. Marchetto, M. Leross, D. Louie, R. Laplante, R. Laxdal, M. McDonald, G. J. Wiebe, V. Wang, and F. Yan, *A multicharge ion source (Supernanogan) for the OLIS facility at ISAC/TRIUMF*, *The Review of scientific instruments* **81**, 02A331 (2010).
- [KA84] T. Kajino and A. Arima, *Resonanting-Group Calculation of Radiative Capture Reactions $\alpha(^3\text{He}, \gamma)^7\text{Be}$ and $\alpha(t, \gamma)^7\text{Li}$ at Astrophysical Low Energies*, *Physical Review Letters* **52**, 739 (1984).
- [Kaj86] T. Kajino, *The $^3\text{He}(\alpha, \gamma)^7\text{Be}$ and $^3\text{He}(\alpha, \gamma)^7\text{Li}$ reactions at astrophysical energies*, *Nuclear Physics A* **460**, no. 3, 559–580 (1986).
- [KBB82] H. Kräwinkel, H. W. Becker, L. Buchmann, K. U. Kettner, W. E. Kieser, R. Santo, P. Schmalbrock, H. P. Trautvetter, A. Vlieks, C. Rolls, J. W. Hammer, W.S. Rodney, R.E. Azuma, and W.S. Rodney, *The $^3\text{He}(\alpha, \gamma)^7\text{Be}$ Reaction and the Solar Neutrino Problem*, *Zeitschrift für Physik A: Atoms and Nuclei* **304**, 307–332 (1982).
- [KBR64] Hsin-Min Kuan, T. W. Bonner, and J. R. Risser, *An investigation of the $\text{C}^{12} + \text{He}^3$ Reactions at bombarding energies between 1.8 and 5.4 MeV*, *Nuclear Physics* **51**, 481–517 (1964).
- [KD11] O.S. Kirsebom and B. Davids, *One fewer solution to the cosmological lithium problem*, *Physical Review C* **84**, 058801 (2011).
- [KDN09] E. Komatsu, J. Dunkley, M. R.olta, C. L. Bennett, B. Gold, G. Hinshaw, N. Jarosik, D. Larson, M. Limon, L. Page, D. N. Spergel, M. Halpern, R. S. Hill, A. Kogut, S. S. Meyer, G. S. Tucker, J. L. Weiland, E. Wollack, and E. L. Wright, *Five-Year Wilkinson Microwave Anisotropy Probe Observations: Cosmological Interpretation*, *The Astrophysical Journal Supplement Series* **180**, 330–376 (2009).
- [KIN81] B.T. Kim, T. Izumoto, and K. Nagatani, *Radiative capture reaction $^3\text{He}(\alpha, \gamma)^7\text{Be}$ at low energies*, *Physical Review C* **23**, no. 1, 33 (1981).
- [Kir98] T. Kirsten, *GALLEX Solar Neutrino Results*, *Progress in Particle and Nuclear Physics* **40**, 85 (1998).
- [Kno00] Gleen.F. Knoll, *Radiation Detection and Measurement*, John Wiley & Sons, Inc., 2000.
- [KTA87] T. Kajino, H. Toki, and Sam M. Austin, *Radiative Alpha-capture rates leading to $A=7$ nuclei: applications to the solar neutrino problem and big bang nucleosynthesis*, *The Astrophysical Journal* **319**, 531–540 (1987).
- [KUD13] A. Kontos, E. Uberseder, R. DeBoer, J. Görres, C. Akers, A. Best, M. Couder, and M. Wiescher, *Astrophysical S factor of $^3\text{He}(\alpha, \gamma)^7\text{Be}$* , *Physical Review C* **87**, 065804 (2013).
- [Lam01] Michael Joseph. Lamey, *A microchannel detection system for dragon*, Master's thesis, Simon Fraser University, 2001.
- [Lan86] K. Langanke, *Microscopic potential model studies of light nuclear capture reactions*, *Nuclear Physics A* **457**, 351–366 (1986).
- [Leo87] W.R. Leo, *Techniques for Nuclear and Particle Physics Experiments*, Springer-Verlag Berlin Heidelberg, 1987.

- [LIB03] W. Liu, G. Imbriani, L. Buchmann, A. A. Chen, J. M. D. Auria, A. D’Onofrio, S. Engel, L. Gialanella, U. Greife, D. Hunter, A. Hussein, D.A. Hutchon, A. Olin, D. Ottewell, D. Rogalla, J. Rogers, M. Romano, and F. Terrasi, *Charge state studies of low energy heavy ions passing through hydrogen and helium gas*, Nuclear Instruments and Methods in Physics Research **496**, 198–214 (2003).
- [LIS] LISE++, Available en: <http://groups.nsl.msui.edu/lise/lise.html>.
- [Lun] The Lund/LBNL Nuclear Data Search, Available in the web page: <http://nucleardata.nuclear.lu.se/nucleardata/toi/>.
- [MAK93] P. Mohr, H. Abele, H. Krauss, H. Oberhummer, and A. Denker, *Alpha scattering and capture reactions in the A=7 system at low energies*, Physical Review C **48**, no. 3, 1420–1427 (1993).
- [MBH06] C. Matei, L. Buchmann, W. Hannes, D. Hutcheon, C. Ruiz, C. Brune, J. Caggiano, a. Chen, J. D’Auria, a. Laird, M. Lamey, Zh. Li, Wp. Liu, a. Olin, D. Ottewell, J. Pearson, G. Ruprecht, M. Trinczek, C. Vockenhuber, and C. Wrede, *Measurement of the Cascade Transition via the First Excited State of O16 in the $^{12}\text{C}(\alpha,\gamma)^{16}\text{O}$ Reaction, and Its S Factor in Stellar Helium Burning*, Physical Review Letters **97**, no. 24, 242503 (2006).
- [MES] MESYTEC GmbH & Co. KG, <http://www.mesytec.com>.
- [MH86] T. Mertelmeier and H.M. Hofmann, *Consistent Cluster Model Description of the Electromagnetic Properties of Lithium and Beryllium nuclei*, Nuclear Physics A **459**, 387–416 (1986).
- [Mik86] S.P. Mikheyev, A. Yu. Smirnov, Sov. J. Nucl. Phys. **42**, 913 (1986).
- [MM93] Robert A. Malaney and Grant J. Mathews, *Probing the early universe: a review of primordial nucleosynthesis beyond the standard big bang*, Physics Reports **229**, no. 4, 145–219 (1993).
- [MN67] W. Meckbach and I.B. Nemirovsky, *Charge Equilibrium of Helium Ions in Helium Gas from 60 to 840 keV*, Physical Review **153**, no. 1, 13 (1967).
- [MN02] A. M. Mukhamedzhanov and F. M. Nunes, *Low energy behavior of the astrophysical S-factor in radiative captures to loosely bound final states*, Nuclear Physics A **708**, 437–459 (2002).
- [Moh09] Peter Mohr, *Low-energy $^3\text{He}(\alpha,\alpha)^3\text{He}$ elastic scattering and the $^3\text{He}(\alpha,\gamma)^7\text{Be}$ reaction*, Physical Review C **79**, no. 6, 1–10 (2009).
- [Nar13] B. S. Nara Singh, *NEW ADVANCES FOR THE $^3\text{He}(\alpha,\gamma)^7\text{Be}$ SOLAR FUSION REACTION*, Acta Physica Polonica B **44**, no. 3, 511–520 (2013).
- [NDA69] K. Nagatani, M. R. Dwarakanath, and D. Ashery, *THE $^3\text{He}(\alpha,\gamma)^7\text{Be}$ REACTION AT VERY LOW ENERGY*, Nuclear Physics A **128**, 325–332 (1969).
- [Nef11] Thomas Neff, *Microscopic Calculation of the $^3\text{He}(\alpha,\gamma)^7\text{Be}$ and $^3\text{H}(\alpha,\gamma)^7\text{Li}$ Capture Cross Sections Using Realistic Interactions*, Physical Review Letters **106**, no. 4, 1–4 (2011).
- [NEHY07] Y. Nir-El, G. Haquin, Z. Yungreiss, M. Hass, G. Goldring, S. K. Chamoli, B. S. Nara Singh, S. Lakshmi, G. Heidenreich, and S. Teichmann, *Precision measurement of the decay rate of ^7Be in host materials*, Physical Review C (R) **75**, 012801 (2007).
- [NHNEH04] B. S. Nara Singh, M. Hass, Y. Nir-El, and G. Haquin, *New Precision Measurement of the $^3\text{He}(\alpha,\gamma)^7\text{Be}$ Cross Section*, Physical Review Letters **93**, 262503 (2004).
- [NM10] Christophe Normand and M^a José G^a Borge, *Trazando el paisaje nuclear 50 años de historia de la Karlsruher Nuklidkarte*, Revista Española de Física, 76–80 (2010).

BIBLIOGRAPHY

- [Nol01] Kenneth Nollett, *Radiative α -capture cross sections from realistic nucleon-nucleon interactions and variational Monte Carlo wave functions*, Physical Review C **63**, no. 5, 1–13 (2001).
- [NSD12] B. S. Nara Singh, S. K. L. Sjue, B. Davids, M. Hass, P. Adsley, L. Buchmann, M. Carmona-Gallardo, J. Fallis, S. P. Fox, B. Fulton, N. Galinski, U. Hager, D.A. Hutcheon, A. M. Laird, L. Martin, D. Ottewell, S. Reeve, C. Ruiz, G. Ruprecht, A. Shotter, and O. Tengblad, *Cross section measurements of the ${}^3\text{He}(\alpha, \gamma){}^7\text{Be}$ reaction using DRAGON at TRIUMF*, Journal of Physics: Conference Series **337**, 012057 (2012).
- [Nuc] National Nuclear Data Center (Brookhaven National Laboratory), Available in the web page: <http://www.nndc.bnl.gov>.
- [OAB10] Yu. Ts. Oganessian, F. Sh. Abdullin, P. D. Bailey, D. E. Benker, M. E. Bennett, S. N. Dmitriev, J. G. Ezold, J. H. Hamilton, R. a. Henderson, M. G. Itkis, Yu. V. Lobanov, A. N. Mezentsev, K. J. Moody, S. L. Nelson, A. N. Polyakov, C. E. Porter, A. V. Ramayya, F. D. Riley, J. B. Roberto, M. A. Ryabinin, K. P. Rykaczewski, R. N. Sagaidak, D. a. Shaughnessy, I. V. Shirokovsky, M. A. Stoyer, V. G. Subbotin, R. Sudowe, A. M. Sukhov, Yu. S. Tsyganov, V. K. Utyonkov, A. A. Voinov, G. K. Vostokin, and P. A. Wilk, *Synthesis of a New Element with Atomic Number $Z=117$* , Physical Review Letters **104**, 142502 (2010).
- [OBK82] J Osborne, C. A. Barnes, Ralph Kavanagh, R. M Kremer, G. J. Mathews, J. L Zyskind, Parker P.D., and Howard A. J., *Low-Energy ${}^3\text{He}(\alpha, \gamma){}^7\text{Be}$ Cross-Section Measurements*, Physical Review Letters **48**, 1664 (1982).
- [OBK84] J.L. Osborne, C.A. Barnes, R.W. Kavanagh, R.M. Kremer, G.J. Mathews, J.L. Zyskind, P.D. Parker, and A.J. Howard, *Low-energy behavior of the ${}^3\text{He}(\alpha, \gamma){}^7\text{Be}$ cross section*, Nuclear Physics A **419**, 115–132 (1984).
- [ORT] ORTEC[®], <http://www.ortec-online.com/>.
- [OSW00] Keith A. Olive, Gary Steigman, and Terry P. Walker, *Primordial nucleosynthesis: theory and observations*, Physics Reports **333-334**, 389–407 (2000).
- [Pas04] C. Pascual Izarra, *Experimental determination of stopping forces for ions in matter*, Ph.D. thesis, Universidad Autonoma de Madrid, 2004.
- [PK63] P.D. Parker and R.W. Kavanagh, *${}^3\text{He}(\alpha, \gamma){}^7\text{Be}$ Reaction*, Physical Review **131**, no. 6, 2578 (1963).
- [PR64] Philip Pochoda and Hubert Reeves, *A REVISED SOLAR MODEL WITH A SOLAR*, 119–126 (1964).
- [QKT81] Q. K. K. Liu, H. Kanada, and Y.C. Tang, *Microscopic study of ${}^3\text{He}(\alpha, \gamma){}^7\text{Be}$ electric-dipole capture reaction*, Physical Review C **23**, no. 2.
- [RBKR03] Philip R. Benington and D. Keith Robinson, *Data Reduction and Error Analysis for the Physical Science*, McGraw-Hill, 2003.
- [RDB] R. G. H. Robertson, P. Dyer, T. J. Bowles, Ronald E. Brown, Nelson Jarmie, C. J. Maggiore, and Sam M. Austin, *Cross section of the capture reaction ${}^3\text{He}(\alpha, \gamma){}^7\text{Be}$* , Physical Review C **27**, no. 1, 11.
- [Ree12] Sarah Reeve, *Determining the transmission efficiency for ${}^3\text{He}(\alpha, \gamma){}^7\text{Be}$ in DRAGON*, Master's thesis, Simon Fraser University, 2012.
- [Rol88] Clauss E. Rolfs and William S. Rodney, *Cauldrons in the Cosmos*, 1988.
- [ROO] ROOT, A Data Analysis Framework-CERN, available program in: <http://root.cern.ch/drupal/>.

- [RSP80] F. Reines, H. W. Sobel, and E. Pasierb, *Evidence for Neutrino Instability*, Physical Review Letters **45**, no. 16, 1307 (1980).
- [SAA05] C. E. Svensson, P. Amaudruz, C. Andreoiu, A. Andreyev, R. A. E. Austin, G. C. Ball, D. Bandyopadhyay, A. J. Boston, R. S. Chakrawarthy, A. A. Chen, R. Churchman, T. E. Drake, P. Finlay, P. E. Garrett, G. F. Grinyer, G. Hackman, B. Hyland, B. Jones, R. Kanningo, R. Maharaj, J. P. Martin, D. Morris, A. C. Morton, C. J. Pearson, A. A. Phillips, J. J. Ressler, R. Roy, F. Sarazin, M. A. Schumaker, H. C. Scraggs, M. B. Smith, N. Starinsky, J. J. Valiente-Dobón, J. C. Waddington, and L. M. Watters, *TIGRESS: TRIUMF-ISAC gamma-ray escape-suppressed spectrometer*, Journal of Physics G: Nuclear and Particle Physics **31**, S1663–S1668 (2005).
- [Sab03] A. Sabán Iglesias, *Diseño y montaje de una línea en el acelerador de 5 MV de la UAM para física nuclear experimental*, Master's thesis, Universidad Complutense de Madrid, 2003.
- [Sea64] R. L. Sears, *Recoil separator ERNA: charge state distribution, target density, beam heating, and longitudinal acceptance*, The Astrophysical Journal **140**, 477–484 (1964).
- [SH03] K.A. Snover and A.E. Hurd, *Is $e+e-$ pair emission important in the determination of the ${}^3\text{He}+{}^4\text{He}$ S factor?*, Physical Review C **67**, 055801 (2003).
- [SL72] G. R. Satchler and W.G. Love, *Folding model potentials from realistic interactions for heavy-ion scattering*, Physics Reports **55**, no. 1, 183–254 (1972).
- [SN04] N. Summers and F. Nunes, *${}^7\text{Be}$ breakup on heavy and light targets*, Physical Review C **70**, 011602(R) (2004).
- [SR01] Michael S Smith and K Ernst Rehm, *NUCLEAR ASTROPHYSICS MEASUREMENTS WITH RADIOACTIVE BEAMS*, Ann. Rev. Nuclear Part. Sci **51**, 91–130 (2001).
- [SRI] SRIM, The Stopping and Range of Ions in Matter, available program in: <http://www.srim.org/>.
- [SSA13] S.K.L. Sjue, B.S. Nara Singh, P. Adsley, L. Buchmann, M. Carmona-Gallardo, B. Davids, J. Fallis, B.R. Fulton, N. Galinski, U. Hager, M. Hass, D. Howell, D.A. Hutcheon, A.M. Laird, L. Martin, D. Ottewell, S. Reeve, C. Ruiz, G. Ruprecht, and S. Triambak, *Beam suppression of the Dragon recoil separator for ${}^3\text{He}(\alpha,\gamma){}^7\text{Be}$* , Nuclear Instruments and Methods in Physics Research Section A: Accelerators, Spectrometers, Detectors and Associated Equipment **700**, 179–181 (2013).
- [ST67] R. J. Spieger and T.A. Tombrello, *Scattering of He^3 by He^4 and of He^4 by Tritium*, Physical Review **163**, no. 4, 964 (1967).
- [Tay82] Jonh. R. Taylor, *An Introduction to Error Analysis. The study of uncertainties in physical measurements*, University Science Books, 1982.
- [Ten96] O. Tengblad, *Desing of a gas system (internal report)*, 1996.
- [TP61] T.A. Tombrello and G.C. Phillips, *Cluster Nature of Li^7 and Be^7* , Physical Review **122**, no. 1, 224–228 (1961).
- [TP63a] T.A. Tombrello and P.D. Parker, *Direct-Capture Model for the $\text{He}^3(\alpha,\gamma)\text{Be}^7$ and $\text{T}(\alpha,\gamma)\text{Li}^7$ Reactions*, Physical Review **131**, no. 6, 2582 (1963).
- [TP63b] T.A. Tombrello and P.D. Parker, *Scattering of He^3 from He^4* , Physical Review **130**, no. 3, 1112 (1963).
- [VKSW83] H. Volk, H. Kräwinkel, R. Santo, and L. Wallek, *Activation Measurement of the ${}^3\text{He}({}^4\text{He},\gamma){}^7\text{Be}$* , Zeitschrift für Physik A: Atoms and Nuclei **310**, 91–94 (1983).

BIBLIOGRAPHY

- [Vuj01] Brittney Vujcich, *Dragon pumping tube alignment and quadrupole alignment*, Tech. report, Dalhousie University, 201.
- [Wee37] John A. Wheeler, *On the Mathematical Description of Light Nuclei by the Method of Resonating Group Structure*, *Physical Review* **52**, 1107 (1937).
- [Whe37] John Archibald Wheeler, *Molecular Viewpoints in Nuclear Structure*, *Physical Review* **52**, 1983 (1937).
- [WHRD03] Chris Wrede, Ahmed Hussein, Joel G. Rogers, and John D'Auria, *A double sided silicon strip detector as a DRAGON end detector*, *Nuclear Instruments and Methods in Physics Research Section B: Beam Interactions with Materials and Atoms* **204**, 619–624 (2003).
- [WKT84] H. Walliser, H. Kanada, and Y. C. Tang, *Study of the ${}^3\text{He}(\alpha, \gamma){}^7\text{Be}$ radiative-capture reaction with resonating-group wave functions*, *Nuclear Physics A* **419**, 133–147 (1984).
- [WRH00] L. Weissman, R. Raabe, M. Huyse, G. Koops, H. Pattyn, G. Terwagne, and P. Van Duppen, *An implanted ${}^4\text{He}$ target for experiments with radioactive beams*, *Nuclear Instruments and Methods in Physics Research Section B: Beam Interactions with Materials and Atoms* **170**, 266–275 (2000).